# INTRA-TRANSFORM VOLCANISM ALONG THE SIQUEIROS FRACTURE ZONE 8°20’ N – 8°30’ N, EAST PACIFIC RISE

By

MICHELLE RENAE HAYS

A THESIS PRESENTED TO THE GRADUATE SCHOOL
OF THE UNIVERSITY OF FLORIDA IN PARTIAL FULFILLMENT
OF THE REQUIREMENTS FOR THE DEGREE OF
MASTER OF SCIENCE

UNIVERSITY OF FLORIDA

2004

ACKNOWLEDGMENTS

Foremost, I thank Dr. Michael Perfit for all his guidance and support throughout this project. I thank my committee members, Dr. Paul Mueller and Dr. David Foster, for their time and discussion. I give special thanks to Dr. Daniel Fornari, Dr. Ian Ridley, the captain and crew of the Atlantis II, and the Alvin pilots for this project would not have been possible without their efforts. I especially thank Dr. Daniel Fornari and Dr. Ken Simms for their early guidance in my graduate studies. I thank Dr. Leonard Danyushevsky for the Cameca microprobe analysis completed at the University of Tasmania, Dr. Ian Jonasson for the ICP-ASE data from the Geological Survey of Canada, and Dr. Jack Casey of the University of Houston for ICP-MS analysis. I would also like to thank Dr. Robert Shuster and Dr. Harmon Maher from the University of Nebraska for their encouragement and inspiration. Most of all, I thank Troy and the rest of my family for their love, support and everlasting patience. I could not have made it this far without them. This work was supported by The National Science Foundation through grants OCE-90-19154, OCE-90-20404, and OCE-0138088 and by the University of Florida through the Alumni Fellowship.

TABLE OF CONTENTS

LIST OF TABLES

LIST OF FIGURES

Abstract of Thesis Presented to the Graduate School
of the University of Florida in Partial Fulfillment of the
Requirements for the Degree of Master of Science

INTRA-TRANSFORM VOLCANISM ALONG THE SIQUEIROS FRACTURE ZONE
8°20' N – 8°30' N, EAST PACIFIC RISE

By

Michelle Renae Hays

December 2004

Chair: Michael Perfit
Major Department: Geological Sciences

Detailed sampling and sonar mapping of the Siqueiros transform were completed in 1991 during the Atlantis-II 125-25 Research Cruise. Fresh, glassy, volcanic rocks were recovered from small constructional volcanic landforms within leaky transform faults and from troughs within the transform. Three of the troughs within the transform exhibit organized spreading and are believed to be intra-transform spreading centers that have resulted from changes in the relative motions of the Pacific and Cocos plates. The samples recovered include extremely primitive lavas (pricritic and olivine-phyric basalts to high-MgO basalts). Compared to the adjacent 9-10°N segment of the EPR the Siqueiros basalts are more primitive and tend to group on the more depleted end in major and trace element diagrams. Four chemically distinct groups of lavas have been identified within the transform. The spreading centers have erupted only N-MORB type lavas which are similar to those from the EPR. Lavas recovered from shear zones within the transform tend to be more primitive and depleted in incompatible elements with the

most incompatible element depleted lavas (D-MORB) recovered from the A-B fault, the shear zone connecting the two western most spreading centers. The E-MORB samples were only recovered at the western ridge-transform intersection (WRTI) and a group of low $Na_2O$ samples were recovered within spreading center A. Fractional crystallization models indicate that the majority of the N-MORB samples can be explained by 50-60% fractional crystallization of olivine ± spinel + plagioclase + clinopyroxene of 2-3 parental compositions similar to the high-MgO lavas recovered from the A-B fault. Scatter about CaO vs. $Al_2O_3$ trends and ratios among highly incompatible elements, along with variations in phenocrysts compositions, indicate that mixing between primitive and evolved compositions is needed in order to explain the entire range of major and trace element variations. Resorbtion textures and chemical analysis of many the large phenocrysts show they are out of equilibrium with the host magma and were derived from high CaO, high MgO lavas. REE diagrams show that the D-MORB samples from the A-B fault cannot be related to the N-MORB samples by fractional crystallization alone. Mixing models indicate that N-MORB compositions can be produced by mixing of approximately 4-6% of an E-MORB composition with the D-MORB samples. The low $Na_2O$ samples from spreading center A are best explained by mixing with a more depleted source, but $Na_{8.0}$ and $Fe_{8.0}$ data indicate both mixing of sources and variable extents and depths of melting occur within the transform. The compositional variations of the Siqueiros samples can be explained by a petrogenetic model in which lava compositions are controlled by the presence/absence, size, and depth of melt lenses within the transform.

# CHAPTER 1
# INTRODUCTION

The Siqueiros transform fault is a left lateral transform fault located on the Northern East Pacific Rise (NEPR) between 8°20'N and 8°30'N (Figure 1-1). The transform domain is approximately 20 km wide and offsets the NEPR by 138 km (Fornari et al., 1989). It lies along a fast-spreading portion of the EPR with a half-slip rate of approximately 63 km $Ma^{-1}$ (Fornari et al., 1989). In 1991, detailed observational data and extensive sampling revealed 3 intra-transform spreading centers and small eruptive centers within the transform shear zones, all of which exhibit recent volcanism (Perfit et al., 1996).

Transforms faults, such as Siqueiros, theoretically parallel the direction of plate motion and are conservative plate boundaries where no plate construction or destruction is thought to occur. Volcanism within the Siqueiros transform is unusual, but is believed to be the result of counterclockwise changes in the spreading direction between the Pacific and Cocos plates. Rotations in plate motions resulted in an extensional environment within the transform (Pockalny et al., 1997). Petrologic and morphologic data suggest that volcanism does occur within other transform domains that exhibit extension, especially along fast- and superfast-spreading portions of the Mid-Ocean Ridge crest (Perfit et al., 1996; Fornari et al., 1989). Few of these transforms have been sampled or studied in any great detail (Hekinian et al, 1995; Wendt et al., 1999). A few samples have been analyzed from the Raitt transform along the Pacific-Antarctic spreading ridge (Castillo et al., 1988) and some samples have been recovered from the

Blanco transform between the Juan de Fuca and Gorda Ridges (Embley & Wilson, 1992; Tierney, 2003). The Garrett transform on the southern EPR is the only oceanic transform where magmatism has been extensively studied and samples have been analyzed. The processes that formed the lavas erupted in these environments and their relations to the nearby ridges are still poorly understood.

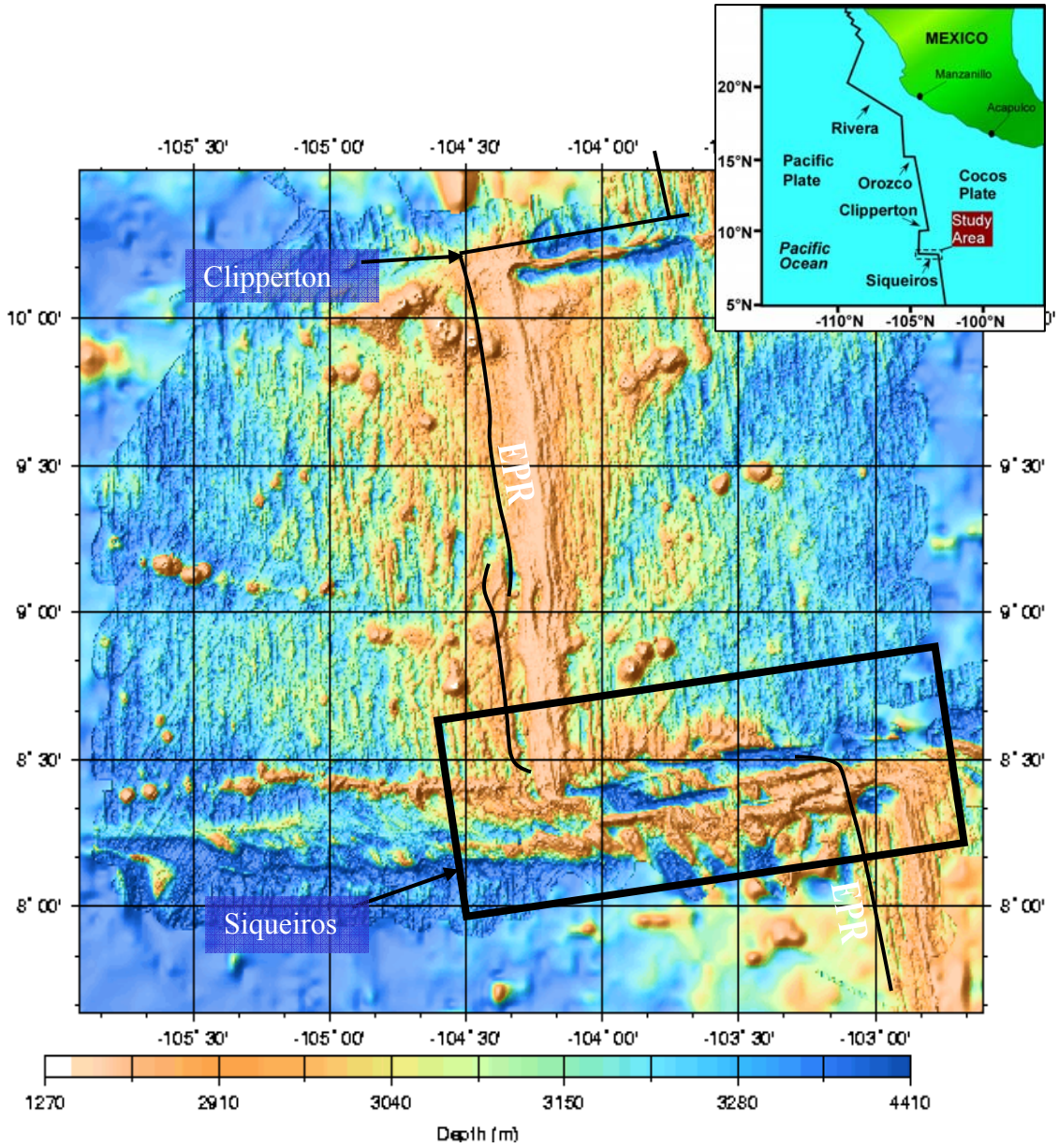


Figure 1-1. Location map of Siqueiros transform.

Because of their presumed colder thermal environment, intra-transform lavas are removed from the large magma chambers beneath the ridge, in which large volumes of melt are mixed. The study of volcanic transforms may provide new insights into the scale of mantle heterogeneities and the compositions of the depleted and enriched mantle because such components may not be thoroughly mixed in areas removed from the larger magma chambers beneath ridge segments. The Siqueiros transform offers a unique look at three, small, focused spreading centers which are separate from the large magma chambers beneath the EPR, which are believed to be sites where different mantle components are mixed. The Siqueiros transform also contains samples of primitive compositions rarely found elsewhere in close proximity to evolved samples.

The goal of this study is to gain a better understanding of the petrologic segmentation and magmatic processes beneath the Siqueiros transform and to compare the basalts of the Siqueiros transform domain with those of the adjacent EPR and Garrett transform. Major and trace element variations in concert with crystallization and mixing models have been used to estimate parental magmatic compositions. Phase chemical data and incompatible element ratios and variations have also been used to evaluate the histories of crystallization and mixing.

## Sampling of the Siqueiros Transform

The study of fracture zones is important because rocks that are believed to compose the lower oceanic crust and upper mantle (gabbroic and ultramafic rocks) are commonly found within fracture zones and rarely found elsewhere in the ocean basins. The Siqueiros transform was originally investigated to complement the knowledge gained from the slow moving Fracture Zone A in the FAMOUS area of the Mid-Atlantic Ridge (Detrick et al., 1973; Crane, 1976). The first near bottom geological and geophysical

survey was conducted at the western intersection of the Siqueiros transform fault and the East Pacific Rise (EPR) using a Deep Tow Fish (Crane, 1976). Samples were also recovered from the western most Siqueiros transform and adjacent EPR by rock dredging (Crane, 1976; Batiza et al., 1977; Natland, 1989). Sampling revealed a broad range of rock types, which include enriched mid-ocean ridge basalts (E-MORBS), normal mid-ocean ridge basalts (N-MORBS), and high-MgO rocks, but a lack of precise locations for the dredged samples made it difficult to interpret the geochemical data in this area of complex sea-floor structure (Natland, 1989). The acquisition of a Sea MARC II sonar survey in July 1987 (Fornari et al., 1989) and Alvin submersible dive observations in May-June 1991 (Fornari et al., 1991) has allowed a better understanding of the seafloor structure. The petrologic, observational, and morphologic data from the 1987 and 1991 cruises revealed what appeared to be sites of intra-transform spreading (Fornari et al., 1989; Fornari et al., 1991; Perfit et al., 1996). Four troughs labeled A, B, C and, D and five strike-slip faults were identified using the bathymetric and side-looking sonar data (Fornari et al., 1989). During Alvin submersible dives, fresh-looking pillow lava flows and sheet flows were identified along the spreading ridges and eruptive centers were found in transform shear zones (Figure 1-2) (Fornari et al., 1991). Despite their location far from the north and south tip of the East Pacific Rise, the basalts recovered from three of the troughs (A, B, and C) still have relatively unaltered glassy rinds, which suggests that they have been recently erupted and do not originate from the spreading associated with the adjacent East Pacific Rise. The forth trough, D, was found to comprise an older volcanic terrain, which has been strongly tectonized. Trough D does not contain any identifiable ridges and any spreading is believed to be focused along transform parallel

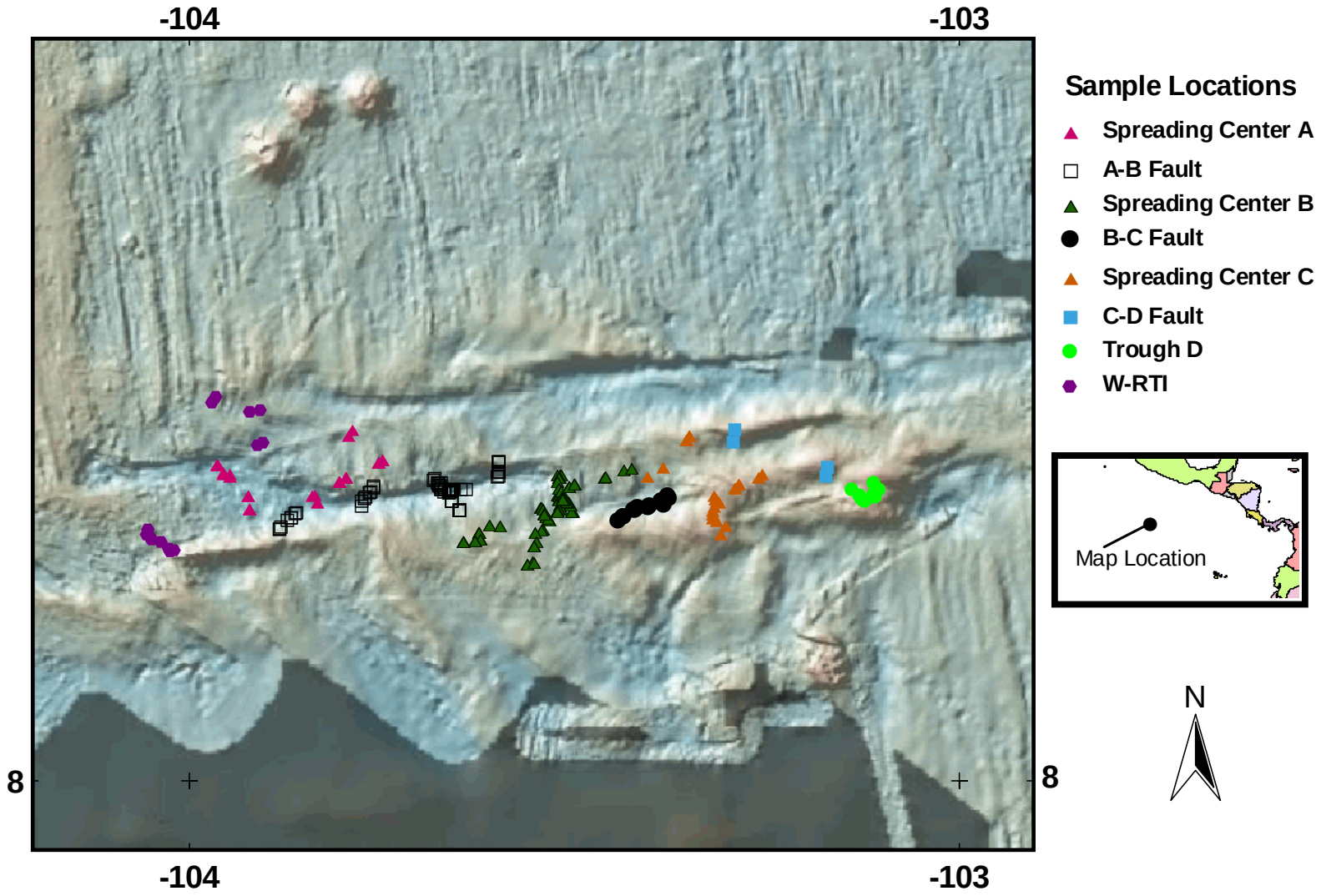


Figure 1-2. Sample location map.

lineaments (Fornari et al., 1991). Troughs A, B, and C are believed to be small intra-transform spreading centers (Fornari et al., 1991) where organized spreading is occurring. The lavas are remarkably fresh with little sediment cover and thick glassy rinds. Small constructional volcanic landforms were found at small offsets within the strike-slip faults connecting the spreading centers. The samples within the A-B fault were unusually mafic, olivine-rich basalts (Perfit et al., 1996). The olivine-phyric basalts are referred to as picritic basalts. In 1996, Perfit and others conducted a detailed study of the young picritic basalts and high-MgO lavas from the A-B fault. The picritic basalts were found to be formed by the accumulation of olivine and minor spinel from high-MgO melts (Perfit et al., 1996). The high-MgO glasses recovered from the strike-slip fault were found to potentially be near-primary melts from incompatible-element depleted oceanic mantle that have been little modified by crustal mixing and or fractionation processes (Perfit et al., 1996). The Siqueiros samples collected in 1991 are petrologically diverse and contain picritic basalts, ferrobasalts, FeTi basalts, N-MORB, incompatible element depleted normal mid-ocean ridge basalts (D-MORB) and E-MORB. This study will combine the previous work completed on the picritic basalts from the A-B fault with a more detailed examination of the samples recovered from other localities within the transform domain in order to gain a better understanding of the petrologic and tectonic evolution of the Siqueiros transform.

## The Transform Fault Effect

Geophysical studies indicate that an axial magma chamber overlain by a thin melt lens is present beneath many sections of the EPR (Sinton & Detrick, 1992; Dunn et al., 2000). The seismic reflector representing the melt lens is <3 to 4 km wide and caps a low compressional wave velocity zone 5-7 km wide. This low velocity zone is believed to

represent the presence of melt mixed with crystals to produce a “mush”. Near 9°30’N on the EPR the axial magma chamber reflector was found to be 1-2 km below the rise. Rosendahl et al. (1976) and Orcutt et al. (1976) demonstrated the existence of a crustal low-velocity zone about 4 km wide and 0.5 to 1.0 km beneath the crest of the EPR in the vicinity of the Siqueiros Fracture Zone. Although seismic studies have not been conducted beneath the Siqueiros fracture zone, seismic studies have shown that the axial magma chamber seismic reflector terminates near fracture zones and is reduced at other discontinuities (Macdonald and Fox, 1988; Macdonald et al., 1991). The lack of a large magma chamber beneath transforms allows for the possible eruption of unmixed mantle components.

Studies have shown that basalts adjacent to fractures zones tend to be characterized by more fractionated compositions (Melson and Thompson, 1971; Hekinian and Thompson, 1976; Natland and Melson, 1980; Christie and Sinton, 1981; LeRoex and Dick, 1981, Sinton et al., 1983; Fornari et al., 1983; Perfit and Fornari, 1983; Perfit et al.,1983; Langmuir and Bender, 1984; Elthon, 1988). At the Siqueiros ridge transform intersection (RTI), highly fractionated E-MORBs along with a few FeTi basalts have been recovered. A wide range of magma compositions including highly–fractionated magmas have been found proximal to fracture zones (Elthon, 1988). These observations have been explained by the “transform fault effect” in which the isotherms are suppressed near the transform due to the juxtaposition of older, cooler lithosphere against the ridge transform intersection (Langmuir & Bender, 1984). The depressed isotherms may allow isolated magma pockets near the ridge transform intersection permitting the highly fractionated magmas to be developed (Perfit and Fornari, 1983).

## Mantle Heterogenities

Initial studies along mid-ocean ridges found axial lavas to be rather homogeneous, but more intensive studies along strike have revealed variations in basalt chemistry that are believed to relate to ridge segmentation and morphology (Thompson et al., 1985; Langmuir and Bender, 1986; Smith et al., 1994; Bazin et al., 2001). Transform faults are first order segments that partition the ridge into distinctive tectonic units which persist for a million years or more and have been found to separate ridge segments with contrasting tectonic and petrological properties (Macdonald et al., 1988). Smaller second and third order segments, such as overlapping spreading centers, deviations in axial linearity (DEVALS), small non-overlapping offsets (SNOOs), and kinks in the ridges, have also been found to correlate with geochemical segmentation (Langmuir and Bender, 1986; Bazin et al., 2001; Smith et al., 2001). The axial discontinuities can be related to the axial magma chamber's depth beneath the seafloor, width, thickness, continuity along the ridge, and the geochemistry of the erupted lavas (Macdonald, 1998). The axial discontinuities have also been found to be related to the volcanic segmentation of the ridge (White et al., 2002). Lava morphology (from sheet to pillow flows) has been found to coincide with boundaries of morphologically defined third-order tectonic segments of the ridge crest and to indicate reduced eruption rates (White et al., 2002).

Studies of mantle heterogeneities have recently focused on across strike sampling in order to study the chemistry of off-axis eruptions, which may tap different sources without mixing in large magma chambers or mush zones. Studies on the East Pacific Rise (ERP) that have focused on across strike variations have found some off-axis lavas that appear to be younger than the surrounding terrain and show greater chemical variability than axial lavas. Remarkably small-scale spatial variations in basalt chemistry

of these off-axis lavas have been found (Reynolds et al., 1992; Perfit et al., 1994; Bideau and Hekinian, 1995; Perfit and Chadwick, 1998; Castillo et al., 2000). Detailed off-axis studies have revealed the existence of lavas with distinctive chemical compositions, both more and less enriched in incompatible elements than those delivered to the axis. Some are similar to depleted lavas recovered from near axis seamounts (Fornari et al., 1988; Perfit et al., 1994; Reynolds and Langmuir, 2000). A nonsystematic distribution of E-MORB lavas was found off-axis in the 9-10° N region of the NEPR (Perfit et al., 1994, Perfit and Chadwick, 1998; Smith et al., 2001). It is believed that these resulted from frequent low-volume off-axis eruptions that did not reflect mixing within the large magma chamber beneath the ridge. Significant chemical variation at 9°31'N was found to be on the scale of 200 m and is believed to result from both rapid changes in magma chamber chemistry and frequent low-volume on-axis and off-axis eruptions (Perfit et al., 1994). Off-axis flows have been documented up to 4 km from the ridge axis along the EPR (Goldstein et al., 1994; Perfit and Chadwick, 1998; Schouten et al., 1999; Reynolds and Langmuir, 2000). The source of these magmas is poorly understood. They may be fed by axial eruptions that flow great distances off-axis or they may be associated with an off-axis magma chamber. Transforms are also removed from the well-mixed large magma chambers associated with the ridge axis. The intra-transform spreading centers can help provide a better understanding of the scale and composition of mantle heterogeneities and may be important in understanding the source of off-axial eruptions.

# CHAPTER 2
# GEOLOGICAL RELATIONSHIPS AND SAMPLE LOCALITIES IN THE SIQUEIROS TRANSFORM

The Siqueiros transform is comprised of a number of different sections that are morphologically distinct (Figure 2-1). The entire transform domain is about 20 km wide and includes the transform valley and adjacent seafloor that has been morphologically or structurally affected by proximity to the transform. Within the transform domain exsists the transform tectonized zone (TTZ) and the transform fault zone (TFZ). The TTZ is defined as the area truncated by abyssal hill topography on opposite sides of the transform valley. The TFZ is usually a 2 km wide continuous swath of lineated ridges, troughs, and closed contoured basins. The Siqueiros transform domain has been found to contain both shear and spreading related features. The shear related features are a series of 5 en echelon TFZ which consist of ridges and troughs that nearly parallel the Pacific-Cocos relative plate motions. The TFZ are approximately 15-25 km long and are the focus of recent strike-slip deformation. The fault troughs are deep (up to 3650 m) and narrow (1-3 km wide) especially in the western portion of the transform (Fornari et al., 1989). The spreading related features consist of four extensional relay zones (ERZ), which are equivalent to continental pull-apart basins. These ERZ are believed to have resulted from a series of counterclockwise changes in spreading direction that occurred at about 3.5, 2.5, 1.5, and 0.5 Ma (Pockalny et al., 1997). Very fresh-looking lava flows and systematic aging of the seafloor across the axis and flanks were found at 3 of the relay zones during Alvin submersible dives confirming that there are three spreading

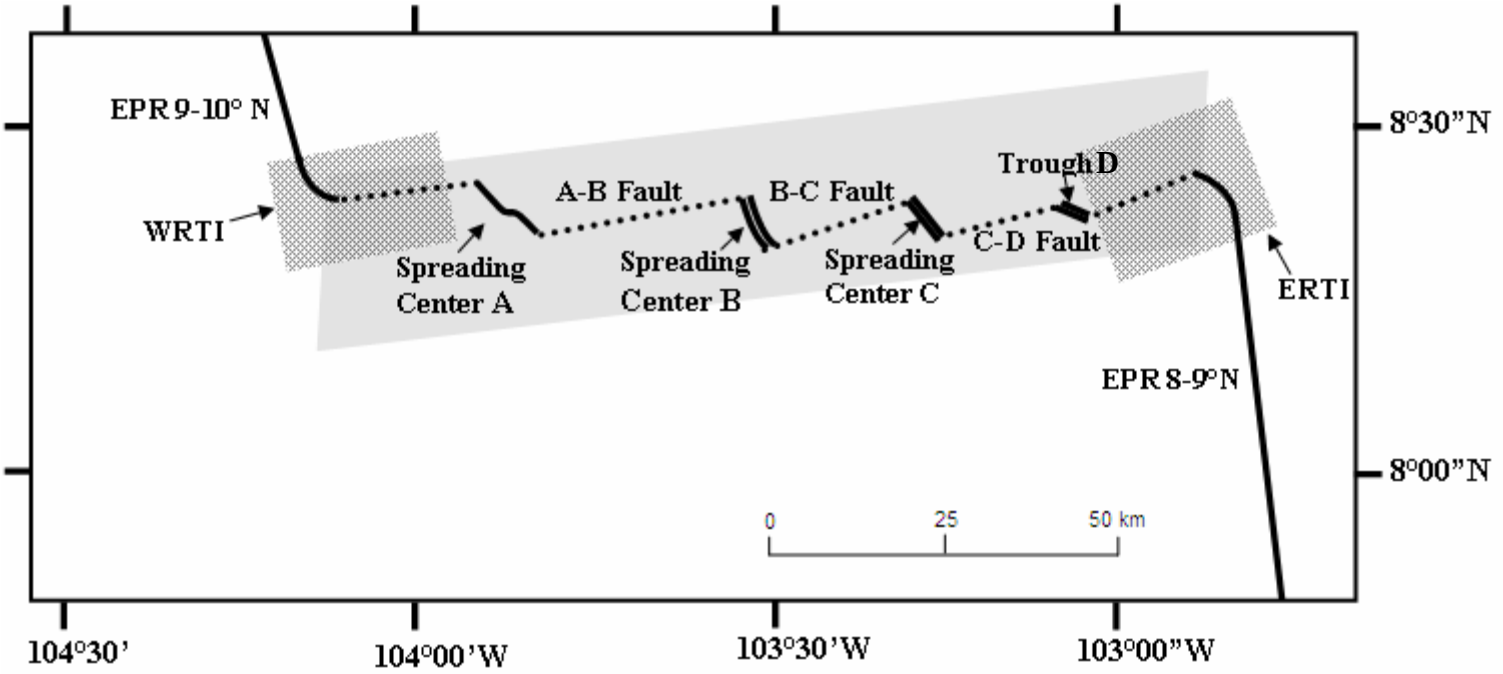


Figure 2-1. Plate boundary geometry of the Siqueiros transform. Locations of the 3 troughs that exhibit intra-transform spreading (A, B, and C) and the fourth trough (D), which has been strongly tectonized and does not exhibit organized spreading are shown. Dashed lines show TFZ (A-B fault, B-C fault, C-D fault) and the two faults that connect the spreading centers to the RTIs (WRTI-A and ERTI-D). Light shaded box depicts the transform domain. Darker shaded boxes represent the WRTI and ERTI. Adjusted from Fornari et al., 1989.

centers (A, B, and C) within the transform. The fourth pull-apart basin (trough D) was strongly tectonized and did not exhibit any organized spreading. The intra-transform spreading centers may have begun as leaky transforms that evolved into small well-developed spreading centers with the persistent change in the plate geometry (Pockalny et al., 1997). The geologic locations referred to in this study include the western ridge transform intersection (WRTI), the eastern ridge transform intersection (ERTI), the 3 spreading centers (A, B, and C), trough D, and the TFZ. For this study, the transform faults were divided into offsets between the three spreading centers (A-B fault, B-C fault, and C-D fault). The A-WRTI and D-ERTI fault offsets were included as part of the WRTI and ERTI, respectively.

At the ridge transform intersections (RTIs) the northern and southern limbs of the EPR axis become slightly deeper and swing into the transform domain, which is morphologically characteristic of transforms at the fast-end of the slip rate spectrum. Both the eastern ridge transform intersection (ERTI) and the western ridge transform intersection (WRTI) have unrifted crest and have abyssal hill topography characteristic of fast to medium spreading ridge segments.

Spreading centers A and B both exhibit bilateral symmetry about the spreading axis out to 20-40 km. Spreading center A is the western most trough and is connected with the WRTI by a TFZ. It is a sigmoid-shaped basin that consists of two ridges (Fornari et al., 1991). Lavas on the northern ridge are older and heavily overprinted. The southern portion has younger pillow lavas, but they are overprinted with faults and fissures, suggesting that transform tectonics are influencing the area (Fornari et al., 1991). East of the southern A axial ridge the volcanic terrain is older and extensively weathered.

West of the spreading center the transform fault intersects the EPR and lavas age to the north as the EPR is approached. Spreading center B is the most well developed spreading center with abyssal hill structures up to 8 km long. The youngest looking flows were found on a small 100 m cone near the central portion of the axis. Spreading center B also consists of pillow walls and constructional pillow escarpments.

Troughs C and D have much smaller swaths of abyssal hill topography (10-20 km). Spreading fabric could only be identified within trough C. Fresh volcanics were found only within the floor of the graben and along the walls of the graben. Many of the flows within C are sheet flows. Trough D was found to contain only strongly tectonized older volcanic terrain. Fresh basalts were recovered north of D suggesting that any spreading at D is focused along a transform-parallel lineament (Fornari et al., 1991).

Transform faults A-B and B-C were chosen for detailed studies using ALVIN and the rock dredge because they link the most morphologically distinct and best organized intra-transform spreading centers. The fault zones are also very clear and have relief between 1000-1500m. Also, the axial deeps and RTI deeps are well-defined. The faults are approximately parallel (078° [A-B] and 075° [B-C]) to the relative plate motion of the Pacific and Cocos plate (082°). Within the A-B transform young glassy picritic basalts and olivine-phyric basalts were collected by dredging and ALVIN sampling. The young volcanic centers were found along the lower parts of the south and north walls of the transform adjacent to and overlying much older highly-sedimented terrain of talus, pelagic sediment, and older manganese encrusted basalt. There is no indication of recent faulting within the young volcanics. The B-C fault is much shorter than the A-B fault (35 km vs. 18 km) and has less relief. N-MORB samples were primarily recovered from

within this transform. The C-D fault and the fault linking trough D and the ERTI are less well-defined and the linearity of the faults are not continuous to the SEPR.

Samples used for this study were collected in 1991 aboard the Atlantis II cruise 125-25 and include rock dredges, rock cores, Alvin submersible dives (Figures 2-2 and 2-3). Eleven SeaBeam surveys were also conducted during the 1991 cruise to add to prior SeaBeam and Sea MARC II survey data. The SeaBeam data allows identification of morphological features that have 10 m or more relief. Seventeen Alvin dives were completed within the Siqueiros transform domain and 171 samples were collected (Table 2-1). Sample localities and geological relationships are based on the ALVIN dive observations and SeaBeam survey data. Alvin dive tracks are based on the ALNAV network and SeaBeam maps with an estimated uncertainty of 100-200 m. Thirty-nine dredges and five rock cores were also conducted in the Siqueiros transform domain (Table 2-2). The dredges consisted of a 50 cm x 1 m mouth frame, 2 m chain bag with fishnet liner, and chain harness, with a 12,000 lb weaklink system. A cylindrical, lead depressor weight was used 100 m up the wire from the dredge mouth. Poor performance of onboard pingers forced the wire to be between 300-400 m greater than bottom depth to insure contact with the bottom. Dredge tracks were kept short (<1 km) to maximize confidence in the sample localities and were located using Global Positioning System (GPS) and by correlating real-time Seabeam depths to existing maps along the sample track.

The Siqueiros volcanic terrain mainly consists of pillow flows found within and around the intra-transform spreading centers and at small eruptive centers in transform shear zones. A few sheet flows have been found within the spreading basins. In contrast,

Table 2-1. Siqueiros transform Alvin dive locations.

| Dive | General Location of Dive | # of Samples | General Sample Descriptions |
|---|---|---|---|
| 2375 | 2nd abyssal hill west of spreading center B axis | 9 | Fresh pillow basalts, one sediment sample |
| 2376 | Southern portion of spreading center B axis | 11 | Fresh to slightly weathered pillow basalts, one ropy lava |
| 2377 | Northern portion of spreading center B axis | 11 | Fresh basalts |
| 2378 | Southern crescent ridge of C and central graben | 11 | Fresh pillow and sheet basalts |
| 2379 | North wall of A-B fault just west of spreading center B intersection | 3 | Sediment covered micro-gabbros |
| 2380 | Southern RTI hole at spreading center B and trough east of spreading center B axis | 12 | Older pillow, lobate, and sheet basalts |
| 2381 | Southern wall of B-C fault | 13 | Older, somewhat weathered basalts |
| 2382 | Southern wall west of spreading center B and plateau south of transform | 11 | Fresh - older sediment covered basalts. Some lobates and sheets. |
| 2383 | Southern ridge of spreading center A | 8 | Very fresh pillow basalts to slightly weathered basalts |
| 2384 | Young cones in axis of A-B fault | 14 | Very fresh, glassy basalts to older basalt fragments |
| 2385 | Northern RTI hole and central rift of spreading center C axis | 9 | Sheet, lobate, and pillow basalts, fresh to slightly weathered |
| 2386 | Trough and northern peak of D | 8 | Somewhat young hackly lava, mostly Mn coated older pillow and lobate basalts |
| 2387 | Cones in axis of B-C fault near intersection with spreading center C | 9 | Fresh-slightly altered basalts, mostly pillows |
| 2388 | A-B fault, cone on south side of axis and traverse up the north wall | 14 | Older sediment covered basalts and microgabbros |
| 2389 | Northern ridge in spreading center A | 8 | Fresh pillow lavas |
| 2390 | WRTI, small ridge that connects EPR to south wall of the A-B fault | 9 | Fresh – sediment covered pillow and lobate basalts |
| 2391 | Small cone built against south wall of the A-B fault west of southern spreading center A ridge | 11 | Sediment covered basalt, microgabbros |

Table 2-2. Siqueiros transform dredge locations.

| Dredge/Rock Core | General Location of Dredge/Rock Core | # of Samples |
|---|---|---|
| A25-D1 | Southern portion of spreading center B | 48 |
| A25-D2 | B-C Fault | 24 |
| A25-D4 | West of spreading center B | 12 |
| A25-D5 | West of spreading center B | 5 |
| A25-D6 | West of spreading center B | 2 |
| A25-D7 | West of spreading center B | 3 |
| D25-D8 | West of spreading center B | 1 |
| A25-D9 | West of spreading center B | No Recovery |
| A25-D10 | West of spreading center B | No Recovery |
| A25-D12 | South of spreading center B | No Recovery |
| A25-D13 | South of spreading center B | 1 |
| A25-D14 | South of spreading center B | 6 |
| A25-D15 | South of spreading center B | 1 |
| A25-D16 | Northwest of A-B fault | No Recovery |
| A25-D17 | Northwest of A-B fault | 10 |
| A25-D18 | Small ridge parallel hill west of spreading center B | 6 |
| A25-D19 | South end of spreading center B | 10 |
| A25-D20 | Small cones near the midpoint of A-B fault | 12 |
| A25-D22 | A-B fault | 5 |
| A25-D23 | A-B fault | 2 |
| A25-D24 | A-B fault | 3 |
| A25-D25 | Southwest side of spreading center C | 7 |
| A25-D26 | North of spreading center C | 10 |
| A25-D27 | West of spreading center C | 5 |
| A25-D28 | Eastern Ridge Transform Intersection | 5 |
| A25-D29 | Eastern Ridge Transform Intersection | 1 |
| A25-D30 | Eastern Ridge Transform Intersection | 8 |
| A25-D31 | Eastern Ridge Transform Intersection | 1 |
| A25-D32 | Spreading center C | 6 |
| A25-D33 | Spreading center C | 5 |
| A25-D34 | Spreading center C | 5 |
| A25-D35 | Southwest of spreading center A | 7 |
| A25-D36 | East of spreading center A | 9 |
| A25-D37 | East of spreading center A | 3 |
| A25-D38 | East of spreading center A | 5 |
| A25-D39 | EPR abyssal hills | 4 |
| A25-D43 | Eastern Ridge Transform Intersection | 5 |
| A25-D44 | Eastern Ridge Transform Intersection | 2 |
| RC-3 | North of spreading center B | Little |
| RC-11 | South of spreading center B | Little |
| RC-40 | Eastern Ridge Transform Intersection | 1 |
| RC-41 | Eastern Ridge Transform Intersection | 1 |
| RC-42 | Eastern Ridge Transform Intersection | 1 |

the EPR north of the transform consists mainly of sheet or lobate flows emanating from the axis and occasional pillow flows, which are found near ridge tips and off axis (Perfit and Chadwick, 1998). Pillow flows are characteristic of low effusion rates suggesting that the intra-transform spreading centers are not as magmatically active as the adjacent EPR segments. The northern segment of the EPR extending up to the Clipperton transform is very well sampled. Little sampling has been done on the southern limb of the EPR.

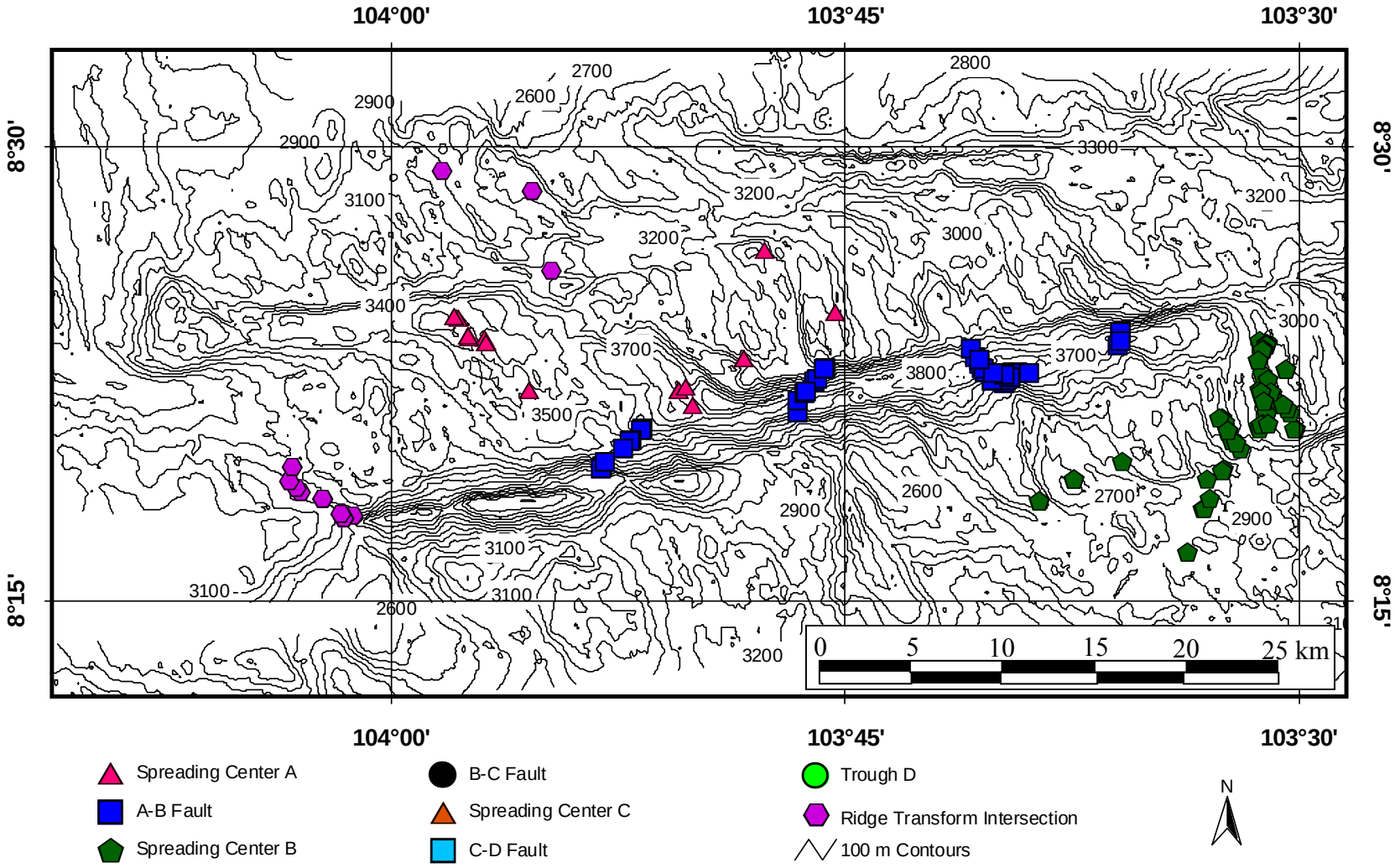


Figure 2-2. Bathymetry and sample locations for west side of the Siqueiros transform.

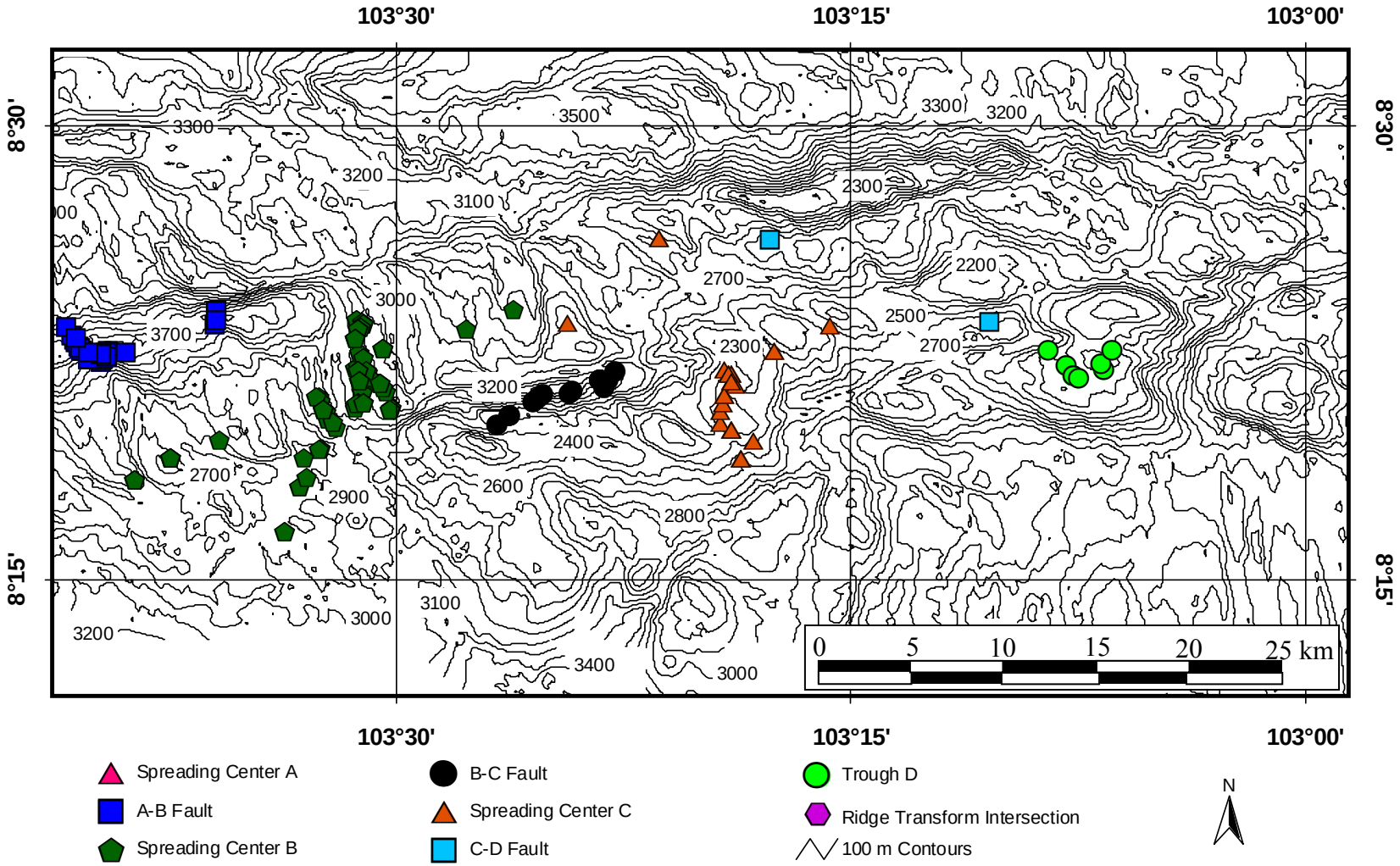


Figure 2-3. Bathymetry and sample locations for east side of the Siqueiros transform.

# CHAPTER 3
# ANALYTICAL METHODS

All Alvin samples were petrographically described and cataloged on ship. Representative dredge samples were inspected and slabbed with a rock saw for thin-section chips and in order to remove surface alteration. Glass rinds were removed from samples with glass and separated for further cleaning. The glass and some whole rocks were crushed in a hardened steel mortar and then cleaned in acetone, 2N HCl, and distilled water in a heated ultrasonic bath. The samples were then inspected under a binocular microscope and any alteration, sediment, or Mn-encrusted glasses were removed. A few samples that were heavily Mn-encrusted could not be completely cleaned and were labeled as "dirty" samples. After cleaning, 7-10 grams of glass or rock chips were crushed and powdered. The remainder of the clean samples was saved for other analyses. Over 150 samples were processed at sea.

Major element analysis of the Siqueiros natural glass samples was done by electron microprobe at the US Geological Survey (USGS) in Denver using an ARL-SEMQ microprobe and JEOL microprobe. An additional data set for major and minor elements was produced for the Siqueiros samples by analysis on a Cameca SX50 electron microprobe at the University of Tasmania (Danyushevsky, personal comm.). For the electron microprobe analysis, sub-samples of the cleaned glass chips were inspected using a binocular microscope and selected for analysis. All probe analyses were normalized to standard glasses VG-A99 and JdF-D2 which were run concurrently with

the Siqueiros glasses. Analyses were corrected using the procedure of Meeker and Quick (1991). Whole-rock samples (glass plus phenocrysts) were also analyzed by microprobe at the USGS after fusion in a rhenium strip furnace.

Most of the Siqueiros samples were analyzed for trace element contents (Co, Cu, Ga, Nb, Ni, Rb, Sr, Y, Zn, Zr, V, Cr, Ba, Sc, K, and Ti) by x-ray fluorescence spectrometery (XRF) in the department of Geological Sciences at the University of Florida using an automated ARL-8420+ spectrometer. Approximately five grams of the powder samples were mixed with an organic binder and pressed into pellets for XRF analysis. Matrix absorption effects were accounted for based on the intensity of the Rh Compton peak (Reynolds, 1963). Standards were run no less frequently than every seven samples in order to correct for any fluctuations in the x-ray intensity or instrument conditions. Replicate analyses of rock standards show that accuracy and precision are generally better than ± 2% for the elements Cu, Zn, V, Ti, Sr, Y, and Zr, better than ± 5% for K, Rb, Nb, Ba, Co, Ga, and Ni, and to within ± 10 % for Sc. Analytical precision is significantly worse (> ± 20%) for Nb, Rb, and Ba when abundances are near detection limits (3, 2, 10 ppm respectively). Direct current plasma (DCP) spectrometry was also used for phenocryst free glass separates at the Lamont-Doherty Earth Observatory. The DCP analysis included major and some minor and trace elements (Ba, Cr, Cu, Ni, Sc, Sr, V, Y, Zr, Mn, and Ti). A few samples were measured for trace elements (Y and Sc) and the rare earth elements (REEs) by inductively coupled plasma- mass spectrometry (ICP-MS) at the University of Houston by Dr. John Casey. Major element and trace element data was also analyzed by the Canadian Geological Survey by ICP-ASE. Chemical

analyses of the Siqueiros picritic basalts were done by microprobe after fusion in a rhenium strip furnace.

Duplicate analyses of selected samples were completed by the different labs and by different methods. Because this has the potential to lead to systematic bias in the data, all of the data were graphically compared (Figure 3-1). The microprobe data from the ARL-SEMQ microprobe and the JEOL microprobe show no apparent analytical offsets. Nor are there any significant differences between the microprobe data and the DCP data. However, the MgO, and $P_2O_5$, data from the Cameca SX50 electron microprobe appear to have a slight offsets when compared to the other Siqueiros electron microprobe data. The Cameca SX50 electron microprobe MgO and $P_2O_5$ data was normalized to match the other electron microprobe MgO and $P_2O_5$ data (Figure 3-2). The normalization method is discussed in Appendix A. The $Cr_2O_3$ contents obtained on the Cameca SX50 electron microprobe are not directly comparable to most of the other Cr data (mostly XRF). Measurements are made on the glass composition whereas the XRF analyses are of the whole rock samples. Therefore, it was not possible to use the microprobe $Cr_2O_3$ contents to compare with the $Cr_2O_3$ contents of the other Siqueiros samples. Since the XRF is a much more accurate method for obtaining Cr contents, only the $Cr_2O_3$ contents determined by XRF were used in this study.

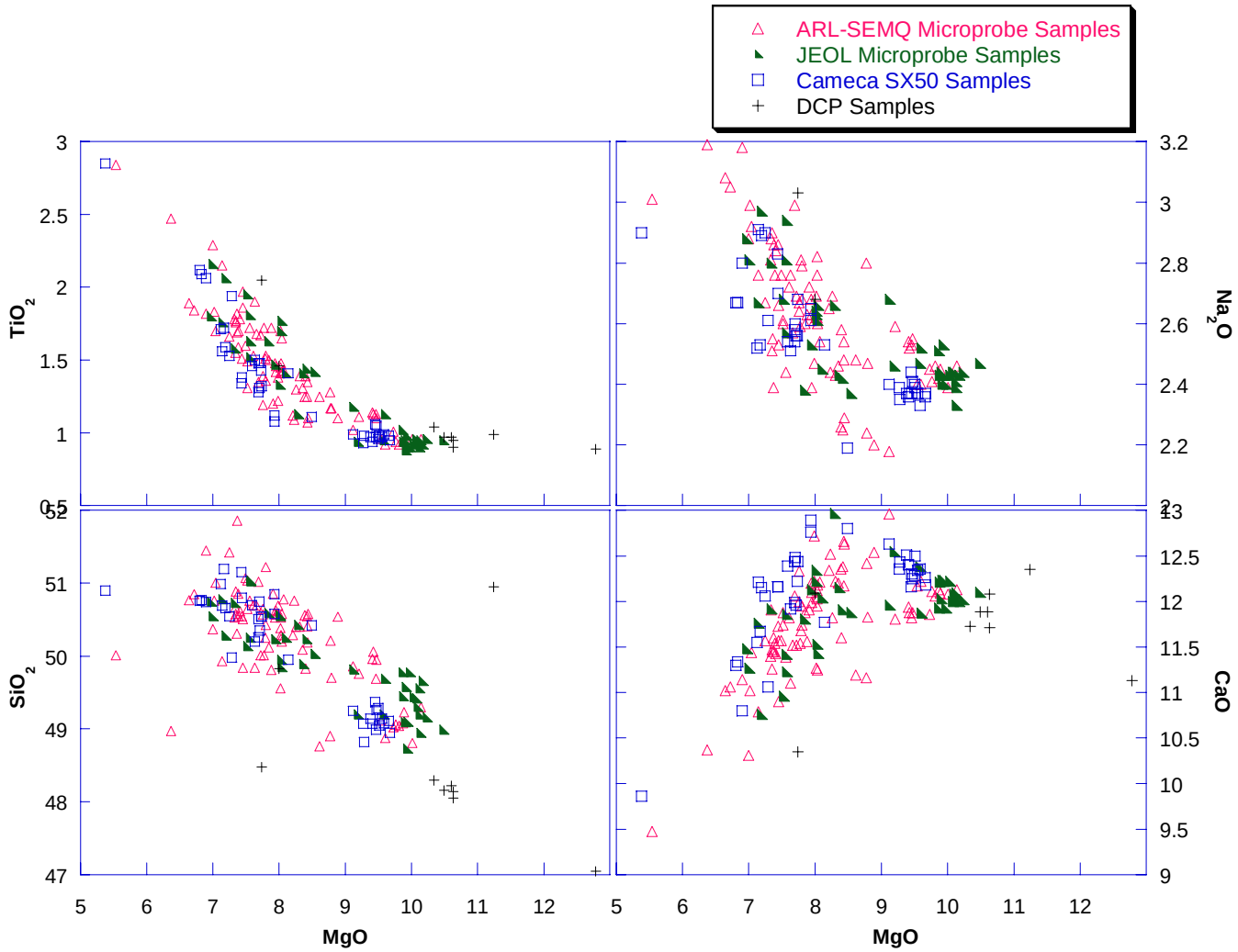


Figure 3-1. Graphical comparison of ARL microprobe, JEOL microprobe, DCP, and Cameca SX50 data before correction of the data.

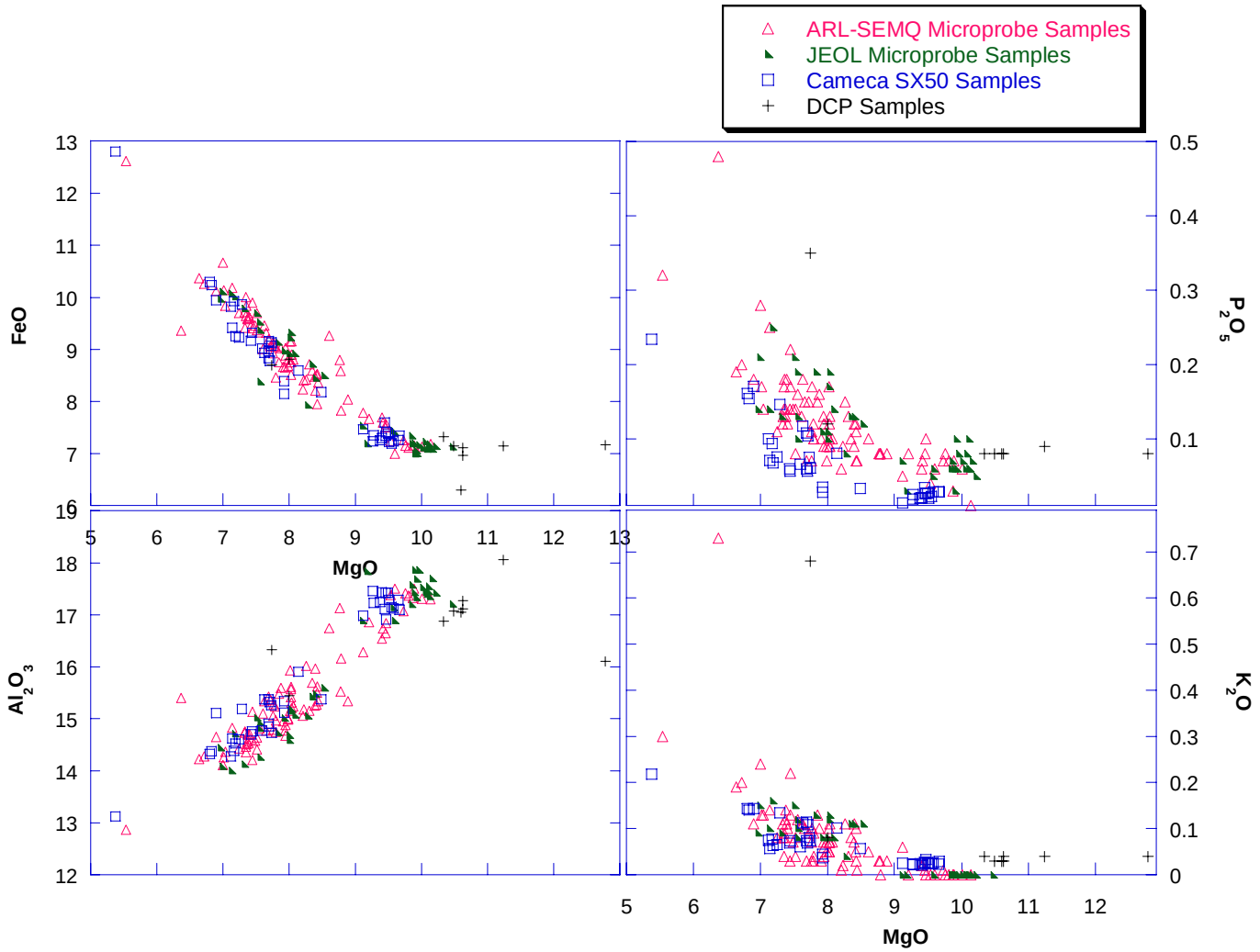


Figure 3-1. Continued.

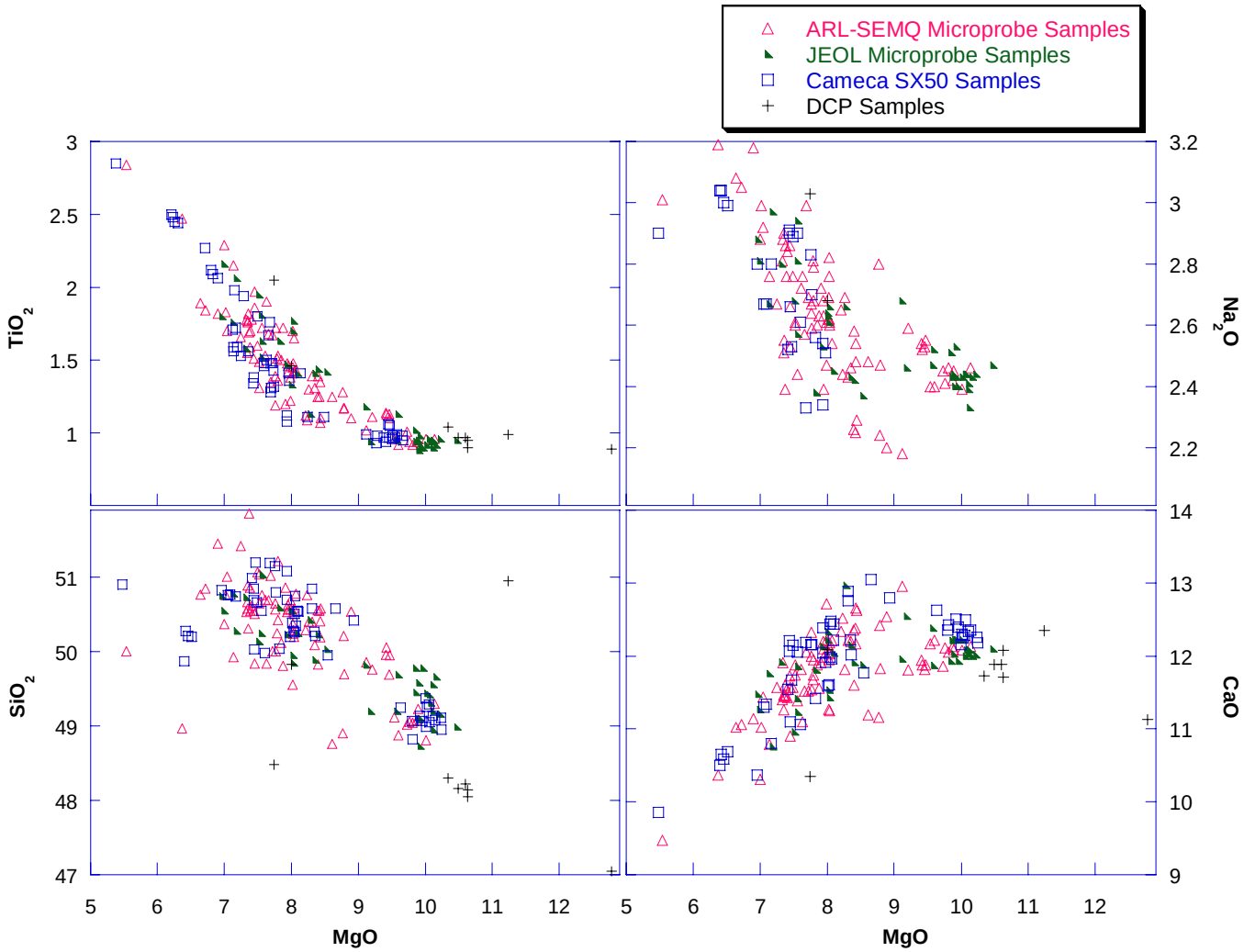


Figure 3-2. Comparison of data after adjustment of the Cameca SX50 MgO and $P_2O_5$ contents.

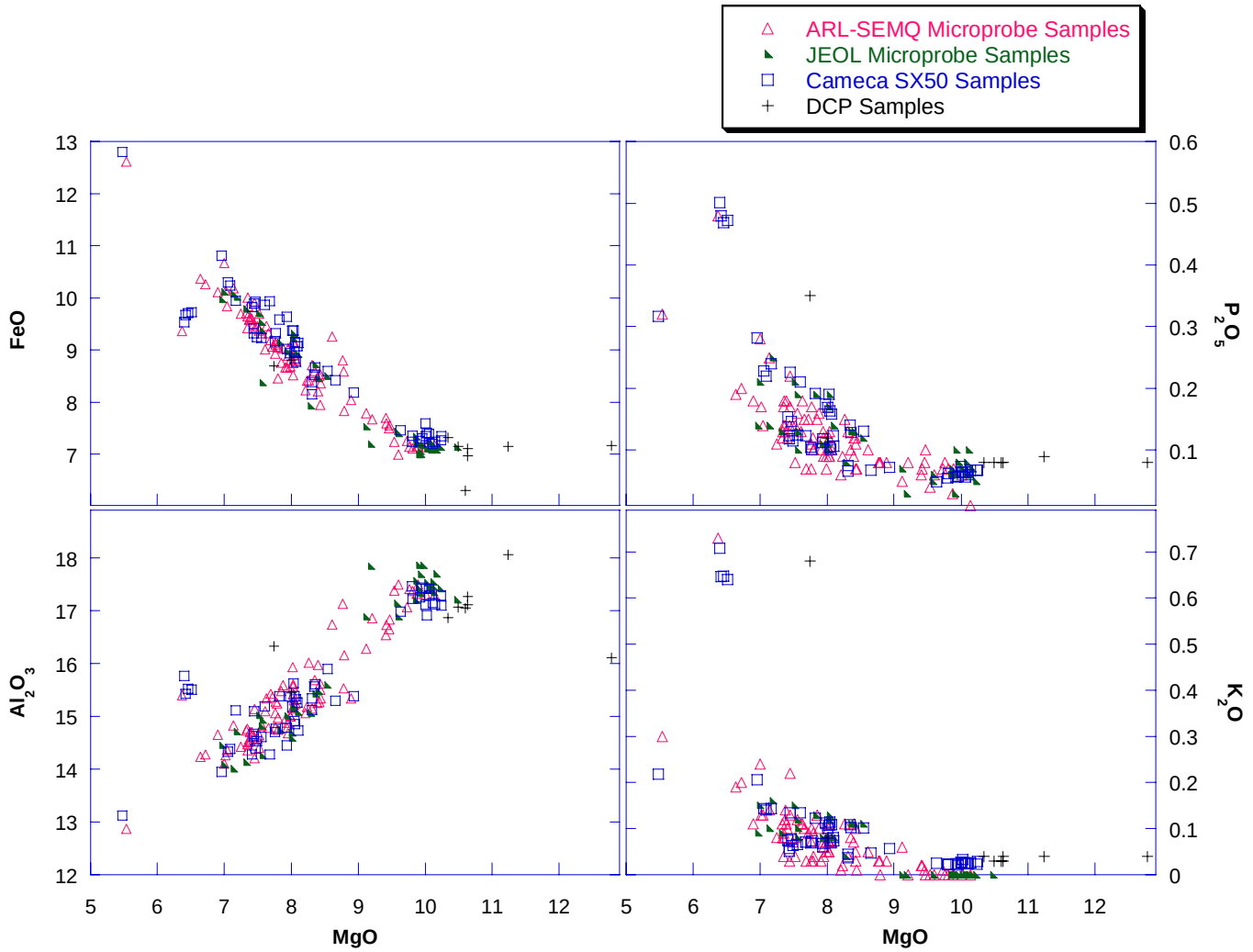


Figure 3-2. Continued.

The chemical characteristics of the samples were determined by comparing their major and trace element abundances to each other and samples from the adjacent East Pacific Rise (EPR) and from the Garrett transform. Liquid lines of descent (LLDs) and rare-earth element diagrams were used to help group samples of similar parental compositions. SeaBeam and SeaMarcII sonar data has also been collected for the Siqueiros transform (Fornari et al., 1989). The sonar data along with the ALVIN submersible dive observations were used to determine sample locations with respect to the local geologic/structural features. The ALVIN submersible observations and dive track data were used to precisely locate samples and to create depth profiles along dive transects. GIS (Arcview) data files were created that consist of latitude/longitude, elevation (depth), geologic location, and chemical characteristics. The data files were then used to create geologic maps of the Siqueiros transform.

Thin-sections of 60 samples were studied with a petrographic microscope to identify the different phases in each sample and to provide information regarding crystallization and mixing histories during petrogenesis. Microprobe analyses of spinel, olivine, and plagioclase phenocrysts were also completed for many of the samples. The compositions of the phenocrysts were then used to better understand crystallization and mixing histories.

# CHAPTER 4
# PETROGRAPHY AND LOCAL GEOLOGIC RELATIONSHIPS

The rocks from the Siqueiros transform include picrites, picritic basalts, basalts, and a few microgabbros. Thin sections examined in this study were cut from the outer glassy rinds as well as the more crystalline interiors of 63 samples. The majority of the samples chosen for thin section analysis were recovered from the A-B fault, but thin sections were made from samples from all spreading centers and faults and of one sample from the RTI. Descriptions of the thin sections examined are provided in Table 4-1 and representative photomicrographs are shown in Figures 4-1, 4-2, and 4-3. A few of the samples are aphyric or vitrophyric, containing less than 1 volume % phenocrysts and microphenocrysts, but most of the samples are phyric containing greater than 5% microphenocrysts.

## Samples from the A-B Fault

The majority of the thin sections are from the A-B fault because these samples are unusually olivine-rich with 5-20 modal% olivine phenocrysts (Perfit et al., 1996). The samples are remarkably fresh and unaltered, with thick glassy rinds which are free of palagonitization and Mn-coatings; indications of the relative youthfulness of the lava (Perfit et al., 1996). The samples differ from the rest of the Siqueiros samples in that they contain only olivine and spinel phenocrysts. Abundant olivine microphenocrysts are found in the glass and at centers of variolites. Near the interiors there is minor dendritic plagioclase microphenocrysts radiating from olivines. Despite the great recovery depths (3000-3900m), many of the olivine-rich basalts from the A-B fault have a greater degree

Table 4-1. Thin section descriptions.

| Sample # | Loc | MgO wt% | glass | Ve | phenocryst texture | | | microphenocryst texture | | | remarks |
|---|---|---|---|---|---|---|---|---|---|---|---|
| | | | | | olivine | plag | spinel | olivine | plag | cpx | |
| 2389-3 | A | ND | Y | Y | Rounded, embayed | Embayed, zoned | None | Hopper - euhedral | Swallow tail - tabular | None | Porphyritic; variolitic; flow features around phenocrysts; few plag clots |
| 2389-8 | A | ND | Y | Y | Very few, rounded | Slight zoning, embayed, skeletal | None | Subhedral | Swallow tail, acicular | None | Porphyritic; plag. clots; variolitic - intersertial |
| 2389-8A | A | ND | Y | Y | Rounded, skeletal | Huge, embayed, skeletal, zoning | None | Subhedral | Acicular - tabular | None | Porphyritic; huge plag. clots up to 9 mm; variolitic |
| 2389-1P | A | 7.35 | Y | Few | Rounded | Oscillatory zoning, skeletal, rounded | None | Variolitic | Variolitic | None | Porphyritic; variolites around ol microphenocrysts |
| 2384-1 | A-B | 9.6 | Y | Y | Up to 6 mm, rounded, skeletal, embayed | None | Skeletal, rounded, inside & outside olivine | Hopper - dendritic | Swallow tail | None | Porphyritic; primarily microphenocrysts; intersertial with opaques |
| 2384-10 | A-B | 9.59 | Y | Few | 1-4 mm, skeletal | None | Inside & outside olivine | Dendritic | Swallow tail | None | Porphyritic; variolitic - dendritic; large ol. clots |
| 2384-11 | A-B | 8.79 | Y | Very few | Few, embayed | None | Few inside olivine microphenocrysts | Hopper-subhedral | Swallow tail | None | Porphyritic; variolitic-intersertial; primarily quenched glass with plag. & ol. microphenocrysts |
| 2384-12 | A-B | 9.11 | Y | Very few | Skeletal, rounded | Very few, skeletal | Rounded; inside & outside olivine | Dendritic | Swallow tail - tabular | None | Porphyritic; ol. & plag. clots; intersertial with opaques |
| 2384-13 | A-B | 8.53 | Y | Y | 1-2 mm, skeletal | None | Inside olivines | Dendritic | Swallow tail | None | Green alteration in vesicals; variolitic-dendritic with opaques; dendritic growth around ol. |
| 2384-3 | A-B | 10.1 | Y | Few | 6-7 mm, rounded, skeletal | None | Skeletal, zoned edges | Hopper | Swallow tail - dendritic | None | Porphyritic; variolitic-dendritic with opaques; primarily microlites |

Table 4-1. Continued.

| Sample # | Loc | MgO wt% | glass | Ve | phenocryst texture | | | microphenocryst texture | | | remarks |
|---|---|---|---|---|---|---|---|---|---|---|---|
| | | | | | olivine | plag | spinel | olivine | plag | cpx | |
| 2384-4B | A-B | ND | Y | Y | Skeletal, embayed | Zoned, embayed, skeletal | None | Hopper | Tabular-swallow tail | Possibly quenched in g.m. | Porphyritic; 6-7 mm clots of ol. & plag.; intersertial g.m. with opaques; alteration inside vesicals |
| 2384-4C | A-B | ND | Y | Y | Rounded, skeletal | Skeletal, zoned, sieve texture | None | Hopper | Swallow tail | Possibly quenched in g.m. | Porphyritic; intersertial with opaques; primarily plag. phenocrysts vs. ol. |
| 2384-6 | A-B | 9.57 | Y | Few | Many, 4-5 mm; skeletal, resorbed | None | Skeletal | Hopper | Tabular-swallow tail | None | Porphyritic; variolitic; euhedral spinel microphenocrysts; 2 populations of plag. microphenocrysts |
| 2384-7 | A-B | 9.9 | Y | None | Skeletal | None | Resorbed | Yes | Swallow tail | None | Porphyritic; sparsely phyric; variolitic with ol. and plag. microphenocrysts |
| 2384-9 | A-B | 9.73 | Y | None | 5-6 mm, embayed, rounded, skeletal | None | Skeletal, variolites around | Variolitic around | None | None | Almost all glass with variolites and ol. microphenocrsts and phenocrysts |
| D20-6 | A-B | 9.87 | Y | Few | 2-3 mm, rounded, embayed, skeletal | None | Inside and next to olivine | Dendritic | Dendritic | None | Porphyritic; primarily glass with microphenocrysts; rounded spinel microphenocrysts; variolitic-dendritic with opaques |
| D20-5 | A-B | 10.6 | Y | None | 2-3 mm, skeletal | None | Skeletal, zoned | Hoppper | Dendritic | None | Porphyritic; glass-variolitic-dendritic |
| 2379-2 | A-B | 6.91 (WR) | Y | Very few | Rounded | Skeletal | None | Tabular | Tabular | None | Poikilitic; intersertial with large opaques; ol. and plag. intergrown |
| 2379-2 | A-B | 6.91 (WR) | Y | Few | 4-6 mm, embayed | Sieve texture | None | Tabular | Tabular | None | Poikilitic; intersertial g.m. with large opaques; ol. and plag. intergrown |

Table 4-1. Continued.

| Sample # | Loc | MgO wt% | glass | Ve | phenocryst texture | | | microphenocryst texture | | | remarks |
|---|---|---|---|---|---|---|---|---|---|---|---|
| | | | | | olivine | plag | spinel | olivine | plag | cpx | |
| 2384-1 | A-B | 9.6 | N | Y | Rounded, skeletal | None | Inside and outside olivine, skeletal, embayed | Tabular | Swallow tail | Possibly quenched in g.m. | Porphyritic; intergranular with opaques |
| 2384-10 | A-B | 9.59 | Y | Y | Few, about 1 mm, rounded | None | Skeletal, zoned | Dendritic | Dendritic - swallow tail | None | Primarily microlitic; variolitic-dendritic |
| 2388-6 | A-B | ND | None | Few | Rounded, altered edges | Zoning, skeletal, embayed | None | Few, rounded | Tabular | Possibly quenched in g.m. | Porphyritic; intergranular with opaques; large plag. & ol. clots 3-4 mm |
| 2388-6WR | A-B | ND | None | Few | Embayed-subhedral, huge | Huge, resorbed edges, skeletal, with very slight zoning | Inside olivines | Rare, rounded | Swallow tail - tabular | Possibly quenched in g.m. | Porphyritic; intergranular; microphenocrysts align around plag. Phenocrysts; plag & ol clots about 5 mm |
| 2388-7 | A-B | ND | None | Few | None | Few, about 4 mm, embayed, skeletal, resorbed rims | None | Rare, broken up, embayed | Subhedral | Possibly quenched in g.m. | Primarily microlitic; intergranular with opaques |
| 2391-10 | A-B | ND | None | Y | None | Embayed | None | Hopper | Tabular - anhedral | Possibly quenched in g.m. | Poikilitic; intersertial with opaques |
| 2391-10 | A-B | ND | None | Y | None | Embayed | None | Subhedral-anhedral | Tabular | Possibly quenched in g.m. | Poikilitic; intersertial with opaques |
| 2391-6 | A-B | ND | Y | Y | Very few, skeletal | Embayed, skeletal, zoning,sieve texture | None | Inter-granular with plagioclase | Tabular - swallow tail | Possibly quenched in g.m. | Porphyritic; intersertial with opaques; clots of plag. phenocrysts |
| 2391-7 | A-B | ND | Y | Y | Skeletal, rounded | Skeletal, embayed, zoning | None | Hopper - subhedral | Acicular - swallow tail | Possibly quenched in g.m. | Porphyritic; intersertial with opaques; plag. clots 3-4 mm |

Table 4-1. Continued.

| Sample # | Loc | MgO wt% | glass | Ve | phenocryst texture | | | microphenocryst texture | | | remarks |
|---|---|---|---|---|---|---|---|---|---|---|---|
| | | | | | olivine | plag | spinel | olivine | plag | cpx | |
| A25-D20-8 | A-B | ND | Y | None | Embayed, skeletal, rounded | None | Rounded, embayed, slightly zoned edges | Hopper-dendritic | Very few, dendritic | None | Phorphyritic; mainly glass; variolitic with hopper ol. microphenocrysts and very few dendritic plag. microphenocrysts |
| D-17B | A-B | ND | Y | Y | Rounded, skeletal | Skeletal | skeletal, zoned edges | Few, dendritic | Dendritic | None | Phorphyritic; ol. & plag. clots; dendritic |
| D17-4 | A-B | ND | None | few | Intergrown with plag | Skeletal, embayed | None | Subhedral | Subhedral | Possibly quenched in g.m. | Poikilitic; intersertial with opaques; green alteration |
| D20-5 | A-B | 10.6 | Y | few | Skeletal, rounded | None | Lots, zoned rims, skeletal | Hopper | Very few; dendritic | None | Sparsely porphyritic; mainly glass; variolitic - dendritic with spinel microphenocrysts |
| D20-6 | A-B | 9.87 | Y | Y | Skeletal, rounded | None | Zoned rims, skeletal | Hopper | Swallow tail - dendritic | Possibly quenched in g.m. | Porphyritic; variolitic - dendritic with opaques; mainly hopper ol. in glass |
| 2384-11 | A-B | 8.79 | Y | Very few | Few, about 1 mm, skeletal, embayed | None | None | Subhedral | Swallow tail - dendritic | None | Primarily microlitic; variolitic-dendritic |
| 2384-11 | A-B | 8.79 | Y | Few | Few, about 1 mm, skeletal, embayed | None | None | Subhedral | Swallow tail - dendritic | None | Primarily microlitic; variolitic-dendritic; aligned plag. microphenocrysts |
| 2384-12 | A-B | 9.11 | Y | Y | Few, skeletal | None | Few, around olivines | Intergown with plagioclase | Swallow tail | Possibly quenched in g.m. | Primarily microlitic; intergranular with opaques |
| 2384-13 | A-B | 8.53 | Y | Y | Skeletal | None | None | Slightly hopper | Swallow tail - dendritic | None | Porphyritic; variolitic - dendritic; ol. clots with dendritic growth of plag around |

Table 4-1. Continued.

| Sample # | Loc | MgO wt% | glass | Ve | phenocryst texture | | | microphenocryst texture | | | remarks |
|---|---|---|---|---|---|---|---|---|---|---|---|
| | | | | | olivine | plag | spinel | olivine | plag | cpx | |
| 2384-14 | A-B | 7.23 | None | Y | 5-6 mm, skeletal, rounded | Skeletal, slight zoning | None | Subhedral | Swallow tail | Possibly quenched in g.m. | Porphyritic; intersertial with opaques clots of ol. and plag. phenocrysts |
| 2384-14 | A-B | 7.23 | None | y | Skeletal | Skeletal | None | Subhedral | Tabular | Possibly quenched in g.m. | Porphyritic; intersertial with opaques |
| 2384-2 | A-B | 9.54 | Y | | Skeletal, 5-6 mm | None | Rounded, zoned rims | Hopper-dendritic | Swallow tail - tabular | None | Porphyritic; intersertial with fine opaques |
| 2384-4 | A-B | ND | Y | Y | Rounded, embayed, in clot | Embayed, skeletal, zoning in some | Inside olivines | Slightly hopper | Swallow tail | Possibly quenched in g.m. | Porphyritic; intersertial with opaques; circular alteration; alignment around clots |
| 2384-4A | A-B | 8.35 | Y | Y | Skeletal, embayed | Skeletal, zoning | Inside olivines | Subhedral-hopper | Swallow tail | None | Porphyritic; intersertial with opaques; huge clots of plag. & ol. |
| 2384-4C | A-B | ND | Y | Y | Skeletal | Embayed, zoning | Inside olivines | Subhedral-hopper | Swallow tail - tabular | None | Porphyritic; intersertial g.m. with opaques; clots of ol & plag 2-3 mm |
| 2388-1 | A-B | ND | N | Many | None | Very few, skeletal | None | Few, skeletal, rounded | Tabular | Possibly quenched in g.m. | Poikilitic; opaques in g.m. |
| 2391-9 | A-B | ND | N | Few, irregular | None | Very resorbed | None | Subhedral -anhedral | Tabular | Possibly quenched in g.m. | Poikilitic |
| 2391-8 | A-B | ND | N | Y, alteration around | Resorbed, skeletal, in clots | Skeletal, resorbed, zoned | Alteration around, rounded | Few, subhedral | Acicular | Possibly quenched in g.m. | Porphyritic; intergranular with opaques; primarily plag. in clots 2-3 mm |
| 2391-2 | A-B | 7.84 | N | Very few | Skeletal, embayed | Skeletal, embayed, zoning | None | Few, hopper-subhedral | Acicular | Possibly quenched in g.m. | Phorphyritic; green-brown alteration; plag. clots |

Table 4-1. Continued.

| Sample # | Loc | MgO wt% | glass | Ve | phenocryst texture | | | microphenocryst texture | | | remarks |
|---|---|---|---|---|---|---|---|---|---|---|---|
| | | | | | olivine | plag | spinel | olivine | plag | cpx | |
| 2376-8 | B | 8.02 | Y | Y | Rounded, skeletal | Skeletal, embayed, sieve texture | None | Hopper-dendritic | Swallow tail - tabular | None | Porphyritic; variolitic - intersertial with opaques; 4-5 mm clots of plag. & ol. |
| 2376-9 | B | ND | Y | Y | Skeletal, embayed | Zoned, skeletal | Zoned rim | Dendritic | Dendritic | None | Porphyritic; 3 mm clots of ol. & plag.; variolitic - dendritic with opaques; 3 populations of plag |
| 2382-10 | B | 6.68 (WR) | Y | None | Skeletal | Sieve texture, rounded, zoned, skeletal | None | Tabular | Swallow tail | Possibly quenched in g.m. | Porphyritic; intersertial with opaques; mainly plag. clots with minor ol. |
| 2376-11 | B | ND | N | | Embayed, rounded | Skeletal, oscillatory zoning, huge | None | Subhedral | Tabular | None | Porphyritic; variolitic - intersertial with opaques; plag. & ol. clots about 4 mm |
| 2387-1 | B-C | ND | Y | Few | Rounded | Sieve texture, zoning, skeletal | None | Tabular | Swallow tail | None | Phorphyritic; intersertial with opaques |
| 2387-2 | B-C | 7.56 | None | Y, glass filled | Out of equilibrium, not as big as plag. | Oscillatory zoning, sieve texture, skeletal | None | Small, subhedral | Swallow tail - tabular | None | Porphyritic; 2-3 mm clots of large plag. with small ol. & plag.; variolitic - intersertial; brown and green alteration |
| 2387-2 | B-C | 7.56 | Y | Y | Few | Embayed, zoning, skeletal, sieve texture | None | Subhedral - euhedral, skeletal | Swallow tail - tabular | None | Porphyritic; 2-3 mm clots of large plag. with small ol. & plag.; variolitic - intersertial; brown and green alteration |
| 2387-5 | B-C | 7.79 | None | Y | Few, embayed, skeletal | Zoning, embayed, sieve texture | None | Subhedral | Tabular | Possibly quenched in g.m. | Porphyritic; 5-6 mm clots of plag. & ol. phenocrysts and microphenocrysts; intersertial with opaques |
| 2387-7 | B-C | ND | None | Y | Very rare, rounded | Zoning, embayed, sieve texture | None | Anhedral | Anhedral | Possibly quenched in g.m. | Poikilitic; 5 mm plag. clots; intergranular with opaques |

Table 4-1. Continued.

| Sample # | Loc | MgO wt% | glass | Ve | phenocryst texture | | | microphenocryst texture | | | remarks |
|---|---|---|---|---|---|---|---|---|---|---|---|
| | | | | | olivine | plag | spinel | olivine | plag | cpx | |
| 2385-1 | C | ND | Y | Few | Embayed, very few | Rounded, skeletal, sieve texture | Zoned, skeletal | Hopper - tabular | Swallow tail | None | Porphyritic; variolitic-intersertial |
| 2385-1 | C | ND | Y | Few | Embayed, very few | Rounded, skeletal, sieve texture | Zoned, skeletal | Hopper - tabular | Swallow tail | None | Porphyritic; variolitic-intersertial |
| D34-2 | C-D | 9.12 | Y | Y | Few, skeletal | Few, skeletal | None | Skeletal | Acicular - tabular | Possibly quenched in g.m. | Microlitic; intersertial with opaques |
| 2386-3 | D | ND | N | Y, many | None | One about 1 mm, embayed | None | Anhedral - subhedral | Subhedral | Possibly quenched in g.m. | Primarily microlitic; few plag. clots; intersertial with opaques |
| 2386-6 | D | ND | N | Y, many | None | Few, small embayed | None | Anhedral - subhedral | Swallow tail - tabular | Possibly quenched in g.m. | Primarily microlitic; few plag. clots |
| 2386-8 | D | ND | None | Y | None | Clots | None | Anhedral - subhedral | Tabular | Possibly quenched in g.m. | Porphyritic; plag. clots; intersertial with opaques |
| 2386-1 | D | ND | Y | | None | One about 1 mm, embayed | None | Subhedral | Subhedral | Possibly quenched in g.m. | Microlitic; intergranular with ol., plag., and opaque microphenocrysts |
| 2390-6 | WRTI | ND | Y | Y | Skeletal | Skeletal, embayed | None | Hopper | Acicular - dendritic | None | Primarily microlitic; intersertial with opaques; primarily plag. |

Notes: ND = no data; Ve = vesicals.

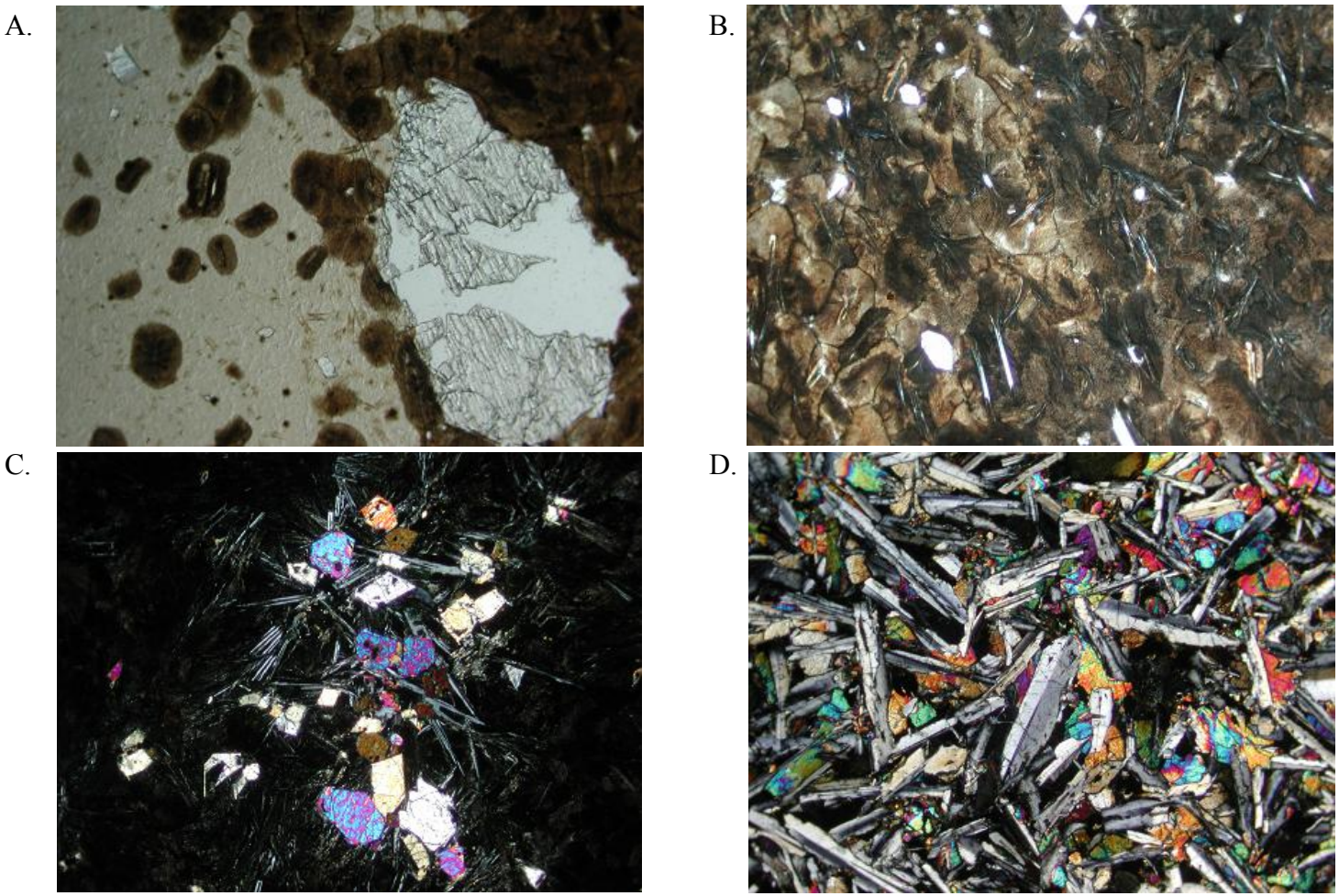


Figure 4-1. Photomicrographs taken under plain light (a & b) and cross polarized light (c & d). Picture width is equal to approximately 1.8 mm. A) Rounded and embayed olivine phenocrysts surrounded by glass and variolites (sample 2384-7). B) Olivine microphenocrysts in transition from variolitic to dentritic texture (sample 2384-7). C) Plagioclase microphenocrysts growing around olivine glomerophenocryst in sample 2384-13 a picritic basalt. D) Plagioclase and olivine phenocrysts in intersertial groundmass with opaques and quenched clinopyroxene (sample 2391-10).

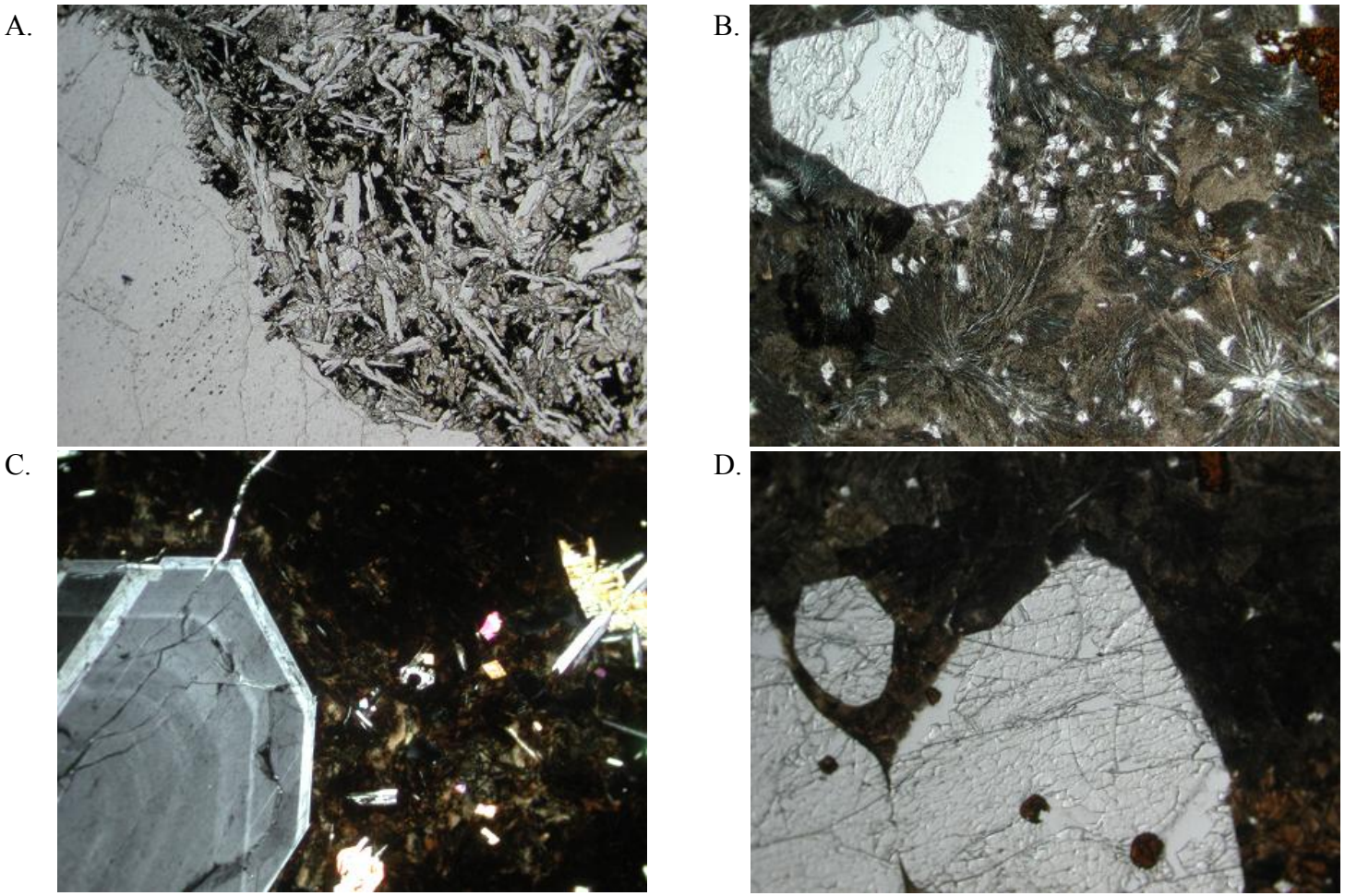


Figure 4-2. Photomicrographs taken under plain light (a, b, & d) and cross polarized light (c). Picture width is equal to approximately 1.8 mm. A) Edge of large plagioclase with very resorbed edge surrounded by olivine, plagioclase and opaque microphenocrysts (sample 2387-7). B) Rounded olivine phenocrysts in dendritic groundmass with hopper olivine microphenocrysts (sample D20-5). C) Plagioclase phenocrysts with oscillatory zoning in variolitic groundmass with olivine and plagioclase microphenocrysts (sample 2389-1). D) Rounded olivine phenocrysts with spinel inside attached in variolitic groundmass (sample 2384-3).

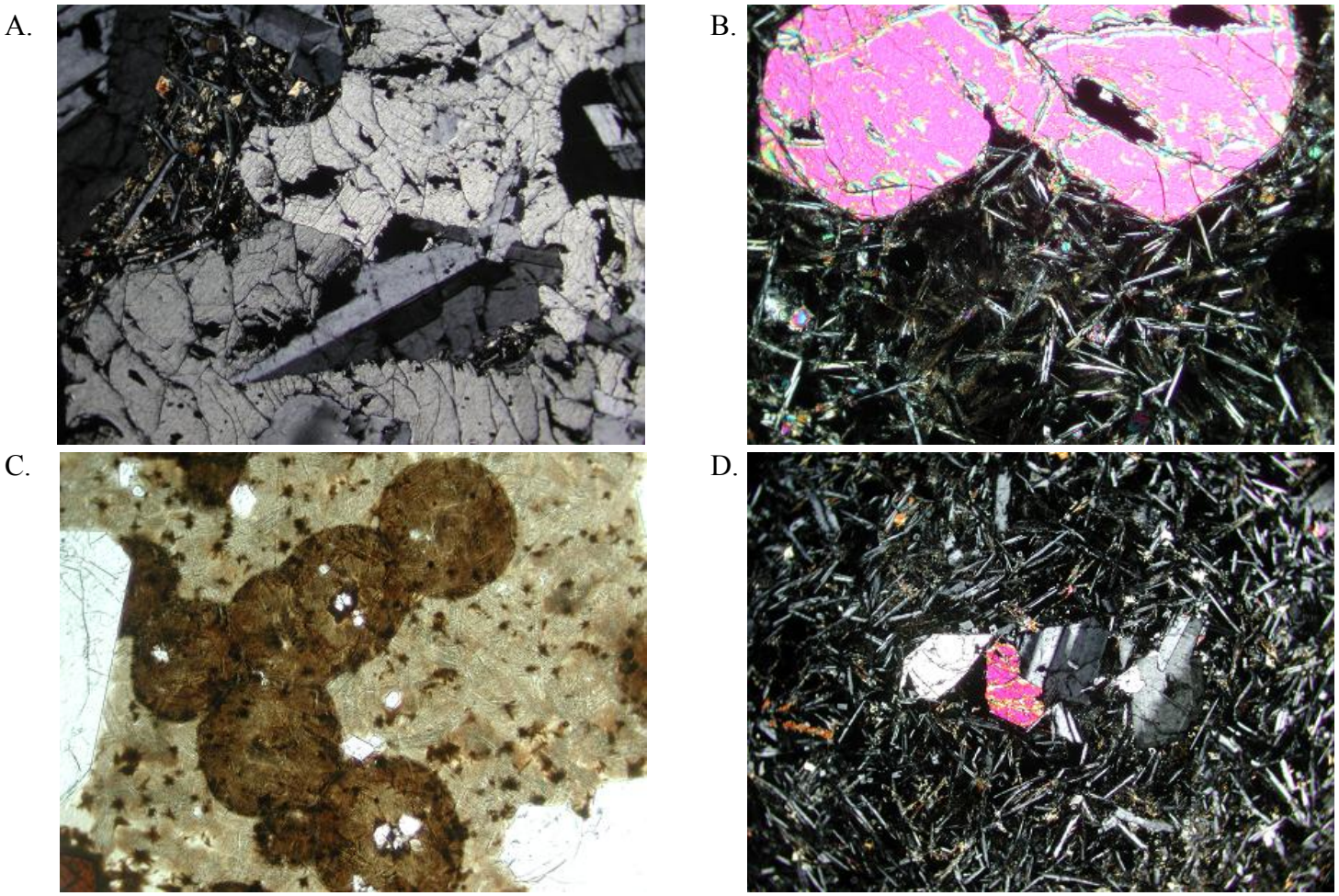


Figure 4-3. Photomicrographs taken under plain light (c) and cross polarized light (a, b, & d). Picture width is equal to approximately 1.8 mm. A) Plagioclase and olivine clot in intersertial groundmass of plagioclase and olivine microphenocrysts (sample 2384-4). B) Rounded olivine phenocrysts in intersertial groundmass of olivine and slightly swallow tail plagioclase microphenocrysts (sample 2384-1). C) Circular variolites with olivine microphenocrysts (sample 2384-9). D) Small olivine plagioclase clot within intersertial groundmass of plagioclase, olivine, and quenched clinopyroxene (sample 2384-4).

of vesicularity than EPR basalts usually found between 2500m to 2800m depth. Several dredges were targeted to sample the cone-shaped features in the axis of the A-B fault. The position of these features, roughly halfway along the fault, suggested they would be located in older volcanic terrane; but their morphology suggested recent constructional volcanism. Dredge D-20 started in an area of small cones near the midpoint of the A-B fault and proceeded up the south wall of the fault valley. Large quantities of young-looking glassy basalts, many of which were picritic were recovered in the dredge. Three additional dredges (D-22, D-23, and D-24) were carried out in the deep areas of the A-B fault, on small, closed-contour peaks and saddles in the axis of the trough, and up the middle to lower walls of the fault valley (Figure 4-4). Young, glassy pillow basalts were found throughout the A-B fault. To more completely document the loci of eruption and tectonic setting of the young-looking, olivine-rich basalts Alvin Dive 2384 traversed the floor of the A-B fault and went up the south wall across on the cone-like features (Figures 4-5). The basalt-floored depression where dive 2384 began was found to be nearly devoid of sediment which is unusual for transform faults. Fresh olivine-phyric basalts were recovered from a volcanic slope characterized by intermingled pillows, broken pillows, and fragments of basalt all fresh and glassy. White to yellow staining, inferred to be hydrothermal in origin, was abundant on the broken basalt surfaces. Another field of fresh basalt flows was found along the base of the south wall of the fault valley. Here nearly intact pillows and tubes were found. The north side of the fault axis consisted of rugged constructional volcanic terrane with occasional steep-sided (up to 70°), flat-topped, volcanic “haystacks”. Glassy picritic basalts with little or no Mn coatings were recovered from a free-standing cone. Around the cone, the seafloor was built of glassy

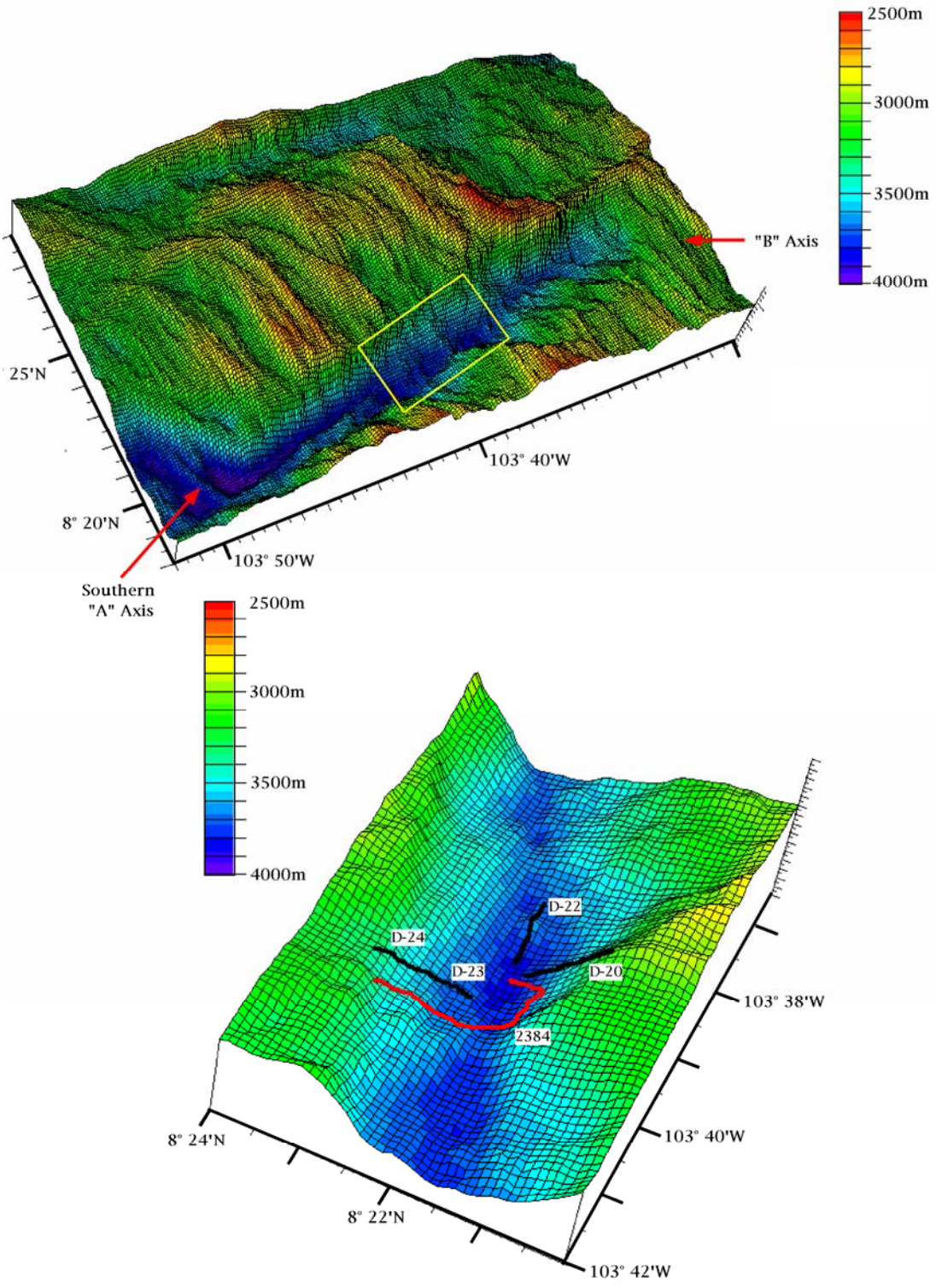


Figure 4-4. Dredge and Alvin dive locations within the A-B fault.

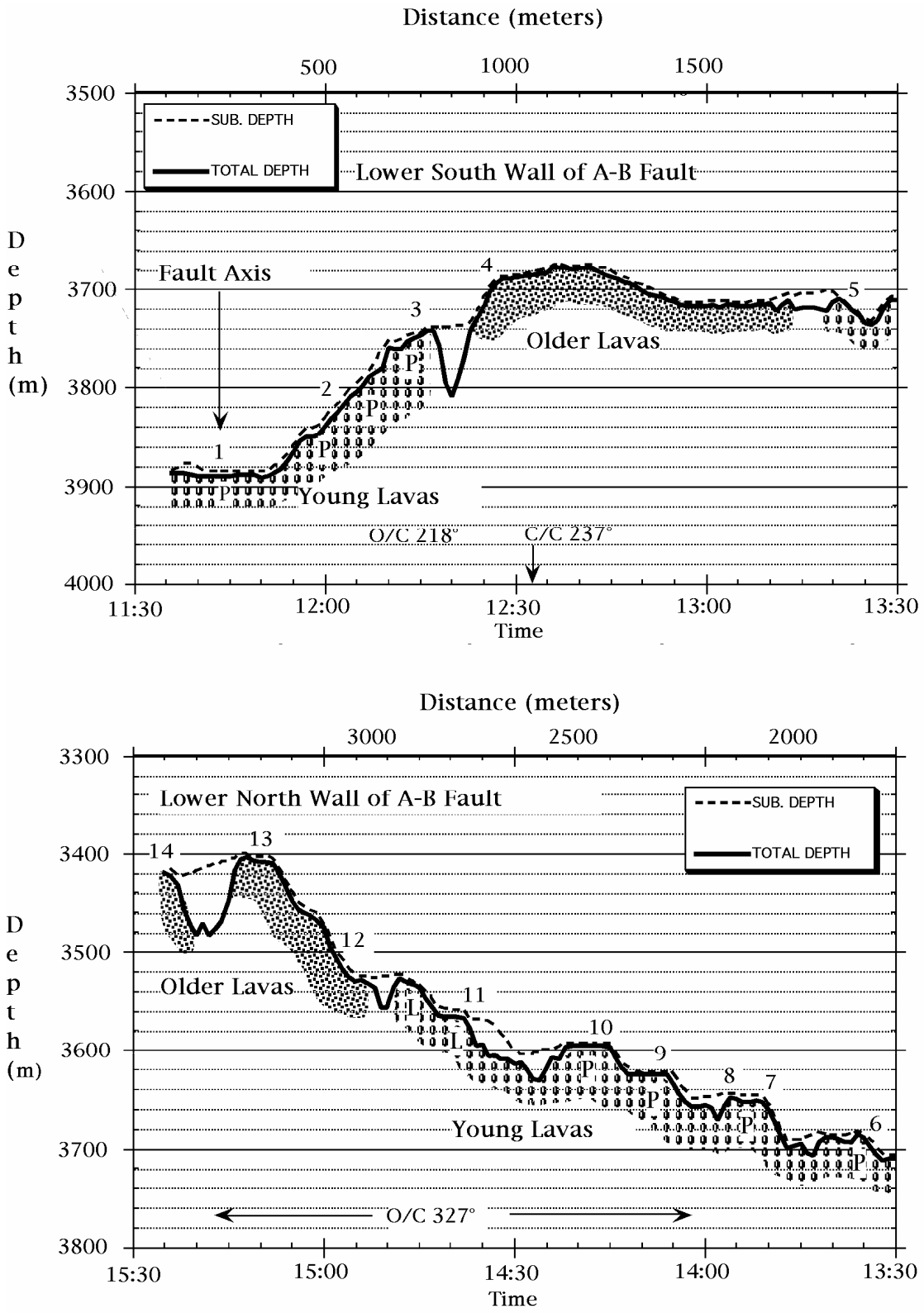


Figure 4-5. Alvin dive 2384 traverse.

basalt flows and veneered with basalt blocks and glass shards. To the north, a bathymetric notch separates the younger volcanic terrane of the south from an older terrane to the north (Figure 4-5). Here sediment was more abundant and glass is absent. Only plagioclase-phyric or olivine + plagioclase-phyric basalts were recovered from the older lava flows.

Within the 28 km long A-B fault, 9 cone like features believed to be constructional volcanic features have been identified (Wendlandt and Ridley, 1994). Bulbous to elongate pillows are the dominant basalt morphology within the A-B fault, similar to that observed along intra-transform spreading centers, but in marked contrast to the lava morphology at the EPR axis, where sheet flows and lobate forms dominate (Ballard et al., 1981; Kastens et al., 1986; Perfit et al., 1991). The erupted lavas overflow a severely tectonized terrane on the valley walls, but the young flows from which the olivine-rich samples were recovered had little structural disruption of the flow surfaces. The olivine rich basalts recovered from the A-B fault valley are inferred to have erupted recently as evidenced by the extreme freshness of the glassy lava surfaces, thin to non-existent sediment cover, and relatively minor structural disruption of the flow surface. The youngest-looking basalts are as glassy as young lavas that floor the axial summit caldera on the EPR between 9°30'-54' N (Haymon et al., 1991, 1993; Fornari et al., 1991; Perfit et al., 1991).

## Siqueiros Sample Petrography

The extremely olivine-rich picrites and picritic samples which lack plagioclase phenocrysts were only recovered within the A-B fault. The older looking, Mn-encrusted basalt samples from the talus and sediment-covered terrains surrounding the fresh flows are plagioclase + olivine ± spinel-phyric, or plagioclase ± spinel-phyric (Perfit et al.,

1996). The samples from the other faults, the three spreading centers, tough D, and the RTIs are also plagioclase + olivine ± spinel-phyric, or plagioclase ± spinel-phyric. Most samples are porphyritic, containing phenocrysts and microphenocrysts.

The olivine-rich samples tend to be hypohyaline having glassy margins with sparse microphenocrysts and variolitic or dendritic interiors. The plagioclase phyric samples range from hypohyaline to hypocrystalline or holocrystalline with nearly completely crystalline interiors and margins and only minor glass in the groundmass. Olivine and plagioclase microphenocrysts are present in almost all of the samples and a few samples had microphenocrysts of spinel. The more crystalline samples have opaques in the groundmass. Clinopyroxene phenocrysts have not been identified, but in the more crystalline samples clinopyroxene appears as a quenched phase in the groundmass. Olivine microphenocrysts are commonly found in centers of variolites or with dendritic growth of plagioclase surrounding them. Olivines range from hopper crystals in the variolitic samples to subhedral in the more crystalline samples. Plagioclase microphenocrysts usually have swallow tail to dendritic forms. Euhedral and subhedral tabular plagioclase crystals are abundant in the more crystalline samples.

In all the samples, including the olivine-rich samples from the A-B fault, the large phenocrysts have textures indicating that they were not in equilibrium with their host melt. Subhedral to euhedral olivine phenocrysts vary from 1 mm to 7 mm in size, but tend to have rounded or embayed edges and are often skeletal. Many of the samples are glomeroporphyritic with clots of olivine and plagioclase growing together. Larger plagioclase phenocrysts are commonly glomeroporphyritic and have skeletal, rounded or embayed edges. Many of the larger plagioclase phenocrysts also exhibit oscillatory

zoning and some have sieve or moth-eaten textures. Spinel phenocrysts exist inside and outside olivine phenocrysts. The spinels were usually rounded, sometimes skeletal, and typically red to brown with darker rims. Clinopyroxene is absent from all samples, which is unusual for MORBs. However, because most of the thin sections were made of the samples from the A-B fault, the samples are fairly primitive and clinopyroxene is not expected on or near the liquidus of more primitive samples at low to moderate pressures.

## Crystal Liquid Equilibria

In addition to thin sections, elemental analyses was completed by microprobe on olivine, plagioclase, and spinel crystals (Appendix B). The olivine microprobe analysis was done on small, medium, and large olivine phenocrysts. A comparison of the Mg# ($Mg^{2+}/ (Mg^{2+} + Fe^{2+})$) of the glass surrounding the olivine and the Fo content of the olivine shows a strong correlation (Figure 4-6). The total compositional range in the Siqueiros basalts is from $Fo_{90.9}$ to $Fo_{80.0}$, which is a slightly greater range than that found in olivine microphenocrysts and microlites within MORBs from the East Pacific Rise at 9°30'N. Olivine phenocrysts in the 9°30'N lavas have been found to range from $Fo_{88}$ to $Fo_{82}$ (Pan and Batiza, 2003). With successive fractional crystallization the Mg# of the melt and the Fo content of the crystallizing olivine both decrease. In the Siqueiros sample suite, there does not seem to be a correlation between the size and Fo content of the olivine. Although the majority of the large olivines have more forsteritic compositions, some of the large olivines have lower Fo contents and some of the small olivines have relatively high Fo contents. For the larger olivine phenocrysts, successive microprobe analyses were done from the center outward to the rim. Individual crystals have little chemical zonation. Some olivines show slight reverse zoning with the Fo content increasing from the core to rim (2384-3-ol1), while other samples are normally

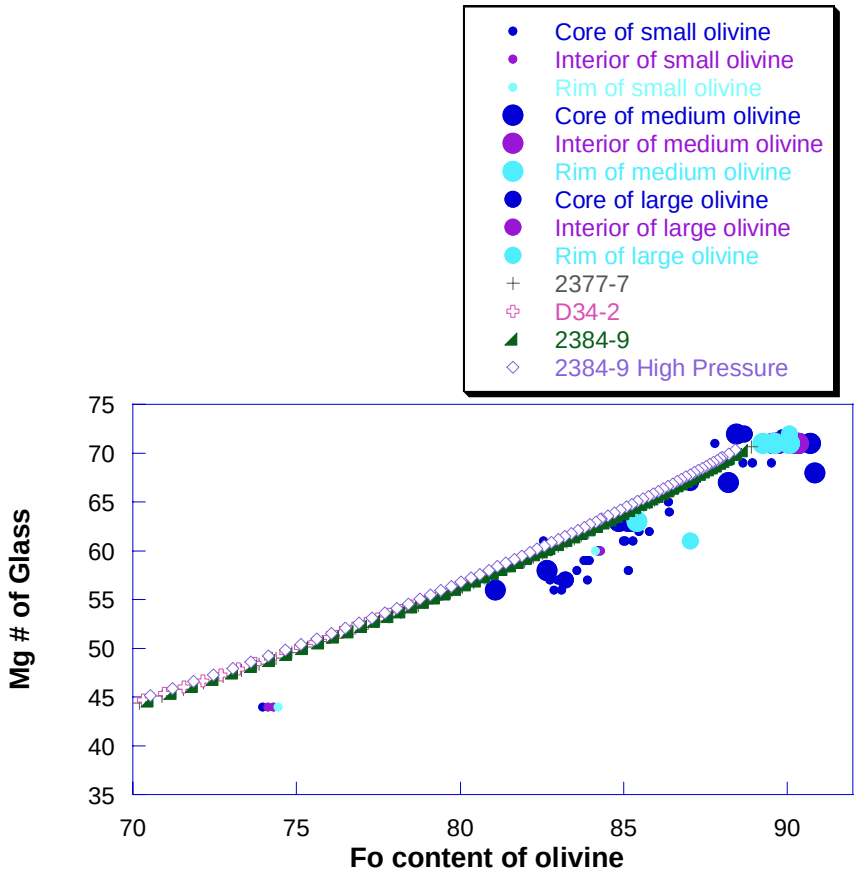


Figure 4-6. Comparison of olivine forsterite content with the Mg# ($Mg^{2+}/(Mg^{2+} + Fe^{2+})$) of the host glass. Modeled equilibrium trends expected during fractional crystallization were calculated using the low pressure model of Danyushevsky (2001) for three different parental compositions. High pressure model of Danyushevsky (2001) also shown for comparison.

zoned and the Fo content decreases slightly from the core to rim (2388-3a-ol1). Liquid-mineral equilbria for olivine (Mg# versus the Fo content) were calculated using the method of Danyushevsky, (2001) (Figure 4-6). Slightly different results were obtained using the ol-liquid equilibria model of Herzberg & O'Hara (2002). Fo-liquid equilbria were determined for three different parental liquids as they fractionally crystallized using the Petrolog program. There is almost no difference for the three parental composition used in the major element models and there is no difference between the high and low

pressure models. The Fo content of olivine steadily decreases as the Mg# of the host magma decreases and as the olivine-melt partition coefficient ($D_{ol\text{-}melt} - Fe^{ol} * Mg^{L}/Mg^{ol} * Fe^{L}$) increases slightly with decreasing temperature. The Herzburg & O'Hara (2002) model calculations predict slightly lower olivine partition coefficients, which fit the observed data better (Figure 4-7). The olivine-melt partition coefficient in MORB lavas has been found to range from approximately 0.31 to 0.28 (Pan and Batiza, 2003). Olivine-liquid pairs in Siqueiros samples fall on the low side of this range of partition coefficients, requiring Kds of less than 0.28 if the olivine phenocrysts are actually in equilibrium with the host magma (Figure 4-8), alternatively, the olivines may be xenocrystic. The more Fo compositions of the Siqueiros olivines suggests that many of the olivine phenocrysts came from more Mg-rich melts and are out of equilibrium with the host magma. This is also suggested by the embayed edges and skeletal textures found in many of the olivine phenocrysts.

Chemical analysis of plagioclase by microprobe shows that the plagioclase phenocrysts have much greater compositional variations than olivine phenocrysts (Appendix B). Analyses were completed on small and large plagioclase crystals and include core, rim, and interior zones. The total compositional range of plagioclase phenocrysts is from $An_{58.0}$ to $An_{88.3,}$ compared to a composition range of $An_{52.1}$ to $An_{83.4}$ for phenocrysts from 9°3'N on the EPR (Pan & Batiza, 2003). The average Siqueiros plagioclase is slightly more calcic ($An_{75.9}$) than the average plagioclase from 9°30'N on the EPR ($An_{68\pm5}$). Many of the large plagioclase crystals show visible zoning. Core to rim analysis show that the zones exhibit oscillatory zoning (Figure 4-9). Overall, the

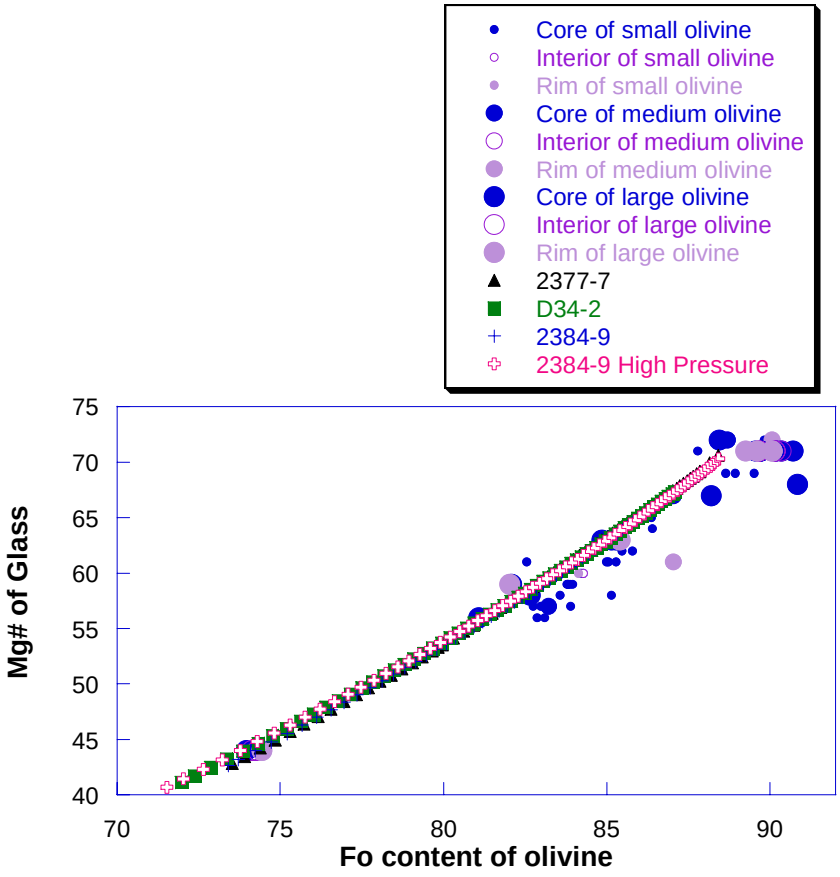


Figure 4-7. Comparison of Olivine forsterite content with the Mg# ($Mg^{2+}/(Mg^{2+} + Fe^{2+})$) of the host glass. Modeled equilibrium trends expected during fractional crystallization were calculated using the low pressure model of Herzburg & O'Hara (2002) for three different parental compositions. High pressure model of Danyushevsky (2001) also shown for comparison.

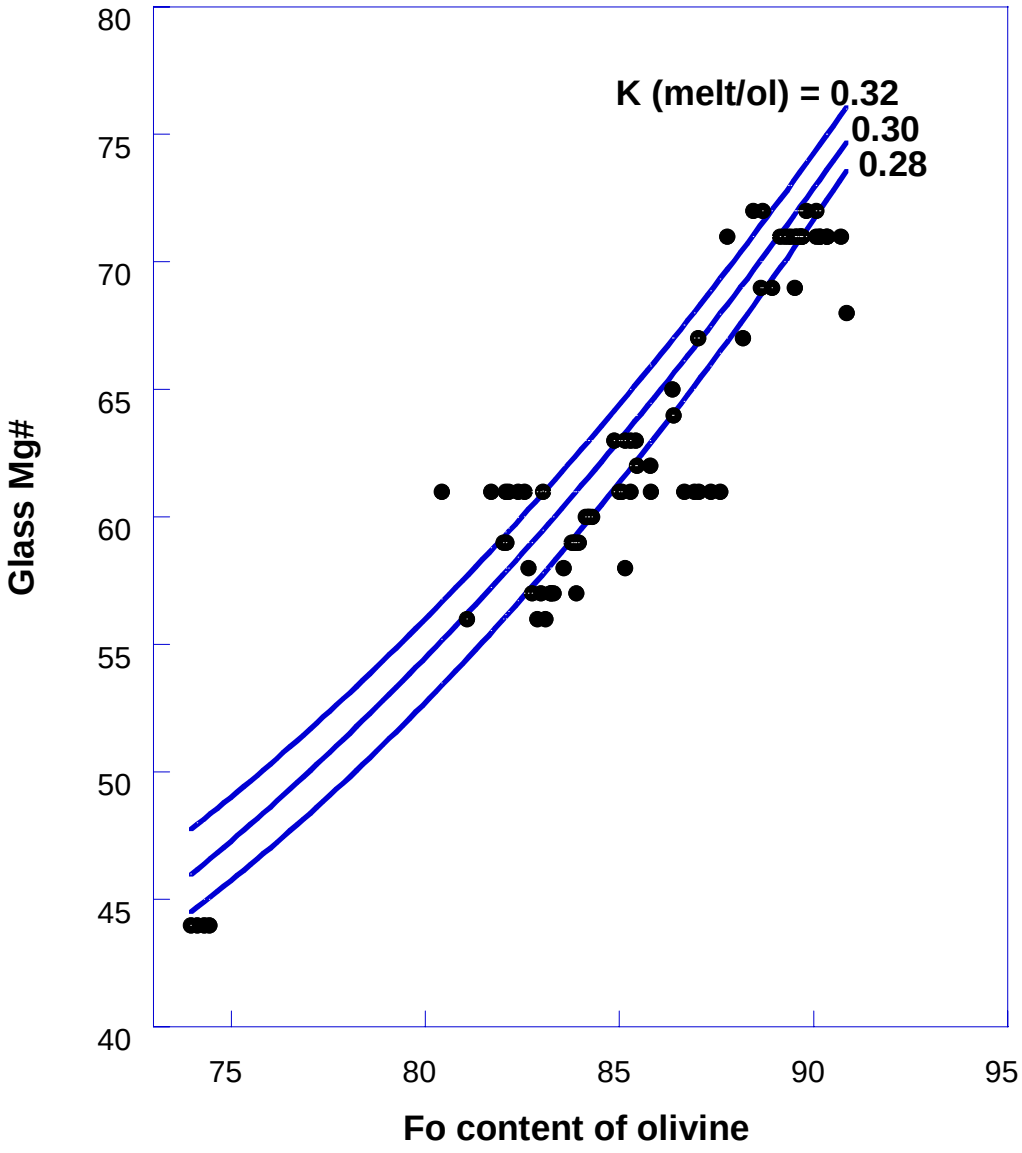


Figure 4-8. Calculated Fo contents of olivine for partition coefficients ranging from 0.28 to 0.32. Siqueiros samples fall on the low side of the acceptable olivine-melt partition coefficients indicating that they are from more mafic magmas than that of the host glass.

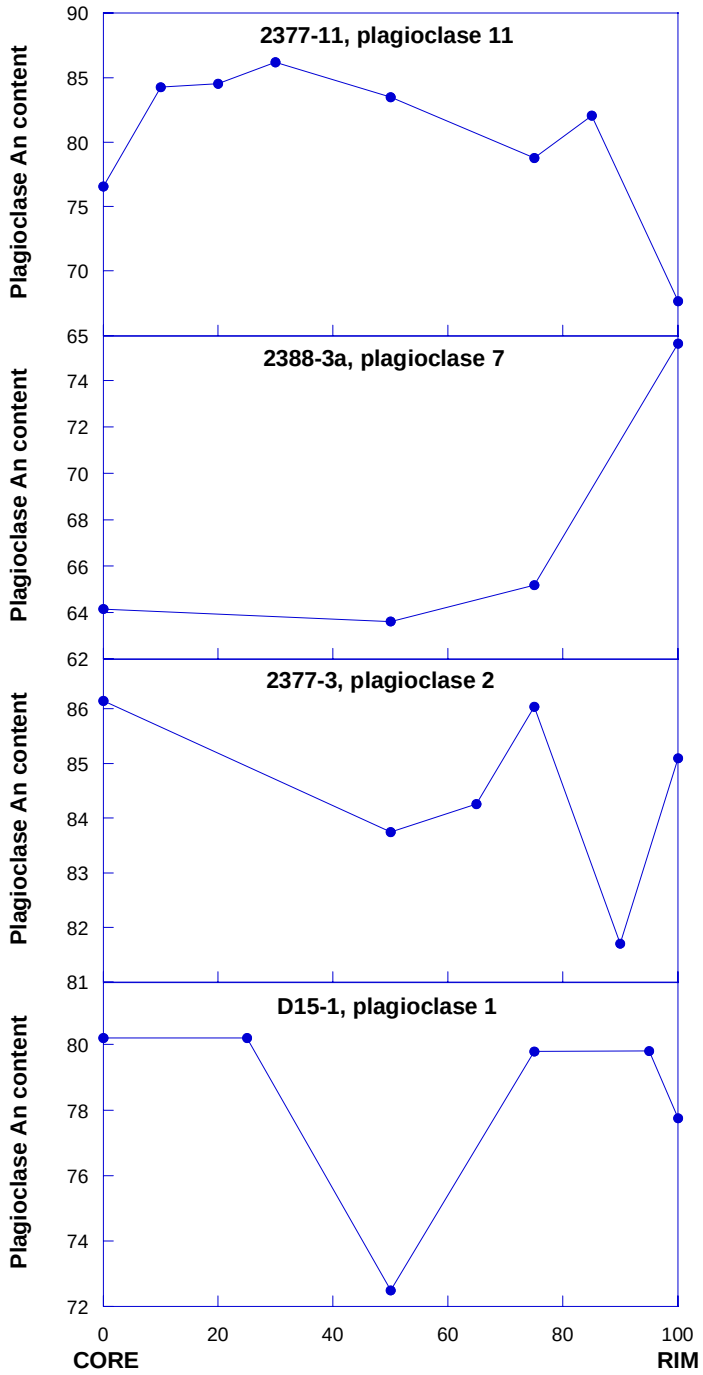


Figure 4-9. An contents for core, interior, and rim locations in Siqueiros plagioclase phenocrysts.

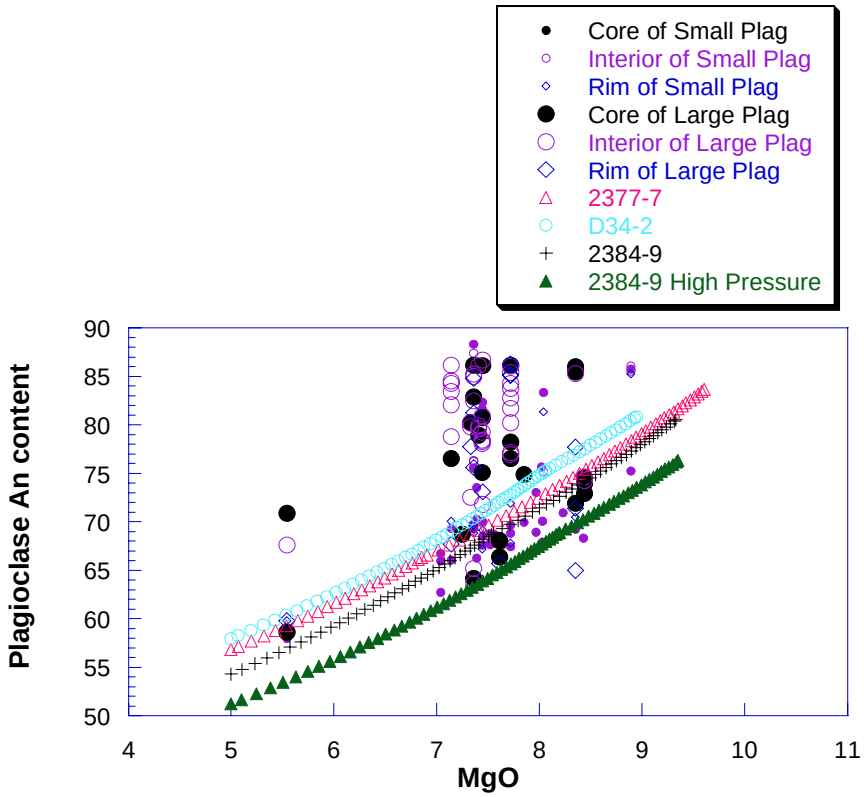


Figure 4-10. Comparison of plagioclase An content from Siqueiros samples and An content evolution for three of the major element parental compositions. Model equilibrium trends expected during fractional crystallization were calculated using low pressure model of Danyushevsky (2001).

smaller plagioclase laths have lower An contents (Avg. An content = 69.9) than the larger laths (Avg. An content = 78.3). Anorthite contents of the small plagioclase phenocrysts exhibit a decrease with magma evolution (decreasing MgO) as predicted in the fractional crystallization models (Figure 4-10). Larger plagioclase phenocrysts and a few of the smaller phenocrysts have higher An contents (for a given MgO or CaO) than predicted and have large variations in An content from core to rim (core-rim), suggesting that the phenocrysts are out of equilibrium with the host glass.

The relationship between An content and the Ca# (Ca/(Ca + Na)) of the magma is complicated. Calculated plagioclase-liquid equilbria indicate that the Ca# initially

decreases slowly with fractionation, but once clinopyroxene begins fractionating from the liquid the Ca# decreases rapidly. Models that describe the relationship between the Ca# of the magma and the coexisting plagioclase An content were produced using the alogrithims of Danyushevsky, (2001) and Langmuir et al. (1992) (Fig. 4-11 and 4-12). The best fit to the observed data were produced using the plagioclase-liquid equilbria model of Danyushevsky, (2001). The compositions of most of the small plagioclase crystals follow the general trend predicted for fractional crystallization, suggesting plagioclase compositions are controlled by the evolving magma chemistry. Large phenocrysts have higher An contents than predicted by the model (Figure 4-11). The higher An contents suggest that the phenocrysts Ca# content. Such high Ca# plagioclase phenocrysts have been found by others, but high Ca# melts are not commonly found in MORB (Ridley et al., in prep; Pan and Batiza, 2003).

Chemical analyses of cores of small spinel phenocrysts and cores, interiors, and rims of the larger spinel phenocrysts are presented in Appendix B. The Cr# (100*Cr/(Cr + Al)) of the spinels range from 25-58 and generally decrease from core to rim (Figure 4-13). The $Fe_2O_3$ content (2.08-7.07 wt. %) and $TiO_2$ content (0.12-0.98 wt. %) of the spinels are low; similar to other spinels from MORB (Dick and Bullen, 1984; Allan et al., 1988). The $Fe^{3+}/(Cr + Al + Fe^{3+})$ vs. $Fe^{2+}/(Mg + Fe^{2+})$ compositions of the Siqueiros spinels fall within the range and have trends observed in spinels from other MORB lavas (Figures 4-14). The Siqueiros spinels generally follow the Cr-Al trend observed in other spinel suites, but the larger phenocrysts in particular, have low $Fe^{2+}/(Mg + Fe^{2+})$ for a

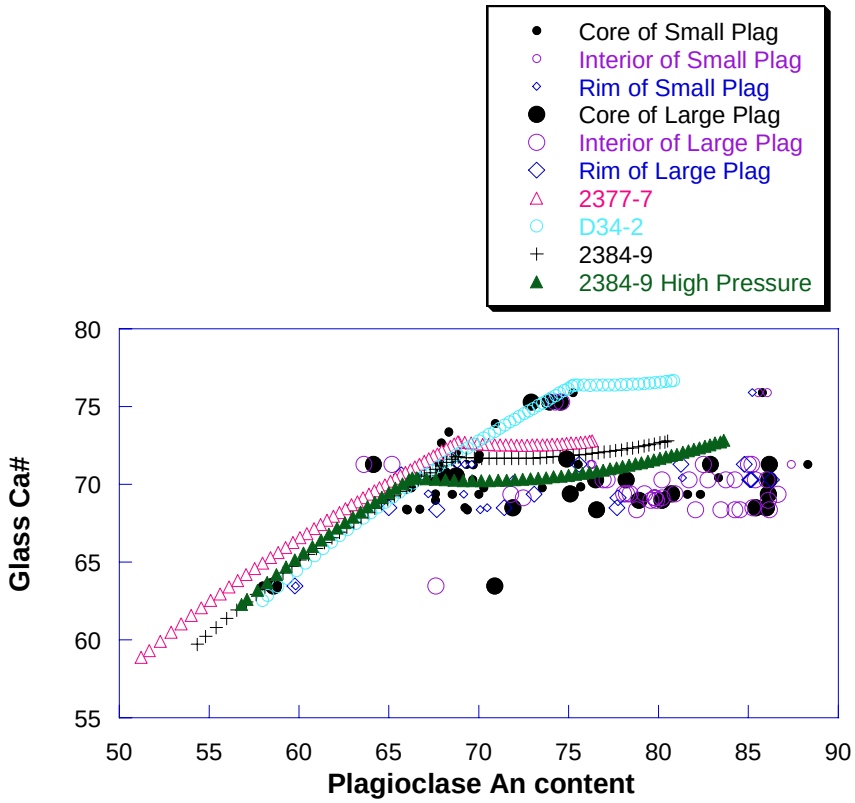


Figure 4-11. Comparison of the host glass Ca# (100*Ca/(Ca + Na) with the plagioclase An content. Modeled equilibrium trends expected during fractional crystallization were calculated using low pressure model of Danyushevsky (2001). Modeled trends fit the many of the smaller plagioclase crystals, but are unable to explain many of the samples that have high An contents compared with the Ca# of their host glass.

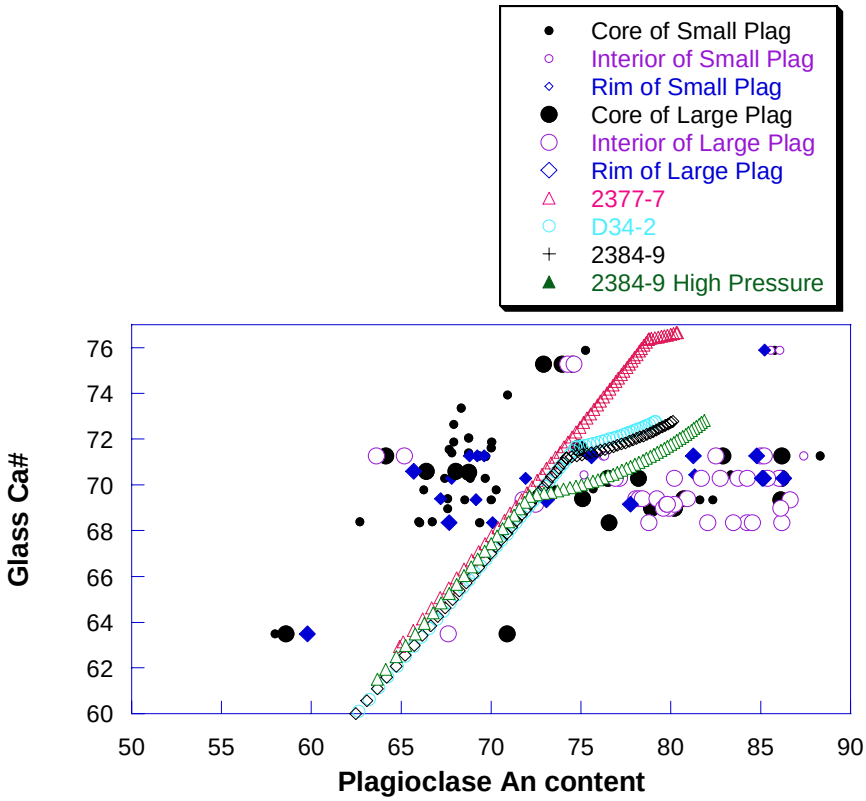


Figure 4-12. Comparison of Siqueiros plagioclase An content vs. glass Ca# (100*Ca/(Ca +Na)). Modeled equilibrium trends expected during fractional crystallization were calculated using the low pressure model of Langmuir et al. (1992). High pressure model is also shown for comparison. The Langmuir et al., 1992 model does not provide a good fit to any of the Siqueiros plagioclase compositions.

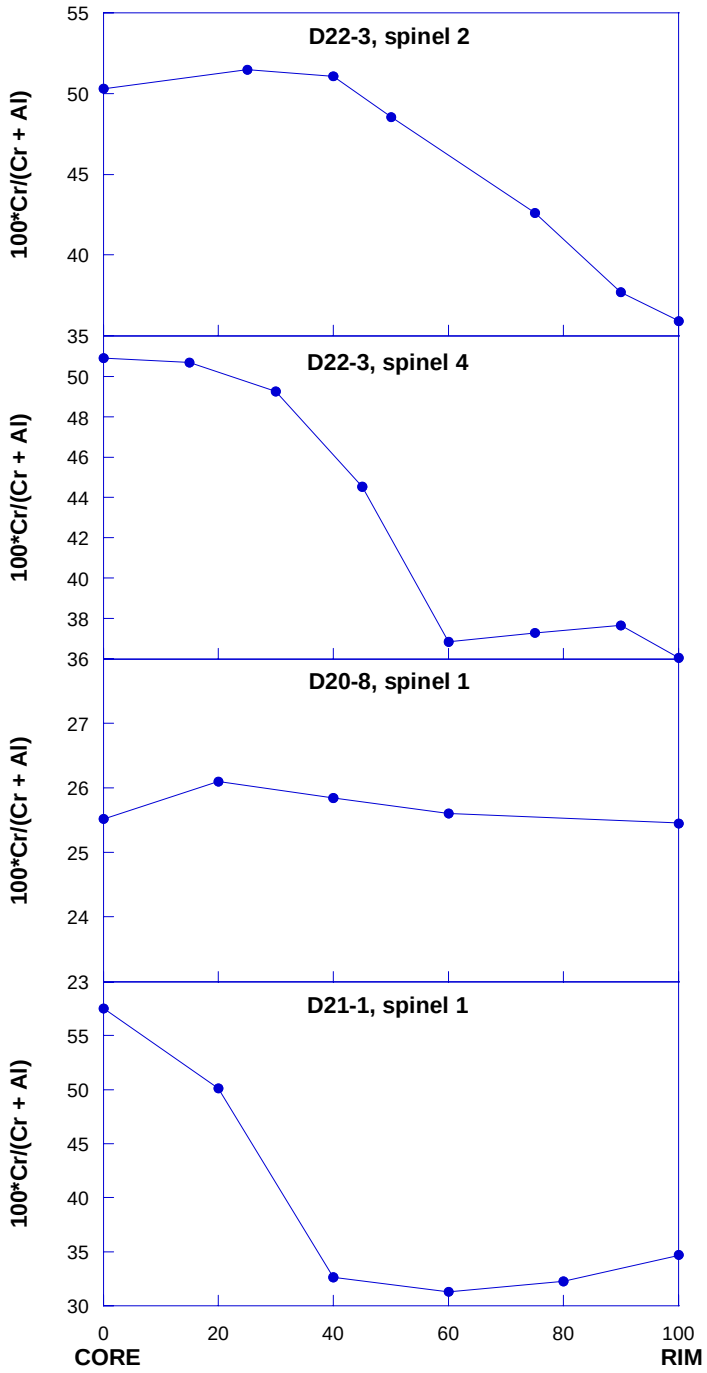


Figure 4-13. Spinel Cr# for core, interior, and rim locations.

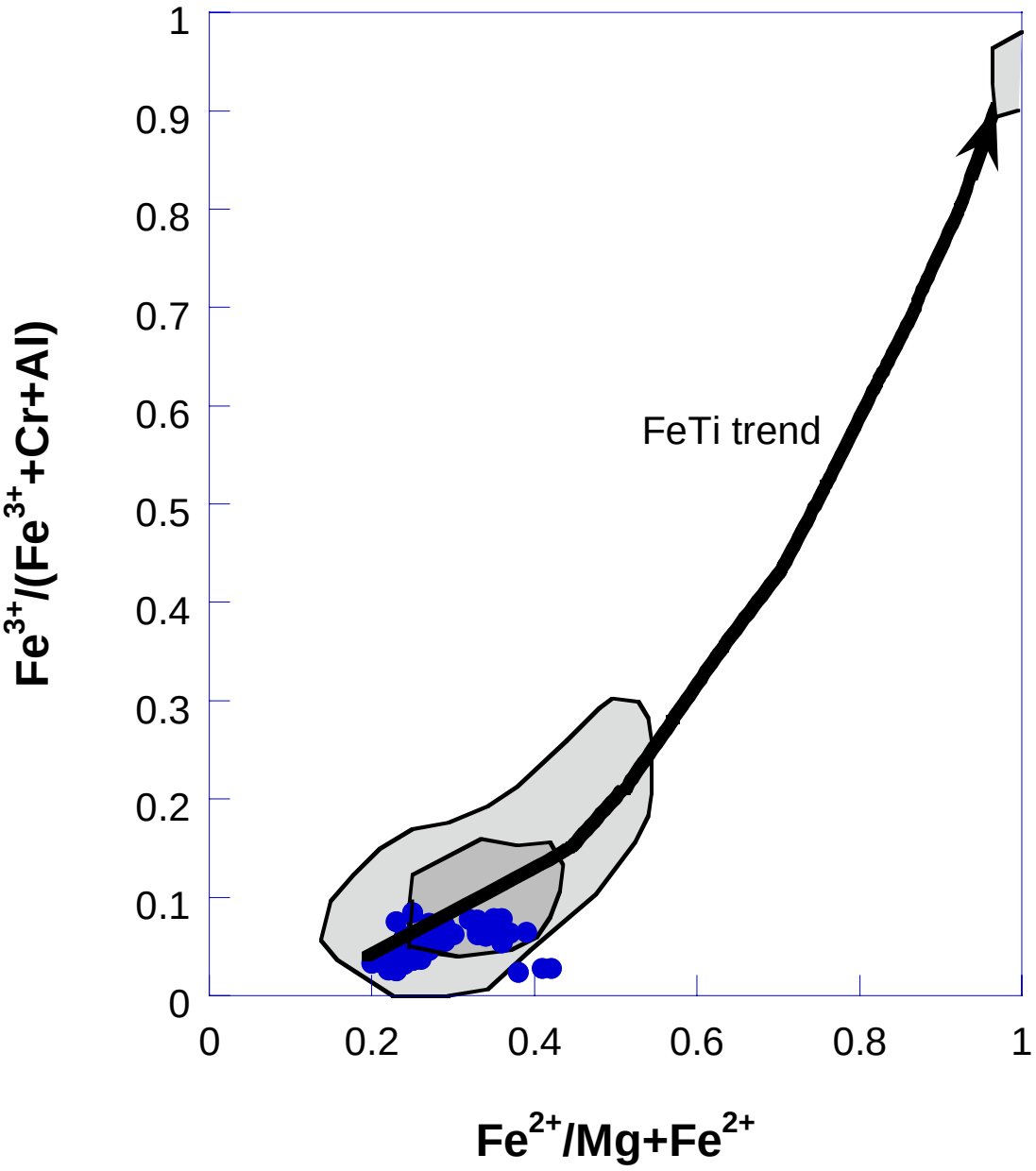


Figures 4-14. $Fe^{3+}/(Cr + Al + Fe^{3+})$ vs. $Fe^{2+}/(Mg + Fe^{2+})$ plots for tholeiitic basalts. Fields are from Barnes & Roeder, 2001 and enclose 50% (dark shading) and 90% (light shading) of the MORB data points.

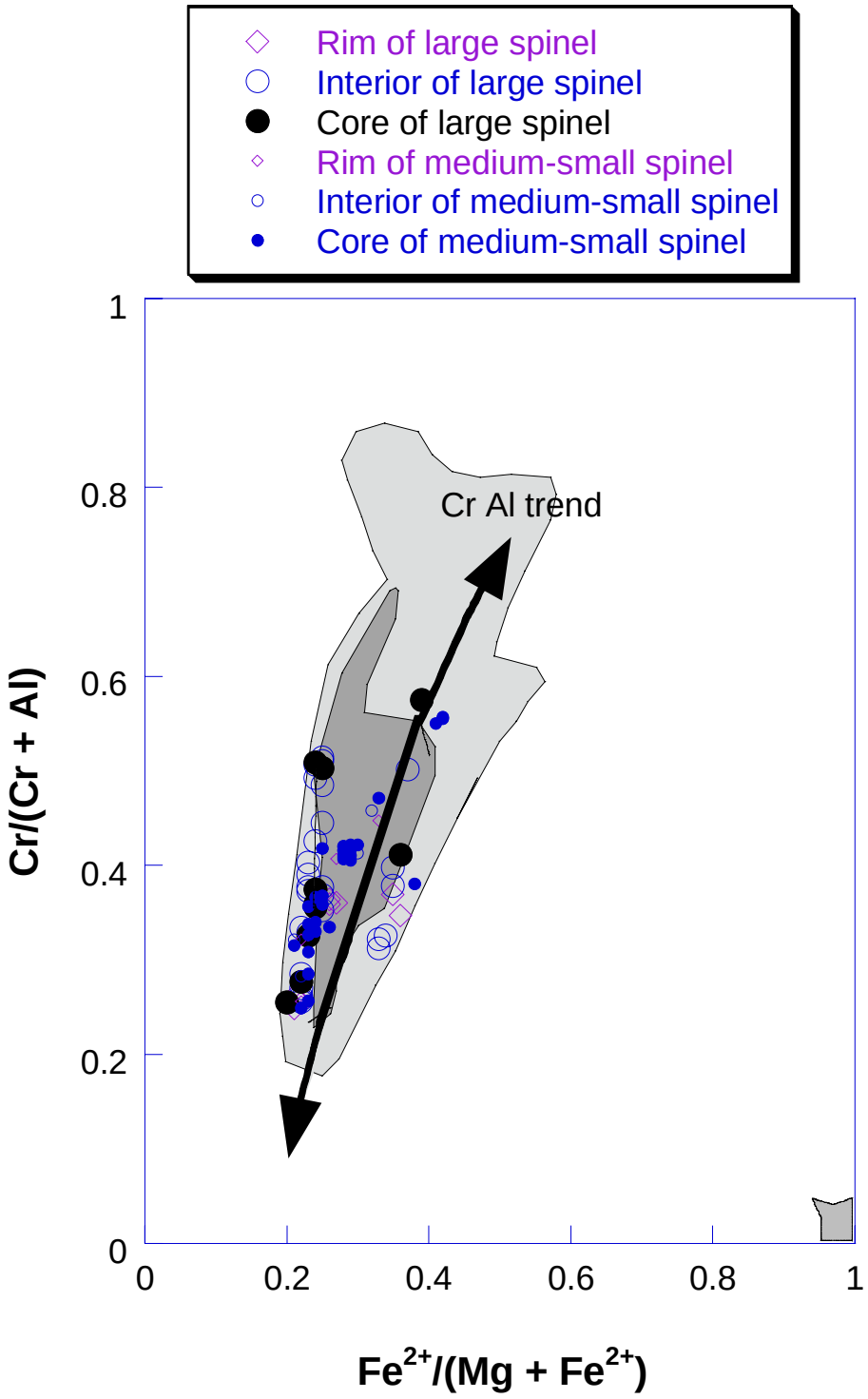


Figure 4-15. Cr/(Cr + Al) vs. $Fe^{2+}/(Mg + Fe^{2+})$ plot for tholeiitic basalts. Fields enclose 50% (dark shading) and 90% (light shading) of the MORB data points. MORB fields are from Barnes & Roeder, 2001.

given Cr/(Cr + Al) when compared to other MORB spinels (Figure 4-15). Comparison of the host-glass compositions with spinel compositions shows a strong correlation between the Al content of spinel rims and glass, but not for core and interior compositions (Figure 4-16). Similar correlations between Al content of the host rock and spinel have been found in other MORB lavas (Sigurdsson and Schilling, 1976, Allan et al. 1988, Dick and Bullen, 1984). A strong correlation also exists between the Mg# of the host glass and the Mg# of the spinels, with the strongest correlation observed for rim compositions (Figure 4-17). The Cr# of the Siqueiros spinels is independent of the host MgO content (Figure 4-18) as found in the Lamont Seamounts (Allan et al., 1988) but contrary to the results of Irvine (1976). Some small spinels are present in the groundmass glass. These show Mg# and Cr# correlations similar to those observed in the larger spinels attached or enclosed in olivines (Figure 4-19). There was no correlation between glass Mg# and spinel Cr# for either type of spinel phenocrysts (Figure 4-20).

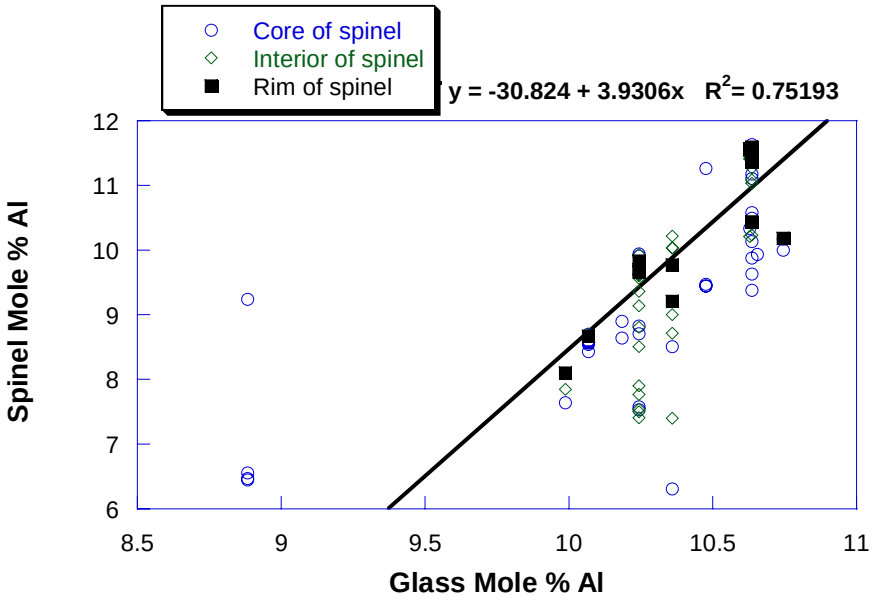


Figure 4-16. Molecular percentage aluminum in glass versus molecular percentage aluminum in spinel. There is a fairly linear relationship for rim compositions of the spinels, but the there is less of a relationship for core and interior compositions.

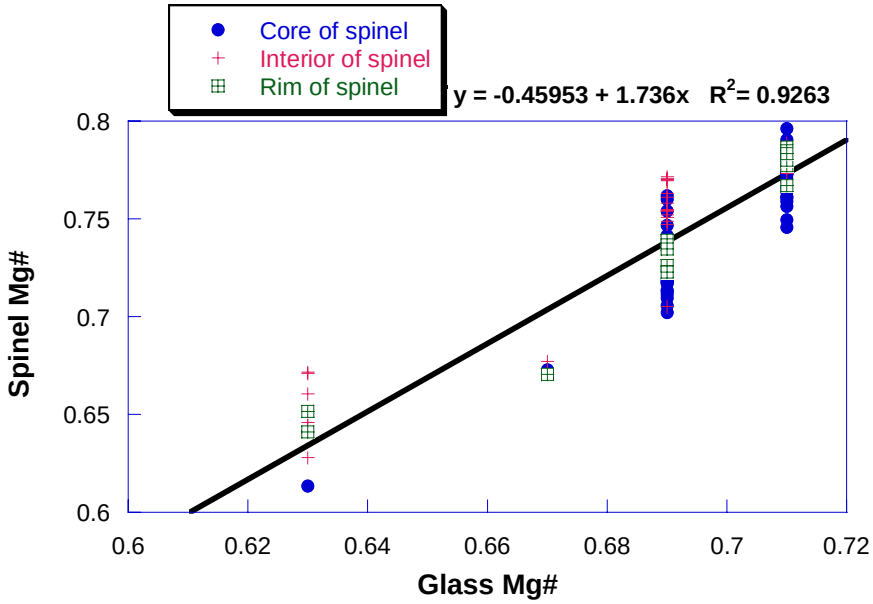


Figure 4-17. Comparison of the composition of the cores, interiors, and rims of spinels found in the groundmasses and within olivines with the composition of the host glass. A strong correlation can be seen between spinel and glass Mg#.

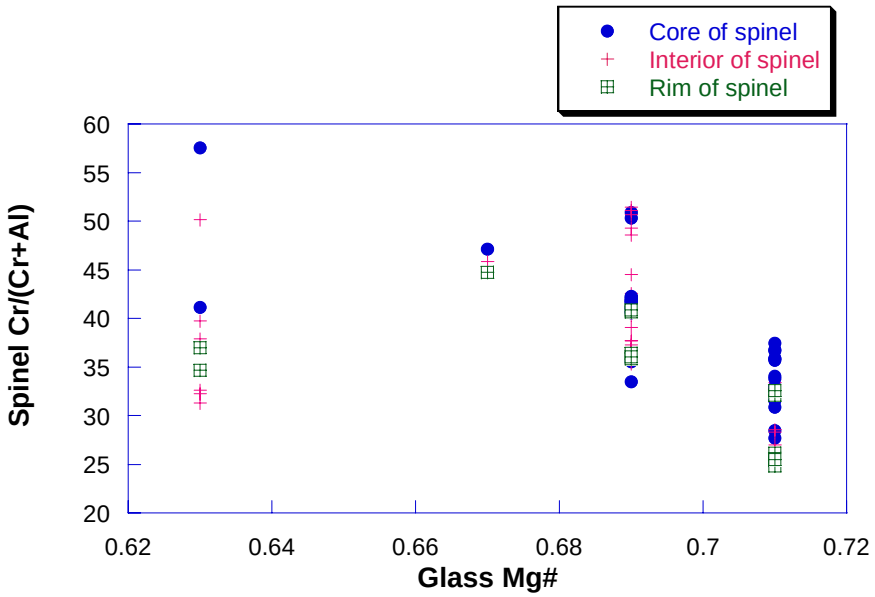


Figure 4-18. Comparison of the composition of the cores, interiors, and rims of spinels found in the groundmasses and within olivines with the composition of the host glass. There is a poor correlation between host glass and spinel Cr/(Cr + Al).

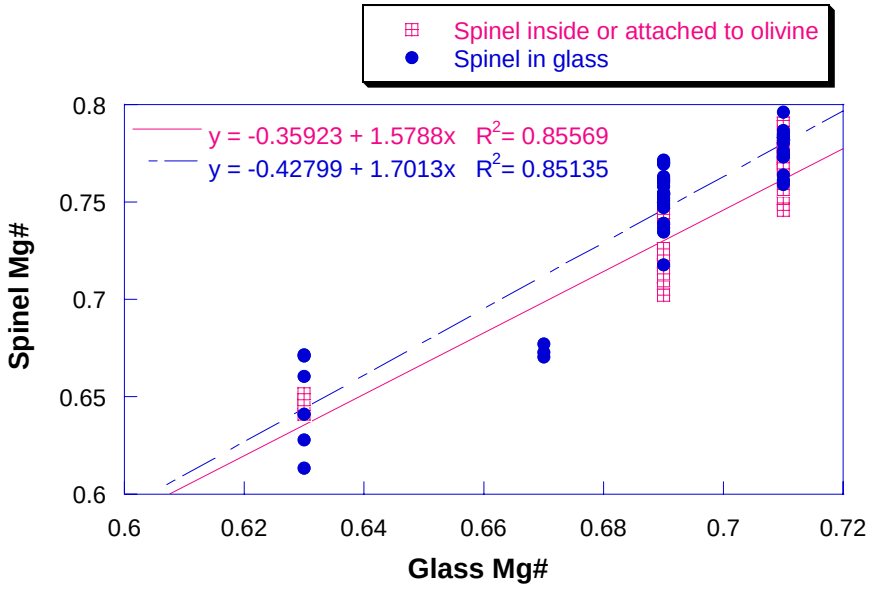


Figure 4-19. Comparison of the composition of the spinels found inside olivines and spinels found in the glass with the composition of the host glass. A strong correlation between spinel and glass Mg# exists for both types of spinels.

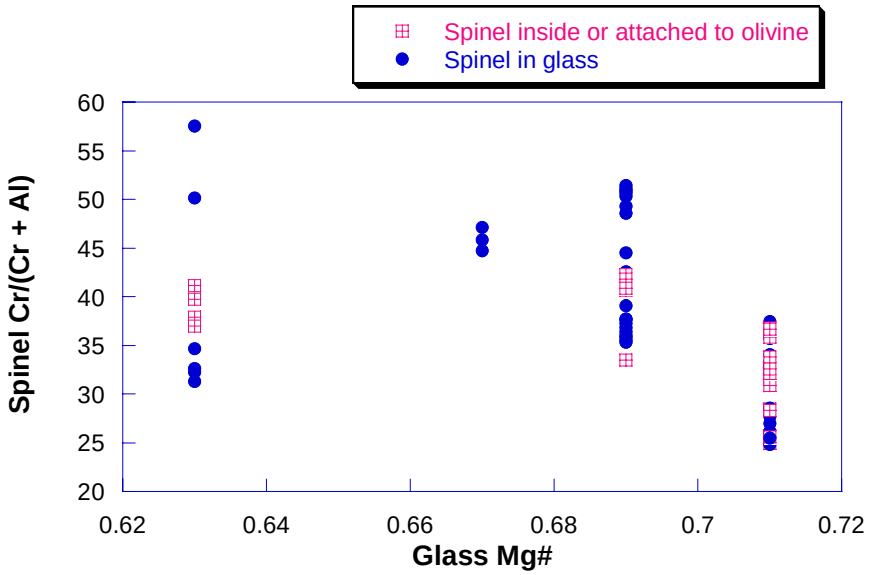


Figure 4-20. Comparison of the composition of the spinels found inside olivines and spinels found in the glass with the composition of the host glass. There is poor correlation between host glass Mg# and spinel Cr/(Cr + Al) for both types of spinels.

# CHAPTER 5
# MAJOR AND TRACE ELEMENT CHEMISTRY

## Major Element Trends

The major element compositions of Siqueiros basalt samples are presented in Appendix C and are shown in Figures 5-1 and 5-2. For comparative purposes, the samples in Figures 5-1 and 5-2 are divided into groups according to the geologic setting from which they were recovered. Basalt samples analyzed in this study include samples from the three spreading centers (A, B, and C), trough D, the 3 connecting transform faults (A-B, B-C, and C-D), the western ridge transform intersection (WRTI), and the eastern ridge transform intersection (ERTI). The lavas from the Siqueiros transform domain can be classified as tholeiitic basalts having low $K_2O$ and total alkali contents as well as showing FeO enrichment trends with decreasing MgO; characteristic of tholeiitic suites (Tilley, 1950). The MORB recovered include picrites, picritic basalts, basalts, ferrobasalts, and a few Fe- and Ti-enriched (FeTi) basalts. Classification of a ferrobasalt is defined as containing greater than 12 wt. % FeO, but less than 2 wt. % $TiO_2$, while FeTi basalts are defined as containing greater than 12 wt. % FeO and $TiO_2$ contents greater than 2 wt. % . The MORB can be further divided into N-MORB (normal, incompatible element-depleted mid-ocean ridge basalts), D-MORBs (exceptionally depleted, incompatible element-depleted mid-ocean ridge basalts), E-MORB (incompatible element-enriched mid-ocean ridge basalts), and T-MORB (mid-ocean ridge basalts transitional between N-MORB and E-MORB). There is currently some debate over the nomenclature of high-MgO volcanic rocks (Kerr and Arndt, 2001;

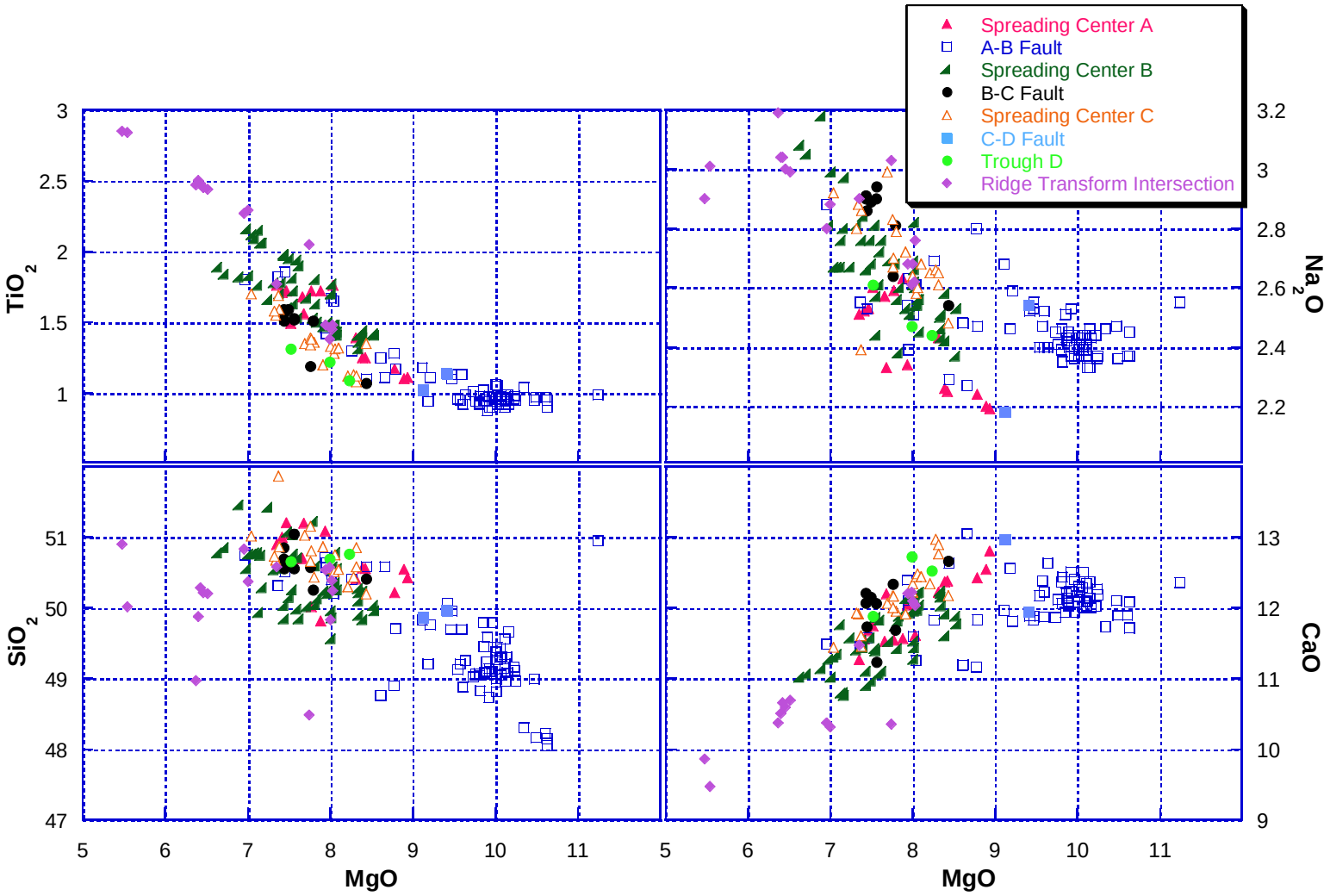


Figure 5-1. Major element variation diagrams for glasses from the Siqueiros transform domain. Samples are distinguished according to their geologic locations within the transform. Picritic basalts and picrites are not shown on this diagram.

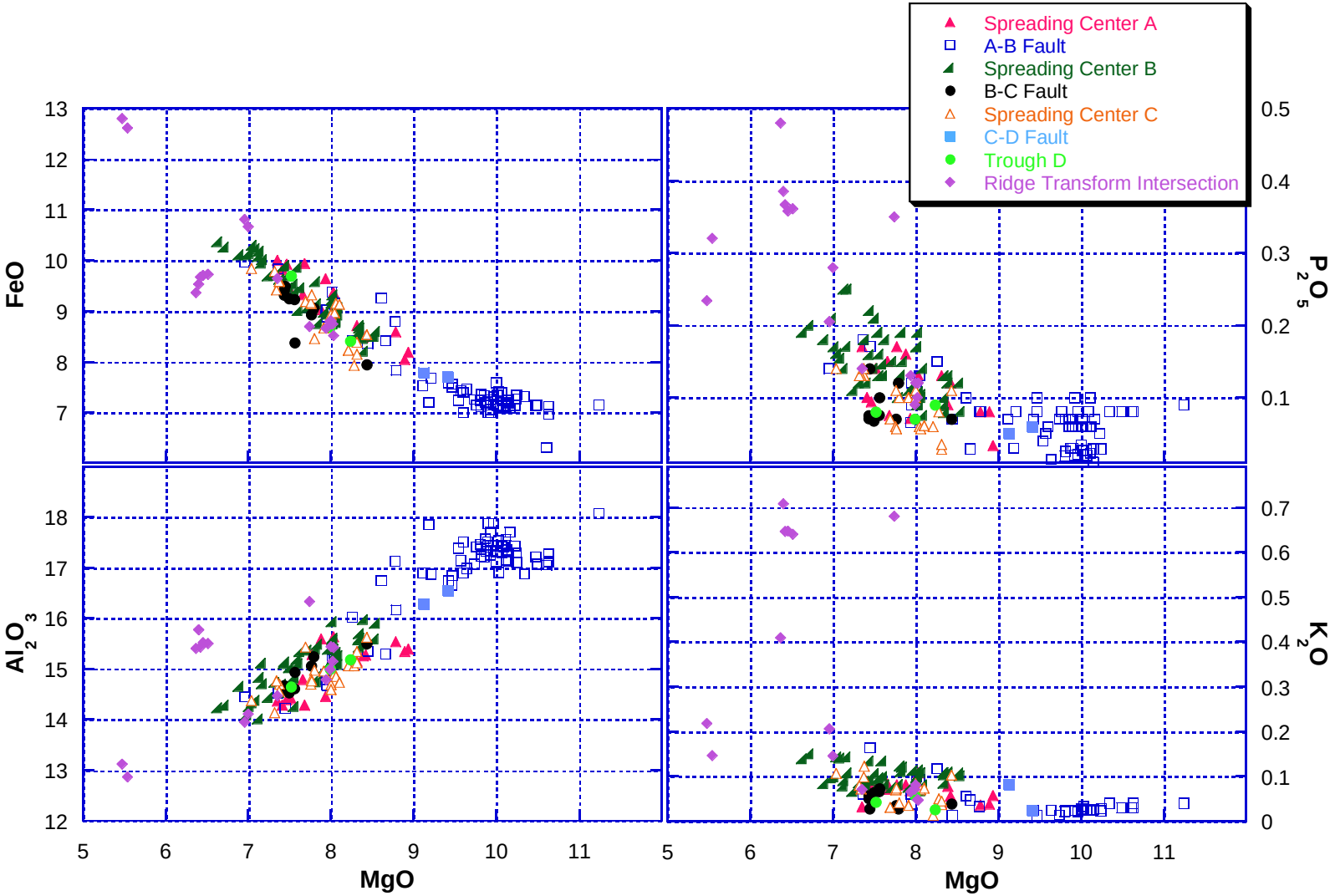


Figure 5-1. Continued.

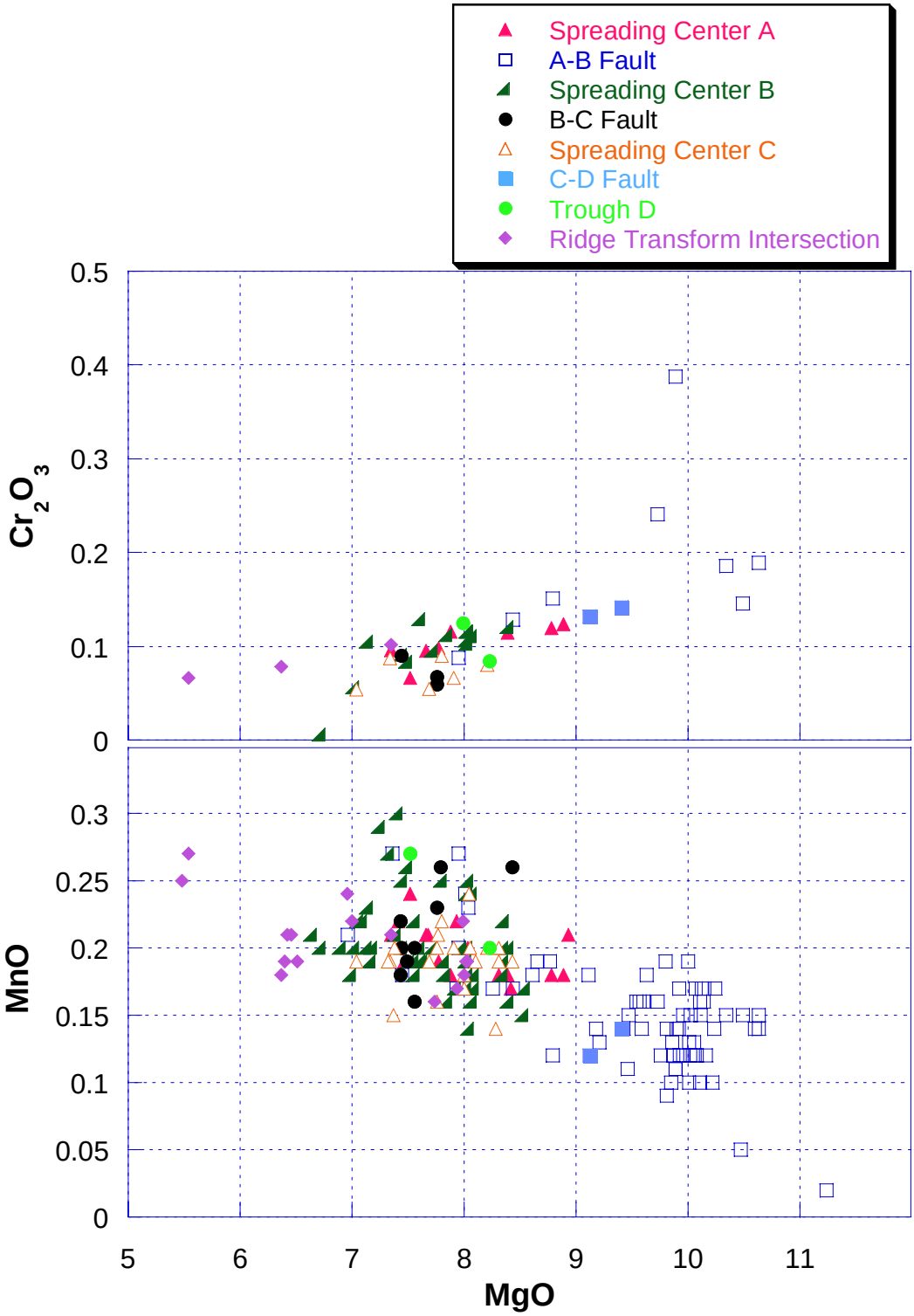


Figure 5-1. Continued.

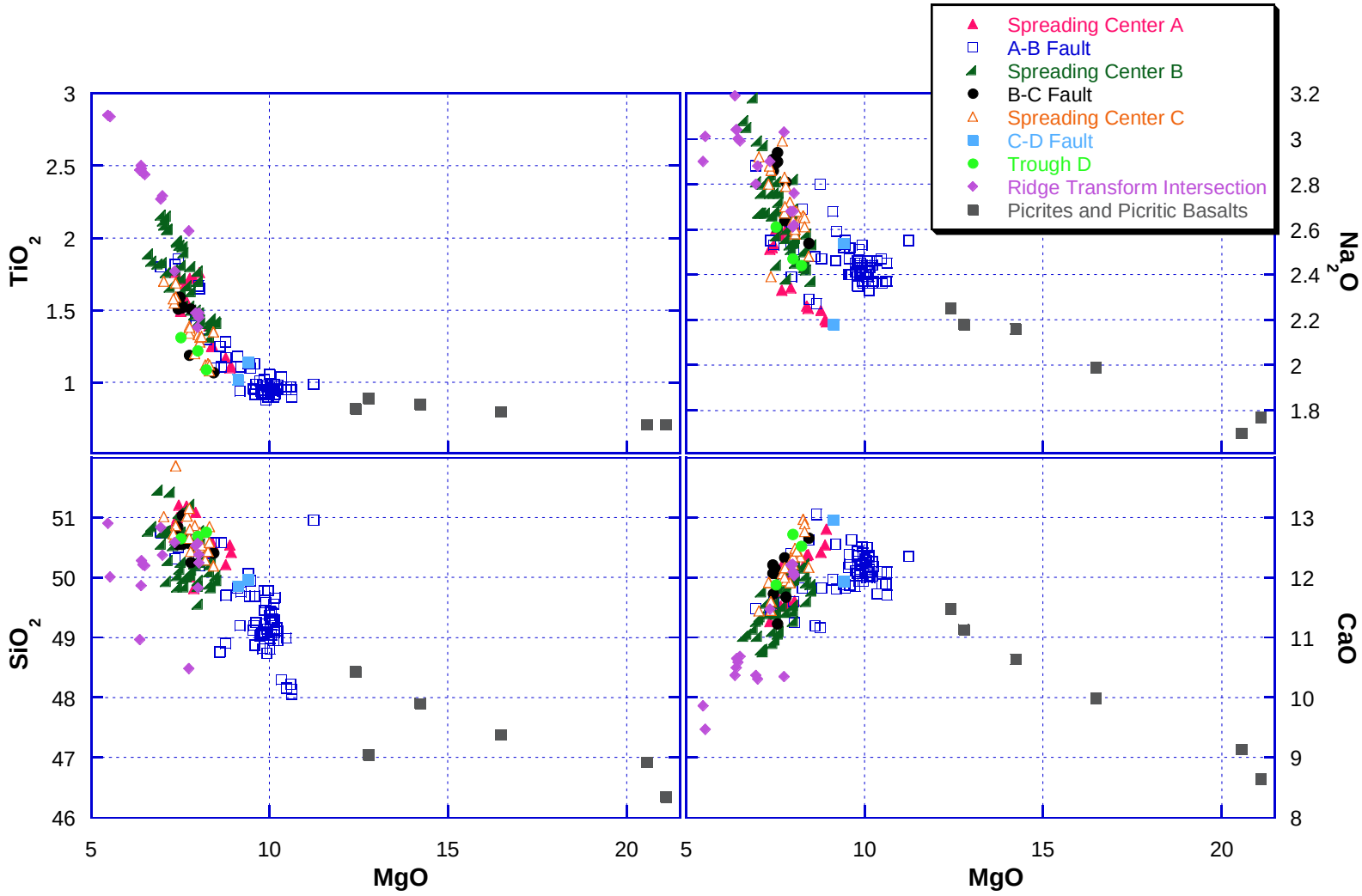


Figure 5-2. Major element variation diagrams showing the Siqueiros picrites and picritic basalts relative to more evolved MORB as in Figure 5-1. Picrites and picritic basalts were only recovered within the A-B fault.

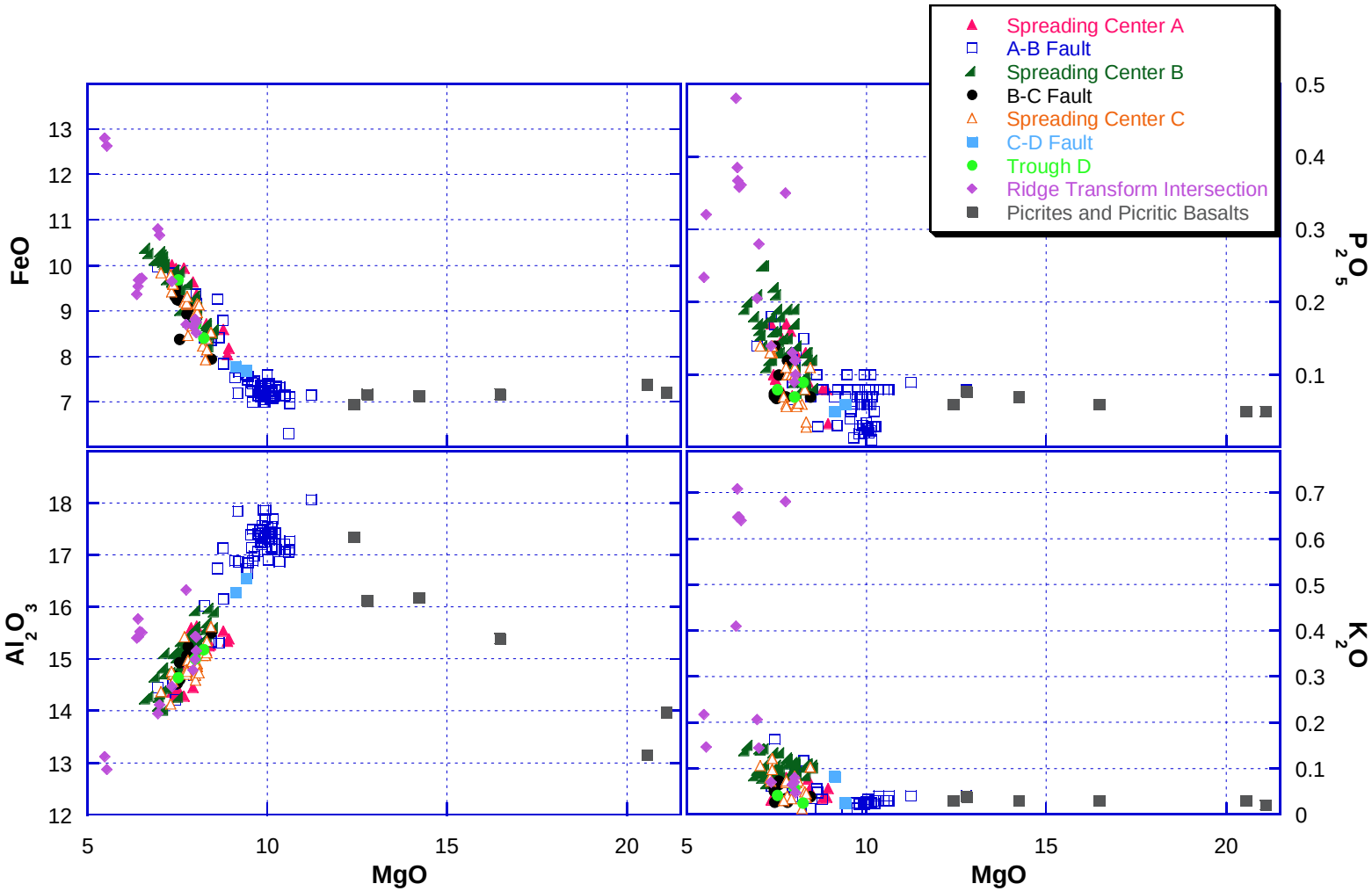


Figure 5-2. Continued.

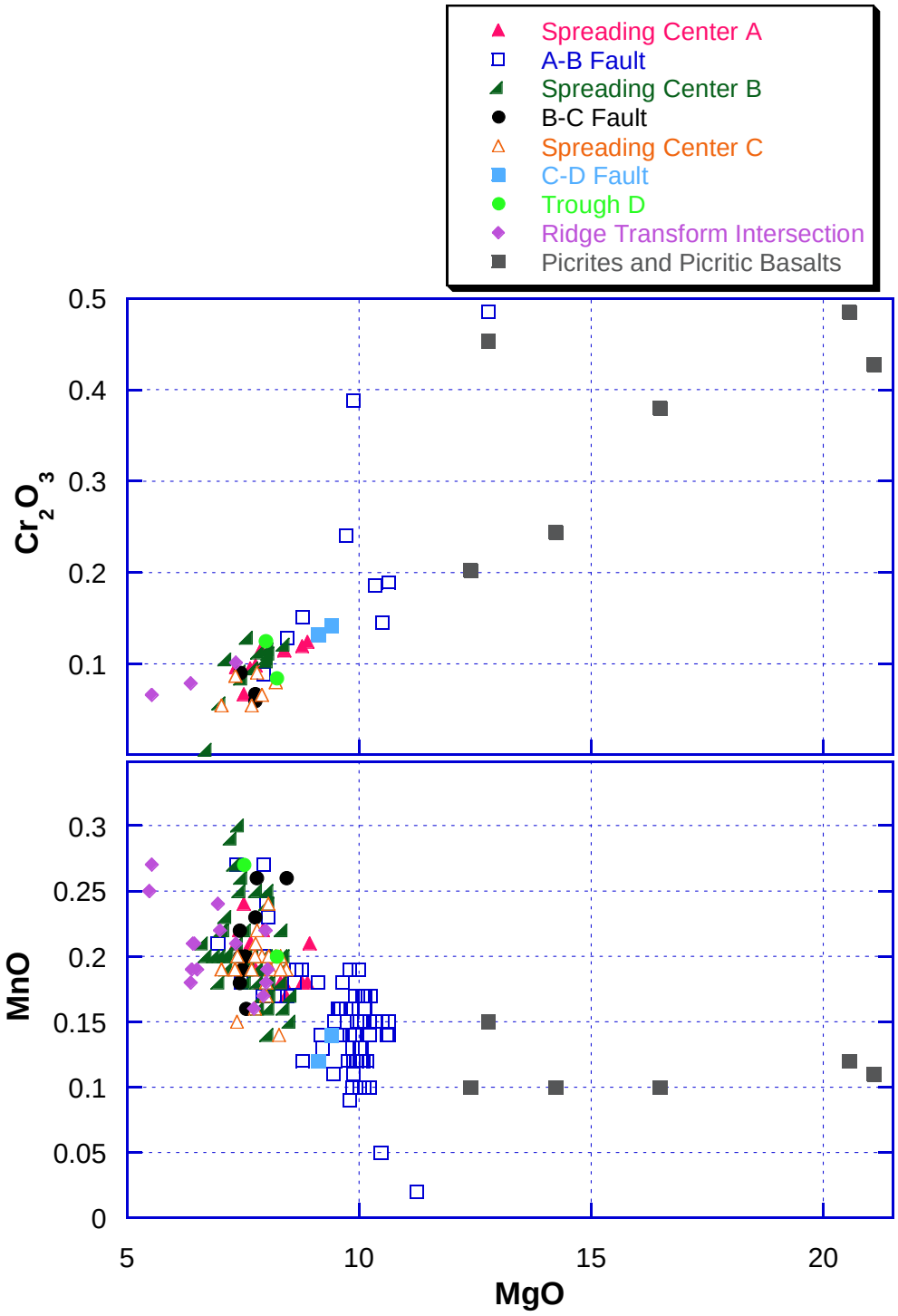


Figure 5-2. Continued.

Le Bas, 2001). The IUGS classification (Le Bas, 2001) for a picrite is >18 wt% MgO with between 1 and 2 wt% total alkalis. This definition is based entirely on the chemistry of the rock. Others (Kerr and Arndt, 2001) advocate for a definition that places greater emphasis on the texture of the rock, which reflects the conditions of crystallization. Such definitions require an abundance of olivine phenocrysts in order for a rock to be classified as a picrite. Of the rocks analyzed for this study, only two can be classified as picrites by the IUGS classification. These two rocks are also rich in olivine phenocrysts and fit into the textural definition of a picrite. The term picritic basalt is used to describe highly magnesian rocks that are also olivine phyric, but have MgO contents too low (12-18 wt% MgO) to be classified as picrites. The picrites and picritic basalts have only been found within the A-B fault.

Where trace element analyzes are not available the ratio of $K_2O$ to $TiO_2$ can be used as a proxy to discriminate between depleted (Ce/Yb < 1) and enriched (Ce/Yb > 1) samples (Perfit et al., 1994.) In the database for the 9°-10°N segment of the EPR there is a natural break at $K_2O/TiO_2 = 0.11$. Samples with $K_2O/TiO_2$ values < 0.11 are considered N-MORB, which have normal incompatible element-depleted signatures (Smith et al., 2001). The majority of samples recovered from the 9°-10°N area are N-MORB, but a small percentage (~15%) of samples found off-axis (300-500 m) have values > 0.11 and are transitional to incompatible element enriched basalt (T-MORB or E-MORB). For the 11-12° segment of the EPR, the depleted versus enriched sample break was found to correlate with a $K_2O/TiO_2$ value of 0.25 (Hekinian et al., 1989). The $K_2O/TiO_2$ ratios of the Siqueiros samples are shown in Figure 5-3. In the Siqueiros samples there is a break between $K_2O/TiO_2$ values < 0.10 and $K_2O/TiO_2$ values greater

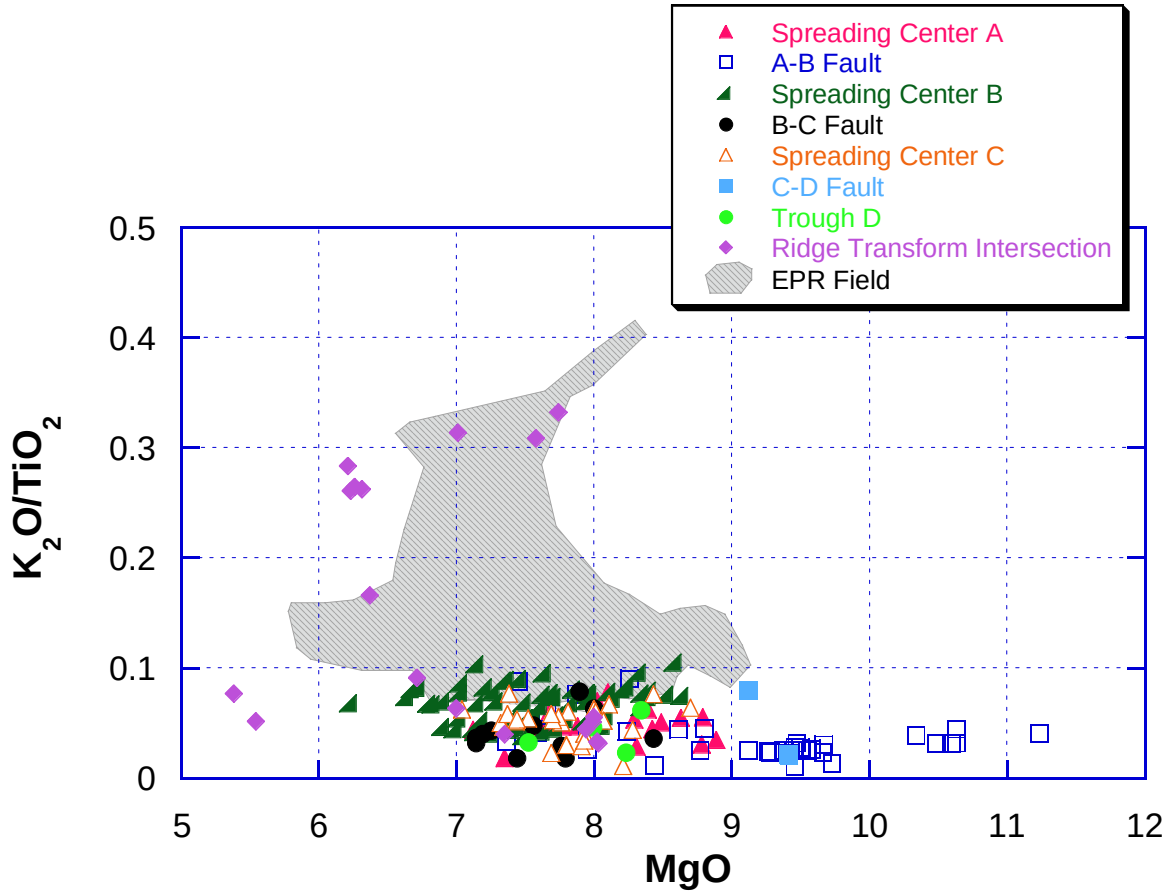


Figure 5-3. Comparison of $K_2O/TiO_2$ of Siqueiros samples with samples from the EPR. A $K_2O/TiO_2 > 0.11$ indicates an enriched sample. The Siqueiros samples are very depleted when compared to the EPR field.

than 0.15. All of the samples with $K_2O/TiO_2$ values greater than 0.15 are from the RTI and the group includes sample 2390-1, which is well documented to be incompatible element enriched as well as to have higher $^{87}Sr/^{86}Sr$ than all other MORB from the region (Lundstrom et al., 1999). For the Siqueiros sample suite, $K_2O/TiO_2$ values $\leq 0.11$ correlate with depleted Ce/Yb ratios (Discussed in Trace Element Trends section).

Unlike the EPR, none of the Siqueiros samples have transitional $K_2O/TiO_2$ values between 0.15 and 0.25 (Figure 5-3). Compared to the EPR, Siqueiros samples are significantly more depleted and include very few enriched samples. Only the samples from spreading center B that have higher $K_2O/TiO_2$ values and the enriched RTI samples overlap with the EPR field.

The Siqueiros samples have a narrow range in MgO content with a relatively primitive average of 8.31 wt. % MgO. The most primitive MORB are found within the A-B fault (MgO contents of ~ 10-10.5 wt. %), but were recovered near basalts that had MgO contents of ~7 wt. %. The most evolved MORB are found near the RTIs (MgO contents of 5.38 wt. %) and were recovered with samples that have as much as ~8 wt. % MgO. The most primitive samples have FeO, and $TiO_2$ contents (in wt. %) of 7.13% and 0.93%, respectively and the most evolved samples have FeO and $TiO_2$ contents of 12.79%, and 2.85%, respectively.

Most of the variation seen in major elements on the segment scale is due to low-pressure crystallization in shallow magma chambers (Perfit et al., 1983; Langmuir et al., 1992; Batiza and Niu, 1992). Low-pressure crystallization results in changes in melt compositions that vary systematically with MgO, which has been shown to decreases during cooling due to the removal of olivine from the melt (Langmuir et al., 1992). The

basalts from the Siqueiros transform exhibit major element variations that appear to mainly reflect the effects of crystal fractionation (Figures 5-1 and 5-2). In the Siqueiros sample suite, FeO and $Na_2O$ contents steadily increase with decreasing MgO content. $P_2O_5$, $K_2O$, and $TiO_2$ also increase with decreasing MgO, but to greater relative extents. MnO and $SiO_2$ show a little more scatter, but also generally increase with decreasing MgO. $Cr_2O_3$ decreases with decreasing MgO and CaO and $Al_2O_3$ both initially increase and then decrease with decreasing MgO. These variations are compatible with initial olivine fractionation, followed by plagioclase fractionation, and finally clinopyroxene fractionation (Batiza et al., 1977; Perfit et al., 1996).

Comparison of the 3 spreading centers shows that the major element variations of lavas from the 3 spreading centers are generally very similar. Spreading center B does contain samples that are slightly more evolved (MgO < 7%) and has some samples with slightly higher $TiO_2$, $Al_2O_3$, $P_2O_5$, and $K_2O$ for a given MgO when compared to the other spreading centers and the faults. Spreading center A has a group of samples with lower $Na_2O$ for a given MgO content when compared with all other Siqueiros samples (Figure 5-2). The most primitive samples were recovered from the A-B fault and all of the picritic basalts were found within this fault. The other faults, B-C and C-D, also contain some samples that are relatively primitive in comparison to the spreading centers. When compared to the other localities within the Siqueiros transform, samples from the B-C fault have low $TiO_2$, $K_2O$, FeO, and $P_2O_5$ values. Fault B-C has the most evolved samples of the 3 intra-transform shear zones. The most evolved samples from the entire transform domain were recovered along the western ridge transform intersection (WRTI). A subset of these samples from the WRTI are very different and do not appear to be

related by fractional crystallization to the other Siqueiros samples. Compared to all other samples from the Siqueiros transform, these RTI samples have higher $Al_2O_3$ and lower $P_2O_5$, $K_2O$, $Na_2O$, and CaO contents for a given MgO.

The samples from spreading center B, which exhibits the most symmetric spreading pattern, were compared to determine whether or not there is symmetry of lava composition about the axis and to determine if there is a systematic change in lava chemistry with time (distance from axis) for the intra-transform spreading centers. As basalts are carried off-axis by spreading, they record the chemical composition of the axial melt lens at the time they were erupted. If the basalts are not buried beneath younger, off-axis flows, the distribution of lava compositions may show systematic differences in magma chamber chemistry with time.

Spreading center B was chosen because it is the most well sampled and it appears to be the most well developed spreading center in the Siqueiros transform. Morphological symmetry of ridges can be identified up to 30-40 km from the axis of spreading. This suggest that spreading center B has been active longer than the other spreading centers, which only exhibit symmetry 10-20 km from the spreading centers. Variations in MgO content and depth to seafloor were compared with the sample's distance from the axis of B (Figure 5-4). Samples recovered from the axis have a wide range in MgO contents (~7-8.5 wt. %). Most of the samples with the highest MgO contents were found within the axis, but high MgO samples were also found on the western side. The most evolved samples were found furthest east from the axis. Smooth fit lines of depth and MgO variation with distance from the axis show no correlation between sample depth and MgO content. Based on the samples recovered, there does not

appear to be a symmetrical variation in MgO contents or any systematic change in lava chemistry with distance or depth, but sampling is too sparse off axis to truly evaluate this.

**Comparison of Siqueiros Samples to the Adjacent EPR and Garrett Transform**

MORB mantle compositional heterogeneities exist on various scales: global, regional and local. Local variability can exist on segment and sub-segment scales with compositional variations along and across axis for individual segments and even within individual lava flows (Perfit & Chadwick, 1998). In order to better understand global and regional variability, the major element contents of the Siqueiros samples were compared to that of the adjacent EPR and the Garrett transform in order to determine how the samples relate to the regional chemistry of the EPR and the chemistry of lavas erupted in other fast slipping transforms (Figures 5-5 and 5-6).

The major element compositions of Siqueiros samples can be compared to the well studied 9-10°N segment of the EPR, which is directly north of the transform. Most of the Siqueiros samples from the 3 intra-transform spreading centers fall within the EPR fields. Siqueiros samples from the faults are less evolved and slightly more depleted in $K_2O$ and $P_2O_5$ than the EPR samples with the picrites and the picritic basalts from the A-B fault and some of the samples from the C-D fault being particularly less evolved than the EPR lavas. A few of the samples from the RTIs fall outside the EPR field and are unlikely to be related to the EPR samples by fractional crystallization.

Siqueiros samples from the 3 intra-transform spreading centers and transform shear zones are similar to Garrett transform basalts, but have slightly lower $P_2O_5$, $K_2O$, and $TiO_2$ contents. Lavas from spreading center A, which were found to be depleted in $Na_2O$

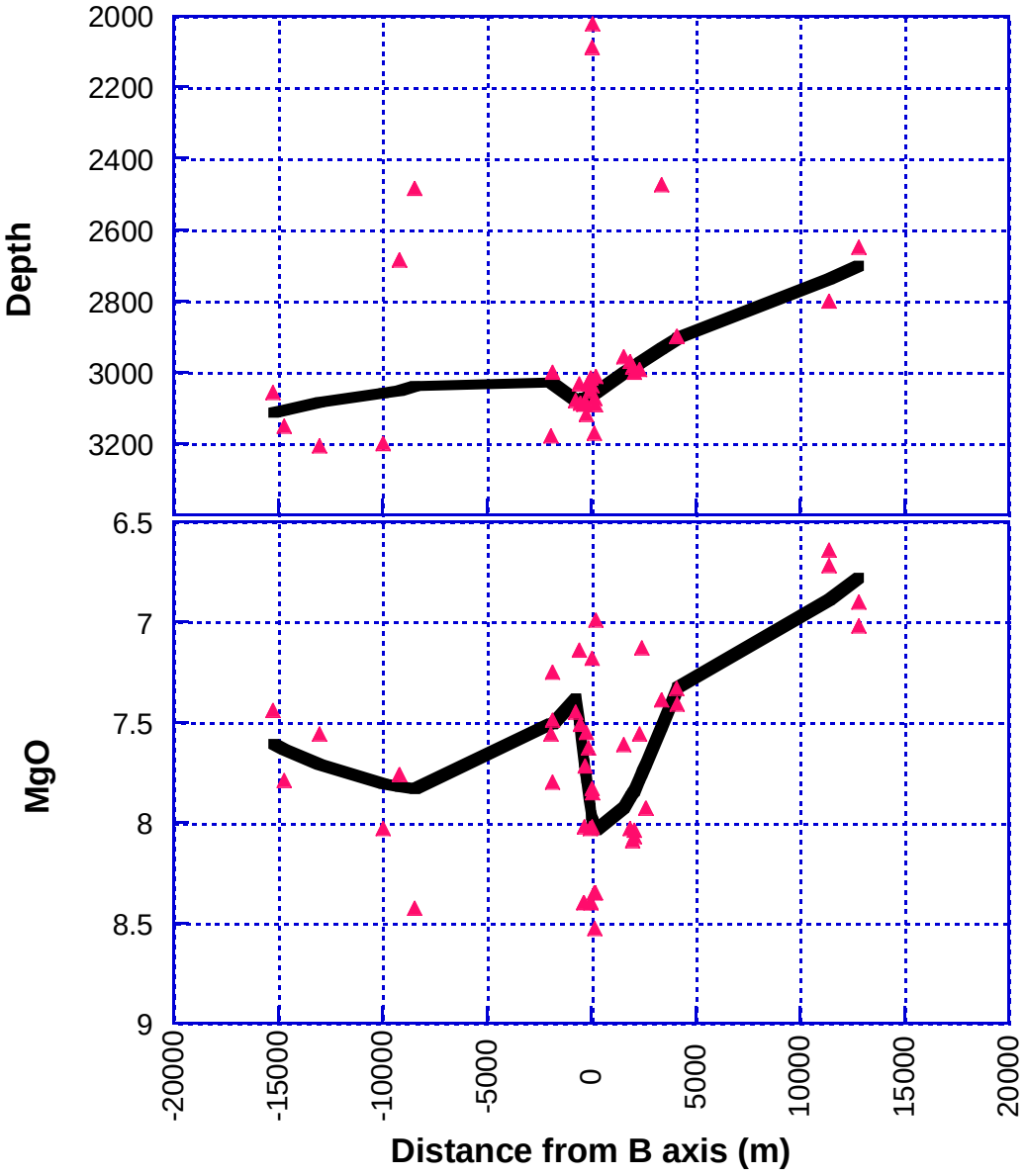


Figure 5-4. MgO (wt. %) and depth to seafloor versus distance from the axis of spreading center B. Negative values are west of the axis and positive values are east of the axis. Thick line is smooth fit trend.

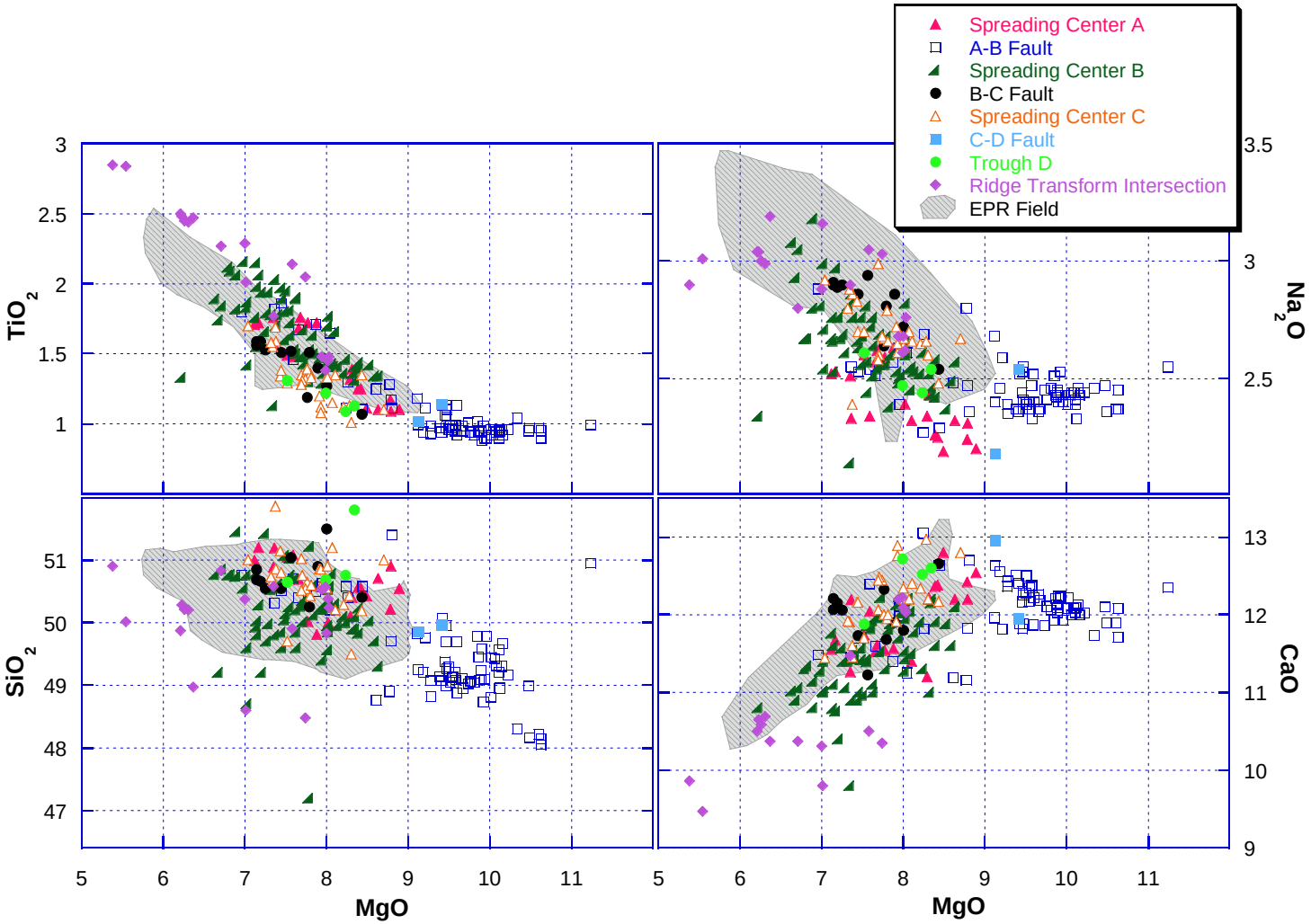


Figure 5-5. Variation diagrams comparing Siqueiros lava compositions with basalts from the 9-10°N segment of the EPR (Perfit et al., personal communication).

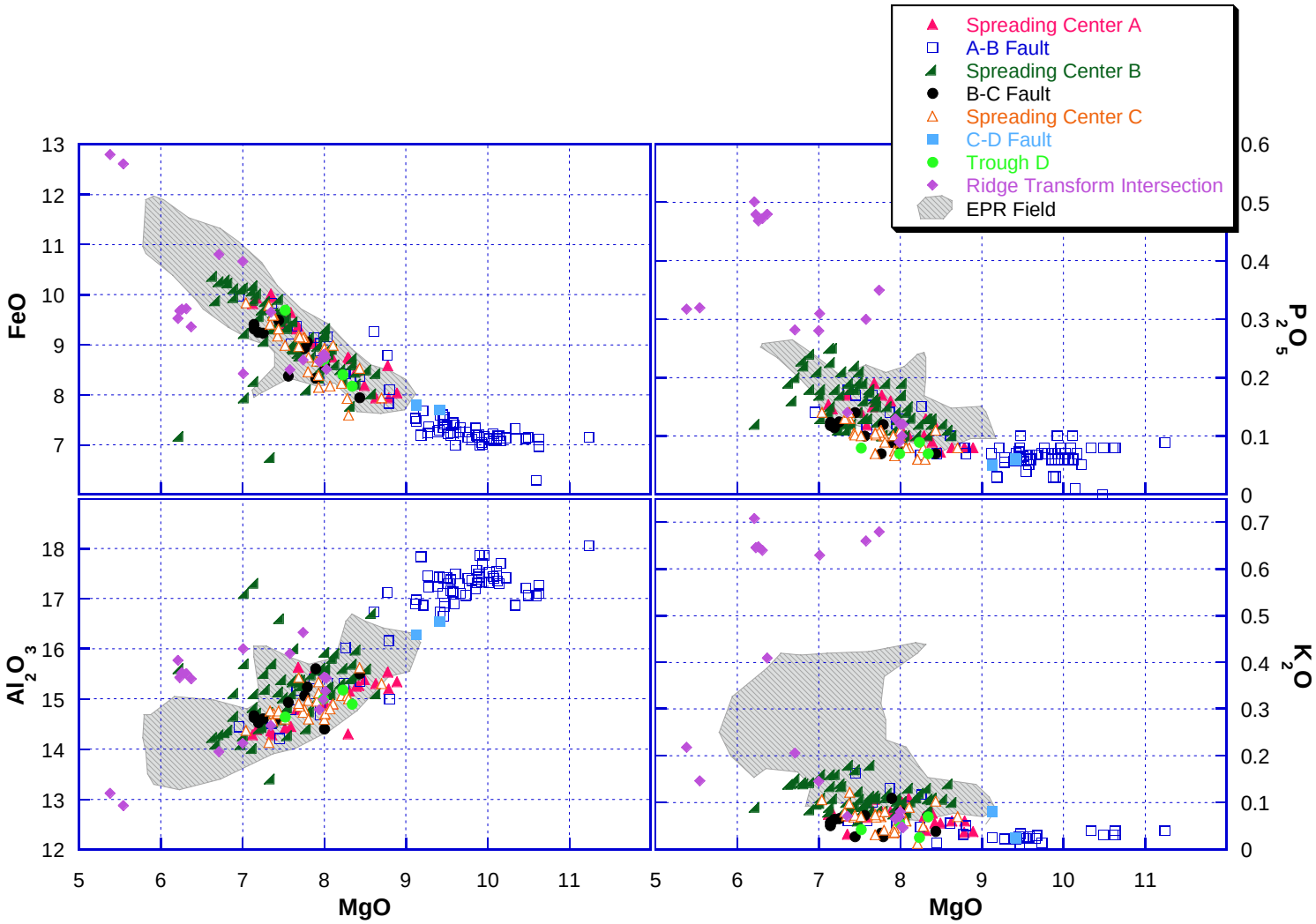


Figure 5-5. Continued.

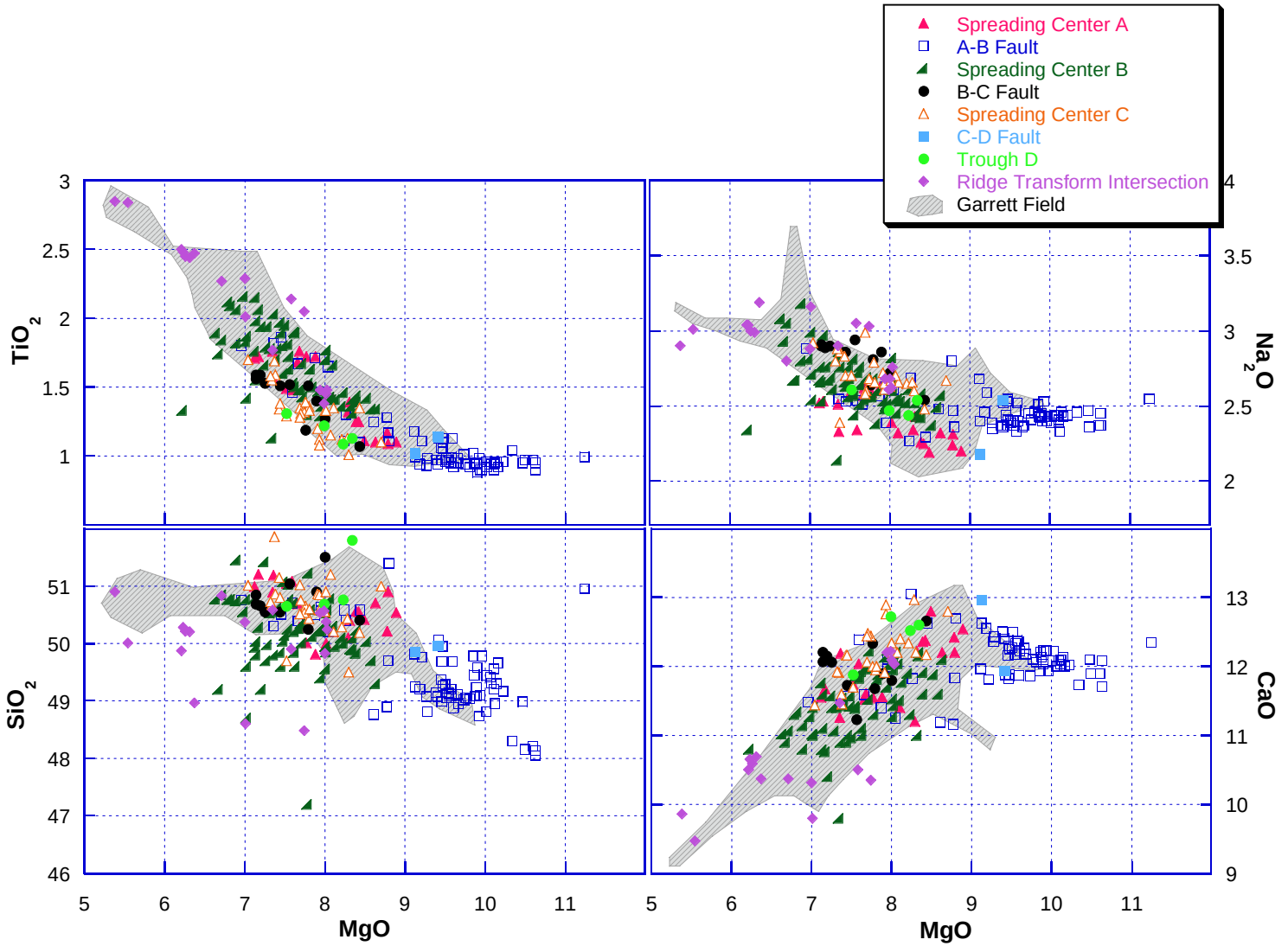


Figure 5-6. Variation diagrams comparing the compositions of the Siqueiros and Garrett samples (from Hekinian et al., 1995).

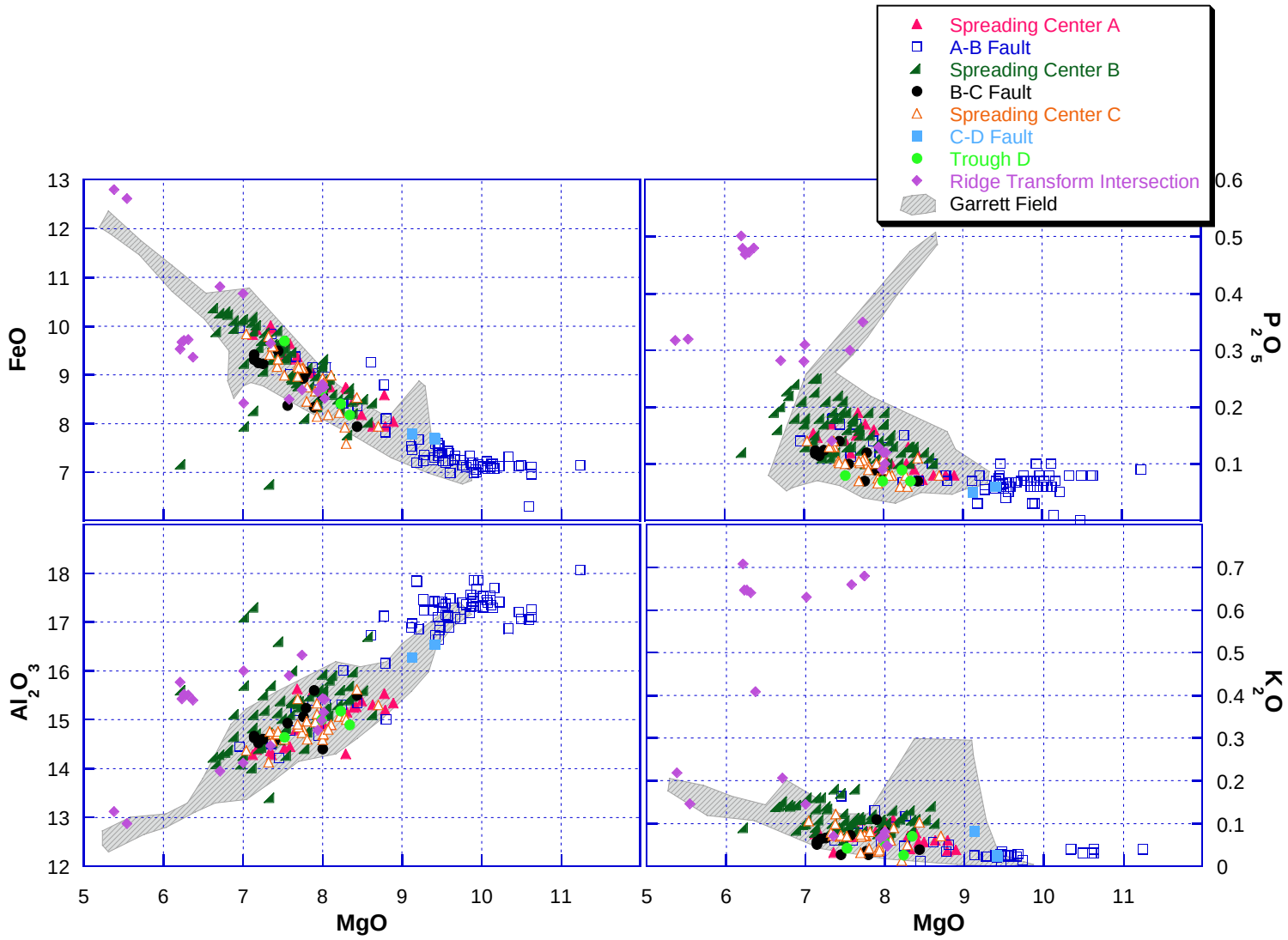


Figure 5-6. Continued.

compared to other Siqueiros samples, are also slightly depleted in $Na_2O$ compared to the Garrett samples. On average the RTI samples are more evolved than the Garret samples and are more enriched in $K_2O$ and $P_2O_5$.

## Trace Element Trends

The trace element contents of the Siqueiros samples are presented in Appendix D. Selected trace elements were plotted against $TiO_2$ and Zr, which both behave incompatibly during crystal fractionation and mantle melting (Figures 5-7 and 5-8). Incompatible element contents generally increase with increasing fractional crystallization, while compatible element contents decrease with magmatic evolution. The trace elements Ni and Cr behave compatibly exhibiting relatively coherent trends that decrease with increasing $TiO_2$ and Zr. Ni is compatible in olivine and initially decreases with fractionation. Cr is compatible in spinel and olivine and exhibits a very high initial decrease with fractionation. Y, V, and Zr all behave incompatibly and increase smoothly with increasing magma evolution. Sr, which is compatible in plagioclase, initially increases with increasing $TiO_2$ and Zr, but then levels off increasing only slightly with further magmatic differentiation.

In general the samples show a narrow range in total abundance for each trace element except for the RTI samples. Samples 2390-1, 2390-3A, 2390-3B, 2390-4, 2390-5, and 2390-8 are enriched in the trace element Sr and depleted in Y. Samples 2390-1 and 2390-5 are also slightly enriched in Ni when compared to the other evolved samples. These samples from the RTI do not appear to be related to the other samples by fractional crystallization and are classified as E-MORBs based on their Ce/Yb ratios. Samples RC-41 and D30-1 (both from the ERTI) and sample 2390-9 (from the WRTI) do not group with the other samples from the RTI, but appear more similar to those from the spreading

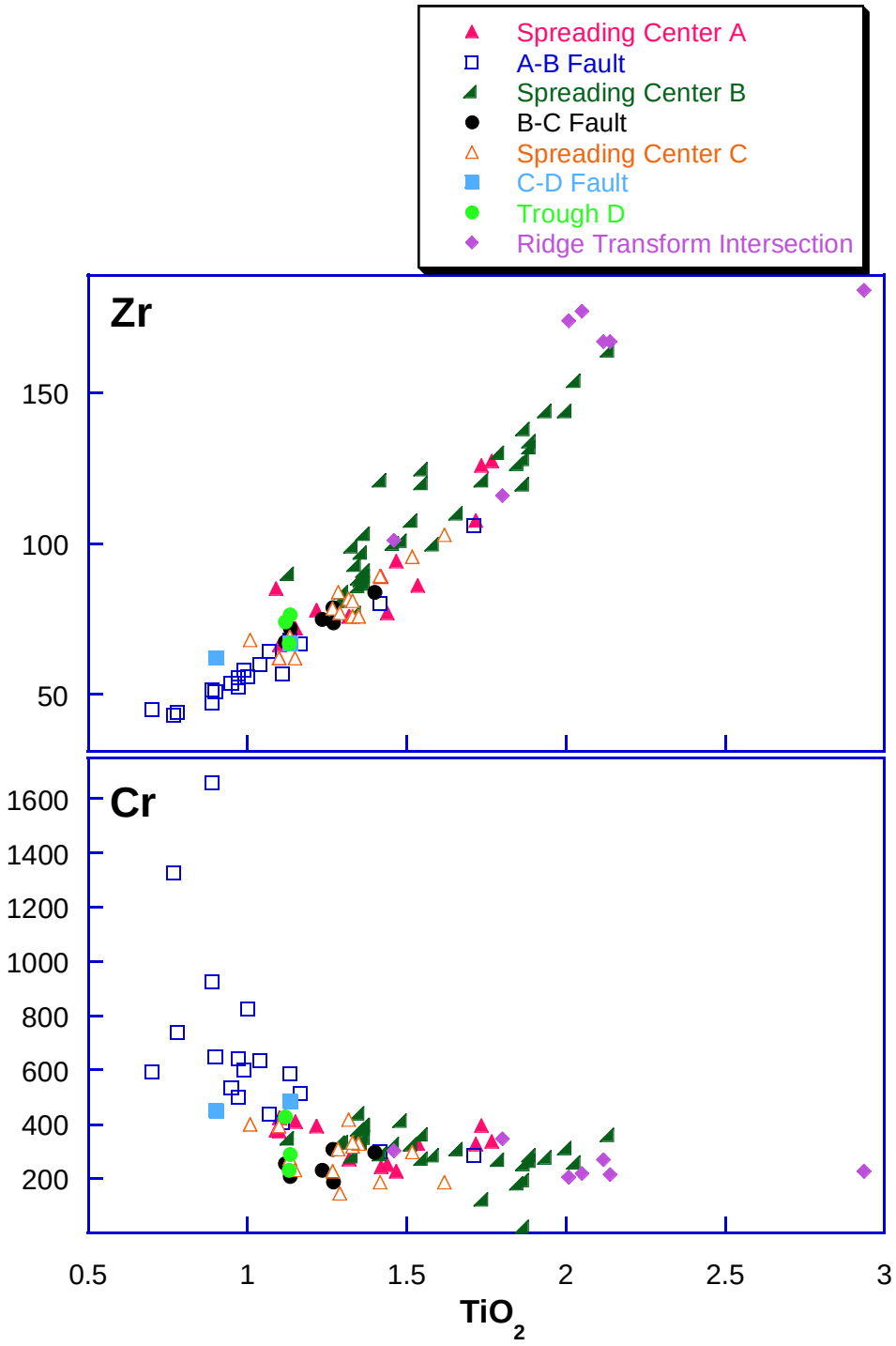


Figure 5-7. Trace elements versus $TiO_2$. Ti behaves incompatibly and increases with magma evolution. Trace element data from XRF and DCP analysis.

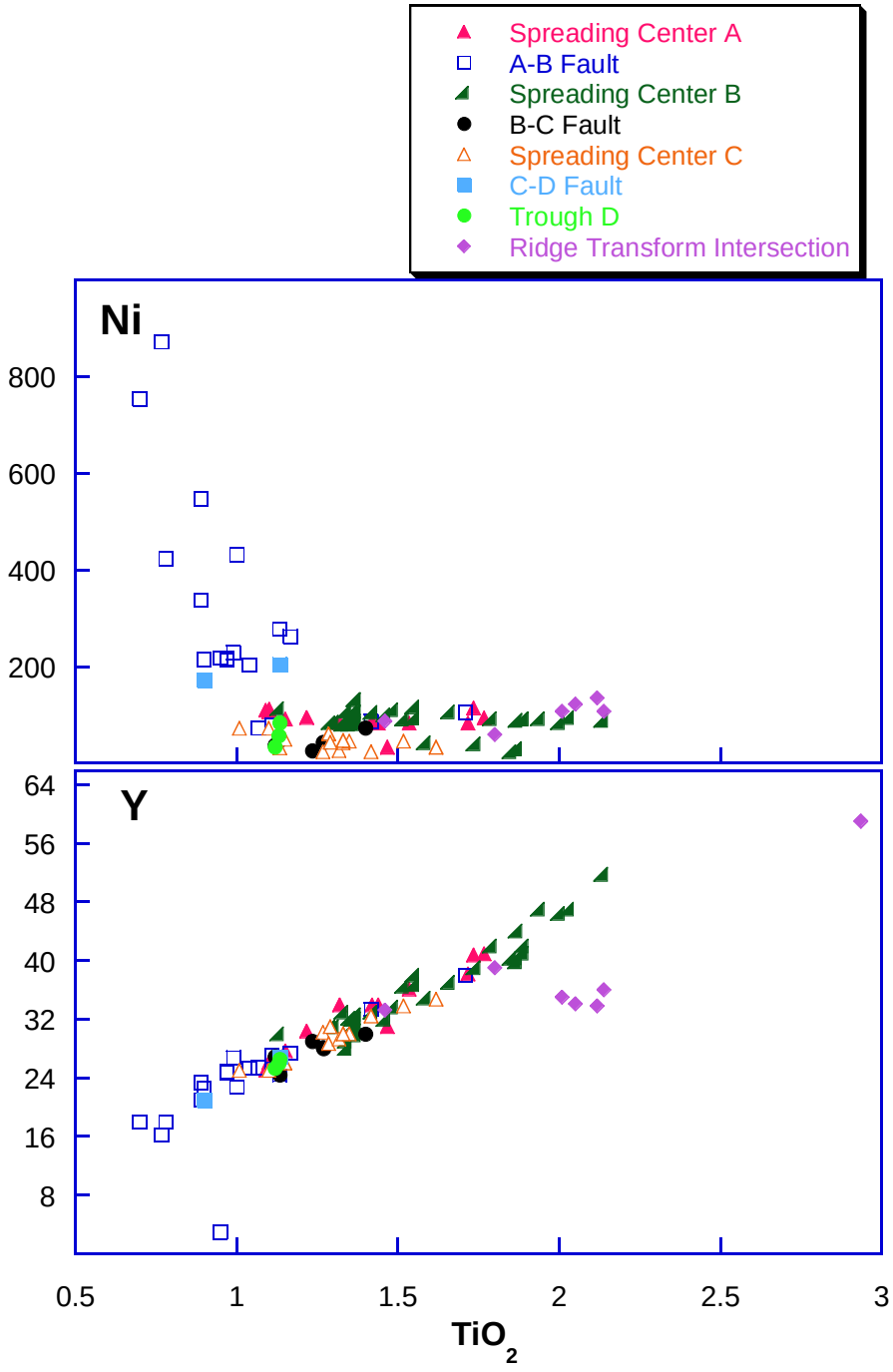


Figure 5-7. Continued.

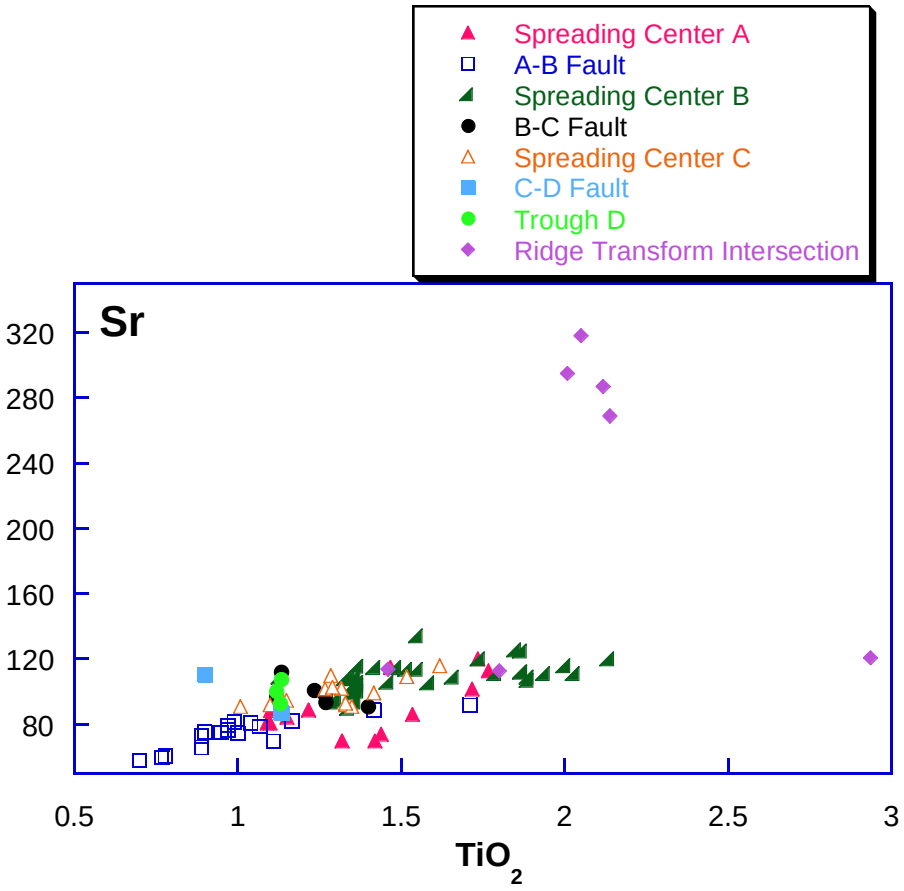


Figure 5-7. Continued.

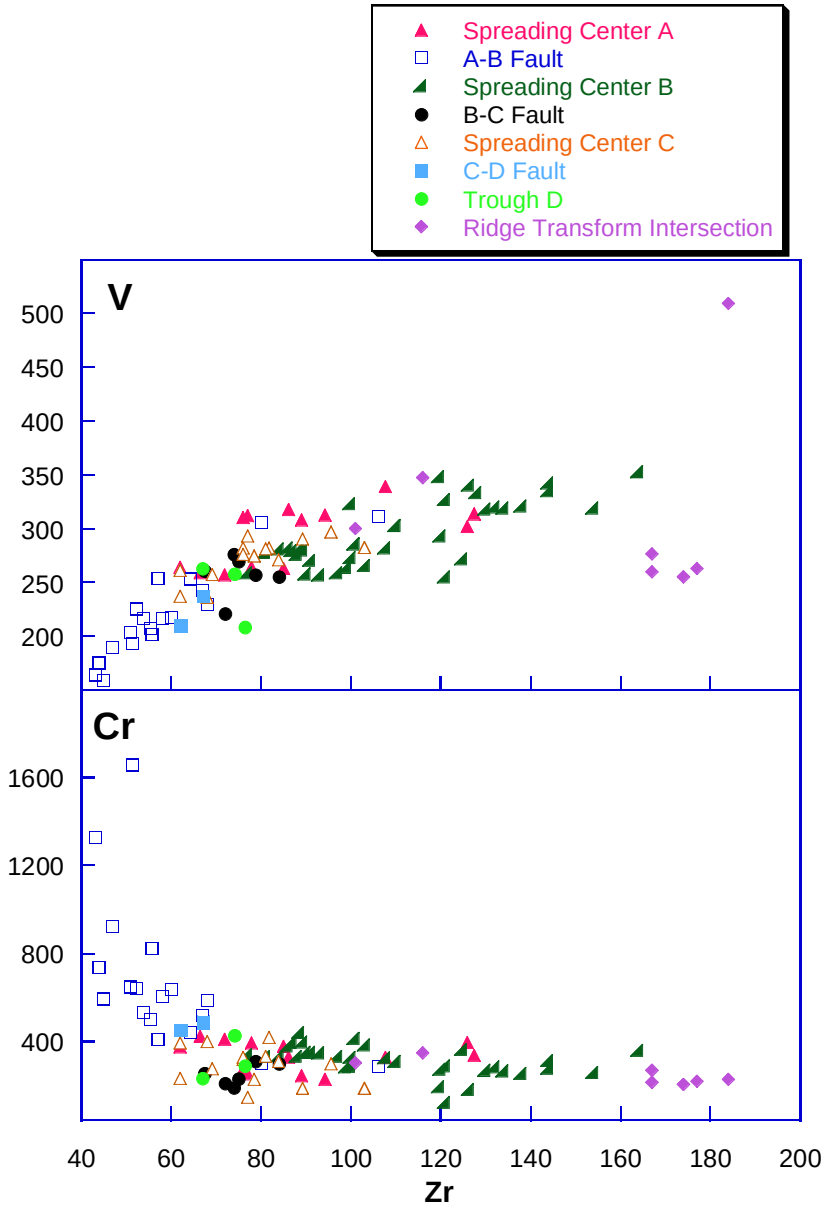


Figure 5-8. Trace elements versus Zr. Zr behaves incompatibly and increases with magma evolution. Trace element data from XRF and DCP analysis.

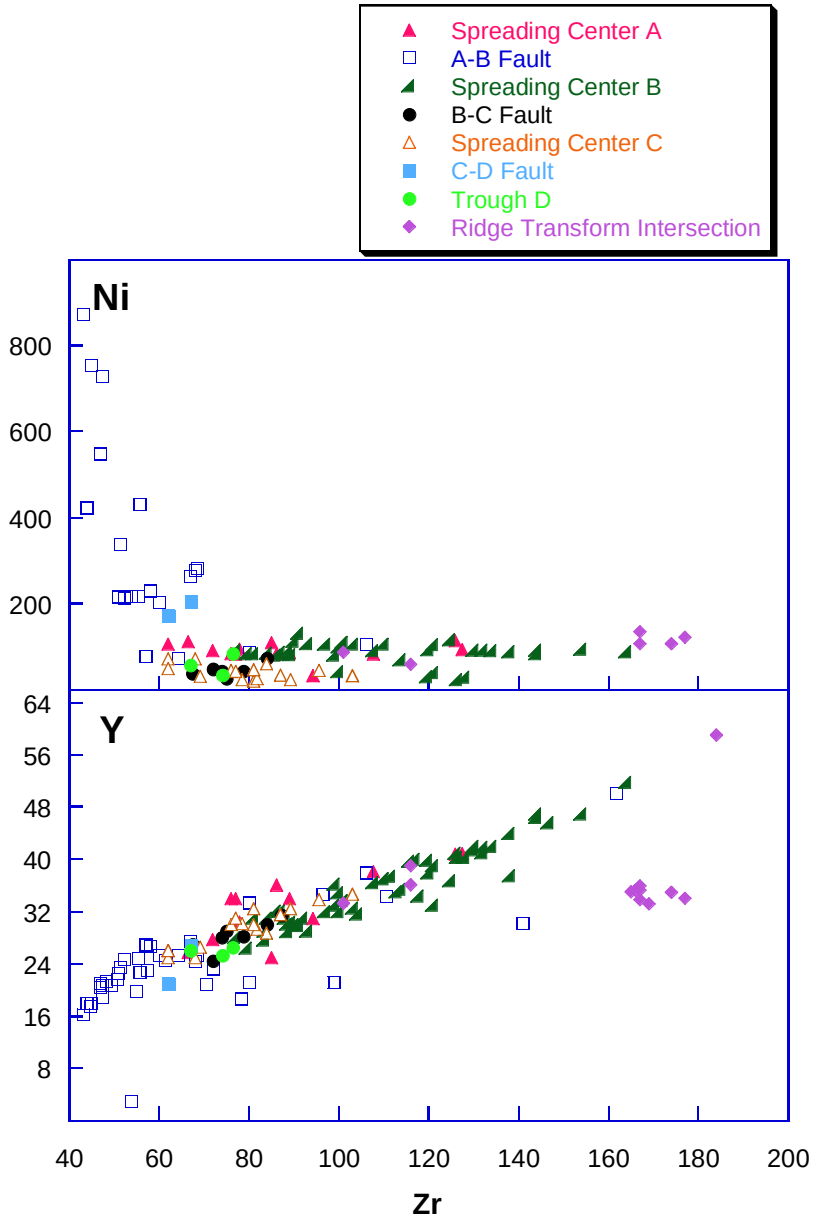


Figure 5-8. Continued.

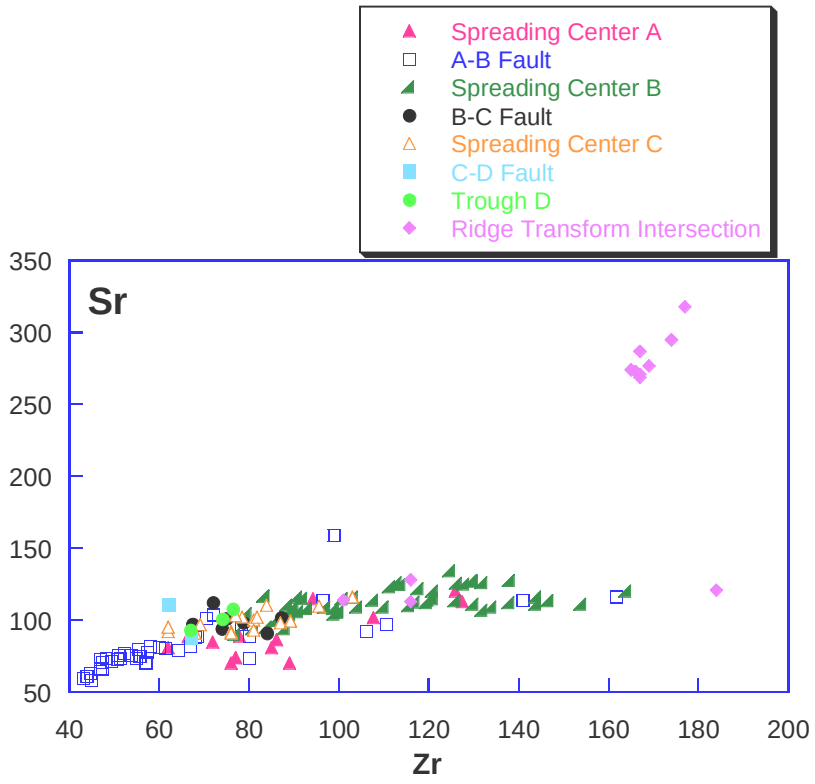


Figure 5-8. Continued.

centers and faults. Samples from spreading center B show a slightly greater range in abundance of the trace elements than the samples from the other spreading centers and faults. A few samples from spreading center A show a slight depletion at given $TiO_2$ and Zr values in Sr contents relative to other moderately evolved samples found within the Siqueiros transform.

The relative enrichment factors for the trace elements Nb, Sr, Zr, and Y, which have been precisely determined by XRF, were computed by dividing the highest value by the lowest value for each morphotectonic location in the transform domain (Table 5-1). The most incompatible element (Nb) shows the greatest relative enrichment for each location with the exception of the C-D fault in which trace element analysis was only completed for two samples from the fault. Nb and Zr, the most incompatible elements, show a lower enrichment than Y and Sr in the two C-D samples. This is because the REE patterns of these samples cross and they cannot be related by fractional crystallization. Sr, the most compatible element, generally shows the least amount of enrichment for each location.

Table 5-1. Nb, Sr, Zr, and Y enrichment factors for Siqueiros transform morphotectonic locations.

| | **Enrichment Factors** | | | |
|---|---|---|---|---|
| | Nb | Zr | Y | Sr |
| Spreading Center A | 3.00 | 2.05 | 1.63 | 1.73 |
| A-B Fault | 6.59 | 3.75 | 3.35 | 2.74 |
| Spreading Center B | 2.72 | 2.13 | 2.10 | 1.53 |
| B-C Fault | 2.25 | 2.33 | 1.29 | 1.24 |
| Spreading Center C | 3.85 | 1.66 | 1.39 | 1.29 |
| C-D Fault | 1.07 | 1.05 | 1.24 | 1.22 |
| Trough D | 1.38 | 1.15 | 1.05 | 1.19 |
| Ridge Transform Intersection* | 1.79 | 1.82 | 1.77 | 1.13 |

*E-MORBs not included in calculation of RTI enrichment factors.

As previously discussed, the $K_2O/TiO_2$ ratio has been used as a proxy for degree of enrichment based on comparison with (Ce/Yb) ratios. The (Ce/Yb) ratio compares a light rare earth element (LREE), Ce, to a heavy rare-earth element (HREE), Yb. When normalized to chondrites a $(Ce/Yb_n)$ ratio of 1 indicates no enrichment or depletion of the LREE to HREE relative to chondrites. A $(Ce/Yb_n)$ ratio greater than one indicates that a sample is LREE enriched and a $(Ce/Yb_n)$ ratio less than one indicates LREE depletion. The $(Ce/Yb_n)$ values can be used to determine what $K_2O/TiO_2$ value matches the boundary between enriched and depleted samples. The measured $K_2O/TiO_2$ value of a sample can then be used to classify samples in which trace element analysis has not been completed as enriched or depleted. Figure (5-9) shows the $(Ce/Yb_n)$ vs. $K_2O/TiO_2$. All samples except for the RTI samples are depleted compared to chondrites. Sample 2390-9 has a $(Ce/Yb_n)$ ratio about equal to one and samples 2390-1, 2390-5, and 2390-3B are enriched compared to chondrites. The $(Ce/Yb_n)$ break in enriched vs. depleted samples is roughly at about $K_2O/TiO_2 = 0.11$. Consequently, most of the Siqueiros samples are classified as depleted and only a few samples from the RTI show an enriched signature.

The samples from the spreading centers and the faults for the most part fall into narrow $(Ce/Yb_n)$ groups based on their location (Figure 5-10). The samples from spreading center B and the C-D fault have higher $(Ce/Yb_n)$ ratios indicating that they are more enriched overall than the other Siqueiros samples. Samples from the A-B fault and spreading center A (except for a few samples) have the most depleted $(Ce/Yb_n)$ values. Of all the samples for which trace element analysis was done only sample 2390-9 exhibits transitional trace element characteristics.

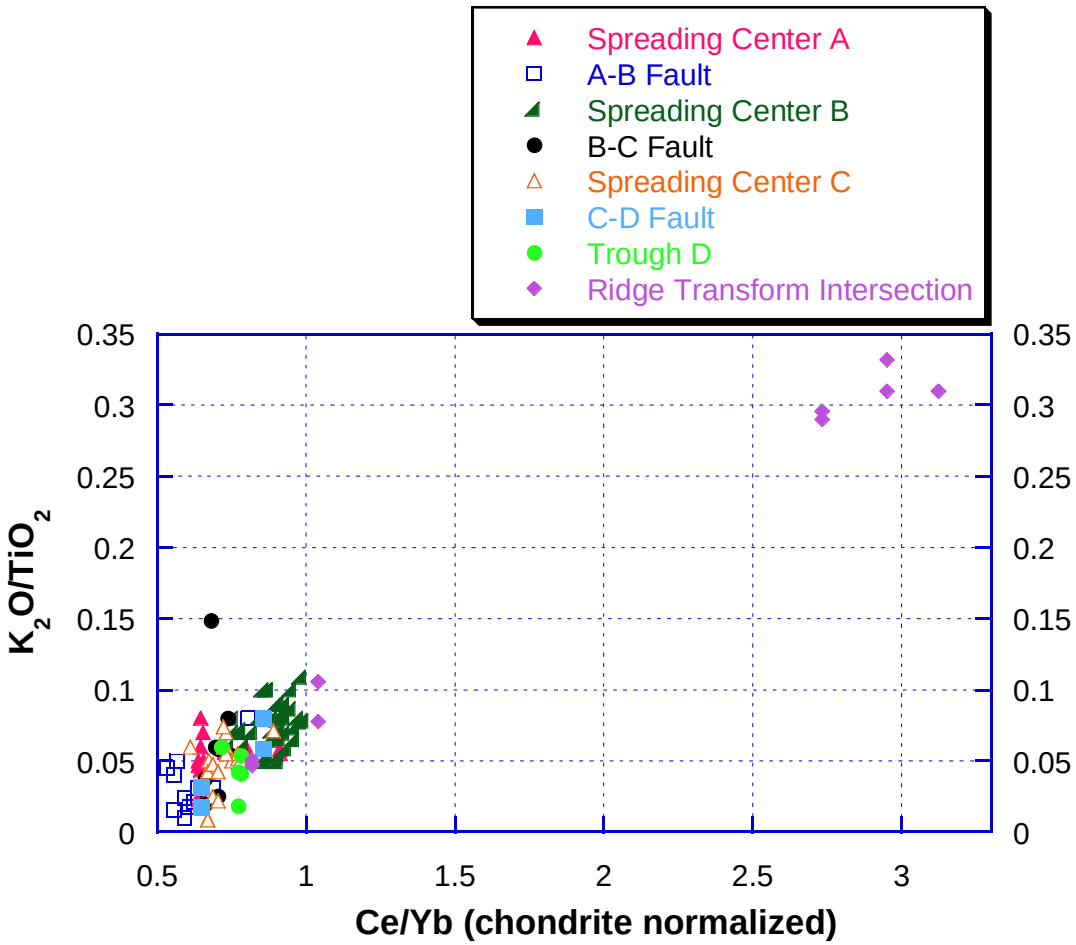


Figure 5-9. $Ce/Yb_n$ vs. $K_2O/TiO_2$ of the Siqueiros samples.

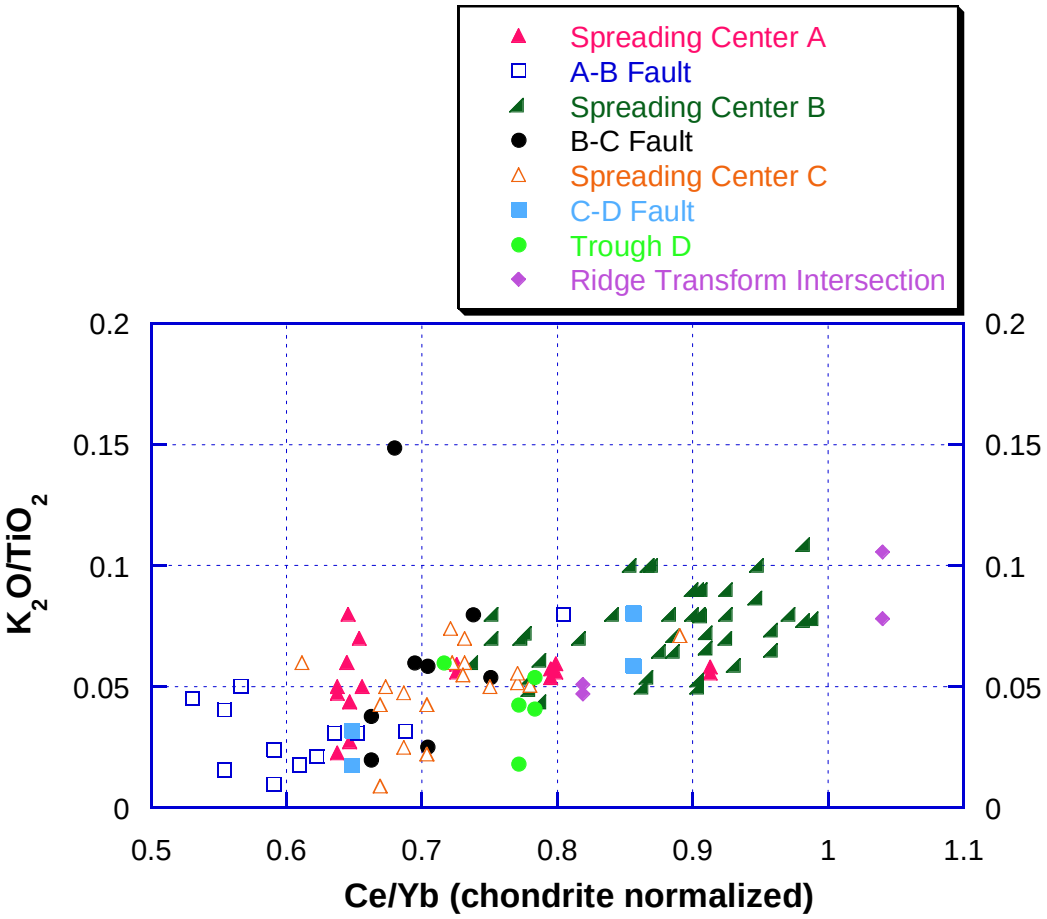


Figure 5-10. Chondrite normalized Ce/Yb ratios for Siqueiros morphotectonic locations.

The samples chosen for ICP-MS analysis range from strongly, light rare earth element depleted to moderately enriched. Most of the samples from the transform faults and the spreading centers generally have 6-20x chondritic values for all REE (Figure 5-11). The samples from the spreading centers and the faults all show strong LREE depletion. Samples from the A-B fault and sample 2382-10WR from spreading center B show the strongest depletions in the LREE, having enrichments as low as 2.5x chondritic values. Samples from the RTI contain two groups. The first group contains the E-MORBs which are enriched in the LREE (samples 2390-8, 2390-5, 2390-4, 2390-1, and 2390-3) with enrichments up to 60x chondritic values, while enrichments in the HREE are only 20x chondritic values. The REE patterns of the E-MORB samples cross those of the "normal" samples and cannot be related by fractional crystallization to any other samples found in the Siqueiros transform. The other group has REE patterns parallel to samples from the spreading centers and faults, yet more enriched overall in REE indicating that they are more fractionated. This group includes sample 2390-9, which is classified as a FeTi basalt. It is the most evolved sample found within the Siqueiros transform domain and the REE patterns parallel those from the spreading centers. Spreading center B, which has the most differentiated samples (lower MgO contents) other than the RTI FeTi basalt, has samples with higher REE abundances than any of the other Siqueiros spreading centers or faults. The most evolved samples from spreading center B (highest REE abundances) have well developed negative Eu anomalies. Eu anomalies are absent in samples from the other spreading centers and the faults, but can be found in sample 2386-5 from tough D and sample 2390-9, the FeTi basalt from the RTI. Samples 2391-10wr and 2391-5 from the A-B fault show positive Eu anomalies.

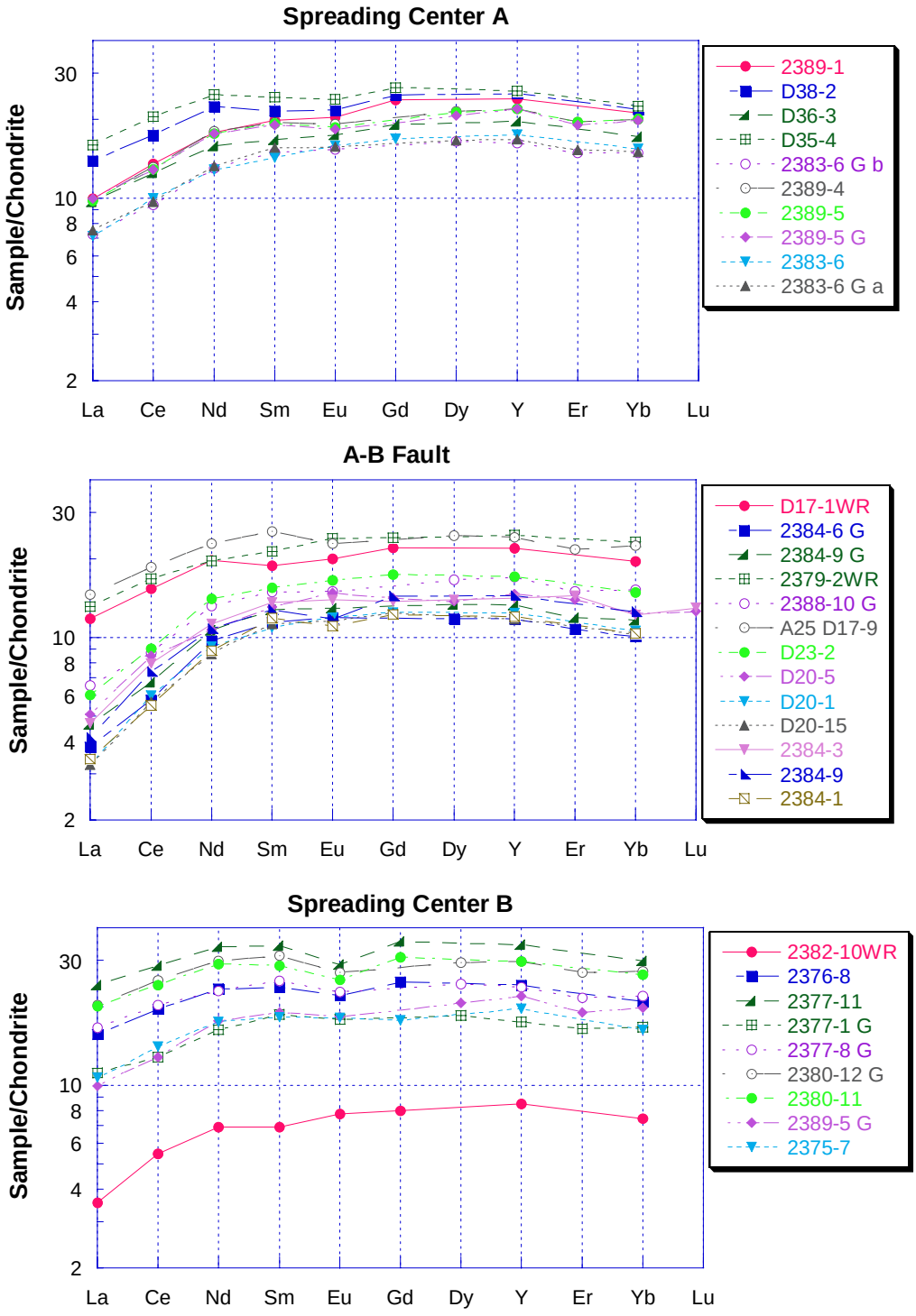


Figure 5-11. Chondrite normalized REE diagrams. Representative samples were chosen for each morphotectonic location. REE analysis by ICP-MS at the University of Houston and by ICP-MS at the Geological Survey of Canada. Chondritic normalization factors are from Sun and McDonough, 1989.

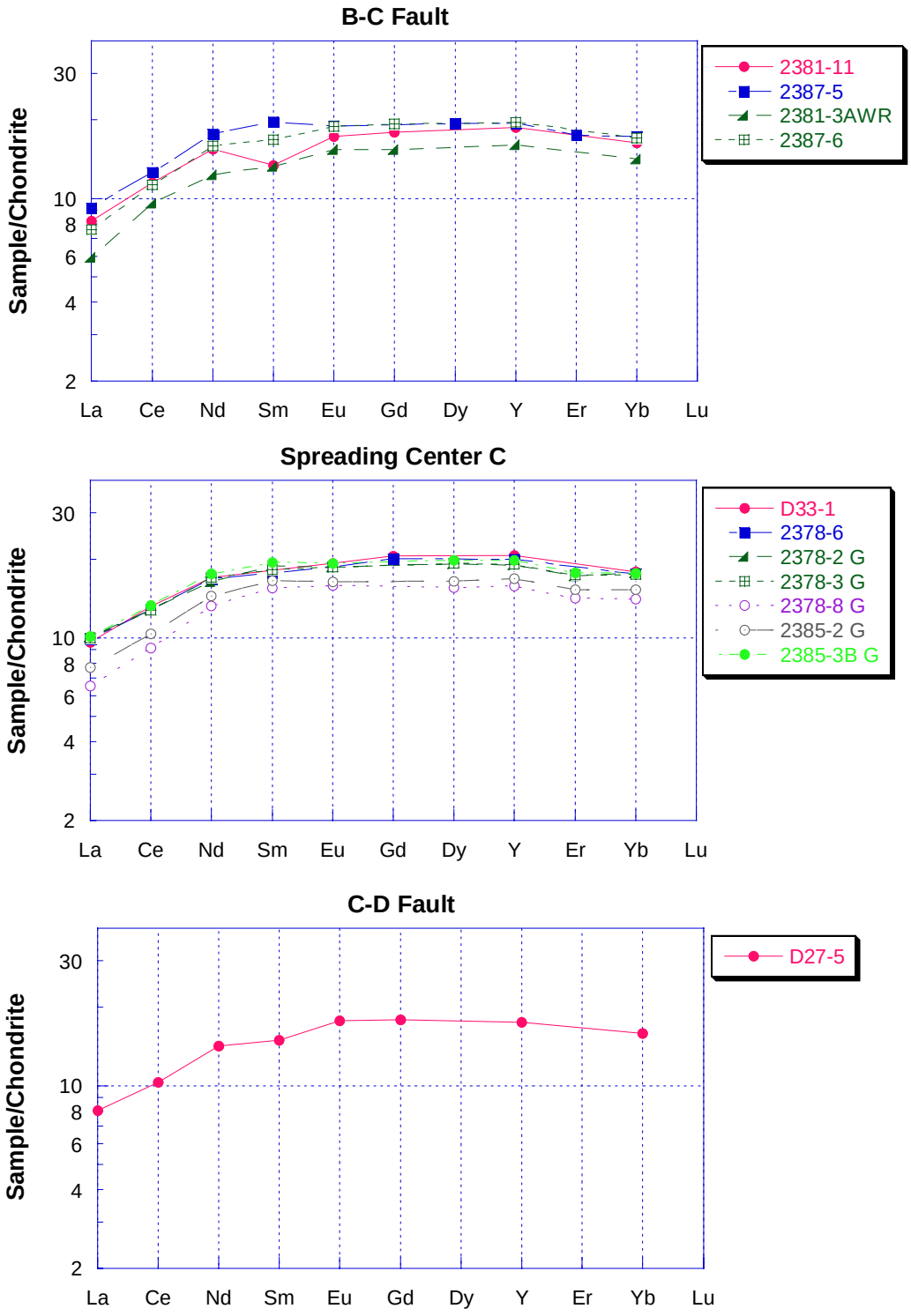


Figure 5-11. Continued.

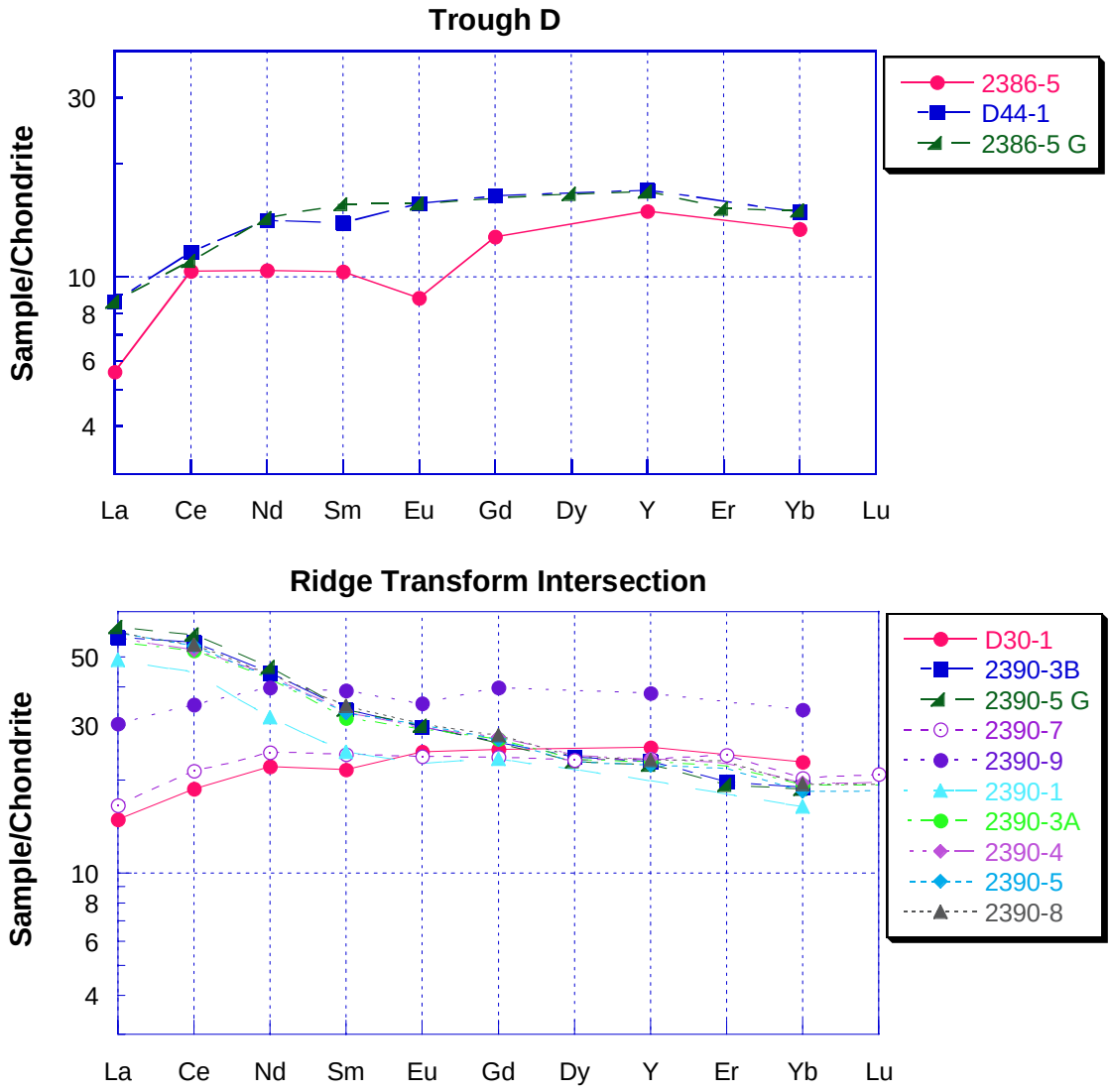


Figure 5-11. Continued.

Other than the more depleted samples from the A-B fault and E-MORB samples from the RTI, samples from the spreading centers and faults generally have parallel REE patterns. A few of the samples do have patterns that are slightly different and cross other REE patterns (eg. samples 2389-1 and 2383-2 from spreading center A) indicating that more than one "normal" parental composition is required to produce all samples within the Siqueiros transform.

The $(La/Sm)_n$ values for the entire suite range from 0.289 (sample 2384-1 from the A-B fault) to 1.98 (sample 2390-1 from the RTI) and have an median value of 0.596. The (Sm/Yb)n values range from 0.649 (sample 2391-5 from the A-B fault) to 1.803 (sample 2390-5G from the RTI). This indicates that the Sm/Yb portion of the rare-earth element curves are flatter than the La-Sm portion and that the samples are more depleted in the LREE.

N-MORB normalized REE diagrams are shown in figure 5-12. Samples from spreading centers A and C are fairly flat and parallel to each other. The samples are all close to N-MORB values with a range of 0.2x – 2x N-MORB. All samples from spreading center B, except for sample 2383-10WR, have REE values that are overall enriched compared to N-MORB. Samples from fault C-D and trough D are flat, but overall are slightly depleted when compared to N-MORB. The B-C and A-B faults are also slightly depleted when compared to N-MORB, but have stronger depletions in the LREE then the HREE. The A-B fault is the most depleted in the LREE. The samples from the RTI range from parallel to and slightly enriched in the LREE to enriched in the LREE.

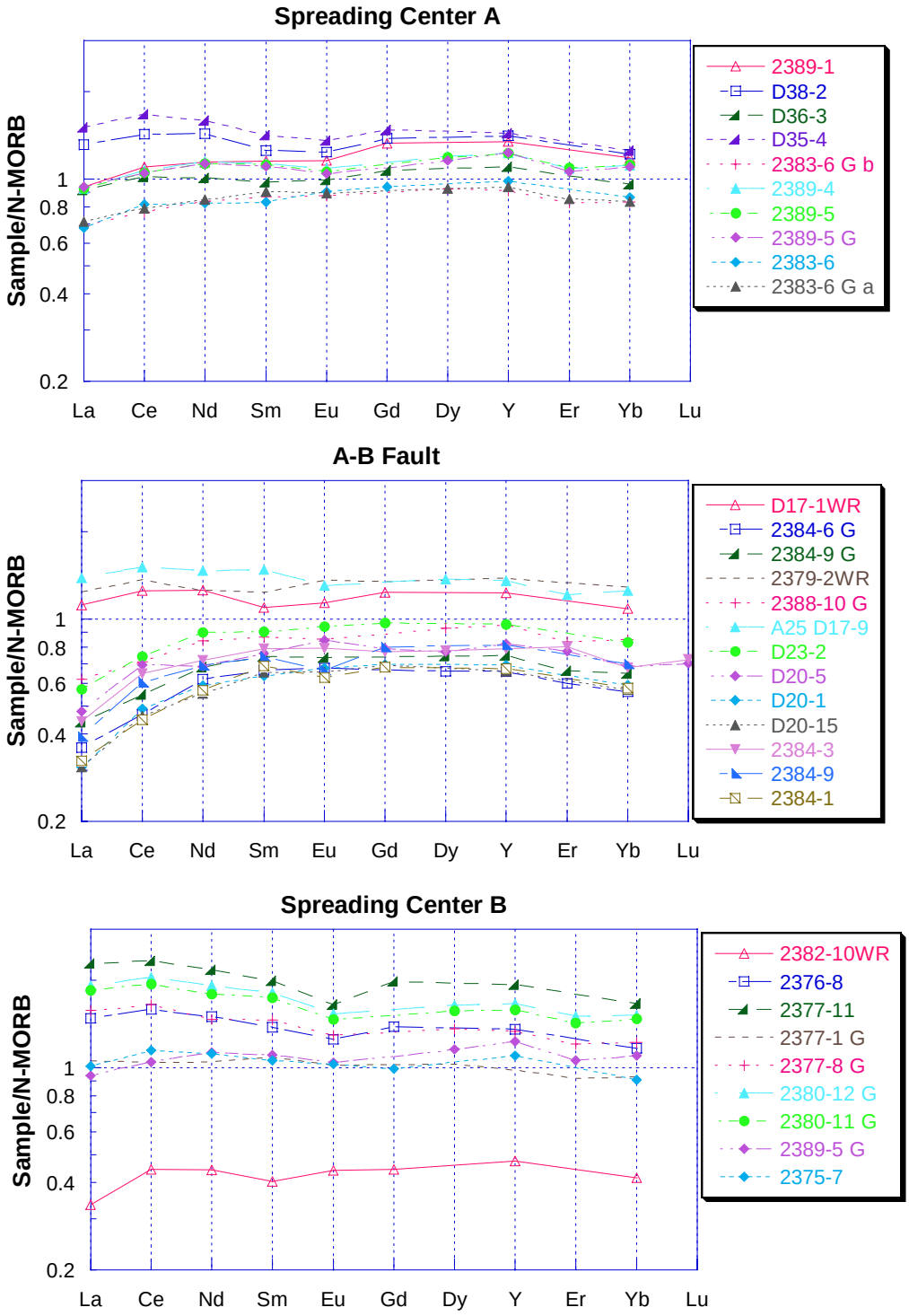


Figure 5-12. N-Morb normalized REE diagrams. Representative samples were chosen for each morphotectonic location. REE analysis by ICP-MS at the University of Houston and by ICP-MS at the Geological Survey of Canada. N-MORB normalization factors are from Sun and McDonough, 1989.

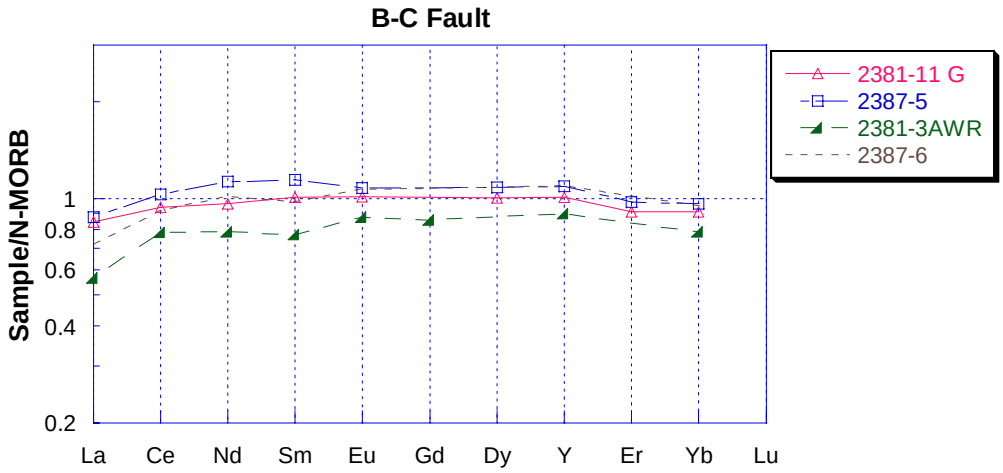


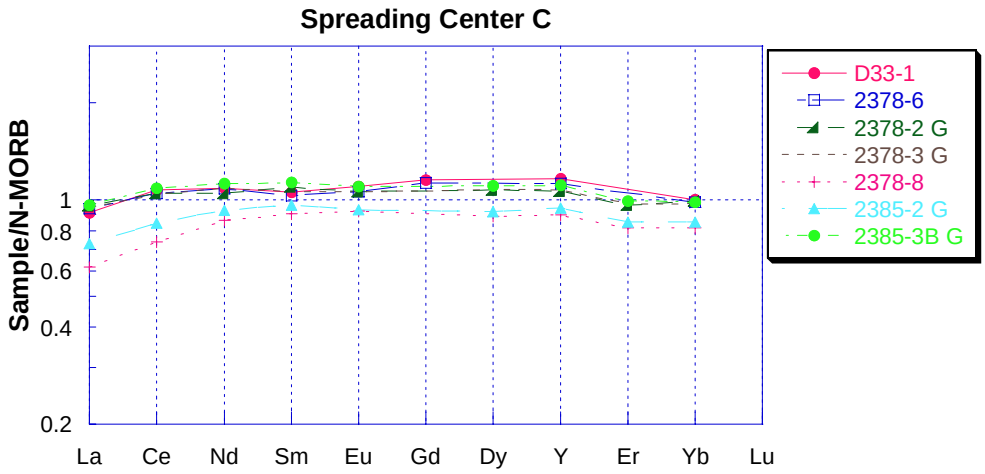


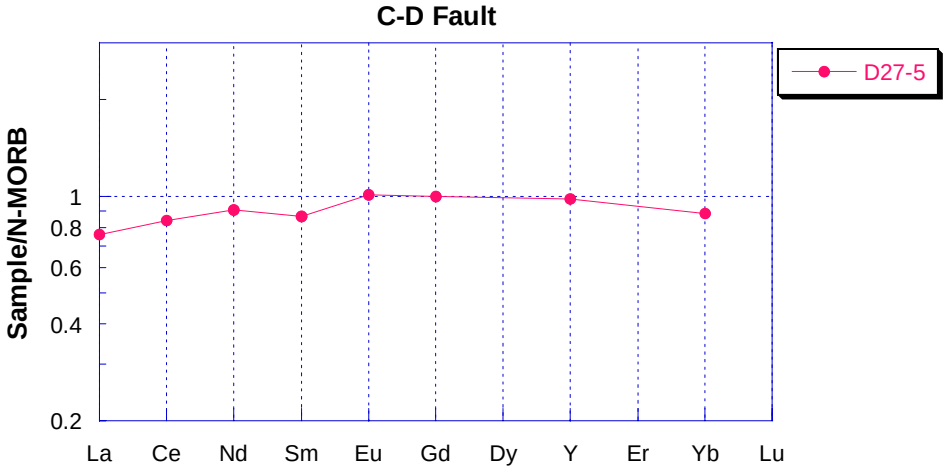


Figure 5-12. Continued.

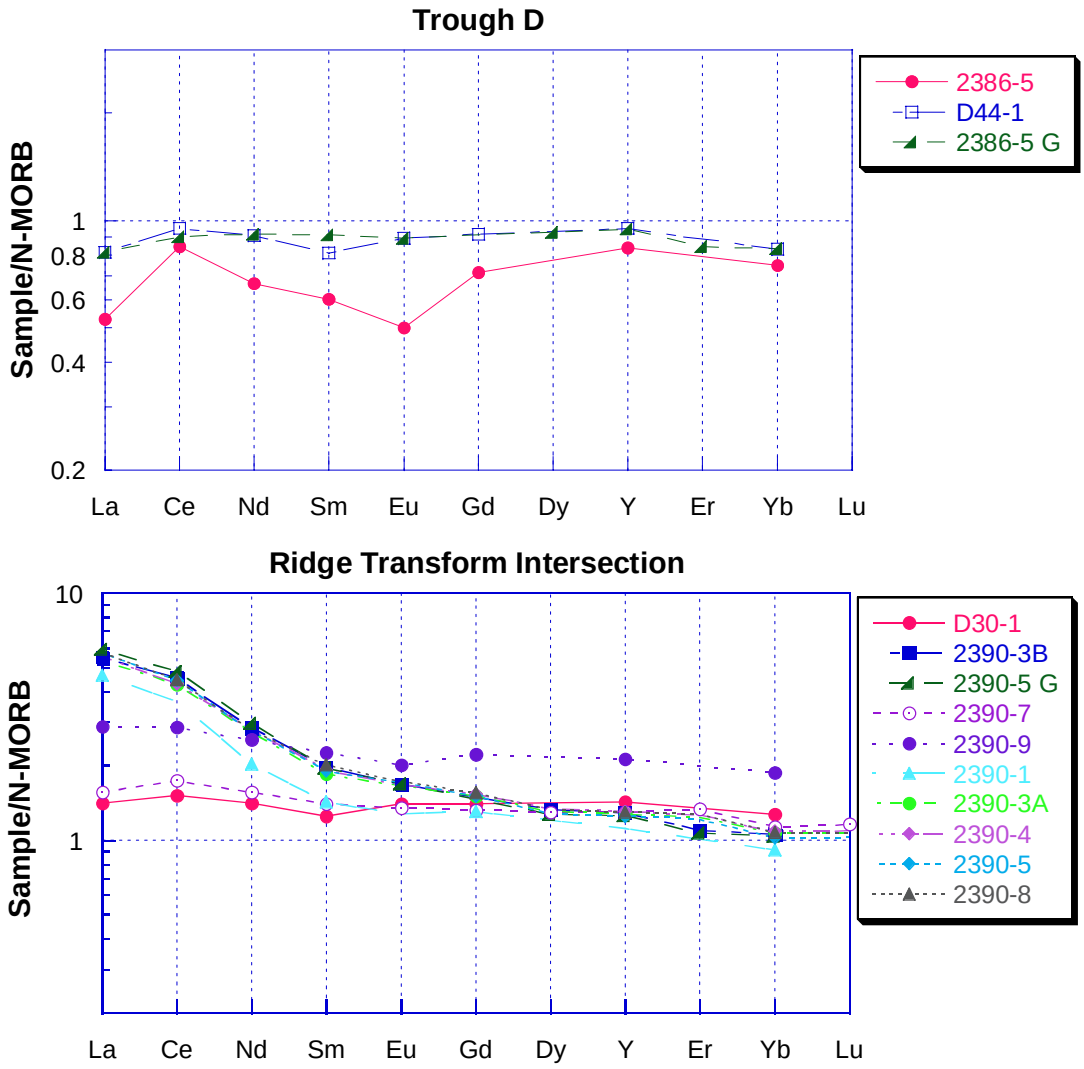


Figure 5-12. Continued.

It is important to note that the majority of the N-MORB samples have lower K/Ti ratios than typical MORB from the northern EPR. This was also noted for samples from the Garrett transform relative to lavas from the southern EPR. All of the low K/Ti Garrett samples were categorized as "D-MORB" (Hekinian et al., 1995). The K/Ti ratio by itself is not an adequate characteristic to distinguish D-MORB from N-MORB in the Siqueiros sample suite because the REE patterns of many of the low K/Ti samples are not sufficiently depleted in LREE to be "depleted" relative to NMORB (Figure 5-12). Only Siqueiros lavas from the A-B fault with unusually depleted LREE patterns are considered "DMORB." When normalized to the N-MORB value of Sun & McDonough (1989) some of the other samples from the Siqueiros transform domain are depleted in the LREE and have Ce/Y (N-MORB normalized) values < 1.0, however, only samples from the highly depleted samples from the A-B fault were classified as D-MORB. This corresponds to a Ce/Y N-MORB normalized value of < 0.80 (Figure 5-13).

When normalized to E-MORB values, the Siqueiros E-MORB are slightly more evolved with REE values around 2x that of E-MORB abundances (Figure 5-14). The Siqueiros E-MORB are also slightly more enriched in the LREE. The Siqueiros E-MORB patterns all parallel each other indicating that they could be derived from a common parental composition. There is also very little difference in REE abundances indicating little difference in fractional crystallization history between the Siqueiros E-MORB samples.

Primitive mantle normalized trace element diagrams are shown in figure 5-15. All of the Siqueiros samples other than the E-MORB found at the RTI have low concentrations of incompatible elements and large-ion-lithophile elements. Samples

2388-10G and 2384-9G are exceptionally depleted in the large-ion-lithophile and incompatible elements. Many of the samples show negative Sr anomalies. E-MORB incompatible element abundances indicate that they do not share a common parental magma with the other Siqueiros samples.

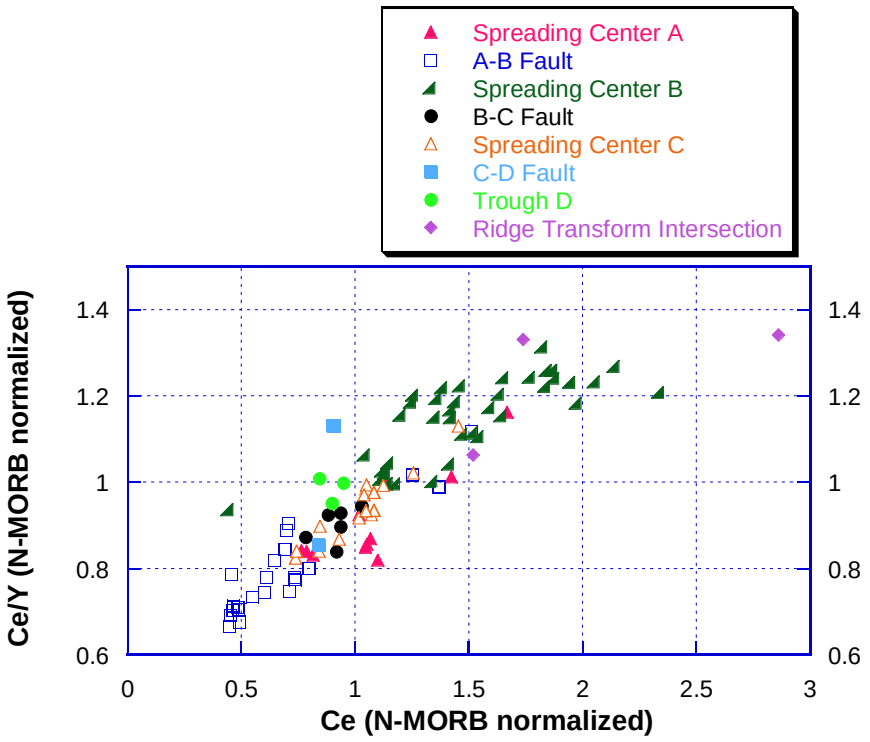


Figure 5-13. N-MORB normalized Ce/Y ratios for Siqueiros transform morphotectonic locations. E-MORB samples from the WRTI are not included.

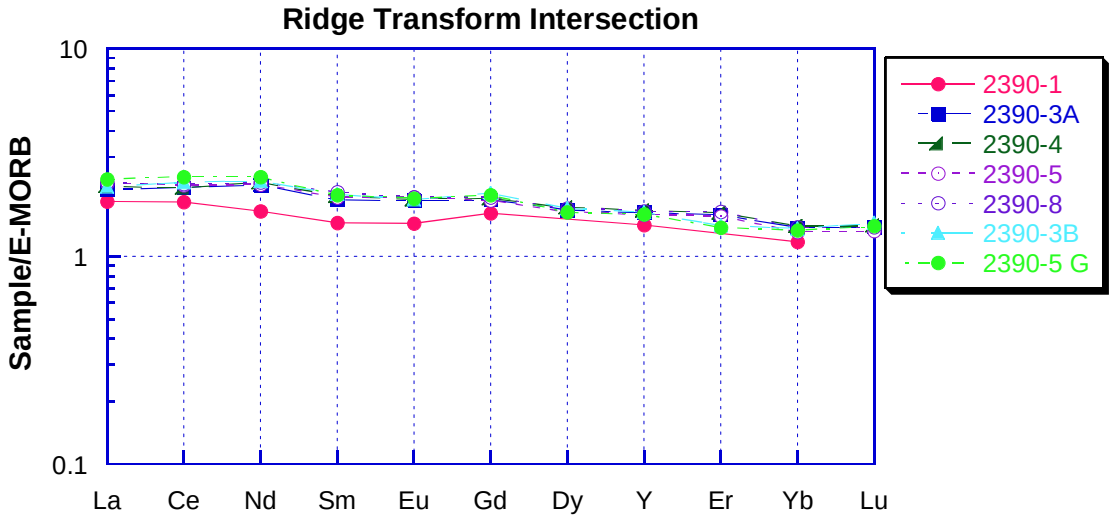


Figure 5-14. REE diagram of RTI E-MORBs plotted relative to E-MORB values. REE analysis by ICP-MS at the University of Houston and by ICP-MS at the Geological Survey of Canada. E-MORB normalization factors are from Sun and McDonough, 1989.

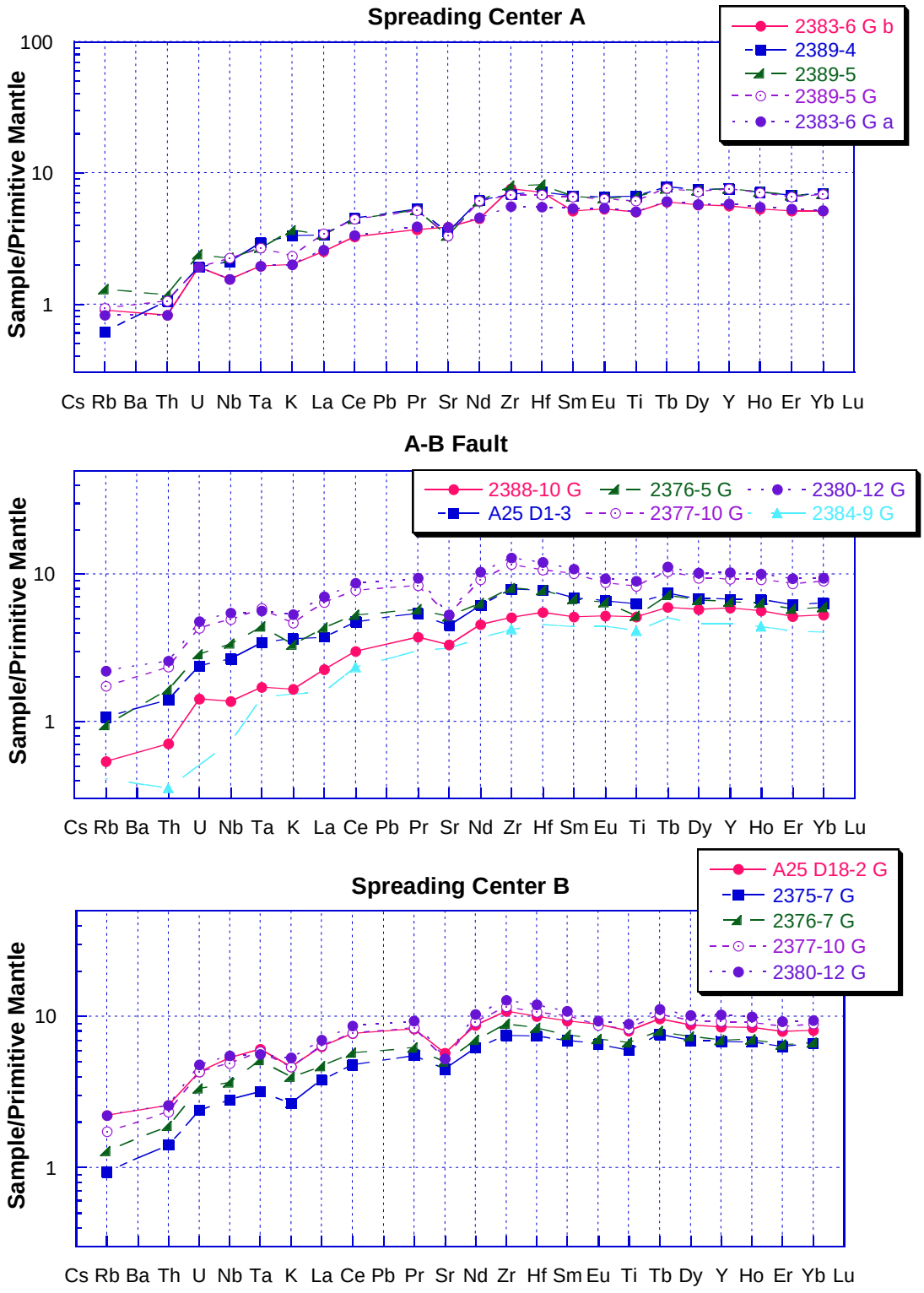


Figure 5-15. Primitive mantle-normalized trace element diagrams. Trace element data completed by ICP-MS at the Geological Survey of Canada. Primitive mantle normalizing factors are from Sun and McDonough, 1989. Elements are listed from right to left in order of increasing incompatibility during mantle melting.

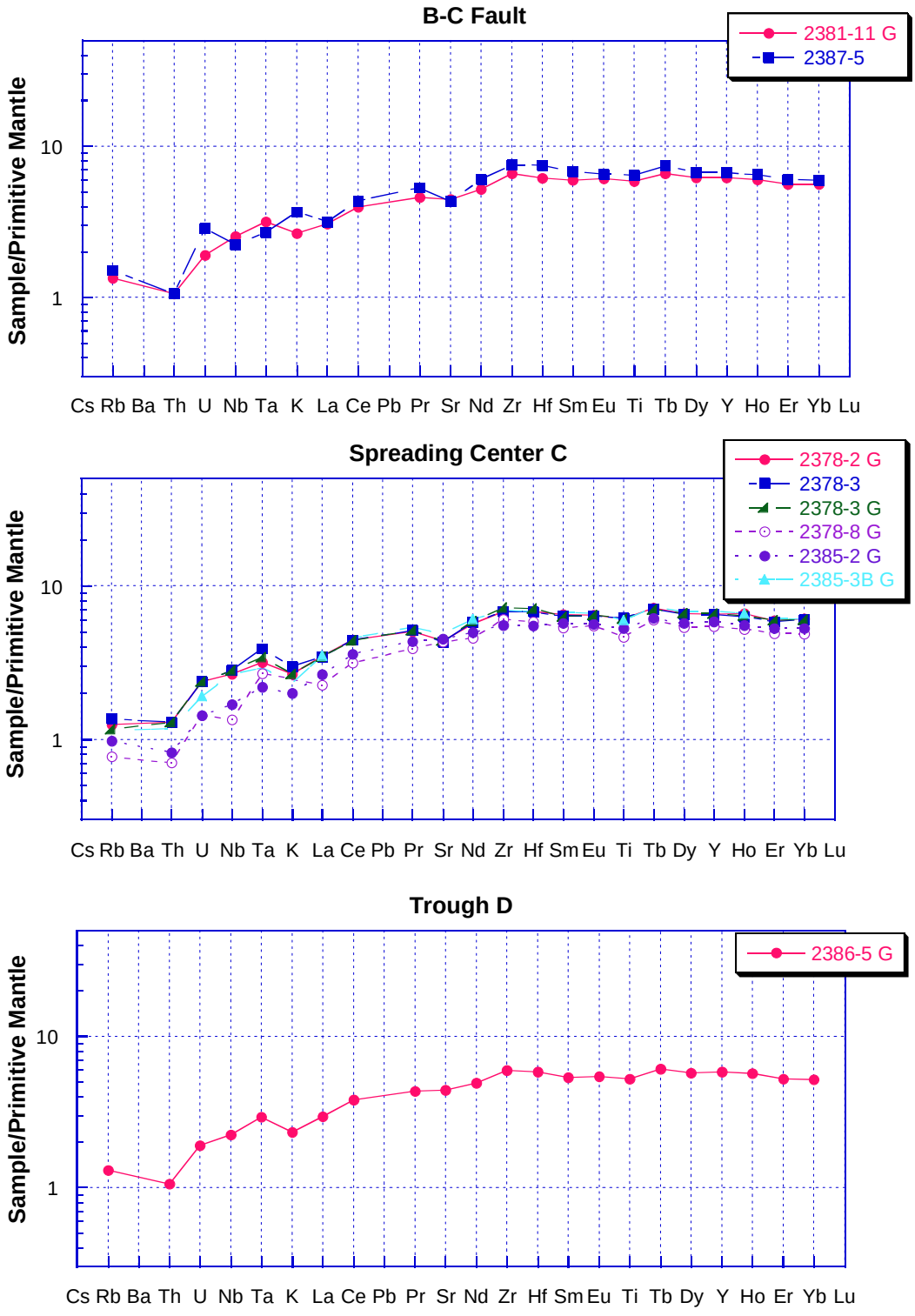


Figure 5-15. Continued.

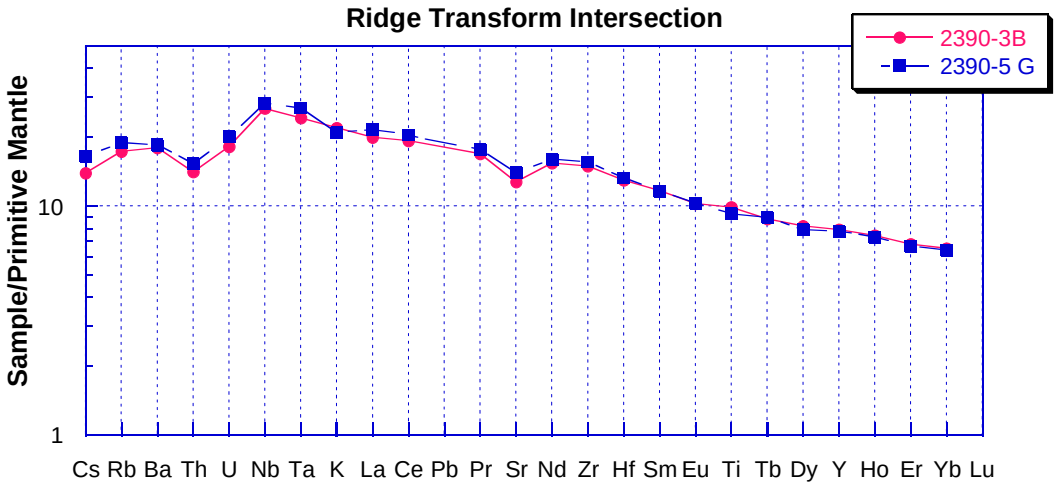


Figure 5-15. Continued.

# CHAPTER 6
# PETROGENESIS

## Major Element Models

Liquid lines of descent were calculated using the program PETROLOG 2.1 (Danyushevsky et al., 1996), which determines the major element contents of sequential residual liquids by fractional crystallization of a given parental composition (Appendix E). The program calculates liquidus minerals and temperatures for the range of melt compositions. The minerals on the liquidus are incrementally removed and residual liquid compositions are re-calculated. The chemistry of these residual liquids determine the liquid line of descent for a given parent. The liquid lines of descent are theoretical magmatic evolutionary paths that show how the magma composition might change with decreasing temperatures and progressive fractionation.

The program input requires an initial composition, the $H_2O$ content of the initial composition, the pressure of crystallization, the amount of crystallization between steps, and the potential minerals in equilibrium during crystallization. Models were run using a variety of samples with relatively high MgO contents as parental compositions. Sample 2377-7, a moderately evolved sample (MgO content of 8.03 wt. %), was also used because of its relative enrichment in some of the more incompatible elements ($TiO_2$, $P_2O_5$, and $K_2O$). In order to provide a relatively primitive parental composition, the composition of sample 2377-7 was run backwards using reverse crystal fractionation in Petrolog. The reverse crystal fractionation option in Petrolog allows chosen minerals to be added until a specified MgO content is reached. Plagioclase and olivine were both

added until a MgO content of 10.5 wt. % was reached. This new composition, 2377-7P, was then used to run the crystal fractionation liquid line of descent. All other parental compositions were taken directly from the major element microprobe analysis of sample and are designated by the sample number plus the letter "P" (eg. D34-2P refers to the parental composition based on the major element analysis of sample D34-2). Olivine, plagioclase, and clinopyroxene were chosen as potential minerals in equilibrium for all samples and spinel was also used for samples for which Cr contents were available. All models were run with 1% melt increments between calculations and were stopped when liquids reached 5 wt. % MgO. The initial calculations were run under anhydrous conditions and at a pressure of 0.33 kbar to estimate the depth of the melt lens at 1 km (Rosendahl et al., 1976). The Danyushevsky (2001) olivine, plagioclase, and clinopyroxene crystal fractionation models and the Ariskin & Nikolaev (1996) spinel crystal fractionation model were chosen.

Under low pressure, the parental liquids begin to first crystallize at about 1260-1380°C. Spinel is the first mineral to crystallize. Only a small amount of spinel crystallizes and the liquid cools to 1200-1250°C before the onset of olivine crystallization which is followed closely by plagioclase crystallization. Clinopyroxene does not begin to crystallize until the liquids cool to around 1160-1180°C, which corresponds to a MgO contents of 6.8-8.0 wt. % (Figure 6-1). The results suggest that nearly 50-55 wt. % total crystallization is required to explain the most evolved samples from the spreading centers and faults and up 70 wt. % total crystallization is required to explain the most evolved samples (other than the E-MORB) from the RTI. The crystallization occurs in two steps:

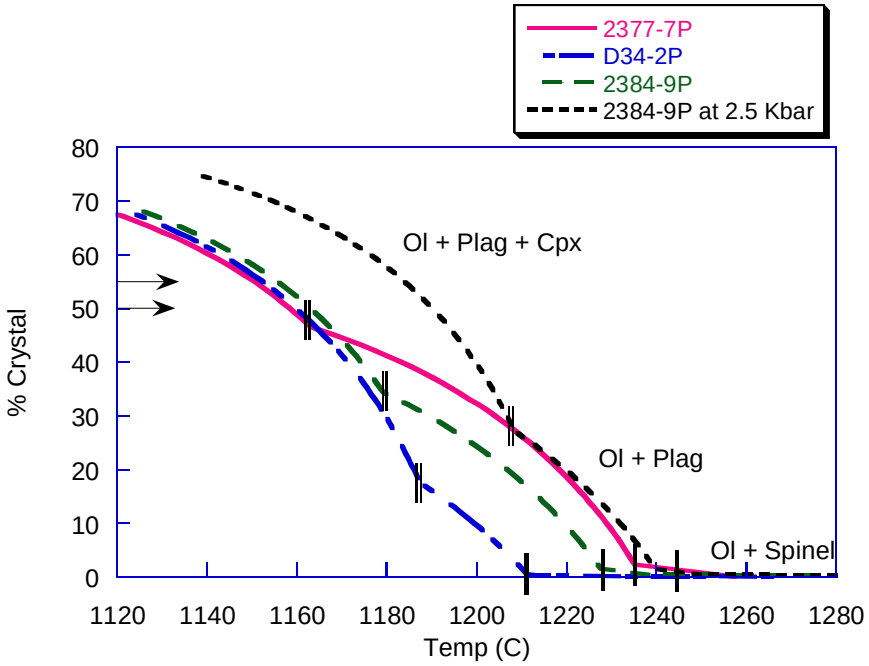


Figure 6-1. Percentage of crystals removed as a function of temperature. Solid lines mark onset of plagioclase fractionation. Double lines mark onset of clinopyroxene fractionation. Top arrow indicates amount of crystal fractionation required in order to model the most evolved sample from the RTI and second arrow indicates amount required to produce that most evolved samples from the spreading centers and faults.

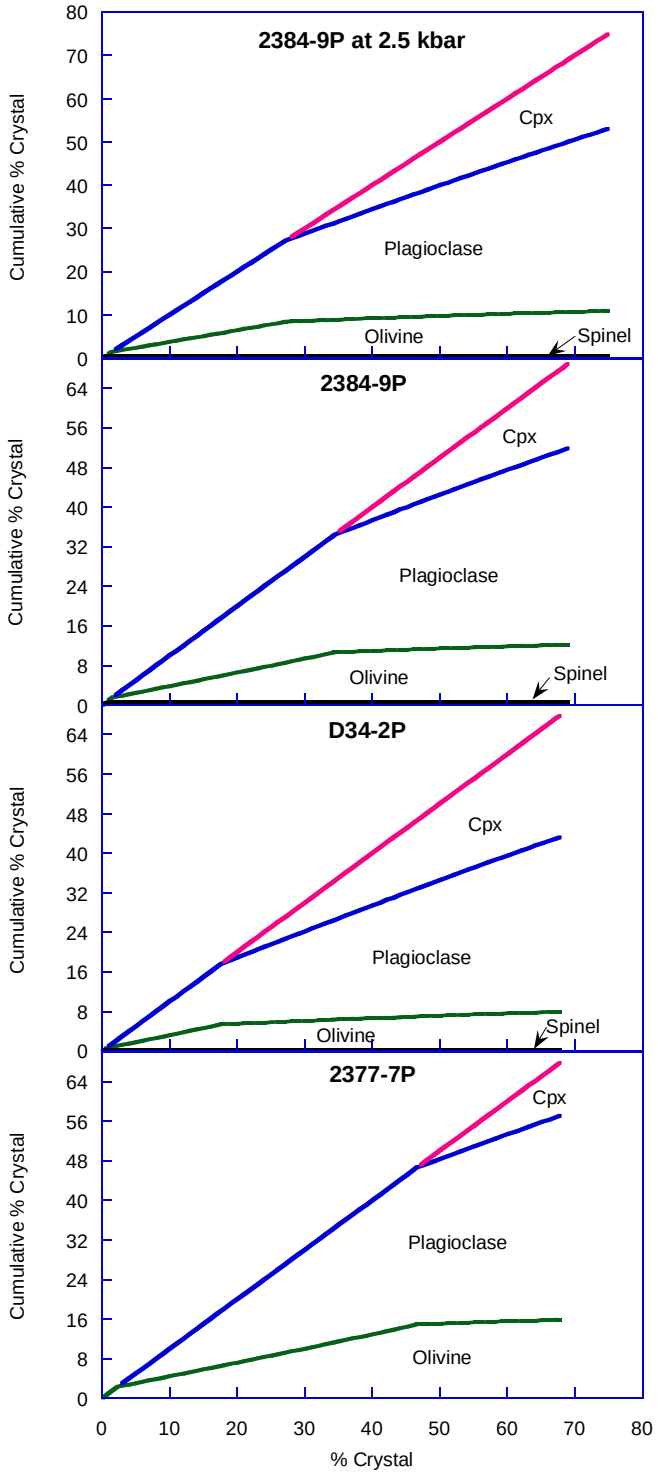


Figure 6-2. Percentage of liquid and removed crystals as a function of percentage of crystals removed from magma for 2377P, D34-2P and 2384-9P. Fractional crystallization models calculated using low pressure model of Danyushevsky (2001). High pressure model of 2384-9P is also shown for comparison.

an initial 18-47 wt. % crystallization of olivine plus plagioclase with minor spinel crystallization followed by 8-37 wt. % crystallization of olivine, plagioclase, and clinopyroxene is predicted by the models (Figure 6-2). The models are in agreement with low pressure experiments completed on sample 2384-1, which predicted initial temperatures of crystallization

around 1297-1306°C and olivine ± spinel as liquidus phases for pressures below 12-13 kbar when a plagioclase lherzolite source is assumed (Wendlandt et al., 1994).

In order to explain the major element variability observed in the entire suite of samples, three parental compositions were chosen (Figure 6-3). 2377-7P from spreading center B provides the best fit to the samples that are more enriched in the slightly incompatible major elements such as $TiO_2$, $K_2O$, and $P_2O_5$. D34-2P from the C-D fault is more depleted in the incompatible major elements and has anomalously low $Na_2O$ and 2384-9P is one of the high-MgO basalts from the A-B fault and provides a good fit for samples with lower FeO and higher $Na_2O$ contents. Most of the samples can be explained by low pressure fractional crystallization of these three parents (2377-7P, D34-2P, 2384-9P). However the low pressure, anhydrous models were unable to account for the lower CaO wt. % samples and high $Al_2O_3$ wt. % samples. Higher pressure (2.5 kbars) fractional crystallization of 2384-9P stabilized clinopyroxene earlier and provided a better fit to the low CaO data (Figure 6-3). High pressure crystal fractionation could occur at the base of the crust where a second low velocity zone has been identified in geophysical surveys (Solomon and Toomey, 1992). Hydrous calculations were also run for 2377-7P, D34-2P, and 2384-9P (Figure 6-4). The hydrous calculations were run with 0.15 wt. % $H_2O$, based on the average $H_2O$ content reported in the Cameca SX50 electron

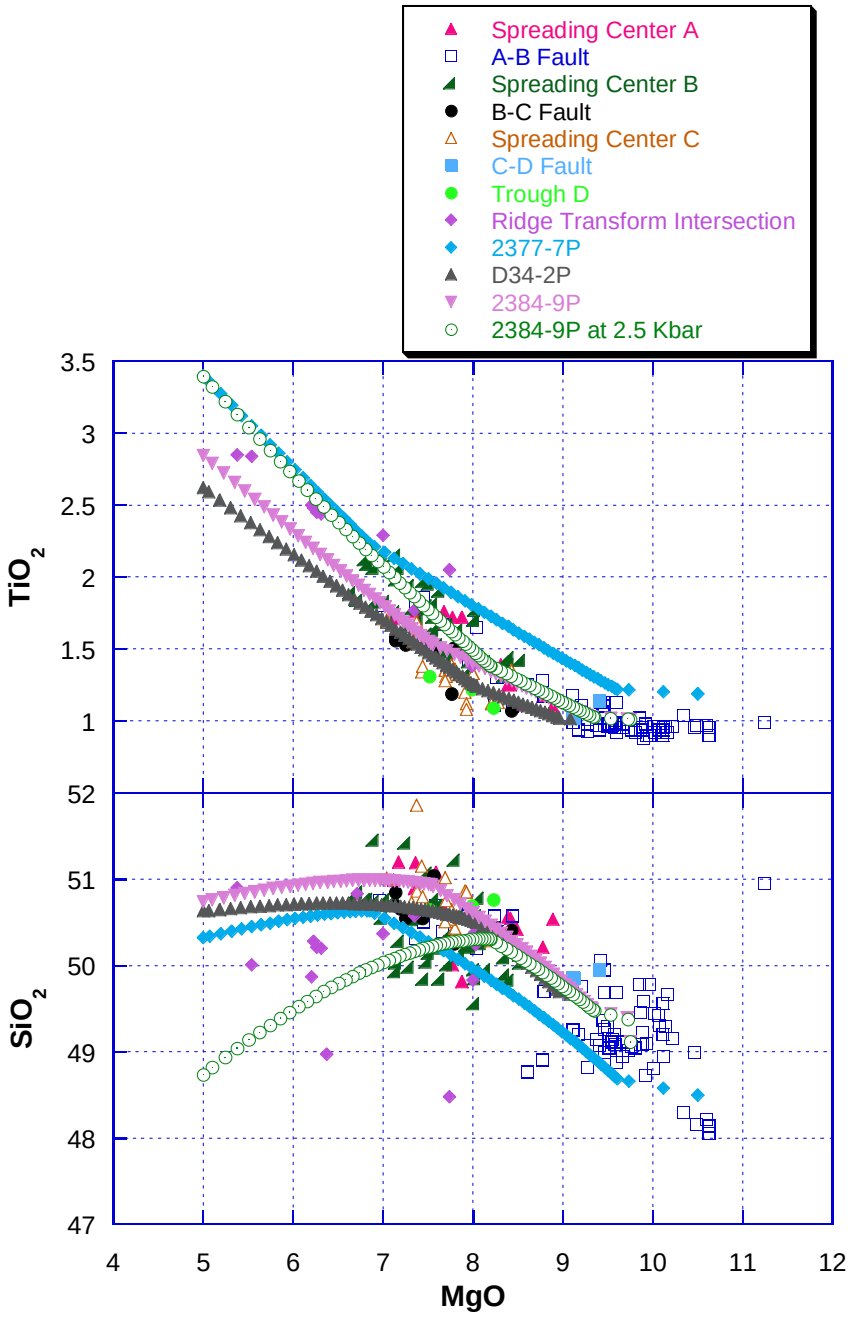


Figure 6-3. Comparison of major element data with LLD models calculated using the olivine, plagioclase, and clinopyroxene fractionation models of Danyushevsky (2001). 2377-7P and D34-2P were run at low pressure (<1 kbar) and 2384-9P was run at low pressure (< 1 kbar) and 2.5 kbar.

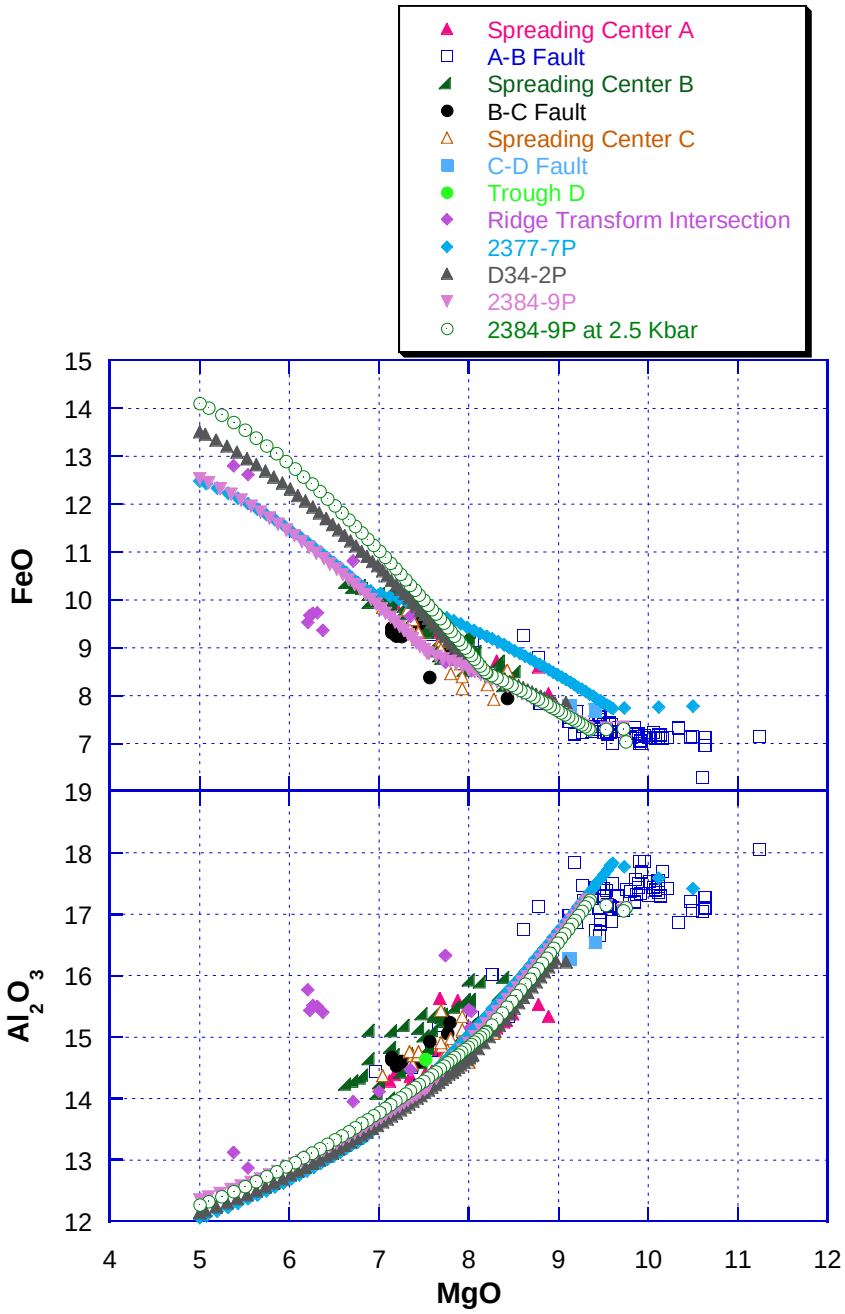


Figure 6-3. Continued.

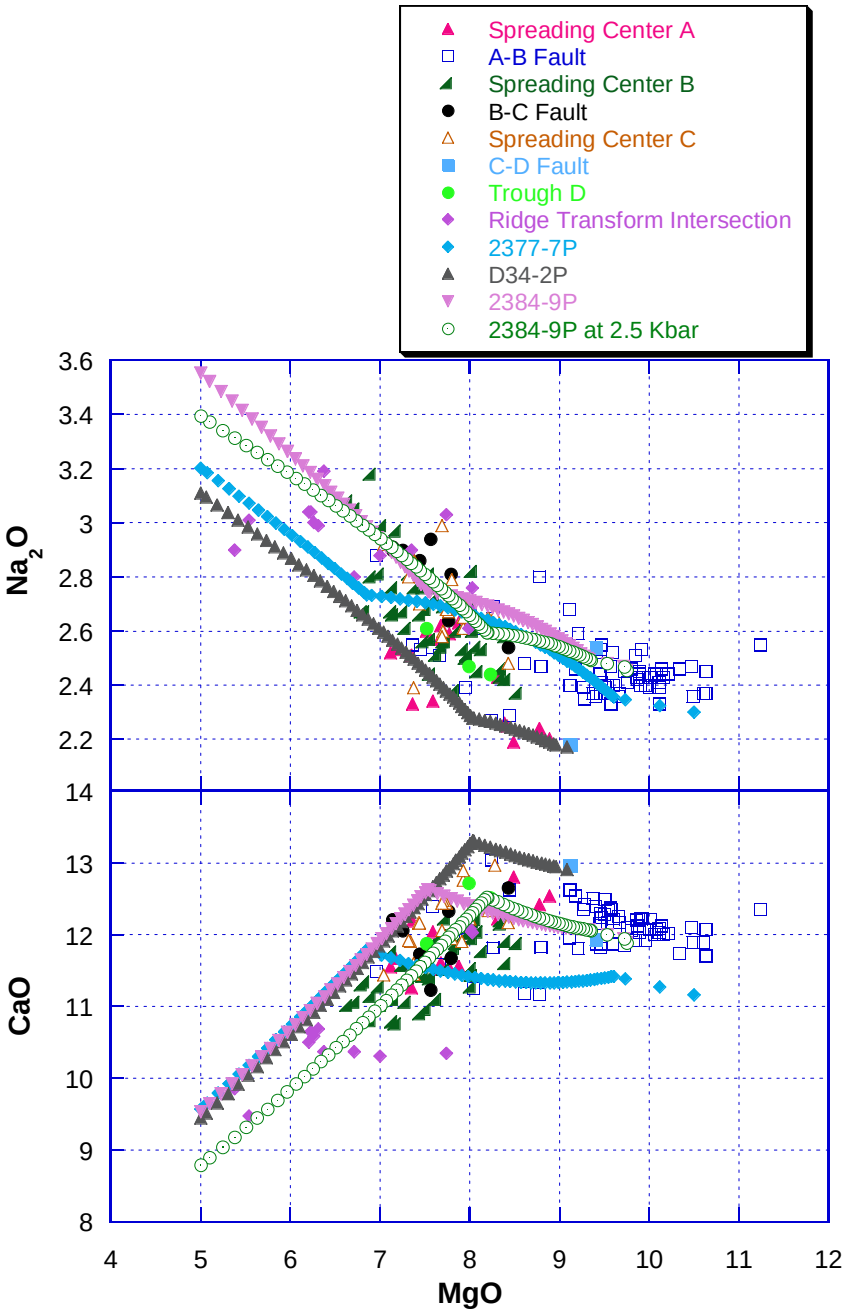


Figure 6-3. Continued.

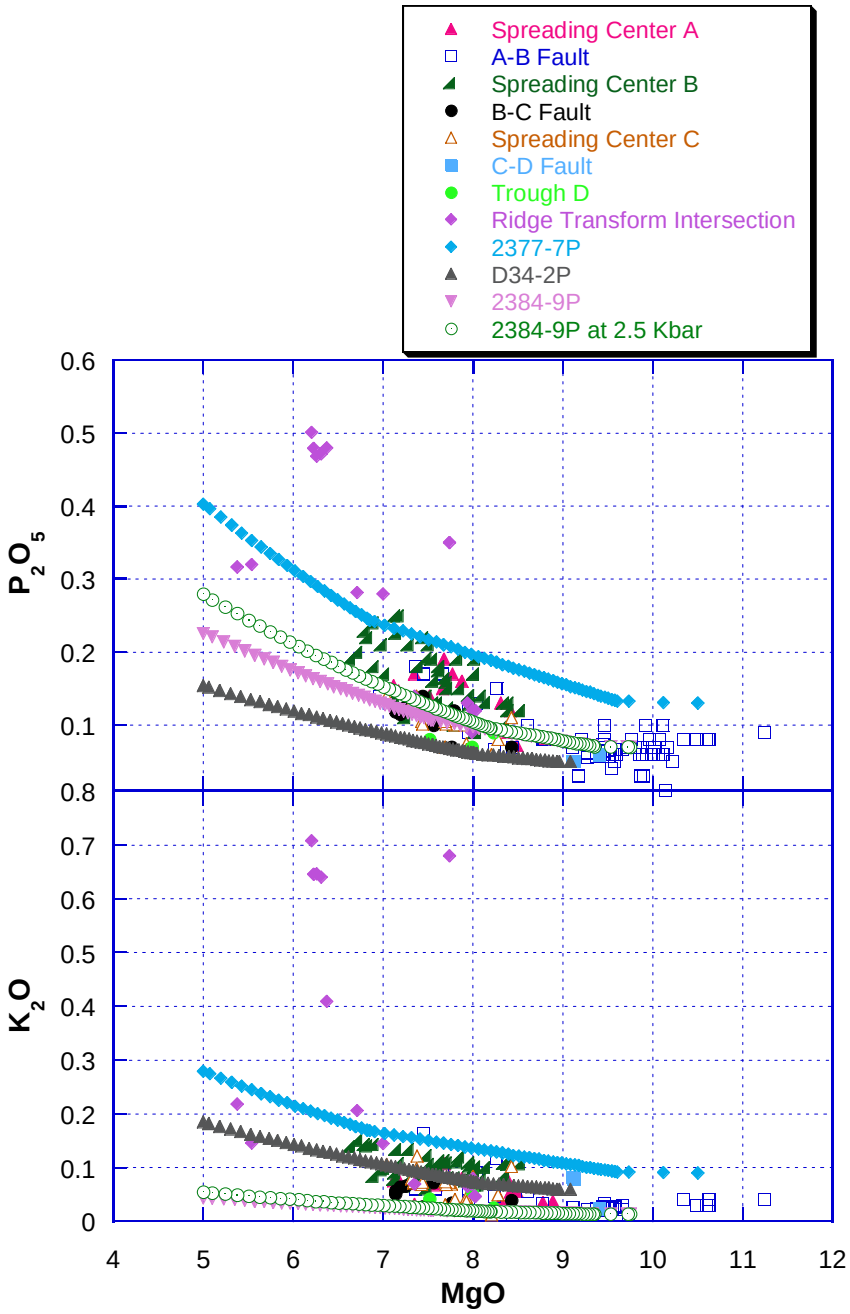


Figure 6-3. Continued.

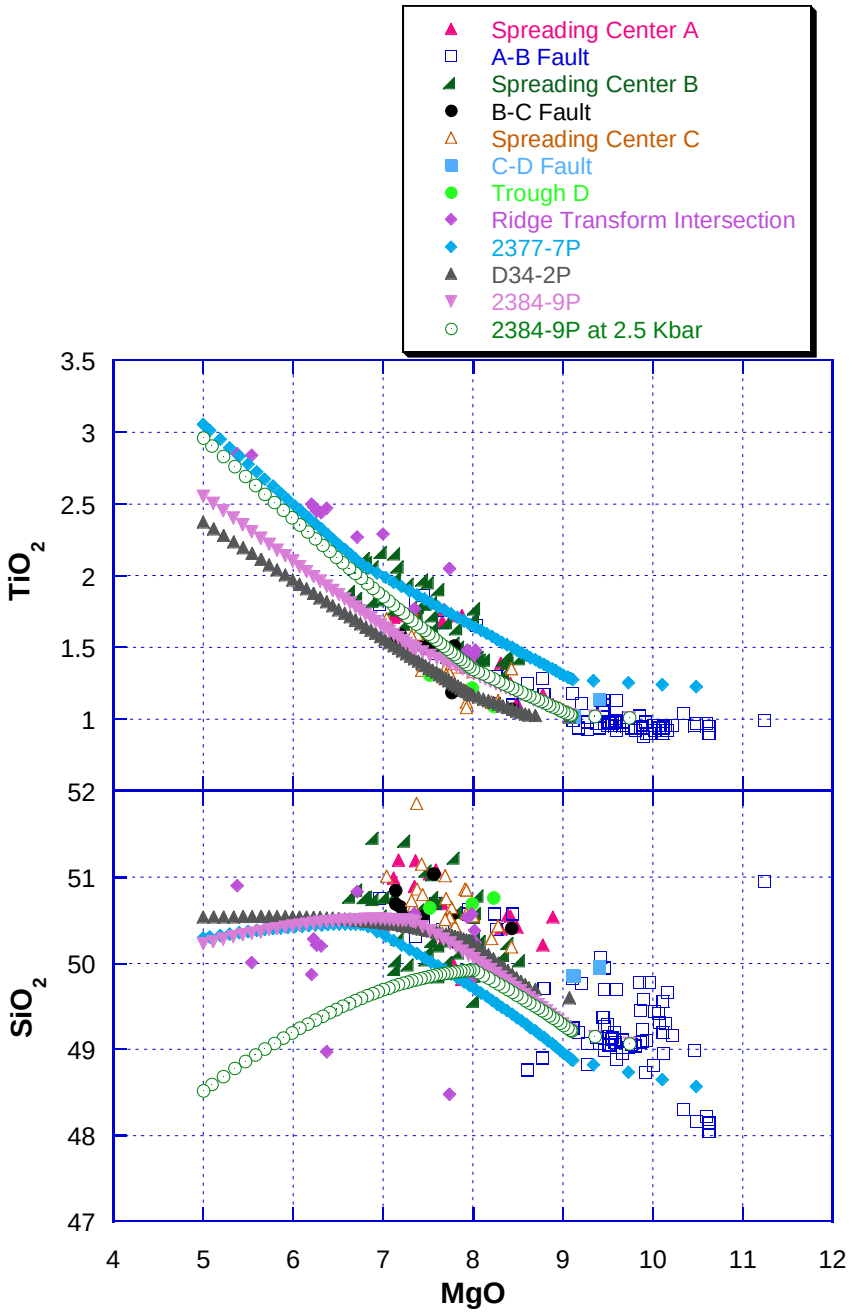


Figure 6-4. Comparison of major element data with hydrous LLD models calculated using the olivine, plagioclase and clinopyroxene fractionation models of Danyushevsky (2001). Calculations include 0.15 wt. % $H_2O$. The hydrous LLD models provide a better fit for the $Al_2O_3$ data, but do not considerably change the fractionation trends. 2377-7P and D34-2P were run at low pressure (< 1 kbar) and 2384-9P was run at low pressure (< 1 kbar) and at 2.5 kbar.

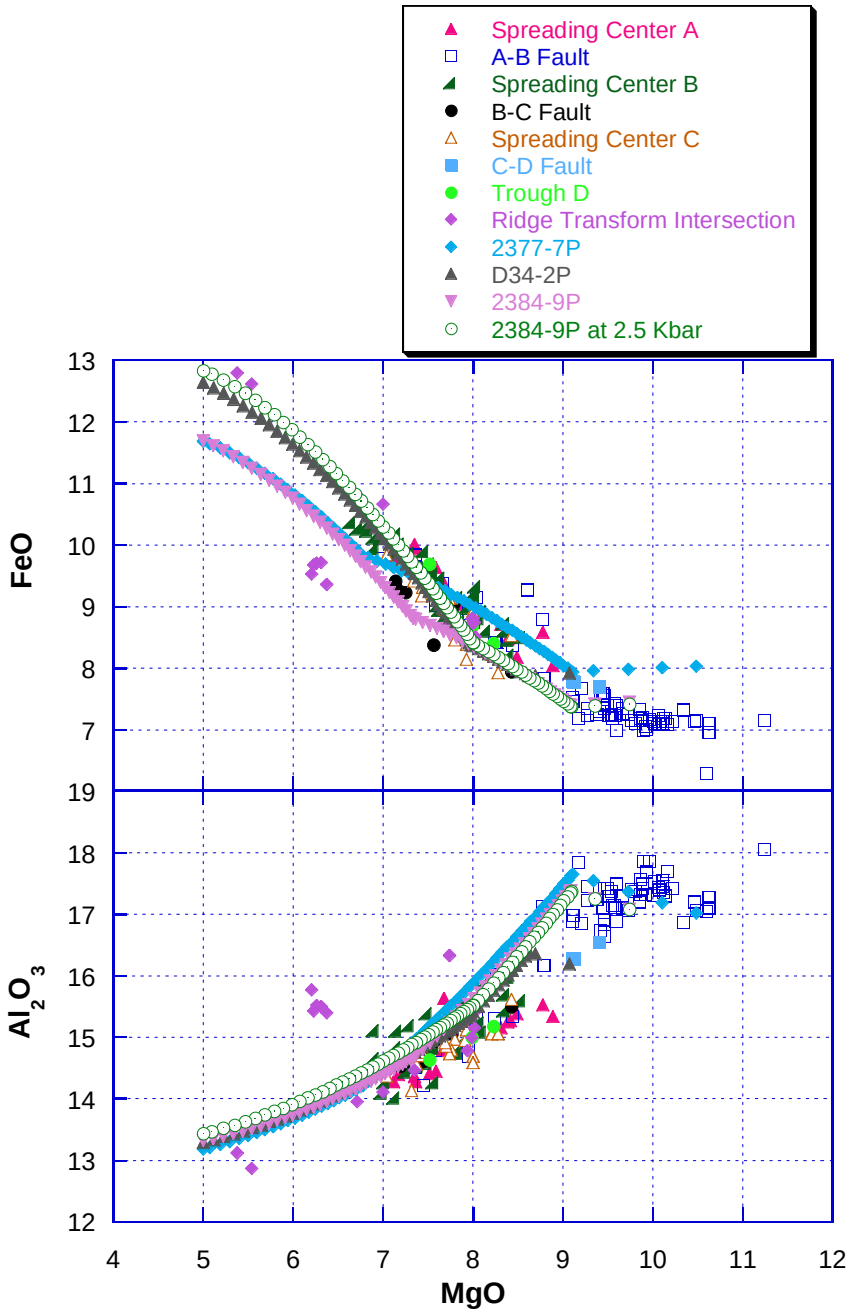


Figure 6-4. Continued.

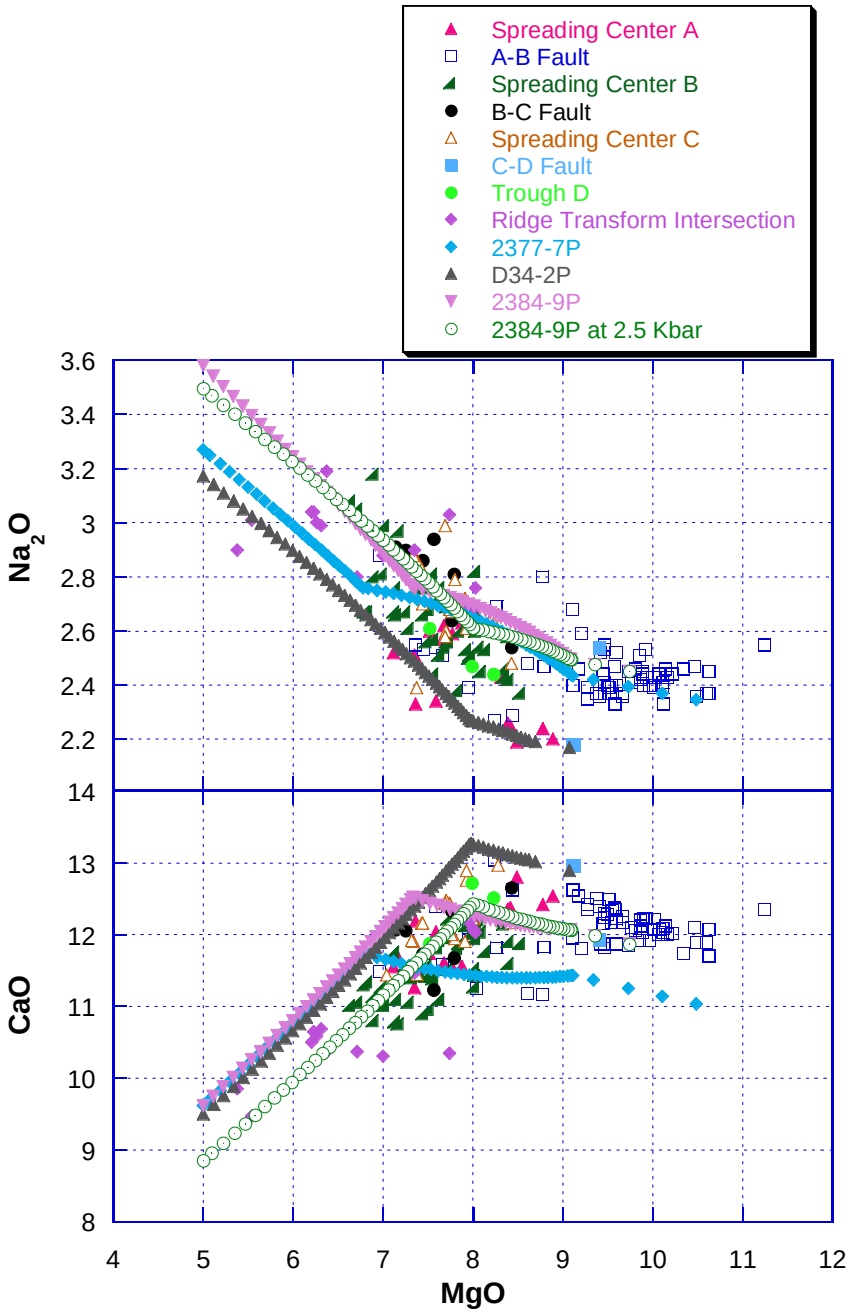


Figure 6-4. Continued.

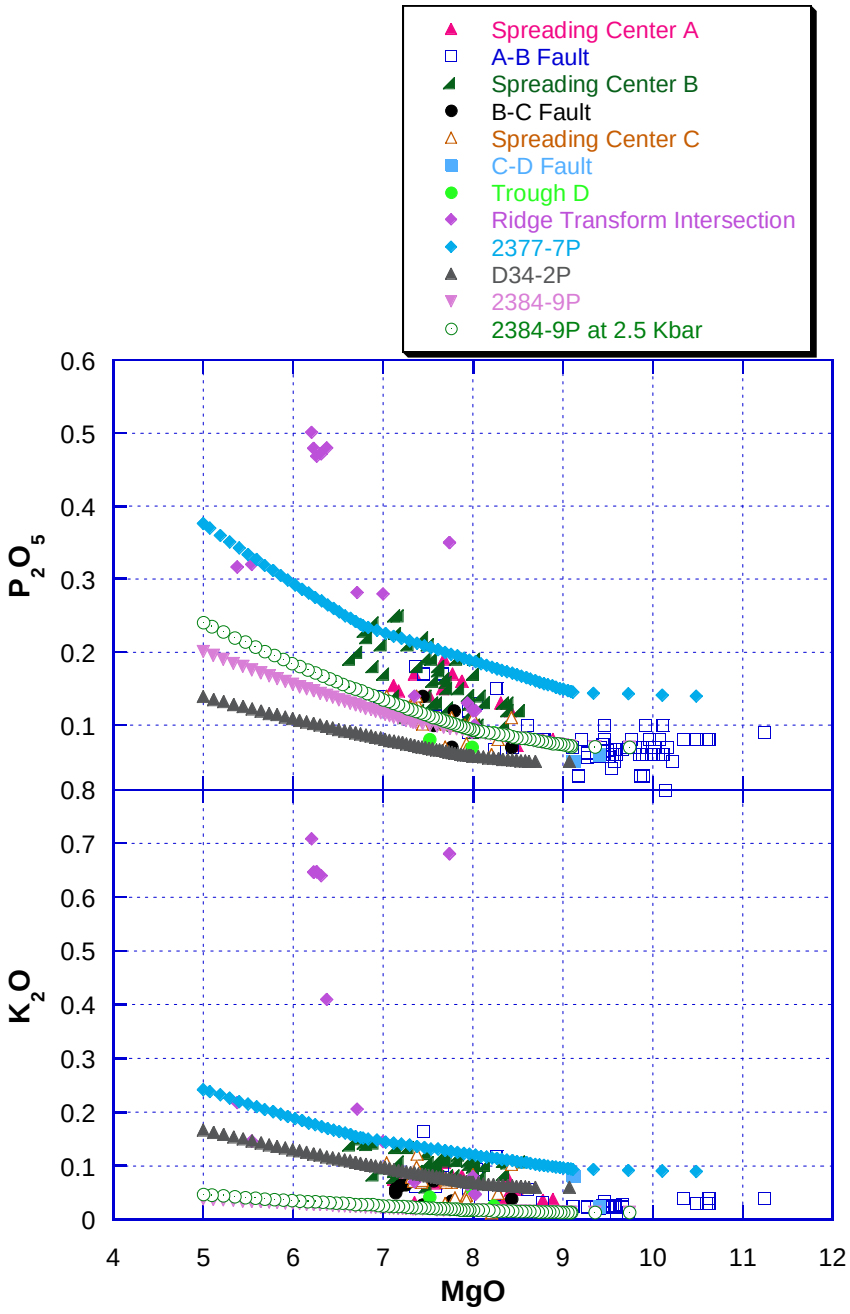


Figure 6-4. Continued.

microprobe analysis. The hydrous calculations cause the liquids to crystallize at lower temperatures (1175-1220°C) and cause plagioclase and clinopyroxene to stabilize a little bit later. The slight delay in the onset of plagioclase crystallization is enough to raise the $Al_2O_3$ of the liquid lines of descent. Since the water resulted in later crystallization of clinopyroxene, hydrous calculations were unable to account for the low CaO samples.

For comparison, liquid line of descent models were also run using the Langmuir et al. (1992) crystal fractionation models for olivine, plagioclase, and clinopyroxene. The two models produced almost identical liquid lines of descent except for the CaO and $Al_2O_3$ major elements. The Langmuir modeled liquid lines of descent fall on the high side of the observed CaO data, but provide a better fit to the $Al_2O_3$ data without requiring hydrous calculations (Figure 6-5). In order to fit the CaO data, high pressure (2.5 kbars) liquid lines of descent are still required.

For the most part, the Siqueiros major element variability can be explained by low pressure crystallization of parental magmas similar in composition to 2377-7P, D34-2P, and 2377-7P. In order to explain the entire range of CaO variability, high pressure fractionation is required to stabilize clinopyroxene early, which results in a reduction in CaO in relatively mafic lavas. $Al_2O_3$ variability can be explained by either the Langmuir et al. (1992) fractionation models or by a small amount of water in the magma as observed in the microprobe data. E-MORB samples from the RTI can not be explained by crystal fractionation of the other Siqueiros samples. A parental composition that is more enriched in $Al_2O_3$ and more depleted in CaO and FeO is required to explain the E-MORB samples.

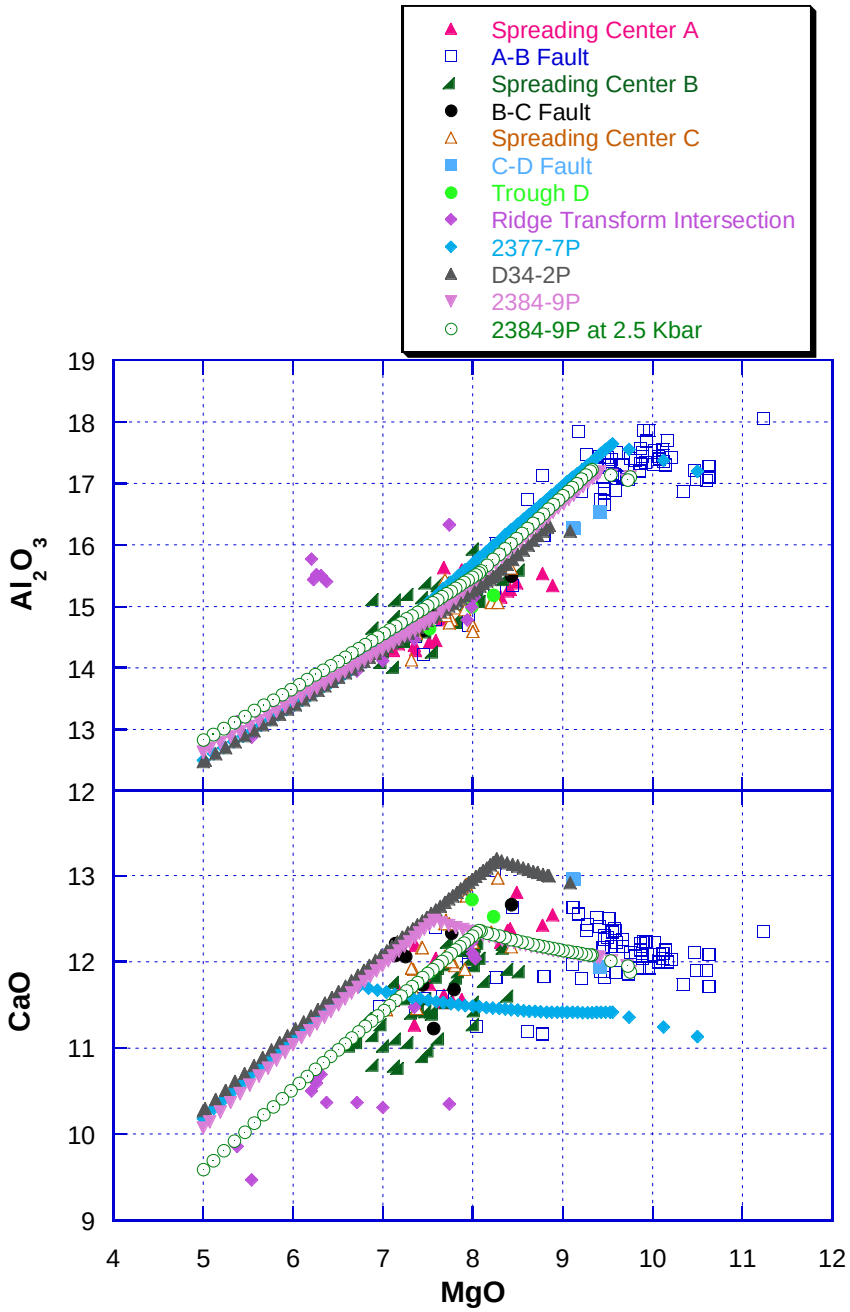


Figure 6-5. Comparison of CaO and $Al_2O_3$ data with LLD models calculated using the olivine, plagioclase, and clinopyroxene fractionation models of Langmuir et al. (1992). Parental compositions 2377-7 and D34-2 were run at low pressure (< 1 kbar) and 2384-9 was run at low pressure (<1 kbar) and at 2.5 k bars.

## Trace Element Models

Trace element systematics can be used to better constrain how fractional crystallization and magma mixing have affected the chemical evolution of the magmas (e.g., Perfit et al., 1983; Hekinian et al., 1989; Batiza and Niu, 1992). The concentrations of Cr, Sr, Zr, Y, Ni, and V in the residual liquid ($C_l$) were modeled using the Rayleigh fractionation equation ($C_l = C_o * F^{(D-1)}$) (Langmuir et al., 1992). The fraction of melt remaining (F) and the proportions of crystals used in each step were taken from the results of the major element LLD calculations produced in Petrolog for low pressure crystal fractionation (33 bars). D34-2P, D20-15P and 2384-9P were chosen as representative parents because they are relatively primitive and have significantly different compositions from one another that might represent different parental melts. The elements chosen to model have a wide range of partition coefficients (Kd) for the liquidus minerals observed in the samples (olivine, plagioclase, clinopyroxene, and spinel). In order to give an idea of the possible range of compositions that could reasonably be generated by fractional crystallization, trace element LLDs were produced for the highest and lowest bulk partition coefficients determined for basaltic systems (Villemant et al., 1981; Johnson & Kinzler, 1989; Skulski et al.,1994; Bindeman et al., 1998; Hart & Dunn, 1993; Duke, 1976; Bougault & Hekinian, 1974; Ulmer, 1989; Ringwood, 1970; Hauri et al., 1994; Takahashi, 1978; Beattie, 1993; Sun et al., 1974; McKay et al., 1994; Smith, 1993; Perfit et al., 1983; Henderson, 1986; Ragland, 1989; Rollinson, 1993) and are graphically shown in Figure 6-6. Partition coefficients with intermediate values were determined that best fit the observed data and the results of those calculations are shown in Figure 6-7. High, low, and best fit partition coefficients are shown in Table 6-1.

Table 6-1. List of partition coefficients.

| | Olivine | | | Plagioclase | | | Clinopyroxene | | | Spinel | | |
|---|---|---|---|---|---|---|---|---|---|---|---|---|
| Element | High | Low | Best | High | Low | Best | High | Low | Best | High | Low | Best |
| Zr | 0.06[a] | 0.007[b] | 0.007[b] | 0.27[a] | 0.005[b] | 0.005[b] | 0.27[c] | 0.001[d] | 0.001[d] | 0 | 0 | 0 |
| Y | 0.01[e] | 0.0036[b] | 0.0036[b] | 0.031[f] | 0.02[b] | 0.02[b] | 1.71[d] | 0.29[d] | 0.467[g] | 0 | 0 | 0 |
| V | 0.09[h] | 0.02[i] | 0.02[i] | 0.1[j] | 0[h] | 0[h] | 6.18[d] | 0.22[i] | 1.31[k] | 38[l] | 0 | 0 |
| Cr | 2.1[m] | 0.63[b] | 1[n] | 10[m] | 0[h] | 0[h] | 36[i] | 1.66[o] | 1.66[o] | 77[l] | 5[n] | 5[n] |
| Ni | 48[i] | 2.86[p] | 12[n] | 0.5[a] | 0.01[m] | 0.01[m] | 10[i] | 1.2[i] | 1.2[i] | 10[n] | 10[n] | 10[n] |
| Sr | 0.014[q] | 0.0000154[r] | 0.0000154[r] | 10[a] | 1.5[l] | 1.5[l] | 0.449[s] | 0.04[t] | 0.04[t] | 0.01[n] | 0.01[n] | 0.01[n] |

Notes: Partition coefficients derived from the following references in the Geochemical Earth Reference Model (GERM) at http://www.earthref.org/GERM/main.htm: Villemant et al., 1981a; Johnson & Kinzler, 1989c; Skulski et al.,1994d; Bindeman et al., 1998f; Hart & Dunn, 1993g; Duke, 1976i; Bougault & Hekinian, 1974j; Ulmer, 1989k; Ringwood, 1970l; Hauri et al., 1994o; Takahashi, 1978p; Beattie, 1993r; Sun et al., 1974s; McKay et al., 1994t. Other sources not found in GERM are Smith, 1993b; Perfit et al., 1983h; Henderson, 1986m; Ragland, 1989n; Rollinson, 1993q.

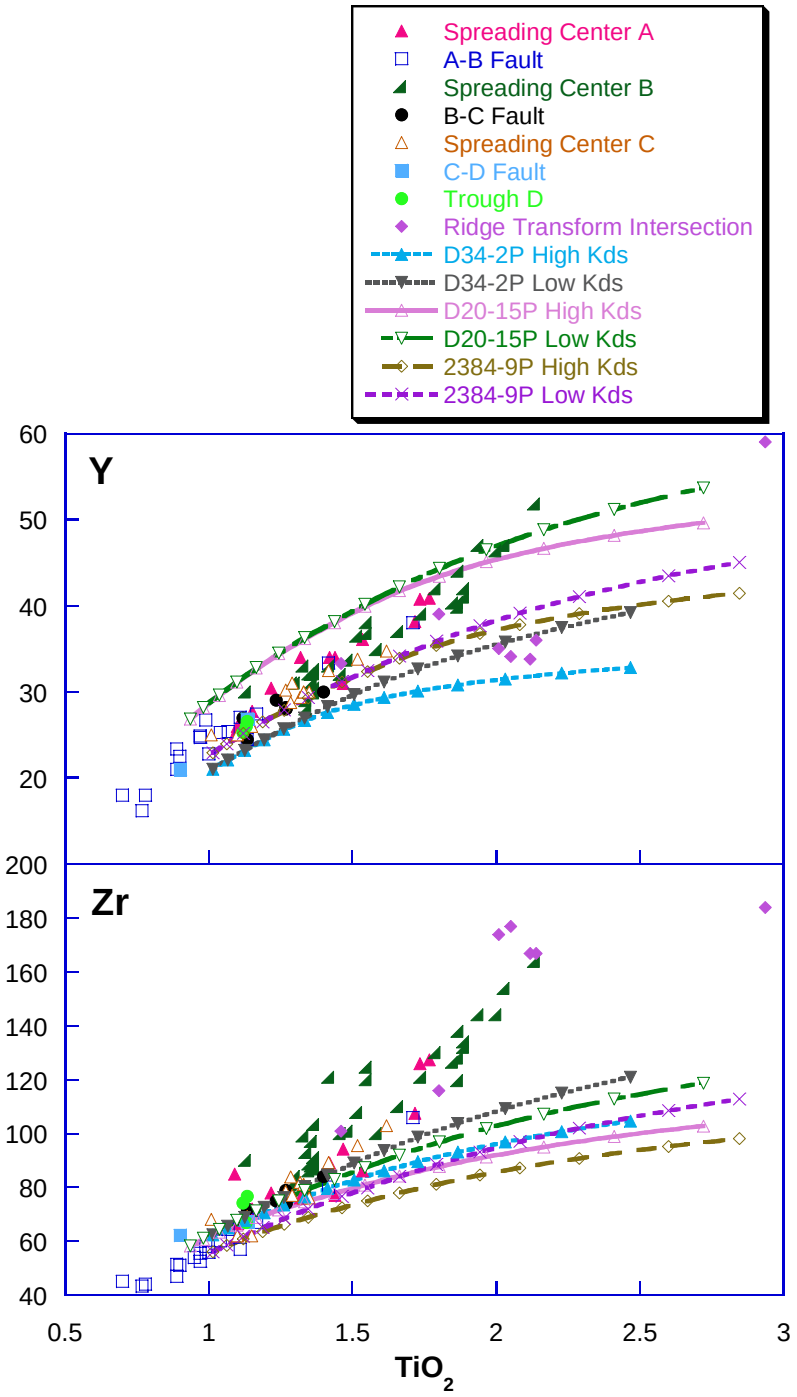


Figure 6-6. Comparison of observed trace element data with modeled fractionation trends calculated assuming perfect Rayleigh fractional crystallization. Fractionation trends were calculated for parental compositions D34-2P, D20-15P, and 2384-9P using the highest and lowest reported partition coefficients for olivine, plagioclase, clinopyroxene, and spinel.

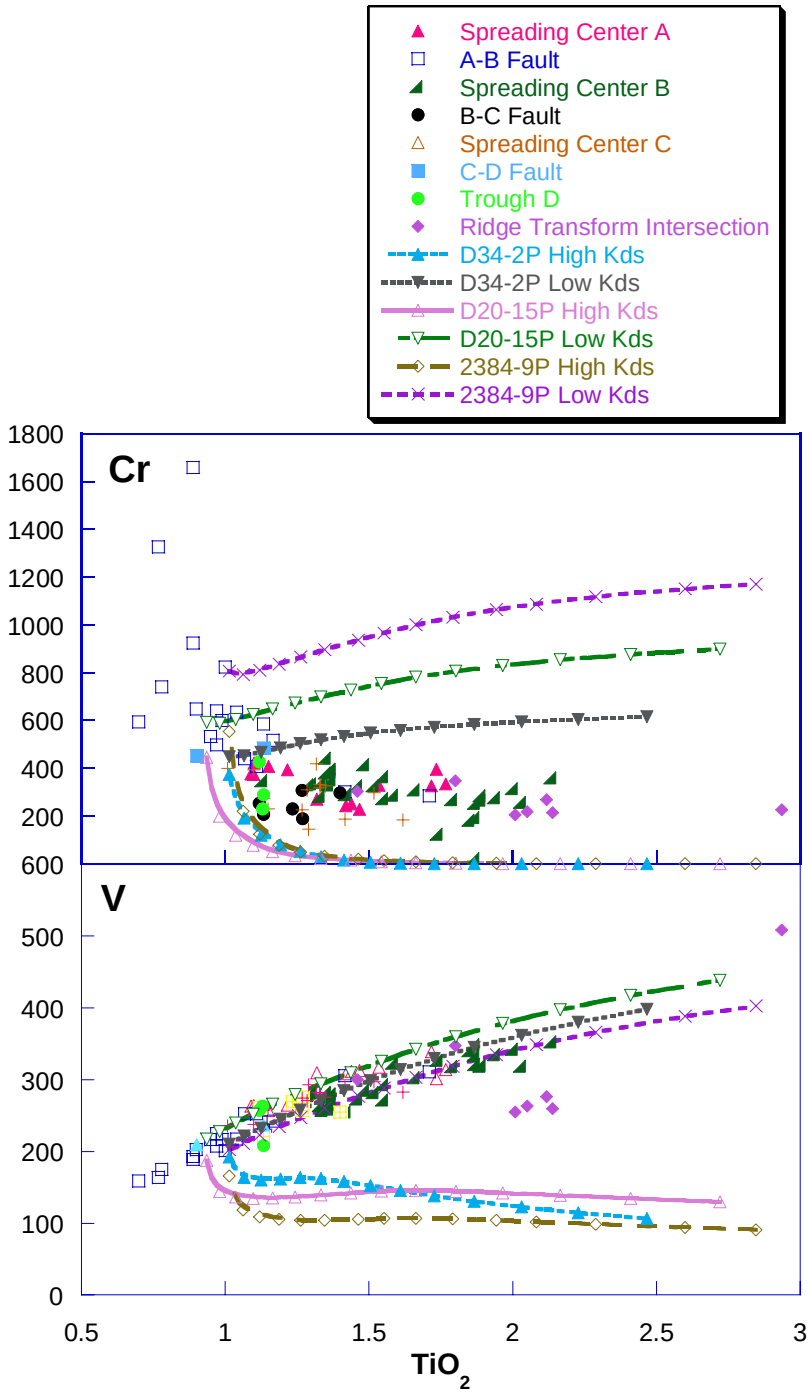


Figure 6-6. Continued.

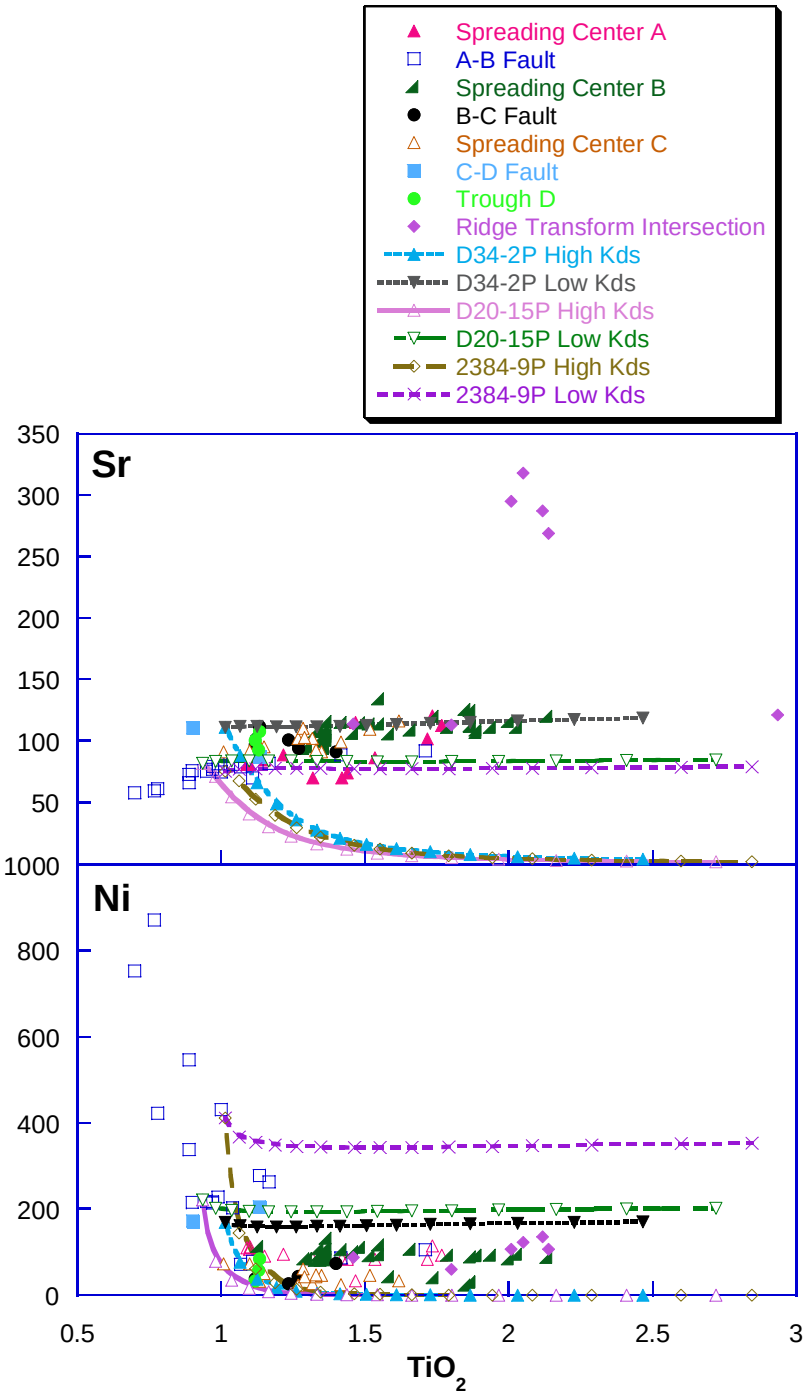


Figure 6-6. Continued.

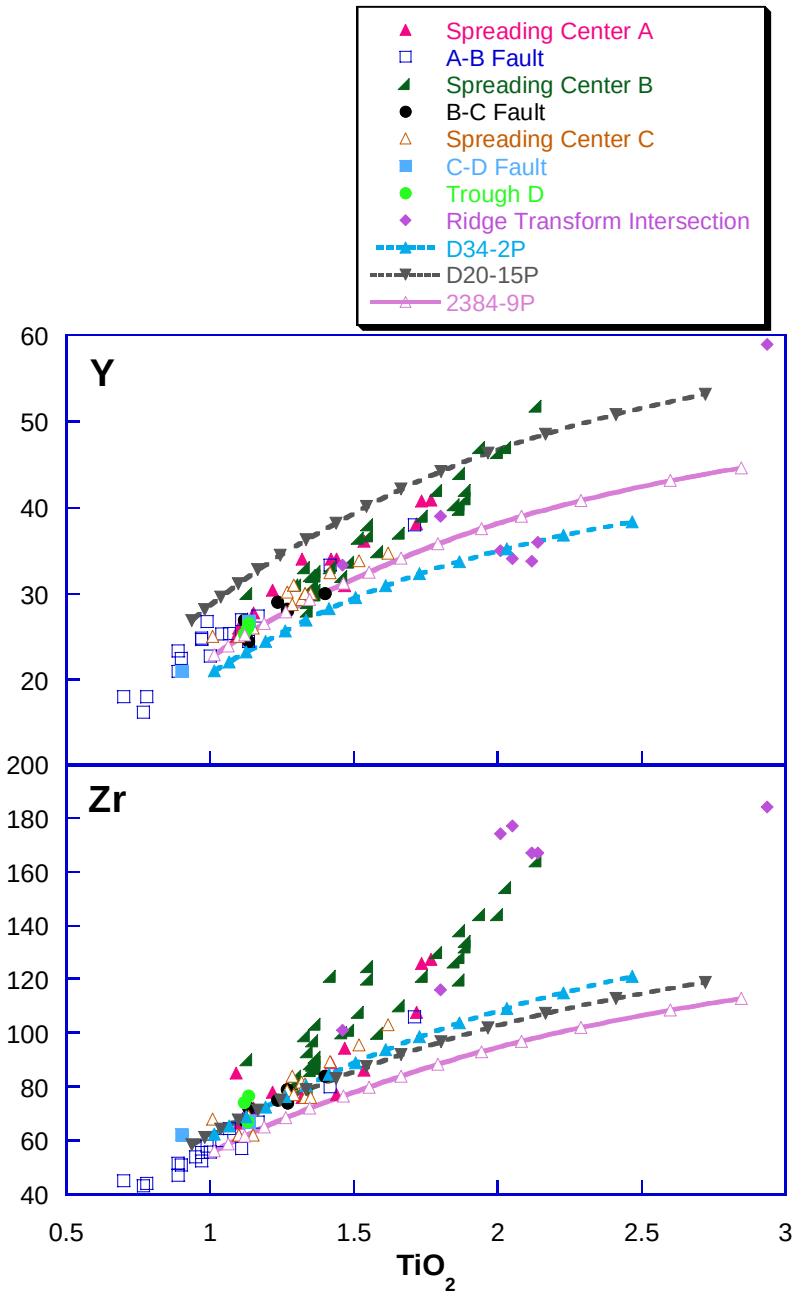


Figure 6-7. Comparison of observed trace element data versus $TiO_2$ with modeled fractionation trends calculated assuming perfect Rayleigh fractional crystallization. Fractionation trends were calculated for parental compositions D34-2P, D20-15P, and 2384-9P using the olivine, plagioclase, clinopyroxene, and spinel partition coefficients that provided the best fit to the observed trends.

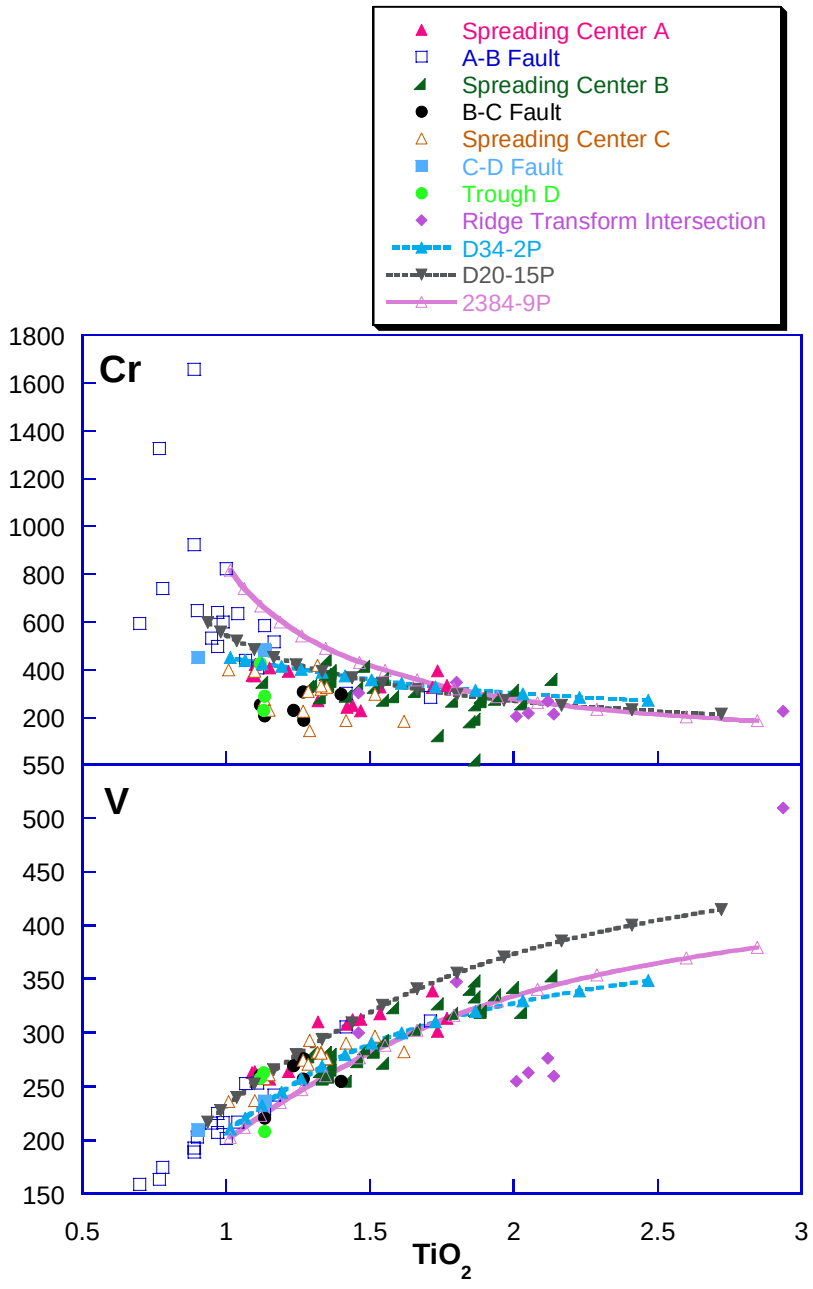


Figure 6-7. Continued.

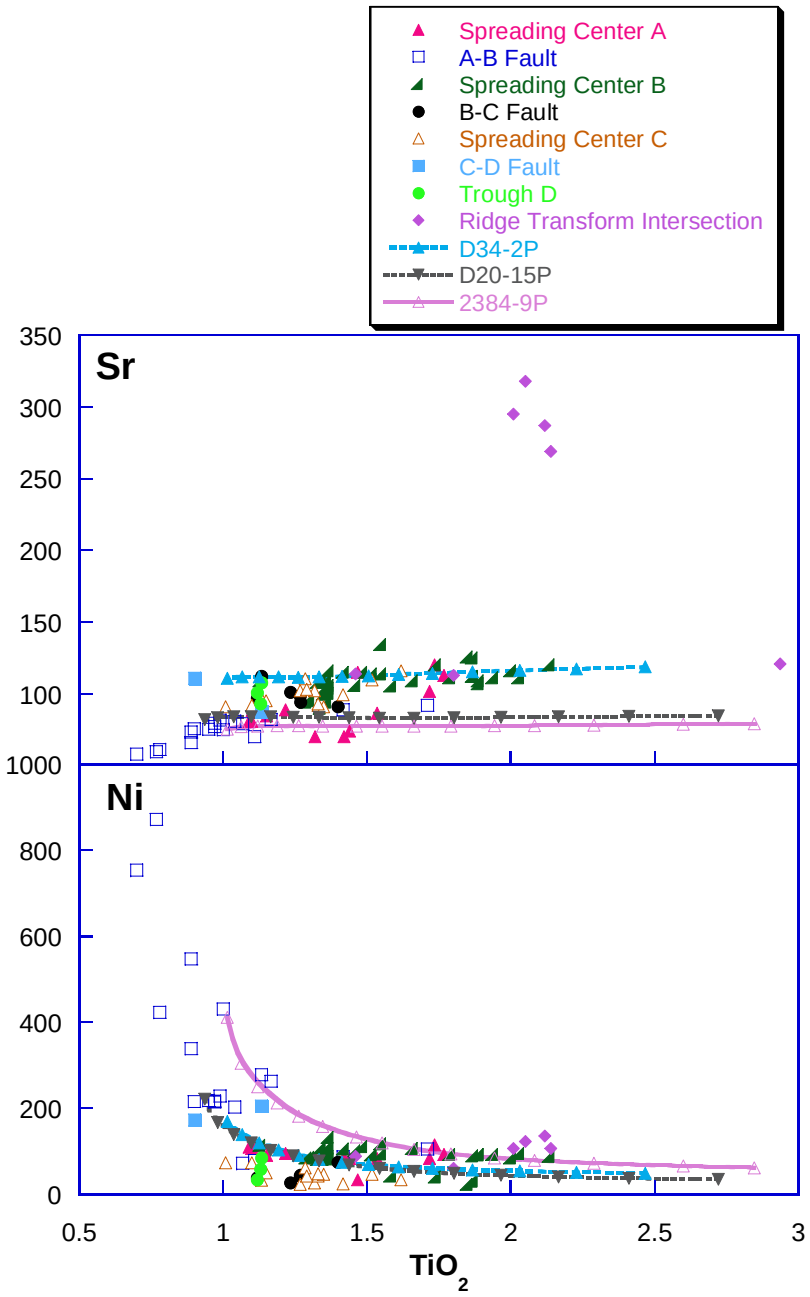


Figure 6-7. Continued.

Figures 6-6 and 6-7 show the calculated liquid lines of descent for increments of 5% fractional crystallization for Zr, Y, V, Cr, Ni, and Sr vs. $TiO_2$. In each fractionation step, the percentage of residual liquid has been calculated from the major element LLDs. The parental liquid and fractionating phase compositions were continually changed after each 5% increment. The fractionating phase compositions were calculated by averaging the phase compositions calculated in the major element variations over the 5% increment. This produces a model in which each parent-to-differentiate step is considered a separate event rather than assuming that the differentiates are a cumulative result of fractionation from one parental composition.

The LLDs produced using the highest and lowest available partition coefficients bracket the observed trace element data (except the E-MORB compositions) for all elements other than Zr (Figure 6-6). When intermediate partition coefficients were used, the liquid lines of descent from the three assumed parental liquids fit the observed Ni, Cr, Sr, and V trends well and can explain the abundances measured in most samples other than the E-MORBS found at the WRTI (Figure 6-7). The E-MORBs are more enriched in the highly incompatible elements and more depleted in Y and V relative to the "normal samples" and require a very different parental composition. The liquid lines of descent bracket the Sr data, but parental compositions D20-15P and 2384-9P do not fit the Sr data as well as they do the other trace elements. When preparing the samples for XRF analysis care was taken to remove all phenocrysts, however, microphenocrysts of plagioclase typically remain and could result in higher Sr contents in some samples which may explain why the Sr contents are slightly higher and could explain the slightly higher observed Sr contents than predicted by the models.

The calculated fractional crystallization paths for Cr and Ni do not reach some of the most depleted samples using the partition coefficients chosen for the best fit (Figure 6-7). The higher partition coefficients do produce fractionation paths more depleted in Cr and Ni than the observed data (Figure 6-6), suggesting that the actual partition coefficients for the samples may be between that chosen for the best fit models and that of the highest partition coefficients.

Although the Y calculated fractional crystallization paths bracket the observed Y values, the shape of the fractionation trend does not fit the trend of the observed data and the measured Zr values are generally higher than the calculated trends. Zr and Y are both highly incompatible elements and over-enrichments in highly incompatible elements compared to what is calculated by Raleigh fractionation is commonly observed in MORB suites (Perfit et al, 1983; Bryan et al., 1979). Slightly greater enrichments in Zr and Y can be obtained by modeling the magma system as one batch that crystallizes to a greater extent (Figure 6-8). In a batch model, the parental liquid composition is not adjusted with each increment and in such a model if any intermediate lavas are removed the more fractionated daughters could not be obtained. It does provide a method to explain how more evolved liquids enriched in highly incompatible elements could be created, which might mix with other less evolved melts given the entire range observed in the Siqueiros samples.

In summary, calculated trace element variations due to fractional crystallization using the parental compositions of D34-2P, D20-15P, and 2384-9P fit the observed data fairly well as shown in trace element-Zr plots (Figure 6-9). In order to explain the majority of the samples from the spreading centers and shear zones, between 55-60%

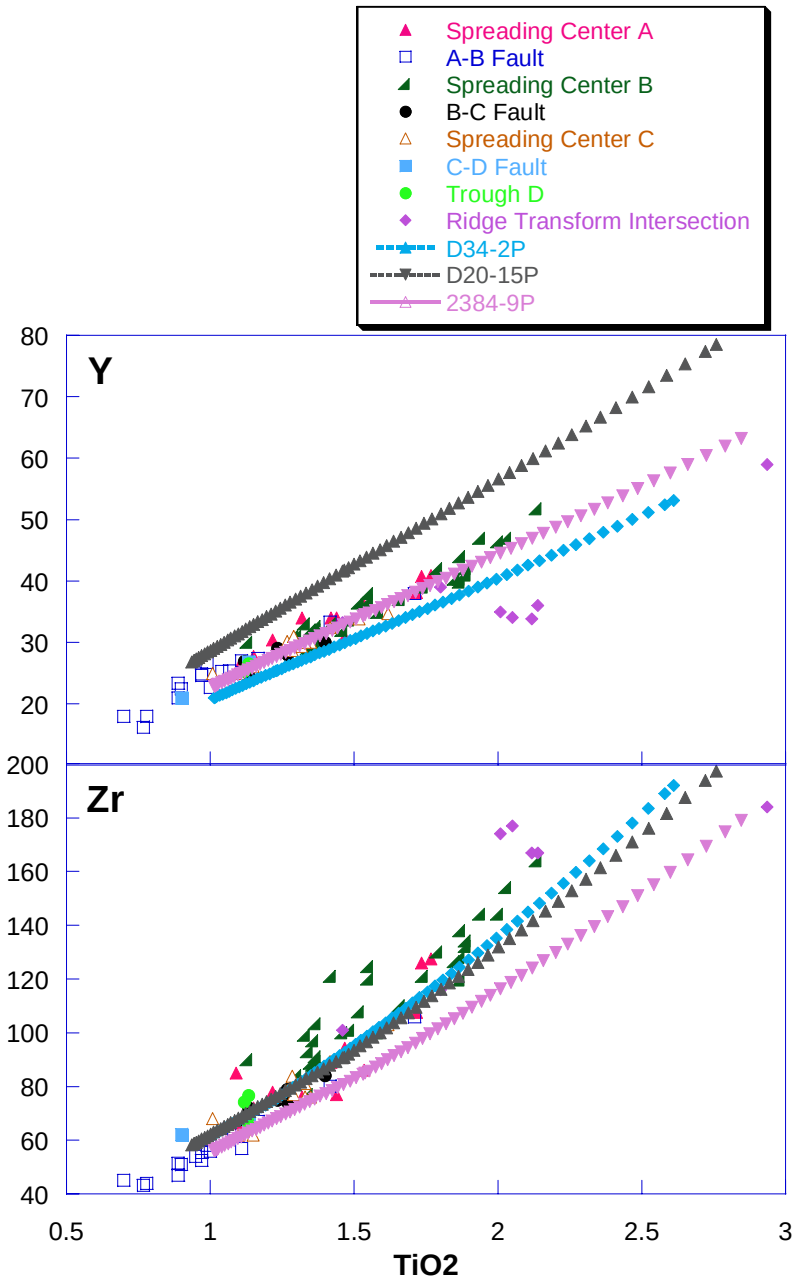


Figure 6-8. . Comparison of observed trace element data versus $TiO_2$ with modeled fractionation trends calculated assuming perfect Rayleigh fractional crystallization. Fractionation trends were calculated as one batch melt in which the parental composition of the derivative magma was not recalculated in 5% increments.

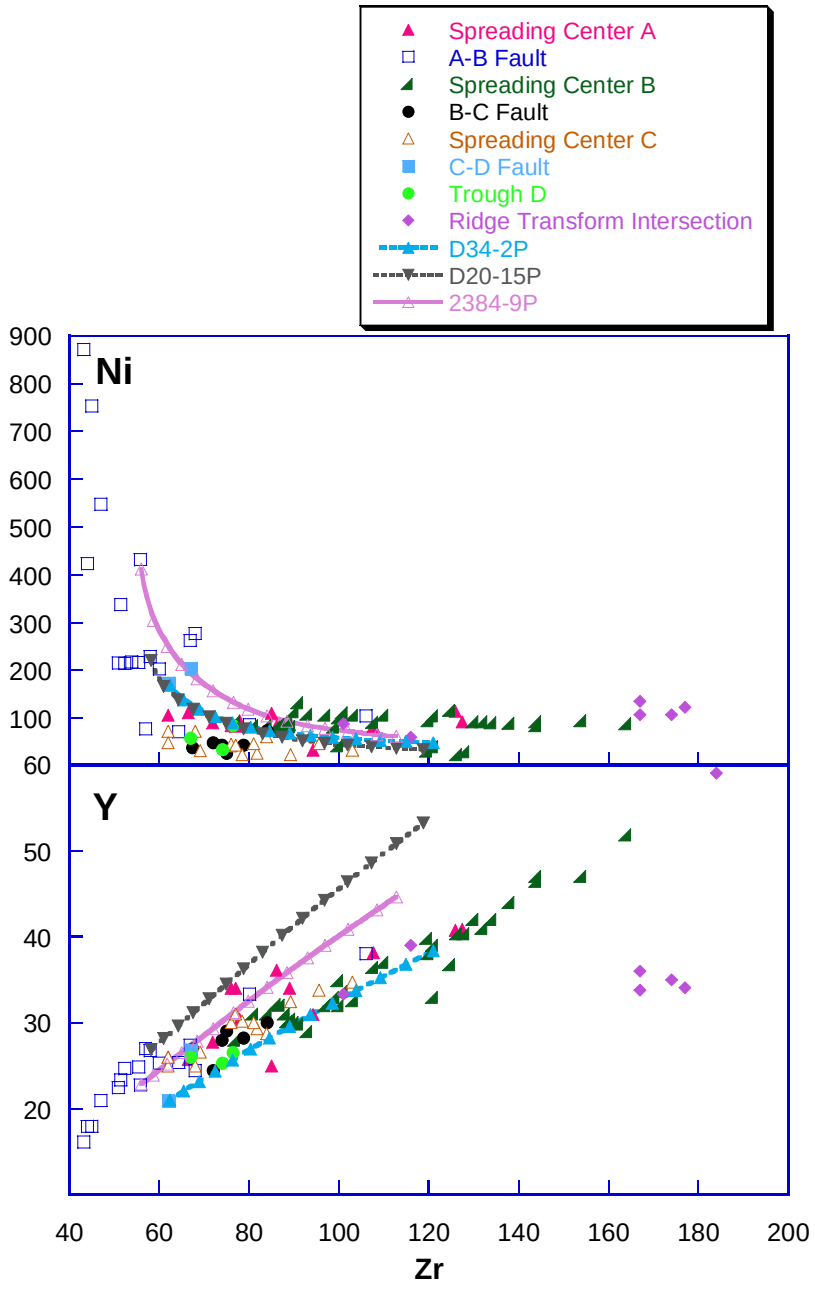


Figure 6-9. Comparison of observed trace element data versus Zr with modeled fractionation trends calculated assuming perfect Rayleigh fractional crystallization. Fractionation trends were calculated for D34-2P, D20-15P, and 2384-9P using the olivine, plagioclase, clinopyroxene, and spinel partition coefficients that provided the best fit to the observed trends.

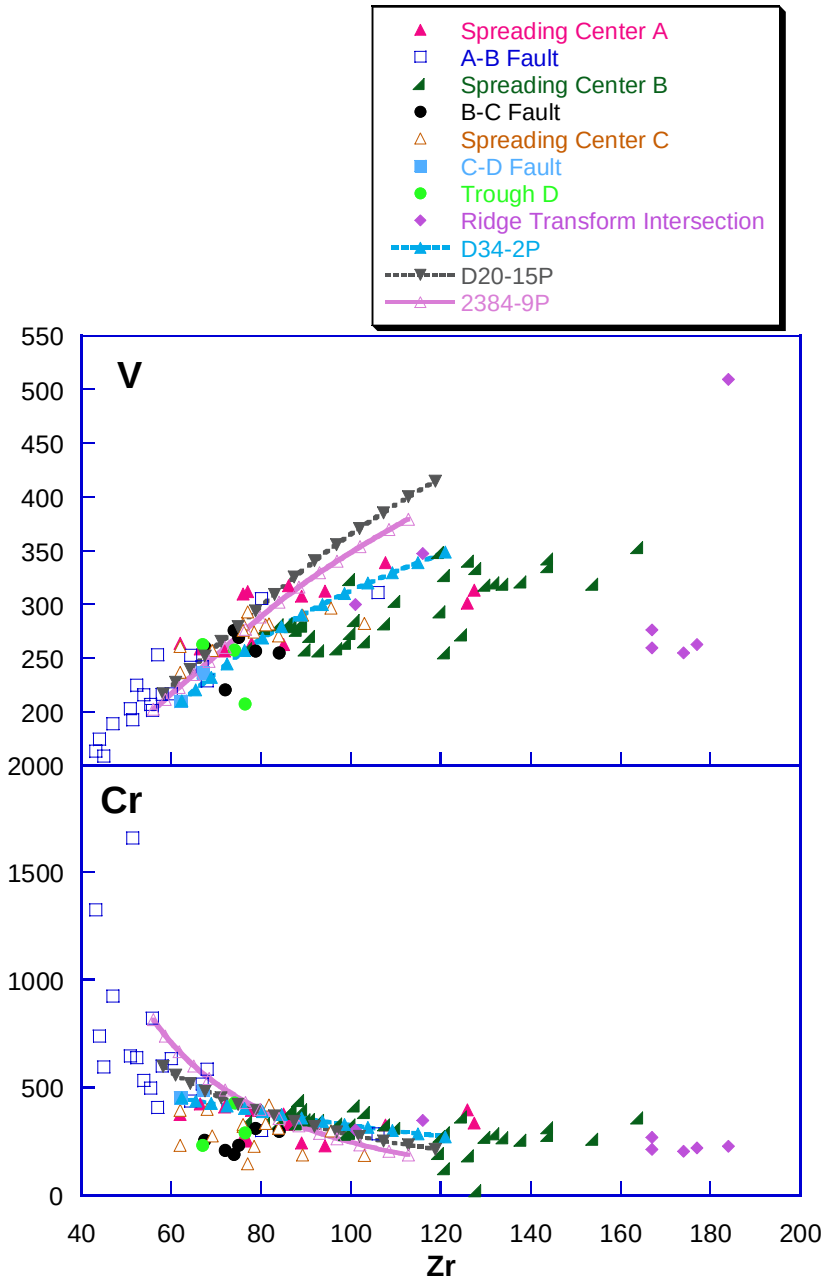


Figure 6-9. Continued.

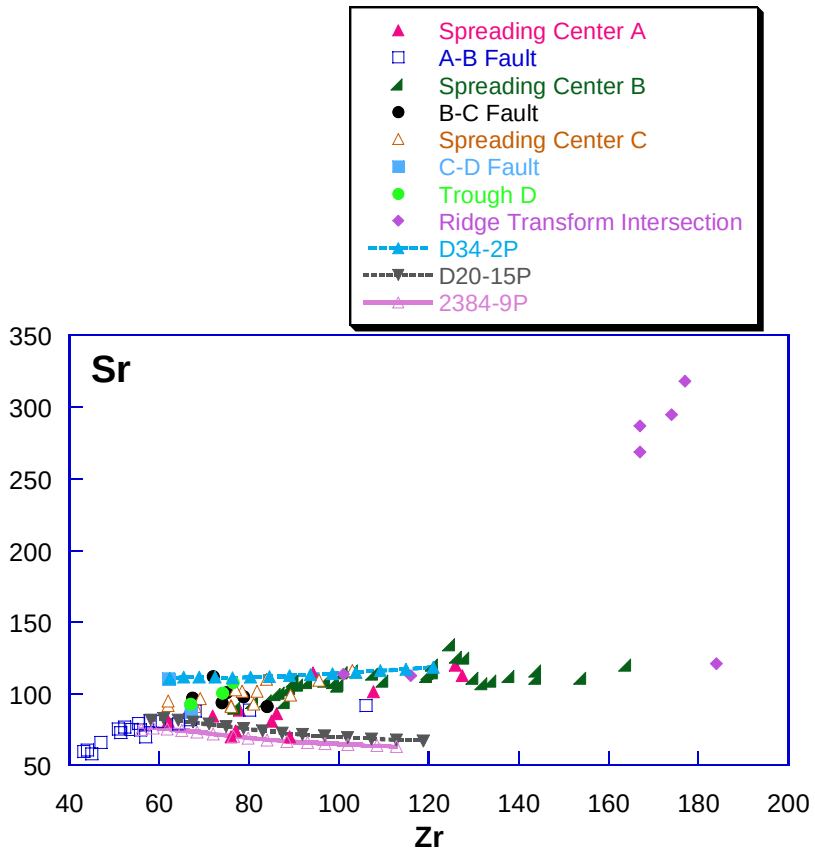


Figuer 6-9. Continued.

fractional crystallization of these parental compositions was required. In order to explain the most evolved sample found at the WRTI, sample 2390-9, over 70% crystal fractionation was required. Parental compositions D20-15P and 2384-9P produce residual liquids slightly more enriched in V and Y for a given Zr content, but this may be due to the under-enrichment of Zr generated by the calculations compared to the observed Zr concentrations. None of the models can be used to explain the observed concentrations in the E-MORB samples using the N-MORB samples as parental compositions. Overall, parental composition D34-2P produces the best liquid line of descent for all the modeled trace elements, but it is clear that more than one liquid line of

descent is needed to fit the entire range of data implying that multiple N-MORB parents are required in the Siqueiros transform domain.

## REE Models

The rare earth elements (REE) are particularly sensitive to magma genesis and fractional crystallization processes (Perfit et al., 1993). The REE trends show that samples from the A-B fault are more depleted in the LREE than those from the spreading centers and transforms. For this reason, REE models were produced using D20-15P (A-B Fault) and 2375-7P (spreading center B) as parental compositions. The modeled REE trends are shown in figures 6-10 and 6-11. The calculated liquid lines of descent are shown for 10% fractional crystallization increments. The parental composition and fractionating phase compositions were recalculated at 5% increments. Trace elements La, Ce, Sm, Y, and Yb were modeled. The partition coefficients are shown in Table 6-2.

The REE patterns modeled by D20-15P are more depleted in the LREE than the REE patterns of samples from the other fault zones and spreading centers (Figure 6-11). Fractional crystallization models of D20-15P do provide a close fit to samples recovered in the A-B fault, but some samples from the A-B fault, such as A25 D17-9, have REE patterns that are better explained by fractionation from a parental magma closer in composition to 2375-7P (Figure 6-12). The REE pattern modeled by 2375-7P from spreading center B provides a much better fit to the REE patterns observed at the other fault zones and spreading centers. 2375-7P is more enriched than other observed compositions which require a more primitive parental composition. The calculations predict that over 60% fractional crystallization would be required to produce the most evolved samples from the RTI from 2375-7P.

Table 6-2. REE partition coefficients.

| | Olivine | Plagioclase | Clinopyroxene |
|---|---|---|---|
| **La** | 0.007 | 0.19 | 0.056 |
| **Ce** | 0.006 | 0.1 | 0.09 |
| **Sm** | 0.007 | 0.039 | 0.445 |
| **Y** | 0.01 | 0.03 | 0.9 |
| **Yb** | 0.014 | 0.067 | 0.62 |

Notes: Data from Rollinson, 1993.

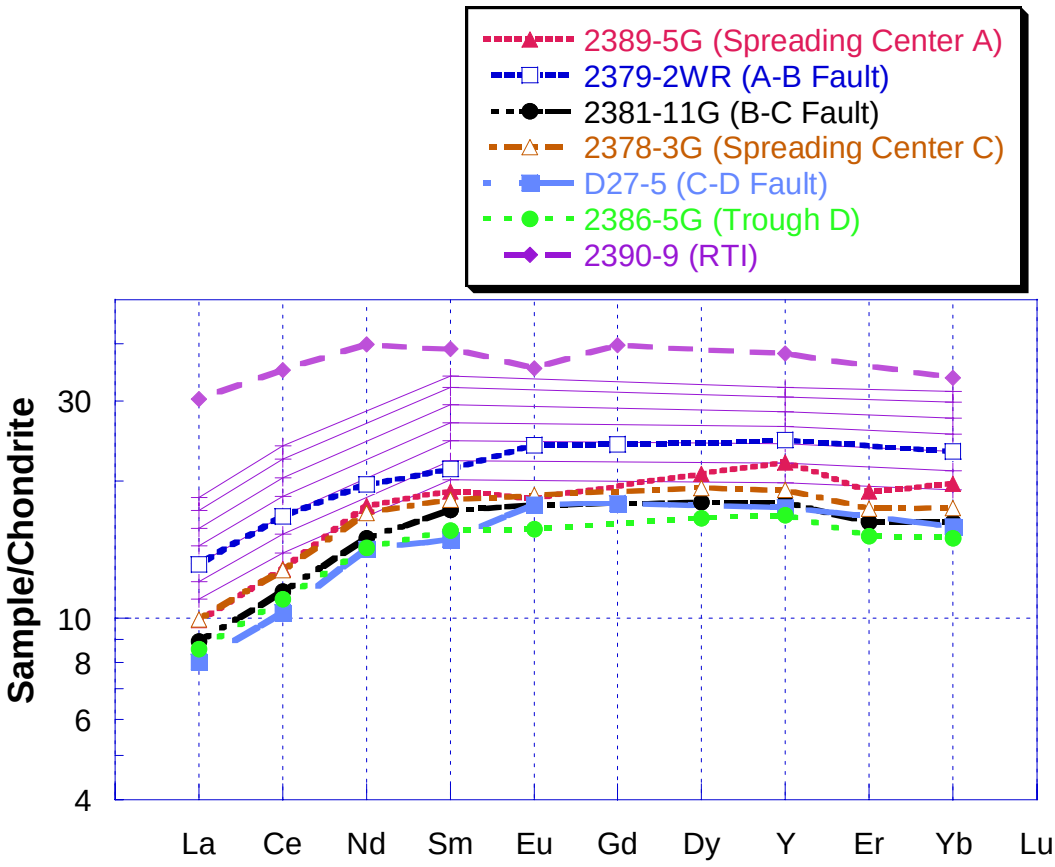


Figure 6-10. Comparison of observed REE trends with modeled REE fractionation trends calculated for 2375-7P from spreading center B. Thin solid purple lines are modeled REE fractionation trends for increments of 10% crystal fractionation. Partition coefficients for La, Ce, Sm, Y, and Yb are shown in Table 6-2.

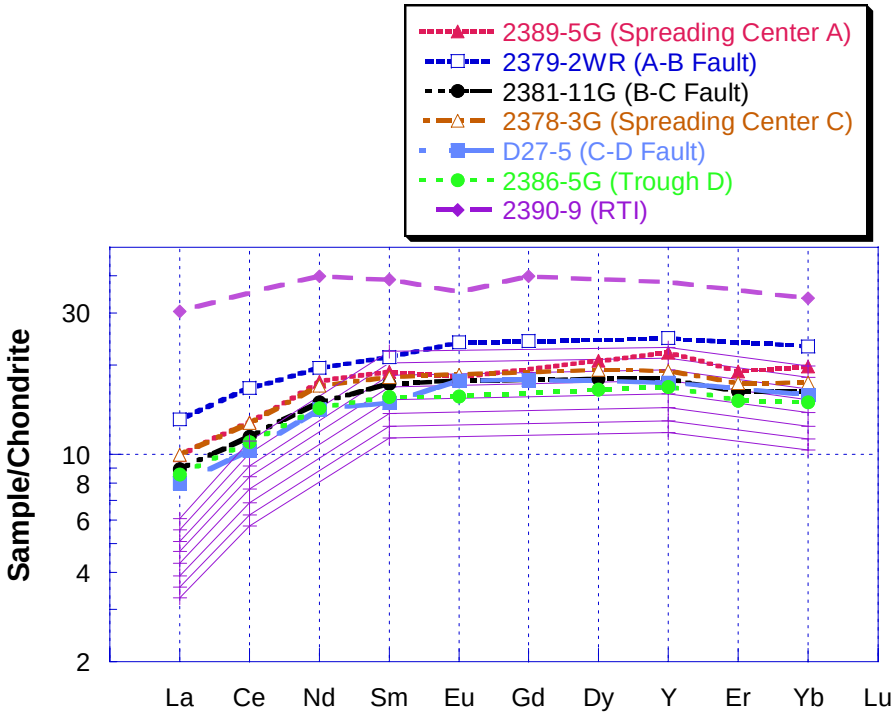


Figure 6-11. Comparison of observed REE trends with modeled REE fractionation trends calculated for D20-15P from the A-B fault. Thin solid purple lines are modeled REE fractionation trends for increments of 10% crystal fractionation. Partition coefficients for La, Ce, Sm, Y, and Yb are shown in Table 6-2.

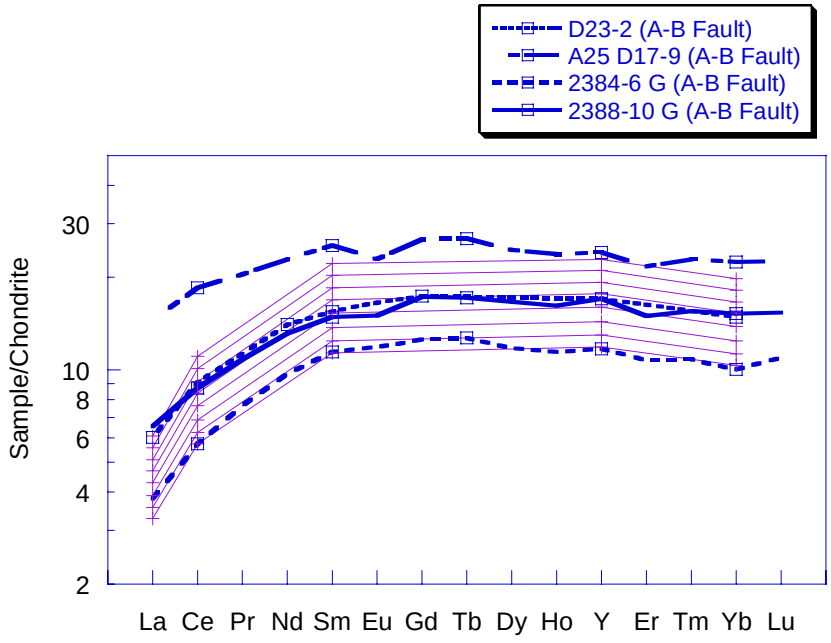


Figure 6-12. Comparison of observed A-B fault REE trends with modeled REE fractionation trends calculated for D20-15P. Thin solid purple lines are modeled REE fractionation trends for increments of 10% crystal fractionation. Partition coefficients for La, Ce, Sm, Y, and Yb are shown in Table 6-2.

Compared to the major element models, greater amounts of fractional crystallization are needed to explain the LREE enrichments of the evolved samples from the RTI. Again greater enrichments can be obtained by modeling the magma system as one batch that crystallizes to a greater extent (Figure 6-13). As discussed in Chapter 7, LREE can also be affected by mixing with E-MORB compositions. Mixing with E-MORB prior to fractional crystallization can also explain some of the LREE enrichment seen in the more evolved samples.

The REE trends of the E-MORBs found at the WRTI are much more enriched in the LREE. Neither 2375-7 nor D20-15 are reasonable parental compositions for the E-MORB samples.

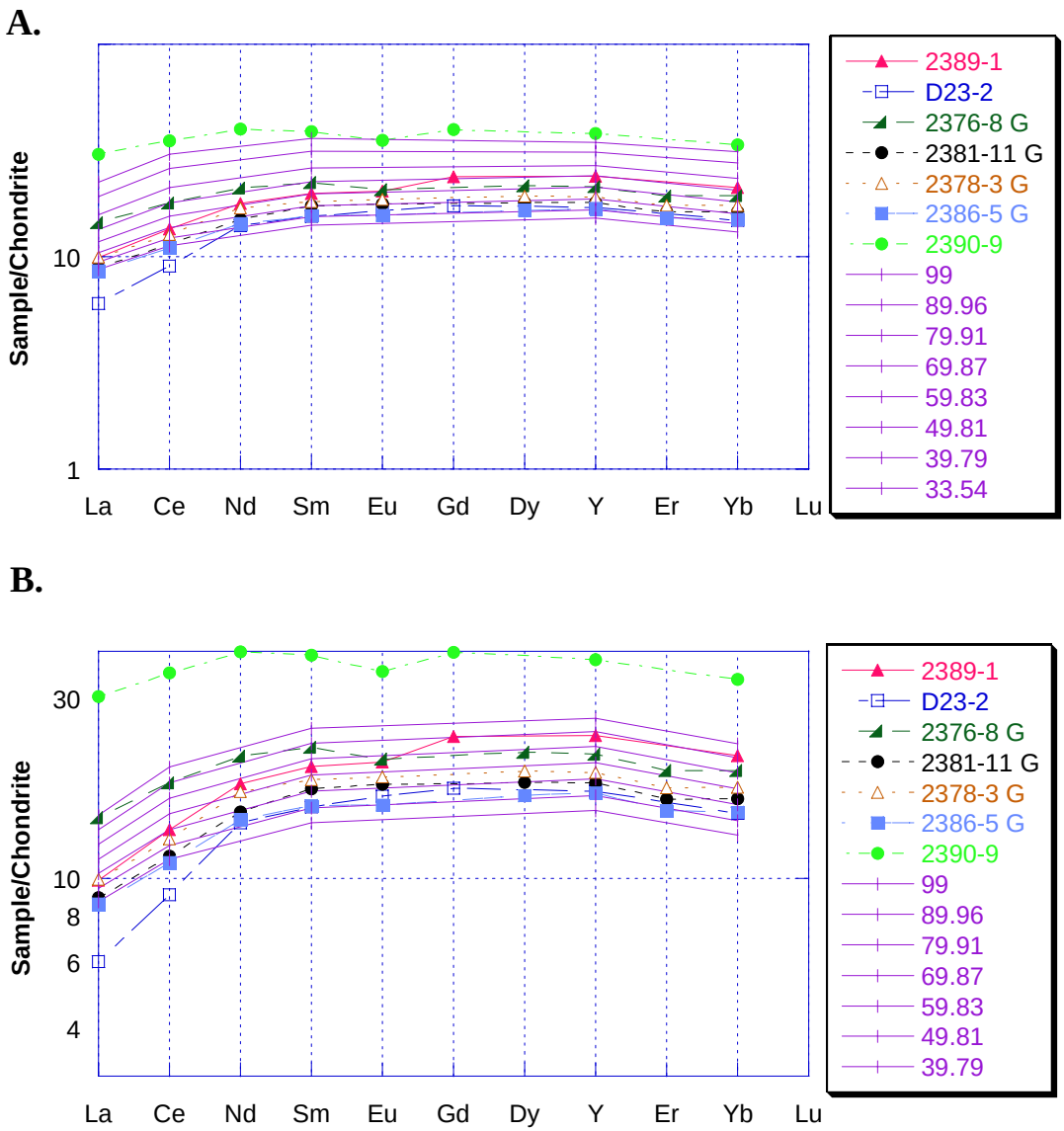


Figure 6-13. Rayleigh fractionation model for REE. Models produced by mixing 2384-9 with 6% E-MORB followed by fractional crystallization shown for 10% increments. A. Batch fractional crystallization model where the magma chamber is fractionated to a great extend without removal of liquid. B. Fractional crystallization model in which the liquid composition is re-calculated at 5% increments. Batch crystallization is able to produce greater enrichment in the REE.

# CHAPTER 7
# DISCUSSION

Major and trace element data indicate that the Siqueiros transform domain contains a wide variety of lavas and that there are at least four groups of MORB with distinct chemical compositions. These groups are: 1) normal incompatible element depleted samples recovered from the three intra-transform spreading centers, the faults, and trough D; 2) low $Na_2O$ samples found at spreading center A; 3) D-MORB found within the A-B transform; 4) E-MORB found at the WRTI. The chemical composition of erupted lavas is generally controlled by 5 factors. These include the composition and mineralogy of the source that melts to form the parental magmas, the depth and extent of mantle melting, the type of melting (e.g. batch, fractional, or polybaric), the amount of mixing between different magma bodies, and the amount of fractional crystallization that the magma experiences after melting (Langmuir et al., 1992; Grove, 2000; Sinton and Detrick, 1992; Perfit and Chadwick, 1988).

## Fractional Crystallization

The majority of the samples from the Siqueiros transform have N-MORB chemical characteristics and were recovered from all of the intra-transform spreading centers, faults, and even from the RTIs. Most of the chemical variation in the N-MORB can be explained by low-pressure fractional crystallization as shown by the major element and trace element factional crystallization paths. The majority of the major element data can be explained by 50-55 wt. % fractional crystallization of spinel, olivine, plagioclase, and clinopyroxene from three different primitive N-MORB parental compositions. The

parental compositions used include D34-2P (a low sodium parent), 2384-9P, and 2377-7P (a parental composition based on reverse fractional crystallization of a more evolved lava composition). The trace element data are consistent with major element models indicating that the majority of Siqueiros samples formed by 55-60 % fractional crystallization from an N-MORB source similar in composition to primitive samples recovered within the Siqueiros transform. Three of the lavas with primitive compositions were used as potential parental magma compositions. D34-2P provided the best overall fit to the observed trace element trends and, although the calculated fractionation trends of D20-15P provide a good fit to much of the observed trace element data, the REE trends of D20-15P indicate that it is even more depleted in the light REE than the typical N-MORB and cannot be related to the N-MORB by fractional crystallization alone. Additionally, the incompatible elements Zr and Y could not be well modeled with the fractionation trends of the three parental compositions. The over enrichment of Zr relative to Ti is better modeled by extensive fractional crystallization of one magma body in which fractionated liquids are not incrementally removed (See Chapter 6).

It is clear that, although most of major and trace element variation could be explained by fractional crystallization, there is enough variability in the elemental data that more than one parental composition is required in order to explain the entire variation in compositions observed. Scatter of the major element data around the calculated LLDs indicate that at least 2-3 parental compositions are required or that multiple physical conditions were involved (e.g., slightly different fO2, pressure, water content). The low pressure models of Danyushevsky (2001) do not provide a good fit to the entire range of CaO and $Al_2O_3$ data. Better fits to the CaO and $Al_2O_3$ data are

obtained by invoking fractional crystallization at moderate pressures (~2.5 kbar) using the model of Langmuir et al. (1992). It is also apparent that many of the more evolved samples are more enriched in incompatible elements (e.g. $TiO_2$, $P_2O_5$, and $K_2O$) than predicted by the fractionation of primitive lavas found within Siqueiros. A parental composition similar to 2377-7P is needed in order to explain these "over-enriched" samples by fractional crystallization alone, yet all primitive lavas recovered within the Siqueiros transform are more depleted in the most highly incompatible elements than 2377-7P.

## Magma Mixing and Assimilation

Magma mixing can occur between primitive magmas derived from different mantle sources or between primitive and evolved magmas from a similar source. Radiogenic isotopic compositions of individual samples provide the best method to determine whether or not different sources were responsible for variations in chemical compositions because the isotopic variations cannot be affected by melting processes, but reflect long-term differences in the compositions of sources. Isotopic measurements (Sr, Nd, and Pb) have been completed on a few of the Siqueiros samples (Sims et al., 2002; Lundstrom et al., 1999), but have confirmed that the E-MORB samples found at the WRTI are isotopically distinct from the N-MORB samples found within the transform and along the adjacent EPR. This indicates that at least two different sources, a typical "depleted MORB source" and a more "enriched" source exist beneath the Siqueiros transform domain. Isotopic analysis of a few D-MORB samples showed that they are not significantly different than N-MORB samples, suggesting that D-MORB and N-MORB sources are similar and that any depletions or enrichments of radiogenic elements (and other incompatible elements) must have occurred relatively recently (in geologic terms).

Isotopic variations between the varieties of MORB recovered form the Siqueiros domain limit the amount of mixing between depleted and enriched end members to less than about 5% (see below) however, there is ample petrologic and chemical evidence that magma ± crystal mixing has occurred between MORB with different major and trace element compositions.

The observed scatter in major and trace elements might be the result of mixing of evolved and relatively primitive melts (+/- crystals). Seismic evidence has shown that a small body of magma (melt lens) overlying a broad crystal mush zone (crystals + melt) exists beneath most fast spreading ridges (MacLeod and Yaouancq, 2000; Detrick et al., 1987; Sinton and Detrick, 1992). Little is understood about the role the melt lenses play in storage and mixing of MORB. A theory proposed by Pan and Batiza (2003) suggests that the seismically detected shallow melt lenses actually contain highly evolved magma, formed by expelled interstitial melt during crystal network compaction. They believe that the composition of many MORB lavas result from more primitive magmas that pass through and possibly mix with the evolved melts in the shallow melt lens. This process is supported by evidence from xenocrysts and diverse melt inclusions found in many magmas along the EPR (Pan and Batiza, 2003; Pan and Batiza, 2002; Ridley et al, 2002; Danyushevsky et al., 2003; Kohut and Nielsen, 2003). More evidence for mixing of diverse magma compositions comes from a gabbroic xenolith recovered in a young lava from the EPR that contains cumulus anorthite (An > 90) and forsteristic olivine that are out of equilibrium relative to the interstitial glass between grains and the host rock compositions. Both the plagioclase and olivine crystals appear to have originated from different melts and the anorthitic phenocrysts likely crystallized from a high Ca/Na

primitive melt prior to accumulating with the olivine crystals. Anorthitic phenocrysts or xenocrysts are present in many MORB, yet such anorthitic crystals cannot have precipitated from any typical N-MORB melt (Kohut and Nielsen 2003; Ridley et al., in prep).

A number of textural and compositional features in Siqueiros lavas suggest that magma mixing may have occurred during petrogenesis of the suite. Phenocryst compositions in the Siqueiros samples include calcic plagioclase phenocrysts (An 75-80) that are out of equilibrium with their host glasses and have partially resorbed textures. Large olivine phenocrysts in Siqueiros samples also have partially resorbed rims and Fo contents (Fo = 90) too mafic to have originated from their host glasses. In addition, the composition of melt inclusions found in olivine phenocrysts from one of the Siqueiros transform picritic basalts are quite diverse and some have compositions believed to reflect assimilation of gabbroic material into hot primitive magma. This assimilation is believed to occur as crystallization begins within the crystal mush zone (Danyushevsky et al., 2003). The presence of phenocrysts (xenocrysts) that are clearly out of equilibrium with their host rocks and the diverse compositions of melt inclusions indicate mixing of different compositions such as high-MgO melts and high Ca/Na melts prior to eruption. The role of magma mixing in generating some of the chemical variability observed in the Siqueiros suite can be evaluated using some major element variations. Most plots of individual major element oxides in this suite of lavas show no distinct inflection points, and as such, provide little or no information regarding the role of magma mixing in the generation of the lavas because with near linear arrays, mixing lines between samples extend along the trend established by differentiation and are consequently

indistinguishable from them. However, prominent inflection points observed in $Al_2O_3$, CaO, and $CaO/Al_2O_3$ vs. MgO plots (Figure 7-1); consequences of the onset of plagioclase crystallization and clinopyroxene crystallization respectively, can provide clues about magma mixing. Lavas with intermediate compositions that deviate from the predicted LLD trends could be a result of mixing between various evolved liquids with more restricted primitive compositions. For example, mixing a primitive melt, with a composition such as sample 2384-9, with a ferrobasaltic melt (like that from spreading center B: 2377-3) or a FeTi basalt (from the RTI: 2390-9) produces mixed melts with intermediate MgO contents and relatively low $CaO/Al_2O_3$ values (Figure 7-1). The scatter observed in $CaO/Al_2O_3$, the departure of the data from calculated LLDs, and the low CaO contents in some samples are consistent with mixing of relatively primitive and moderately evolved magmas rather than requiring multiple LLDs produced at higher pressure and/or with different $H_2O$ contents. If all of the scatter were a result of evolution along different liquid lines of descent, greater degrees of scatter along other major element liquid lines of descent might be expected. Mixing of more and less evolved magmas is supported by the disequilibrium phase chemical data discussed above. The mixing of magmas cannot however account for the group of low $Na_2O$ samples found within spreading center A. These low $Na_2O$ samples must either result from partial melting of a low Na source or from greater extents of melting of the mantle beneath spreading center A.

Mixing models also provide better fits to some of the observed trends in trace element data than fractional crystallization models. Mixing curves were calculated assuming primitive melt with a composition of 2384-9P mixes with evolved melts with

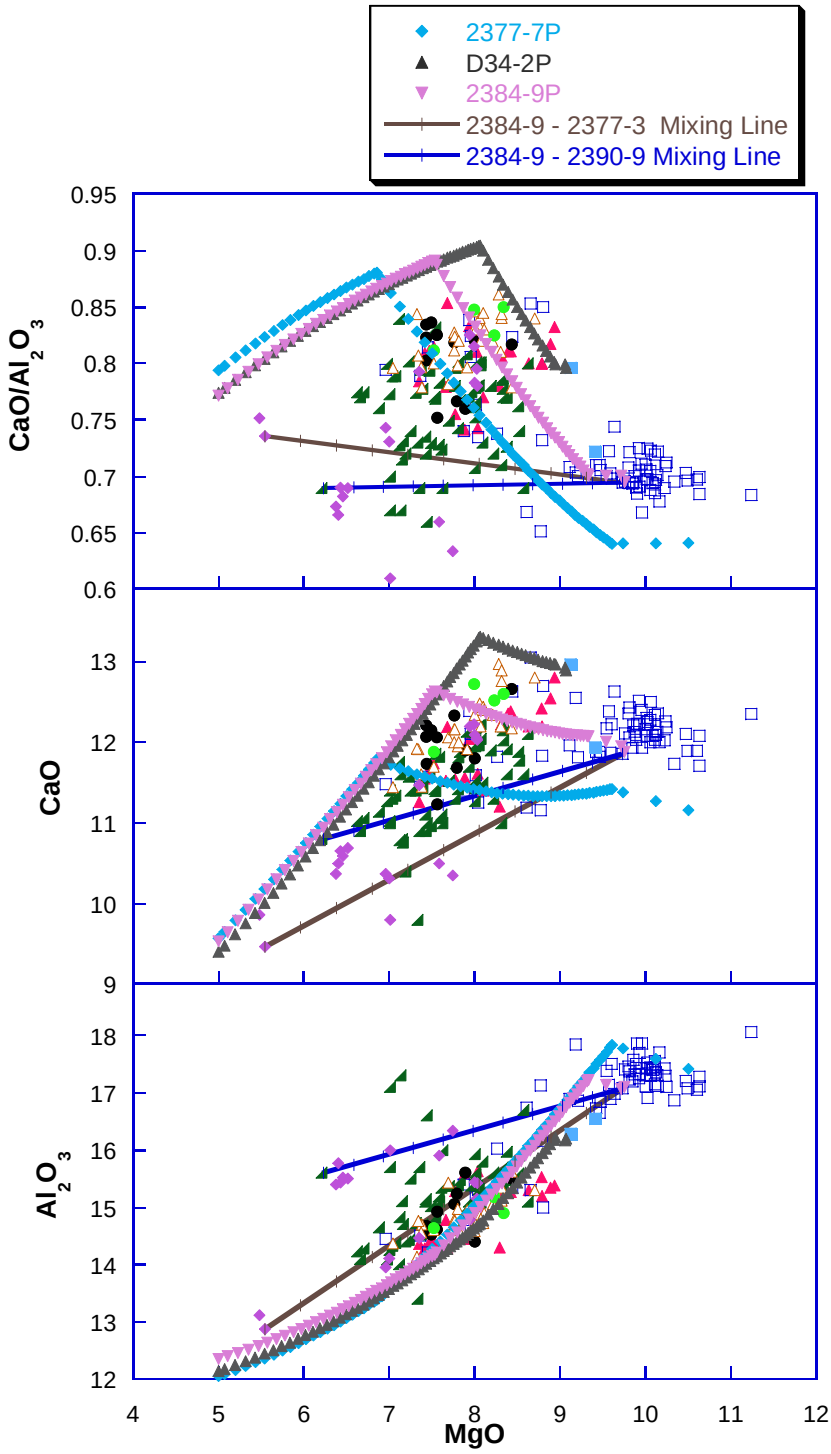


Figure 7-1. Mixing lines between primitive and evolved sample compositions from the Siqueiros transform. Sample 2384-9 was mixed with a ferrobasalt from spreading center B (2377-3) and a FeTi basalt from the RTI (2390-9). Tick marks on mixing line indicate increments of 10% mixing.

the compositions of samples 2377-11 or 2390-9 (FeTi basalt from WRTI) (Figure 7-2). Mixing between magmas with such evolved and primitive compositions can explain the observed enrichment in Zr and Y better than fractional crystallization alone. In these models, the evolved samples must either be derived from a source more enriched in incompatible elements than primitive samples or from melts that have been created by extensive fractional crystallization. Such highly fractionated magma bodies may be represented by the melt lens which has been proposed to represent interstitial melt expelled from the extensive mush zone that underlies ridges (Pan and Batiza, 2003; Natland and Dick, in prep.).

Plots of incompatible element ratios (Figure 7-3) also suggest mixing of melts from different sources may have occurred. The ratio of two highly incompatible elements is relatively insensitive to the effects of fractional crystallization, therefore, relatively large differences in the ratios of incompatible elements (e.g. Zr/Y; Figure 7-3) are likely to have been inherited from the source region (either because of low extents of melting or because the mantle is heterogeneous). Mixing curves calculated using primitive D-MORB samples as one end-member and evolved samples or E-MORB as the enriched end-members are shown in Figure 7-3. The calculated mixing curves suggest that variations in incompatible element ratios can be related to mixing of different magmas that erupted along the Siqueiros transform. Almost the entire range of observed Zr/Y data can be accounted for by mixing of primitive to moderately evolved melts with either E-MORB and/or more evolved N-MORB magmas represented by lavas found within the Siqueiros transform. Three samples from the A-B fault have high Zr/Y ratios and fall above the mixing curves. These samples have low Y contents and positive Eu anomalies

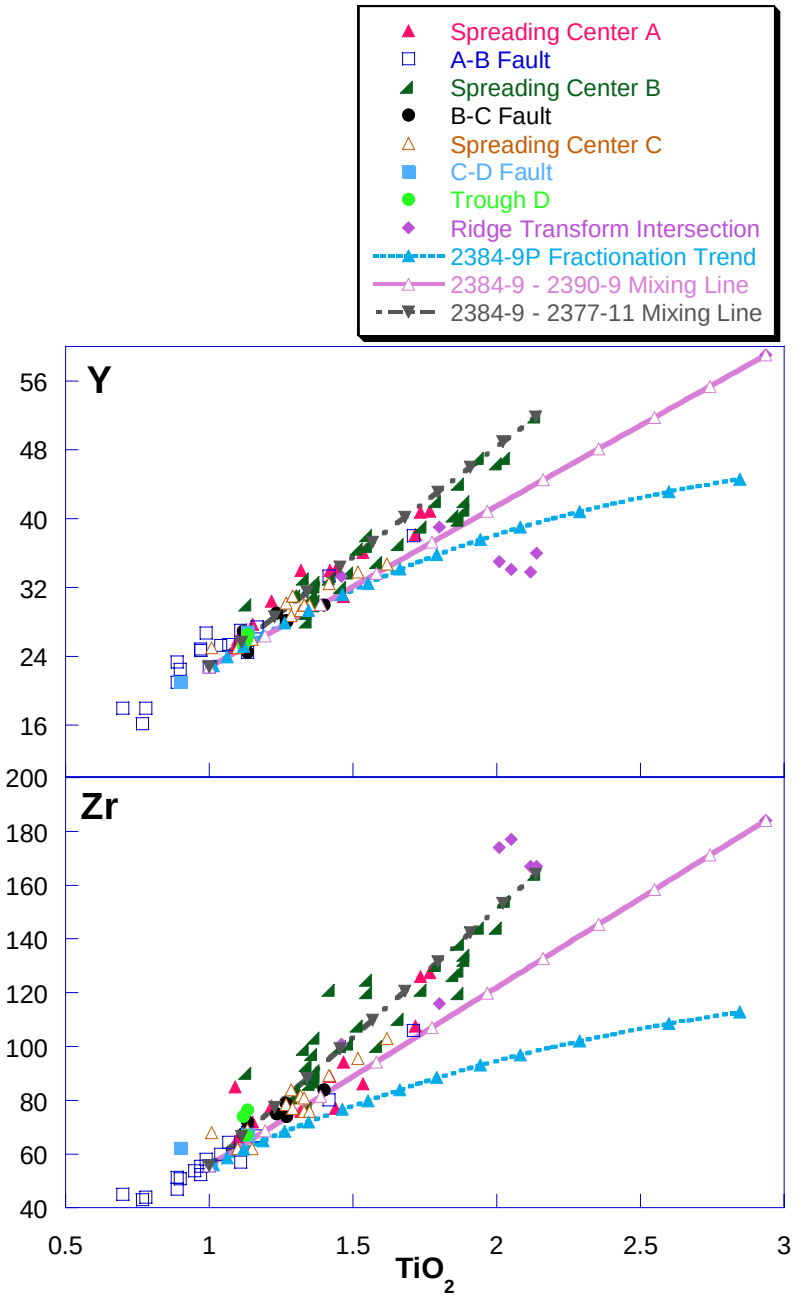


Figure 7-2. Trace element mixing lines between primitive and evolved samples. Mixing increments are 10%. Fractionation trend for sample 2384-9P is shown for comparison.

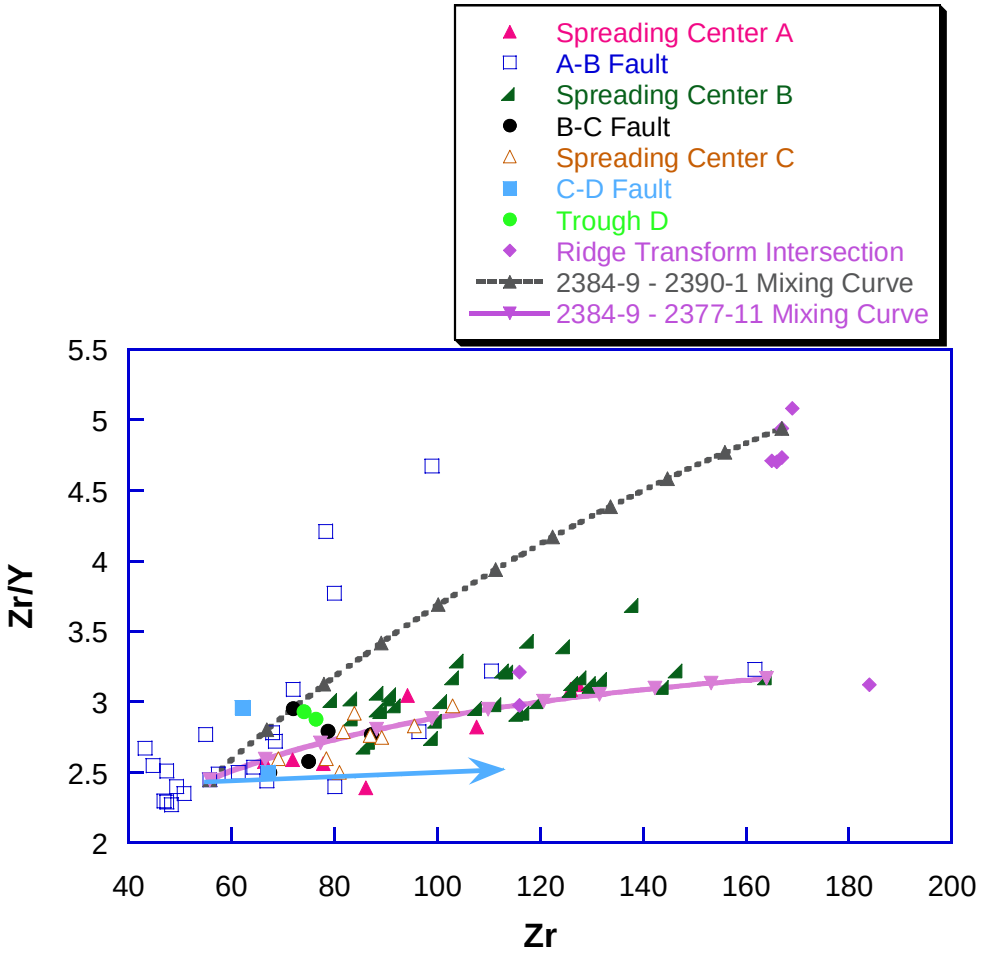


Figure 7-3. Calculated mixing curves between sample 2384-9 and an evolved sample from spreading center B (2377-11) and an E-MORB from the RTI (2390-1). Blue arrow indicates fractionation trend for 2384-9P.

suggesting that the lavas have either accumulated plagioclase or assimilated plagioclase-rich gabbroic material and thus do not represent true liquid compositions.

**D-MORBs and E-MORBs**

REE element abundances and ratios in lavas from the Siqueiros transform domain exhibit a wide range of values not typical for most MORB suites. A nearly continuous trend in Ce/Y and Ce/Yb ratios (measures of LREE to HREE fractionation) can be seen in the Siqueiros sample suite extending from typical N-MORB LREE depleted patterns to patterns almost as depleted as the D-MORB samples found within the A-B fault (Figure 7-4). The overall observed variations in Ce/Y and Ce/Yb ratios cannot be produced by fractional crystallization alone although the variations observed in N-MORB from proximal locations can largely be explained by the effects of crystal fractionation. Even moderate to high percents of crystal fractionation of olivine, plagioclase, and clinopyroxene only enrich the LREE compared to the HREE by approximately 10 relative percent as shown in Figure 7-4. La/Sm ratios (a measure of relative LREE depletion or enrichment) show the extreme LREE depletions that the samples from the A-B fault have compared to other tectonic locations within the transform (Figure 7-5).

Mixing calculations suggest that the overall range of observed REE patterns (and Ce/Y) could be generated by mixing of depleted and enriched magmas. Typical N-MORB samples could be produced by mixing D-MORB with approximately 2-6 % of an E-MORB composition (Figures 7-4 & 7-6). Because the E-MORB are moderately fractionated it is assumed that they have higher overall REE abundances than their less evolved parents. Consequently, if mixing of parental magmas took place, the amount of E-MORB required could double. In either case, such a small percentage of the enriched melt does not significantly alter the major element composition, but does cause

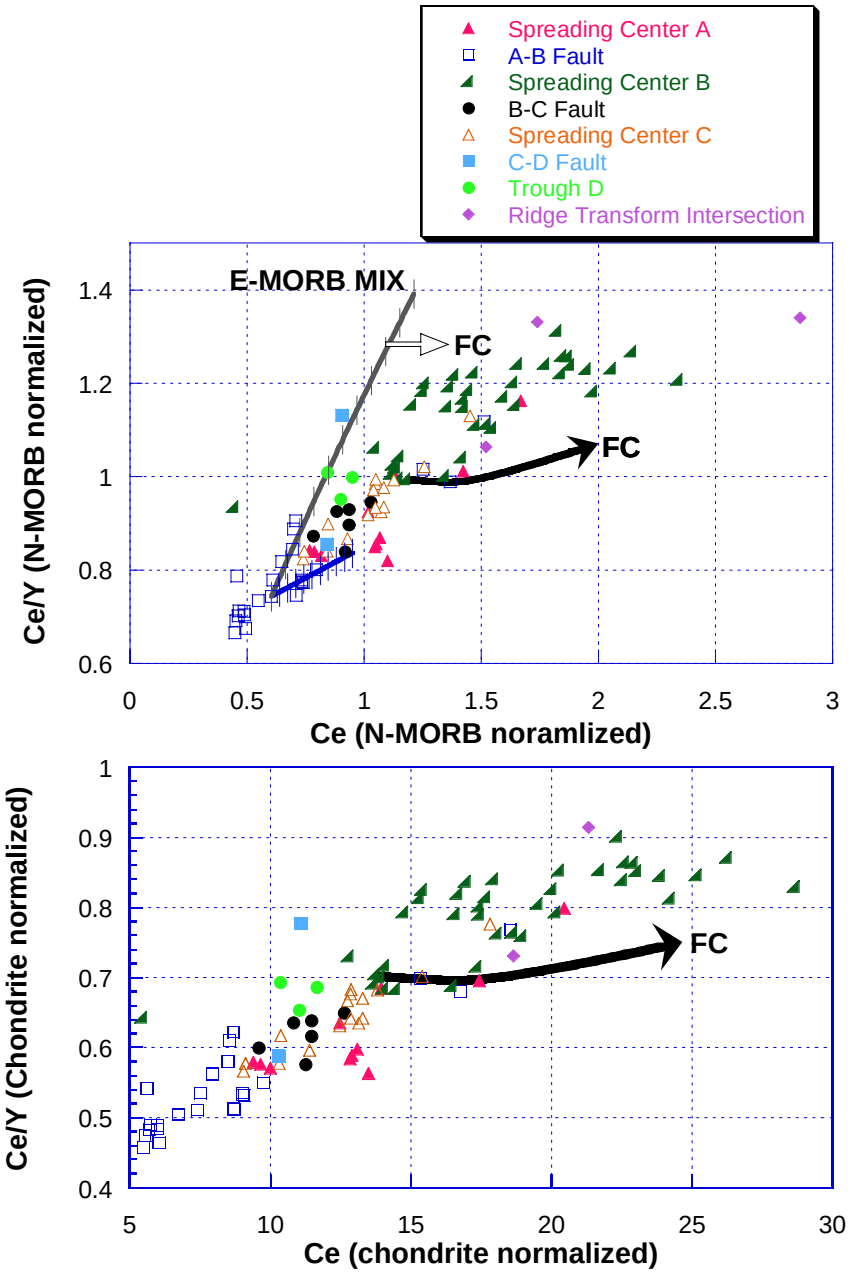


Figure 7-4. Chondrite and N-MORB normalized Ce/Y ratios for Siqueiros transform morphotectonic locations. E-MORB samples from the WRTI are not included. Solid arrow shows fractional crystallization trend for sample 2375-9. Thin black line shows mixing line between sample 2384-9 (D-MORB) and sample 2390-1 (E-MORB). Blue line shows mixing line between sample 2384-9 (D-MORB) and sample 2377-11 (FeTi basalt). Tick marks indicate increments of 2%.

noticeable enrichment in the incompatible elements which may provide an explanation for the N-MORB that are relatively enriched in $TiO_2$, $P_2O_5$, and $K_2O$ (Figure 7-7).

Once mixed with 6% E-MORB, approximately 36% fractional crystallization is required to produce higher overall REE abundances similar to those of the N-MORB compositions recovered from the spreading centers (Figure 7-8). Mixing calculations were also done between 2384-9P (D-MORB) and sample 2377-11 (FeTi basalt). Mixing with a more evolved N-MORB compositions will increase the Ce/Y ratios, but does not provide a high enough increase to explain the variations in Ce/Y ratios seen between the spreading centers and faults (Figure 7-4).

**Controls on Spatial Variability in Lava Chemistry**

A diverse group of samples has been found within the Siqueiros transform, however, the spatial distribution of compositionally distinct samples is very limited and for the most part samples from a common morphotectonic location are geochemically very similar (Figure 7-4 and 7-9). E-MORB samples were only recovered from the western ridge transform intersection (WRTI). The extremely incompatible element depleted D-MORB samples were exclusively recovered from the A-B fault. The rest of the samples recovered from the transform domain range from N-MORB to slightly depleted N-MORB (Figure 7-9). The most evolved N-MORB (ferrobasalts and FeTi basalts) were all recovered from the western RTI. Previous dredging of the western section of the transform also recovered a diverse group of samples with similar spacial distributions of E-MORB and N-MORB (Natland, 1989). Spreading center A has a few normal N-MORB, but for the most part contains low-$Na_2O$, low Ce/Y N-MORB samples. The A-B fault contains all of the picritic basalts and picrites recovered within the transform. All of the samples from the A-B fault are unusually primitive when compared

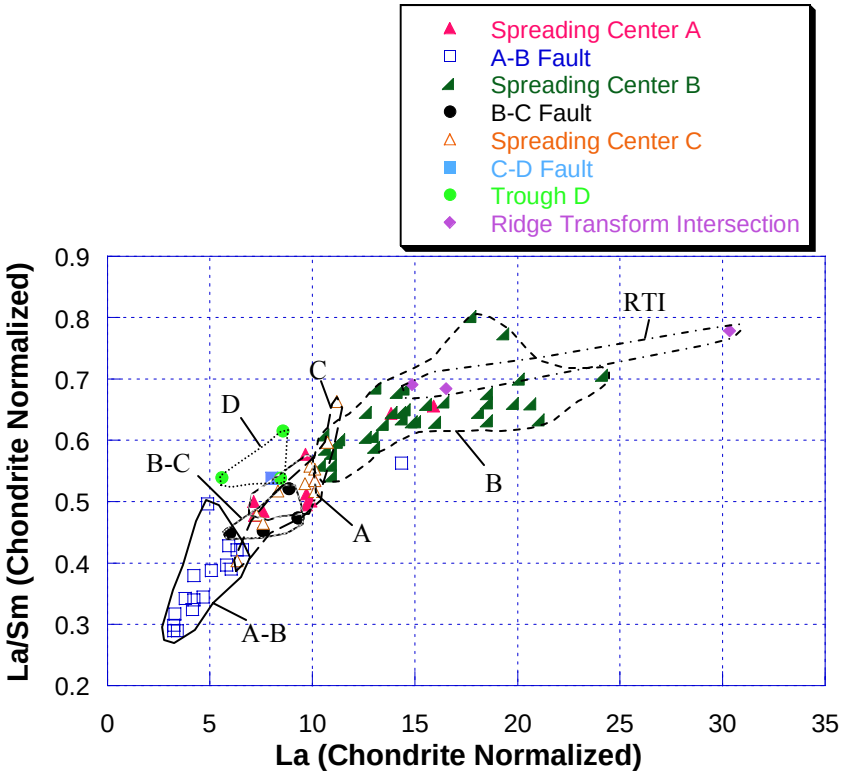


Figure 7-5. Chondrite normalized La/Sm ratios for Siqueiros transform morphotectonic locations. Arrow shows fractional crystallization trend. E-MORB samples from the WRTI are not included.

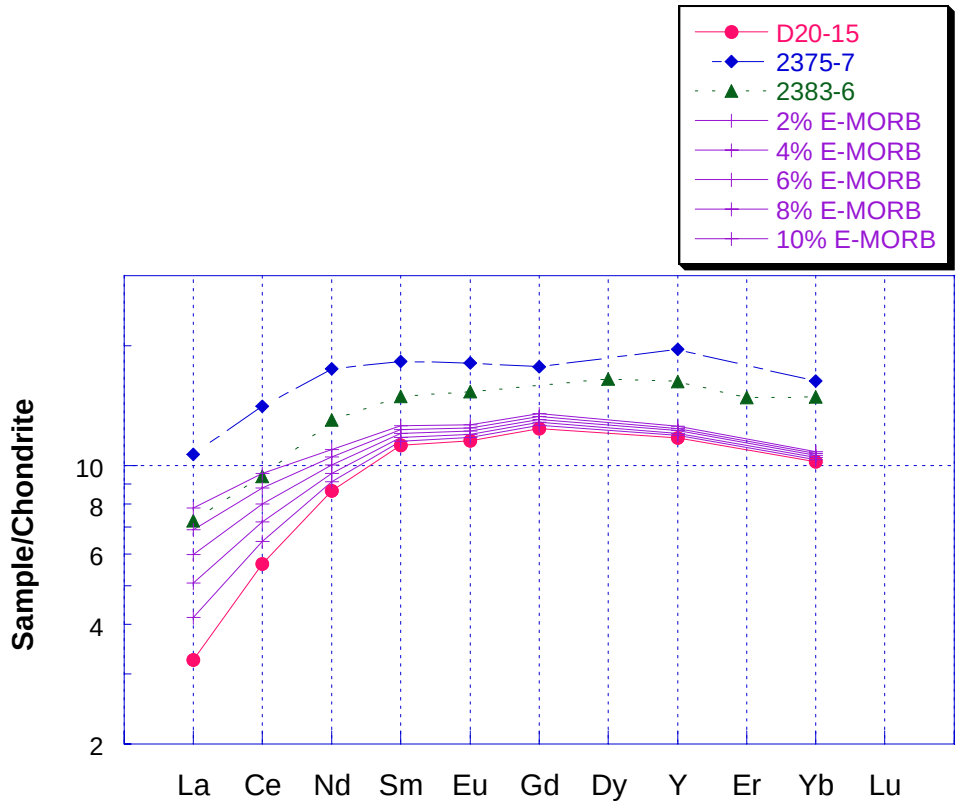


Figure 7-6. Calculated mixing between sample D20-15 (D-MORB compositions) and sample 2390-1 (E-MORB composition). Mixing lines (solid purple lines) represent increments of mixing with 2% E-MORB. Approximately 6% mixing with an E-MORB composition is required to produce REE patterns parallel to patterns of N-MORB composition (e.g. 2375-7 and 2383-6).

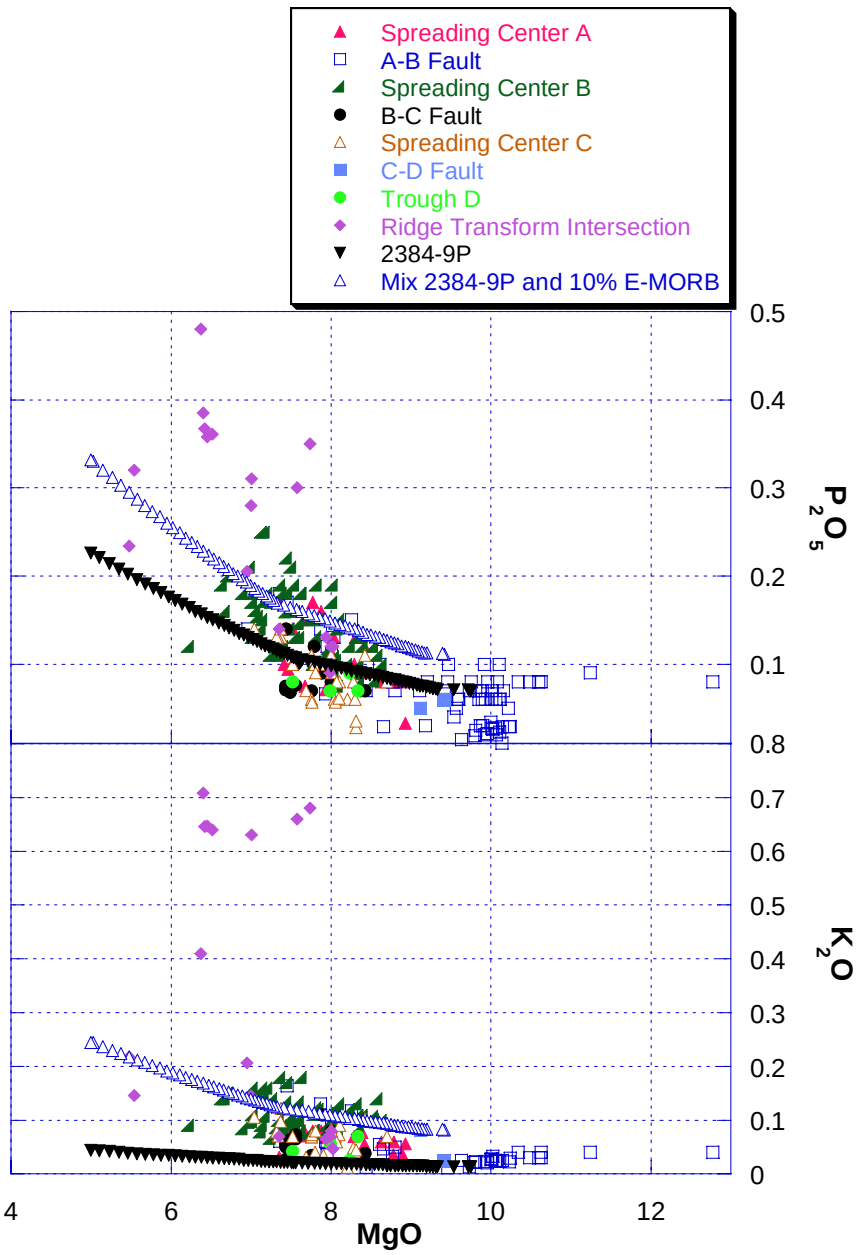


Figure 7-7. LLD for 2384-9P after mixing with 10% E-MORB. Mixing with an E-MORB composition can explain some of the enrichment in the incompatible major elements

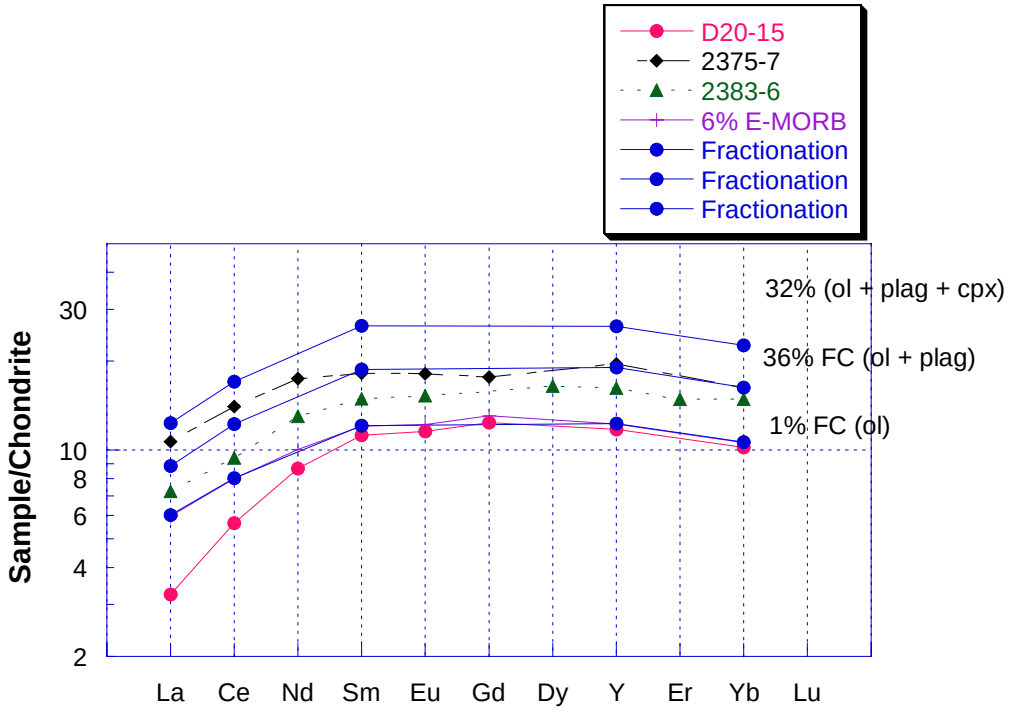


Figure 7-8. Modeled fractional crystallization path of 6% mixing line from figure 7-6. Approximately 36% fractional crystallization is required to produce REE patterns similar to N-MORB compositions found within the spreading centers (e.g. 2375-7 and 2383-6).

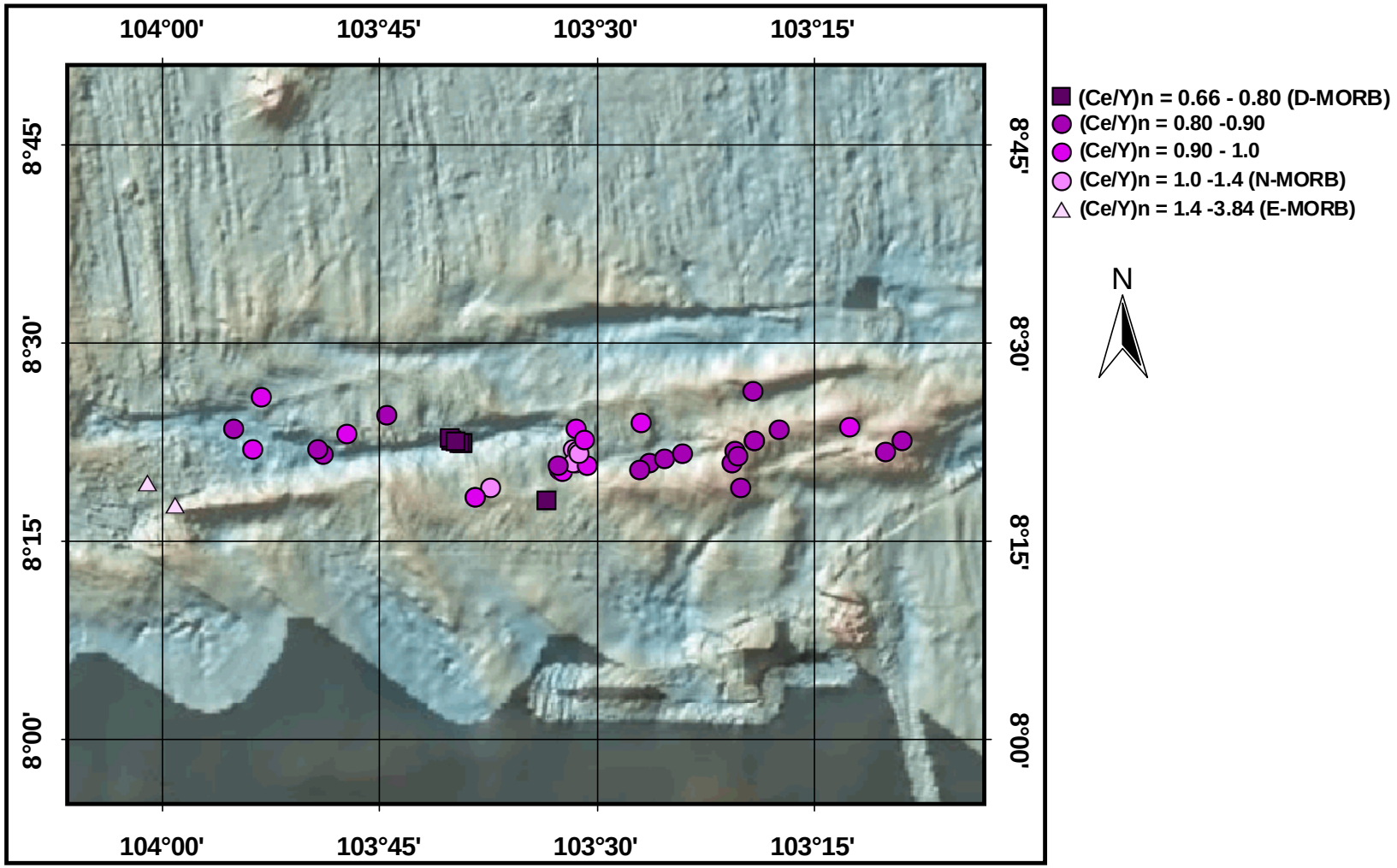


Figure 7-9. Location map of E-MORB, N-MORB, and D-MORB samples within the Siqueiros transform based on Ce/Y ratios. Ce/Y values normalized to N-MORB.

to the other Siqueiros samples and to samples collected along the northern EPR (Batiza & Nui, 1992; Pan and Batiza, 2003; Perfit et al., 1994 and in prep; Smith et al., 2001). The majority of samples from the A-B fault are D-MORB, however, they were recovered in close proximity to N-MORB samples. Spreading center B is the most densely sampled location. It contains the greatest range in compositions and has the most evolved samples of the 3 spreading centers. Spreading center B also has lavas with a greater range in $Na_{8.0}$ and $Fe_{8.0}$ than the other spreading centers. The B-C and C-D faults, spreading center C, and trough D are not as heavily sampled as the other locations, but samples from these locations form fairly tight groups on variation diagrams, $Na_{8.0}$- $Fe_{8.0}$ plots and $K_2O/TiO_2$ plots (Figures 5-1 and 5-9).

**Tectonic Controls on Magmagenesis and Melting Systematics**

Transform faults are plate boundaries which divide active ridge segments and are believed to be places where crust is neither created nor destroyed. This assumes that there is no component of extension or spreading in transform domains and that zones of faulting and tectonism dominate the morphologic features. The Siqueiros intra-transform spreading centers are believed to result from a series of plate motion changes occurring about 2.5 Ma, 1.5 Ma, and 0.5 Ma that generated extension across the transform. (Pockalny et al., 1997) (Figure 7-10). The formation of the intra-transform spreading centers appears to be the result of tears or propagation events initiated near the trace of the transform fault (Pockalny et al., 1997). The tensional environment caused a scissor-like opening of the transform and propagation of the WRTI southward (Pockalny et al., 1997). Structural trends within the swath of terrain generated at spreading center B range from oblique to nearly ridge parallel indicating that the intra-transform spreading centers may begin as leaky transforms, evolving to a transform parallel volcanic ridge as

extension occurs (Pockalny et al., 1997). The recent volcanism within the A-B fault may be a result of current extension within the transform. Continued extension may lead to more volcanism within the A-B fault and eventually the formation of a new spreading center.

Where spreading ridges intersect transform faults (RTI) the thermal regime is believed to be cooler than the ridge due to the juxtaposition of thin, young, hot lithosphere against thicker, older and colder lithosphere. Oceanic crust has been found to be thin proximal to ridge/transform intersections (Fox et al., 1981, Stroup and Fox, 1981; Detrick and Purdy, 1980), leading to the idea that the cold edge of lithosphere abutting the end of a segment might affect processes of basalt generation at the RTI boundary. The processes that lead to the occurrence of a wider range in magma compositions, magmas of lower temperature, liquid lines of descent that are offset to higher $TiO_2$ and

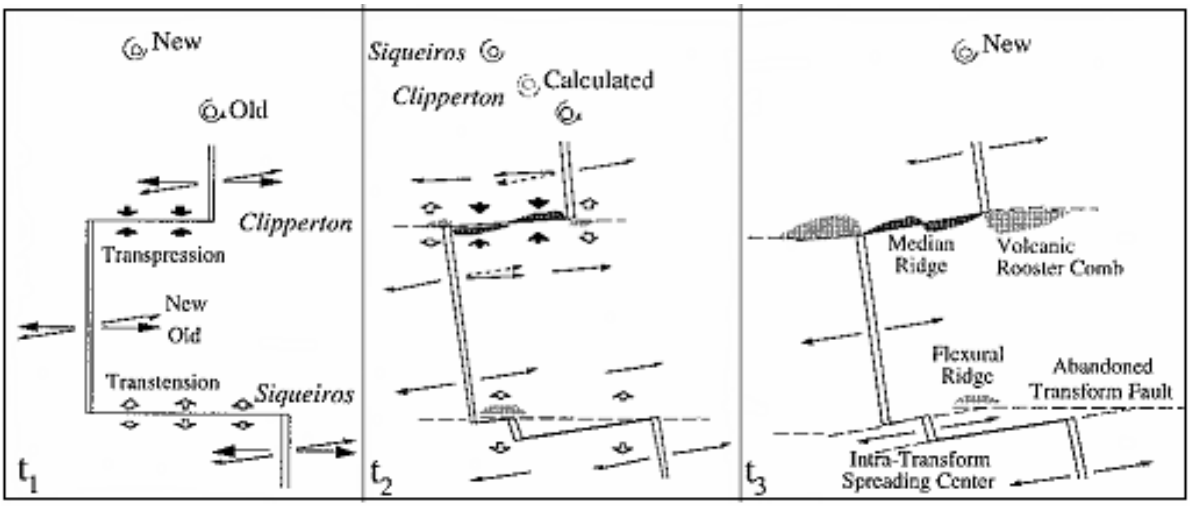


Figure 7-10. Position of "apparent" Euler poles associated with a counterclockwise change in spreading direction along the Clipperton and Siqueiros Fracture Zones. t1 = onset of spreading direction change resulting in tension along the Siqueiros transform. t2 = New spreading direction within the Siqueiros Fracture Zone. t3 = extension produced intra-transform spreading centers, a flexural transverse ridge and the abandoned transform fault trace with the Siqueiros transform. (Pockalny et al., 1997).

FeO, and magmas with greater incompatible element abundances near transform faults has been referred to as the transform fault effect (TFE) (Bender et al., 1984). It has been suggested that the TFE is caused by either greater extents of low pressure fractionation (Christie and Sinton, 1981) and/or lower extents of melting at the RTI (Bender et al., 1984). It has been proposed that lower extents of melting may lead to preferential sampling of enriched portions of the mantle (E-MORB) (Hanson, 1977; Bender et al., 1984). At the Siqueiros WRTI the intersection high is a broad, tongue-like feature with over 300m of relief that spills over the transform domain suggesting that the RTI has attempted to propagate southward in the recent past (Pockalny et al., 1997). As a propagating rift moves into older, thicker, and colder crust and this may lead to increased cooling and crystal fractionation (Christie and Sinton, 1981).

At the WRTI of the Siqueiros transform, highly fractionated ferrobasalts and a FeTi basalt were recovered along with E-MORB lavas. Relative to other Siqueiros N-MORB samples the RTI ferrobasalts and FeTi basalt are more enriched overall in REE and incompatible trace elements indicating that they are more evolved and have undergone greater extents of low pressure fractionation. The RTI N-MORB are also slightly more enriched in incompatible elements compared to other Siqueiros N-MORB. For example, La/Sm (chondrite normalized) ratios of samples from the WRTI (avg. = 0.72, median = 0.69, not including E-MORB samples) are on average greater than the La/Sm (chondrite normalized) ratios of samples from the intra-transform spreading centers (avg. = 0.60, median = 0.62).

It might be expected that all of the intra-transform lavas would exhibit chemical characteristics indicative of the TFE because lithosphere within the transform is also

older and would be assumed to be colder than lithosphere along the adjacent ridge segments. Instead, lavas within the Siqueiros transform and other transforms which exhibit intra-transform volcanism have been found to be more porphyritic, less evolved, and have lower concentrations of incompatible trace elements compared lavas from adjacent ridge segments (Wendt et al., 1999, Perfit et al., 1996).

**Constraints on Melting –Na-Fe Systematics**

Mid-ocean ridge basalts (MORB) are produced by decompression melting of the upper mantle in response to plate separation. Low pressure crystallization results in major element variations that form rather smooth trends on plots of oxide abundances as a function of MgO. As magma cools MgO, which is compatible in olivine, decreases during low-pressure crystallization (Langmuir et al., 1992). The cooling and crystallization of olivine produces changes in the concentrations of all the elements. These chemical changes must be corrected for in order to see trends caused by more complex fractionation processes, processes of melt generation and segregation, or source heterogeneity (Langmuir et al., 1992). The effects of fractional crystallization can be corrected for by normalizing the major element concentrations to a constant MgO.

The Siqueiros sample $Na_2O$ and FeO contents were normalized to a MgO content of 8.0 wt. % in order to observe any local variability in composition due to processes other than fractional crystallization (Appendix F). The Siqueiros transform $Na_{8.0}$ and $Fe_{8.0}$ data group in the center of the global $Na_{8.0}$-$Fe8_{.0}$ field (Figure 7-11). For the most part the samples from common morphotectonic locations group together, except for samples from the A-B fault and spreading center B, which have a wide range in $Na_{8.0}$ and $Fe_{8.0}$ (Figure 7-12).

Globally, $Na_{8.0}$ and $Fe_{8.0}$ values have been found to vary in basalts from normal ridges, basalts from back-arc basins, and for basalts from ridge segments that have been influenced by certain hotspots. Normal ridge $Na_{8.0}$ and $Fe_{8.0}$ values in MORB correlate strongly with axial depth assuming mantle major element compositions are approximately the same worldwide (Langmuir et al., 1992). Deeper axial depths have been found to correlate with higher $Na_{8.0}$ and lower $Fe_{8.0}$ values. The global $Na_{8.0}$-$Fe_{8.0}$ trend has been attributed to variations in mantle temperature. Axial depth variations are a response to variations in mantle temperature beneath the ocean ridge depth. Hotter mantle has undergone a higher extent of melting and correlates with a more inflated axial ridge (Grove, 2000). This results in a global trend that has a negative correlation between $Na_{8.0}$ and $Fe_{8.0}$. $Na_2O$ behaves as a moderately incompatible element; therefore, shallow melt regimes with a short melt column (low % of melt) will have high $Na_2O$, whereas deeper melts with a longer melt column (high % of melt) will have lower $Na_2O$. Mantle temperatures have been found to have the opposite effect on FeO concentrations because deeper melt columns have higher average pressures, which have been found to correlate with higher FeO. Variation in the temperature of the mantle is the only process that has been found to produce a negative correlation between $Na_{8.0}$ and $Fe_{8.0}$ (Klein and Langmuir, 1987). In addition to these global variations, finer "local" variations that are opposite the global trend have been observed that indicate distinct chemical signatures for individual sections of the ocean ridge system. The regional data for slow-spreading ridges form trends that parallel the global trend, but each local region has trends that are oblique to the global trend. These trends appear to reflect processes that occur beneath individual ridge segments (Langmuir et al., 1992).

Local variability of data from the East Pacific Rise (EPR) is much different than that of slow-spreading ridges (Langmuir et al., 1992) because the EPR shows much less depth variation than slow spreading ridges like the Mid-Atlantic Ridge. The $Na_{8.0}$ and $Fe_{8.0}$ data sets for the EPR parallel the global vector and the range for individual segments are almost as large as the global range. The average EPR data plot in the middle of the global field. The variability observed in EPR lavas occurs over distances as small as 50 km. Examination of other major elements suggest that the scatter of the $Na_{8.0}$ and $Fe_{8.0}$ data may be due to two components of local variability, one within the 'normal' MORB (N-MORB, with low $K_2O/TiO_2$), and one between N-MORB and 'transitional' MORB (T-MORB, with higher K contents). Local variations emerge when the N-MORB is considered alone. However, the EPR does not have a striking $Na_{8.0}$-$Fe_{8.0}$ negative correlation because N-MORB exhibit little variation in $Na_{8.0}$. The variation in $Na_{8.0}$ comes from mixing N-MORB with T-MORB or E-MORB, which have low FeO and high $Na_2O$.

When compared to the global field for normal ridge segments the Siqueiros samples parallel the global vector, and there is significant variability in the $Na_{8.0}$ (Figure 7-11). Although there is variability in $Fe_{8.0}$ it is not as great. Unlike other normal ridge segments the $Na_{8.0}$ and $Fe_{8.0}$ does not show a correlation with axial depth (Figure 7-17). Brodholt and Batiza (1989) found that the global trends are strongly defined by samples from very shallow and very deep ridges and that the $Fe_{8.0}$ trend is particularly weak for normal depths (1500-4000m). The Siqueiros samples were only collected for depths ranging from 1990m to 3909m and would not be expected to show the entire range in the global $Na_{8.0}$-$Fe_{8.0}$ variations. The general trend of the Siqueiros data suggests that there

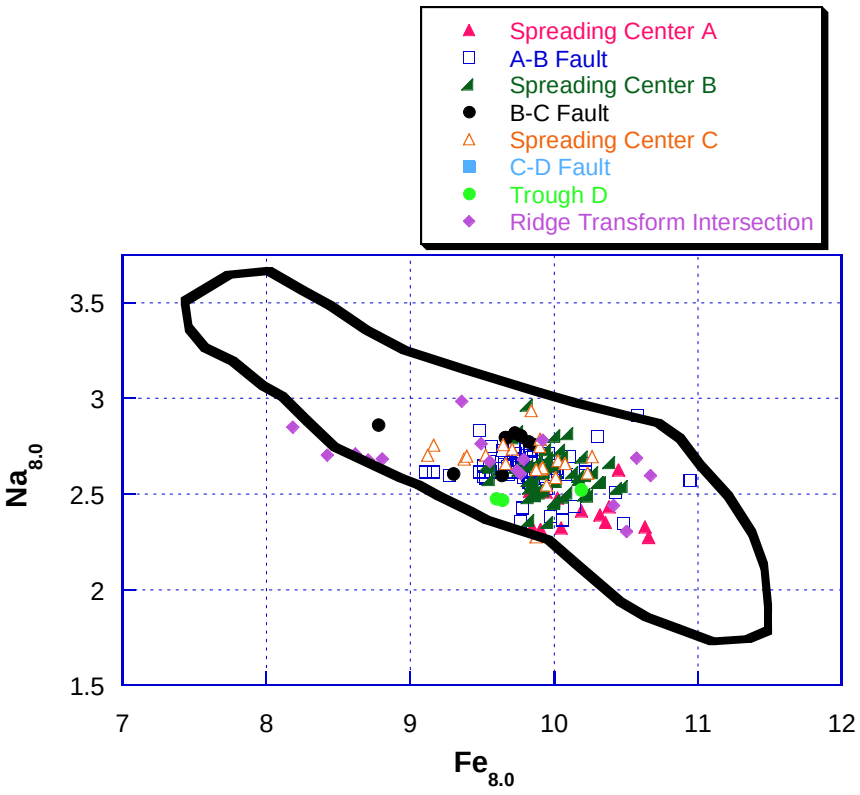


Figure 7-11. Siqueiros $Na_{8.0}$ and $Fe_{8.0}$ data compared with global field for normal ridge segments (Langmuir et al., 1992).

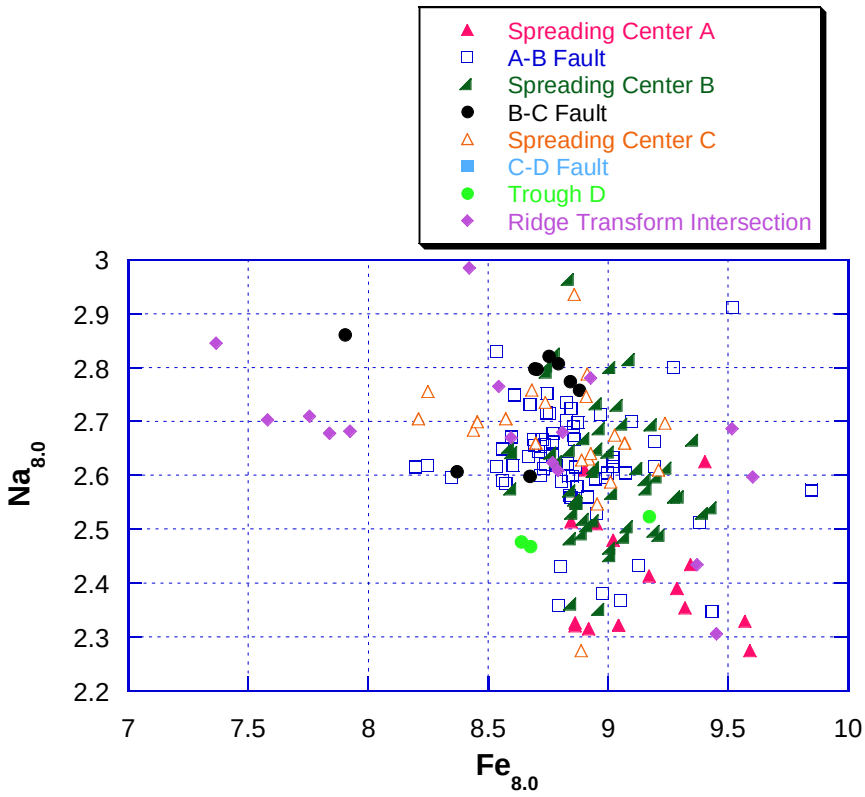


Figure 7-12. $Na_{8.0}$ vs. $Fe_{8.0}$. The RTI samples form a group with high $Na_{8.0}$, low $Fe_{8.0}$ and samples from spreading center A group in the low $Na_{8.0}$, high $Fe_{8.0}$ region. All iron is calculated as FeO.

are different mantle temperatures controlling the Siqueiros $Na_{8.0}$-$Fe_{8.0}$; however, the greater variability in $Na_{8.0}$ may result from local trends in the $Na_{8.0}$ and $Fe_{8.0}$ that are opposite to the observed global trends.

The local trend in the Siqueiros data may result from varying source compositions. In other EPR lavas, $Na_{8.0}$ abundances have been found to correlate with higher $K_2O/TiO_2$ contents. Locations that exhibit a wide range in $Na_{8.0}$ abundances also exhibit ranges in $K_2O/TiO_2$ and Ce/Y contents (Figure 7-13 and 7-14). A subset of RTI samples are characterized by higher $Na_{8.0}$ and lower $Fe_{8.0}$, correlate with the high $K_2O/TiO_2$ E-MORB samples from the RTI. The low $Na_2O$, high FeO samples from spreading center A correlate with low Ce/Y (N-MORB normalized) suggesting that the $Na_{8.0}$ variations may result from mixing between depleted and enriched sources (Figure 7-15). As a whole the Siqueiros $Na_{8.0}$ data does not correlate with Ce/Y (N-MORB normalized) or $K_2O/TiO_2$ (Figures 7-14 and 7-16).

Another important consideration is that the global data set was produced from regional averages of lava chemistry and depth (Klein and Langmuir, 1987). Using averages results in an average of the depth and pressure of melting for a particular region. Prior to averaging of the data melts may exist that result from the eruption of lavas originating from different depths or pressures within the melting column. If one considers shallow, high percent melts and deep, low percent melts in MOR mantle it is possible to generate more variability in $Na_{8.0}$, $Fe_{8.0}$ by producing high $Fe_{8.0}$, high $Na_{8.0}$ deep melts and low $Fe_{8.0}$, low $Na_{8.0}$ shallow melts (Figure 7-18). The lack of correlation between $Na_{8.0}$-$Fe_{8.0}$ systematics with depth, $K_2O/TiO_2$, or Ce/Y indicates that $Na_{8.0}$ and

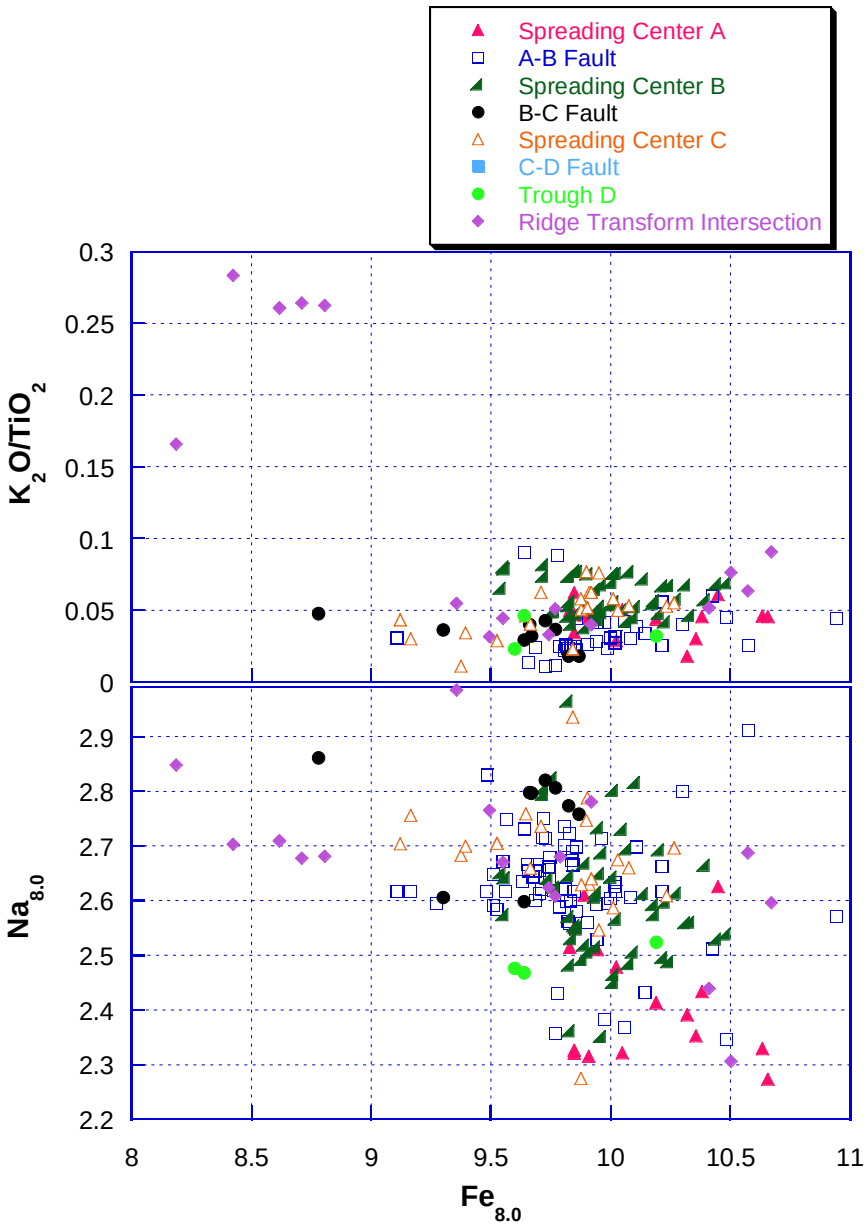


Figure 7-13. $Na_{8.0}$ vs. $Fe_{8.0}$ and $K_2O/TiO_2$. The RTI samples form a group with high $Na_{8.0}$, low $Fe_{8.0}$ and samples from spreading center A group in the low $Na_{8.0}$, high $Fe_{8.0}$ region. All iron is calculated as FeO.

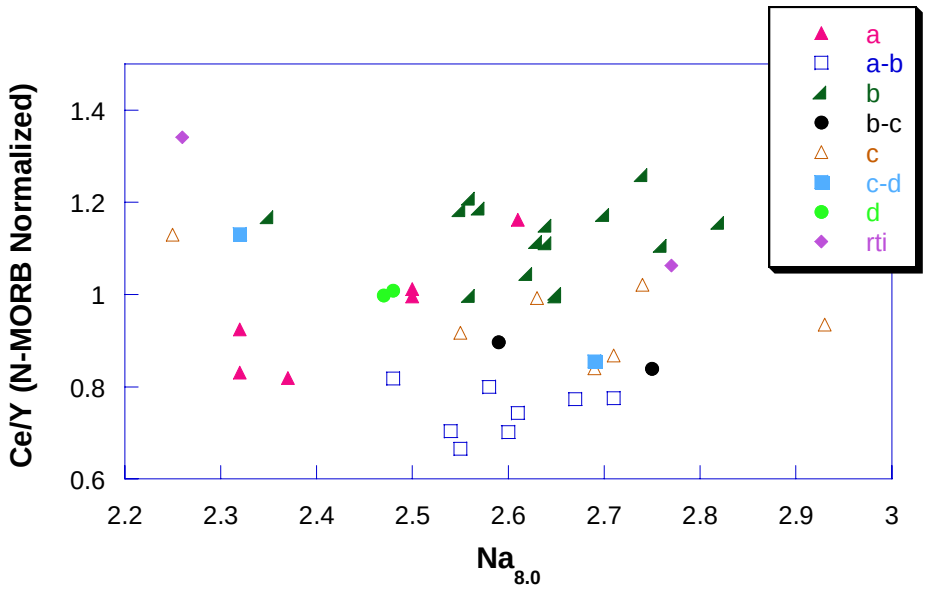


Figure 7-14. Ce/Y ratios vs. $Na_{8.0}$ values for all Siqueiros transform samples.

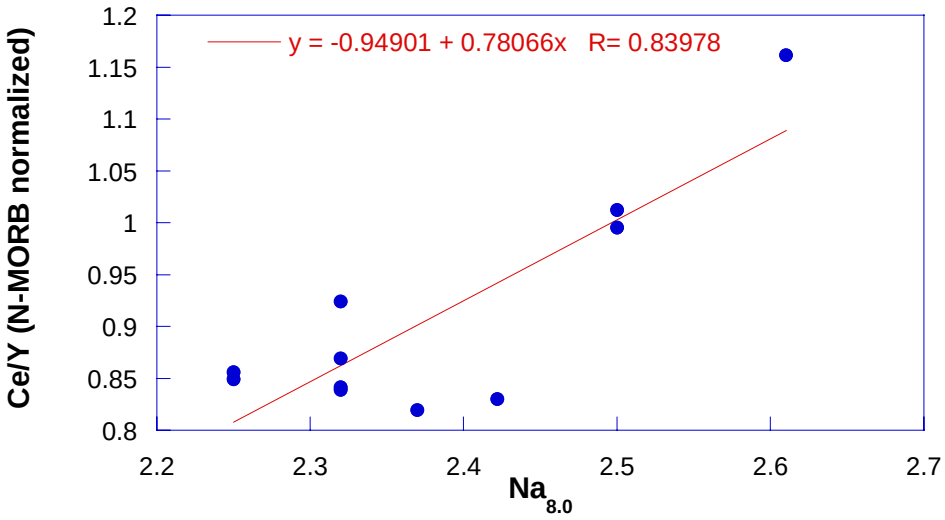


Figure 7-15. Ce/Y ratios vs. $Na_{8.0}$ values for samples from spreading center A. A best fit line shows that there is a good correlation between LREE enrichments and higher $Na_2O$ in samples from this spreading center.

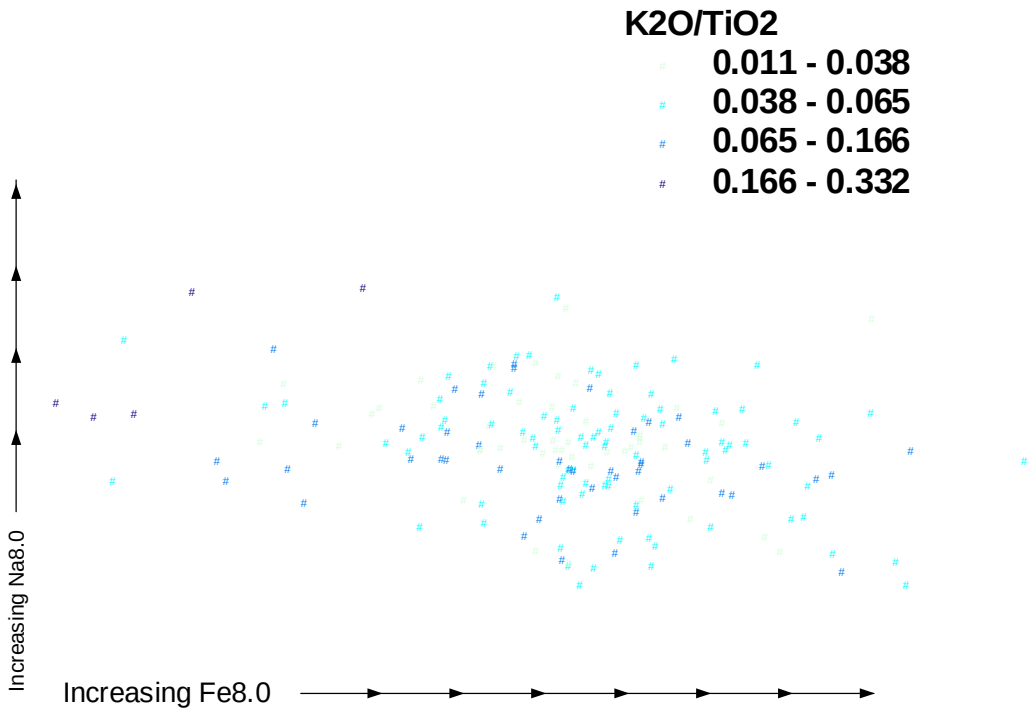


Figure 7-16. $K_2O/TiO_2$ ratios of Siqueiros samples compared with their $Na_{8.0}$, $Fe_{8.0}$ data.

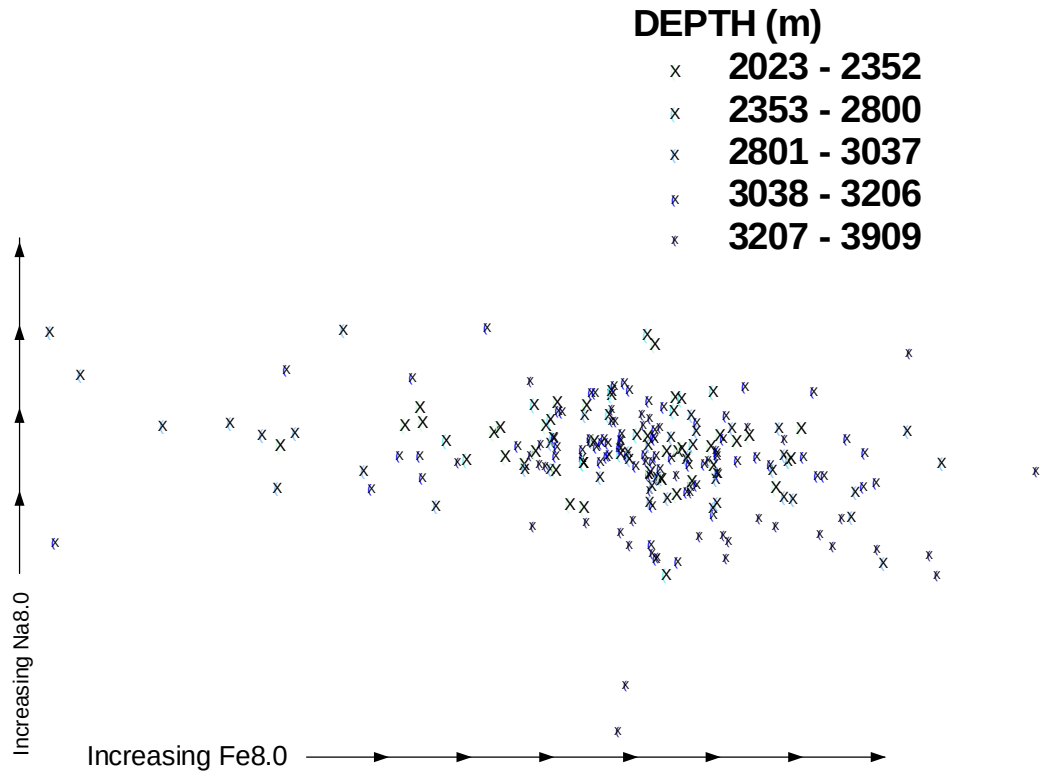


Figure 7-17. $Fe_{8.0}$ versus $Na_{8.0}$ and axial depth.

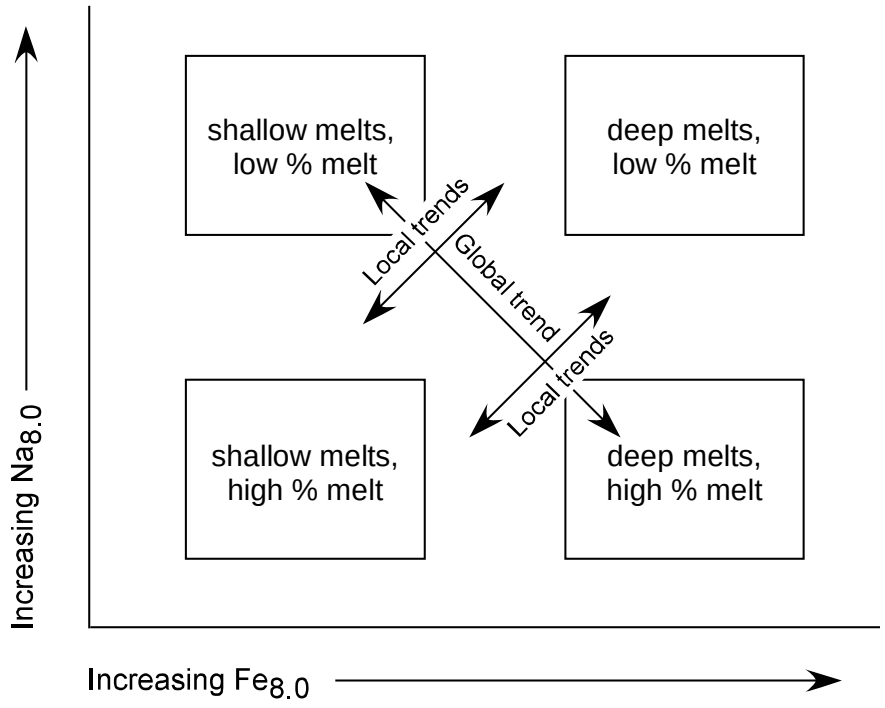


Figure 7-18. Variations in $Na_{8.0}$ and $Fe_{8.0}$ systematics due to variable depths and extents of melting.

$Fe_{8.0}$ systematics result from two components of local variability, one due to variable mixing with enriched sources and the other due to variable depths and extents of melting.

**Models for Volcanism in Transform Domains.**

Perfit and others (1996) hypothesize that the high-magnesian samples are only found within the A-B fault because of their greater density. Since the A-B fault is deeper than other areas, it was suggested that the transform might tap the high-MgO lavas stored in a magma chamber that are too dense to erupt at shallower locations. In order to evaluate this, the densities of each Siqueiros sample were calculated (using the method of Lange & Carmichael, 1987) in order to see if density is related to sample depth of recovery. The density of the samples does not correlate with depth and a best-fit line

actually shows an extremely poor inverse correlation with denser samples coming from shallower regions (Figure 7-19). A comparison of MgO contents with depth was also made and although the high MgO lavas are found at the deepest locations, there does not seem to be any other correlation between MgO content and depth for the Siqueiros sample suite (Figure 7-20). When the olivine phenocrysts contained in the picritic and olivine rich basalts are taken into account, a large difference in sample density can be seen. The picritic basalts have been found to contain up to 20 modal% olivine. The addition of 5-20 modal% olivine phenocrysts to the liquids of the picritic and olivine rich samples greatly increases their sample density (Figure 7-21). The picritic and olivine basalts were recovered in the deepest sample locations and an addition of only 5% olivine phenocrysts to these samples shows that a correlation can be made between density and sample depth (Figure 7-22).

Another theory regarding the eruption of high-MgO lavas only within transform domains is that the relatively primitive and porphyritic basalts result from rapid transport of magmas to the surface without extensive cooling and fractionation in crustal magma chambers (Hekinian et al., 1995; Wendt et al., 1999). Hekinian and other (1995) propose that the ascent of magma through narrow fissures or dykes in the fast cooling environment of the transform would increase the magma's viscosity as well as the rate of crystal nucleation and therefore prevent crystal settling, leading to the extrusion of highly porphyritic lavas. The high-MgO samples were only recovered in the A-B fault located away from areas of organized spreading were it is unlikely that a large magma chamber exists. The narrow range in lava MgO content in the A-B fault is consistent with limited mixing and fractional crystallization.

Geophysical evidence indicates that shallow melt lenses may contain > 70% crystals, whereas dikes and lavas generally have < 10% (Hussenoeder et al., 1996). Yet dikes and lavas erupted along the EPR have Mg#s too high to have formed from > 70% crystallization of mantle-derived liquids. Many researchers believe that the lavas instead have a deeper source such as a sill near the Moho that supplies magmas erupted at the surface and that the shallow melt lenses are unrelated to lavas erupted at the surface (Kelemen et al., 1997; Natland & Dick, in prep; Pan & Batiza, 2003). Studies of ophiolites have recently led many to the conclusion that lower gabbros and perhaps much of the oceanic crust forms from sills (Kelemen et al., 1997). Calculated liquids for gabbro sills in the Oman mantle transition zone are identical to the composition of sheeted dikes. Also, PmS refractions near the Moho within 30 km of the EPR may indicate the presence of sills (Kelemen et al., 1997). Recent compliance techniques discussed in Kelemen and others (1997) and studies of ophiolites support the existence of lower crustal sills (Natland & Dick, in prep). Compliance techniques indicate that in addition to an upper melt lens at ~1.5 km below many ridges, a lower melt lens exists at the base of the crust. Natland & Dick (in prep.) propose that the lower melt lens corresponds to a zone where picritic melts are neutrally buoyant causing olivine-rich magmas to laterally intrude the lower crust. Natland & Dick (in prep.) also propose that both plagioclase-rich & picrite basalts can be erupted due to flowage differentiation of crystals in the dikes or sills.

**Garrett Transform Models**

Insights into the petrogenesis within Siqueiros can be gained from published studies of other intra-transform domains. The Garrett transform on the SEPR is one of the only well studied transforms exhibiting intra-transform volcanism. Within the Garrett transform the majority of lavas were found to be more porphyritic and less evolved than

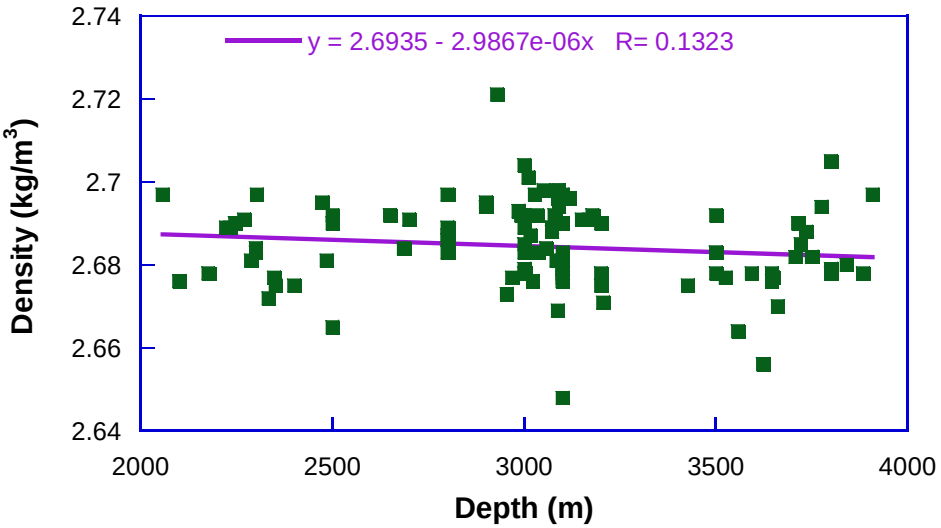


Figure 7-19. Sample density versus recovery depth for Siqueiros samples. Best fit linear line shows a very poor reverse correlation between sample density and depth.

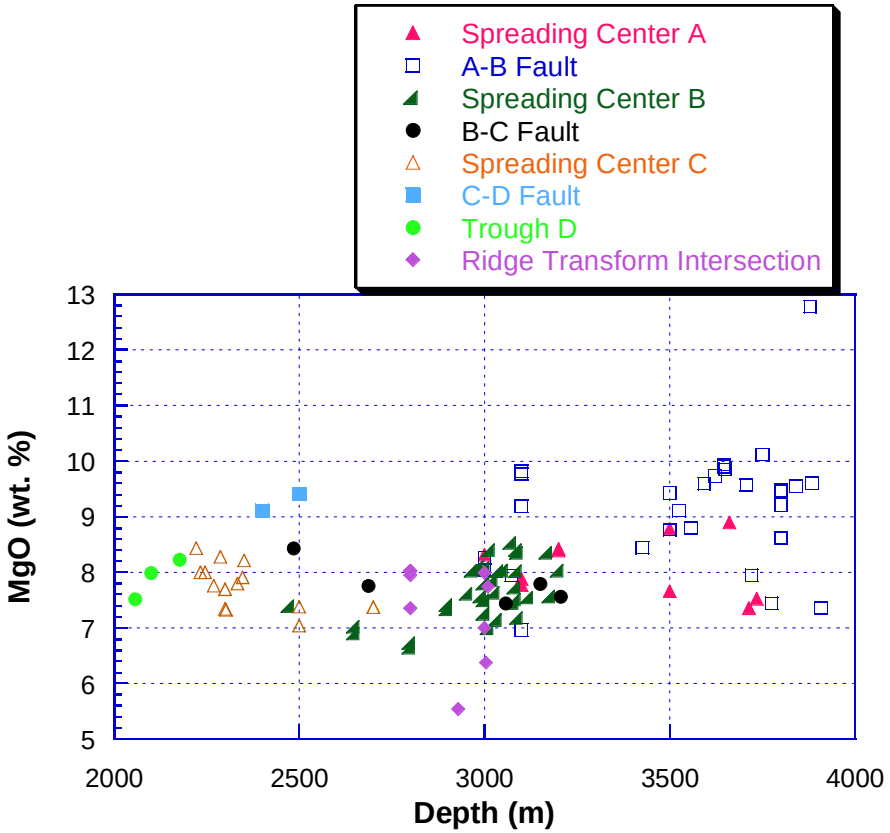


Figure 7-20. Sample MgO content versus recovery depth for Siqueiros samples.

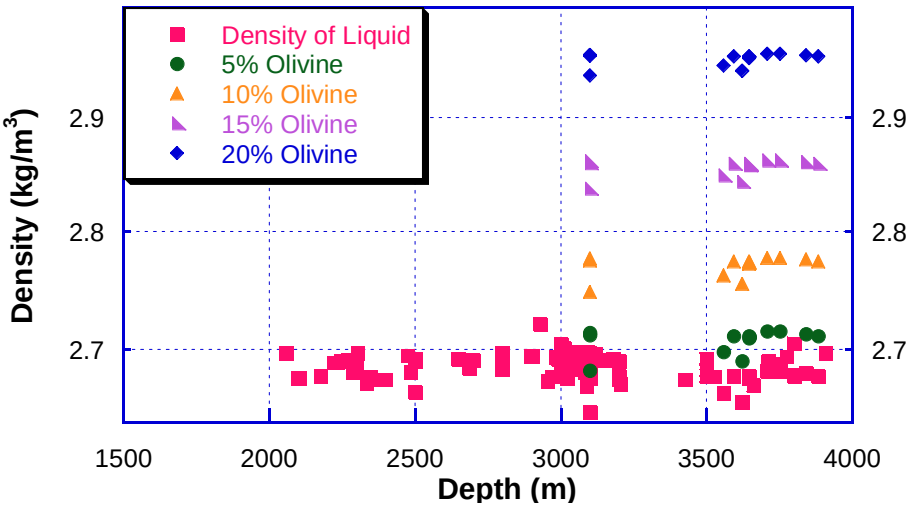


Figure 7-21. Density of samples vs. depth with addition of olivine phenocrysts. Between 5-20% olivine phenocrysts were included in the calculation of the sample density.

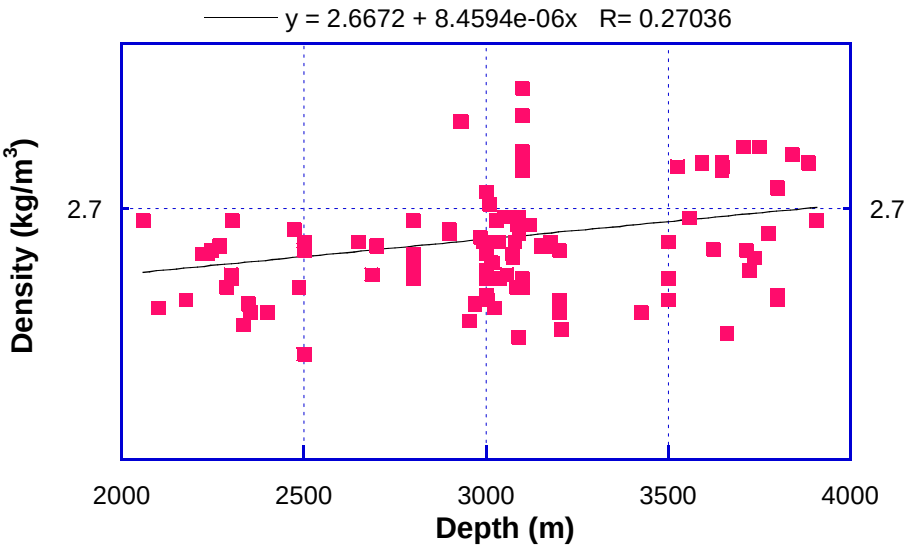


Figure 7-22. Density vs. depth of Siqueiros samples with 5 modal % olivine added to picritic and olivine rich basalts.

those along the adjacent South East Pacific Rise (SEPR) (Hekinian et al., 1995). The lavas are more depleted having lower concentrations of incompatible trace elements than normal MORB (Wendt et al., 1999). Sr, Nd, and Pb isotope compositions overlap those in the depleted end of the Pacific mid-ocean ridge basalts, but extend to less radiogenic Sr and Pb isotopes and more radiogenic Nd isotope values (Wendt et al., 1999). The Garrett transform also contains ferrobasalts, which fall along elemental trends suggesting extensive fractional crystallization.

Two models have been proposed to explain the existence of highly depleted basalts and the absence of enriched basalts in the Garrett transform domain. The first model proposes that enriched melts are generated in the transform, but because of their small volume and the cooler thermal regime they freeze in the lithosphere before extrusion (Hekinian et al., 1995). With continued and more extensive melting the ascent of magmas leads to reheating of the lithosphere allowing depleted, primitive melts to be extruded. Small magma chambers may be produced where only small extents of fractional crystallization and mixing take place. Crystallization and accumulation in the magmatic reservoir may later lead to the extrusion of more evolved and aphyric lavas (Hekinian et al., 1995). Wendt and others (1999) point out that this model requires a unique process that causes enriched and depleted melts from the same source to remain separate beneath transforms. Wendt and others (1999) instead proposed a second model in which the D-MORBs are believed to result from the melting of a two-component mantle beneath a transform. The model of Wendt and others (1999) requires that the upper mantle material currently melting beneath the Garrett transform has lost the enriched, easily melted component during previous partial melting beneath the SEPR, yet

remains sufficiently fertile to undergo decompression melting during lithospheric extension with the Garrett transform. Wendt and others propose that beneath the EPR deeper melts undergo less melting and remain fertile enough to melt underneath the Garrett transform where melting is occurring deeper due to the colder thermal regime. Such a model would require that that the melting beneath the EPR axis was very minimal because even a small amount of melt results in a refractory mantle that is very difficult to melt and yields melts very different from N-MORBs (Falloon et al., 1997). The model also implies that the Garrett transform is hot enough to melt the residual material that was not melted beneath the EPR axis suggesting the isotherms are higher than under normal ridges.

**Siqueiros Transform Models**

The Siqueiros transform differs from the Garrett transform in that the majority of samples recovered within Siqueiros, although depleted in K/Ti, have REE patterns and isotope compositions similar to N-MORBs (Lundstrom et al., 1999) and unlike Garrett, E-MORBs have been recovered at the WRTI. D-MORB samples were recovered within the Siqueiros transform, but the highly depleted LREE samples are only found within the A-B fault, whereas, D-MORB were recovered from the faults zones and the intra-transform ridges within the Garrett transform. Samples from the other spreading centers and faults have Ce/Y ratios that range from N-MORB to slightly depleted N-MORB (Figure 7-9).

U-series disequilibria measurements of Siqueiros lavas revealed that there is an inverse correlation between $^{230}$Th excess and $^{226}$Ra excess (Lundstrom et al., 1999; Sims et al., 2002). The $^{226}$Ra and $^{230}$Th excesses are found to vary with composition. $^{226}$Ra excesses are found in the D-MORBs and are positively correlated with Mg# (Mg/(Mg +

Fe)). Lundstrom and others (1999) explained the inverse correlation as a result of heterogeneous source compositions and suggest that N-MORBs, which have intermediate $^{226}Ra$ excesses, result from mixing of a D-MORB source with 5-10% E-MORB. Lundstrom and others (1999) concluded that these mixing trends indicate that intra-transform lavas undergo melting processes similar to those beneath the ridge. Recently U-series disequilibria coupled with $^{87}Sr/^{86}Sr$ data has been used to argue for melting processes rather than source heterogeneity as the dominant control on variations in Th/U (Sims et al., 1999). Incompatible enriched melts which have only been found at the RTIs in Garrett and Siqueiros have high Th/U and $^{230}Th$ excesses, while the most depleted incompatible element melts are found at leaky transform faults and are characterized by low Th/U and low $^{230}Th$ excesses. Melts intermediate in Th/U and $^{230}Th$ excesses were found at the intra-transform spreading centers in Garrett and Siqueiros. The cause of variation could be either different long-lived sources or melting processes. Recent studies have shown that a significant amount of trace element and U-series nuclides variability can occur as a result of melting processes (Speigelman and Kelemen, 2002). The Sr, Nd, Pb, and Hf isotopic compositions of the 9-10°N EPR N-MORB and Siqueiros D-MORB samples measured by Sims et al. 1999, were found to be relatively homogeneous, but the Siqueiros E-MORB is isotopically enriched. Based on the isotopic similarities of the D-MORB and N-MORB samples it was concluded that a melting process such as progressive source depletion during polybaric melting is the dominant control on variations in Th/U. However, isotopically depleted source components have been found at the Lamont Seamounts and suggest that an isotopically depleted component does exist in the 9°N area (Fornari et al., 1988; Tepley et al., 2004). The

Siqueiros REE patterns indicate that D-MORB only require 4-6% E-MORB to produce REE patterns similar to N-MORB. When 4-6% E-MORB is mixed with the D-MORB samples from Siqueiros the $^{87}Sr/^{86}Sr$ ratios are within the range of Siqueiros N-MORB $^{87}Sr/^{86}Sr$ ratios reported by Sims and others (2002), indicating that the U-series disequilibria could still be a result of source heterogeneity.

**Proposed Model**

The Siqueiros transform petrogenetic model must account for the following observations: 1) Like the Garrett transform, the samples from the Siqueiros transform are more primitive and porphyritic than those recovered along the EPR. 2) Major element variations indicate that fractional crystallization is occurring beneath the transform. The greater range in MgO contents found at the spreading centers indicates that they have undergone greater amounts of fractional crystallization than samples recovered from the fault zones. 3) Radiogenic isotope analysis confirms that there are at least two different sources beneath the transform (E-MORB and N-MORB). 4) REE patterns of D-MORB samples indicate that they cannot be related to N-MORB by fractional crystallization, but require mixing with 4-6% E-MORB to produce REE patterns similar to N-MORB samples. 5) Evidence for mixing is seen in phenocrysts/xenocryst textures and compositions. Mixing model between evolved and primitive samples provide better fits to major and trace element data. 6) Samples from similar morphotectonic locations group together on Ce/Y and $Na_{8.0}$, $Fe_{8.0}$ diagrams, but Ce/Y ratios from different locations cannot be produced by fractional crystallization. Ce/Y ratios are can be best explained by variable extents of mixing with an E-MORB source. $Na_{8.0}$, $Fe_{8.0}$ data cannot be easily explained by mixing different sources or by variability in the depth and extents

of melting. Instead, the $Na_{8.0}$-$Fe_{8.0}$ variability appears to result from a combination of source variability and variability in extents and depths of melting.

The above observations can be fit by a petrogenetic model in which lava compositions are controlled by the presence, size, and depth of melt lenses located within the transform (Figure 7-23). The eruption of N-MORB and evolved samples from the spreading centers opposed to the D-MORB and primitive basalts erupted within the faults can be explained by the existence of melt lenses located beneath the spreading centers that mix depleted and enriched sources and fractional crystallize magma prior to eruption. The fairly narrow range of compositions found at individual tectonic locations suggests that some homogenization does occur within melt lenses located beneath the spreading centers. The melt lenses are probably truncated by the fault zones resulting in the eruption of more depleted, primitive basalts within the faults. The more depleted nature of the samples from the A-B fault suggests that sources may be mixed with lower percents E-MORB or none at all. The narrow range in MgO contents and lack of ferrobasalts recovered from the faults indicates that limited fractional crystallization is occurring beneath the faults (i.e. magmas may not be mixed in a shallow level magma chamber). The higher density of the picritic samples may have caused them to erupt within the A-B fault because it is deep enough to tap a lower melt lens or because it is not filtered through an upper melt lens. The WRTI may tap the very edge of the EPR melt lens where highly evolved samples can be erupted along with E-MORB samples due greater amounts of fractional crystallization in a colder thermal regime.

Similar models (Natland and Dick, 1996 and in prep.; Kelemen et al., 1997, Boudier et al., 1996) have been proposed in which sills located at various depths feed

erupted lavas (Figure 7-23). These include the upper melt lens located beneath the sheeted dikes and a lower melt lens located at the base of the crust where picritic basalts are neutrally buoyant, but may also include small melt lenses located at variable depths in between. Larger sills where magmas mix to a greater extend might be located beneath the more homogenized and fractionated spreading centers, while the deeper faults tap smaller sills of variable depths that have not undergone as much mixing and fractionation. Such a model can be used to explain the $Na_{8.0}$ and $Fe_{8.0}$ data which suggests eruptions of variable depths and melt percents and also to explain the variability in sample composition found at small spatial intervals.

Mixing of compositions may also occur as lavas are channeled to the surface. Numerical models suggest that large variations in primary magma composition can be caused by channelized melt transport through the mantle (Spiegelman and Kelemen, 2003). The centers of channels can contain enriched melts from depth, while the edges of the channels transport highly depleted melts extracted from the inter-channel regions at shallower levels (Spiegelman & Keleman, 2003). If channelized melt transport is occurring in Siqueiros transform, it would help explain the wide variations in $Na_{8.0}$, $Fe_{8.0}$ data found at the spreading center B and the A-B fault. Within the melt column deep melts will carry one $Na_{8.0}$, $Fe_{8.0}$ signature, while melts equilibrated at shallow depths along the outside of the column may carry a completely different $Na_{8.0}$, $Fe_{8.0}$ signature. Models for channelized melt transport, melt inclusions, and anorthitic plagioclase phenocrysts indicate that there is a wide range of compositions which are rarely erupted, but most likely are a component of MORB parental magmas.

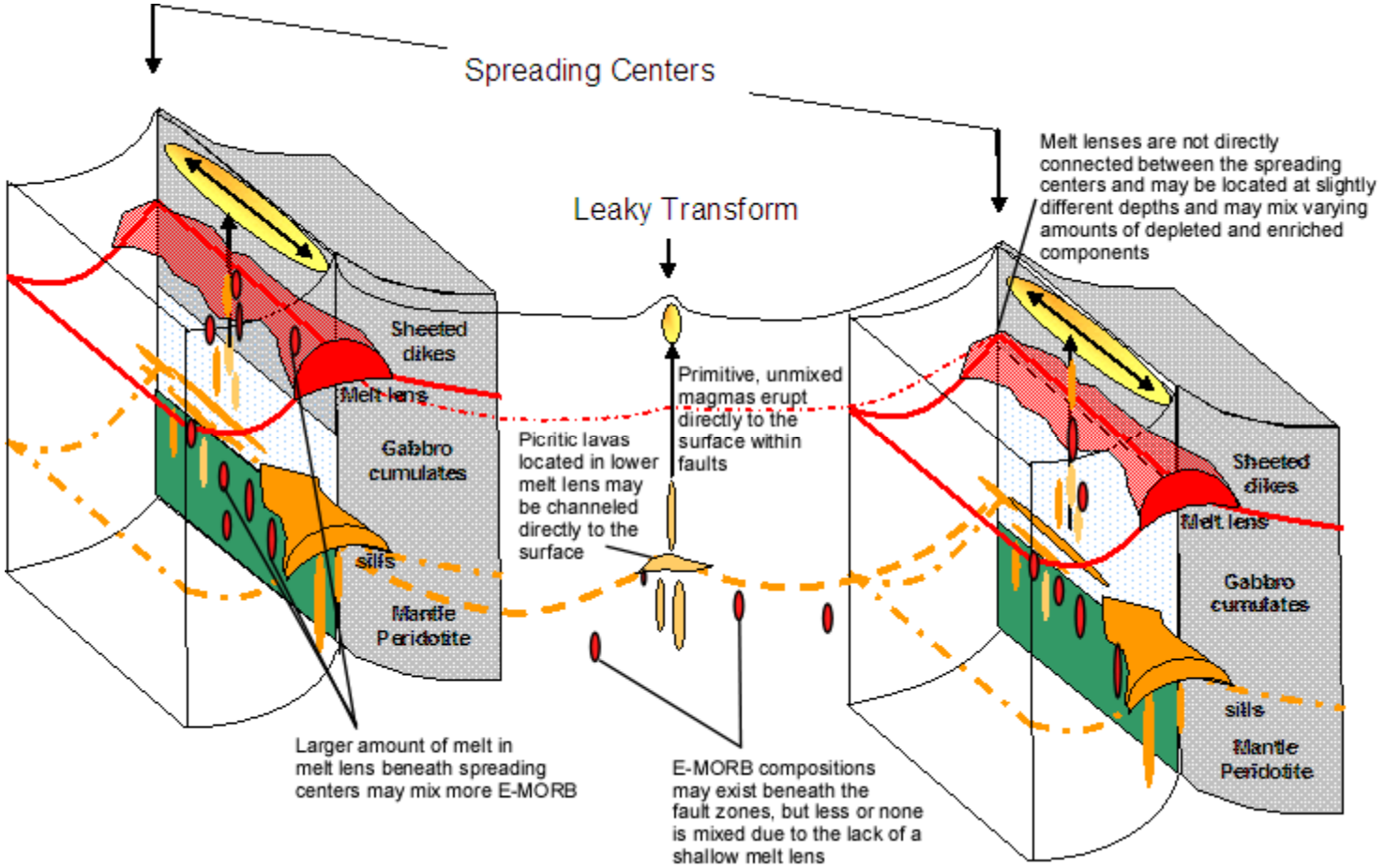


Figure 7-23. Magma transport within the Siqueiros transform (modified from Natland & Dick, in prep.).

# CHAPTER 8
# CONCLUSIONS

Based on major and trace element models, mixing models, and the spatial locations of samples the following conclusions can be made about the Siqueiros transform.

1. Elemental fractionation trends similar to that seen in samples recovered from the EPR suggest that similar magmatic processes are occurring within the transform domain. The majority of the Siqueiros major and trace element variations can be explained by fractional crystallization of parental compositions similar to the high MgO basalts recovered form the A-B fault, with the most evolved samples requiring 50-60% fractional crystallization of spinel + olivine ± plagioclase ± clinopyroxene. Samples from a common morphotectonic location can generally be related by fractional crystallization and the spreading centers show the greatest range in MgO, appearing to have undergone more fractionation than those from the faults. The majority of samples recovered from the spreading centers are also N-MORB. These characteristics suggest that fairly long-lived magma chambers or melt lenses capable of fractionating mixing magma bodies exist beneath the spreading centers. This is in agreement with tectonic models suggesting that "normal" crustal accretion has been occurring along the spreading centers for a few million years.

2. Although most of the chemical variability in the lavas can be explained by fractionation, variations in the major and trace element data are great enough to require at least 2-3 different parental compositions. The A-B fault contains both D-MORB and N-MORB and E-MORB are present at the nearby RTI. The close proximity of these chemical types suggests that mantle heterogeneities exist on a very small scale.

3. Well evolved melt lenses or long-lived sills probably do not exist beneath the faults. The more primitive and porphyritic nature of samples from the A-B fault, along with the occurrence of variably depleted samples may result from the lack of well developed melt lenses with the fault zones. Here the lavas may be channeled directly to the surface with limited fractionation in sills or channels. The result is the eruption of more primitive, porphyritic samples, due to the lack of a melt lens in which crystals are removed and melts are filtered.

4. Mixing of some magmas prior to eruption within the transform is supported by presence of the phenocrysts/xenocrysts that have textures and compositions that indicate that they are out of equilibrium with their host rocks.

5. Incompatible element ratios, CaO, $Al_2O_3$, Zr, and Y trends can be best fit by mixing models between primitive and evolved compositions. Evolved compositions may be mixed with primitive magmas in the upper melt lens, which has been recently proposed to contain highly evolved interstitial melt expelled during crystal network compaction.

6. Radiogenic isotopic analysis of N-MORB and E-MORB, REE patterns of D-MORB, Ce/Y (N-MORB normalized) ratios, and $Na_{8.0}$-$Fe_{8.0}$ data all suggest variable mixing between enriched and depleted sources. Melt lenses beneath the spreading centers may mix larger volumes of melt resulting in the eruption of only N-MORB, but variable extents of enriched material may be mixed at each spreading center resulting in variable Ce/Y and $Na_{8.0}$-$Fe_{8.0}$ that cannot be explained by fractional crystallization. The faults between spreading centers, which are not believed to have well developed melt lenses, are not able to thoroughly mix depleted and enriched components and also may undergo much smaller extents of melting resulting in less enriched material being tapped.

7. The crystal mush zones beneath each spreading center may be of variable sizes resulting in different extents of melting. Channels and sills that erupt within faults or feed melt lenses may be of variable sizes and located at different depths. The variability in extents and depths of melting can explain the $Na_{8.0}$ and $Fe_{8.0}$ variations that cannot be explained by source variations. Fractional crystallization at moderate pressures (~2-8 Kb)are also likely to play a role in the major element variations..

8. The petrogenesis of the samples within Siqueiros may be controlled by the presence, size, and depth of melt lenses located within the transform. Melt lenses are believed to be located beneath the spreading centers which exhibit fractional crystallization trends and N-MORB compositions. More depleted and primitive samples found within the A-B fault may result from the lack of a shallow melt lens capable of mixing enriched and depleted components.

# APPENDIX A
# NORMALIZATION OF CAMECA MICROPROBE DATA

Graphical comparison of the Cameca electron microprobe data and the other microprobe and DCP data showed that there appears to be systematic analytical biases in the MgO and $P_2O_5$ contents of the data sets. The MgO contents obtained from the Cameca electron microprobe are consistently higher than the MgO contents of the ARL and JEOL electron microprobes and the $P_2O_5$ contents of the Cameca electron microprobe data are consistently lower than the $P_2O_5$ contents of the ARL and JEOL electron microprobes. The Cameca electron microprobe data was normalized to be consistent with the ARL and JEOL electron microprobe data.

Normalizations were made to the Cameca electron microprobe MgO and $P_2O_5$ concentrations by plotting the Cameca electron microprobe MgO and $P_2O_5$ values versus the other microprobe MgO and $P_2O_5$ contents for replicate samples (Figure A-1). A best fit line was matched to the data. For a perfect fit, the best fit line would have a slope of 1. In order to remove the analytical offset, the MgO and $P_2O_5$ contents of the Cameca electron microprobe data were shifted to make a best fit line with a slope equal to 1 (Figure A-2).

The following equation was used to correct the MgO contents:

$$MgO_{corrected} = (MgO_{Cameca} + 0.026281) / 0.82046$$

The following equation was used to correct the $P_2O_5$ contents:

$$P_2O_{5corrected} = (P_2O_{5Cameca} - 0.44722) / 0.90029$$

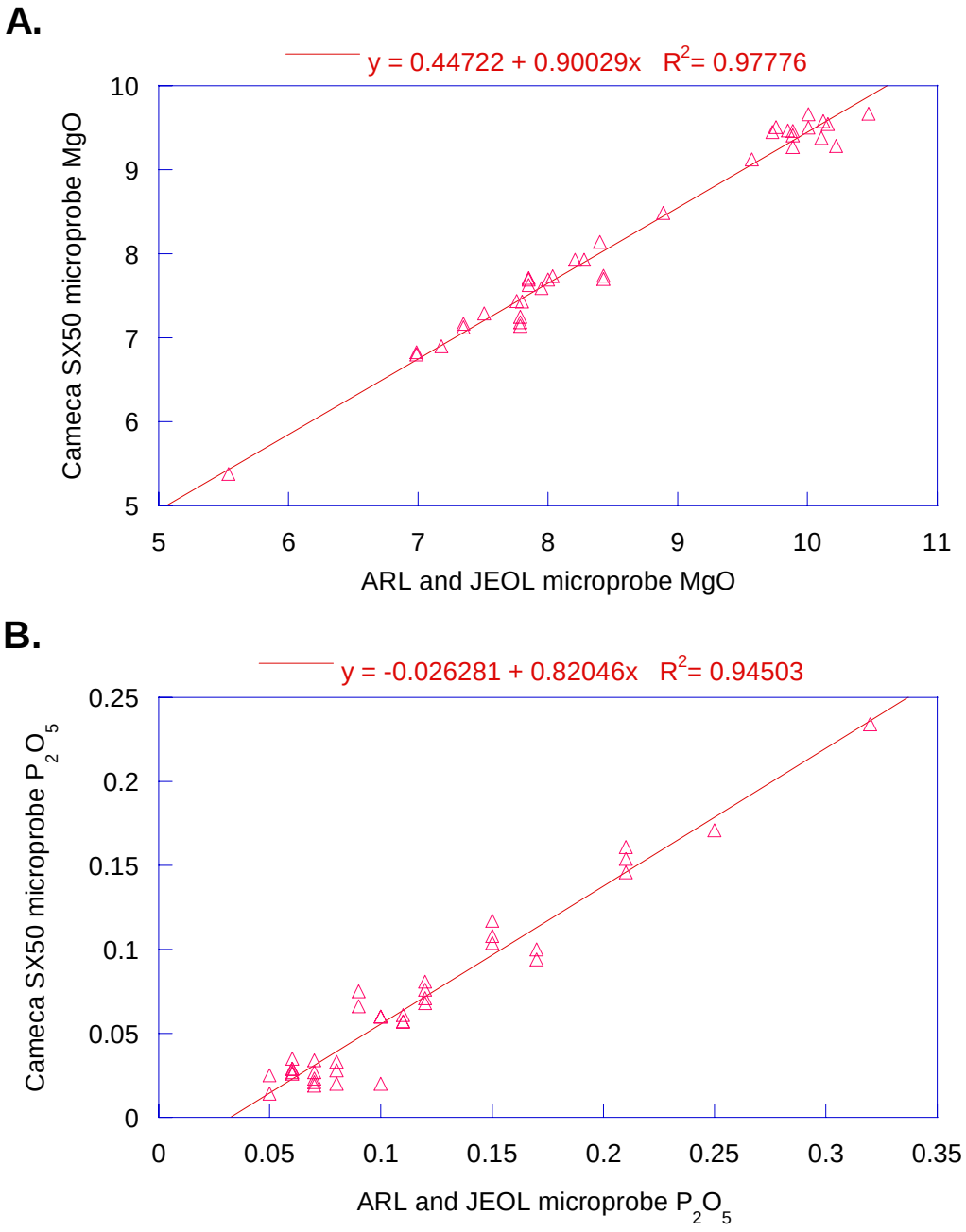


Figure A-1. Cameca microprobe data versus ARL and JEOL microprobe data. A. Best fit line showing the offset between the Cameca microprobe MgO contents and the ARL and JEOL microprobe MgO contents. B. Best fit line showing the offset between the Cameca microprobe $P_2O_5$ contents and the ARL and JEOL microprobe $P_2O_5$ contents. The equations for the best fit lines are displayed at top of graphs along with the $R^2$ value.

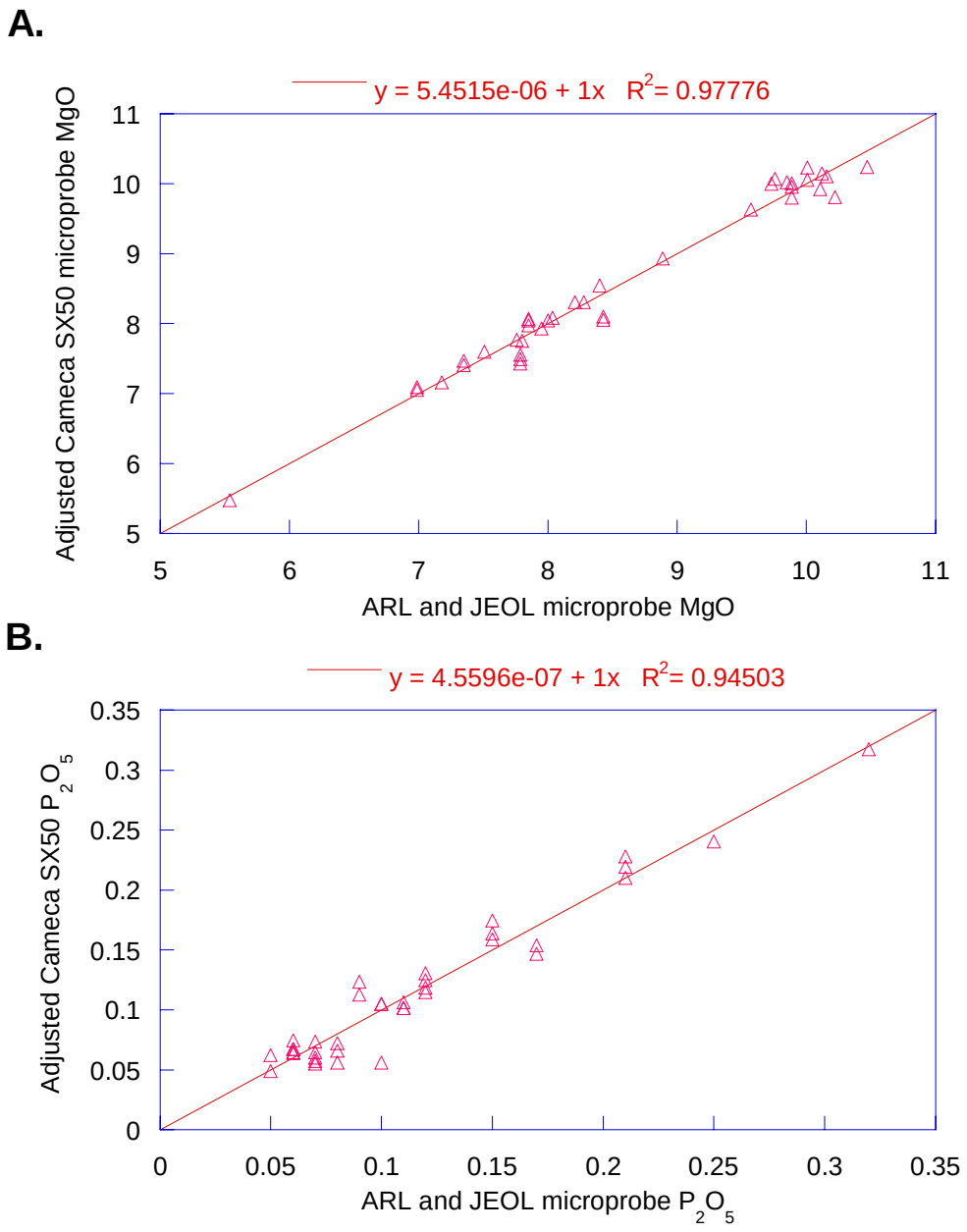


Figure A-2. Normalized Cameca microprobe data. A. Normalized Cameca microprobe MgO contents versus ARL and JEOL microprobe MgO contents. B. Normalized Cameca microprobe $P_2O_5$ contents versus ARL and JEOL microprobe $P_2O_5$ contents. The MgO and $P_2O_5$ contents were shifted to fit a slope of 1. The equation for the best fit line is displayed at the top of graphs along with the $R^2$ value.

# APPENDIX B
# OLIVINE, PLAGIOCLASE AND SPINEL MICROPROBE ANALYSIS

Table B-1. Microprobe analysis of olivine phenocrysts in the Siqueiros samples.

| Sample # | Description | Mg* | $SiO_2$ | $FeO_T$ | MnO | MgO | CaO | Total | Si | Ti | Fe | Mn | Mg | Ca | Cr | O | Fo | Fa |
|---|---|---|---|---|---|---|---|---|---|---|---|---|---|---|---|---|---|---|
| **2375-9-ol1** | ctr. sm. euh. | 0.6 | 39.8 | 15.08 | 0.12 | 45.05 | 0.38 | 100.43 | 1.00 | 0.00 | 0.32 | 0.00 | 1.68 | 0.01 | 0 | 4 | 84.19 | 15.81 |
| | 50% outward | 0.6 | 39.7 | 14.79 | 0.17 | 44.54 | 0.38 | 99.58 | 1.00 | 0.00 | 0.31 | 0.00 | 1.67 | 0.01 | 0 | 4 | 84.29 | 15.71 |
| | rim | 0.6 | 39.55 | 14.92 | 0.2 | 44.4 | 0.39 | 99.46 | 1.00 | 0.00 | 0.32 | 0.00 | 1.67 | 0.01 | 0 | 4 | 84.14 | 15.86 |
| **2376-3-ol1** | ctr. sm. euh. | 0.62 | 40.14 | 13.52 | 0.16 | 45.79 | 0.28 | 99.89 | 1.00 | 0.00 | 0.28 | 0.00 | 1.70 | 0.01 | 0 | 4 | 85.79 | 14.21 |
| **2376-8-ol1** | ctr. sm. euh. | 0.61 | 40.13 | 14.09 | 0.16 | 45.81 | 0.26 | 100.45 | 1.00 | 0.00 | 0.29 | 0.00 | 1.70 | 0.01 | 0 | 4 | 85.28 | 14.72 |
| **2377-4-ol1** | ctr. sm. euh | 0.59 | 39.75 | 15.33 | 0.19 | 44.56 | 0.31 | 100.14 | 1.00 | 0.00 | 0.32 | 0.00 | 1.67 | 0.01 | 0 | 4 | 83.82 | 16.18 |
| **2377-4-ol2** | lge. anh. | 0.59 | 39.51 | 16.91 | 0.21 | 43.46 | 0.23 | 100.32 | 1.00 | 0.00 | 0.36 | 0.00 | 1.64 | 0.01 | 0 | 4 | 82.08 | 17.92 |
| | rim | 0.59 | 39.73 | 16.98 | 0.16 | 43.45 | 0.24 | 100.56 | 1.00 | 0.00 | 0.36 | 0.00 | 1.63 | 0.01 | 0 | 4 | 82.02 | 17.98 |
| **2377-11-ol1** | ctr. lge. euh. | 0.56 | 39.59 | 17.88 | 0.22 | 42.99 | 0.27 | 100.95 | 1.00 | 0.00 | 0.38 | 0.00 | 1.62 | 0.01 | 0 | 4 | 81.08 | 18.92 |
| **2378-7-ol1** | ctr. sm. euh. | 0.6 | 39.84 | 15.09 | 0.19 | 45.2 | 0.33 | 100.65 | 0.99 | 0.00 | 0.32 | 0.00 | 1.68 | 0.01 | 0 | 4 | 84.22 | 15.78 |
| **2378-7-ol2** | ctr. sm. euh. | 0.6 | 39.75 | 14.84 | 0.16 | 44.67 | 0.33 | 99.75 | 1.00 | 0.00 | 0.31 | 0.00 | 1.68 | 0.01 | 0 | 4 | 84.29 | 15.71 |
| **2380-4-ol1** | ctr. sm. euh. | 0.59 | 39.92 | 15.43 | 0.21 | 44.73 | 0.25 | 100.54 | 1.00 | 0.00 | 0.32 | 0.00 | 1.67 | 0.01 | 0 | 4 | 83.78 | 16.22 |
| **2380-11-ol1** | ctr. sm. euh. | 0.61 | 39.68 | 16.55 | 0.2 | 43.93 | 0.25 | 100.61 | 1.00 | 0.00 | 0.35 | 0.00 | 1.65 | 0.01 | 0 | 4 | 82.55 | 17.45 |
| **2381-11-0l1** | ctr. sm. euh. | 0.61 | 39.41 | 14.19 | 0.13 | 45.08 | 0.37 | 99.18 | 1.00 | 0.00 | 0.30 | 0.00 | 1.70 | 0.01 | 0 | 4 | 84.99 | 15.01 |
| **2381-11-ol2** | ctr. sm. euh. | 0.61 | 40.11 | 12.53 | 0.14 | 46.82 | 0.34 | 99.94 | 1.00 | 0.00 | 0.26 | 0.00 | 1.73 | 0.01 | 0 | 4 | 86.94 | 13.06 |
| **2381-11-ol1a** | ctr. sm. euh. | 0.61 | 39.92 | 14.24 | 0.18 | 45.48 | 0.37 | 100.19 | 1.00 | 0.00 | 0.30 | 0.00 | 1.69 | 0.01 | 0 | 4 | 85.06 | 14.94 |
| **2382-7-0l1** | glomero. w. cpx+plag | 0.58 | 40.03 | 16.47 | 0.2 | 44.02 | 0.26 | 100.98 | 1.00 | 0.00 | 0.34 | 0.00 | 1.64 | 0.01 | 0 | 4 | 82.65 | 17.35 |
| **2383-2-ol1** | ctr. sm. euh | 0.59 | 39.63 | 15.38 | 0.26 | 44.7 | 0.28 | 100.25 | 1.00 | 0.00 | 0.32 | 0.00 | 1.67 | 0.01 | 0 | 4 | 83.82 | 16.18 |
| **2383-6-ol1** | ctr. med. euh. | 0.67 | 40.6 | 12.55 | 0.13 | 47.25 | 0.26 | 100.79 | 1.00 | 0.00 | 0.26 | 0.00 | 1.73 | 0.01 | 0 | 4 | 87.03 | 12.97 |
| | rim | 0.61 | 40.55 | 12.51 | 0.15 | 47.16 | 0.33 | 100.7 | 1.00 | 0.00 | 0.26 | 0.00 | 1.73 | 0.01 | 0 | 4 | 87.04 | 12.96 |
| **2384-1-ol1** | ctr. lge. anh. | 0.71 | 41.22 | 10.09 | 0.14 | 48.53 | 0.28 | 100.26 | 1.01 | 0.00 | 0.21 | 0.00 | 1.77 | 0.01 | 0 | 4 | 89.55 | 10.45 |
| **2384-1-ol2** | rim | 0.71 | 41.21 | 10.35 | 0.11 | 48.28 | 0.48 | 100.43 | 1.01 | 0.00 | 0.21 | 0.00 | 1.76 | 0.01 | 0 | 4 | 89.26 | 10.74 |
| **2384-3-ol1** | ctr. med. subh. | 0.72 | 40.82 | 10.9 | 0.09 | 47.98 | 0.26 | 100.05 | 1.00 | 0.00 | 0.22 | 0.00 | 1.76 | 0.01 | 0 | 4 | 88.69 | 11.31 |
| | rim | 0.72 | 41.29 | 9.66 | 0.09 | 49.14 | 0.3 | 100.48 | 1.01 | 0.00 | 0.20 | 0.00 | 1.78 | 0.01 | 0 | 4 | 90.07 | 9.93 |
| **2384-3-ol2** | ctr. sm. euh. | 0.72 | 41.21 | 9.85 | 0.1 | 48.76 | 0.3 | 100.22 | 1.01 | 0.00 | 0.20 | 0.00 | 1.78 | 0.01 | 0 | 4 | 89.82 | 10.18 |
| **2384-3-ol3** | ctr. lge. anh. | 0.72 | 40.68 | 11.15 | 0.09 | 47.93 | 0.49 | 100.34 | 1.00 | 0.00 | 0.23 | 0.00 | 1.76 | 0.01 | 0 | 4 | 88.45 | 11.55 |
| **2384-9-ol1** | ctr. sm. euh. | 0.71 | 39.99 | 11.7 | 0.12 | 47.15 | 0.28 | 99.24 | 1.00 | 0.00 | 0.24 | 0.00 | 1.75 | 0.01 | 0 | 4 | 87.78 | 12.22 |
| **2384-9-ol2** | ctr. sm. euh. | 0.71 | 40.73 | 9.95 | 0.1 | 48.39 | 0.28 | 99.45 | 1.00 | 0.00 | 0.21 | 0 | 1.78 | 0.01 | 0 | 4 | 89.66 | 10.34 |
| **2384-9-ol3** | ctr. sm. euh. | 0.71 | 40.7 | 10.56 | 0.06 | 48.68 | 0.26 | 100.26 | 1.00 | 0.00 | 0.22 | 0 | 1.78 | 0.01 | 0 | 4 | 89.15 | 10.85 |

Table B-1. Continued.

| Sample # | Description | Mg* | $SiO_2$ | $FeO_T$ | MnO | MgO | CaO | Total | Si | Ti | Fe | Mn | Mg | Ca | Cr | O | Fo | Fa |
|---|---|---|---|---|---|---|---|---|---|---|---|---|---|---|---|---|---|---|
| **2384-9-ol4** | ctr. sm. euh. | 0.71 | 40.57 | 9.91 | 0.09 | 48.17 | 0.33 | 99.07 | 1.00 | 0.00 | 0.21 | 0.00 | 1.78 | 0.01 | 0 | 4 | 89.65 | 10.35 |
| **2384-9-ol5** | ctr. sm. euh. | 0.71 | 40.76 | 10.12 | 0.05 | 48.61 | 0.27 | 99.81 | 1.00 | 0.00 | 0.21 | 0.00 | 1.78 | 0.01 | 0 | 4 | 89.54 | 10.46 |
| **2384-11-ol1** | ctr. lge. anh. | 0.67 | 40.47 | 11.4 | 0.13 | 47.77 | 0.25 | 100.02 | 1.00 | 0.00 | 0.24 | 0.00 | 1.76 | 0.01 | 0 | 4 | 88.19 | 11.81 |
| **2386-5-ol1** | ctr. sm. euh. | 0.64 | 39.73 | 12.92 | 0.15 | 46.03 | 0.36 | 99.19 | 1.00 | 0.00 | 0.27 | 0.00 | 1.72 | 0.01 | 0 | 4 | 86.39 | 13.61 |
| **2386-7-ol1** | ctr. sm. euh. | 0.58 | 38.7 | 15.42 | 0.21 | 44.02 | 0.34 | 98.69 | 0.99 | 0.00 | 0.33 | 0.00 | 1.68 | 0.01 | 0 | 4 | 83.57 | 16.43 |
| **2387-1-ol1** | ctr. sm. euh. | 0.58 | 40.17 | 14.15 | 0.14 | 45.48 | 0.28 | 100.22 | 1.00 | 0.00 | 0.30 | 0.00 | 1.69 | 0.01 | 0 | 4 | 85.14 | 14.86 |
| **2387-6-ol1** | ctr. sm. euh. | 0.59 | 39.44 | 15.26 | 0.19 | 44.83 | 0.32 | 100.04 | 0.99 | 0.00 | 0.32 | 0.00 | 1.68 | 0.01 | 0 | 4 | 83.96 | 16.04 |
| **2387-6-ol2** | ctr. sm. euh. | 0.59 | 39.61 | 15.29 | 0.21 | 44.65 | 0.34 | 100.1 | 1.00 | 0.00 | 0.32 | 0.00 | 1.67 | 0.01 | 0 | 4 | 83.88 | 16.12 |
| **2388-3a-ol1** | ctr. sm. euh. | 0.57 | 39.31 | 15.3 | 0.2 | 44.72 | 0.27 | 99.8 | 0.99 | 0.00 | 0.32 | 0.00 | 1.68 | 0.01 | 0 | 4 | 83.89 | 16.11 |
| | rim | 0.57 | 39.51 | 15.7 | 0.17 | 43.94 | 0.32 | 99.64 | 1.00 | 0.00 | 0.33 | 0.00 | 1.66 | 0.01 | 0 | 4 | 83.30 | 16.70 |
| **2388-3a-ol2** | ctr. med. euh. | 0.57 | 39.61 | 15.86 | 0.18 | 44.13 | 0.27 | 100.05 | 1.00 | 0.00 | 0.33 | 0.00 | 1.66 | 0.01 | 0 | 4 | 83.22 | 16.78 |
| **2388-10-ol1** | ctr. sm. euh. | 0.65 | 39.94 | 13.08 | 0.14 | 46.49 | 0.3 | 99.95 | 0.99 | 0.00 | 0.27 | 0.00 | 1.73 | 0.01 | 0 | 4 | 86.37 | 13.63 |
| **2389-1-ol1** | ctr. sm. euh. | 0.57 | 39.6 | 15.77 | 0.17 | 43.96 | 0.3 | 99.8 | 1.00 | 0.00 | 0.33 | 0.00 | 1.65 | 0.01 | 0 | 4 | 83.24 | 16.76 |
| **2389-1-ol2** | ctr. sm. euh | 0.57 | 39.58 | 15.98 | 0.15 | 43.73 | 0.29 | 99.73 | 1.00 | 0.00 | 0.34 | 0.00 | 1.65 | 0.01 | 0 | 4 | 82.98 | 17.02 |
| **2390-9-ol1** | ctr. wormy | 0.44 | 38.38 | 24.02 | 0.29 | 38.29 | 0.28 | 101.26 | 0.99 | 0.00 | 0.52 | 0.01 | 1.48 | 0.01 | 0 | 4 | 73.96 | 26.04 |
| | 50% outward | 0.44 | 38.33 | 23.9 | 0.33 | 38.43 | 0.26 | 101.25 | 0.99 | 0.00 | 0.52 | 0.01 | 1.48 | 0.01 | 0 | 4 | 74.13 | 25.87 |
| | 75% outward | 0.44 | 38.51 | 23.78 | 0.31 | 38.57 | 0.28 | 101.45 | 0.99 | 0.00 | 0.51 | 0.01 | 1.48 | 0.01 | 0 | 4 | 74.30 | 25.70 |
| | rim | 0.44 | 38.3 | 23.62 | 0.3 | 38.58 | 0.32 | 101.12 | 0.99 | 0.00 | 0.51 | 0.01 | 1.49 | 0.01 | 0 | 4 | 74.43 | 25.57 |
| **D1-5-ol1** | ctr. sm. euh. | 0.62 | 40.12 | 13.9 | 0.14 | 45.86 | 0.33 | 100.35 | 1.00 | 0.00 | 0.29 | 0.00 | 1.70 | 0.01 | 0 | 4 | 85.46 | 14.54 |
| **D4-2-ol1** | ctr. sm. euh. | 0.57 | 39.3 | 16.18 | 0.2 | 43.53 | 0.28 | 99.49 | 1.00 | 0.00 | 0.34 | 0.00 | 1.65 | 0.01 | 0 | 4 | 82.74 | 17.26 |
| **D20-7-ol1** | ctr. sm. euh. | 0.71 | 40.69 | 9.94 | 0.05 | 48.68 | 0.26 | 99.62 | 1.00 | 0.00 | 0.20 | 0.00 | 1.79 | 0.01 | 0 | 4 | 89.72 | 10.28 |
| **D20-7-ol2** | ctr. lge. anh. | 0.71 | 41.05 | 9.27 | 0.1 | 48.72 | 0.23 | 99.37 | 1.01 | 0.00 | 0.19 | 0.00 | 1.78 | 0.01 | 0 | 4 | 90.35 | 9.65 |
| | 50% outward | 0.71 | 40.9 | 9.36 | 0.09 | 49.12 | 0.25 | 99.72 | 1.00 | 0.00 | 0.19 | 0.00 | 1.79 | 0.01 | 0 | 4 | 90.34 | 9.66 |
| **D20-8-ol1** | ctr. sm subh. | 0.71 | 40.48 | 10.21 | 0.1 | 48.46 | 0.27 | 99.52 | 1.00 | 0.00 | 0.21 | 0.00 | 1.78 | 0.01 | 0 | 4 | 89.43 | 10.57 |
| **D20-30-ol1** | ctr. sm. euh. | 0.71 | 41.04 | 10.51 | 0.13 | 49.5 | 0.26 | 101.44 | 0.99 | 0.00 | 0.21 | 0.00 | 1.79 | 0.01 | 0 | 4 | 89.35 | 10.65 |
| **D20-30-ol2** | ctr. lge. anh. | 0.71 | 40.83 | 9.92 | 0.05 | 48.45 | 0.28 | 99.53 | 1.00 | 0.00 | 0.20 | 0.00 | 1.78 | 0.01 | 0 | 4 | 89.70 | 10.30 |
| **D20-30-ol3** | ctr. lge. anh. | 0.71 | 41 | 8.97 | 0.08 | 49.12 | 0.25 | 99.42 | 1.01 | 0.00 | 0.18 | 0.00 | 1.80 | 0.01 | 0 | 4 | 90.71 | 9.29 |
| **D20-30-ol4** | ctr. lge. anh. | 0.71 | 40.96 | 9.98 | 0.08 | 48.66 | 0.28 | 99.96 | 1.00 | 0.00 | 0.20 | 0.00 | 1.78 | 0.01 | 0 | 4 | 89.68 | 10.32 |
| | 30% outward | 0.71 | 40.73 | 10.01 | 0.08 | 48.58 | 0.25 | 99.65 | 1.00 | 0.00 | 0.21 | 0.00 | 1.78 | 0.01 | 0 | 4 | 89.64 | 10.36 |
| | 60% outward | 0.71 | 40.69 | 10.01 | 0.09 | 48.72 | 0.26 | 99.77 | 1.00 | 0.00 | 0.21 | 0.00 | 1.79 | 0.01 | 0 | 4 | 89.66 | 10.34 |

Table B-1. Continued.

| Sample # | Description | Mg* | $SiO_2$ | $FeO_T$ | MnO | MgO | CaO | Total | Si | Ti | Fe | Mn | Mg | Ca | Cr | O | Fo | Fa |
|---|---|---|---|---|---|---|---|---|---|---|---|---|---|---|---|---|---|---|
| | rim | 0.71 | 40.86 | 10.11 | 0.08 | 48.89 | 0.29 | 100.23 | 1.00 | 0.00 | 0.21 | 0.00 | 1.78 | 0.01 | 0 | 4 | 89.60 | 10.40 |
| **D20-30-ol5** | ctr. lge. anh. | 0.71 | 40.86 | 9.53 | 0.09 | 49.07 | 0.26 | 99.81 | 1.00 | 0.00 | 0.20 | 0.00 | 1.79 | 0.01 | 0 | 4 | 90.17 | 9.83 |
| | 50% outward | 0.71 | 41.04 | 9.52 | 0.03 | 48.9 | 0.25 | 99.74 | 1.01 | 0.00 | 0.20 | 0.00 | 1.79 | 0.01 | 0 | 4 | 90.15 | 9.85 |
| | rim | 0.71 | 41.3 | 9.6 | 0.1 | 48.88 | 0.26 | 100.14 | 1.01 | 0.00 | 0.20 | 0.00 | 1.78 | 0.01 | 0 | 4 | 90.07 | 9.93 |
| **D20-30-ol6** | ctr. lge. anh. | 0.71 | 41.05 | 9.98 | 0.07 | 48.8 | 0.31 | 100.21 | 1.00 | 0.00 | 0.20 | 0.00 | 1.78 | 0.01 | 0 | 4 | 89.71 | 10.29 |
| **D20-30-ol7** | ctr. lge. anh. | 0.71 | 40.96 | 9.98 | 0.08 | 48.66 | 0.28 | 99.96 | 1.00 | 0.00 | 0.20 | 0.00 | 1.78 | 0.01 | 0 | 4 | 89.68 | 10.32 |
| | 30% outward | 0.71 | 40.73 | 10.01 | 0.08 | 48.58 | 0.25 | 99.65 | 1.00 | 0.00 | 0.21 | 0.00 | 1.78 | 0.01 | 0 | 4 | 89.64 | 10.36 |
| | 60% outward | 0.71 | 40.69 | 10.01 | 0.09 | 48.72 | 0.26 | 99.77 | 1.00 | 0.00 | 0.21 | 0.00 | 1.79 | 0.01 | 0 | 4 | 89.66 | 10.34 |
| | rim | 0.71 | 40.86 | 10.11 | 0.08 | 48.89 | 0.29 | 100.23 | 1.00 | 0.00 | 0.21 | 0.00 | 1.78 | 0.01 | 0 | 4 | 89.60 | 10.40 |
| **D20-30-ol8** | ctr. lge. anh. | 0.71 | 40.86 | 9.53 | 0.09 | 49.07 | 0.26 | 99.81 | 1.00 | 0.00 | 0.20 | 0.00 | 1.79 | 0.01 | 0 | 4 | 90.17 | 9.83 |
| | 50% outward | 0.71 | 41.04 | 9.52 | 0.03 | 48.9 | 0.25 | 99.74 | 1.01 | 0.00 | 0.20 | 0.00 | 1.79 | 0.01 | 0 | 4 | 90.15 | 9.85 |
| | rim | 0.71 | 41.3 | 9.6 | 0.1 | 48.88 | 0.26 | 100.14 | 1.01 | 0.00 | 0.20 | 0.00 | 1.78 | 0.01 | 0 | 4 | 90.07 | 9.93 |
| **D20-30-ol9** | ctr. lge. anh. | 0.71 | 41.05 | 9.98 | 0.07 | 48.8 | 0.31 | 100.21 | 1.00 | 0.00 | 0.20 | 0.00 | 1.78 | 0.01 | 0 | 4 | 89.71 | 10.29 |
| **D21-1-ol1** | ctr. lge. anh. | 0.63 | 40.15 | 14.19 | 0.14 | 45.63 | 0.24 | 100.35 | 1.00 | 0.00 | 0.30 | 0.00 | 1.69 | 0.01 | 0 | 4 | 85.14 | 14.86 |
| | rim | 0.63 | 40.1 | 14.03 | 0.1 | 46.08 | 0.24 | 100.55 | 1.00 | 0.00 | 0.29 | 0.00 | 1.71 | 0.01 | 0 | 4 | 85.41 | 14.59 |
| **D21-1-ol2** | ctr. lge. anh. | 0.63 | 40.23 | 14.09 | 0.16 | 45.79 | 0.26 | 100.53 | 1.00 | 0.00 | 0.29 | 0.00 | 1.70 | 0.01 | 0 | 4 | 85.28 | 14.72 |
| **D21-1-ol3** | ctr. lge. anh. | 0.63 | 40.17 | 14.43 | 0.13 | 45.37 | 0.21 | 100.31 | 1.00 | 0.00 | 0.30 | 0.00 | 1.69 | 0.01 | 0 | 4 | 84.86 | 15.14 |
| **D22-3-ol1** | ctr. sm. euh. | 0.69 | 40.63 | 10.18 | 0.06 | 48.75 | 0.24 | 99.86 | 1.00 | 0.00 | 0.21 | 0.00 | 1.79 | 0.01 | 0 | 4 | 89.51 | 10.49 |
| **D22-4-ol1** | ctr. lge. anh. | 0.68 | 41.29 | 8.88 | 0.08 | 49.46 | 0.24 | 99.95 | 1.01 | 0.00 | 0.18 | 0.00 | 1.80 | 0.01 | 0 | 4 | 90.85 | 9.15 |
| **D26-6-ol1** | ctr. sm. anh. | 0.56 | 39.17 | 15.75 | 0.18 | 43.43 | 0.34 | 98.87 | 1.00 | 0.00 | 0.34 | 0.00 | 1.65 | 0.01 | 0 | 4 | 83.09 | 16.91 |
| **D26-6-ol2** | ctr. sm. euh. | 0.56 | 39.35 | 16.03 | 0.18 | 43.52 | 0.34 | 99.42 | 1.00 | 0.00 | 0.34 | 0.00 | 1.65 | 0.01 | 0 | 4 | 82.87 | 17.13 |
| **D27-5-ol1** | ctr sm. euh. att.spin. | 0.69 | 40.37 | 10.89 | 0.12 | 47.67 | 0.27 | 99.32 | 1.00 | 0.00 | 0.23 | 0.00 | 1.76 | 0.01 | 0 | 4 | 88.64 | 11.36 |
| **D27-5-ol2** | ctr. sm. euh. att. spin. | 0.69 | 40.52 | 10.69 | 0.09 | 48.18 | 0.25 | 99.73 | 1.00 | 0.00 | 0.22 | 0.00 | 1.77 | 0.01 | 0 | 4 | 88.93 | 11.07 |
| **2384-4a** | ol | 0.61 | 40.222 | 12.638 | 0.345 | 46.116 | 0.296 | 99.617 | 1.00 | 0.00 | 0.264 | 0.007 | 1.71 | 0.01 | 0 | 4 | 86.67 | 13.33 |
| | Marj olv | 0.61 | 39.659 | 10.91 | 0.287 | 43.25 | 0.049 | 94.155 | 1.03 | 0.00 | 0.238 | 0.006 | 1.68 | 0.00 | 0 | 4 | 87.60 | 12.40 |
| **2384-4a** | ol core | 0.61 | 39.96 | 11.907 | 0.297 | 46.19 | 0.277 | 98.631 | 1.00 | 0.00 | 0.25 | 0.006 | 1.73 | 0.01 | 0 | 4 | 87.36 | 12.64 |
| | ol rim | 0.61 | 39.735 | 18.344 | 0.28 | 42.286 | 0.281 | 100.926 | 1.00 | 0.00 | 0.388 | 0.006 | 1.59 | 0.01 | 0 | 4 | 80.42 | 19.58 |
| **2384-4a** | ol in clot | 0.61 | 40.341 | 13.543 | 0.163 | 45.962 | 0.266 | 100.275 | 1.00 | 0.00 | 0.282 | 0.003 | 1.70 | 0.01 | 0 | 4 | 85.81 | 14.19 |

Table B-1. Continued.

| Sample # | Description | Mg* | $SiO_2$ | FeO | MnO | MgO | CaO | Total | Si | Ti | Fe | Mn | Mg | Ca | Cr | O | Fo | Fa |
|---|---|---|---|---|---|---|---|---|---|---|---|---|---|---|---|---|---|---|
| **2384-4a** | big ol | 0.61 | 38.174 | 16.597 | 0.183 | 42.866 | 0.26 | 98.08 | 0.99 | 0.00 | 0.359 | 0.004 | 1.65 | 0.01 | 0 | 4 | 82.15 | 17.85 |
| **2384-4a** | big ol | 0.61 | 38.287 | 16.227 | 0.361 | 42.635 | 0.284 | 97.794 | 0.99 | 0.00 | 0.352 | 0.008 | 1.65 | 0.01 | 0 | 4 | 82.40 | 17.60 |
| | big ol | 0.61 | 38.733 | 15.746 | 0.349 | 43.246 | 0.287 | 98.361 | 0.99 | 0.00 | 0.338 | 0.008 | 1.66 | 0.01 | 0 | 4 | 83.03 | 16.97 |
| | big ol nearer edge | 0.61 | 38.393 | 17.034 | 0.251 | 42.647 | 0.296 | 98.621 | 0.99 | 0.00 | 0.367 | 0.005 | 1.64 | 0.01 | 0 | 4 | 81.69 | 18.31 |
| **2384-4a** | ol next to plag | 0.61 | 37.715 | 16.585 | 0.162 | 42.586 | 0.274 | 97.322 | 0.98 | 0.00 | 0.362 | 0.004 | 1.66 | 0.01 | 0 | 4 | 82.06 | 17.94 |

Notes: * Mg = 100 * Mg/(Mg + $Fe^{2+}$) of the host glass. Oxides expressed in wt. %. Fo = fosterite content. Fa = fayalite content.

Table B-2. Microprobe analysis of plagioclase phenocrysts in the Siqueiros samples.

| Sample | Description | Mg* | $SiO_2$ | $Al_2O_3$ | FeO | MgO | CaO | $Na_2O$ | $K_2O$ | Total | Si | Al | Fe | Mg | Ca | Na | K | O | An | Ab | Or |
|---|---|---|---|---|---|---|---|---|---|---|---|---|---|---|---|---|---|---|---|---|---|
| **2375-7-pl1** | ctr. sm lath | 0.62 | 51.66 | 29.48 | 0.67 | 0.15 | 13.58 | 3.54 | 0.01 | 99.09 | 2.37 | 1.59 | 0.03 | 0.01 | 0.67 | 0.31 | 0.001 | 8 | 67.91 | 32.03 | 0.06 |
| **2375-7-pl2** | ctr. sm. lath | | 51.03 | 29.71 | 0.68 | 0.18 | 13.91 | 3.28 | 0.01 | 98.8 | 2.34 | 1.60 | 0.03 | 0.01 | 0.68 | 0.29 | 0.001 | 8 | 70.05 | 29.89 | 0.06 |
| **2375-9-pl1** | ctr. sm. lath | 0.6 | 51.2 | 29.63 | 0.89 | 0.66 | 13.85 | 3.5 | 0.02 | 99.75 | 2.36 | 1.61 | 0.03 | 0.05 | 0.68 | 0.31 | 0.001 | 8 | 68.54 | 31.34 | 0.12 |
| **2375-9-pl2** | ctr. lge. subh. phen. | | 51.49 | 28.96 | 0.92 | 0.28 | 13.25 | 3.7 | 0.01 | 98.61 | 2.38 | 1.58 | 0.04 | 0.02 | 0.66 | 0.33 | 0.001 | 8 | 66.39 | 33.55 | 0.06 |
| | rim | | 51.71 | 28.49 | 0.98 | 0.35 | 13.01 | 3.74 | 0.02 | 98.3 | 2.38 | 1.54 | 0.04 | 0.02 | 0.64 | 0.33 | 0.001 | 8 | 65.70 | 34.18 | 0.12 |
| **2375-9-pl3** | ctr. lge. euh. phen. | | 51.75 | 29.7 | 0.67 | 1.21 | 13.56 | 3.52 | | 100.41 | 2.36 | 1.60 | 0.03 | 0.08 | 0.66 | 0.31 | 0.000 | 8 | 68.04 | 31.96 | 0.00 |
| **2376-3-pl1** | ctr. sm plag lath | 0.62 | 51.42 | 30.29 | 0.58 | 0.2 | 14.04 | 3.32 | 0.01 | 99.86 | 2.34 | 1.62 | 0.02 | 0.01 | 0.68 | 0.29 | 0.001 | 8 | 69.99 | 29.95 | 0.06 |
| **2376-3-pl2** | ctr. lge. anh. phen. | | 49.75 | 31.65 | 0.45 | 0.18 | 15.07 | 2.79 | | 99.89 | 2.28 | 1.71 | 0.02 | 0.01 | 0.74 | 0.25 | 0.000 | 8 | 74.90 | 25.10 | 0.00 |
| **2376-8-pl1** | ctr. sm lath | 0.61 | 49.77 | 31.88 | 0.47 | 0.11 | 15.17 | 2.69 | 0.01 | 100.1 | 2.27 | 1.71 | 0.02 | 0.01 | 0.74 | 0.24 | 0.001 | 8 | 75.66 | 24.28 | 0.06 |
| **2377-3-pl1** | ctr. lge anh. phen. | 0.61 | 48.66 | 32.23 | 0.27 | 0.15 | 15.77 | 2.43 | | 99.51 | 2.23 | 1.74 | 0.01 | 0.01 | 0.78 | 0.22 | 0.000 | 8 | 78.20 | 21.80 | 0.00 |
| | 50% outward | | 49.1 | 32.01 | 0.65 | 0.12 | 15.99 | 2.18 | | 100.05 | 2.25 | 1.73 | 0.02 | 0.01 | 0.79 | 0.19 | 0.000 | 8 | 80.21 | 19.79 | 0.00 |
| | 75% outward | | 49.29 | 31.82 | 0.33 | 0.17 | 15.4 | 2.52 | | 99.53 | 2.25 | 1.71 | 0.01 | 0.01 | 0.75 | 0.22 | 0.000 | 8 | 77.15 | 22.85 | 0.00 |
| | rim | | 47.3 | 33.67 | 0.37 | 0.06 | 17.3 | 1.52 | | 100.22 | 2.17 | 1.82 | 0.01 | 0.00 | 0.85 | 0.14 | 0.000 | 8 | 86.28 | 13.72 | 0.00 |
| **2377-3-pl2** | ctr. lge. anh. phen. | | 46.72 | 33.43 | 0.31 | 0.04 | 17.22 | 1.53 | | 99.25 | 2.17 | 1.83 | 0.01 | 0.00 | 0.86 | 0.14 | 0.000 | 8 | 86.15 | 13.85 | 0.00 |
| | 50% outward | | 47.76 | 33.4 | 0.28 | 0.11 | 16.69 | 1.79 | | 100.03 | 2.19 | 1.80 | 0.01 | 0.01 | 0.82 | 0.16 | 0.000 | 8 | 83.75 | 16.25 | 0.00 |
| | 65% outward | | 47.59 | 33.51 | 0.27 | 0.1 | 16.76 | 1.73 | | 99.96 | 2.18 | 1.81 | 0.01 | 0.01 | 0.82 | 0.15 | 0.000 | 8 | 84.26 | 15.74 | 0.00 |
| | 75% outward | | 46.54 | 33.87 | 0.22 | 0.04 | 17.18 | 1.54 | | 99.39 | 2.15 | 1.85 | 0.01 | 0.00 | 0.85 | 0.14 | 0.000 | 8 | 86.04 | 13.96 | 0.00 |
| | 90% outward | | 47.96 | 32.87 | 0.23 | 0.08 | 16.4 | 2.03 | | 99.57 | 2.20 | 1.78 | 0.01 | 0.01 | 0.81 | 0.18 | 0.000 | 8 | 81.70 | 18.30 | 0.00 |
| | rim | | 47.01 | 33.78 | 0.35 | 0.09 | 16.85 | 1.63 | | 99.71 | 2.17 | 1.84 | 0.01 | 0.01 | 0.83 | 0.15 | 0.000 | 8 | 85.10 | 14.90 | 0.00 |
| **2377-3-pl3** | ctr. lge. anh. phen. | | 50.04 | 31.68 | 0.32 | 0.13 | 15.54 | 2.63 | 0.01 | 100.35 | 2.27 | 1.69 | 0.01 | 0.01 | 0.76 | 0.23 | 0.001 | 8 | 76.51 | 23.43 | 0.06 |
| | 25% outward | | 48.17 | 33.69 | 0.31 | 0.06 | 16.75 | 1.93 | | 100.91 | 2.19 | 1.80 | 0.01 | 0.00 | 0.81 | 0.17 | 0.000 | 8 | 82.75 | 17.25 | 0.00 |
| | 50% outward | | 47.44 | 34.04 | 0.31 | 0.04 | 17.25 | 1.63 | | 100.71 | 2.17 | 1.83 | 0.01 | 0.00 | 0.84 | 0.14 | 0.000 | 8 | 85.40 | 14.60 | 0.00 |
| | 75% outward | | 49.67 | 32.06 | 0.39 | 0.16 | 15.73 | 2.6 | 0.01 | 100.62 | 2.25 | 1.71 | 0.01 | 0.01 | 0.76 | 0.23 | 0.001 | 8 | 76.93 | 23.01 | 0.06 |
| | rim | | 47.38 | 33.76 | 0.41 | 0.09 | 17.35 | 1.67 | | 100.66 | 2.19 | 1.84 | 0.02 | 0.01 | 0.86 | 0.15 | 0.000 | 8 | 85.17 | 14.83 | 0.00 |
| **2377-3-pl4** | ctr. sm lath | | 52.52 | 30.17 | 0.5 | 0.13 | 13.68 | 3.64 | 0.02 | 100.66 | 2.37 | 1.61 | 0.02 | 0.01 | 0.66 | 0.32 | 0.001 | 8 | 67.42 | 32.46 | 0.12 |
| | rim | | 51.82 | 30.1 | 0.57 | 0.09 | 13.77 | 3.6 | 0.02 | 99.97 | 2.36 | 1.61 | 0.02 | 0.01 | 0.67 | 0.32 | 0.001 | 8 | 67.80 | 32.08 | 0.12 |
| **2377-3-pl5** | ctr. sm. lath | | 51.95 | 30.69 | 0.52 | 0.14 | 14.01 | 3.5 | 0.01 | 100.82 | 2.34 | 1.63 | 0.02 | 0.01 | 0.68 | 0.31 | 0.001 | 8 | 68.83 | 31.12 | 0.06 |
| | rim | | 51.21 | 30.7 | 0.56 | 0.14 | 14.45 | 3.11 | 0.01 | 100.18 | 2.33 | 1.65 | 0.02 | 0.01 | 0.70 | 0.27 | 0.001 | 8 | 71.93 | 28.01 | 0.06 |
| **2377-3-pl6** | ctr. tiny lath | | 51.36 | 30.6 | 0.83 | 0.13 | 14.08 | 3.38 | 0.01 | 100.39 | 2.34 | 1.64 | 0.03 | 0.01 | 0.69 | 0.30 | 0.001 | 8 | 69.67 | 30.27 | 0.06 |
| **2377-4-pl1** | ctr. tiny lath | 0.59 | 52.09 | 29.93 | 0.86 | 0.19 | 13.53 | 3.57 | 0.02 | 100.19 | 2.36 | 1.60 | 0.03 | 0.01 | 0.66 | 0.31 | 0.001 | 8 | 67.60 | 32.28 | 0.12 |
| **2377-11-pl1** | ctr. tiny lath | 0.56 | 51.14 | 30.46 | 0.77 | 0.19 | 13.98 | 3.4 | 0.02 | 99.96 | 2.34 | 1.65 | 0.03 | 0.01 | 0.69 | 0.30 | 0.001 | 8 | 69.36 | 30.52 | 0.12 |

Table B-2. Continued.

| Sample | Description | Mg* | $SiO_2$ | $Al_2O_3$ | FeO | MgO | CaO | $Na_2O$ | $K_2O$ | Total | Si | Al | Fe | Mg | Ca | Na | K | O | An | Ab | Or |
|---|---|---|---|---|---|---|---|---|---|---|---|---|---|---|---|---|---|---|---|---|---|
| **2377-11-pl2** | ctr med. euh. | | 52.22 | 29.57 | 0.61 | 0.1 | 13.19 | 3.74 | 0.01 | 99.44 | 2.38 | 1.59 | 0.02 | 0.01 | 0.64 | 0.33 | 0.001 | 8 | 66.05 | 33.89 | 0.06 |
| | rim | | 51.21 | 30.36 | 0.79 | 0.06 | 14.07 | 3.32 | | 99.81 | 2.34 | 1.63 | 0.03 | 0.00 | 0.69 | 0.29 | 0.000 | 8 | 70.08 | 29.92 | 0.00 |
| **2377-11-pl3** | ctr. lge anh. phen. | | 50.01 | 31.68 | 0.35 | 0.19 | 15.12 | 2.56 | | 99.91 | 2.27 | 1.70 | 0.01 | 0.01 | 0.74 | 0.23 | 0.000 | 8 | 76.55 | 23.45 | 0.00 |
| | 10% outward | | 47.27 | 33.3 | 0.22 | 0.03 | 16.95 | 1.75 | | 99.52 | 2.18 | 1.81 | 0.01 | 0.00 | 0.84 | 0.16 | 0.000 | 8 | 84.26 | 15.74 | 0.00 |
| | 20% outward | | 47.46 | 33.14 | 0.25 | 0.07 | 16.89 | 1.71 | | 99.52 | 2.18 | 1.80 | 0.01 | 0.00 | 0.83 | 0.15 | 0.000 | 8 | 84.52 | 15.48 | 0.00 |
| | 30% outward | | 47.22 | 33.54 | 0.28 | 0.07 | 17.25 | 1.53 | | 99.89 | 2.18 | 1.82 | 0.01 | 0.00 | 0.85 | 0.14 | 0.000 | 8 | 86.17 | 13.83 | 0.00 |
| | 50% outward | | 47.83 | 33.4 | 0.27 | 0.07 | 16.54 | 1.81 | | 99.92 | 2.20 | 1.81 | 0.01 | 0.00 | 0.81 | 0.16 | 0.000 | 8 | 83.47 | 16.53 | 0.00 |
| | 75% outward | | 48.87 | 32.36 | 0.27 | 0.11 | 15.71 | 2.34 | | 99.66 | 2.24 | 1.75 | 0.01 | 0.01 | 0.77 | 0.21 | 0.000 | 8 | 78.77 | 21.23 | 0.00 |
| | 85% outward | | 47.74 | 32.76 | 0.33 | 0.09 | 16.23 | 1.96 | | 99.11 | 2.22 | 1.80 | 0.01 | 0.01 | 0.81 | 0.18 | 0.000 | 8 | 82.07 | 17.93 | 0.00 |
| | rim | | 51.79 | 30.59 | 0.56 | 0.09 | 13.5 | 3.55 | 0.02 | 100.1 | 2.34 | 1.63 | 0.02 | 0.01 | 0.65 | 0.31 | 0.001 | 8 | 67.68 | 32.20 | 0.12 |
| **2378-6-pl1** | ctr. sm ueh. | | 51.65 | 30.23 | 0.78 | 0.16 | 13.94 | 3.46 | 0.01 | 100.23 | 2.35 | 1.62 | 0.03 | 0.01 | 0.68 | 0.31 | 0.001 | 8 | 68.96 | 30.98 | 0.06 |
| **2378-6-pl2** | ctr. sm. euh. | | 50.57 | 31.06 | 0.49 | 0.12 | 14.51 | 2.96 | | 99.71 | 2.31 | 1.68 | 0.02 | 0.01 | 0.71 | 0.26 | 0.000 | 8 | 73.04 | 26.96 | 0.00 |
| **2380-4-pl1** | ctr. sm. lath | 0.59 | 51.51 | 30.17 | 0.53 | 0.14 | 13.75 | 3.44 | 0.02 | 99.56 | 2.34 | 1.61 | 0.02 | 0.01 | 0.67 | 0.30 | 0.001 | 8 | 68.75 | 31.13 | 0.12 |
| **2380-11-pl1** | ctr. lge. anh. phen. | 0.58 | 46.61 | 33.98 | 0.23 | 0.09 | 17.07 | 1.52 | | 99.5 | 2.15 | 1.85 | 0.01 | 0.01 | 0.84 | 0.14 | 0.000 | 8 | 86.12 | 13.88 | 0.00 |
| | 50% outward | | 46.78 | 33.98 | 0.27 | 0.09 | 17.27 | 1.47 | | 99.86 | 2.17 | 1.86 | 0.01 | 0.01 | 0.86 | 0.13 | 0.000 | 8 | 86.65 | 13.35 | 0.00 |
| | 95% outward | | 50.57 | 31.13 | 0.54 | 0.1 | 14.4 | 3.12 | 0.01 | 99.87 | 2.31 | 1.68 | 0.02 | 0.01 | 0.70 | 0.28 | 0.001 | 8 | 71.79 | 28.15 | 0.06 |
| | rim | | 50.13 | 31.21 | 0.61 | 0.09 | 14.51 | 2.95 | | 99.5 | 2.30 | 1.69 | 0.02 | 0.01 | 0.71 | 0.26 | 0.000 | 8 | 73.10 | 26.90 | 0.00 |
| **2380-11-pl2** | ctr. sm. lath | | 51.3 | 30.43 | 0.66 | 0.12 | 13.91 | 3.28 | 0.02 | 99.72 | 2.34 | 1.64 | 0.03 | 0.01 | 0.68 | 0.29 | 0.001 | 8 | 70.01 | 29.87 | 0.12 |
| **2380-11-pl3** | ctr. sm. lath | | 51.45 | 30.28 | 0.7 | 0.07 | 13.73 | 3.47 | 0.02 | 99.72 | 2.35 | 1.63 | 0.03 | 0.00 | 0.67 | 0.31 | 0.001 | 8 | 68.54 | 31.34 | 0.12 |
| | rim | | 51.38 | 30.43 | 0.76 | 0.09 | 13.83 | 3.4 | 0.01 | 99.9 | 2.33 | 1.62 | 0.03 | 0.01 | 0.67 | 0.30 | 0.001 | 8 | 69.17 | 30.77 | 0.06 |
| **2380-11-pl4** | ctr. sm. euh. | | 48.23 | 32.46 | 0.58 | 0.04 | 16.39 | 2.04 | | 99.74 | 2.22 | 1.76 | 0.02 | 0.00 | 0.81 | 0.18 | 0.000 | 8 | 81.62 | 18.38 | 0.00 |
| **2380-11-pl5** | ctr. med. anh. phen. | | 48.44 | 16.44 | 0.38 | 0.1 | 16.44 | 1.95 | | 83.75 | 2.68 | 1.07 | 0.02 | 0.01 | 0.97 | 0.21 | 0.000 | 8 | 82.33 | 17.67 | 0.00 |
| **2381-14a-pl1** | ctr. sm. lath | 0.66 | 51.71 | 29.47 | 0.59 | 0.22 | 13.61 | 3.48 | 0.01 | 99.09 | 2.37 | 1.59 | 0.02 | 0.02 | 0.67 | 0.31 | 0.001 | 8 | 68.33 | 31.61 | 0.06 |
| **2382-7-pl1** | ctr. sm lath | 0.58 | 52.27 | 29.55 | 0.7 | 0.15 | 13.34 | 3.74 | 0.02 | 99.77 | 2.41 | 1.60 | 0.03 | 0.01 | 0.66 | 0.33 | 0.001 | 8 | 66.26 | 33.62 | 0.12 |
| **2382-7-pl2** | ctr. glomero. w . cpx+ol | | 53.4 | 29.45 | 0.59 | 0.14 | 12.91 | 2.57 | | 99.06 | 2.40 | 1.56 | 0.02 | 0.01 | 0.62 | 0.22 | 0.000 | 8 | 73.52 | 26.48 | 0.00 |
| **2382-7-pl2** | ctr.glomero.w. cpx+ol | | 51.02 | 30.34 | 0.59 | 0.09 | 14.11 | 3.29 | 0.01 | 99.45 | 2.34 | 1.64 | 0.02 | 0.01 | 0.69 | 0.29 | 0.001 | 8 | 70.28 | 29.66 | 0.06 |
| **2383-2-pl1** | ctr. sm. lath | 0.59 | 51.69 | 30.6 | 0.52 | 0.1 | 13.77 | 3.45 | 0.01 | 100.14 | 2.34 | 1.64 | 0.02 | 0.01 | 0.67 | 0.30 | 0.001 | 8 | 68.76 | 31.18 | 0.06 |
| **2383-2-pl2** | ctr. sm. lath | | 52.29 | 30.42 | 0.6 | 0.18 | 13.65 | 3.57 | 0.02 | 100.73 | 2.34 | 1.60 | 0.02 | 0.01 | 0.65 | 0.31 | 0.001 | 8 | 67.80 | 32.09 | 0.12 |
| **2383-6-pl1** | ctr. med subh. | 0.67 | 46.94 | 34.02 | 0.25 | 0.11 | 17.23 | 1.58 | | 100.13 | 2.16 | 1.84 | 0.01 | 0.01 | 0.85 | 0.14 | 0.000 | 8 | 85.77 | 14.23 | 0.00 |

Table B-2. Continued.

| Sample | Description | Mg* | $SiO_2$ | $Al_2O_3$ | FeO | MgO | CaO | $Na_2O$ | $K_2O$ | Total | Si | Al | Fe | Mg | Ca | Na | K | O | An | Ab | Or |
|---|---|---|---|---|---|---|---|---|---|---|---|---|---|---|---|---|---|---|---|---|---|
| | 30% outward | | 47.25 | 33.8 | 0.26 | 0.04 | 17.2 | 1.54 | | 100.09 | 2.17 | 1.83 | 0.01 | 0.00 | 0.85 | 0.14 | 0.000 | 8 | 86.06 | 13.94 | 0.00 |
| | 60% outward | | 47.41 | 33.93 | 0.24 | 0.09 | 17.05 | 1.59 | | 100.31 | 2.17 | 1.83 | 0.01 | 0.01 | 0.83 | 0.14 | 0.000 | 8 | 85.56 | 14.44 | 0.00 |
| | rim | | 47.46 | 33.94 | 0.34 | 0.11 | 17.02 | 1.63 | | 100.5 | 2.18 | 1.84 | 0.01 | 0.01 | 0.84 | 0.14 | 0.000 | 8 | 85.23 | 14.77 | 0.00 |
| **2383-6-pl2** | ctr. sm lath | | 50.24 | 31.76 | 0.4 | 0.21 | 15.08 | 2.74 | | 100.43 | 2.29 | 1.71 | 0.02 | 0.01 | 0.74 | 0.24 | 0.000 | 8 | 75.26 | 24.74 | 0.00 |
| **2386-5-pl1** | ctr. tiny lath | 0.64 | 50.4 | 30.53 | 0.72 | 0.21 | 13.98 | 3.16 | 0.01 | 99.01 | 2.32 | 1.66 | 0.03 | 0.01 | 0.69 | 0.28 | 0.001 | 8 | 70.93 | 29.01 | 0.06 |
| **2386-7-pl1** | ctr. tiny lath | 0.58 | 52.29 | 30.43 | 0.73 | 0.17 | 13.43 | 3.54 | 0.01 | 100.6 | 2.34 | 1.61 | 0.03 | 0.01 | 0.64 | 0.31 | 0.001 | 8 | 67.66 | 32.28 | 0.06 |
| **2387-1-pl1** | ctr. lge anh. phen. | 0.64 | 46.33 | 34.99 | 0.2 | 0.06 | 17.43 | 1.35 | | 100.36 | 2.12 | 1.89 | 0.01 | 0.00 | 0.86 | 0.12 | 0.000 | 8 | 87.71 | 12.29 | 0.00 |
| | 50% outward | | 47.01 | 34.26 | 0.21 | 0.06 | 16.97 | 1.63 | 0.06 | 100.2 | 2.15 | 1.85 | 0.01 | 0.00 | 0.83 | 0.14 | 0.004 | 8 | 84.89 | 14.75 | 0.36 |
| | 75% outward | | 46.56 | 34.05 | 0.23 | 0.05 | 17.44 | 1.4 | | 99.73 | 2.14 | 1.85 | 0.01 | 0.00 | 0.86 | 0.13 | 0.000 | 8 | 87.32 | 12.68 | 0.00 |
| | 90% outward | | 46.51 | 34.51 | 0.3 | 0.07 | 17.35 | 1.45 | | 100.19 | 2.14 | 1.87 | 0.01 | 0.00 | 0.85 | 0.13 | 0.000 | 8 | 86.86 | 13.14 | 0.00 |
| | 95% outward | | 46.69 | 34.55 | 0.24 | 0.06 | 17.22 | 1.42 | | 100.18 | 2.15 | 1.87 | 0.01 | 0.00 | 0.85 | 0.13 | 0.000 | 8 | 87.02 | 12.98 | 0.00 |
| **2387-1-pl2** | ctr. lge. anh. phen. | | 48.85 | 31.97 | 0.29 | 0.1 | 15.73 | 2.38 | | 99.32 | 2.25 | 1.73 | 0.01 | 0.01 | 0.78 | 0.21 | 0.000 | 8 | 78.51 | 21.49 | 0.00 |
| | 50% outward | | 49.08 | 32.61 | 0.32 | 0.09 | 15.93 | 2.3 | | 100.33 | 2.25 | 1.76 | 0.01 | 0.01 | 0.78 | 0.20 | 0.000 | 8 | 79.28 | 20.72 | 0.00 |
| **2387-1-pl2** | ctr. sm. lath | | 51.06 | 30.6 | 0.59 | 0.12 | 14.05 | 3.24 | 0.01 | 99.67 | 2.31 | 1.64 | 0.02 | 0.01 | 0.68 | 0.28 | 0.001 | 8 | 70.51 | 29.43 | 0.06 |
| **2387-1-pl3** | ctr. lge anh. phen. | | 46.98 | 33.64 | 0.23 | 0.05 | 17.27 | 1.53 | | 99.7 | 2.18 | 1.84 | 0.01 | 0.00 | 0.86 | 0.14 | 0.000 | 8 | 86.18 | 13.82 | 0.00 |
| | rim | | 50.2 | 31.3 | 0.35 | 0.12 | 14.82 | 2.7 | | 99.49 | 2.28 | 1.68 | 0.01 | 0.01 | 0.72 | 0.24 | 0.000 | 8 | 75.21 | 24.79 | 0.00 |
| **2387-1-pl4** | ctr. lge anh. phen. | | 46.35 | 33.89 | 0.23 | 0.07 | 17.39 | 1.4 | | 99.33 | 2.15 | 1.85 | 0.01 | 0.00 | 0.86 | 0.13 | 0.000 | 8 | 87.28 | 12.72 | 0.00 |
| | 50% outward | | 46.27 | 33.91 | 0.2 | 0.04 | 17.42 | 1.32 | | 99.16 | 2.14 | 1.85 | 0.01 | 0.00 | 0.87 | 0.12 | 0.000 | 8 | 87.94 | 12.06 | 0.00 |
| | 75% outward | | 47.26 | 33.74 | 0.25 | 0.05 | 17.14 | 1.51 | | 99.95 | 2.17 | 1.83 | 0.01 | 0.00 | 0.84 | 0.13 | 0.000 | 8 | 86.25 | 13.75 | 0.00 |
| | rim | | 47.75 | 33.13 | 0.28 | 0.09 | 16.41 | 1.92 | | 99.58 | 2.21 | 1.81 | 0.01 | 0.01 | 0.81 | 0.17 | 0.000 | 8 | 82.53 | 17.47 | 0.00 |
| **2387-1-pl5** | ctr. med. euh. | | 51.12 | 30.69 | 0.49 | 0.11 | 13.96 | 3.42 | | 99.79 | 2.33 | 1.65 | 0.02 | 0.01 | 0.68 | 0.30 | 0.000 | 8 | 69.28 | 30.72 | 0.00 |
| **2387-6-pl1** | ctr. sm. lath | 0.59 | 51.64 | 30.16 | 0.73 | 0.16 | 13.5 | 3.57 | 0.01 | 99.77 | 2.35 | 1.62 | 0.03 | 0.01 | 0.66 | 0.32 | 0.001 | 8 | 67.59 | 32.35 | 0.06 |
| | rim | | 51.99 | 29.89 | 0.81 | 0.18 | 13.48 | 3.63 | 0.01 | 99.99 | 2.37 | 1.60 | 0.03 | 0.01 | 0.66 | 0.32 | 0.001 | 8 | 67.20 | 32.74 | 0.06 |
| **2387-6-pl2** | ctr. lge. wormy anh. | | 49.31 | 30.91 | 0.37 | 0.1 | 14.84 | 2.72 | | 98.25 | 2.28 | 1.69 | 0.01 | 0.01 | 0.74 | 0.24 | 0.000 | 8 | 75.09 | 24.91 | 0.00 |
| | 10% outward | | 48.96 | 32.07 | 0.4 | 0.07 | 15.56 | 2.41 | 0.01 | 99.48 | 2.25 | 1.74 | 0.02 | 0.00 | 0.77 | 0.21 | 0.001 | 8 | 78.06 | 21.88 | 0.06 |
| **2387-6-pl3** | ctr. lge. wormy anh. | | 47.91 | 32.7 | 0.37 | 0.06 | 15.99 | 2.11 | | 99.14 | 2.21 | 1.78 | 0.01 | 0.00 | 0.79 | 0.19 | 0.000 | 8 | 80.72 | 19.28 | 0.00 |
| | 20% outward | | 48.89 | 32.23 | 0.33 | 0.1 | 15.55 | 2.39 | | 99.49 | 2.24 | 1.74 | 0.01 | 0.01 | 0.76 | 0.21 | 0.000 | 8 | 78.24 | 21.76 | 0.00 |
| | 40% outward | | 48.52 | 32.2 | 0.34 | 0.07 | 15.73 | 2.39 | | 99.25 | 2.23 | 1.75 | 0.01 | 0.00 | 0.78 | 0.21 | 0.000 | 8 | 78.43 | 21.57 | 0.00 |
| | 60% outward | | 48.12 | 32.9 | 0.3 | 0.09 | 16.27 | 2.12 | | 99.8 | 2.21 | 1.78 | 0.01 | 0.01 | 0.80 | 0.19 | 0.000 | 8 | 80.92 | 19.08 | 0.00 |
| | 80% outward | | 48.44 | 32.34 | 0.39 | 0.12 | 15.95 | 2.31 | | 99.55 | 2.24 | 1.76 | 0.02 | 0.01 | 0.79 | 0.21 | 0.000 | 8 | 79.23 | 20.77 | 0.00 |
| **2388-3a-pl1** | ctr. sm lath | 0.57 | 51.7 | 30.92 | 0.55 | 0.17 | 13.82 | 3.37 | 0.01 | 100.54 | 2.34 | 1.65 | 0.02 | 0.01 | 0.67 | 0.30 | 0.001 | 8 | 69.34 | 30.60 | 0.06 |
| | rim | | 51.81 | 30.6 | 0.76 | 0.17 | 13.81 | 3.33 | | 100.48 | 2.33 | 1.62 | 0.03 | 0.01 | 0.67 | 0.29 | 0.000 | 8 | 69.62 | 30.38 | 0.00 |
| **2388-3a-pl2** | ctr. lge. phen. | | 48.09 | 33.6 | 0.3 | 0.08 | 16.64 | 1.9 | | 100.61 | 2.19 | 1.81 | 0.01 | 0.01 | 0.81 | 0.17 | 0.000 | 8 | 82.88 | 17.12 | 0.00 |

Table B-2. Continued.

| Sample | Description | Mg* | $SiO_2$ | $Al_2O_3$ | FeO | MgO | CaO | $Na_2O$ | $K_2O$ | Total | Si | Al | Fe | Mg | Ca | Na | K | O | An | Ab | Or |
|---|---|---|---|---|---|---|---|---|---|---|---|---|---|---|---|---|---|---|---|---|---|
| | 50% outward | | 48.22 | 33.46 | 0.26 | 0.06 | 16.47 | 1.93 | | 100.4 | 2.20 | 1.80 | 0.01 | 0.00 | 0.81 | 0.17 | 0.000 | 8 | 82.50 | 17.50 | 0.00 |
| | rim | | 48.4 | 33.35 | 0.32 | 0.07 | 16.18 | 2.06 | | 100.38 | 2.20 | 1.78 | 0.01 | 0.00 | 0.79 | 0.18 | 0.000 | 8 | 81.27 | 18.73 | 0.00 |
| **2388-3a-pl3** | ctr. med. euh. | | 46.73 | 35.26 | 0.37 | 0.11 | 17.64 | 1.29 | | 101.4 | 2.12 | 1.89 | 0.01 | 0.01 | 0.86 | 0.11 | 0.000 | 8 | 88.31 | 11.69 | 0.00 |
| | 50% outward | | 46.94 | 34.35 | 0.38 | 0.1 | 17.45 | 1.39 | | 100.61 | 2.17 | 1.87 | 0.01 | 0.01 | 0.86 | 0.12 | 0.000 | 8 | 87.40 | 12.60 | 0.00 |
| | rim | | 51.98 | 30.5 | 0.58 | 0.09 | 13.64 | 3.41 | 0.01 | 100.21 | 2.34 | 1.62 | 0.02 | 0.01 | 0.66 | 0.30 | 0.001 | 8 | 68.81 | 31.13 | 0.06 |
| **2388-3a-pl4** | ctr. lge. euh. | | 46.76 | 34.15 | 0.28 | 0.04 | 17.14 | 1.52 | | 99.89 | 2.15 | 1.85 | 0.01 | 0.00 | 0.84 | 0.14 | 0.000 | 8 | 86.17 | 13.83 | 0.00 |
| | 50% outward | | 46.97 | 33.88 | 0.27 | 0.1 | 17.23 | 1.68 | | 100.13 | 2.16 | 1.84 | 0.01 | 0.01 | 0.85 | 0.15 | 0.000 | 8 | 85.00 | 15.00 | 0.00 |
| | 75% outward | | 47.33 | 33.81 | 0.28 | 0.08 | 17 | 1.63 | | 100.13 | 2.17 | 1.83 | 0.01 | 0.01 | 0.84 | 0.14 | 0.000 | 8 | 85.21 | 14.79 | 0.00 |
| | rim | | 47.12 | 34.4 | 0.34 | 0.07 | 16.83 | 1.67 | | 100.43 | 2.16 | 1.86 | 0.01 | 0.00 | 0.83 | 0.15 | 0.000 | 8 | 84.78 | 15.22 | 0.00 |
| **2388-3a-pl5** | ctr. med. euh. | | 49.89 | 32.34 | 0.6 | 0.12 | 14.96 | 2.67 | 0.01 | 100.59 | 2.27 | 1.73 | 0.02 | 0.01 | 0.73 | 0.24 | 0.001 | 8 | 75.54 | 24.40 | 0.06 |
| | 50% outward | | 49.29 | 32.59 | 0.4 | 0.1 | 15.07 | 2.59 | 0.01 | 100.05 | 2.25 | 1.75 | 0.02 | 0.01 | 0.74 | 0.23 | 0.001 | 8 | 76.23 | 23.71 | 0.06 |
| | 75% outward | | 49.84 | 32.58 | 0.5 | 0.09 | 15.1 | 2.59 | | 100.7 | 2.25 | 1.73 | 0.02 | 0.01 | 0.73 | 0.23 | 0.000 | 8 | 76.31 | 23.69 | 0.00 |
| **2388-3a-pl6** | ctr. med. euh. | | 47.78 | 33.8 | 0.34 | 0.08 | 16.57 | 1.87 | | 100.44 | 2.20 | 1.83 | 0.01 | 0.01 | 0.82 | 0.17 | 0.000 | 8 | 83.04 | 16.96 | 0.00 |
| | rim | | 51.75 | 30.35 | 0.65 | 0.22 | 13.69 | 3.35 | 0.02 | 100.03 | 2.36 | 1.63 | 0.02 | 0.01 | 0.67 | 0.30 | 0.001 | 8 | 69.23 | 30.65 | 0.12 |
| **2388-3a-pl7** | ctr. lge. anh. phen. | | 53.04 | 29.93 | 0.55 | 0.05 | 12.8 | 3.94 | 0.02 | 100.33 | 2.40 | 1.59 | 0.02 | 0.00 | 0.62 | 0.35 | 0.001 | 8 | 64.15 | 35.73 | 0.12 |
| | 50% outward | | 52.41 | 30.18 | 0.52 | 0.04 | 12.7 | 4 | 0.02 | 99.87 | 2.38 | 1.61 | 0.02 | 0.00 | 0.62 | 0.35 | 0.001 | 8 | 63.62 | 36.26 | 0.12 |
| | 75% outward | | 52.09 | 30.52 | 0.54 | 0.05 | 12.96 | 3.82 | 0.01 | 99.99 | 2.35 | 1.62 | 0.02 | 0.00 | 0.63 | 0.33 | 0.001 | 8 | 65.18 | 34.76 | 0.06 |
| | rim | | 49.24 | 32.71 | 0.43 | 0.11 | 15.01 | 2.68 | | 100.18 | 2.24 | 1.76 | 0.02 | 0.01 | 0.73 | 0.24 | 0.000 | 8 | 75.58 | 24.42 | 0.00 |
| **2388-10-pl1** | ctr. lge lath | 0.65 | 49.83 | 31.69 | 0.39 | 0.15 | 14.88 | 2.81 | | 99.75 | 2.28 | 1.71 | 0.01 | 0.01 | 0.73 | 0.25 | 0.000 | 8 | 74.53 | 25.47 | 0.00 |
| **2388-10-pl2** | ctr. lge anh. phen | | 50.59 | 31.15 | 0.51 | 0.23 | 14.65 | 3 | 0.01 | 100.14 | 2.30 | 1.67 | 0.02 | 0.02 | 0.71 | 0.26 | 0.001 | 8 | 72.92 | 27.02 | 0.06 |
| **2388-10-pl3** | ctr. lge. euh. | | 50.13 | 31.74 | 0.52 | 0.21 | 14.79 | 2.88 | | 100.27 | 2.28 | 1.70 | 0.02 | 0.01 | 0.72 | 0.25 | 0.000 | 8 | 73.94 | 26.06 | 0.00 |
| | 50% outward | | 50.38 | 31.44 | 0.55 | 0.15 | 14.72 | 2.82 | | 100.06 | 2.29 | 1.69 | 0.02 | 0.01 | 0.72 | 0.25 | 0.000 | 8 | 74.26 | 25.74 | 0.00 |
| | 75% outward | | 50.49 | 31.49 | 0.54 | 0.25 | 14.9 | 2.8 | | 100.47 | 2.31 | 1.69 | 0.02 | 0.02 | 0.73 | 0.25 | 0.000 | 8 | 74.62 | 25.38 | 0.00 |
| **2389-1-pl1** | ctr. med. lath | 0.57 | 51.43 | 30.59 | 0.47 | 0.13 | 13.78 | 3.31 | | 99.71 | 2.34 | 1.64 | 0.02 | 0.01 | 0.67 | 0.29 | 0.000 | 8 | 69.70 | 30.30 | 0.00 |
| **2390-9-pl1** | ctr. lge anh. | 0.44 | 50.92 | 30.83 | 0.53 | 0.06 | 14.3 | 3.24 | 0.01 | 99.89 | 2.34 | 1.67 | 0.02 | 0.00 | 0.70 | 0.29 | 0.001 | 8 | 70.88 | 29.06 | 0.06 |
| | rim | | 53.67 | 28.83 | 0.74 | 0.03 | 11.95 | 4.43 | 0.02 | 99.67 | 2.43 | 1.54 | 0.03 | 0.00 | 0.58 | 0.39 | 0.001 | 8 | 59.78 | 40.10 | 0.12 |
| | 50% outward | | 51.82 | 30.55 | 0.49 | 0.02 | 13.55 | 3.58 | 0.01 | 100.02 | 2.36 | 1.64 | 0.02 | 0.00 | 0.66 | 0.32 | 0.001 | 8 | 67.61 | 32.33 | 0.06 |
| **2390-9-pl2** | ctr. lge. subh. | | 54.04 | 28.55 | 0.73 | 0.05 | 11.86 | 4.61 | 0.03 | 99.87 | 2.45 | 1.53 | 0.03 | 0.00 | 0.58 | 0.41 | 0.002 | 8 | 58.60 | 41.22 | 0.18 |
| **2390-9-pl3** | ctr. sm. lath | | 53.3 | 28.01 | 0.75 | 0.02 | 11.57 | 4.61 | 0.04 | 98.3 | 2.46 | 1.52 | 0.03 | 0.00 | 0.57 | 0.41 | 0.002 | 8 | 57.97 | 41.80 | 0.24 |
| | rim | | 52.87 | 28.35 | 0.79 | 0.02 | 11.77 | 4.36 | 0.02 | 98.18 | 2.42 | 1.53 | 0.03 | 0.00 | 0.58 | 0.39 | 0.001 | 8 | 59.80 | 40.08 | 0.12 |
| **D1-5-pl1** | ctr. tiny lath | 0.62 | 52.2 | 30.33 | 0.65 | 0.27 | 13.69 | 3.56 | 0.02 | 100.72 | 2.36 | 1.62 | 0.02 | 0.02 | 0.66 | 0.31 | 0.001 | 8 | 67.92 | 31.96 | 0.12 |
| **D4-2-pl1** | ctr. sm. lath | 0.57 | 51.97 | 30.59 | 0.56 | 0.1 | 13.71 | 3.5 | 0.01 | 100.44 | 2.35 | 1.63 | 0.02 | 0.01 | 0.66 | 0.31 | 0.001 | 8 | 68.36 | 31.58 | 0.06 |
| **D4-2-pl2** | ctr. sm. lath | | 52.35 | 30.23 | 0.66 | 0.11 | 13.69 | 3.47 | 0.02 | 100.53 | 2.37 | 1.61 | 0.02 | 0.01 | 0.66 | 0.30 | 0.001 | 8 | 68.47 | 31.41 | 0.12 |

Table B-2. Continued.

| Sample | Description | Mg* | $SiO_2$ | $Al_2O_3$ | FeO | MgO | CaO | $Na_2O$ | $K_2O$ | Total | Si | Al | Fe | Mg | Ca | Na | K | O | An | Ab | Or |
|---|---|---|---|---|---|---|---|---|---|---|---|---|---|---|---|---|---|---|---|---|---|
| **D4-2-pl3** | ctr. lge. anh. phen | | 51.73 | 30.49 | 0.5 | 0.11 | 13.71 | 3.43 | 0.02 | 99.99 | 2.34 | 1.63 | 0.02 | 0.01 | 0.66 | 0.30 | 0.001 | 8 | 68.75 | 31.13 | 0.12 |
| **D13-1-pl1** | ctr. lge anh. phen | 0.58 | 49.06 | 32.4 | 0.36 | 0.08 | 15.65 | 2.31 | | 99.86 | 2.24 | 1.74 | 0.01 | 0.01 | 0.76 | 0.20 | 0.000 | 8 | 78.92 | 21.08 | 0.00 |
| | 50% outward | | 46.84 | 34.05 | 0.33 | 0.07 | 17.07 | 1.52 | | 99.88 | 2.16 | 1.85 | 0.01 | 0.00 | 0.84 | 0.14 | 0.000 | 8 | 86.12 | 13.88 | 0.00 |
| | 75% outward | | 48.64 | 32.82 | 0.54 | 0.09 | 15.83 | 2.2 | | 100.12 | 2.22 | 1.77 | 0.02 | 0.01 | 0.78 | 0.20 | 0.000 | 8 | 79.90 | 20.10 | 0.00 |
| | 95% outward | | 48.74 | 32.59 | 0.44 | 0.09 | 15.8 | 2.24 | | 99.9 | 2.23 | 1.76 | 0.02 | 0.01 | 0.78 | 0.20 | 0.000 | 8 | 79.58 | 20.42 | 0.00 |
| **D15-1-pl1** | ctr. lge anh. phen. | 0.58 | 48.23 | 32.66 | 0.35 | 0.09 | 15.91 | 2.17 | | 99.41 | 2.22 | 1.77 | 0.01 | 0.01 | 0.79 | 0.19 | 0.000 | 8 | 80.20 | 19.80 | 0.00 |
| | 25% outward | | 48.45 | 32.74 | 0.33 | 0.06 | 15.83 | 2.16 | | 99.57 | 2.23 | 1.78 | 0.01 | 0.00 | 0.78 | 0.19 | 0.000 | 8 | 80.20 | 19.80 | 0.00 |
| | 50% outward | | 49.9 | 31.39 | 0.41 | 0.13 | 14.43 | 3.02 | 0.01 | 99.29 | 2.28 | 1.69 | 0.02 | 0.01 | 0.71 | 0.27 | 0.001 | 8 | 72.49 | 27.45 | 0.06 |
| | 75% outward | | 48.73 | 32.71 | 0.4 | 0.07 | 15.86 | 2.22 | | 99.99 | 2.23 | 1.76 | 0.02 | 0.00 | 0.78 | 0.20 | 0.000 | 8 | 79.79 | 20.21 | 0.00 |
| | 95% outward | | 48.26 | 32.84 | 0.53 | 0.06 | 15.8 | 2.21 | | 99.7 | 2.22 | 1.78 | 0.02 | 0.00 | 0.78 | 0.20 | 0.000 | 8 | 79.80 | 20.20 | 0.00 |
| | rim | | 48.92 | 32.11 | 0.62 | 0.07 | 15.3 | 2.42 | | 99.44 | 2.24 | 1.74 | 0.02 | 0.00 | 0.75 | 0.22 | 0.000 | 8 | 77.75 | 22.25 | 0.00 |
| **D17-10-pl1** | ctr med. euh. | 0.61 | 47.4 | 33.22 | 0.47 | 0.09 | 16.37 | 1.81 | | 99.36 | 2.20 | 1.82 | 0.02 | 0.01 | 0.81 | 0.16 | 0.000 | 8 | 83.33 | 16.67 | 0.00 |
| | 50% outward | | 49.23 | 31.3 | 0.51 | 0.14 | 14.74 | 2.69 | | 98.61 | 2.27 | 1.70 | 0.02 | 0.01 | 0.73 | 0.24 | 0.000 | 8 | 75.17 | 24.83 | 0.00 |
| | rim | | 47.93 | 32.5 | 0.51 | 0.08 | 16.01 | 2.03 | | 99.06 | 2.24 | 1.79 | 0.02 | 0.01 | 0.80 | 0.18 | 0.000 | 8 | 81.34 | 18.66 | 0.00 |
| **D26-6-pl1** | ctr. med euh. | 0.56 | 52.82 | 28.98 | 0.8 | 0.12 | 12.41 | 4.06 | 0.03 | 99.22 | 2.42 | 1.56 | 0.03 | 0.01 | 0.61 | 0.36 | 0.002 | 8 | 62.70 | 37.12 | 0.18 |
| **D26-6-pl2** | ctr. med euh. | | 51.92 | 29.21 | 0.62 | 0.12 | 12.85 | 3.65 | 0.02 | 98.39 | 2.39 | 1.58 | 0.02 | 0.01 | 0.63 | 0.33 | 0.001 | 8 | 65.97 | 33.91 | 0.12 |
| **D26-6-pl3** | Ctr sm. lath | | 52.28 | 30.26 | 0.59 | 0.12 | 13.37 | 3.67 | 0.02 | 100.31 | 2.65 | 1.81 | 0.02 | 0.01 | 0.73 | 0.36 | 0.001 | 8 | 66.73 | 33.15 | 0.12 |
| **2384-4a** | plag in clot core | 0.61 | 46.61 | 33.51 | 0.33 | 0.20 | 17.44 | 1.57 | 0.01 | 99.65 | 2.15 | 1.82 | 0.01 | 0.01 | 0.86 | 0.14 | 0.000 | 8 | 86.00 | 13.99 | 0.02 |
| | plag in clot rim | 0.61 | 48.17 | 29.44 | 0.56 | 0.20 | 14.65 | 3.24 | 0.02 | 96.28 | 2.28 | 1.64 | 0.02 | 0.01 | 0.74 | 0.30 | 0.001 | 8 | 71.41 | 28.57 | 0.05 |
| | smaller plag c in ol | 0.61 | 51.36 | 30.28 | 0.56 | 0.21 | 14.19 | 3.49 | 0.02 | 100.10 | 2.32 | 1.61 | 0.02 | 0.01 | 0.69 | 0.31 | 0.001 | 8 | 69.24 | 30.74 | 0.07 |
| | smaller plag rim in ol | 0.61 | 51.00 | 30.42 | 0.58 | 0.20 | 14.27 | 3.30 | 0.02 | 99.79 | 2.31 | 1.63 | 0.02 | 0.01 | 0.69 | 0.29 | 0.001 | 8 | 70.46 | 29.52 | 0.07 |
| | med plag core in ol | 0.61 | 50.14 | 30.34 | 0.49 | 0.20 | 14.74 | 3.19 | 0.02 | 99.12 | 2.29 | 1.64 | 0.02 | 0.01 | 0.72 | 0.28 | 0.001 | 8 | 71.86 | 28.12 | 0.07 |
| | med plag rim in ol | 0.61 | 49.17 | 29.81 | 0.58 | 0.17 | 14.64 | 3.17 | 0.02 | 97.56 | 2.29 | 1.64 | 0.02 | 0.01 | 0.73 | 0.29 | 0.001 | 8 | 71.86 | 28.13 | 0.07 |
| | plag pheno in matrix core | 0.61 | 50.02 | 30.39 | 0.44 | 0.18 | 14.54 | 3.14 | 0.03 | 98.74 | 2.29 | 1.64 | 0.02 | 0.01 | 0.71 | 0.28 | 0.001 | 8 | 71.90 | 28.08 | 0.07 |
| | plag pheno in matrix rim | 0.61 | 46.34 | 30.65 | 0.52 | 0.14 | 15.95 | 2.53 | 0.02 | 96.14 | 2.21 | 1.72 | 0.02 | 0.01 | 0.81 | 0.23 | 0.001 | 8 | 77.71 | 22.28 | 0.05 |
| | plag mega core | 0.61 | 46.88 | 33.57 | 0.31 | 0.15 | 17.47 | 1.65 | 0.01 | 100.03 | 2.15 | 1.82 | 0.01 | 0.01 | 0.86 | 0.15 | 0.000 | 8 | 85.43 | 14.57 | 0.02 |
| | plag mega half rim | 0.61 | 45.83 | 32.30 | 0.30 | 0.14 | 17.43 | 1.67 | 0.01 | 97.68 | 2.16 | 1.79 | 0.01 | 0.01 | 0.88 | 0.15 | 0.000 | 8 | 85.26 | 14.73 | 0.03 |
| | plag mega rim | 0.61 | 48.78 | 27.98 | 0.70 | 0.21 | 13.32 | 3.96 | 0.04 | 94.99 | 2.32 | 1.57 | 0.03 | 0.01 | 0.68 | 0.37 | 0.001 | 8 | 65.01 | 34.95 | 0.10 |

Notes: * Mg = 100 * Mg/(Mg + $Fe^{2+}$) of the host glass. Oxides expressed in wt. %. An = anorthite content. Ab = albite content Or = Orthoclase content.

Table B-3. Microprobe analysis of spinel phenocrysts in the Siqueiros samples.

| Sample # | Description | Mg* | $TiO_2$ | $Al_2O_3$ | $Cr_2O_3$ | $Fe_2O_3$ | FeO | MnO | MgO | NiO | CaO | Total | Ti | Al | Cr | $Fe^{3+}$ | $Fe^{2+}$ | Mn | Mg | Ni | Ca | TET | OCT | O | FE* | CR* |
|---|---|---|---|---|---|---|---|---|---|---|---|---|---|---|---|---|---|---|---|---|---|---|---|---|---|---|
| **D20-8-sp1** | ctr. lg. wormy | 0.71 | 0.14 | 44.09 | 22.50 | 2.98 | 8.78 | 0.02 | 19.24 | 0.19 | 0.02 | 97.96 | 0.02 | 11.50 | 3.94 | 0.53 | 1.62 | 0.00 | 6.34 | 0.03 | 0.00 | 15.98 | 8.01 | 32 | 20.38 | 25.50 |
| | 20% outward | 0.71 | 0.16 | 44.67 | 23.54 | 2.97 | 9.57 | 0.02 | 19.34 | 0.16 | 0.01 | 100.44 | 0.03 | 11.41 | 4.03 | 0.52 | 1.73 | 0.00 | 6.25 | 0.03 | 0.00 | 15.98 | 8.01 | 32 | 21.73 | 26.12 |
| | 40% outward | 0.71 | 0.16 | 44.87 | 23.32 | 2.92 | 9.56 | 0.02 | 19.35 | 0.17 | 0.01 | 100.38 | 0.03 | 11.45 | 3.99 | 0.51 | 1.73 | 0.00 | 6.25 | 0.03 | 0.00 | 15.98 | 8.01 | 32 | 21.70 | 25.85 |
| | 60% outward | 0.71 | 0.19 | 44.95 | 23.07 | 2.94 | 9.52 | 0.02 | 19.40 | 0.12 | 0.01 | 100.21 | 0.03 | 11.48 | 3.95 | 0.51 | 1.72 | 0.00 | 6.27 | 0.02 | 0.00 | 15.98 | 8.02 | 32 | 21.58 | 25.61 |
| | rim | 0.71 | 0.16 | 43.70 | 22.26 | 2.35 | 9.20 | 0.04 | 18.66 | 0.14 | 0.02 | 96.53 | 0.03 | 11.57 | 3.95 | 0.42 | 1.73 | 0.01 | 6.25 | 0.03 | 0.00 | 15.98 | 8.02 | 32 | 21.67 | 25.47 |
| **D20-8-sp2** | ctr. lg wormy | 0.71 | 0.24 | 39.78 | 28.74 | 3.34 | 9.78 | 0.08 | 18.86 | 0.05 | 0.02 | 100.90 | 0.04 | 10.33 | 5.01 | 0.59 | 1.80 | 0.01 | 6.19 | 0.01 | 0.00 | 15.97 | 8.03 | 32 | 22.54 | 32.64 |
| | 60% outward | 0.71 | 0.19 | 38.97 | 28.53 | 4.04 | 9.71 | 0.02 | 18.59 | 0.18 | 0.05 | 100.29 | 0.03 | 10.21 | 5.02 | 0.72 | 1.81 | 0.00 | 6.16 | 0.03 | 0.01 | 15.98 | 8.02 | 32 | 22.67 | 32.93 |
| **D20-15-sp1** | euh. within glass | 0.71 | 0.49 | 37.35 | 28.75 | 4.38 | 10.13 | 0.03 | 18.14 | 0.09 | 0.14 | 99.50 | 0.08 | 9.93 | 5.13 | 0.79 | 1.91 | 0.01 | 6.10 | 0.02 | 0.03 | 15.93 | 8.06 | 32 | 23.86 | 34.05 |
| **D20-30-sp1** | euh. within oliv. | 0.71 | 0.22 | 40.56 | 27.02 | 3.54 | 9.75 | 0.15 | 18.60 | 0.19 | 0.08 | 100.10 | 0.04 | 10.58 | 4.73 | 0.63 | 1.80 | 0.03 | 6.14 | 0.03 | 0.02 | 15.97 | 8.02 | 32 | 22.73 | 30.88 |
| **D20-30-sp2** | euh. within glass | 0.71 | 0.31 | 38.83 | 28.52 | 4.48 | 10.23 | 0.10 | 18.27 | 0.15 | 0.29 | 101.18 | 0.05 | 10.13 | 4.99 | 0.79 | 1.89 | 0.02 | 6.03 | 0.03 | 0.07 | 15.96 | 8.03 | 32 | 23.91 | 33.01 |
| **D20-30-sp3** | euh. within glass | 0.71 | 0.70 | 35.34 | 29.25 | 6.63 | 9.64 | 0.15 | 18.46 | 0.10 | 0.14 | 100.41 | 0.12 | 9.38 | 5.21 | 1.20 | 1.82 | 0.03 | 6.20 | 0.02 | 0.03 | 15.90 | 8.09 | 32 | 22.66 | 35.70 |
| **D20-30-sp1** | ctr.lg. euh. within glass | 0.71 | 0.14 | 43.50 | 24.87 | 2.81 | 9.61 | 0.04 | 19.16 | 0.10 | 0.02 | 100.25 | 0.02 | 11.18 | 4.29 | 0.49 | 1.75 | 0.01 | 6.23 | 0.02 | 0.00 | 15.98 | 8.01 | 32 | 21.96 | 27.72 |
| | 50% outward | 0.71 | 0.16 | 44.10 | 24.33 | 2.99 | 9.50 | 0.02 | 19.36 | 0.16 | 0.02 | 100.64 | 0.03 | 11.27 | 4.17 | 0.52 | 1.72 | 0.00 | 6.26 | 0.03 | 0.00 | 15.98 | 8.01 | 32 | 21.59 | 27.01 |
| | rim | 0.71 | 0.14 | 45.32 | 22.33 | 3.15 | 9.37 | 0.02 | 19.40 | 0.17 | 0.02 | 99.92 | 0.02 | 11.59 | 3.83 | 0.55 | 1.70 | 0.00 | 6.27 | 0.03 | 0.00 | 15.99 | 8.01 | 32 | 21.32 | 24.84 |
| **D20-30-sp2** | ctr.lg. euh. within glass | 0.71 | 0.22 | 36.22 | 32.35 | 2.92 | 10.21 | 0.02 | 18.07 | 0.07 | 0.01 | 100.09 | 0.04 | 9.63 | 5.77 | 0.53 | 1.93 | 0.00 | 6.08 | 0.01 | 0.00 | 15.97 | 8.03 | 32 | 24.08 | 37.47 |
| | near center | 0.71 | 0.21 | 37.20 | 31.05 | 2.88 | 10.02 | 0.04 | 18.20 | 0.05 | 0.01 | 99.67 | 0.04 | 9.88 | 5.53 | 0.52 | 1.89 | 0.01 | 6.11 | 0.01 | 0.00 | 15.97 | 8.02 | 32 | 23.61 | 35.89 |
| | 50% outward | 0.71 | 0.19 | 39.07 | 29.23 | 3.24 | 9.62 | 0.06 | 18.72 | 0.09 | 0.01 | 100.24 | 0.03 | 10.23 | 5.14 | 0.58 | 1.79 | 0.01 | 6.20 | 0.02 | 0.00 | 15.98 | 8.02 | 32 | 22.38 | 33.42 |
| | 75% outward | 0.71 | 0.12 | 43.01 | 25.62 | 3.07 | 9.43 | 0.03 | 19.33 | 0.09 | 0.01 | 100.72 | 0.02 | 11.03 | 4.41 | 0.54 | 1.72 | 0.01 | 6.27 | 0.02 | 0.00 | 15.99 | 8.01 | 32 | 21.50 | 28.55 |
| | rim | 0.71 | 0.18 | 44.36 | 23.42 | 3.28 | 9.44 | 0.03 | 19.33 | 0.19 | 0.02 | 100.25 | 0.03 | 11.36 | 4.02 | 0.57 | 1.71 | 0.01 | 6.26 | 0.03 | 0.00 | 15.98 | 8.02 | 32 | 21.50 | 26.15 |
| **D20-30-sp3** | ctr. subh. within oliv. | 0.71 | 0.18 | 42.96 | 25.53 | 2.35 | 10.04 | 0.02 | 18.81 | 0.11 | 0.02 | 100.02 | 0.03 | 11.11 | 4.43 | 0.41 | 1.84 | 0.00 | 6.15 | 0.02 | 0.00 | 15.98 | 8.02 | 32 | 23.05 | 28.50 |
| | 50% outward | 0.71 | 0.15 | 43.17 | 25.44 | 2.77 | 9.69 | 0.02 | 19.12 | 0.15 | 0.02 | 100.53 | 0.02 | 11.09 | 4.38 | 0.48 | 1.77 | 0.00 | 6.21 | 0.03 | 0.00 | 15.98 | 8.01 | 32 | 22.14 | 28.33 |
| | rim | 0.71 | 0.18 | 44.56 | 22.89 | 2.83 | 9.72 | 0.02 | 19.03 | 0.15 | 0.01 | 99.38 | 0.03 | 11.49 | 3.96 | 0.50 | 1.78 | 0.00 | 6.21 | 0.03 | 0.00 | 15.98 | 8.02 | 32 | 22.27 | 25.63 |
| **D20-30-sp4** | euh. within oliv. | 0.71 | 0.15 | 45.40 | 22.50 | 2.68 | 9.77 | 0.02 | 19.17 | 0.12 | 0.02 | 99.84 | 0.02 | 11.63 | 3.86 | 0.47 | 1.78 | 0.00 | 6.21 | 0.02 | 0.00 | 15.98 | 8.01 | 32 | 22.25 | 24.95 |
| **D20-30-sp5** | ctr. round in oliv. | 0.71 | 0.20 | 40.46 | 27.79 | 3.52 | 9.09 | 0.03 | 19.25 | 0.14 | 0.02 | 100.49 | 0.03 | 10.49 | 4.83 | 0.62 | 1.67 | 0.01 | 6.31 | 0.02 | 0.00 | 15.98 | 8.02 | 32 | 20.94 | 31.54 |
| | 50% outward | 0.71 | 0.20 | 39.99 | 28.30 | 3.44 | 9.15 | 0.02 | 19.18 | 0.10 | 0.01 | 100.38 | 0.03 | 10.40 | 4.94 | 0.61 | 1.69 | 0.00 | 6.31 | 0.02 | 0.00 | 15.98 | 8.02 | 32 | 21.11 | 32.19 |
| | rim | 0.71 | 0.24 | 39.95 | 28.17 | 3.13 | 9.49 | 0.02 | 18.88 | 0.14 | 0.01 | 100.03 | 0.04 | 10.44 | 4.94 | 0.56 | 1.76 | 0.00 | 6.24 | 0.02 | 0.00 | 15.97 | 8.03 | 32 | 22.00 | 32.11 |
| **D21-1-sp1** | ctr. lg. anhedra | 0.63 | 0.34 | 21.95 | 44.31 | 5.24 | 15.18 | 0.08 | 13.52 | 0.01 | 0.01 | 100.65 | 0.06 | 6.31 | 8.55 | 1.03 | 3.10 | 0.02 | 4.92 | 0.00 | 0.00 | 15.95 | 8.04 | 32 | 38.65 | 57.52 |

Table B-3. Continued.

| Sample # | Description | Mg* | $TiO_2$ | $Al_2O_3$ | $Cr_2O_3$ | $Fe_2O_3$ | FeO | MnO | MgO | NiO | CaO | Total | Ti | Al | Cr | $Fe^{3+}$ | $Fe^{2+}$ | Mn | Mg | Ni | Ca | TET | OCT | O | FE* | CR* |
|---|---|---|---|---|---|---|---|---|---|---|---|---|---|---|---|---|---|---|---|---|---|---|---|---|---|---|
| D21-1-sp1 | ctr. lg. anhedra | 0.63 | 0.34 | 21.95 | 44.31 | 5.24 | 15.18 | 0.08 | 13.52 | 0.01 | 0.01 | 100.65 | 0.06 | 6.31 | 8.55 | 1.03 | 3.10 | 0.02 | 4.92 | 0.00 | 0.00 | 15.95 | 8.04 | 32 | 38.65 | 57.52 |
| | 20% outward | 0.63 | 0.41 | 26.46 | 39.67 | 5.38 | 15.03 | 0.10 | 14.25 | 0.01 | 0.01 | 101.32 | 0.07 | 7.40 | 7.44 | 1.02 | 2.98 | 0.02 | 5.04 | 0.00 | 0.00 | 15.94 | 8.05 | 32 | 37.18 | 50.14 |
| | 40% outward | 0.63 | 0.50 | 37.72 | 27.25 | 5.29 | 14.39 | 0.11 | 15.72 | 0.12 | 0.08 | 101.18 | 0.08 | 10.03 | 4.86 | 0.96 | 2.72 | 0.02 | 5.29 | 0.02 | 0.02 | 15.93 | 8.06 | 32 | 33.93 | 32.64 |
| | 60% outward | 0.63 | 0.47 | 38.49 | 26.11 | 5.49 | 13.98 | 0.11 | 16.04 | 0.06 | 0.03 | 100.78 | 0.08 | 10.22 | 4.65 | 0.99 | 2.63 | 0.02 | 5.38 | 0.01 | 0.01 | 15.94 | 8.06 | 32 | 32.85 | 31.27 |
| | 80% outward | 0.63 | 0.47 | 37.47 | 26.59 | 5.79 | 13.90 | 0.06 | 15.92 | 0.02 | 0.05 | 100.27 | 0.08 | 10.03 | 4.77 | 1.05 | 2.64 | 0.01 | 5.39 | 0.00 | 0.01 | 15.94 | 8.06 | 32 | 32.88 | 32.25 |
| | rim | 0.63 | 0.58 | 35.95 | 28.45 | 4.60 | 14.94 | 0.09 | 14.99 | 0.01 | 0.10 | 99.71 | 0.10 | 9.77 | 5.19 | 0.85 | 2.88 | 0.02 | 5.15 | 0.00 | 0.02 | 15.91 | 8.08 | 32 | 35.87 | 34.68 |
| D21-1-sp2 | ctr lg. euh. att. oliv. | 0.63 | 0.94 | 30.78 | 32.06 | 6.59 | 14.77 | 0.08 | 14.81 | 0.06 | 0.15 | 100.24 | 0.17 | 8.51 | 5.94 | 1.24 | 2.90 | 0.02 | 5.18 | 0.01 | 0.04 | 15.85 | 8.14 | 32 | 35.88 | 41.13 |
| | 50% outward | 0.63 | 0.89 | 31.34 | 30.84 | 6.51 | 14.50 | 0.07 | 14.84 | 0.02 | 0.12 | 99.12 | 0.16 | 8.72 | 5.75 | 1.23 | 2.86 | 0.01 | 5.22 | 0.00 | 0.03 | 15.86 | 8.13 | 32 | 35.40 | 39.76 |
| | 75% outward | 0.63 | 0.85 | 32.97 | 29.98 | 6.67 | 14.65 | 0.06 | 15.17 | 0.05 | 0.11 | 100.51 | 0.15 | 9.00 | 5.49 | 1.24 | 2.84 | 0.01 | 5.24 | 0.01 | 0.03 | 15.87 | 8.12 | 32 | 35.14 | 37.89 |
| | rim | 0.63 | 0.74 | 33.71 | 29.50 | 6.19 | 14.48 | 0.07 | 15.21 | 0.01 | 0.11 | 100.02 | 0.13 | 9.21 | 5.40 | 1.15 | 2.81 | 0.01 | 5.25 | 0.00 | 0.03 | 15.89 | 8.10 | 32 | 34.82 | 36.99 |
| D22-2-sp1 | euh. att. oliv. | 0.69 | 0.46 | 32.70 | 33.29 | 4.77 | 11.88 | 0.10 | 16.62 | 0.11 | 0.03 | 99.96 | 0.08 | 8.90 | 6.08 | 0.88 | 2.29 | 0.02 | 5.72 | 0.02 | 0.01 | 15.93 | 8.06 | 32 | 28.63 | 40.58 |
| D22-2-sp2 | euh. att. oliv. | 0.69 | 0.60 | 31.46 | 33.48 | 5.30 | 11.56 | 0.11 | 16.64 | 0.02 | 0.08 | 99.25 | 0.11 | 8.64 | 6.17 | 0.99 | 2.25 | 0.02 | 5.78 | 0.00 | 0.02 | 15.91 | 8.08 | 32 | 28.05 | 41.65 |
| D22-3-sp1 | euh. att. oliv. | 0.69 | 0.53 | 31.80 | 32.98 | 5.65 | 11.64 | 0.01 | 16.61 | 0.01 | 0.18 | 99.41 | 0.09 | 8.71 | 6.06 | 1.05 | 2.26 | 0.00 | 5.76 | 0.00 | 0.04 | 15.92 | 8.07 | 32 | 28.22 | 41.03 |
| D22-3-sp2 | lg. round within glass | 0.69 | 0.18 | 27.40 | 41.40 | 3.61 | 10.02 | 0.02 | 17.25 | 0.01 | 0.02 | 99.91 | 0.03 | 7.58 | 7.68 | 0.68 | 1.97 | 0.00 | 6.04 | 0.00 | 0.01 | 15.98 | 8.02 | 32 | 24.59 | 50.34 |
| | 25% outward | 0.69 | 0.24 | 26.82 | 42.38 | 3.46 | 10.16 | 0.02 | 17.20 | 0.07 | 0.01 | 100.37 | 0.04 | 7.41 | 7.86 | 0.65 | 1.99 | 0.00 | 6.01 | 0.01 | 0.00 | 15.97 | 8.03 | 32 | 24.90 | 51.46 |
| | 40% outward | 0.69 | 0.22 | 26.99 | 42.02 | 3.21 | 10.26 | 0.03 | 17.03 | 0.06 | 0.01 | 99.83 | 0.04 | 7.50 | 7.83 | 0.61 | 2.02 | 0.01 | 5.98 | 0.01 | 0.00 | 15.97 | 8.03 | 32 | 25.27 | 51.08 |
| | 50% outward | 0.69 | 0.22 | 28.64 | 40.29 | 3.10 | 10.27 | 0.03 | 17.18 | 0.09 | 0.01 | 99.83 | 0.04 | 7.90 | 7.45 | 0.58 | 2.01 | 0.01 | 5.99 | 0.02 | 0.00 | 15.97 | 8.03 | 32 | 25.11 | 48.55 |
| | 75% outward | 0.69 | 0.20 | 32.73 | 36.19 | 3.24 | 10.13 | 0.04 | 17.80 | 0.08 | 0.01 | 100.43 | 0.03 | 8.81 | 6.54 | 0.59 | 1.94 | 0.01 | 6.06 | 0.01 | 0.00 | 15.97 | 8.02 | 32 | 24.21 | 42.58 |
| | 90% outward | 0.69 | 0.22 | 36.10 | 32.55 | 3.26 | 10.44 | 0.05 | 18.00 | 0.09 | 0.02 | 100.74 | 0.04 | 9.56 | 5.78 | 0.59 | 1.96 | 0.01 | 6.03 | 0.02 | 0.00 | 15.97 | 8.02 | 32 | 24.56 | 37.69 |
| | rim | 0.69 | 0.24 | 36.94 | 30.81 | 3.31 | 11.05 | 0.02 | 17.57 | 0.10 | 0.02 | 100.06 | 0.04 | 9.83 | 5.50 | 0.60 | 2.09 | 0.00 | 5.91 | 0.02 | 0.00 | 15.97 | 8.03 | 32 | 26.09 | 35.88 |
| D22-3-sp3 | ctr. lg anh. in glass | 0.69 | 0.19 | 38.03 | 31.30 | 2.91 | 10.34 | 0.01 | 18.39 | 0.11 | 0.01 | 101.29 | 0.03 | 9.94 | 5.49 | 0.52 | 1.92 | 0.00 | 6.08 | 0.02 | 0.00 | 15.98 | 8.02 | 32 | 23.98 | 35.57 |
| | 30% outward | 0.69 | 0.23 | 35.46 | 33.91 | 3.14 | 9.74 | 0.02 | 18.47 | 0.14 | 0.02 | 101.12 | 0.04 | 9.36 | 6.01 | 0.56 | 1.82 | 0.00 | 6.17 | 0.03 | 0.00 | 15.97 | 8.03 | 32 | 22.83 | 39.08 |
| | 60% outward | 0.69 | 0.22 | 34.32 | 34.62 | 3.34 | 9.73 | 0.01 | 18.25 | 0.16 | 0.02 | 100.68 | 0.04 | 9.14 | 6.19 | 0.61 | 1.84 | 0.00 | 6.15 | 0.03 | 0.00 | 15.97 | 8.02 | 32 | 23.03 | 40.36 |
| | 90% outward | 0.69 | 0.20 | 37.78 | 30.75 | 3.34 | 10.61 | 0.02 | 18.09 | 0.12 | 0.02 | 100.93 | 0.03 | 9.93 | 5.42 | 0.60 | 1.98 | 0.00 | 6.01 | 0.02 | 0.00 | 15.98 | 8.02 | 32 | 24.77 | 35.32 |
| | rim | 0.69 | 0.26 | 36.52 | 31.18 | 4.06 | 11.22 | 0.03 | 17.62 | 0.09 | 0.02 | 101.00 | 0.04 | 9.66 | 5.53 | 0.73 | 2.11 | 0.01 | 5.89 | 0.02 | 0.00 | 15.97 | 8.03 | 32 | 26.32 | 36.42 |
| D22-3-sp4 | ctr lg. round in glass | 0.69 | 0.25 | 27.52 | 42.52 | 3.14 | 9.82 | 0.03 | 17.63 | 0.06 | 0.02 | 100.98 | 0.04 | 7.53 | 7.81 | 0.58 | 1.91 | 0.01 | 6.10 | 0.01 | 0.00 | 15.97 | 8.03 | 32 | 23.80 | 50.89 |
| | 15% outward | 0.69 | 0.25 | 27.63 | 42.35 | 3.38 | 9.78 | 0.04 | 17.69 | 0.09 | 0.02 | 101.23 | 0.04 | 7.54 | 7.75 | 0.63 | 1.89 | 0.01 | 6.11 | 0.02 | 0.00 | 15.97 | 8.03 | 32 | 23.67 | 50.69 |
| | 30% outward | 0.69 | 0.23 | 28.48 | 41.23 | 3.32 | 9.87 | 0.03 | 17.66 | 0.06 | 0.02 | 100.90 | 0.04 | 7.77 | 7.54 | 0.62 | 1.91 | 0.01 | 6.09 | 0.01 | 0.00 | 15.97 | 8.03 | 32 | 23.88 | 49.27 |
| | 45% outward | 0.69 | 0.26 | 31.69 | 37.91 | 3.16 | 10.29 | 0.04 | 17.76 | 0.11 | 0.04 | 101.26 | 0.04 | 8.51 | 6.83 | 0.58 | 1.96 | 0.01 | 6.03 | 0.02 | 0.01 | 15.96 | 8.03 | 32 | 24.53 | 44.52 |
| | 60% outward | 0.69 | 0.21 | 36.54 | 31.78 | 3.93 | 10.50 | 0.05 | 18.05 | 0.13 | 0.05 | 101.24 | 0.04 | 9.62 | 5.61 | 0.70 | 1.96 | 0.01 | 6.01 | 0.02 | 0.01 | 15.98 | 8.02 | 32 | 24.62 | 36.85 |
| | 75% outward | 0.69 | 0.20 | 36.65 | 32.51 | 3.20 | 9.83 | 0.04 | 18.48 | 0.15 | 0.03 | 101.09 | 0.03 | 9.64 | 5.73 | 0.57 | 1.83 | 0.01 | 6.14 | 0.03 | 0.01 | 15.98 | 8.02 | 32 | 22.99 | 37.30 |

Table B-3. Continued.

| Sample # | Description | Mg* | $TiO_2$ | $Al_2O_3$ | $Cr_2O_3$ | $Fe_2O_3$ | FeO | MnO | MgO | NiO | CaO | Total | Ti | Al | Cr | $Fe^{3+}$ | $Fe^{2+}$ | Mn | Mg | Ni | Ca | TET | OCT | O | FE* | CR* |
|---|---|---|---|---|---|---|---|---|---|---|---|---|---|---|---|---|---|---|---|---|---|---|---|---|---|---|
| | 90% outward | 0.69 | 0.23 | 36.41 | 32.82 | 2.98 | 9.77 | 0.04 | 18.43 | 0.19 | 0.06 | 100.93 | 0.04 | 9.60 | 5.80 | 0.53 | 1.83 | 0.01 | 6.14 | 0.03 | 0.01 | 15.97 | 8.03 | 32 | 22.93 | 37.68 |
| | rim | 0.69 | 0.28 | 36.45 | 30.67 | 4.10 | 11.23 | 0.05 | 17.46 | 0.09 | 0.03 | 100.36 | 0.05 | 9.70 | 5.47 | 0.74 | 2.12 | 0.01 | 5.88 | 0.02 | 0.01 | 15.96 | 8.03 | 32 | 26.52 | 36.08 |
| **D22-3-sp5** | sm. round in oliv. | 0.69 | 0.57 | 37.35 | 28.01 | 5.17 | 11.04 | 0.04 | 17.78 | 0.12 | 0.02 | 100.10 | 0.10 | 9.91 | 4.98 | 0.93 | 2.08 | 0.01 | 5.96 | 0.02 | 0.00 | 15.92 | 8.08 | 32 | 25.83 | 33.47 |
| **D22-3-sp6** | euh. within glass | 0.69 | 0.51 | 32.26 | 32.97 | 5.25 | 11.71 | 0.03 | 16.70 | 0.08 | 0.01 | 99.52 | 0.09 | 8.82 | 6.04 | 0.98 | 2.27 | 0.01 | 5.77 | 0.01 | 0.00 | 15.93 | 8.07 | 32 | 28.23 | 40.67 |
| **D27-5-sp1** | ctr euh. att. to olivine | 0.69 | 0.68 | 31.93 | 33.18 | 5.47 | 12.22 | 0.21 | 16.45 | 0.01 | 0.08 | 100.24 | 0.12 | 8.70 | 6.06 | 1.01 | 2.36 | 0.04 | 5.67 | 0.00 | 0.02 | 15.90 | 8.09 | 32 | 29.43 | 41.07 |
| | 50% outward | 0.69 | 0.54 | 31.83 | 33.40 | 5.36 | 12.16 | 0.18 | 16.32 | 0.07 | 0.08 | 99.94 | 0.09 | 8.70 | 6.13 | 1.00 | 2.36 | 0.04 | 5.64 | 0.01 | 0.02 | 15.92 | 8.07 | 32 | 29.48 | 41.31 |
| | rim | 0.69 | 0.57 | 31.68 | 32.40 | 6.25 | 11.26 | 0.20 | 16.75 | 0.05 | 0.09 | 99.25 | 0.10 | 8.69 | 5.96 | 1.17 | 2.19 | 0.04 | 5.81 | 0.01 | 0.02 | 15.92 | 8.07 | 32 | 27.38 | 40.69 |
| **D27-5-sp2** | euh. within sm. oliv. | 0.69 | 0.49 | 31.29 | 34.05 | 5.33 | 11.87 | 0.18 | 16.45 | 0.02 | 0.02 | 99.70 | 0.09 | 8.58 | 6.27 | 0.99 | 2.31 | 0.04 | 5.71 | 0.00 | 0.00 | 15.93 | 8.06 | 32 | 28.83 | 42.20 |
| **D27-5 -sp3** | euh. within sm. oliv. | 0.69 | 0.54 | 30.17 | 32.33 | 7.07 | 10.22 | 0.18 | 16.92 | 0.10 | 0.03 | 97.56 | 0.10 | 8.43 | 6.06 | 1.34 | 2.03 | 0.04 | 5.98 | 0.02 | 0.01 | 15.92 | 8.07 | 32 | 25.31 | 41.82 |
| **D27-5-sp4** | ctr euh att. oliv. | 0.69 | 0.58 | 31.05 | 33.48 | 5.62 | 11.54 | 0.19 | 16.42 | 0.02 | 0.20 | 99.10 | 0.10 | 8.56 | 6.19 | 1.05 | 2.26 | 0.04 | 5.73 | 0.00 | 0.05 | 15.91 | 8.08 | 32 | 28.29 | 41.97 |
| **D27-5-sp5** | ctr euh.att. oliv. | 0.69 | 0.52 | 31.27 | 34.11 | 5.33 | 12.23 | 0.20 | 16.17 | 0.10 | 0.11 | 100.03 | 0.09 | 8.57 | 6.27 | 0.99 | 2.38 | 0.04 | 5.60 | 0.02 | 0.03 | 15.92 | 8.07 | 32 | 29.79 | 42.25 |
| **D27-5-sp6** | ctr euh. att. oliv. | 0.69 | 0.53 | 30.87 | 32.97 | 5.97 | 11.79 | 0.15 | 16.16 | 0.05 | 0.14 | 98.63 | 0.09 | 8.57 | 6.14 | 1.13 | 2.32 | 0.03 | 5.67 | 0.01 | 0.04 | 15.92 | 8.07 | 32 | 29.05 | 41.74 |
| **D27-5-sp7** | ctr med. att. oliv. | 0.69 | 0.57 | 31.26 | 33.23 | 5.94 | 11.59 | 0.14 | 16.55 | 0.09 | 0.09 | 99.47 | 0.10 | 8.59 | 6.12 | 1.11 | 2.26 | 0.03 | 5.75 | 0.02 | 0.02 | 15.92 | 8.07 | 32 | 28.21 | 41.63 |
| | rim | 0.69 | 0.56 | 31.57 | 32.57 | 6.17 | 11.34 | 0.13 | 16.60 | 0.05 | 0.25 | 99.24 | 0.10 | 8.67 | 6.00 | 1.15 | 2.21 | 0.03 | 5.76 | 0.01 | 0.06 | 15.92 | 8.07 | 32 | 27.71 | 40.90 |
| **D27-5-sp8** | ctr. euh. in glass | 0.69 | 0.52 | 30.99 | 33.52 | 5.82 | 11.50 | 0.11 | 16.41 | 0.10 | 0.22 | 99.18 | 0.09 | 8.54 | 6.20 | 1.09 | 2.25 | 0.02 | 5.72 | 0.02 | 0.06 | 15.93 | 8.07 | 32 | 28.22 | 42.05 |
| **D27-5-sp9** | euh. within oliv. | 0.69 | 0.50 | 31.00 | 33.17 | 5.63 | 11.69 | 0.10 | 16.32 | 0.05 | 0.02 | 98.48 | 0.09 | 8.60 | 6.17 | 1.06 | 2.30 | 0.02 | 5.73 | 0.01 | 0.01 | 15.93 | 8.06 | 32 | 28.67 | 41.78 |
| **2384-9-sp1** | euh. att. oliv. | 0.71 | 0.30 | 43.45 | 22.40 | 4.27 | 10.13 | 0.10 | 18.63 | 0.16 | 0.06 | 99.50 | 0.05 | 11.26 | 3.90 | 0.75 | 1.86 | 0.02 | 6.11 | 0.03 | 0.01 | 15.96 | 8.03 | 32 | 23.37 | 25.70 |
| **2384-9-sp2** | euh. att. oliv. | 0.71 | 0.40 | 35.34 | 30.64 | 5.11 | 10.55 | 0.04 | 17.72 | 0.12 | 0.09 | 100.01 | 0.07 | 9.45 | 5.50 | 0.93 | 2.00 | 0.01 | 5.99 | 0.02 | 0.02 | 15.95 | 8.05 | 32 | 25.04 | 36.77 |
| **2384-9-sp3** | euh. att. oliv. | 0.71 | 0.97 | 35.44 | 29.56 | 5.02 | 10.82 | 0.05 | 17.80 | 0.19 | 0.13 | 99.98 | 0.17 | 9.47 | 5.30 | 0.91 | 2.05 | 0.01 | 6.02 | 0.03 | 0.03 | 15.85 | 8.14 | 32 | 25.44 | 35.88 |
| **2384-9-sp4** | euh. att. oliv. | 0.71 | 0.40 | 35.24 | 30.40 | 5.24 | 10.21 | 0.08 | 17.81 | 0.12 | 0.10 | 99.61 | 0.07 | 9.45 | 5.47 | 0.96 | 1.94 | 0.02 | 6.04 | 0.02 | 0.02 | 15.95 | 8.05 | 32 | 24.34 | 36.66 |
| **2384-1-sp1** | euh. att. oliv. | 0.71 | 0.25 | 37.60 | 28.65 | 4.49 | 9.70 | 0.09 | 18.25 | 0.17 | 0.02 | 99.22 | 0.04 | 10.00 | 5.11 | 0.81 | 1.83 | 0.02 | 6.14 | 0.03 | 0.00 | 15.97 | 8.02 | 32 | 22.97 | 33.82 |
| **2384-1-sp2** | ctr. euh. att. oliv. | 0.71 | 0.31 | 38.55 | 27.87 | 4.53 | 9.70 | 0.12 | 18.54 | 0.03 | 0.03 | 99.67 | 0.05 | 10.17 | 4.93 | 0.81 | 1.81 | 0.02 | 6.18 | 0.01 | 0.01 | 15.96 | 8.03 | 32 | 22.69 | 32.66 |
| | rim | 0.71 | 0.30 | 38.48 | 27.74 | 4.43 | 9.92 | 0.08 | 18.31 | 0.09 | 0.03 | 99.37 | 0.05 | 10.19 | 4.93 | 0.80 | 1.86 | 0.02 | 6.13 | 0.02 | 0.01 | 15.96 | 8.03 | 32 | 23.31 | 32.59 |

Table B-3. Continued.

| Sample # | Description | Mg* | $TiO_2$ | $Al_2O_3$ | $Cr_2O_3$ | $Fe_2O_3$ | FeO | MnO | MgO | NiO | CaO | Total | Ti | Al | Cr | $Fe^{3+}$ | $Fe^{2+}$ | Mn | Mg | Ni | Ca | TET | OCT | O | FE* | CR* |
|---|---|---|---|---|---|---|---|---|---|---|---|---|---|---|---|---|---|---|---|---|---|---|---|---|---|---|
| 2384-11-sp1 | euh. within glass | 0.67 | 0.98 | 27.29 | 36.29 | 6.35 | 13.33 | 0.08 | 15.39 | 0.02 | 0.11 | 99.85 | 0.18 | 7.64 | 6.82 | 1.21 | 2.65 | 0.02 | 5.45 | 0.00 | 0.03 | 15.84 | 8.15 | 32 | 32.71 | 47.15 |
| | 50% outward | 0.67 | 0.83 | 28.02 | 35.34 | 6.43 | 13.10 | 0.06 | 15.42 | 0.01 | 0.14 | 99.34 | 0.15 | 7.85 | 6.64 | 1.23 | 2.61 | 0.01 | 5.47 | 0.00 | 0.04 | 15.87 | 8.12 | 32 | 32.28 | 45.83 |
| | rim | 0.67 | 0.72 | 28.81 | 34.75 | 5.76 | 13.28 | 0.03 | 15.17 | 0.02 | 0.19 | 98.73 | 0.13 | 8.10 | 6.56 | 1.10 | 2.65 | 0.01 | 5.40 | 0.00 | 0.05 | 15.89 | 8.10 | 32 | 32.94 | 44.72 |
| 2384-4a-sp1 | in oliv. | 0.61 | 0.77 | 21.938 | 40.01 | 2.1894 | 17.7 | 0.33 | 14.3 | 0 | 0 | 97.12 | 0.15 | 6.552 | 8.019 | 0.42 | 3.76 | 0.1 | 5.4 | 0 | 0 | 15.14 | 9.22 | 32 | 41.12 | 55.03 |
| 2384-4a-sp2 | in oliv. | 0.61 | 0.685 | 21.424 | 39.995 | 2.199 | 17.8 | 0.21 | 14 | 0 | 0 | 96.17 | 0.13 | 6.472 | 8.109 | 0.42 | 3.82 | 0 | 5.4 | 0 | 0 | 15.14 | 9.23 | 32 | 41.65 | 55.61 |
| 2384-4a-sp3 | in oliv. | 0.61 | 0.69 | 21.395 | 40.153 | 2.2297 | 18.1 | 0.19 | 13.9 | 0 | 0 | 96.51 | 0.13 | 6.449 | 8.122 | 0.43 | 3.87 | 0 | 5.3 | 0 | 0.01 | 15.13 | 9.23 | 32 | 42.11 | 55.74 |
| 2384-4a-sp4 | in oliv. Clot | 0.61 | 0.513 | 33.341 | 30.581 | 2.0761 | 16.8 | 0.27 | 15.7 | 0 | 0 | 99.17 | 0.09 | 9.24 | 5.687 | 0.37 | 3.31 | 0.1 | 5.5 | 0 | 0.01 | 15.39 | 8.88 | 32 | 37.55 | 38.10 |

Notes: Notes: * Mg = 100 * Mg/(Mg + $Fe^{2+}$) of the host glass. Oxides expressed in wt. %. FE* = $Fe^{2+}$/($Fe^{2+}$ + Mg). CR* = Cr/(Cr + Al).

# APPENDIX C
# MAJOR ELEMENT COMPOSITIONS OF THE SIQUEIROS SAMPLES

Table C-1. ARL, JEOL, and DCP electron microprobe major element analyses of basalts from the Siqueiros transform.

| Sample | Location | Depth (m) | $SiO_2$ | $TiO_2$ | $Al_2O_3$ | FeO | $Fe_2O_3$ | MnO | MgO | CaO | $Na_2O$ | K2O | $P_2O_5$ | Total | Mg# | $Na_{8.0}$ | $Fe_{8.0}$ |
|---|---|---|---|---|---|---|---|---|---|---|---|---|---|---|---|---|---|
| **Weight percent by microprobe*** | | | | | | | | | | | | | | | | | |
| 2375-1 | B | ND | 50.23 | 1.47 | 15.01 | 8.97 | 1.11 | 0.17 | 7.93 | 12.13 | 2.53 | 0.08 | 0.11 | 99.46 | 61.14 | 2.51 | 9.88 |
| 2375-2 | B | ND | 50.78 | 1.76 | 14.01 | 10.07 | 1.24 | 0.2 | 7.13 | 11.76 | 2.67 | 0.1 | 0.14 | 99.54 | 55.75 | 2.47 | 10.06 |
| 2375-4 | B | 2992 | 51.03 | 1.63 | 14.26 | 9.37 | 1.16 | 0.18 | 7.56 | 11.86 | 2.57 | 0.1 | 0.13 | 99.55 | 58.97 | 2.48 | 9.86 |
| 2375-6 | B | 2985 | 50.25 | 1.41 | 15.08 | 8.92 | 1.10 | 0.18 | 8.09 | 12.04 | 2.45 | 0.08 | 0.14 | 99.46 | 61.76 | 2.47 | 10.02 |
| 2375-7 | B | 2968 | 50.29 | 1.41 | 15.57 | 8.76 | 1.08 | 0.2 | 8.03 | 12.12 | 2.62 | 0.07 | 0.1 | 100.08 | 62.01 | 2.62 | 9.77 |
| 2375-9 | B | 2955 | 50.7 | 1.53 | 15.1 | 9.01 | 1.11 | 0.19 | 7.61 | 11.82 | 2.72 | 0.11 | 0.13 | 99.86 | 60.06 | 2.65 | 9.53 |
| 2376-1 | B | 3073 | 50.03 | 1.42 | 15.59 | 8.50 | 1.05 | 0.15 | 8.53 | 11.88 | 2.37 | 0.11 | 0.12 | 99.48 | 64.13 | 2.45 | 10.03 |
| 2376-2 | B | ND | 50.59 | 1.63 | 14.74 | 9.14 | 1.13 | 0.18 | 7.83 | 11.81 | 2.38 | 0.13 | 0.19 | 99.46 | 60.4 | 2.35 | 9.96 |
| 2376-3 | B | 2023 | 50.12 | 1.5 | 15.48 | 8.76 | 1.08 | 0.16 | 7.85 | 11.88 | 2.6 | 0.13 | 0.15 | 99.55 | 61.48 | 2.57 | 9.55 |
| 2376-4 | B | 3015 | 50.23 | 1.44 | 15.48 | 8.45 | 1.04 | 0.16 | 8.4 | 11.91 | 2.42 | 0.11 | 0.13 | 99.53 | 63.9 | 2.49 | 9.85 |
| 2376-7 | B | 3092 | 49.83 | 1.39 | 15.97 | 8.21 | 1.01 | 0.2 | 8.4 | 11.6 | 2.58 | 0.11 | 0.12 | 99.27 | 64.56 | 2.64 | 9.58 |
| 2376-8 | B | 3037 | 49.56 | 1.7 | 15.93 | 9.16 | 1.13 | 0.19 | 8.02 | 11.27 | 2.69 | 0.1 | 0.17 | 99.76 | 60.91 | 2.7 | 10.2 |
| 2376-12 | B | ND | 49.89 | 1.41 | 15.43 | 8.72 | 1.08 | 0.19 | 8.35 | 12.15 | 2.43 | 0.11 | 0.13 | 99.6 | 63.02 | 2.49 | 10.08 |
| 2377-1 | B | 31701 | 50.09 | 1.31 | 15.69 | 8.60 | 1.06 | 0.2 | 8.35 | 12.2 | 2.46 | 0.08 | 0.1 | 99.99 | 63.36 | 2.52 | 9.95 |
| 2377-2 | B | 3119 | 50.25 | 1.81 | 14.82 | 9.53 | 1.18 | 0.19 | 7.55 | 11.42 | 2.81 | 0.12 | 0.19 | 99.54 | 58.51 | 2.72 | 10.03 |
| 2377-3 | B | 3083 | 50.01 | 1.67 | 15.37 | 9.06 | 1.12 | 0.2 | 7.72 | 11.52 | 2.69 | 0.09 | 0.15 | 99.44 | 60.26 | 2.64 | 9.73 |
| 2377-4 | B | 3028 | 49.84 | 1.9 | 15.34 | 9.46 | 1.17 | 0.19 | 7.63 | 11.1 | 2.76 | 0.11 | 0.18 | 99.51 | 58.95 | 2.68 | 10.06 |
| 2377-5 | B | 3090 | 50.28 | 2.06 | 14.71 | 10.02 | 1.24 | 0.2 | 7.18 | 10.76 | 2.97 | 0.16 | 0.25 | 99.5 | 56.08 | 2.79 | 10.08 |
| 2377-6 | B | 3011 | 50.55 | 2.16 | 14.09 | 10.11 | 1.25 | 0.18 | 6.99 | 11.27 | 2.81 | 0.15 | 0.21 | 99.46 | 55.16 | 2.57 | 9.91 |
| 2377-7 | B | 3051 | 49.85 | 1.77 | 15.19 | 9.32 | 1.15 | 0.18 | 8.03 | 11.43 | 2.66 | 0.13 | 0.19 | 99.6 | 60.53 | 2.67 | 10.4 |
| 2377-8 | B | 3087 | 49.95 | 1.7 | 15.15 | 9.23 | 1.14 | 0.17 | 8.02 | 11.53 | 2.61 | 0.12 | 0.17 | 99.5 | 60.75 | 2.61 | 10.28 |
| 2377-10 | B | 3085 | 50.14 | 1.95 | 15.02 | 9.69 | 1.20 | 0.19 | 7.51 | 10.96 | 2.68 | 0.15 | 0.21 | 99.39 | 57.99 | 2.58 | 10.16 |
| 2377-11 | B | 3033 | 49.93 | 2.15 | 14.83 | 10.18 | 1.26 | 0.23 | 7.14 | 10.79 | 2.76 | 0.14 | 0.25 | 99.48 | 55.53 | 2.56 | 10.2 |
| 2378-1 | C | 2303 | 50.73 | 1.58 | 14.13 | 9.78 | 1.21 | 0.19 | 7.32 | 11.92 | 2.8 | 0.09 | 0.13 | 99.58 | 57.12 | 2.66 | 10.01 |
| 2378-2 | C | 2223 | 50.19 | 1.35 | 15.62 | 8.53 | 1.05 | 0.19 | 8.43 | 12.17 | 2.48 | 0.1 | 0.11 | 100.08 | 63.76 | 2.55 | 9.97 |
| 2378-3 | C | 2234 | 50.56 | 1.33 | 14.69 | 8.92 | 1.10 | 0.17 | 8 | 12.22 | 2.63 | 0.08 | 0.1 | 99.52 | 61.51 | 2.63 | 9.91 |
| 2378-5 | C | 2246 | 50.55 | 1.33 | 14.59 | 8.93 | 1.10 | 0.18 | 8 | 12.34 | 2.64 | 0.08 | 0.11 | 99.58 | 61.48 | 2.64 | 9.92 |
| 2378-7 | C | 2270 | 50.65 | 1.39 | 14.79 | 9.14 | 1.13 | 0.2 | 7.76 | 12 | 2.67 | 0.07 | 0.11 | 99.75 | 60.17 | 2.63 | 9.87 |
| 2378-8 | C | 2287 | 50.43 | 1.13 | 15.06 | 7.93 | 0.98 | 0.14 | 8.28 | 12.97 | 2.66 | 0.04 | 0.08 | 99.45 | 65.03 | 2.7 | 9.14 |

Table C-1. Continued.

| Sample | Location[u] | Depth (m) | $SiO_2$ | $TiO_2$ | $Al_2O_3$ | FeO | $Fe_2O_3$ | MnO | MgO | CaO | $Na_2O$ | K2O | $P_2O_5$ | Total | Mg# | $Na_{8.0}$ | $Fe_{8.0}$ |
|---|---|---|---|---|---|---|---|---|---|---|---|---|---|---|---|---|---|
| **Weight percent by microprobe*** | | | | | | | | | | | | | | | | | |
| 2380-4 | B | 3178 | 50.76 | 1.72 | 14.82 | 9.32 | 1.15 | 0.22 | 7.56 | 11.39 | 2.44 | 0.12 | 0.16 | 99.5 | 59.08 | 2.35 | 9.82 |
| 2380-11 | B | 3079 | 49.84 | 1.97 | 15.14 | 9.90 | 1.22 | 0.25 | 7.45 | 10.9 | 2.66 | 0.13 | 0.22 | 99.5 | 57.26 | 2.55 | 10.31 |
| 2381-11 | B-C | 2686 | 50.57 | 1.19 | 15.06 | 8.93 | 1.10 | 0.23 | 7.76 | 12.33 | 2.64 | 0.03 | 0.07 | 99.75 | 60.74 | 2.59 | 9.63 |
| 2381-11WR | B-C | 2686 | 50.57 | 1.19 | 15.06 | 8.93 | 1.10 | 0.23 | 7.76 | 12.33 | 2.64 | 0.03 | 0.07 | 99.75 | 60.74 | 2.59 | 9.63 |
| 2381-14A | B-C | 2485 | 50.41 | 1.07 | 15.5 | 7.95 | 0.98 | 0.26 | 8.43 | 12.66 | 2.54 | 0.03 | 0.07 | 99.76 | 65.38 | 2.61 | 9.32 |
| 2382-7 | B | 2474 | 50.55 | 1.7 | 14.53 | 9.63 | 1.19 | 0.21 | 7.39 | 11.54 | 2.76 | 0.11 | 0.18 | 99.61 | 57.74 | 2.63 | 9.93 |
| 2383-2 | A | 3735 | 51.04 | 1.49 | 14.41 | 9.37 | 1.16 | 0.24 | 7.52 | 11.74 | 2.6 | 0.08 | 0.14 | 99.64 | 58.83 | 2.5 | 9.81 |
| 2383-6 | A | 3661 | 50.54 | 1.1 | 15.34 | 8.04 | 0.99 | 0.18 | 8.89 | 12.54 | 2.2 | 0.03 | 0.08 | 99.83 | 66.32 | 2.32 | 9.89 |
| 2384-1 | A-B | 3884 | 48.88 | 0.92 | 17.5 | 6.99 | 0.86 | 0.16 | 9.6 | 12.22 | 2.4 | ND | 0.06 | 99.46 | 70.96 | 2.55 | 9.37 |
| 2384-2 | A-B | 3841 | 49.12 | 0.96 | 17.38 | 7.25 | 0.89 | 0.16 | 9.54 | 12.17 | 2.4 | ND | 0.04 | 99.78 | 70.1 | 2.55 | 9.6 |
| 2384-3 | A-B | 3751 | 48.95 | 0.95 | 17.35 | 7.18 | 0.89 | 0.17 | 10.12 | 12.09 | 2.33 | ND | 0.06 | 99.97 | 71.5 | 2.48 | 9.97 |
| 2384-6 | A-B | 3707 | 49.2 | 0.95 | 17.14 | 7.43 | 0.92 | 0.16 | 9.57 | 12.38 | 2.47 | ND | 0.05 | 99.98 | 69.62 | 2.63 | 9.84 |
| 2384-7A | A-B | 3646 | 49.58 | 0.88 | 17.86 | 6.99 | 0.86 | 0.14 | 9.9 | 12.23 | 2.4 | ND | 0.03 | 100.59 | 71.59 | 2.55 | 9.6 |
| 2384-7B | A-B | 3646 | 49.1 | 0.9 | 17.69 | 7.00 | 0.86 | 0.12 | 9.93 | 12.23 | 2.43 | ND | 0.06 | 100.04 | 71.63 | 2.59 | 9.64 |
| 2384-8 | A-B | 3648 | 49.78 | 1.02 | 17.2 | 7.34 | 0.90 | 0.1 | 9.85 | 11.93 | 2.51 | ND | 0.06 | 100.38 | 70.51 | 2.66 | 9.95 |
| 2384-9 | A-B | 3623 | 49.02 | 1.01 | 17.07 | 7.25 | 0.89 | 0.16 | 9.73 | 11.86 | 2.45 | 0.01 | 0.07 | 99.4 | 70.48 | 2.61 | 9.76 |
| 2384-10 | A-B | 3593 | 49.69 | 1.13 | 16.89 | 7.40 | 0.91 | 0.14 | 9.59 | 11.87 | 2.52 | ND | 0.06 | 99.9 | 69.77 | 2.67 | 9.81 |
| 2384-11 | A-B | 3558 | 49.7 | 1.17 | 16.16 | 7.83 | 0.97 | 0.12 | 8.79 | 11.83 | 2.47 | ND | 0.08 | 99.99 | 66.65 | 2.58 | 9.56 |
| 2384-12 | A-B | 3525 | 49.82 | 1.18 | 16.89 | 7.53 | 0.93 | 0.18 | 9.11 | 11.96 | 2.68 | ND | 0.07 | 100.04 | 68.28 | 2.82 | 9.54 |
| 2385-2 | C | 2352 | 50.29 | 1.12 | 15.06 | 8.23 | 1.01 | 0.2 | 8.21 | 12.34 | 2.65 | 0.01 | 0.06 | 99.02 | 63.99 | 2.69 | 9.38 |
| 2385-3A | C | 2333 | 50.43 | 1.36 | 14.97 | 8.46 | 1.04 | 0.22 | 7.8 | 11.95 | 2.79 | 0.04 | 0.1 | 98.98 | 62.14 | 2.75 | 9.16 |
| 2385-6T | C | 2347 | 50.86 | 1.2 | 14.95 | 8.67 | 1.07 | 0.2 | 7.91 | 11.91 | 2.72 | 0.03 | 0.1 | 99.45 | 61.9 | 2.71 | 9.52 |
| 2386-5 | D | 2176 | 50.76 | 1.09 | 15.18 | 8.41 | 1.04 | 0.2 | 8.23 | 12.52 | 2.44 | 0.02 | 0.09 | 99.81 | 63.54 | 2.48 | 9.61 |
| 2386-7 | D | 2058 | 50.65 | 1.31 | 14.64 | 9.69 | 1.20 | 0.27 | 7.52 | 11.88 | 2.61 | 0.04 | 0.08 | 99.71 | 58 | 2.51 | 10.17 |
| 2387-2 (3) | B-C | 3206 | 51.04 | 1.52 | 14.93 | 8.38 | 1.03 | 0.16 | 7.56 | 11.23 | 2.94 | 0.08 | 0.1 | 98.71 | 61.6 | 2.85 | 8.76 |
| 2387-5 | B-C | 3150 | 50.25 | 1.51 | 15.24 | 9.06 | 1.12 | 0.26 | 7.79 | 11.68 | 2.81 | 0.03 | 0.12 | 99.69 | 60.48 | 2.77 | 9.82 |
| 2387-6 | B-C | 3057 | 50.55 | 1.51 | 14.61 | 9.50 | 1.17 | 0.2 | 7.44 | 11.73 | 2.86 | 0.03 | 0.14 | 99.55 | 58.25 | 2.75 | 9.85 |
| 2388-3A | A-B | 3909 | 50.31 | 1.82 | 14.51 | 9.84 | 1.21 | 0.27 | 7.36 | 11.45 | 2.55 | 0.08 | 0.18 | 99.41 | 57.12 | 2.42 | 10.12 |
| 2388-10 | A-B | 3057 | 50.58 | 1.1 | 15.34 | 8.36 | 1.03 | 0.17 | 8.44 | 12.63 | 2.29 | 0.01 | 0.07 | 99.9 | 64.25 | 2.36 | 9.79 |
| 2389-1 | A | 3714 | 50.89 | 1.76 | 14.36 | 10.01 | 1.23 | 0.21 | 7.35 | 11.26 | 2.51 | 0.04 | 0.17 | 99.63 | 56.66 | 2.37 | 10.3 |
| 2390-1 | W-RTI | 3004 | 48.97 | 2.47 | 15.4 | 9.36 | 1.15 | 0.18 | 6.37 | 10.37 | 3.19 | 0.73 | 0.48 | 98.48 | 54.78 | 2.76 | 8.16 |

Table C-1. Continued.

| Sample | Location[μ] | Depth (m) | $SiO_2$ | $TiO_2$ | $Al_2O_3$ | FeO | $Fe_2O_3$ | MnO | MgO | CaO | $Na_2O$ | K2O | $P_2O_5$ | Total | Mg# | $Na_{8.0}$ | $Fe_{8.0}$ |
|---|---|---|---|---|---|---|---|---|---|---|---|---|---|---|---|---|---|
| **Weight percent by microprobe*** | | | | | | | | | | | | | | | | | |
| 2390-9 | W-RTI | 2930 | 50.01 | 2.84 | 12.87 | 12.62 | 1.56 | 0.27 | 5.54 | 9.47 | 3.01 | 0.3 | 0.32 | 98.58 | 43.87 | 2.26 | 10.4 |
| 2391-1 | A-B | 3721 | 50.63 | 1.42 | 14.88 | 9.03 | 1.11 | 0.27 | 7.95 | 11.99 | 2.39 | 0.06 | 0.12 | 99.68 | 61.06 | 2.38 | 9.97 |
| D1-3 | B | 3000 | 50.58 | 1.42 | 15.21 | 8.90 | 1.10 | 0.25 | 8.04 | 12.18 | 2.6 | 0.07 | 0.09 | 100.28 | 61.66 | 2.6 | 9.94 |
| D1-5 | B | 3000 | 50.78 | 1.43 | 15.24 | 8.80 | 1.09 | 0.24 | 8.07 | 12.21 | 2.54 | 0.07 | 0.1 | 100.41 | 62.01 | 2.56 | 9.86 |
| D4-2 | B | 3000 | 51.42 | 1.66 | 14.43 | 9.69 | 1.20 | 0.29 | 7.25 | 11.57 | 2.67 | 0.08 | 0.11 | 100.21 | 57.11 | 2.51 | 9.81 |
| D4-4 | B | 3000 | 51.22 | 1.53 | 14.75 | 9.05 | 1.12 | 0.25 | 7.8 | 11.74 | 2.68 | 0.09 | 0.1 | 100.15 | 60.53 | 2.64 | 9.82 |
| D4-6 | B | 3000 | 51.07 | 1.6 | 14.58 | 9.46 | 1.17 | 0.26 | 7.49 | 11.57 | 2.76 | 0.07 | 0.14 | 99.99 | 58.5 | 2.65 | 9.87 |
| D6-1 | B | 3200 | 50.53 | 1.41 | 15.61 | 8.75 | 1.08 | 0.24 | 8.03 | 11.95 | 2.82 | 0.07 | 0.09 | 100.41 | 62.04 | 2.82 | 9.76 |
| D13-1 | B | 2900 | 50.62 | 1.78 | 14.7 | 9.60 | 1.18 | 0.3 | 7.41 | 11.43 | 2.84 | 0.1 | 0.12 | 99.9 | 57.87 | 2.72 | 9.93 |
| D15-1 | B | 2900 | 50.53 | 1.78 | 14.73 | 9.71 | 1.20 | 0.27 | 7.33 | 11.4 | 2.81 | 0.11 | 0.12 | 99.81 | 57.33 | 2.67 | 9.94 |
| D17-10 | A-B | 3000 | 50.2 | 1.65 | 15.31 | 9.15 | 1.13 | 0.23 | 8.04 | 11.25 | 2.61 | 0.11 | 0.13 | 99.65 | 61 | 2.61 | 10.22 |
| D17-11 | A-B | 3000 | 50.4 | 1.3 | 16.02 | 8.42 | 1.04 | 0.17 | 8.26 | 11.82 | 2.69 | 0.11 | 0.15 | 100.2 | 63.6 | 2.74 | 9.65 |
| D18-3 | B | 2800 | 50.85 | 1.84 | 14.28 | 10.26 | 1.27 | 0.2 | 6.72 | 11.06 | 3.05 | 0.2 | 0.2 | 99.74 | 53.83 | 2.74 | 9.69 |
| D18-4 | B | 2800 | 50.77 | 1.89 | 14.23 | 10.37 | 1.28 | 0.21 | 6.64 | 11.02 | 3.08 | 0.19 | 0.19 | 99.67 | 53.27 | 2.75 | 9.69 |
| D19-2 | B | 2650 | 50.76 | 1.83 | 14.26 | 10.13 | 1.25 | 0.2 | 7.02 | 11.02 | 2.99 | 0.13 | 0.17 | 99.58 | 55.22 | 2.76 | 9.99 |
| D19-9 | B | 2650 | 51.45 | 1.82 | 14.65 | 10.12 | 1.25 | 0.2 | 6.9 | 11.14 | 3.18 | 0.11 | 0.18 | 100.8 | 54.84 | 2.92 | 9.79 |
| D20-1 | A-B | 3100 | 48.81 | 0.96 | 17.31 | 7.13 | 0.88 | 0.1 | 10.01 | 12.08 | 2.39 | ND | 0.06 | 99.61 | 71.43 | 2.54 | 9.83 |
| D20-2 | A-B | 3100 | 49.42 | 0.96 | 17.44 | 7.23 | 0.89 | 0.12 | 10.06 | 12 | 2.44 | ND | 0.06 | 100.33 | 71.25 | 2.59 | 9.98 |
| D20-3 | A-B | 3100 | 49.45 | 0.94 | 17.57 | 7.19 | 0.89 | 0.13 | 9.86 | 12.21 | 2.43 | ND | 0.07 | 100.44 | 70.94 | 2.59 | 9.79 |
| D20-4 | A-B | 3100 | 49.2 | 0.94 | 17.84 | 7.19 | 0.89 | 0.14 | 9.18 | 12.55 | 2.46 | ND | 0.03 | 100.14 | 69.44 | 2.6 | 9.23 |
| D20-6 | A-B | 3100 | 49.08 | 0.94 | 17.32 | 7.15 | 0.88 | 0.12 | 9.87 | 12.13 | 2.42 | ND | 0.03 | 99.65 | 71.09 | 2.58 | 9.75 |
| D20-7 | A-B | 3100 | 49.06 | 0.94 | 17.41 | 7.15 | 0.88 | 0.12 | 9.76 | 12.11 | 2.41 | ND | 0.08 | 99.78 | 70.86 | 2.56 | 9.67 |
| D20-8 | A-B | 3100 | 49.04 | 0.92 | 17.37 | 7.11 | 0.88 | 0.09 | 9.81 | 12.06 | 2.46 | ND | 0.07 | 99.69 | 71.07 | 2.62 | 9.67 |
| D20-12 | A-B | 3100 | 50.75 | 1.8 | 14.45 | 9.97 | 1.23 | 0.21 | 6.96 | 11.48 | 2.88 | 0.09 | 0.14 | 99.59 | 55.41 | 2.64 | 9.72 |
| D20-13 | A-B | 3100 | 49.16 | 0.96 | 17.42 | 7.14 | 0.88 | 0.1 | 10.22 | 12.02 | 2.44 | ND | 0.05 | 100.11 | 71.83 | 2.59 | 9.99 |
| D20-14 | A-B | 3100 | 49.56 | 0.9 | 17.45 | 7.11 | 0.88 | 0.1 | 10.11 | 12.09 | 2.41 | ND | 0.06 | 100.39 | 71.68 | 2.56 | 9.88 |
| D20-15 | A-B | 3100 | 49.23 | 0.94 | 17.5 | 7.16 | 0.88 | 0.11 | 9.89 | 12.09 | 2.45 | ND | 0.07 | 100.2 | 71.11 | 2.6 | 9.78 |
| D20-16 | A-B | 3100 | 49.31 | 0.94 | 17.4 | 7.08 | 0.87 | 0.12 | 10.08 | 12.08 | 2.44 | ND | 0.08 | 100.11 | 71.7 | 2.59 | 9.83 |

Table C-1. Continued.

| Sample | Location[µ] | Depth (m) | $SiO_2$ | $TiO_2$ | $Al_2O_3$ | FeO | $Fe_2O_3$ | MnO | MgO | CaO | $Na_2O$ | K2O | $P_2O_5$ | Total | Mg# | $Na_{8.0}$ | $Fe_{8.0}$ |
|---|---|---|---|---|---|---|---|---|---|---|---|---|---|---|---|---|---|
| **Weight percent by microprobe*** | | | | | | | | | | | | | | | | | |
| D20-18 | A-B | 3100 | 49.78 | 0.9 | 17.86 | 7.16 | 0.88 | 0.12 | 9.96 | 11.93 | 2.4 | ND | 0.08 | 100.79 | 71.22 | 2.55 | 9.84 |
| D20-19 | A-B | 3100 | 49.44 | 0.92 | 17.53 | 7.11 | 0.88 | 0.12 | 10.02 | 12.22 | 2.43 | ND | 0.07 | 100.45 | 71.5 | 2.58 | 9.82 |
| D20-20 | A-B | 3100 | 48.99 | 0.95 | 17.21 | 7.13 | 0.88 | 0.05 | 10.47 | 12.1 | 2.47 | ND | ND | 99.96 | 72.34 | 2.61 | 10.14 |
| D20-21 | A-B | 3100 | 49.3 | 0.96 | 17.3 | 7.18 | 0.89 | 0.16 | 10.14 | 12.13 | 2.46 | ND | 0.01 | 100.23 | 71.54 | 2.61 | 9.98 |
| D20-30 | A-B | 3100 | 49.09 | 0.95 | 17.43 | 7.20 | 0.89 | 0.11 | 9.89 | 12.03 | 2.44 | ND | 0.06 | 99.96 | 70.98 | 2.59 | 9.83 |
| D20-31 | A-B | 3100 | 49.66 | 0.92 | 17.7 | 7.08 | 0.87 | 0.12 | 10.16 | 12 | 2.43 | ND | 0.07 | 100.71 | 71.86 | 2.58 | 9.89 |
| D20-33 | A-B | 3100 | 48.73 | 0.98 | 17.33 | 7.06 | 0.87 | 0.14 | 9.92 | 12.22 | 2.53 | ND | 0.1 | 99.59 | 71.45 | 2.68 | 9.69 |
| D20-40 | A-B | 3100 | 49.2 | 0.94 | 17.55 | 7.13 | 0.88 | 0.16 | 10.11 | 12.03 | 2.39 | ND | 0.1 | 100.2 | 71.63 | 2.54 | 9.9 |
| D21-1 | A-B | 3800 | 48.76 | 1.25 | 16.74 | 9.26 | 1.14 | 0.18 | 8.61 | 11.19 | 2.48 | 0.05 | 0.1 | 99.6 | 62.34 | 2.57 | 10.97 |
| D22-2 | A-B | 3800 | 49.69 | 1.13 | 16.65 | 7.50 | 0.92 | 0.11 | 9.46 | 11.82 | 2.53 | 0.01 | 0.08 | 99.77 | 69.2 | 2.69 | 9.81 |
| D22-3 | A-B | 3800 | 49.95 | 1.1 | 16.84 | 7.56 | 0.93 | 0.15 | 9.47 | 11.88 | 2.55 | ND | 0.1 | 100.4 | 69.04 | 2.71 | 9.89 |
| D22-4 | A-B | 3800 | 49.76 | 1.11 | 16.86 | 7.67 | 0.95 | 0.13 | 9.21 | 11.81 | 2.59 | ND | 0.08 | 100.02 | 68.14 | 2.73 | 9.78 |
| D23-2 | A-B | 3800 | 50.06 | 1.13 | 16.73 | 7.60 | 0.94 | 0.14 | 9.42 | 11.88 | 2.52 | 0.02 | 0.07 | 100.4 | 68.83 | 2.67 | 9.89 |
| D25-6 | C | 2700 | 51.86 | 1.69 | 14.56 | 9.59 | 1.18 | 0.15 | 7.37 | 11.6 | 2.39 | 0.12 | 0.14 | 100.5 | 57.79 | 2.25 | 9.86 |
| D26-4 | C | 2500 | 50.86 | 1.59 | 14.7 | 9.59 | 1.18 | 0.2 | 7.38 | 11.45 | 2.86 | 0.14 | 0.13 | 99.91 | 57.8 | 2.73 | 9.88 |
| D26-6 | C | 2500 | 51.01 | 1.7 | 14.37 | 9.84 | 1.21 | 0.19 | 7.04 | 11.44 | 2.92 | 0.13 | 0.14 | 99.8 | 56.03 | 2.7 | 9.68 |
| D27-5 | C-D | 2500 | 49.96 | 1.14 | 16.54 | 7.70 | 0.95 | 0.14 | 9.41 | 11.94 | 2.54 | 0.02 | 0.06 | 100.3 | 68.52 | 2.69 | 9.99 |
| D30-1 | E-RTI | 2800 | 50.58 | 1.77 | 14.47 | 9.65 | 1.19 | 0.21 | 7.35 | 11.47 | 2.9 | 0.09 | 0.14 | 99.65 | 57.56 | 2.77 | 9.9 |
| D32-1 | C | 2300 | 51.02 | 1.35 | 15.43 | 9.19 | 1.13 | 0.19 | 7.69 | 12.06 | 2.99 | 0.03 | 0.07 | 101 | 59.84 | 2.93 | 9.83 |
| D32-3 | C | 2300 | 50.67 | 1.55 | 14.76 | 9.41 | 1.16 | 0.19 | 7.34 | 11.91 | 2.88 | 0.08 | 0.13 | 99.91 | 58.13 | 2.74 | 9.63 |
| D34-2 | C-D | 2400 | 49.86 | 1.02 | 16.28 | 7.79 | 0.96 | 0.12 | 9.12 | 12.96 | 2.18 | 0.06 | 0.05 | 100.3 | 67.59 | 2.32 | 9.83 |
| D35-3 | A | 3100 | 50.01 | 1.72 | 15.28 | 9.11 | 1.12 | 0.19 | 7.77 | 11.54 | 2.59 | 0.1 | 0.17 | 99.44 | 60.3 | 2.54 | 9.84 |
| D35-4 | A | 3100 | 49.81 | 1.72 | 15.59 | 9.03 | 1.11 | 0.18 | 7.88 | 11.56 | 2.63 | 0.1 | 0.16 | 99.62 | 60.85 | 2.61 | 9.89 |
| D36-3 | A | 3200 | 50.56 | 1.25 | 15.25 | 8.48 | 1.05 | 0.18 | 8.39 | 12.36 | 2.26 | 0.07 | 0.09 | 99.8 | 63.79 | 2.32 | 9.86 |
| D36-4 | A | 3200 | 50.55 | 1.25 | 15.27 | 8.51 | 1.05 | 0.17 | 8.42 | 12.38 | 2.25 | 0.05 | 0.12 | 99.87 | 63.8 | 2.31 | 9.93 |
| D37-2 | A | 3000 | 50.4 | 1.39 | 15.15 | 8.71 | 1.07 | 0.18 | 8.31 | 12.22 | 2.43 | 0.04 | 0.13 | 99.9 | 62.94 | 2.48 | 10.04 |
| D38-1 | A | 3500 | 50.21 | 1.17 | 15.53 | 8.59 | 1.06 | 0.18 | 8.78 | 12.42 | 2.24 | 0.03 | 0.08 | 100.1 | 64.55 | 2.35 | 10.39 |
| D38-2 | A | 3500 | 50.69 | 1.68 | 14.78 | 9.32 | 1.15 | 0.21 | 7.66 | 11.52 | 2.57 | 0.1 | 0.15 | 99.65 | 59.42 | 2.5 | 9.93 |
| D39-1 | W-RTI | 3000 | 50.37 | 2.29 | 14.11 | 10.67 | 1.32 | 0.22 | 7 | 10.31 | 2.88 | 0.24 | 0.28 | 99.49 | 53.89 | 2.65 | 10.55 |
| D43-2 | W-RTI | 3000 | 50.57 | 1.38 | 14.99 | 8.80 | 1.09 | 0.22 | 7.99 | 12.22 | 2.61 | 0.07 | 0.09 | 99.87 | 61.78 | 2.61 | 9.77 |
| D44-1 | DW | 2100 | 50.69 | 1.22 | 15 | 8.69 | 1.07 | ND | 7.99 | 12.72 | 2.47 | 0.05 | 0.07 | 100 | 62.09 | 2.47 | 9.64 |

Table C-1. Continued.

| Sample | Location[μ] | Depth (m) | $SiO_2$ | $TiO_2$ | $Al_2O_3$ | FeO | $Fe_2O_3$ | MnO | MgO | CaO | $Na_2O$ | K2O | $P_2O_5$ | Total | Mg# | $Na_{8.0}$ | $Fe_{8.0}$ |
|---|---|---|---|---|---|---|---|---|---|---|---|---|---|---|---|---|---|
| **Weight percent by microprobe*** | | | | | | | | | | | | | | | | | |
| 2388-2 | A-B | 3500 | 48.9 | 1.28 | 17.13 | 8.79 | 1.08 | 0.19 | 8.77 | 11.16 | 2.8 | 0.03 | 0.08 | 99.89 | 63.97 | 2.91 | 10.61 |
| 2388-5 | A-B | 3775 | 50.51 | 1.86 | 14.21 | 9.41 | 1.16 | 0.18 | 7.45 | 11.57 | 2.53 | 0.22 | 0.17 | ND | 58.51 | 2.41 | 9.76 |
| 2388-13 | A-B | 3072 | 50.57 | 1.46 | 14.68 | 8.88 | 1.10 | 0.2 | 7.95 | 12.1 | 2.63 | 0.04 | 0.09 | ND | 61.44 | 2.62 | 9.81 |
| RC-40 | E-RTI | 2800 | 50.53 | 1.48 | 14.78 | 8.66 | 1.07 | 0.17 | 7.94 | 12.2 | 2.68 | 0.07 | 0.13 | ND | 62.02 | 2.67 | 9.55 |
| Rc -41 | E-RTI | 2800 | 50.38 | 1.45 | 15.15 | 8.75 | 1.08 | 0.19 | 8.02 | 12.05 | 2.62 | 0.05 | 0.1 | ND | 62.01 | 2.62 | 9.74 |
| RC -42 | E-RTI | 2800 | 50.24 | 1.48 | 15.42 | 8.51 | 1.05 | 0.19 | 8.03 | 12.03 | 2.76 | 0.05 | 0.12 | ND | 62.67 | 2.76 | 9.5 |
| **Weight percent by microprobe for picritic basalts and picrites[ϕ]** | | | | | | | | | | | | | | | | | |
| 2384-6 | A-B | 3707 | 48.43 | 0.82 | 17.35 | 6.95 | 0.86 | 0.1 | 12.41 | 11.48 | 2.25 | 0.03 | 0.06 | 100.73 | 76.10 | 2.72 | 8.99 |
| 2384-1 | A-B | 3884 | 47.05 | 0.89 | 16.11 | 7.16 | 0.88 | 0.15 | 12.78 | 11.13 | 2.18 | 0.039 | 0.077 | 98.45 | 76.00 | 2.67 | 9.24 |
| 2384-3 | A-B | 3751 | 47.9 | 0.85 | 16.18 | 7.13 | 0.88 | 0.1 | 14.24 | 10.64 | 2.16 | 0.03 | 0.07 | 100.18 | 78.10 | 2.75 | 9.32 |
| D20-1 | A-B | 3100 | 47.38 | 0.8 | 15.38 | 7.17 | 0.88 | 0.1 | 16.48 | 9.98 | 1.99 | 0.03 | 0.06 | 100.26 | 80.40 | 2.72 | 9.54 |
| 2384-2 | A-B | 3841 | 46.93 | 0.71 | 13.15 | 7.37 | 0.91 | 0.12 | 20.57 | 9.14 | 1.7 | 0.03 | 0.05 | 100.68 | 83.20 | 2.70 | 10.07 |
| D20-15 | A-B | 3100 | 46.35 | 0.71 | 13.96 | 7.21 | 0.89 | 0.11 | 21.1 | 8.64 | 1.77 | 0.02 | 0.05 | 100.81 | 83.00 | 2.80 | 9.95 |
| **Weight percent by DCP^** | | | | | | | | | | | | | | | | | |
| 2384-1 | A-B | 3884 | 47.05 | 0.89 | 16.11 | 7.17 | 0.88 | 0.15 | 12.78 | 11.13 | 2.18 | 0.04 | 0.08 | 99.25 | 76.06 | 2.67 | 9.24 |
| 2384-3 | A-B | 3751 | 48.16 | 0.97 | 17.07 | 7.15 | 0.88 | 0.15 | 10.49 | 11.89 | 2.36 | 0.03 | 0.08 | 100.04 | 72.33 | 2.70 | 9.04 |
| 2384-7B | A-B | 3646 | 48.14 | 0.90 | 17.27 | 6.96 | 0.86 | 0.15 | 10.63 | 12.08 | 2.45 | 0.04 | 0.08 | 100.33 | 73.11 | 2.80 | 8.86 |
| 2384-8 | A-B | 3648 | 48.30 | 1.04 | 16.87 | 7.32 | 0.90 | 0.15 | 10.34 | 11.73 | 2.46 | 0.04 | 0.08 | 100.05 | 71.56 | 2.80 | 9.20 |
| 2390-5 | W-RTI | 3110 | 48.48 | 2.05 | 16.33 | 8.70 | 1.07 | 0.16 | 7.74 | 10.35 | 3.03 | 0.68 | 0.35 | 99.92 | 61.32 | 2.97 | 8.42 |
| D20-5 | A-B | 3100 | 48.05 | 0.95 | 17.11 | 7.11 | 0.88 | 0.14 | 10.63 | 11.71 | 2.37 | 0.03 | 0.08 | 99.85 | 72.70 | 2.72 | 9.01 |
| D20-13 | A-B | 3100 | 48.22 | 0.97 | 17.05 | 6.30 | 0.78 | 0.14 | 10.60 | 11.89 | 2.37 | 0.03 | 0.08 | 99.14 | 74.98 | 2.72 | 8.20 |
| D20-15 | A-B | 3100 | 50.95 | 0.99 | 18.06 | 7.15 | 0.88 | 0.02 | 11.24 | 12.35 | 2.55 | 0.04 | 0.09 | 105.25 | 73.69 | 2.94 | 9.10 |
| RC-41 | E-RTI | 2800 | 49.83 | 1.46 | 15.44 | 8.81 | 1.09 | 0.18 | 8.00 | 12.09 | 2.68 | 0.08 | 0.12 | 100.75 | 61.80 | 2.68 | 8.81 |

[μ]Locations: A = spreading center A, A-B = fault separating spreading centers A and B, B = spreading center B, B-C = fault separating spreading centers B and C, C = spreading center C, C-D = fault separating spreading center C and trough D, D = trough D, WRTI = western ridge transform intersection, ERTI = eastern ridge transform intersection. *Microprobe analysis was completed on natural glass samples at the US Geological Survey in Denver using an ARL-SEMQ microprobe and JEOL microprobe. [ϕ]Major element analysis of the picritic basalts and picrites determined by electron microprobe analysis of fused glasses + phenocrysts. ^DCP analysis was completed on phenocrysts-free samples at the Lamont-Doherty Earth Observatory. ND = not detected; Mg# = Mg/(Mg + $Fe^{2+}$); $Fe^{2+}$ is assumed to be 0.9 Fe total. All probe analyses were normalized to standard glasses VG-A99 and JdF-D2 which were run concurrently with the Siqueiros glasses. $Na_{8.0}$ = $Na_2O$ contents normalized to 8.0 wt. % MgO. $Fe_{8.0}$ = FeO contents normalized to 8.0 wt. % MgO.

Table C-2. Siqueiros glass major element analysis.

| Sample # | Loc.[µ] | Depth (m) | $SiO_2$ | $TiO_2$ | $Al_2O_3$ | $FeO_t$ | MnO | MgO* | CaO | $Na_2O$ | $K_2O$ | $P_2O_5$** | $CR_2O_3$ | Total | Mg # | $Na_{8.0}$ | $Fe_{8.0}$ | $H_2O$ | S | CL |
|---|---|---|---|---|---|---|---|---|---|---|---|---|---|---|---|---|---|---|---|---|
| **Weight percent by microprobe^** | | | | | | | | | | | | | | | | | | | | |
| 2390-9 | W-RTI | 2930 | 50.9 | 2.85 | 13.12 | 14.2 | 0.25 | 5.48 | 9.86 | 2.9 | 0.22 | 0.32 | 0.01 | 100.1 | 43.27 | 2.27 | 10.09 | 0.391 | 0.202 | 0.058 |
| 2390-5 | W-RTI | 3010 | 49.87 | 2.5 | 15.77 | 10.6 | 0.19 | 6.40 | 10.5 | 3.04 | 0.71 | 0.50 | 0.04 | 100.1 | 54.47 | 2.64 | 7.81 | 0.649 | 0.149 | 0.035 |
| 2390-3B/ar2 | W-RTI | 2934 | 50.28 | 2.48 | 15.43 | 10.8 | 0.21 | 6.42 | 10.65 | 3.04 | 0.65 | 0.48 | 0.03 | 100.4 | 54.19 | 2.65 | 7.98 | 0.636 | 0.156 | 0.032 |
| 2390-3B/ar1 | W-RTI | 2934 | 50.21 | 2.45 | 15.52 | 10.8 | 0.21 | 6.46 | 10.59 | 3 | 0.65 | 0.47 | 0.02 | 100.3 | 54.22 | 2.62 | 8.05 | 0.634 | 0.156 | 0.033 |
| 2390-4 | W-RTI | 2938 | 50.2 | 2.44 | 15.5 | 10.8 | 0.19 | 6.51 | 10.69 | 2.99 | 0.64 | 0.47 | 0.03 | 100.4 | 54.41 | 2.62 | 8.12 | 0.632 | 0.148 | 0.032 |
| D39-1 | W-RTI | 3000 | 50.83 | 2.27 | 13.95 | 12 | 0.24 | 6.96 | 10.37 | 2.8 | 0.21 | 0.28 | 0.03 | 99.9 | 53.42 | 2.54 | 9.69 | 0.332 | 0.166 | 0.067 |
| 2377-6/ar1 | B | 3011 | 50.76 | 2.12 | 14.33 | 11.4 | 0.22 | 7.06 | 11.3 | 2.67 | 0.13 | 0.23 | 0.04 | 100.3 | 54.98 | 2.44 | 9.28 | 0.290 | 0.149 | 0.018 |
| 2377-6/ar2 | B | 3011 | 50.77 | 2.09 | 14.38 | 11.4 | 0.22 | 7.09 | 11.34 | 2.67 | 0.14 | 0.22 | 0.06 | 100.3 | 55.24 | 2.44 | 9.26 | 0.295 | 0.153 | 0.018 |
| 2377-5 | B | 2090 | 50.74 | 2.06 | 15.11 | 11.1 | 0.19 | 7.17 | 10.8 | 2.8 | 0.13 | 0.24 | 0.04 | 100.3 | 56.22 | 2.59 | 9.05 | 0.341 | 0.139 | 0.022 |
| 2389-1/ar1 | A | 3714 | 50.99 | 1.71 | 14.28 | 10.9 | 0.22 | 7.41 | 11.55 | 2.52 | 0.08 | 0.15 | 0.03 | 99.8 | 57.35 | 2.37 | 9.19 | 0.146 | 0.149 | 0.004 |
| 2387-5/p1/ar1 | B-C | 3150 | 50.85 | 1.59 | 14.67 | 10.4 | 0.18 | 7.43 | 12.07 | 2.9 | 0.05 | 0.12 | 0.05 | 100.2 | 58.69 | 2.76 | 8.72 | 0.135 | 0.141 | 0.004 |
| 2387-5/p1/ar2 | B-C | 3150 | 50.69 | 1.56 | 14.63 | 10.5 | 0.22 | 7.43 | 12.21 | 2.91 | 0.06 | 0.12 | 0.03 | 100.3 | 58.45 | 2.77 | 8.81 | 0.136 | 0.130 | 0.003 |
| 2380-12 | BE | 3069 | 50.03 | 1.98 | 15.1 | 11 | 0.2 | 7.45 | 11.1 | 2.66 | 0.13 | 0.23 | 0.04 | 99.9 | 57.28 | 2.52 | 9.30 | 0.308 | 0.142 | 0.019 |
| 2389-1/ar2 | A | 3714 | 51.2 | 1.72 | 14.39 | 11 | 0.19 | 7.47 | 11.67 | 2.53 | 0.08 | 0.15 | 0.05 | 100.4 | 57.27 | 2.40 | 9.36 | 0.147 | 0.151 | 0.004 |
| 2387-5/p2/ar1 | B-C | 3150 | 50.66 | 1.59 | 14.53 | 10.3 | 0.19 | 7.49 | 12.15 | 2.89 | 0.06 | 0.11 | 0.03 | 100.0 | 59.05 | 2.76 | 8.70 | 0.130 | 0.132 | 0.002 |
| 2387-5/p2/ar2 | B-C | 3150 | 50.55 | 1.53 | 14.61 | 10.3 | 0.2 | 7.56 | 12.06 | 2.9 | 0.07 | 0.12 | 0.04 | 99.9 | 59.32 | 2.79 | 8.76 | 0.125 | 0.142 | 0.003 |
| 2377-10 | B | 3085 | 49.98 | 1.94 | 15.19 | 11 | 0.2 | 7.60 | 11.06 | 2.61 | 0.13 | 0.21 | 0.02 | 99.9 | 57.86 | 2.51 | 9.44 | 0.289 | 0.142 | 0.018 |
| 2389-5 | A | 3552 | 51.19 | 1.56 | 14.28 | 11 | 0.21 | 7.68 | 12.19 | 2.33 | 0.07 | 0.12 | 0.03 | 100.7 | 57.93 | 2.25 | 9.59 | 0.133 | 0.142 | 0.002 |
| 2378-7 | C | 2278 | 50.8 | 1.38 | 14.76 | 10.4 | 0.21 | 7.77 | 12.16 | 2.7 | 0.07 | 0.10 | 0.04 | 100.3 | 59.77 | 2.64 | 9.07 | 0.141 | 0.122 | 0.009 |
| 2385-3B | C | 2332 | 51.15 | 1.34 | 14.7 | 10.2 | 0.16 | 7.76 | 12.16 | 2.83 | 0.07 | 0.11 | 0.03 | 100.5 | 60.11 | 2.77 | 8.91 | 0.118 | 0.132 | 0.003 |
| 2380-9 | B | 3135 | 50.04 | 1.8 | 15.38 | 10.7 | 0.19 | 7.82 | 11.42 | 2.56 | 0.12 | 0.19 | 0.06 | 100.2 | 59.25 | 2.52 | 9.39 | 0.263 | 0.136 | 0.014 |
| 2388-13 | A-B | 3072 | 50.7 | 1.46 | 14.78 | 10 | 0.17 | 7.93 | 12.39 | 2.54 | 0.06 | 0.11 | 0.05 | 100.2 | 61.05 | 2.52 | 8.95 | 0.142 | 0.133 | 0.007 |
| 2389-4 | A | 3555 | 51.08 | 1.48 | 14.45 | 10.7 | 0.22 | 7.93 | 12.04 | 2.34 | 0.07 | 0.12 | 0.05 | 100.4 | 59.46 | 2.32 | 9.57 | 0.127 | 0.138 | 0.001 |
| 2376-3/p2 | B | 2023 | 50.2 | 1.5 | 15.38 | 9.93 | 0.2 | 7.98 | 11.92 | 2.51 | 0.11 | 0.17 | 0.05 | 99.9 | 61.40 | 2.50 | 8.91 | 0.213 | 0.121 | 0.010 |
| D17-9 | A-B | 3000 | 50.39 | 1.67 | 15.18 | 10.4 | 0.24 | 8.01 | 11.59 | 2.51 | 0.10 | 0.17 | 0.04 | 100.3 | 60.37 | 2.51 | 9.38 | 0.214 | 0.133 | 0.010 |
| D35-4 | A | 3100 | 50.28 | 1.76 | 15.63 | 10.4 | 0.2 | 8.03 | 11.61 | 2.62 | 0.11 | 0.19 | 0.04 | 100.8 | 60.44 | 2.63 | 9.41 | 0.238 | 0.138 | 0.007 |
| 2376-3/p1/ar1 | B | 2023 | 50.26 | 1.48 | 15.38 | 9.81 | 0.14 | 8.04 | 11.99 | 2.54 | 0.11 | 0.16 | 0.04 | 99.9 | 61.88 | 2.55 | 8.88 | 0.213 | 0.135 | 0.011 |
| 2378-3 | C | 2234 | 50.51 | 1.28 | 14.91 | 9.96 | 0.24 | 8.04 | 12.44 | 2.58 | 0.07 | 0.11 | 0.05 | 100.1 | 61.52 | 2.59 | 9.01 | 0.125 | 0.129 | 0.010 |
| 2378-2/p2 | C | 2223 | 50.75 | 1.31 | 14.85 | 10.2 | 0.2 | 8.06 | 12.48 | 2.6 | 0.07 | 0.10 | 0.05 | 100.6 | 61.06 | 2.61 | 9.21 | 0.127 | 0.134 | 0.008 |

Table C-2. Continued.

| Sample # | Loc.[μ] | Depth (m) | $SiO_2$ | $TiO_2$ | $Al_2O_3$ | $FeO_t$ | MnO | MgO* | CaO | $Na_2O$ | $K_2O$ | $P_2O_5$** | $CR_2O_3$ | Total | Mg # | $Na_{8.0}$ | $Fe_{8.0}$ | $H_2O$ | S | CL |
|---|---|---|---|---|---|---|---|---|---|---|---|---|---|---|---|---|---|---|---|---|
| **Weight percent by microprobe^** | | | | | | | | | | | | | | | | | | | | |
| 2376-3/p1/ar2 | B | 2023 | 50.35 | 1.48 | 15.32 | 9.75 | 0.16 | 8.07 | 11.96 | 2.56 | 0.11 | 0.16 | 0.06 | 99.9 | 62.09 | 2.58 | 8.85 | 0.210 | 0.127 | 0.009 |
| D1-3 | B | 3000 | 50.55 | 1.43 | 15.26 | 10.1 | 0.17 | 8.09 | 12.22 | 2.56 | 0.08 | 0.12 | 0.06 | 100.6 | 61.37 | 2.58 | 9.17 | 0.167 | 0.125 | 0.023 |
| 2378-2/p1 | C | 2223 | 50.54 | 1.32 | 14.73 | 10.2 | 0.19 | 8.10 | 12.44 | 2.68 | 0.07 | 0.11 | 0.04 | 100.3 | 61.24 | 2.70 | 9.24 | 0.130 | 0.134 | 0.007 |
| 2378-8 | C | 2287 | 50.58 | 1.08 | 15.34 | 9.05 | 0.19 | 8.31 | 12.89 | 2.65 | 0.04 | 0.07 | 0.05 | 100.2 | 64.51 | 2.73 | 8.48 | 0.083 | 0.118 | 0.002 |
| 2385-2 | C | ND | 50.85 | 1.12 | 15.12 | 9.32 | 0.2 | 8.31 | 12.76 | 2.61 | 0.05 | 0.07 | 0.04 | 100.4 | 63.84 | 2.69 | 8.72 | 0.092 | 0.117 | 0.003 |
| 2376-5/ar1 | B | 3034 | 50.27 | 1.41 | 15.57 | 9.47 | 0.18 | 8.34 | 12.23 | 2.5 | 0.11 | 0.14 | 0.07 | 100.2 | 63.56 | 2.59 | 8.89 | 0.183 | 0.127 | 0.008 |
| 2376-5/ar2 | B | 3034 | 50.21 | 1.36 | 15.61 | 9.63 | 0.22 | 8.36 | 12.02 | 2.51 | 0.10 | 0.13 | 0.05 | 100.1 | 63.20 | 2.60 | 9.05 | 0.182 | 0.134 | 0.008 |
| 2376-7 | B | 3092 | 49.95 | 1.41 | 15.9 | 9.55 | 0.17 | 8.54 | 11.77 | 2.53 | 0.10 | 0.13 | 0.06 | 100.1 | 63.91 | 2.67 | 9.18 | 0.188 | 0.129 | 0.016 |
| 2388-5 | A-B | 3797 | 50.58 | 1.11 | 15.3 | 9.36 | 0.19 | 8.66 | 13.05 | 2.27 | 0.05 | 0.07 | 0.06 | 100.6 | 64.67 | 2.43 | 9.13 | 0.080 | 0.119 | 0.002 |
| 2383-6 | A | 3661 | 50.42 | 1.11 | 15.38 | 9.09 | 0.21 | 8.93 | 12.8 | 2.19 | 0.06 | 0.07 | 0.06 | 100.3 | 66.05 | 2.42 | 9.18 | 0.087 | 0.124 | 0.000 |
| 2384-6 | A-B | 3707 | 49.25 | 0.99 | 16.98 | 8.29 | 0.18 | 9.63 | 12.63 | 2.4 | 0.03 | 0.05 | 0.05 | 100.4 | 69.70 | 2.69 | 9.21 | 0.054 | 0.100 | 0.001 |
| D20-15/p1 | A-B | 3100 | 49.07 | 0.93 | 17.46 | 8.04 | 0.19 | 9.80 | 12.36 | 2.39 | 0.02 | 0.06 | 0.05 | 100.3 | 70.70 | 2.69 | 9.87 | 0.064 | 0.105 | 0.003 |
| D20-13 | A-B | 3100 | 48.82 | 0.98 | 17.23 | 8.17 | 0.14 | 9.81 | 12.43 | 2.35 | 0.02 | 0.06 | 0.06 | 100.0 | 70.39 | 2.65 | 10.00 | 0.065 | 0.110 | 0.002 |
| D20-40 | A-B | 3100 | 49.14 | 0.97 | 17.25 | 8.06 | 0.17 | 9.92 | 12.51 | 2.37 | 0.02 | 0.06 | 0.04 | 100.5 | 70.90 | 2.68 | 9.90 | 0.065 | 0.099 | 0.002 |
| D20-15/p3 | A-B | 3100 | 49.07 | 0.94 | 17.43 | 8.11 | 0.15 | 9.96 | 12.4 | 2.36 | 0.02 | 0.06 | 0.06 | 100.5 | 70.85 | 2.67 | 9.96 | 0.066 | 0.102 | 0.002 |
| 2384-9 | A-B | 3623 | 49.37 | 1.06 | 17.11 | 8.44 | 0.19 | 10.00 | 12.16 | 2.44 | 0.03 | 0.07 | 0.05 | 100.9 | 70.11 | 2.75 | 10.29 | 0.075 | 0.104 | 0.003 |
| D20-15/p2 | A-B | 3100 | 48.99 | 0.97 | 17.42 | 8.16 | 0.13 | 10.01 | 12.3 | 2.37 | 0.03 | 0.06 | 0.05 | 100.4 | 70.83 | 2.68 | 10.01 | 0.065 | 0.112 | 0.002 |
| 2384-8 | A-B | 3648 | 49.26 | 1.05 | 16.91 | 8.23 | 0.15 | 10.02 | 12.25 | 2.41 | 0.03 | 0.06 | 0.06 | 100.4 | 70.68 | 2.72 | 10.08 | 0.080 | 0.116 | 0.004 |
| D20-1/p1 | A-B | 3100 | 49.29 | 0.96 | 17.42 | 8.21 | 0.13 | 10.06 | 12.28 | 2.4 | 0.03 | 0.06 | 0.06 | 100.8 | 70.80 | 2.72 | 10.06 | 0.064 | 0.103 | 0.003 |
| D20-7 | A-B | 3100 | 49.05 | 0.98 | 17.29 | 8.03 | 0.17 | 10.07 | 12.5 | 2.39 | 0.02 | 0.06 | 0.06 | 100.6 | 71.28 | 2.71 | 9.88 | 0.062 | 0.108 | 0.002 |
| D20-31 | A-B | 3100 | 49.14 | 0.97 | 17.15 | 7.99 | 0.15 | 10.11 | 12.34 | 2.37 | 0.02 | 0.06 | 0.04 | 100.3 | 71.47 | 2.69 | 9.85 | 0.063 | 0.105 | 0.003 |
| 2384-3 | A-B | 3751 | 49.08 | 0.99 | 17.12 | 8.04 | 0.17 | 10.14 | 12.36 | 2.33 | 0.03 | 0.07 | 0.06 | 100.3 | 71.41 | 2.65 | 9.90 | 0.063 | 0.107 | 0.003 |
| D20-1/p2 | A-B | 3100 | 49.11 | 0.98 | 17.29 | 8.07 | 0.14 | 10.23 | 12.26 | 2.36 | 0.02 | 0.07 | 0.05 | 100.5 | 71.51 | 2.69 | 9.94 | 0.066 | 0.110 | 0.002 |
| D20-20 | A-B | 3100 | 48.95 | 0.95 | 17.1 | 8.16 | 0.17 | 10.24 | 12.18 | 2.37 | 0.03 | 0.07 | 0.06 | 100.2 | 71.31 | 2.70 | 10.03 | 0.064 | 0.105 | 0.001 |

[μ]Locations same as Table C-1. ^Major element analysis of Siqueiros natural glasses completed at the University of Tasmania using a Cameca SX50 electron microprobe (Danyushevsky, personal communication). *MgO contents have been corrected using MgO* = MgO - 0.44722/0.90029. **P2O3 contents have been corrected using $^{**}P_2O_3 = P_2O_3 + 0.026281/0.82046$.

$Na_{8.0}$ = $Na_2O$ contents normalized to 8.0 wt. % MgO. $Fe_{8.0}$ = FeO contents normalized to 8.0 wt. % MgO.

Table C-3. ICP-MS major element analysis of Siqueiros transform basalts.

| Sample | Location[µ] | Depth (m) | $SiO_2$ | $TiO_2$ | $Al_2O_3$ | FeO | $Fe_2O_3$ | MnO | MgO | CaO | $Na_2O$ | $K_2O$ | $P_2O_5$ | Total | $Na_{8.0}$ | $Fe_{8.0}$ |
|---|---|---|---|---|---|---|---|---|---|---|---|---|---|---|---|---|
| **ICP Major Element Analysis (wt. %)** | | | | | | | | | | | | | | | | |
| 2375-7 G | B | 2968 | 47.20 | 1.30 | 14.40 | 8.10 | 1.00 | 0.16 | 7.79 | 11.30 | 2.56 | 0.08 | 0.10 | 95.00 | 2.52 | 7.88 |
| 2376-3 G | B | 3022 | 49.90 | 1.36 | 15.40 | 7.77 | 0.96 | 0.16 | 8.33 | 11.00 | 2.52 | 0.13 | 0.13 | 98.60 | 2.57 | 8.10 |
| 2376-5 | B | 3034 | 49.70 | 1.34 | 16.70 | 8.02 | 0.99 | 0.16 | 8.59 | 11.60 | 2.49 | 0.14 | 0.11 | 100.80 | 2.58 | 8.59 |
| 2376-5 G | B | 3034 | 42.30 | 1.13 | 13.40 | 6.75 | 0.83 | 0.14 | 7.35 | 9.80 | 2.14 | 0.10 | 0.11 | 84.90 | 2.02 | 6.03 |
| 2376-7 G | B | 3088 | 50.00 | 1.46 | 15.60 | 8.26 | 1.02 | 0.17 | 8.24 | 11.30 | 2.61 | 0.12 | 0.12 | 99.90 | 2.65 | 8.50 |
| 2376-8 G | B | 3037 | 48.70 | 1.42 | 17.10 | 7.94 | 0.98 | 0.15 | 7.03 | 11.40 | 2.54 | 0.11 | 0.13 | 98.50 | 2.35 | 6.82 |
| 2377-1 G | B | 3170 | 49.30 | 1.34 | 15.10 | 8.42 | 1.04 | 0.17 | 8.64 | 12.10 | 2.57 | 0.10 | 0.10 | 99.90 | 2.67 | 9.04 |
| 2377-10 | B | 3085 | 49.60 | 1.89 | 16.60 | 9.56 | 1.18 | 0.19 | 7.46 | 11.00 | 2.63 | 0.17 | 0.18 | 101.60 | 2.53 | 8.96 |
| 2377-10 G | B | 3085 | 49.70 | 1.79 | 15.50 | 9.07 | 1.12 | 0.18 | 7.27 | 11.40 | 2.69 | 0.14 | 0.17 | 100.20 | 2.55 | 8.25 |
| 2377-3 G | B | 3083 | 45.00 | 1.33 | 15.60 | 7.17 | 0.88 | 0.14 | 6.23 | 10.80 | 2.34 | 0.09 | 0.12 | 90.60 | 1.96 | 4.97 |
| 2377-5 | B | 3090 | 49.80 | 2.03 | 15.70 | 9.31 | 1.15 | 0.19 | 7.37 | 10.90 | 2.86 | 0.18 | 0.19 | 100.80 | 2.74 | 8.62 |
| 2377-6 | B | 3011 | 49.60 | 1.89 | 16.00 | 8.91 | 1.10 | 0.19 | 7.64 | 11.00 | 2.64 | ND | ND | 100.40 | 2.58 | 8.52 |
| 2377-8 G | B | 3087 | 50.30 | 1.66 | 15.80 | 8.91 | 1.10 | 0.18 | 8.11 | 11.50 | 2.55 | ND | ND | 101.50 | 2.57 | 9.02 |
| 2378-2 G | C | 2223 | 50.60 | 1.33 | 14.60 | 8.75 | 1.08 | 0.18 | 7.81 | 12.00 | 2.66 | 0.08 | 0.09 | 100.30 | 2.63 | 8.55 |
| 2378-3 | C | 2234 | 50.20 | 1.35 | 14.90 | 8.99 | 1.11 | 0.18 | 8.11 | 12.40 | 2.66 | 0.09 | 0.08 | 101.20 | 2.68 | 9.10 |
| 2378-3 G | C | 2234 | 50.90 | 1.33 | 14.70 | 8.83 | 1.09 | 0.18 | 8.01 | 12.20 | 2.67 | 0.08 | 0.09 | 101.20 | 2.67 | 8.84 |
| 2378-8 | C | 2287 | 51.00 | 1.10 | 15.30 | 7.94 | 0.98 | 0.17 | 8.70 | 12.80 | 2.67 | 0.07 | 0.08 | 101.80 | 2.77 | 8.60 |
| 2378-8 G | C | 2287 | 49.50 | 1.01 | 15.00 | 7.59 | 0.94 | 0.15 | 8.30 | 12.20 | 2.60 | ND | 0.06 | 98.30 | 2.65 | 7.89 |
| 2380-11 G | B | 3079 | 49.60 | 1.87 | 15.70 | 9.23 | 1.14 | 0.18 | 7.03 | 11.00 | 2.71 | 0.16 | 0.18 | 100.00 | 2.52 | 8.12 |
| 2380-12 G | B | 3069 | 49.20 | 1.94 | 14.40 | 9.56 | 1.18 | 0.19 | 7.21 | 10.40 | 2.76 | 0.16 | 0.18 | 98.40 | 2.61 | 8.67 |
| 2380-9 G | B | 3135 | 49.80 | 1.55 | 17.30 | 8.26 | 1.02 | 0.17 | 7.15 | 11.60 | 2.53 | 0.16 | 0.15 | 100.70 | 2.37 | 7.30 |
| 2381-11 G | B-C | 2686 | 51.50 | 1.27 | 14.40 | 8.58 | 1.06 | 0.18 | 8.00 | 11.80 | 2.72 | 0.08 | 0.08 | 100.70 | 2.72 | 8.58 |
| 2383-6 G a | A | 3661 | 50.70 | 1.10 | 15.30 | 7.94 | 0.98 | 0.16 | 8.63 | 12.20 | 2.32 | ND | ND | 100.50 | 2.41 | 8.54 |
| 2383-6 G b | A | 3661 | 50.90 | 1.09 | 15.20 | 7.94 | 0.98 | 0.16 | 8.79 | 12.20 | 2.31 | ND | ND | 100.70 | 2.42 | 8.68 |
| 2384-3 G | A-B | 3751 | 48.80 | 0.70 | 14.20 | 7.06 | 0.87 | 0.13 | 17.10 | 9.07 | 1.98 | ND | 0.06 | 101.00 | 1.21 | 6.78 |
| 2384-6 G | A-B | 3707 | 47.90 | 0.78 | 14.00 | 6.92 | 0.85 | 0.13 | 14.30 | 10.00 | 2.00 | ND | 0.05 | 97.90 | 1.96 | 8.78 |
| 2384-9 G | A-B | 3623 | 48.00 | 0.89 | 14.20 | 7.31 | 0.90 | 0.13 | 15.10 | 9.60 | 2.03 | ND | 0.07 | 99.30 | 1.82 | 8.76 |
| 2385-2 G | C | 2352 | 51.20 | 1.15 | 14.80 | 8.18 | 1.01 | 0.17 | 8.07 | 12.20 | 2.70 | 0.06 | 0.08 | 100.60 | 2.71 | 8.25 |
| 2385-3B G | C | 2333 | 49.70 | 1.29 | 14.60 | 8.99 | 1.11 | 0.20 | 7.52 | 11.70 | 2.70 | ND | ND | 99.10 | 2.61 | 8.47 |
| 2386-5 G | D | 2178 | 51.80 | 1.13 | 14.90 | 8.18 | 1.01 | 0.18 | 8.34 | 12.60 | 2.54 | ND | ND | 101.80 | 2.59 | 8.52 |

Table C-3. Continued.

| Sample | Location[μ] | Depth (m) | $SiO_2$ | $TiO_2$ | $Al_2O_3$ | FeO | $Fe_2O_3$ | MnO | MgO | CaO | $Na_2O$ | $K_2O$ | $P_2O_5$ | Total | $Na_{8.0}$ | $Fe_{8.0}$ |
|---|---|---|---|---|---|---|---|---|---|---|---|---|---|---|---|---|
| **ICP Major Element Analysis (wt. %)** | | | | | | | | | | | | | | | | |
| 2388-10 G | A-B | 3057 | 51.40 | 1.11 | 15.00 | 8.10 | 1.00 | 0.17 | 8.80 | 12.70 | 2.36 | 0.05 | 0.07 | 101.80 | 2.48 | 8.85 |
| 2389-4 | A | 3555 | 50.00 | 1.44 | 14.90 | 8.75 | 1.08 | 0.18 | 8.02 | 12.10 | 2.39 | ND | ND | 100.10 | 2.39 | 8.77 |
| 2389-5 | A | 3552 | 50.20 | 1.42 | 14.90 | 8.75 | 1.08 | 0.18 | 8.10 | 11.40 | 2.32 | ND | ND | 99.60 | 2.34 | 8.85 |
| 2389-5 G | A | 3552 | 50.10 | 1.32 | 14.30 | 8.75 | 1.08 | 0.17 | 8.29 | 11.20 | 2.34 | 0.07 | 0.10 | 98.80 | 2.39 | 9.04 |
| 2390-3B | WRTI | 2934 | 49.90 | 2.14 | 15.90 | 8.50 | 1.05 | 0.17 | 7.58 | 10.50 | 3.05 | 0.66 | 0.30 | 100.80 | 2.98 | 8.05 |
| 2390-5 G | WRTI | 3010 | 48.60 | 2.01 | 16.00 | 8.42 | 1.04 | 0.17 | 7.01 | 9.80 | 3.16 | 0.63 | 0.31 | 98.20 | 2.97 | 7.29 |
| A25 D1-3 | B | 3000 | 50.10 | 1.36 | 15.30 | 8.50 | 1.05 | 0.17 | 8.21 | 11.90 | 2.52 | 0.11 | 0.10 | 100.40 | 2.55 | 8.71 |
| A25 D1-3 G | B | 3000 | 49.40 | 1.29 | 15.10 | 8.34 | 1.03 | 0.18 | 7.95 | 11.70 | 2.48 | ND | ND | 98.70 | 2.47 | 8.29 |
| A25 D17-9 | A-B | 3000 | 50.50 | 1.71 | 15.40 | 9.15 | 1.13 | 0.18 | 7.87 | 11.40 | 2.57 | 0.13 | 0.14 | 101.30 | 2.55 | 9.01 |
| A25 D18-2 G | B | 2800 | 49.20 | 1.74 | 14.10 | 9.88 | 1.22 | 0.18 | 6.68 | 10.90 | 2.93 | ND | ND | 98.30 | 2.66 | 8.31 |

*ICP-MS analysis was completed at the Geological Survey of Canada on Siqueiros. WR indicates whole rock samples. G indicates glass samples. [μ]Locations same as Table C-1. Mg# = Mg/(Mg + $Fe^{2+}$); $Fe^{2+}$ is assumed to be 0.9 Fe total. $Na_{8.0}$ = $Na_2O$ contents normalized to 8.0 wt. % MgO. $Fe_{8.0}$ = FeO contents normalized to 8.0 wt. % MgO.

# APPENDIX D
# TRACE ELEMENT CONTENTS OF THE SIQUEIROS SAMPLES

Table D-1. XRF trace element concentrations for the Siqueiros transform basalts.

| Sample # | Dec. Lat. | Dec. Long. | Location* | MgO (wt.%) | Co | Cu | Ga | Nb | Ni | Rb | Sr | Y | Zn | Zr | V | Cr | Ba | Ti | Sc | K |
|---|---|---|---|---|---|---|---|---|---|---|---|---|---|---|---|---|---|---|---|---|
| **XRF analysis (ppm)^** | | | | | | | | | | | | | | | | | | | | |
| 2375-7 | 8.34 | -103.54 | B | 8.03 | 45 | 80 | 17 | 3.9 | 82 | 1.4 | 104 | 30 | 92 | 89 | 280 | 397 | 22 | 8200 | 43.4 | |
| 2375-9 | 8.34 | -103.53 | B | 7.61 | 47 | 79 | 18 | 2.7 | 88 | 1.6 | 103 | 30 | 92 | 89 | 282 | 441 | 19 | 8100 | 42.3 | |
| 2376-10 | 8.35 | -103.52 | B | | | | | | | | 110 | 29 | | 89 | | | | | | |
| 2376-3 | 8.37 | -103.52 | B | 7.85 | 46 | 76 | 19 | 3.2 | 107 | 3.1 | 116 | 33 | 74 | 103 | 265 | 385 | 22 | 8200 | 32.5 | |
| 2376-5 | 8.36 | -103.52 | B | | | | | | | | 115 | 31 | | 92 | | | | | | |
| 2376-6 | 8.35 | -103.52 | B | | | | | | | | 116 | 30 | | 91 | | | | | | |
| 2376-7 | 8.35 | -103.52 | B | 8.4 | 44 | 77 | 18 | 2.3 | 111 | 2.1 | 115 | 34 | 139 | 101 | 285 | 414 | 22 | 8900 | 37.1 | |
| 2376-8 | 8.35 | -103.52 | B | 8.02 | 44 | 65 | 19 | 3.7 | 117 | 2.1 | 134 | 37 | 80 | 125 | 272 | 364 | 25 | 9300 | 33.5 | |
| 2376-9 | 8.35 | -103.52 | B | | | | | | | | 117 | 29 | | 84 | | | | | | |
| 2377-11 | 8.36 | -103.52 | B | 7.14 | 47 | 63 | 21 | 5.4 | 88 | 2.1 | 120 | 52 | 107 | 164 | 353 | 360 | 40 | 12800 | 42.3 | 1300 |
| 2377-3 | 8.39 | -103.52 | B | 7.72 | 40 | 70 | 18 | 3.5 | 91 | 1.3 | 114 | 36 | 80 | 108 | 282 | 326 | 15 | 9100 | 33.9 | |
| 2378-2 | 8.32 | -103.31 | C | 8.43 | 49 | 89 | 18 | 2.4 | 21 | 2.0 | 100 | 32 | 78 | 81 | | | | | | |
| 2378-6 | 8.35 | -103.32 | C | | 48 | 83 | 18 | 3.6 | 26 | 2.3 | 102 | 29 | 77 | 82 | 282 | 419 | 20 | 7900 | 42.0 | 600 |
| 2379-2WR | 8.39 | -103.60 | A-B | | | | | | | | 114 | 30 | | 141 | | | | | | |
| 2380-11 | 8.36 | -103.51 | B | 7.45 | 48 | 65 | 19 | 4.2 | 84 | 3.5 | 116 | 46 | 92 | 144 | 342 | 313 | 39 | 12000 | 36.7 | 1200 |
| 2380-12 | 8.36 | -103.51 | B | | | | | | | 1.7 | 114 | 46 | | 147 | | | | | | |
| 2380-3 | 8.34 | -103.50 | B | | | | | | | 1.1 | 112 | 40 | | 117 | | | | | | |
| 2380-4 | 8.34 | -103.50 | B | 7.56 | 45 | 68 | 19 | 3.1 | 71 | 2.3 | 125 | 35 | 112 | 114 | | | | | | |
| 2380-5 | 8.35 | -103.51 | B | | | | | | | 0.7 | 126 | 35 | | 113 | | | | | | |
| 2380-7 | 8.36 | -103.51 | B | | | | | | | 1.0 | 110 | 40 | | 116 | | | | | | |
| 2380-9 | 8.36 | -103.51 | B | | | | | | | 1.3 | 114 | 41 | | 126 | | | | | | |
| 2381-11 | 8.34 | -103.44 | B-C | 7.76 | 47 | 79 | 18 | 3.2 | 26 | 2.9 | 101 | 29 | 74 | 75 | 270 | 231 | 12 | 7400 | 44.0 | 600 |
| 2381-11WR | 8.34 | -103.44 | B-C | 7.76 | | | | | | | | | | | 275 | 204 | 16 | 7700 | 41.4 | 1200 |
| 2381-3AWR | 8.35 | -103.42 | B-C | | 35 | 68 | 19 | 3.4 | 49 | 4.4 | 112 | 24 | 59 | 72 | 221 | 208 | 10 | 6800 | 29.2 | 1400 |
| 2382-10WR | 8.30 | -103.55 | B | | 39 | 66 | 19 | 2.5 | 85 | 0.9 | 104 | 26 | 67 | 80 | | | | | | |
| 2382-9 | 8.31 | -103.55 | B | | | | | | | 0.9 | 117 | 28 | | 84 | | | | | | |
| 2383-2 | 8.36 | -103.83 | A | 7.52 | 50 | 73 | 18 | 2.3 | 33 | 1.7 | 115 | 31 | 84 | 94 | 313 | 228 | 20 | 8800 | 45.3 | 700 |
| 2383-6 | 8.37 | -103.84 | A | 8.89 | 45 | 81 | 18 | 2.4 | 111 | 1.7 | 89 | 26 | 70 | 66 | 259 | 423 | 11 | 6600 | 39.8 | 400 |
| 2384-1 | 8.38 | -103.66 | A-B | 9.6 | | | | 1.3 | | | 63 | 18 | | 45 | | | | | | |
| 2384-10 | 8.38 | -103.67 | A-B | 9.59 | | | | | | 0.3 | 81 | 25 | | 61 | | | | | | |

Table D-1. Continued.

| Sample # | Dec. Lat. | Dec. Long. | Location* | MgO (wt.%) | Co | Cu | Ga | Nb | Ni | Rb | Sr | Y | Zn | Zr | V | Cr | Ba | Ti | Sc | K |
|---|---|---|---|---|---|---|---|---|---|---|---|---|---|---|---|---|---|---|---|---|
| **XRF analysis (ppm)μ** | | | | | | | | | | | | | | | | | | | | |
| 2384-11 | 8.38 | -103.68 | A-B | 8.79 | 50 | 71 | 17 | 2.3 | 263 | 0.5 | 82 | 27 | 69 | 67 | 242 | 516 | 17 | 7000 | 32.7 | 300 |
| 2384-12 | 8.38 | -103.68 | A-B | 9.11 | | | | | | 0.8 | 104 | 23 | | 72 | | | | | | |
| 2384-13 | 8.38 | -103.68 | A-B | | | | | | | 0.4 | 114 | 35 | | 97 | | | | | | |
| 2384-14 | 8.39 | -103.68 | A-B | | | | | | | 2.9 | 97 | 34 | | 111 | | | | | | |
| 2384-2 | 8.37 | -103.66 | A-B | 9.54 | | | | 0.8 | | 0.4 | 71 | 21 | | 49 | | | | | | |
| 2384-3 | 8.37 | -103.66 | A-B | 10.12 | | | | 1.2 | | 0.6 | 73 | 22 | | 51 | | | | | | |
| 2384-4 | 8.37 | -103.66 | A-B | | | | | | | 1.4 | 116 | 50 | | 162 | | | | | | |
| 2384-6 | 8.37 | -103.67 | A-B | 9.57 | | | | 0.8 | | 0.5 | 73 | 20 | | 47 | | | | | | |
| 2384-7A | 8.38 | -103.67 | A-B | 9.9 | | | | 1.0 | | | 71 | 21 | | 48 | | | | | | |
| 2384-7B | 8.38 | -103.67 | A-B | 9.93 | | | | 1.2 | | 0.7 | 73 | 21 | | 48 | | | | | | |
| 2384-8 | 8.38 | -103.67 | A-B | 9.85 | | | | 1.1 | | 0.3 | 78 | 23 | | 58 | | | | | | |
| 2384-9 | 8.38 | -103.67 | A-B | 9.73 | 53 | 73 | 16 | 2.1 | 431 | 0.1 | 75 | 23 | 63 | 56 | 202 | 823 | 7 | 6000 | 26.8 | 200 |
| 2385-2 | 8.36 | -103.32 | C | 8.21 | 47 | 87 | 18 | 2.8 | 32 | 0.8 | 97 | 27 | 69 | 69 | 258 | 274 | 16 | 6800 | 83.6 | 400 |
| 2385-3A | 8.36 | -103.32 | C | 7.8 | 42 | 74 | 19 | 1.8 | 61 | 1.2 | 110 | 29 | 70 | 84 | 271 | 309 | 21 | 7700 | 42.6 | 500 |
| 2385-6T | 8.36 | -103.31 | C | 7.91 | 47 | 79 | 19 | 3.7 | 24 | 1.7 | 102 | 30 | 73 | 79 | 275 | 227 | 13 | 7600 | 46.8 | 500 |
| 2386-5 | 8.36 | -103.13 | D | 8.23 | 36 | 60 | 17 | 1.7 | 85 | 0.7 | 108 | 27 | 59 | 76 | 208 | 289 | 13 | 6800 | 23.4 | 400 |
| 2387-1 | 8.35 | -103.41 | B-C (e) | | 47 | 85 | 17 | 3.6 | 38 | 2.0 | 97 | 27 | 96 | 68 | 261 | 255 | 12 | 6700 | 43.0 | 500 |
| 2387-5 | 8.36 | -103.39 | B-C (e) | 7.79 | | | | | | 1.1 | 102 | 31 | | 87 | | | | | | |
| 2387-6 | 8.36 | -103.38 | B-C (e) | 7.44 | 40 | 6 | 17 | 3.0 | 43 | 1.9 | 98 | 28 | 70 | 79 | 257 | 309 | 14 | 7600 | 34.2 | 400 |
| 2388-1 | 8.35 | -103.78 | A-B | | | | | | | | 159 | 21 | | 99 | | | | | | |
| 2388-10 | 8.37 | -103.77 | A-B | 8.44 | 46 | 91 | 17 | 2.4 | 72 | 3.2 | 79 | 25 | 69 | 64 | 253 | 439 | 10 | 6400 | 37.2 | 300 |
| 2388-14 | 8.38 | -103.76 | A-B | | | | | | | | 73 | 21 | | 80 | | | | | | |
| 2388-7 | 8.37 | -103.77 | A-B | | | | | | | | 73 | 20 | | 55 | | | | | | |
| 2389-1 | 8.39 | -103.95 | A | 7.35 | 44 | 60 | 19 | 2.6 | 83 | 1.1 | 86 | 36 | 81 | 86 | 318 | 328 | 19 | 9200 | 34.1 | 600 |
| 2390-1 | 8.30 | -104.02 | W-RTI | 6.37 | 44 | 55 | 19 | 16.2 | 135 | 10.6 | 287 | 34 | 81 | 167 | 276 | 269 | 144 | 12700 | 27.5 | 5100 |
| 2390-3A | 8.29 | -104.03 | W-RTI | | | | | | | 9.0 | 271 | 35 | | 167 | | | | | | |
| 2390-3B | 8.29 | -104.03 | W-RTI | | | | | | | 9.1 | 274 | 35 | | 165 | | | | | | |
| 2390-4 | 8.30 | -104.03 | W-RTI | | | | | | | 9.3 | 273 | 35 | | 166 | | | | | | |
| 2390-7 | 8.31 | -104.05 | W-RTI | | | | | | | 1.6 | 128 | 36 | | 116 | | | | | | |
| 2390-8 | 8.32 | -104.06 | W-RTI | | | | | | | 10.4 | 277 | 33 | | 169 | | | | | | |

Table D-1. Continued.

| Sample # | Dec. Lat. | Dec. Long. | Location* | MgO (wt.%) | Co | Cu | Ga | Nb | Ni | Rb | Sr | Y | Zn | Zr | V | Cr | Ba | Ti | Sc | K |
|---|---|---|---|---|---|---|---|---|---|---|---|---|---|---|---|---|---|---|---|---|
| **XRF analysis (ppm)$^{\mu}$** | | | | | | | | | | | | | | | | | | | | |
| 2390-9 | 8.32 | -104.06 | W-RTI | 5.54 | 53 | 58 | 24 | 5.9 | | 4.2 | 121 | 59 | 120 | 184 | 509 | 227 | 76 | 17600 | 54.4 | 1900 |
| 2391-1 | 8.35 | -103.86 | A-B | 7.95 | 47 | 70 | 20 | 2.7 | 86 | 0.9 | 89 | 33 | 80 | 80 | 305 | 301 | 26 | 8500 | 42.2 | 600 |
| 2391-5 | 8.34 | -103.87 | A-B | | | | | | | 0.7 | 97 | 19 | | 78 | | | | | | |
| 2391-9wr | 8.33 | -103.88 | A-B | | | | | | | | 101 | 21 | | 71 | | | | | | |
| D1-3 | 8.34 | -103.54 | B | 8.04 | 45 | 80 | 18 | 3.2 | 87 | 0.7 | 100 | 32 | 110 | 87 | 280 | 396 | 17 | 8200 | 53.8 | 600 |
| D1-5 | 8.34 | -103.54 | B | 8.07 | 44 | 76 | 19 | 2.6 | 81 | 0.6 | 99 | 32 | 74 | 86 | 282 | 380 | 22 | 8100 | 40.8 | 600 |
| D18-1WR | 8.32 | -103.62 | BW | | | | | | | 4.7 | 128 | 38 | | 138 | | | | | | |
| D18-2 | 8.32 | -103.62 | BW | | | | | | | 2.1 | 128 | 42 | | 130 | | | | | | |
| D18-3 | 8.32 | -103.62 | BW | 6.72 | 48 | 72 | 20 | 4.5 | 30 | 2.5 | 125 | 40 | 91 | 128 | 334 | 21 | 40 | 11200 | 49.4 | 1200 |
| D18-4 | 8.32 | -103.62 | BW | 6.64 | | | | | | 1.4 | 126 | 42 | | 132 | | | | | | |
| D18-5 | 8.32 | -103.62 | BW | | | | | | | 1.2 | 127 | 42 | | 130 | | | | | | |
| D19-1 | 8.31 | -103.64 | BW | | 47 | 74 | 22 | 4.2 | 24 | 1.3 | 126 | 40 | 89 | 126 | 340 | 182 | 38 | 11100 | 54.3 | 1200 |
| D19-2 | 8.31 | -103.64 | BW | 7.02 | 48 | 70 | 21 | 4.5 | 31 | 1.1 | 112 | 40 | 89 | 120 | 348 | 194 | 37 | 11200 | 48.6 | 1000 |
| D19-5wr | 8.31 | -103.64 | BW | | | | | 3.3 | | 3.7 | 109 | 32 | | 104 | | | | | | |
| D20-1 | 8.37 | -103.66 | A-B | 10.01 | 66 | 68 | 13 | 1.0 | 727 | 1.8 | 66 | 19 | 60 | 47 | | | | | | |
| D20-15 | 8.37 | -103.66 | A-B | 9.89 | 71 | 62 | 13 | 0.8 | 871 | | 60 | 16 | 59 | 43 | 164 | 1326 | 39 | 4600 | 56.5 | 100 |
| D22-1 | 8.37 | -103.66 | A-B | | 47 | 71 | 17 | 1.5 | 277 | 1.7 | 88 | 24 | 64 | 68 | 229 | 586 | 7 | 6800 | 31.2 | 200 |
| D23-2 | 8.38 | -103.67 | A-B | 9.42 | 49 | 74 | 17 | 2.1 | 282 | 1.9 | 89 | 25 | 68 | 69 | | | | | | |
| D26-6 | 8.44 | -103.36 | C | 7.04 | 48 | 76 | 20 | 3.0 | 33 | 2.0 | 116 | 35 | 84 | 103 | 282 | 186 | 29 | 9700 | 45.7 | 1000 |
| D27-5 | 8.44 | -103.29 | C-D | 9.41 | 46 | 76 | 17 | 2.5 | 204 | 0.2 | 87 | 27 | 68 | 67 | 237 | 485 | 14 | 6800 | 32.1 | 300 |
| D30-1 | 8.43 | -103.91 | E-RTI | 7.35 | 46 | 72 | 20 | 3.3 | 60 | 1.4 | 113 | 39 | 86 | 116 | 347 | 347 | 25 | 10800 | 47.4 | 700 |
| D32-1 | 8.38 | -103.29 | C | 7.69 | 48 | 75 | 19 | 2.3 | 24 | 1.6 | 99 | 32 | 78 | 89 | 290 | 187 | 18 | 8500 | 42.5 | 500 |
| D32-3 | 8.38 | -103.29 | C | 7.34 | 47 | 74 | 20 | 2.9 | 47 | 1.3 | 110 | 34 | 85 | 96 | 297 | 298 | 25 | 9100 | 19.0 | 700 |
| D33-1 | 8.39 | -103.26 | C | | 48 | 77 | 19 | 3.5 | 34 | 1.0 | 98 | 32 | 82 | 87 | | | | | | |
| D34-2 | 8.39 | -103.17 | C-D | 9.12 | 45 | 75 | 14 | 3.0 | 173 | 1.2 | 111 | 21 | 60 | 62 | 210 | 451 | 11 | 5400 | 28.0 | 600 |
| D35-3 | 8.38 | -103.81 | A | 7.77 | 47 | 67 | 19 | 3.3 | 93 | 1.1 | 113 | 41 | 84 | 127 | 314 | 336 | 23 | 10600 | 41.7 | 900 |
| D35-4 | 8.38 | -103.81 | A | 7.88 | 47 | 66 | 18 | 2.7 | 114 | 0.9 | 120 | 41 | 80 | 126 | 302 | 396 | 29 | 10400 | 38.2 | 800 |
| D36-3 | 8.41 | -103.76 | A | 8.39 | 45 | 75 | 19 | 2.6 | 95 | 0.3 | 89 | 30 | 72 | 78 | 264 | 393 | 23 | 7300 | 39.6 | 600 |
| D38-1 | 8.37 | -103.92 | A | 8.78 | 47 | 85 | 19 | 2.0 | 91 | 0.6 | 85 | 28 | 72 | 72 | 257 | 409 | 16 | 6900 | 37.1 | 400 |
| D38-2 | 8.37 | -103.92 | A | 7.66 | 46 | 66 | 20 | 3.1 | 83 | 1.3 | 102 | 38 | 87 | 108 | 339 | 326 | 28 | 10300 | 52.5 | 800 |

Table D-1. Continued.

| Sample # | Dec. Lat. | Dec. Long. | Location | MgO (wt.%) | Co | Cu | Ga | Nb | Ni | Rb | Sr | Y | Zn | Zr | V | Cr | Ba | Ti | Sc | K |
|---|---|---|---|---|---|---|---|---|---|---|---|---|---|---|---|---|---|---|---|---|
| **XRF analysis (ppm)** | | | | | | | | | | | | | | | | | | | | |
| D4-3 | 8.38 | -103.51 | B | | | | | | | 0.6 | 104 | 36 | | 99 | | | | | | |
| D44-1 | 8.38 | -103.11 | D | 7.99 | 47 | 84 | 18 | 2.2 | 34 | 2.1 | 101 | 25 | 40 | 74 | 258 | 428 | 16 | 6700 | 38.7 | 500 |
| D4-6 | 8.38 | -103.51 | B | 7.49 | 46 | 73 | 18 | 2.3 | 43 | 2.4 | 106 | 35 | 84 | 100 | 323 | 287 | 26 | 9500 | 50.0 | 800 |
| D5-5 | 8.39 | -103.46 | B | | | | | | | 1.6 | 123 | 37 | | 111 | | | | | | |
| D6-1 | 8.40 | -103.44 | BE | 8.03 | 52 | 82 | 24 | 2.5 | 132 | 1.2 | 106 | 30 | 78 | 91 | 270 | 351 | 36 | 8200 | 39.6 | 600 |
| D8-1wr | 8.33 | -103.60 | BW | | | | | | | 2.4 | 122 | 34 | | 118 | | | | | | |

* Locations A = spreading center A, A-B = fault separating spreading centers A and B, B = spreading center B, B-C = fault separating spreading centers B and C, C = spreading center C, C-D = fault separating spreading center C and trough D, D = trough D, WRTI = western ridge transform intersection, ERTI = eastern ridge transform intersection. $^{\mu}$XRF whole rock and glass powders analyzed at the University of Florida. MgO values from Table C-1.

Table D-2. ICP Trace element concentrations for the Siqueiros transform basalts.

| Sample # | Dec. Lat. | Dec. Long. | Location* | MgO wt. % | La | Ce | Nd | Sm | Eu | Gd | Dy | Y | Er | Yb | Lu | Sc | (Ce/Yb)n |
|---|---|---|---|---|---|---|---|---|---|---|---|---|---|---|---|---|---|
| **ICP Analysis (ppm)[μ]** | | | | | | | | | | | | | | | | | |
| 2375-7 | 8.34 | -103.54 | BW | 8.03 | 2.53 | 8.61 | 8.17 | 2.79 | 1.05 | 3.64 | | 30.8 | | 2.77 | | 36.2 | 0.86 |
| 2375-9 | 8.34 | -103.53 | BW | 7.61 | 2.67 | 8.84 | 8.77 | 2.89 | 1.12 | 4.33 | | 33.2 | | 3.16 | | 40.3 | 0.78 |
| 2376-3 | 8.37 | -103.52 | BS | 7.85 | 3.44 | 10.81 | 9.98 | 3.25 | 1.19 | 4.55 | | 34.0 | | 3.17 | | 36.0 | 0.95 |
| 2376-7 | 8.35 | -103.52 | BE | 8.4 | 3.36 | 10.67 | 9.4 | 3.2 | 1.19 | 4.7 | | 34.6 | | 3.27 | | 37.3 | 0.91 |
| 2376-8 | 8.35 | -103.52 | BS | 8.02 | 3.7 | 11.94 | 10.95 | 3.63 | 1.28 | 5.1 | | 38.0 | | 3.56 | | 34.8 | 0.93 |
| 2377-11 | 8.36 | -103.52 | BN | 7.14 | 5.73 | 17.54 | 15.86 | 5.24 | 1.68 | 7.32 | | 54.2 | | 5.08 | | 39.0 | 0.96 |
| 2377-3 | 8.39 | -103.52 | BN | 7.72 | 3.42 | 11.05 | 10.05 | 3.48 | 1.23 | 4.91 | | 37.1 | | 3.54 | | 36.4 | 0.87 |
| 2378-2 | 8.32 | -103.31 | CW | 8.43 | 2.19 | 7.63 | 7.21 | 2.34 | 0.98 | 3.94 | | 31.0 | | 2.94 | | 41.2 | 0.72 |
| 2378-6 | 8.35 | -103.32 | CW | | 2.34 | 7.86 | 7.88 | 2.71 | 1.08 | 4.14 | | 31.4 | | 2.99 | | 42.0 | 0.73 |
| 2378-7 | 8.35 | -103.32 | CW | 7.76 | 2.65 | 8.45 | 7.91 | 2.58 | 1.14 | 4.04 | | 31.8 | | 3.01 | | 40.2 | 0.78 |
| 2379-2WR | 8.39 | -103.60 | A-B | | 3.11 | 10.26 | 9.18 | 3.26 | 1.39 | 4.95 | | 38.7 | | 3.94 | | 41.7 | 0.72 |
| 2380-11 | 8.36 | -103.51 | BE | 7.45 | 4.77 | 14.82 | 13.58 | 4.4 | 1.47 | 6.34 | | 46.8 | | 4.52 | | 37.8 | 0.91 |
| 2380-4 | 8.34 | -103.50 | BE | 7.56 | 3.11 | 10.66 | 8.9 | 2.93 | 1.1 | 4.43 | | 34.1 | | 3.2 | | 36.5 | 0.93 |
| 2380-7 | 8.36 | -103.51 | BE | | 3.57 | 12.34 | 10.99 | 3.66 | 1.39 | 5.1 | 6.34 | 39.9 | 4.22 | 3.8 | 0.59 | 44.0 | 0.90 |
| 2381-11 | 8.34 | -103.44 | B-C | 7.76 | 1.94 | 7.02 | 7.21 | 2.05 | 1 | 3.67 | | 29.2 | | 2.77 | | 41.8 | 0.70 |
| 2381-3AWR | 8.35 | -103.42 | B-C | | 1.41 | 5.87 | 5.75 | 2.03 | 0.89 | 3.15 | | 25.1 | | 2.4 | | 35.2 | 0.68 |
| 2382-10WR | 8.30 | -103.55 | B (SW) | | 0.84 | 3.34 | 3.23 | 1.06 | 0.45 | 1.64 | | 13.3 | | 1.27 | | 18.0 | 0.73 |
| 2382-7 | 8.32 | -103.55 | B (SW) | 7.39 | 3.53 | 11.39 | 10.7 | 3.62 | 1.32 | 5.09 | | 38.2 | | 3.61 | | 42.0 | 0.88 |
| 2383-2 | 8.36 | -103.83 | A | 7.52 | 2.31 | 8.53 | 7.61 | 2.32 | 1.05 | 3.95 | | 32.0 | | 2.98 | | 38.9 | 0.80 |
| 2383-6 | 8.37 | -103.84 | A | 8.89 | 1.69 | 6.12 | 6 | 2.18 | 0.92 | 3.46 | | 27.5 | | 2.63 | | 39.0 | 0.65 |
| 2384-1 | 8.38 | -103.66 | A-B | 9.6 | 0.81 | 3.36 | 4.14 | 1.81 | 0.64 | 2.51 | | 18.9 | | 1.76 | | 25.3 | 0.53 |
| 2384-11 | 8.38 | -103.68 | A-B | 8.79 | 1.56 | 5.97 | 6.55 | 2.39 | 0.95 | 3.64 | | 27.9 | | 2.61 | | 34.4 | 0.64 |
| 2384-3 | 8.37 | -103.66 | A-B | 10.12 | 1.11 | 4.86 | 5.26 | 2.08 | 0.81 | 2.83 | 3.54 | 22.2 | 2.39 | 2.07 | 0.33 | 29.0 | 0.65 |
| 2384-9 | 8.38 | -103.67 | A-B | 9.73 | 0.98 | 4.53 | 5.04 | 1.95 | 0.68 | 2.95 | | 22.7 | | 2.13 | | 29.0 | 0.59 |
| 2385-2 | 8.36 | -103.32 | C | 8.21 | 1.72 | 6.31 | 6.77 | 2.32 | 0.95 | 3.57 | | 28.1 | | 2.62 | | 42.3 | 0.67 |
| 2385-6T | 8.36 | -103.31 | C | 7.91 | 1.97 | 6.97 | 6.97 | 2.46 | 1.04 | 3.79 | | 30.0 | | 2.82 | | 41.5 | 0.69 |
| 2386-5 | 8.36 | -103.13 | D | 8.23 | 1.32 | 6.33 | 4.85 | 1.58 | 0.51 | 2.63 | | 23.4 | | 2.28 | | 37.8 | 0.77 |
| 2387-1 | 8.35 | -103.41 | B-C (e) | | 1.75 | 6.62 | 6.94 | 2.23 | 0.95 | 3.46 | | 26.7 | | 2.45 | | 30.3 | 0.75 |
| 2387-6 | 8.36 | -103.38 | B-C (e) | 7.44 | 1.8 | 6.89 | 7.42 | 2.57 | 1.09 | 3.97 | | 30.7 | | 2.89 | | 37.4 | 0.66 |
| 2388-1 | 8.35 | -103.78 | A-B | | 1.32 | 5.31 | 4.65 | 1.68 | 0.89 | 2.61 | 3.49 | 21.9 | 2.4 | 2.32 | 0.37 | 42.7 | 0.64 |

Table D-2. Continued.

| Sample # | Dec. Lat. | Dec. Long. | Location* | MgO wt. % | La | Ce | Nd | Sm | Eu | Gd | Dy | Y | Er | Yb | Lu | Sc | (Ce/Yb)n |
|---|---|---|---|---|---|---|---|---|---|---|---|---|---|---|---|---|---|
| **ICP Analysis (ppm)[µ]** | | | | | | | | | | | | | | | | | |
| 2388-14 | 8.38 | -103.76 | A-B | | 1.16 | 4.59 | 3.99 | 1.51 | 0.75 | 2.45 | 3.43 | 22.0 | 2.4 | 2.28 | 0.34 | 40.2 | 0.56 |
| 2388-7 | 8.37 | -103.77 | A-B | | 0.78 | 3.7 | 3.69 | 1.59 | 0.8 | 2.44 | 3.25 | 20.5 | 2.23 | 2.05 | 0.31 | 38.7 | 0.50 |
| 2389-1 | 8.39 | -103.95 | A | 7.35 | 2.35 | 8.26 | 8.33 | 3.03 | 1.18 | 4.88 | | 37.6 | | 3.6 | | 37.5 | 0.64 |
| 2390-1 | 8.30 | -104.02 | W-RTI | 6.37 | 11.58 | 27.37 | 14.85 | 3.77 | 1.31 | 4.79 | | 31.1 | | 2.78 | | 25.6 | 2.73 |
| 2390-3A | 8.29 | -104.03 | W-RTI | | 13.25 | 32.09 | 19.9 | 4.86 | 1.69 | 5.55 | 5.94 | 35.9 | 3.66 | 3.26 | 0.49 | 30.6 | 2.73 |
| 2390-4 | 8.30 | -104.03 | W-RTI | | 13.72 | 32.21 | 20.42 | 5.08 | 1.71 | 5.64 | 6.11 | 36.6 | 3.75 | 3.31 | 0.5 | 31.3 | 2.70 |
| 2390-5 | 8.31 | -104.04 | W-RTI | | 14.17 | 33.15 | 20.06 | 5.03 | 1.75 | 5.54 | 5.83 | 35.0 | 3.6 | 3.12 | 0.47 | 29.1 | 2.95 |
| 2390-7 | 8.31 | -104.05 | W-RTI | | 3.91 | 13.05 | 11.41 | 3.69 | 1.38 | 4.86 | 5.88 | 36.6 | 3.97 | 3.45 | 0.53 | 40.3 | 1.05 |
| 2390-8 | 8.32 | -104.06 | W-RTI | | 14.34 | 33.47 | 20.47 | 5.3 | 1.76 | 5.73 | 6.05 | 36.3 | 3.79 | 3.28 | 0.49 | 30.3 | 2.83 |
| 2390-9 | 8.32 | -104.06 | W-RTI | 5.54 | 7.19 | 21.46 | 18.62 | 5.96 | 2.05 | 8.18 | | 59.8 | | 5.73 | | 42.2 | 1.04 |
| 2391-10wr | 8.32 | -103.88 | A-B | | 0.79 | 3.43 | 2.88 | 1.16 | 0.65 | 1.9 | 2.57 | 16.3 | 1.81 | 1.69 | 0.26 | 40.2 | 0.56 |
| 2391-5 | 8.34 | -103.87 | A-B | | 0.86 | 3.66 | 3.17 | 1.21 | 0.65 | 2.07 | 3.02 | 19.2 | 2.14 | 2.07 | 0.31 | 40.6 | 0.49 |
| 2391-9wr | 8.33 | -103.88 | A-B | | 1.29 | 5.23 | 4.91 | 1.73 | 0.81 | 2.69 | 3.55 | 22.0 | 2.38 | 2.14 | 0.32 | 44.3 | 0.68 |
| D1-5 | 8.34 | -103.54 | B | 8.07 | 2.51 | 8.59 | 8.4 | 2.66 | 1.1 | 4.14 | | 32.2 | | 3.06 | | 39.2 | 0.78 |
| D17-1WR | 8.40 | -103.60 | A-B | | 2.8 | 9.4 | 9.19 | 2.88 | 1.16 | 4.54 | | 34.5 | | 3.32 | | 38.3 | 0.79 |
| D18-1WR | 8.32 | -103.62 | BW | | 3.22 | 10.61 | 10.28 | 3.25 | 1.34 | 5.09 | | 38.0 | | 3.61 | | 41.5 | 0.82 |
| D18-3 | 8.32 | -103.62 | BW | 6.72 | 4.59 | 14.01 | 12.63 | 3.83 | 1.5 | 5.62 | | 41.6 | | 3.96 | | 42.8 | 0.98 |
| D19-1 | 8.31 | -103.64 | BW | | 4.21 | 13.28 | 11.54 | 3.39 | 1.24 | 5.45 | | 39.9 | | 3.73 | | 41.5 | 0.99 |
| D19-2 | 8.31 | -103.64 | BW | 7.02 | 3.45 | 11.59 | 10.13 | 3.43 | 1.3 | 5.11 | | 39.1 | | 3.63 | | 40.3 | 0.89 |
| D20-1 | 8.37 | -103.66 | A-B | 10.01 | 0.77 | 3.67 | 4.3 | 1.67 | 0.69 | 2.56 | | 19.5 | | 1.8 | | 25.4 | 0.57 |
| D20-15 | 8.37 | -103.66 | A-B | 9.89 | 0.77 | 3.47 | 4.04 | 1.72 | 0.67 | 2.55 | | 18.5 | | 1.74 | | 25.1 | 0.55 |
| D20-5 | 8.37 | -103.66 | A-B | | 1.2 | 5.2 | 5 | 2 | 0.86 | 2.9 | 3.5 | 23.0 | 2.3 | 2.1 | 0.32 | 30.0 | 0.69 |
| D22-1 | 8.37 | -103.66 | A-B | | 1.4 | 5.51 | 6.37 | 2.11 | 0.93 | 3.42 | | 26.4 | | 2.46 | | 32.3 | 0.62 |
| D22-3 | 8.37 | -103.66 | A-B | 9.47 | 1.38 | 5.51 | 6.47 | 2.25 | 0.89 | 3.44 | | 26.5 | | 2.45 | | 32.6 | 0.62 |
| D23-2 | 8.38 | -103.67 | A-B | 9.42 | 1.43 | 5.55 | 6.56 | 2.37 | 0.96 | 3.57 | | 26.8 | | 2.53 | | 33.2 | 0.61 |
| D25-6 | 8.39 | -103.41 | CW | 7.37 | 3.26 | 10.9 | 10.25 | 3.06 | 1.29 | 4.76 | | 36.0 | | 3.4 | | 42.2 | 0.89 |
| D27-5 | 8.44 | -103.29 | C-D | 9.41 | 1.9 | 6.3 | 6.63 | 2.28 | 1.03 | 3.67 | | 27.5 | | 2.7 | | 34.9 | 0.65 |
| D30-1 | 8.43 | -103.91 | E-RTI | 7.35 | 3.52 | 11.41 | 10.31 | 3.29 | 1.43 | 5.16 | | 40.1 | | 3.87 | | 41.9 | 0.82 |
| D32-1 | 8.38 | -103.29 | CE | 7.69 | 2.54 | 8.13 | 7.75 | 2.75 | 1.19 | 4.26 | | 32.5 | | 3.21 | | 42.4 | 0.70 |
| D32-3 | 8.38 | -103.29 | CE | 7.34 | 2.87 | 9.43 | 9.32 | 2.78 | 1.24 | 4.55 | | 34.5 | | 3.4 | | 41.2 | 0.77 |

Table D-2. Continued.

| Sample # | Dec. Lat. | Dec. Long. | Location* | MgO wt. % | La | Ce | Nd | Sm | Eu | Gd | Dy | Y | Er | Yb | Lu | Sc | (Ce/Yb)n |
|---|---|---|---|---|---|---|---|---|---|---|---|---|---|---|---|---|---|
| **ICP Analysis (ppm)[μ]** | | | | | | | | | | | | | | | | | |
| D33-1 | 8.39 | -103.26 | CE | | 2.28 | 8.05 | 7.94 | 2.78 | 1.12 | 4.23 | | 32.5 | | 3.05 | | 41.6 | 0.73 |
| D34-2 | 8.39 | -103.17 | C-D | 9.12 | 2.21 | 6.78 | 5.88 | 1.75 | 0.82 | 2.94 | | 22.4 | | 2.2 | | 34.5 | 0.86 |
| D35-4 | 8.38 | -103.81 | AE | 7.88 | 3.77 | 12.52 | 11.63 | 3.71 | 1.38 | 5.43 | | 40.2 | | 3.81 | | 38.6 | 0.91 |
| D36-3 | 8.41 | -103.76 | AE | 8.39 | 2.29 | 7.63 | 7.36 | 2.56 | 1.01 | 3.93 | | 30.8 | | 2.92 | | 38.4 | 0.73 |
| D38-2 | 8.37 | -103.92 | A | 7.66 | 3.28 | 10.67 | 10.44 | 3.29 | 1.26 | 5.08 | | 39.4 | | 3.71 | | 40.3 | 0.80 |
| D44-1 | 8.38 | -103.11 | DW | 7.99 | 2.03 | 7.13 | 6.61 | 2.13 | 0.91 | 3.37 | | 26.7 | | 2.53 | | 40.6 | 0.78 |
| D4-6 | 8.38 | -103.51 | B | 7.49 | 3.08 | 10.07 | 9.96 | 3.28 | 1.28 | 5.03 | | 37.5 | | 3.55 | | 42.9 | 0.79 |
| D6-1 | 8.40 | -103.44 | BE | 8.03 | 2.89 | 9.02 | 7.35 | 2.27 | 0.94 | 3.9 | | 29.1 | | 2.77 | | 35.6 | 0.90 |
| D8-1wr | 8.33 | -103.60 | BW | | 2.47 | 8.62 | 8.72 | 2.85 | 1.27 | 4.56 | | 14.8 | | 3.42 | | 44.4 | 0.70 |

*Locations same as Table D-1. [μ]ICP-MS analysis completed at the University of Houston by Dr. Jack Casey.
MgO values from Table C-1.

Table D-3. DCP trace element concentrations for the Siqueiros transform basalts.

| Sample # | Dec. Lat. | Dec. Long | Location* | MgO wt.% | $TiO_2$ wt.% | $K_2O$ wt% | Mn | Ba | Cr | Cu | Ni | Sc | Sr | V | Y | Zr |
|---|---|---|---|---|---|---|---|---|---|---|---|---|---|---|---|---|
| **DCP Analysis (ppm)$^{\mu}$** | | | | | | | | | | | | | | | | |
| 2384-1 | 8.38 | -103.66 | A-B | 12.78 | 0.93 | 0.04 | 0.15 | 2 | 1659 | 80 | 338 | 31 | 73 | 193 | 23 | 51 |
| 2384-3 | 8.37 | -103.66 | A-B | 10.49 | 1.00 | 0.03 | 0.15 | 2 | 498 | 82 | 216 | 32 | 79 | 207 | 25 | 56 |
| 2384-7B | 8.38 | -103.67 | A-B | 10.63 | 0.90 | 0.04 | 0.15 | 1 | 647 | 88 | 215 | 30 | 76 | 203 | 23 | 51 |
| 2384-8 | 8.38 | -103.67 | A-B | 10.34 | 1.04 | 0.04 | 0.15 | 1 | 635 | 78 | 203 | 32 | 81 | 217 | 25 | 60 |
| 2390-5 | 8.31 | -104.04 | W-RTI | 7.74 | 2.02 | 0.64 | 0.16 | 141 | 219 | 55 | 123 | 29 | 318 | 263 | 34 | 177 |
| D20-13 | 8.37 | -103.66 | A-B | 10.60 | 0.95 | 0.03 | 0.14 | 2 | 640 | 83 | 214 | 32 | 77 | 225 | 25 | 52 |
| D20-15 | 8.37 | -103.66 | A-B | 11.24 | 1.00 | 0.04 | 0.15 | 12 | 601 | 90 | 229 | 33 | 82 | 216 | 27 | 58 |
| D20-5 | 8.37 | -103.66 | A-B | 10.63 | 0.93 | 0.03 | 0.14 | 3 | 534 | 85 | 218 | 31 | 75 | 216 | 3 | 54 |
| RC-41 | | | E-RTI | 8.00 | 1.46 | 0.08 | 0.18 | 5 | 303 | 79 | 88 | 41 | 114 | 300 | 33 | 101 |

*Locations same as Table D-1. $^{\mu}$DCP analysis completed on phenocrysts-free samples at Lamont Doherty Earth Observatory. MgO values from Table C-1.

Table D-4. ICP trace element concentrations of the Siqueiros transform basalts.

| Sample | 2375-7G | 2376-3G | 2376-5 | 2376-5G | 2376-7G | 2376-8G | 2377-1G | 2377-10 | 2377-10G |
|---|---|---|---|---|---|---|---|---|---|
| Location* | B | B | B | B | B | B | B | B | B |
| ICP Trace Element Analysis (ppm)[µ] | | | | | | | | | |
| Ag | 0.10 | 0.10 | ND | ND | ND | 0.20 | 0.30 | 0.10 | ND |
| Ba | ND | ND | ND | ND | ND | ND | ND | ND | ND |
| Be | ND | ND | ND | ND | ND | ND | ND | ND | ND |
| Bi | ND | ND | ND | ND | ND | ND | 0.2 | ND | ND |
| Cd | 1.1 | ND | ND | 0.2 | 0.3 | 0.5 | 0.5 | 0.2 | 0.2 |
| Cl | 207 | ND | 700 | 1036 | 117 | 2008 | 887 | 826 | ND |
| Co | 38 | 36 | 37 | 37 | 38 | 33 | 38 | 35 | 35 |
| Cr | 334 | 331 | 348 | 349 | 327 | 289 | 341 | 266 | 269 |
| Cs | ND | ND | ND | ND | ND | ND | ND | ND | ND |
| Cu | 77 | 72 | 76 | 75 | 73 | 60 | 79 | 61 | 61 |
| F | 123 | ND | 126 | 127 | 136 | 137 | 113 | 182 | ND |
| Ga | 16 | 16 | 16 | 16 | 16 | 16 | 15 | 19 | 17 |
| Hf | 2.30 | 2.60 | 2.40 | 2.40 | 2.60 | 3.10 | 2.10 | 3.50 | 3.30 |
| In | 0.09 | ND | 0.08 | ND | ND | 0.07 | 0.36 | 0.08 | ND |
| Mo | ND | 0.2 | ND | 0.2 | 0.3 | 0.4 | 0.4 | 0.3 | 0.3 |
| Nb | 2.00 | 2.60 | 2.30 | 2.40 | 2.60 | 2.60 | 2.50 | 3.50 | 3.50 |
| Ni | 85 | 106 | 108 | 113 | 101 | 105 | 92 | 91 | 92 |
| Rb | 0.59 | 0.77 | 0.83 | 0.60 | 0.81 | 1.10 | 1.10 | 1.20 | 1.10 |
| Sb | ND | ND | ND | ND | ND | ND | ND | ND | ND |
| Sc | 37 | 33 | 33 | 33 | 33 | 30 | 33 | 35 | 35 |
| Sn | 0.80 | 1.00 | 1.30 | 0.70 | 0.90 | 1.20 | 1.10 | 1.10 | 1.00 |
| Sr | 95 | 109 | 108 | 109 | 106 | 115 | 90 | 109 | 111 |
| Ta | 0.13 | 0.20 | 0.16 | 0.18 | 0.21 | 0.19 | 0.14 | 0.25 | 0.24 |
| Te | ND | ND | ND | ND | ND | ND | ND | ND | ND |
| Th | 0.12 | 0.16 | 0.14 | 0.14 | 0.16 | 0.15 | 0.12 | 0.21 | 0.2 |
| Tl | ND | ND | ND | ND | ND | ND | ND | ND | ND |
| U | 0.05 | 0.07 | 0.06 | 0.06 | 0.07 | 0.08 | 0.06 | 0.09 | 0.09 |
| V | 281 | 259 | 257 | 258 | 273 | 255 | 259 | 319 | 318 |
| Zn | 71 | 70 | 68 | 67 | 71 | 72 | 67 | 85 | 84 |
| Zr | 84 | 97 | 93 | 90 | 100 | 121 | 77 | 134 | 130 |
| Ce | 8.50 | 10.38 | 9.43 | 9.36 | 10.20 | 10.98 | 7.83 | 14.09 | 13.78 |
| Dy | 5.09 | 5.22 | 4.98 | 4.89 | 5.43 | 5.49 | 4.69 | 7.04 | 6.92 |
| Er | 3.03 | 3.05 | 2.87 | 2.79 | 3.13 | 3.20 | 2.73 | 4.08 | 4.12 |
| Eu | 1.10 | 1.17 | 1.12 | 1.08 | 1.19 | 1.20 | 1.04 | 1.45 | 1.47 |
| Gd | 4.44 | 4.57 | 4.27 | 4.26 | 4.74 | 4.86 | 4.08 | 6.23 | 6.16 |
| Ho | 1.11 | 1.11 | 1.05 | 1.04 | 1.16 | 1.18 | 1.00 | 1.49 | 1.50 |
| La | 2.61 | 3.34 | 3.02 | 2.97 | 3.21 | 3.43 | 2.64 | 4.40 | 4.40 |
| Lu | 0.48 | 0.48 | 0.45 | 0.46 | 0.50 | 0.52 | 0.44 | 0.68 | 0.67 |
| Nd | 8.35 | 9.65 | 8.93 | 8.60 | 9.44 | 9.84 | 7.63 | 12.56 | 12.45 |
| Pr | 1.52 | 1.78 | 1.60 | 1.59 | 1.72 | 1.86 | 1.37 | 2.35 | 2.31 |
| Sm | 3.07 | 3.30 | 3.17 | 2.98 | 3.35 | 3.41 | 2.86 | 4.34 | 4.48 |
| Tb | 0.82 | 0.83 | 0.78 | 0.77 | 0.86 | 0.87 | 0.73 | 1.12 | 1.12 |
| Tm | 0.48 | 0.49 | 0.46 | 0.46 | 0.50 | 0.52 | 0.44 | 0.66 | 0.68 |
| Y | 31.1 | 31.8 | 29.3 | 29.5 | 31.9 | 33.5 | 27.5 | 42.4 | 42.1 |
| Yb | 3.25 | 3.21 | 2.95 | 2.94 | 3.30 | 3.29 | 2.84 | 4.30 | 4.41 |
| (Ce/Yb)n | 0.73 | 0.90 | 0.89 | 0.89 | 0.86 | 0.93 | 0.77 | 0.91 | 0.87 |

Table D-4. Continued.

| Sample | 2377-3G | 2377-52 | 2377-6 | 2377-8G | 2378-2G | 2378-3 | 2378-3G | 2378-8 | 2378-8G | 2380-11G |
|---|---|---|---|---|---|---|---|---|---|---|
| **Location*** | B | B | B | B | C | C | C | C | C | B |
| **ICP Trace Element Analysis (ppm)[µ]** | | | | | | | | | | |
| **Ag** | 0.10 | 0.20 | 0.30 | ND | 0.10 | ND | ND | ND | ND | ND |
| **Ba** | ND | ND | ND | ND | ND | ND | ND | ND | ND | ND |
| **Be** | ND | 0.5 | ND | ND | ND | ND | ND | ND | ND | 0.50 |
| **Bi** | ND | ND | ND | ND | ND | ND | ND | ND | ND | ND |
| **Cd** | 0.3 | 0.6 | ND | ND | 0.20 | ND | ND | 0.20 | 0.30 | 1.20 |
| **Cl** | 1453 | ND | 557 | ND | ND | ND | ND | 165 | 223 | ND |
| **Co** | 31 | 33 | 35 | 36 | 39 | 39 | 39 | 37 | 37 | 35 |
| **Cr** | 283 | 259 | 285 | 309 | 319 | 328 | 333 | 393 | 399 | 254 |
| **Cs** | ND | ND | ND | ND | ND | ND | ND | ND | ND | ND |
| **Cu** | 62 | 53 | 57 | 65 | 83 | 83 | 86 | 93 | 93 | 59 |
| **F** | 137 | ND | 176 | ND | 112 | 114 | 115 | 96 | 93 | ND |
| **Ga** | 16 | 19 | 19 | 17 | 16 | 15 | 16 | 14 | 15 | 17 |
| **Hf** | 2.60 | 4.10 | 3.40 | 2.80 | 2.10 | 2.10 | 2.20 | 1.70 | 1.80 | 3.60 |
| **In** | ND | 0.09 | ND | ND | ND | ND | ND | ND | ND | 0.13 |
| **Mo** | ND | 0.4 | ND | ND | ND | ND | ND | ND | ND | 0.70 |
| **Nb** | 2.40 | 3.80 | 3.50 | 3.00 | 1.90 | 2.00 | 2.00 | 0.95 | 0.96 | 3.80 |
| **Ni** | 81 | 95 | 92 | 106 | 42 | 46 | 47 | 73 | 73 | 89 |
| **Rb** | 0.89 | 1.60 | 1.40 | 1.10 | 0.79 | 0.87 | 0.74 | 0.34 | 0.49 | 1.50 |
| **Sb** | ND | ND | ND | ND | ND | ND | ND | ND | ND | ND |
| **Sc** | 31 | 34 | 34 | 35 | 39 | 38 | 39 | 39 | 39 | 35 |
| **Sn** | 2.80 | 1.60 | 1.50 | 1.20 | 1.00 | 1.00 | 0.80 | ND | 1.00 | 1.90 |
| **Sr** | 108 | 111 | 107 | 109 | 92 | 91 | 93 | 92 | 91 | 112 |
| **Ta** | 0.17 | 0.25 | ND | ND | 0.13 | 0.16 | 0.14 | 0.19 | 0.11 | 0.26 |
| **Te** | ND | ND | ND | ND | ND | ND | ND | ND | ND | ND |
| **Th** | 0.15 | 0.24 | ND | ND | 0.11 | 0.11 | 0.11 | 0.06 | 0.06 | 0.22 |
| **Tl** | ND | ND | ND | ND | ND | ND | ND | ND | ND | ND |
| **U** | 0.06 | 0.11 | ND | ND | 0.05 | 0.05 | 0.05 | 0.03 | 0.03 | 0.10 |
| **V** | 264 | 319 | 320 | 303 | 282 | 276 | 281 | 237 | 236 | 321 |
| **Zn** | 68 | 90 | 83 | 78 | 72 | 70 | 72 | 70 | 59 | 86 |
| **Zr** | 99 | 154 | 132 | 110 | 76 | 76 | 81 | 62 | 68 | 138 |
| **Ce** | 10.14 | 16.07 | 13.83 | 12.41 | 7.86 | 7.88 | 7.80 | 5.54 | 5.58 | 14.61 |
| **Dy** | 5.53 | 7.89 | 6.67 | 6.20 | 4.87 | 4.83 | 4.90 | 4.04 | 3.96 | 7.13 |
| **Er** | 3.18 | 4.60 | 3.91 | 3.59 | 2.85 | 2.80 | 2.88 | 2.43 | 2.35 | 4.24 |
| **Eu** | 1.18 | 1.62 | 1.38 | 1.32 | 1.08 | 1.07 | 1.08 | 0.94 | 0.92 | 1.50 |
| **Gd** | 4.85 | 7.02 | 5.97 | 5.43 | 4.24 | 4.14 | 4.14 | 3.47 | 3.41 | 6.27 |
| **Ho** | 1.19 | 1.70 | 1.44 | 1.32 | 1.08 | 1.03 | 1.05 | 0.87 | 0.86 | 1.55 |
| **La** | 3.16 | 4.92 | 4.29 | 3.94 | 2.39 | 2.37 | 2.36 | 1.54 | 1.55 | 4.62 |
| **Lu** | 0.51 | 0.74 | 0.62 | 0.58 | 0.47 | 0.44 | 0.45 | 0.38 | 0.38 | 0.67 |
| **Nd** | 9.55 | 14.46 | 12.37 | 10.72 | 7.65 | 7.83 | 7.94 | 6.30 | 6.18 | 13.09 |
| **Pr** | 1.78 | 2.66 | 2.31 | 2.07 | 1.39 | 1.41 | 1.42 | 1.08 | 1.07 | 2.40 |
| **Sm** | 3.38 | 5.10 | 4.32 | 3.84 | 2.88 | 2.82 | 2.79 | 2.37 | 2.37 | 4.59 |
| **Tb** | 0.87 | 1.26 | 1.06 | 0.96 | 0.78 | 0.76 | 0.76 | 0.64 | 0.65 | 1.16 |
| **Tm** | 0.52 | 0.74 | 0.62 | 0.60 | 0.46 | 0.46 | 0.46 | 0.39 | 0.38 | 0.68 |
| **Y** | 32.9 | 47.3 | 41.0 | 37.3 | 29.8 | 29.6 | 30.0 | 25.1 | 24.8 | 44.3 |
| **Yb** | 3.39 | 4.88 | 4.13 | 3.73 | 3.02 | 2.98 | 2.97 | 2.49 | 2.39 | 4.49 |
| **(Ce/Yb)n** | 0.83 | 0.91 | 0.93 | 0.92 | 0.72 | 0.74 | 0.73 | 0.62 | 0.65 | 0.90 |

Table D-4. Continued.

| Sample | 2380-12G | 2380-9G | 2381-11G | 2383-6G a | 2383-6G b | 2384-3G | 2384-6G | 2384-9G |
|---|---|---|---|---|---|---|---|---|
| **Location*** | B | B | B-C | A | A | A-B | A-B | A-B |
| **ICP Trace Element Analysis (ppm)[µ]** | | | | | | | | |
| **Ag** | ND | ND | 0.30 | ND | ND | ND | 0.30 | ND |
| **Ba** | ND | ND | ND | ND | ND | ND | ND | ND |
| **Be** | 0.50 | ND | ND | ND | ND | ND | ND | ND |
| **Bi** | ND | ND | ND | ND | ND | ND | ND | ND |
| **Cd** | ND | ND | 0.2 | ND | 1 | ND | ND | ND |
| **Cl** | ND | ND | ND | ND | ND | ND | ND | 1187 |
| **Co** | 36 | 37 | 39 | 38 | 39 | 60 | 51 | 51 |
| **Cr** | 277 | 273 | 189 | 375 | 377 | 594 | 739 | 924 |
| **Cs** | ND | ND | ND | ND | ND | ND | ND | ND |
| **Cu** | 61 | 64 | 79 | 80 | 79 | 62 | 80 | 69 |
| **F** | 197 | 122 | 106 | 132 | 85 | 62 | 67 | 73 |
| **Ga** | 18 | 17 | 16 | 15 | 15 | 11 | 12 | 12 |
| **Hf** | 3.70 | 3.00 | 1.90 | 1.70 | 2.20 | 1.30 | 1.30 | 1.40 |
| **In** | 0.06 | 0.1 | ND | ND | ND | ND | ND | ND |
| **Mo** | 0.40 | 0.3 | 0.2 | ND | 1 | 0.7 | ND | ND |
| **Nb** | 3.90 | 3.10 | 1.80 | 1.10 | 1.10 | 0.48 | ND | 0.52 |
| **Ni** | 92 | 94 | 44 | 106 | 110 | 753 | 423 | 547 |
| **Rb** | 1.40 | 1.20 | 0.85 | 0.52 | 0.57 | 0.30 | ND | 0.26 |
| **Sb** | ND | ND | ND | ND | ND | 0.2 | ND | ND |
| **Sc** | 36 | 33 | 39 | 36 | 35 | 23 | 24 | 25 |
| **Sn** | 1.30 | 2.80 | 0.70 | 0.80 | 0.50 | ND | 0.90 | ND |
| **Sr** | 111 | 114 | 94 | 81 | 81 | 58 | 61 | 66 |
| **Ta** | 0.23 | 0.20 | 0.13 | ND | ND | ND | ND | 0.06 |
| **Te** | ND | ND | ND | ND | ND | ND | ND | ND |
| **Th** | 0.22 | 0.2 | 0.1 | ND | ND | ND | ND | ND |
| **Tl** | ND | ND | ND | ND | ND | ND | ND | ND |
| **U** | 0.10 | 0.08 | ND | ND | ND | ND | ND | ND |
| **V** | 335 | 293 | 276 | 264 | 263 | 159 | 175 | 189 |
| **Zn** | 90 | 79 | 72 | 67 | 67 | 56 | 74 | 61 |
| **Zr** | 144 | 120 | 74 | 62 | 85 | 45 | 44 | 47 |
| **Ce** | 15.41 | 12.25 | 7.02 | 5.91 | 5.75 | 3.39 | 3.51 | 4.11 |
| **Dy** | 7.49 | 6.09 | 4.57 | 4.22 | 4.19 | 2.97 | 3.00 | 3.39 |
| **Er** | 4.47 | 3.64 | 2.69 | 2.53 | 2.46 | 1.72 | 1.78 | 1.97 |
| **Eu** | 1.57 | 1.30 | 1.03 | 0.91 | 0.89 | 0.66 | 0.69 | 0.75 |
| **Gd** | 6.54 | 5.31 | 3.91 | 3.46 | 3.46 | 2.51 | 2.58 | 2.93 |
| **Ho** | 1.64 | 1.32 | 0.99 | 0.90 | 0.87 | 0.64 | 0.65 | 0.72 |
| **La** | 4.80 | 3.82 | 2.11 | 1.78 | 1.72 | 0.94 | 0.90 | 1.10 |
| **Lu** | 0.70 | 0.58 | 0.43 | 0.39 | 0.39 | 0.28 | 0.28 | 0.32 |
| **Nd** | 14.00 | 10.85 | 7.01 | 6.19 | 6.08 | 4.19 | 4.53 | 4.98 |
| **Pr** | 2.59 | 2.04 | 1.26 | 1.07 | 1.02 | 0.68 | 0.73 | 0.83 |
| **Sm** | 4.79 | 3.90 | 2.65 | 2.38 | 2.28 | 1.68 | 1.75 | 1.95 |
| **Tb** | 1.21 | 1.00 | 0.71 | 0.66 | 0.65 | 0.47 | 0.48 | 0.54 |
| **Tm** | 0.72 | 0.59 | 0.42 | 0.40 | 0.39 | 0.27 | 0.28 | 0.31 |
| **Y** | 46.7 | 38.0 | 28.2 | 26.3 | 25.5 | 18.3 | 18.4 | 20.9 |
| **Yb** | 4.63 | 3.87 | 2.77 | 2.55 | 2.53 | 1.77 | 1.71 | 1.98 |
| **(Ce/Yb)n** | 0.92 | 0.88 | 0.70 | 0.64 | 0.63 | 0.53 | 0.57 | 0.58 |

Table D-4. Continued.

| Sample | 2385-2G | 2385-3BG | 2386-5G | 2387-52 | 2388-10G | 2389-42 | 2389-52 | 2389-G | 2390-3B | 2390-5G |
|---|---|---|---|---|---|---|---|---|---|---|
| Location* | C | C | D | B-C | A-B | A | A | A | WRTI | WRTI |
| **ICP Trace Element Analysis (ppm)[μ]** | | | | | | | | | | |
| Ag | 0.10 | ND | ND | ND | ND | ND | ND | ND | ND | 0.20 |
| Ba | ND | ND | ND | ND | ND | ND | ND | ND | 125 | 129 |
| Be | ND | ND | ND | ND | ND | ND | ND | ND | 0.90 | 0.90 |
| Bi | ND | ND | ND | ND | ND | ND | ND | ND | ND | ND |
| Cd | ND | ND | ND | 2 | ND | ND | ND | 1.10 | 0.20 | 0.30 |
| Cl | ND | ND | ND | 247 | ND | 218 | 1333 | 417 | ND | 271 |
| Co | 38 | 40 | 40 | 37 | 37 | 36 | 37 | 38 | 32 | 33 |
| Cr | 231 | 146 | 231 | 297 | 408 | 251 | 243 | 271 | 214 | 205 |
| Cs | ND | ND | ND | ND | ND | ND | ND | ND | 0.11 | 0.13 |
| Cu | 88 | 77 | 87 | 70 | 93 | 66 | 69 | 66 | 51 | 50 |
| F | 93 | 115 | 98 | 111 | 78 | 110 | 106 | 105 | 313 | 330 |
| Ga | 15 | 16 | 15 | 16 | 15 | 17 | 17 | 17 | 18 | 18 |
| Hf | 1.70 | 2.10 | 1.80 | 2.30 | 1.70 | 2.20 | 2.50 | 2.10 | 4.00 | 4.10 |
| In | ND | ND | ND | ND | 0.07 | ND | ND | 0.05 | 0.06 | 0.15 |
| Mo | ND | ND | ND | ND | ND | ND | ND | 0.30 | 1.00 | 1.50 |
| Nb | 1.20 | 1.90 | 1.60 | 1.60 | 0.98 | 1.50 | 1.60 | 1.60 | 19.00 | 20.00 |
| Ni | 49 | 43 | 58 | 74 | 78 | 83 | 86 | 84 | 107 | 107 |
| Rb | 0.62 | 0.73 | 0.83 | 0.96 | 0.34 | ND | 0.82 | 0.59 | 11.00 | 12.00 |
| Sb | ND | ND | ND | ND | ND | ND | ND | ND | ND | ND |
| Sc | 39 | 41 | 40 | 34 | 36 | 37 | 36 | 36 | 28 | 27 |
| Sn | 0.70 | 0.60 | 0.50 | 0.80 | 0.70 | 0.80 | 1.00 | 0.80 | 1.40 | 1.90 |
| Sr | 95 | 103 | 93 | 91 | 70 | 74 | 70 | 70 | 269 | 295 |
| Ta | 0.09 | ND | ND | ND | 0.07 | ND | ND | 0.11 | 0.99 | 1.10 |
| Te | ND | ND | ND | ND | ND | ND | ND | ND | ND | ND |
| Th | ND | ND | ND | ND | 0.06 | ND | ND | 0.09 | 1.20 | 1.30 |
| Tl | ND | ND | ND | ND | ND | ND | ND | ND | 0.02 | 0.02 |
| U | ND | ND | ND | ND | 0.03 | ND | ND | 0.04 | 0.38 | 0.42 |
| V | 261 | 293 | 263 | 255 | 253 | 312 | 308 | 310 | 260 | 255 |
| Zn | 65 | 76 | 67 | 69 | 65 | 77 | 77 | 77 | 79 | 78 |
| Zr | 62 | 77 | 67 | 84 | 57 | 77 | 89 | 76 | 167 | 174 |
| Ce | 6.35 | 8.13 | 6.75 | 7.72 | 5.33 | 8.01 | 7.89 | 7.85 | 34.08 | 36.18 |
| Dy | 4.18 | 5.02 | 4.21 | 4.92 | 4.23 | 5.45 | 5.40 | 5.26 | 6.03 | 5.81 |
| Er | 2.53 | 2.94 | 2.51 | 2.89 | 2.48 | 3.23 | 3.24 | 3.15 | 3.26 | 3.18 |
| Eu | 0.95 | 1.12 | 0.91 | 1.10 | 0.87 | 1.11 | 1.08 | 1.06 | 1.72 | 1.73 |
| Gd | 3.68 | 4.30 | 3.59 | 4.28 | 3.56 | 4.49 | 4.38 | 4.36 | 6.01 | 5.88 |
| Ho | 0.91 | 1.08 | 0.94 | 1.07 | 0.92 | 1.16 | 1.18 | 1.16 | 1.22 | 1.20 |
| La | 1.82 | 2.40 | 2.03 | 2.18 | 1.55 | 2.32 | 2.31 | 2.35 | 13.71 | 14.82 |
| Lu | 0.40 | 0.48 | 0.39 | 0.44 | 0.39 | 0.53 | 0.53 | 0.52 | 0.51 | 0.50 |
| Nd | 6.75 | 8.19 | 6.68 | 8.22 | 6.14 | 8.38 | 8.23 | 8.24 | 20.75 | 21.70 |
| Pr | 1.19 | 1.48 | 1.20 | 1.47 | 1.03 | 1.46 | 1.44 | 1.43 | 4.66 | 4.85 |
| Sm | 2.53 | 2.98 | 2.39 | 3.01 | 2.28 | 2.97 | 2.94 | 2.91 | 5.18 | 5.15 |
| Tb | 0.66 | 0.79 | 0.66 | 0.80 | 0.64 | 0.85 | 0.82 | 0.83 | 0.95 | 0.96 |
| Tm | 0.40 | 0.47 | 0.40 | 0.46 | 0.40 | 0.54 | 0.52 | 0.52 | 0.51 | 0.50 |
| Y | 26.4 | 31.1 | 26.5 | 30.5 | 26.7 | 34.4 | 34.4 | 34.5 | 36.0 | 35.2 |
| Yb | 2.60 | 3.00 | 2.55 | 2.93 | 2.59 | 3.40 | 3.41 | 3.36 | 3.23 | 3.17 |
| (Ce/Yb)n | 0.68 | 0.75 | 0.74 | 0.73 | 0.57 | 0.66 | 0.64 | 0.65 | 2.93 | 3.17 |

Table D-4. Continued.

| Sample | A25 D1-3 G | A25 D17-9 | A25 D18-2 G |
|---|---|---|---|
| Location* | B | A-B | B |
| **ICP Trace Element Analysis (ppm)μ** | | | |
| **Ag** | 0.40 | 0.10 | 0.20 |
| **Ba** | ND | ND | ND |
| **Be** | ND | ND | 1 |
| **Bi** | ND | ND | ND |
| **Cd** | 5 | 0.20 | ND |
| **Cl** | 1393 | 106 | 218 |
| **Co** | 38 | 37 | 38 |
| **Cr** | 332 | 285 | 124 |
| **Cs** | ND | ND | ND |
| **Cu** | 76 | 66 | 70 |
| **F** | 123 | 157 | 174 |
| **Ga** | 16 | 17 | 18 |
| **Hf** | 2.20 | 2.90 | 3.10 |
| **In** | ND | 0.06 | ND |
| **Mo** | ND | 1.00 | ND |
| **Nb** | 2.00 | 2.70 | 3.80 |
| **Ni** | 84 | 105 | 40 |
| **Rb** | 0.61 | 0.83 | 1.40 |
| **Sb** | ND | ND | ND |
| **Sc** | 36 | 34 | 39 |
| **Sn** | 1.00 | 1.00 | 1.00 |
| **Sr** | 94 | 92 | 120 |
| **Ta** | ND | 0.19 | ND |
| **Te** | ND | ND | ND |
| **Th** | ND | 0.17 | ND |
| **Tl** | ND | ND | ND |
| **U** | ND | 0.07 | ND |
| **V** | 278 | 311 | 327 |
| **Zn** | 71 | 109 | 87 |
| **Zr** | 81 | 106 | 121 |
| **Ce** | 8.36 | 11.35 | 13.68 |
| **Dy** | 5.07 | 6.24 | 6.50 |
| **Er** | 2.98 | 3.60 | 3.81 |
| **Eu** | 1.10 | 1.33 | 1.49 |
| **Gd** | 4.29 | 5.48 | 5.83 |
| **Ho** | 1.10 | 1.35 | 1.39 |
| **La** | 2.56 | 3.46 | 4.34 |
| **Lu** | 0.48 | 0.58 | 0.61 |
| **Nd** | 8.19 | 10.71 | 11.81 |
| **Pr** | 1.46 | 1.95 | 2.28 |
| **Sm** | 2.95 | 3.90 | 4.16 |
| **Tb** | 0.79 | 1.00 | 1.04 |
| **Tm** | 0.47 | 0.58 | 0.61 |
| **Y** | 31.0 | 37.9 | 38.9 |
| **Yb** | 3.11 | 3.82 | 3.97 |
| **(Ce/Yb)n** | 0.75 | 0.82 | 0.96 |

*Locations same as Table D-1. μICP-MS completed at the Geological Survey of Canada. MgO values from Table C-1.

# APPENDIX E
# FRACTIONAL CRYSTALLIZATION MODEL PARAMETERS CALCULATED IN PETROLOG

Table E-1. 2377-7P at low pressure.

| Step | Melt% | T(C) | $SiO_2$ | $TiO_2$ | $Al_2O_3$ | FeO | MgO | CaO | $Na_2O$ | $K_2O$ | $P_2O_5$ | Fo | An | Olv% | Plg% | Cpx% |
|---|---|---|---|---|---|---|---|---|---|---|---|---|---|---|---|---|
| 1 | 100.00 | 1258 | 48.50 | 1.19 | 17.41 | 7.77 | 10.50 | 11.16 | 2.30 | 0.09 | 0.13 | 88.90 | -1 | 0.00 | 0.00 | 0.00 |
| 2 | 99.00 | 1249 | 48.58 | 1.20 | 17.59 | 7.76 | 10.12 | 11.27 | 2.32 | 0.09 | 0.13 | 88.53 | -1 | 1.00 | 0.00 | 0.00 |
| 5 | 96.99 | 1235 | 48.71 | 1.23 | 17.79 | 7.76 | 9.58 | 11.42 | 2.36 | 0.09 | 0.13 | 87.92 | 83.46 | 2.53 | 0.49 | 0.00 |
| 7 | 94.98 | 1233 | 48.78 | 1.25 | 17.64 | 7.85 | 9.51 | 11.40 | 2.38 | 0.10 | 0.14 | 87.70 | 82.87 | 3.07 | 1.95 | 0.00 |
| 12 | 89.96 | 1229 | 48.96 | 1.32 | 17.27 | 8.08 | 9.31 | 11.37 | 2.44 | 0.10 | 0.15 | 87.09 | 81.36 | 4.45 | 5.59 | 0.00 |
| 17 | 84.93 | 1224 | 49.16 | 1.40 | 16.88 | 8.33 | 9.08 | 11.34 | 2.49 | 0.11 | 0.15 | 86.40 | 79.75 | 5.84 | 9.23 | 0.00 |
| 22 | 79.91 | 1218 | 49.36 | 1.49 | 16.44 | 8.60 | 8.84 | 11.33 | 2.54 | 0.11 | 0.16 | 85.62 | 78.02 | 7.23 | 12.85 | 0.00 |
| 27 | 74.90 | 1212 | 49.57 | 1.59 | 15.97 | 8.88 | 8.57 | 11.34 | 2.59 | 0.12 | 0.17 | 84.74 | 76.17 | 8.64 | 16.46 | 0.00 |
| 32 | 69.87 | 1204 | 49.79 | 1.70 | 15.46 | 9.18 | 8.26 | 11.37 | 2.63 | 0.13 | 0.19 | 83.71 | 74.17 | 10.06 | 20.07 | 0.00 |
| 37 | 64.85 | 1195 | 50.02 | 1.84 | 14.89 | 9.49 | 7.91 | 11.44 | 2.67 | 0.14 | 0.20 | 82.51 | 72.00 | 11.50 | 23.65 | 0.00 |
| 42 | 59.83 | 1183 | 50.27 | 1.99 | 14.27 | 9.81 | 7.51 | 11.55 | 2.70 | 0.15 | 0.22 | 81.08 | 69.65 | 12.97 | 27.20 | 0.00 |
| 47 | 54.82 | 1168 | 50.55 | 2.17 | 13.59 | 10.13 | 7.02 | 11.72 | 2.73 | 0.16 | 0.24 | 79.31 | 67.10 | 14.49 | 30.69 | 0.00 |
| 50 | 52.81 | 1162 | 50.64 | 2.25 | 13.35 | 10.27 | 6.82 | 11.74 | 2.74 | 0.17 | 0.25 | 78.53 | 66.11 | 14.97 | 31.95 | 0.27 |
| 53 | 49.81 | 1158 | 50.62 | 2.37 | 13.19 | 10.57 | 6.63 | 11.50 | 2.79 | 0.18 | 0.26 | 77.45 | 65.01 | 15.11 | 33.34 | 1.75 |
| 58 | 44.80 | 1150 | 50.58 | 2.59 | 12.88 | 11.11 | 6.27 | 11.05 | 2.89 | 0.20 | 0.29 | 75.34 | 62.99 | 15.34 | 35.63 | 4.23 |
| 63 | 39.79 | 1140 | 50.51 | 2.86 | 12.57 | 11.67 | 5.84 | 10.54 | 3.00 | 0.23 | 0.33 | 72.75 | 60.75 | 15.56 | 37.88 | 6.77 |
| 68 | 34.78 | 1127 | 50.40 | 3.20 | 12.23 | 12.23 | 5.32 | 9.93 | 3.13 | 0.26 | 0.37 | 69.49 | 58.23 | 15.77 | 40.09 | 9.36 |
| 71 | 32.22 | 1119 | 50.32 | 3.40 | 12.06 | 12.48 | 5.00 | 9.57 | 3.20 | 0.28 | 0.40 | 67.49 | 56.82 | 15.88 | 41.19 | 10.71 |

Notes: The relative proportions (in wt. %) of the major element oxides and crystallizing phases are shown at ~5 wt. % increments of crystallization, except when a new mineral comes on the liquidus. Olv = olivine; Plg = plagioclase; Cpx – clinopyroxene; Spl = spinel; Fo = forsterite content of crystallizing olivine; An = anorthite content of crystallizing plagioclase. The oxides and parameters not used in the liquid line of descent modeling have been omitted.

Table E-2. D34-2P at low pressure.

| Step | Melt% | T(C) | $SiO_2$ | $TiO_2$ | $Al_2O_3$ | FeO | MgO | CaO | $Na_2O$ | $K_2O$ | $P_2O_5$ | $Cr_2O_3$ | Fo | An | Olv% | Plg% | Cpx% | Spl% |
|---|---|---|---|---|---|---|---|---|---|---|---|---|---|---|---|---|---|---|
| 1 | 100.00 | 1297 | 49.59 | 1.02 | 16.19 | 7.64 | 9.07 | 12.89 | 2.17 | 0.06 | 0.05 | 0.131 | -1 | -1 | 0.00 | 0.00 | 0.00 | 0.00 |
| 2 | 99.76 | 1214 | 49.72 | 1.02 | 16.17 | 7.82 | 9.06 | 12.92 | 2.17 | 0.06 | 0.05 | 0.040 | 87.05 | -1 | 0.00 | 0.00 | 0.00 | 0.24 |
| 3 | 99.46 | 1211 | 49.76 | 1.02 | 16.22 | 7.81 | 8.95 | 12.96 | 2.18 | 0.06 | 0.05 | 0.037 | 86.91 | 80.84 | 0.29 | 0.00 | 0.00 | 0.25 |
| 4 | 99.00 | 1211 | 49.77 | 1.02 | 16.18 | 7.83 | 8.93 | 12.97 | 2.18 | 0.06 | 0.05 | 0.037 | 86.85 | 80.71 | 0.42 | 0.34 | 0.00 | 0.25 |
| 8 | 94.98 | 1206 | 49.94 | 1.07 | 15.86 | 7.99 | 8.74 | 13.03 | 2.21 | 0.06 | 0.05 | 0.038 | 86.32 | 79.50 | 1.55 | 3.22 | 0.00 | 0.25 |
| 13 | 89.96 | 1200 | 50.17 | 1.13 | 15.43 | 8.21 | 8.49 | 13.12 | 2.24 | 0.07 | 0.06 | 0.039 | 85.58 | 77.91 | 2.98 | 6.81 | 0.00 | 0.25 |
| 22 | 81.92 | 1187 | 50.54 | 1.24 | 14.70 | 8.57 | 8.05 | 13.29 | 2.28 | 0.07 | 0.06 | 0.040 | 84.19 | 75.20 | 5.19 | 12.44 | 0.21 | 0.25 |
| 24 | 79.91 | 1186 | 50.56 | 1.26 | 14.63 | 8.70 | 7.99 | 13.20 | 2.30 | 0.08 | 0.06 | 0.035 | 83.86 | 74.74 | 5.30 | 13.39 | 1.14 | 0.25 |
| 29 | 74.90 | 1183 | 50.61 | 1.33 | 14.44 | 9.04 | 7.82 | 12.96 | 2.36 | 0.08 | 0.07 | 0.025 | 82.96 | 73.55 | 5.59 | 15.77 | 3.50 | 0.25 |
| 34 | 69.87 | 1180 | 50.66 | 1.41 | 14.24 | 9.41 | 7.64 | 12.70 | 2.42 | 0.09 | 0.07 | 0.019 | 81.93 | 72.26 | 5.87 | 18.14 | 5.87 | 0.25 |
| 39 | 64.85 | 1176 | 50.70 | 1.51 | 14.01 | 9.82 | 7.43 | 12.41 | 2.48 | 0.09 | 0.08 | 0.015 | 80.77 | 70.88 | 6.14 | 20.50 | 8.26 | 0.25 |
| 44 | 59.83 | 1171 | 50.74 | 1.61 | 13.78 | 10.27 | 7.20 | 12.09 | 2.55 | 0.10 | 0.08 | 0.012 | 79.42 | 69.38 | 6.40 | 22.84 | 10.68 | 0.25 |
| 49 | 54.82 | 1166 | 50.77 | 1.73 | 13.52 | 10.76 | 6.94 | 11.74 | 2.63 | 0.11 | 0.09 | 0.010 | 77.84 | 67.75 | 6.66 | 25.17 | 13.11 | 0.25 |
| 54 | 49.81 | 1160 | 50.79 | 1.87 | 13.25 | 11.30 | 6.63 | 11.34 | 2.71 | 0.12 | 0.10 | 0.009 | 75.97 | 65.97 | 6.91 | 27.47 | 15.57 | 0.25 |
| 59 | 44.80 | 1152 | 50.80 | 2.03 | 12.95 | 11.89 | 6.27 | 10.89 | 2.81 | 0.13 | 0.11 | 0.008 | 73.73 | 63.99 | 7.15 | 29.74 | 18.06 | 0.25 |
| 64 | 39.79 | 1143 | 50.79 | 2.23 | 12.64 | 12.51 | 5.84 | 10.37 | 2.91 | 0.15 | 0.13 | 0.008 | 70.96 | 61.80 | 7.39 | 31.98 | 20.60 | 0.25 |
| 69 | 34.78 | 1131 | 50.76 | 2.47 | 12.31 | 13.16 | 5.31 | 9.75 | 3.04 | 0.17 | 0.14 | 0.008 | 67.48 | 59.33 | 7.62 | 34.16 | 23.20 | 0.25 |
| 72 | 32.24 | 1124 | 50.73 | 2.61 | 12.15 | 13.47 | 5.00 | 9.40 | 3.11 | 0.19 | 0.15 | 0.009 | 65.36 | 57.96 | 7.74 | 35.24 | 24.53 | 0.25 |

Notes: The relative proportions (in wt. %) of the major element oxides and crystallizing phases are shown at ~5 wt. % increments of crystallization, except when a new mineral comes on the liquidus. Olv = olivine; Plg = plagioclase; Cpx – clinopyroxene; Spl = spinel; Fo = forsterite content of crystallizing olivine; An = anorthite content of crystallizing plagioclase. The oxides and parameters not used in the liquid line of descent modeling have been omitted.

Table E-3. 2384-9P at low pressure.

| Step | Melt% | T(C) | $SiO_2$ | $TiO_2$ | $Al_2O_3$ | FeO | MgO | CaO | $Na_2O$ | $K_2O$ | $P_2O5$ | $Cr_2O_3$ | Fo | An | Olv% | Plg% | Cpx% | Spl% |
|---|---|---|---|---|---|---|---|---|---|---|---|---|---|---|---|---|---|---|
| 1 | 100.00 | 1380 | 49.12 | 1.01 | 17.10 | 7.04 | 9.75 | 11.88 | 2.46 | 0.01 | 0.07 | 0.241 | -1 | -1 | 0.00 | 0.00 | 0.00 | 0.00 |
| 2 | 99.48 | 1238 | 49.39 | 1.01 | 17.06 | 7.34 | 9.72 | 11.95 | 2.47 | 0.01 | 0.07 | 0.038 | 88.66 | -1 | 0.00 | 0.00 | 0.00 | 0.52 |
| 3 | 99.00 | 1233 | 49.44 | 1.02 | 17.14 | 7.32 | 9.54 | 12.01 | 2.48 | 0.01 | 0.07 | 0.035 | 88.47 | -1 | 0.48 | 0.00 | 0.00 | 0.53 |
| 5 | 97.99 | 1227 | 49.51 | 1.03 | 17.19 | 7.33 | 9.32 | 12.07 | 2.50 | 0.01 | 0.07 | 0.032 | 88.20 | 80.37 | 1.13 | 0.34 | 0.00 | 0.54 |
| 8 | 94.98 | 1225 | 49.62 | 1.06 | 16.97 | 7.45 | 9.20 | 12.08 | 2.53 | 0.01 | 0.07 | 0.033 | 87.86 | 79.49 | 1.95 | 2.53 | 0.00 | 0.54 |
| 13 | 89.96 | 1219 | 49.82 | 1.12 | 16.58 | 7.67 | 8.99 | 12.11 | 2.57 | 0.02 | 0.08 | 0.034 | 87.24 | 77.94 | 3.31 | 6.20 | 0.00 | 0.54 |
| 18 | 84.93 | 1214 | 50.03 | 1.19 | 16.17 | 7.90 | 8.75 | 12.16 | 2.62 | 0.02 | 0.08 | 0.035 | 86.54 | 76.30 | 4.69 | 9.84 | 0.00 | 0.54 |
| 23 | 79.91 | 1207 | 50.24 | 1.26 | 15.71 | 8.14 | 8.49 | 12.23 | 2.66 | 0.02 | 0.09 | 0.036 | 85.75 | 74.53 | 6.06 | 13.48 | 0.00 | 0.54 |
| 28 | 74.90 | 1199 | 50.47 | 1.35 | 15.22 | 8.39 | 8.20 | 12.33 | 2.69 | 0.02 | 0.09 | 0.037 | 84.84 | 72.64 | 7.46 | 17.10 | 0.00 | 0.54 |
| 33 | 69.87 | 1189 | 50.71 | 1.44 | 14.68 | 8.66 | 7.86 | 12.47 | 2.72 | 0.02 | 0.10 | 0.039 | 83.77 | 70.60 | 8.89 | 20.70 | 0.00 | 0.54 |
| 39 | 64.85 | 1179 | 50.94 | 1.55 | 14.15 | 8.95 | 7.51 | 12.59 | 2.76 | 0.02 | 0.11 | 0.039 | 82.54 | 68.51 | 10.17 | 24.11 | 0.33 | 0.54 |
| 44 | 59.83 | 1174 | 50.97 | 1.66 | 13.93 | 9.36 | 7.28 | 12.29 | 2.84 | 0.02 | 0.12 | 0.029 | 81.31 | 66.98 | 10.43 | 26.47 | 2.72 | 0.54 |
| 49 | 54.82 | 1169 | 50.99 | 1.79 | 13.69 | 9.81 | 7.02 | 11.95 | 2.93 | 0.03 | 0.13 | 0.022 | 79.89 | 65.30 | 10.67 | 28.83 | 5.14 | 0.54 |
| 54 | 49.81 | 1163 | 50.99 | 1.94 | 13.44 | 10.32 | 6.73 | 11.57 | 3.03 | 0.03 | 0.14 | 0.018 | 78.19 | 63.46 | 10.91 | 31.16 | 7.59 | 0.54 |
| 59 | 44.80 | 1155 | 50.97 | 2.12 | 13.16 | 10.87 | 6.38 | 11.14 | 3.14 | 0.03 | 0.16 | 0.016 | 76.16 | 61.41 | 11.13 | 33.47 | 10.06 | 0.54 |
| 64 | 39.79 | 1146 | 50.92 | 2.34 | 12.88 | 11.46 | 5.97 | 10.64 | 3.26 | 0.04 | 0.18 | 0.015 | 73.65 | 59.12 | 11.34 | 35.75 | 12.58 | 0.54 |
| 69 | 34.78 | 1134 | 50.84 | 2.60 | 12.58 | 12.08 | 5.46 | 10.05 | 3.42 | 0.04 | 0.20 | 0.015 | 70.49 | 56.53 | 11.55 | 37.98 | 15.15 | 0.54 |
| 73 | 30.99 | 1123 | 50.74 | 2.85 | 12.36 | 12.53 | 5.00 | 9.53 | 3.55 | 0.04 | 0.23 | 0.015 | 67.49 | 54.33 | 11.70 | 39.63 | 17.14 | 0.54 |

Notes: The relative proportions (in wt. %) of the major element oxides and crystallizing phases are shown at ~5 wt. % increments of crystallization, except when a new mineral comes on the liquidus. Olv = olivine; Plg = plagioclase; Cpx – clinopyroxene; Spl = spinel; Fo = forsterite content of crystallizing olivine; An = anorthite content of crystallizing plagioclase. The oxides and parameters not used in the liquid line of descent modeling have been omitted.

Table E-4. 2384-9P at 2 kbar.

| Step | Melt% | T(C) | $SiO_2$ | $TiO_2$ | $Al_2O_3$ | FeO | MgO | CaO | $Na_2O$ | $K_2O$ | $P_2O5$ | $Cr_2O_3$ | Fo | An | Olv% | Plg% | Cpx% | Spl% |
|---|---|---|---|---|---|---|---|---|---|---|---|---|---|---|---|---|---|---|
| 1 | 100.00 | 1380 | 49.12 | 1.01 | 17.10 | 7.04 | 9.75 | 11.88 | 2.46 | 0.01 | 0.07 | 0.241 | -1 | -1 | 0.00 | 0.00 | 0.00 | 0.00 |
| 2 | 99.51 | 1250 | 49.38 | 1.01 | 17.06 | 7.31 | 9.72 | 11.95 | 2.47 | 0.01 | 0.07 | 0.046 | 88.42 | -1 | 0.00 | 0.00 | 0.00 | 0.49 |
| 3 | 99.00 | 1245 | 49.43 | 1.02 | 17.15 | 7.30 | 9.53 | 12.01 | 2.48 | 0.01 | 0.07 | 0.043 | 88.21 | -1 | 0.51 | 0.00 | 0.00 | 0.50 |
| 5 | 97.99 | 1239 | 49.49 | 1.03 | 17.19 | 7.31 | 9.33 | 12.07 | 2.50 | 0.01 | 0.07 | 0.040 | 87.96 | 76.17 | 1.11 | 0.39 | 0.00 | 0.51 |
| 8 | 94.98 | 1237 | 49.58 | 1.06 | 16.98 | 7.43 | 9.22 | 12.09 | 2.51 | 0.01 | 0.07 | 0.041 | 87.63 | 75.42 | 1.91 | 2.60 | 0.00 | 0.51 |
| 13 | 89.96 | 1232 | 49.73 | 1.12 | 16.61 | 7.65 | 9.03 | 12.15 | 2.54 | 0.02 | 0.08 | 0.042 | 87.03 | 74.10 | 3.24 | 6.29 | 0.00 | 0.51 |
| 18 | 84.93 | 1226 | 49.89 | 1.19 | 16.21 | 7.88 | 8.82 | 12.23 | 2.56 | 0.02 | 0.08 | 0.044 | 86.35 | 72.69 | 4.59 | 9.97 | 0.00 | 0.51 |
| 23 | 79.91 | 1220 | 50.06 | 1.26 | 15.77 | 8.12 | 8.58 | 12.33 | 2.58 | 0.02 | 0.09 | 0.046 | 85.59 | 71.19 | 5.95 | 13.63 | 0.00 | 0.51 |
| 28 | 74.90 | 1212 | 50.23 | 1.35 | 15.30 | 8.37 | 8.31 | 12.46 | 2.59 | 0.02 | 0.09 | 0.048 | 84.71 | 69.58 | 7.32 | 17.28 | 0.00 | 0.51 |
| 32 | 71.88 | 1208 | 50.31 | 1.40 | 15.05 | 8.55 | 8.16 | 12.49 | 2.61 | 0.02 | 0.10 | 0.046 | 84.15 | 68.65 | 7.96 | 19.27 | 0.37 | 0.51 |
| 34 | 69.87 | 1207 | 50.31 | 1.44 | 14.97 | 8.70 | 8.10 | 12.40 | 2.63 | 0.02 | 0.10 | 0.041 | 83.79 | 68.19 | 8.08 | 20.29 | 1.25 | 0.51 |
| 39 | 64.85 | 1203 | 50.30 | 1.54 | 14.76 | 9.08 | 7.92 | 12.17 | 2.68 | 0.02 | 0.11 | 0.029 | 82.79 | 66.97 | 8.39 | 22.80 | 3.46 | 0.51 |
| 44 | 59.83 | 1200 | 50.27 | 1.65 | 14.53 | 9.52 | 7.72 | 11.91 | 2.74 | 0.02 | 0.12 | 0.021 | 81.65 | 65.64 | 8.68 | 25.31 | 5.67 | 0.51 |
| 49 | 54.82 | 1195 | 50.21 | 1.78 | 14.29 | 10.00 | 7.50 | 11.63 | 2.81 | 0.03 | 0.13 | 0.016 | 80.33 | 64.19 | 8.97 | 27.80 | 7.90 | 0.51 |
| 54 | 49.81 | 1190 | 50.13 | 1.93 | 14.02 | 10.54 | 7.24 | 11.30 | 2.88 | 0.03 | 0.14 | 0.013 | 78.77 | 62.60 | 9.24 | 30.28 | 10.17 | 0.51 |
| 59 | 44.80 | 1184 | 50.01 | 2.11 | 13.72 | 11.14 | 6.94 | 10.94 | 2.96 | 0.03 | 0.16 | 0.011 | 76.91 | 60.83 | 9.50 | 32.73 | 12.46 | 0.51 |
| 64 | 39.79 | 1176 | 49.84 | 2.33 | 13.40 | 11.82 | 6.59 | 10.52 | 3.05 | 0.04 | 0.18 | 0.010 | 74.66 | 58.84 | 9.75 | 35.17 | 14.79 | 0.51 |
| 69 | 34.78 | 1166 | 49.59 | 2.61 | 13.04 | 12.58 | 6.16 | 10.03 | 3.14 | 0.04 | 0.20 | 0.010 | 71.85 | 56.60 | 9.99 | 37.56 | 17.16 | 0.51 |
| 74 | 29.77 | 1154 | 49.23 | 2.96 | 12.65 | 13.38 | 5.63 | 9.45 | 3.26 | 0.05 | 0.24 | 0.010 | 68.28 | 54.02 | 10.22 | 39.91 | 19.59 | 0.51 |
| 79 | 25.09 | 1138 | 48.74 | 3.39 | 12.27 | 14.11 | 5.00 | 8.79 | 3.39 | 0.06 | 0.28 | 0.012 | 63.93 | 51.23 | 10.41 | 42.05 | 21.94 | 0.51 |

Notes: The relative proportions (in wt. %) of the major element oxides and crystallizing phases are shown at ~5 wt. % increments of crystallization, except when a new mineral comes on the liquidus. Olv = olivine; Plg = plagioclase; Cpx – clinopyroxene; Spl = spinel; Fo = forsterite content of crystallizing olivine; An = anorthite content of crystallizing plagioclase. The oxides and parameters not used in the liquid line of descent modeling have been omitted.

Table E-5. 2377-7P at low pressure, hydrous conditions.

| Step | Melt% | T(C) | $SiO_2$ | $TiO_2$ | $Al_2O_3$ | FeO | MgO | CaO | $Na_2O$ | $K_2O$ | $P_2O_5$ | $H_2O$ | Fo | An | Olv% | Plg% | Cpx% |
|---|---|---|---|---|---|---|---|---|---|---|---|---|---|---|---|---|---|
| 1 | 100.00 | 1223 | 48.57 | 1.23 | 17.02 | 8.03 | 10.49 | 11.04 | 2.35 | 0.09 | 0.14 | 0.15 | 88.51 | -1 | 0.00 | 0.00 | 0.00 |
| 2 | 99.00 | 1214 | 48.65 | 1.24 | 17.19 | 8.01 | 10.11 | 11.14 | 2.37 | 0.09 | 0.14 | 0.15 | 88.13 | -1 | 1.00 | 0.00 | 0.00 |
| 6 | 95.98 | 1186 | 48.89 | 1.28 | 17.63 | 7.95 | 9.09 | 11.43 | 2.44 | 0.09 | 0.15 | 0.16 | 86.98 | 81.81 | 3.72 | 0.30 | 0.00 |
| 7 | 94.98 | 1185 | 48.92 | 1.29 | 17.56 | 8.00 | 9.06 | 11.43 | 2.45 | 0.10 | 0.15 | 0.16 | 86.86 | 81.52 | 3.99 | 1.03 | 0.00 |
| 12 | 89.96 | 1179 | 49.10 | 1.37 | 17.19 | 8.23 | 8.83 | 11.41 | 2.50 | 0.10 | 0.16 | 0.17 | 86.19 | 80.05 | 5.37 | 4.67 | 0.00 |
| 17 | 84.93 | 1173 | 49.29 | 1.45 | 16.80 | 8.47 | 8.60 | 11.40 | 2.55 | 0.11 | 0.17 | 0.18 | 85.43 | 78.47 | 6.76 | 8.30 | 0.00 |
| 22 | 79.91 | 1166 | 49.49 | 1.54 | 16.38 | 8.72 | 8.33 | 11.40 | 2.60 | 0.11 | 0.18 | 0.19 | 84.57 | 76.79 | 8.17 | 11.91 | 0.00 |
| 27 | 74.90 | 1157 | 49.70 | 1.64 | 15.92 | 8.98 | 8.03 | 11.43 | 2.64 | 0.12 | 0.19 | 0.20 | 83.59 | 74.99 | 9.59 | 15.51 | 0.00 |
| 32 | 69.87 | 1147 | 49.92 | 1.76 | 15.42 | 9.26 | 7.69 | 11.48 | 2.69 | 0.13 | 0.20 | 0.21 | 82.45 | 73.04 | 11.03 | 19.10 | 0.00 |
| 37 | 64.85 | 1134 | 50.16 | 1.89 | 14.87 | 9.53 | 7.30 | 11.58 | 2.72 | 0.14 | 0.22 | 0.23 | 81.09 | 70.94 | 12.50 | 22.66 | 0.00 |
| 42 | 59.83 | 1119 | 50.43 | 2.05 | 14.28 | 9.79 | 6.83 | 11.72 | 2.76 | 0.15 | 0.23 | 0.25 | 79.44 | 68.69 | 14.01 | 26.16 | 0.00 |
| 44 | 58.83 | 1116 | 50.46 | 2.09 | 14.20 | 9.86 | 6.75 | 11.71 | 2.77 | 0.15 | 0.24 | 0.26 | 79.10 | 68.30 | 14.21 | 26.75 | 0.21 |
| 48 | 54.82 | 1110 | 50.45 | 2.22 | 14.02 | 10.19 | 6.52 | 11.41 | 2.84 | 0.16 | 0.26 | 0.27 | 77.82 | 67.01 | 14.40 | 28.62 | 2.16 |
| 53 | 49.81 | 1101 | 50.44 | 2.40 | 13.79 | 10.63 | 6.17 | 10.99 | 2.94 | 0.18 | 0.28 | 0.30 | 75.93 | 65.27 | 14.66 | 30.93 | 4.61 |
| 58 | 44.80 | 1090 | 50.40 | 2.62 | 13.55 | 11.08 | 5.78 | 10.51 | 3.06 | 0.20 | 0.31 | 0.33 | 73.67 | 63.35 | 14.89 | 33.21 | 7.10 |
| 63 | 39.79 | 1076 | 50.34 | 2.89 | 13.30 | 11.50 | 5.30 | 9.95 | 3.19 | 0.23 | 0.35 | 0.38 | 70.89 | 61.22 | 15.13 | 35.44 | 9.64 |
| 66 | 37.13 | 1067 | 50.30 | 3.06 | 13.18 | 11.69 | 5.00 | 9.62 | 3.27 | 0.24 | 0.38 | 0.40 | 69.14 | 60.01 | 15.25 | 36.60 | 11.02 |

Notes: The relative proportions (in wt. %) of the major element oxides and crystallizing phases are shown at ~5 wt. % increments of crystallization, except when a new mineral comes on the liquidus. Olv = olivine; Plg = plagioclase; Cpx – clinopyroxene; Spl = spinel; Fo = forsterite content of crystallizing olivine; An = anorthite content of crystallizing plagioclase. The oxides and parameters not used in the liquid line of descent modeling have been omitted.

Table E-6. D34-2P at low pressure, hydrous conditions.

| Step | Melt% | T(C) | $SiO_2$ | $TiO_2$ | $Al_2O_3$ | FeO | MgO | CaO | $Na_2O$ | $K_2O$ | $P_2O_5$ | $Cr_2O_3$ | $H_2O$ | Fo | An | Olv% | Plg% | Cpx% |
|---|---|---|---|---|---|---|---|---|---|---|---|---|---|---|---|---|---|---|
| 1 | 100.00 | 1177 | 49.53 | 1.01 | 16.17 | 7.91 | 9.06 | 12.88 | 2.17 | 0.06 | 0.05 | 0.131 | 0.149 | 86.93 | -1 | 0.00 | 0.00 | 0.00 |
| 2 | 99.00 | 1165 | 49.63 | 1.02 | 16.34 | 7.88 | 8.68 | 13.00 | 2.19 | 0.06 | 0.05 | 0.132 | 0.151 | 86.45 | -1 | 1.00 | 0.00 | 0.00 |
| 4 | 97.99 | 1163 | 49.68 | 1.03 | 16.29 | 7.91 | 8.60 | 13.03 | 2.20 | 0.06 | 0.05 | 0.133 | 0.152 | 86.28 | 80.98 | 1.37 | 0.64 | 0.00 |
| 7 | 94.98 | 1159 | 49.80 | 1.07 | 16.05 | 8.03 | 8.45 | 13.07 | 2.22 | 0.06 | 0.05 | 0.137 | 0.157 | 85.85 | 80.08 | 2.22 | 2.80 | 0.00 |
| 12 | 89.96 | 1151 | 50.03 | 1.13 | 15.63 | 8.23 | 8.18 | 13.16 | 2.25 | 0.07 | 0.06 | 0.143 | 0.166 | 85.06 | 78.51 | 3.66 | 6.38 | 0.00 |
| 18 | 84.93 | 1142 | 50.25 | 1.19 | 15.21 | 8.45 | 7.90 | 13.26 | 2.28 | 0.07 | 0.06 | 0.150 | 0.175 | 84.17 | 76.88 | 5.03 | 9.87 | 0.17 |
| 23 | 79.91 | 1138 | 50.30 | 1.26 | 15.05 | 8.75 | 7.74 | 13.03 | 2.34 | 0.08 | 0.06 | 0.144 | 0.186 | 83.34 | 75.79 | 5.32 | 12.24 | 2.52 |
| 28 | 74.90 | 1134 | 50.36 | 1.33 | 14.88 | 9.08 | 7.56 | 12.78 | 2.40 | 0.08 | 0.07 | 0.140 | 0.199 | 82.39 | 74.62 | 5.62 | 14.61 | 4.87 |
| 33 | 69.87 | 1129 | 50.40 | 1.41 | 14.70 | 9.44 | 7.36 | 12.50 | 2.47 | 0.09 | 0.07 | 0.137 | 0.213 | 81.33 | 73.36 | 5.90 | 16.98 | 7.25 |
| 38 | 64.85 | 1123 | 50.45 | 1.49 | 14.51 | 9.83 | 7.13 | 12.20 | 2.55 | 0.09 | 0.08 | 0.136 | 0.230 | 80.10 | 72.01 | 6.18 | 19.32 | 9.65 |
| 43 | 59.83 | 1117 | 50.49 | 1.60 | 14.30 | 10.25 | 6.88 | 11.86 | 2.63 | 0.10 | 0.08 | 0.138 | 0.249 | 78.69 | 70.55 | 6.44 | 21.65 | 12.08 |
| 48 | 54.82 | 1110 | 50.52 | 1.71 | 14.09 | 10.70 | 6.59 | 11.48 | 2.72 | 0.11 | 0.09 | 0.142 | 0.272 | 77.04 | 68.97 | 6.70 | 23.95 | 14.53 |
| 53 | 49.81 | 1101 | 50.54 | 1.85 | 13.86 | 11.19 | 6.26 | 11.06 | 2.82 | 0.12 | 0.10 | 0.149 | 0.299 | 75.08 | 67.24 | 6.96 | 26.23 | 17.01 |
| 58 | 44.80 | 1091 | 50.55 | 2.00 | 13.62 | 11.69 | 5.86 | 10.57 | 2.93 | 0.13 | 0.11 | 0.161 | 0.333 | 72.72 | 65.34 | 7.20 | 28.47 | 19.53 |
| 63 | 39.79 | 1078 | 50.55 | 2.19 | 13.38 | 12.20 | 5.39 | 10.01 | 3.07 | 0.15 | 0.13 | 0.177 | 0.374 | 69.81 | 63.22 | 7.44 | 30.68 | 22.09 |
| 67 | 36.27 | 1067 | 50.55 | 2.34 | 13.22 | 12.53 | 5.00 | 9.56 | 3.18 | 0.16 | 0.14 | 0.192 | 0.411 | 67.33 | 61.60 | 7.62 | 32.19 | 23.93 |

Notes: The relative proportions (in wt. %) of the major element oxides and crystallizing phases are shown at ~5 wt. % increments of crystallization, except when a new mineral comes on the liquidus. Olv = olivine; Plg = plagioclase; Cpx – clinopyroxene; Spl = spinel; Fo = forsterite content of crystallizing olivine; An = anorthite content of crystallizing plagioclase. The oxides and parameters not used in the liquid line of descent modeling have been omitted.

Table E-7. 2384-9P at low pressure, hydrous conditions.

| Step | Melt% | T(C) | $SiO_2$ | $TiO_2$ | $Al_2O_3$ | FeO | MgO | CaO | $Na_2O$ | $K_2O$ | $P_2O_5$ | $Cr_2O_3$ | $H_2O$ | Fo | An | Olv% | Plg% | Cpx% |
|---|---|---|---|---|---|---|---|---|---|---|---|---|---|---|---|---|---|---|
| 1 | 100.00 | 1200 | 49.07 | 1.01 | 17.09 | 7.45 | 9.74 | 11.87 | 2.45 | 0.01 | 0.07 | 0.241 | 0.150 | 88.54 | -1 | 0.00 | 0.00 | 0.00 |
| 2 | 99.00 | 1189 | 49.16 | 1.02 | 17.26 | 7.42 | 9.35 | 11.99 | 2.48 | 0.01 | 0.07 | 0.243 | 0.152 | 88.13 | -1 | 1.00 | 0.00 | 0.00 |
| 4 | 97.99 | 1181 | 49.23 | 1.03 | 17.36 | 7.41 | 9.07 | 12.07 | 2.50 | 0.01 | 0.07 | 0.245 | 0.153 | 87.80 | 80.97 | 1.78 | 0.23 | 0.00 |
| 7 | 94.98 | 1178 | 49.34 | 1.06 | 17.15 | 7.53 | 8.95 | 12.08 | 2.53 | 0.01 | 0.07 | 0.252 | 0.158 | 87.44 | 80.09 | 2.60 | 2.42 | 0.00 |
| 12 | 89.96 | 1172 | 49.52 | 1.12 | 16.77 | 7.75 | 8.72 | 12.10 | 2.58 | 0.02 | 0.08 | 0.265 | 0.167 | 86.79 | 78.56 | 3.97 | 6.07 | 0.00 |
| 17 | 84.93 | 1164 | 49.72 | 1.19 | 16.36 | 7.97 | 8.47 | 12.15 | 2.62 | 0.02 | 0.08 | 0.280 | 0.177 | 86.04 | 76.93 | 5.36 | 9.70 | 0.00 |
| 22 | 79.91 | 1156 | 49.93 | 1.27 | 15.91 | 8.20 | 8.20 | 12.21 | 2.67 | 0.02 | 0.09 | 0.296 | 0.188 | 85.20 | 75.18 | 6.75 | 13.33 | 0.00 |
| 27 | 74.90 | 1146 | 50.14 | 1.35 | 15.44 | 8.45 | 7.88 | 12.31 | 2.71 | 0.02 | 0.09 | 0.315 | 0.200 | 84.22 | 73.32 | 8.17 | 16.93 | 0.00 |
| 36 | 66.86 | 1127 | 50.50 | 1.51 | 14.63 | 8.86 | 7.31 | 12.49 | 2.77 | 0.02 | 0.11 | 0.350 | 0.225 | 82.31 | 70.13 | 10.34 | 22.50 | 0.31 |
| 38 | 64.85 | 1125 | 50.50 | 1.55 | 14.56 | 9.01 | 7.22 | 12.37 | 2.81 | 0.02 | 0.11 | 0.355 | 0.232 | 81.85 | 69.57 | 10.44 | 23.44 | 1.28 |
| 43 | 59.83 | 1119 | 50.51 | 1.66 | 14.37 | 9.40 | 6.97 | 12.04 | 2.90 | 0.02 | 0.12 | 0.372 | 0.251 | 80.56 | 68.08 | 10.69 | 25.79 | 3.69 |
| 48 | 54.82 | 1111 | 50.51 | 1.78 | 14.17 | 9.82 | 6.69 | 11.68 | 3.00 | 0.03 | 0.13 | 0.394 | 0.274 | 79.06 | 66.44 | 10.93 | 28.12 | 6.14 |
| 53 | 49.81 | 1103 | 50.48 | 1.93 | 13.96 | 10.28 | 6.37 | 11.27 | 3.11 | 0.03 | 0.14 | 0.425 | 0.301 | 77.29 | 64.65 | 11.15 | 30.42 | 8.62 |
| 58 | 44.80 | 1092 | 50.44 | 2.10 | 13.74 | 10.76 | 5.99 | 10.80 | 3.24 | 0.03 | 0.16 | 0.465 | 0.335 | 75.14 | 62.68 | 11.37 | 32.70 | 11.14 |
| 63 | 39.79 | 1079 | 50.35 | 2.31 | 13.52 | 11.25 | 5.54 | 10.26 | 3.40 | 0.03 | 0.18 | 0.518 | 0.377 | 72.50 | 60.47 | 11.57 | 34.93 | 13.71 |
| 68 | 34.85 | 1063 | 50.23 | 2.56 | 13.32 | 11.69 | 5.00 | 9.62 | 3.58 | 0.04 | 0.20 | 0.587 | 0.431 | 69.22 | 58.04 | 11.76 | 37.08 | 16.31 |

Notes: The relative proportions (in wt. %) of the major element oxides and crystallizing phases are shown at ~5 wt. % increments of crystallization, except when a new mineral comes on the liquidus. Olv = olivine; Plg = plagioclase; Cpx – clinopyroxene; Spl = spinel; Fo = forsterite content of crystallizing olivine; An = anorthite content of crystallizing plagioclase. The oxides and parameters not used in the liquid line of descent modeling have been omitted.

Table E-8. 2377-7P at low pressure using fractionation model of Langmuir (1992).

| Step | Melt% | T(C) | $SiO_2$ | $TiO_2$ | $Al_2O_3$ | FeO | MgO | CaO | $Na_2O$ | $K_2O$ | $P_2O_5$ | Fo | An | Olv% | Plg% | Cpx% |
|---|---|---|---|---|---|---|---|---|---|---|---|---|---|---|---|---|
| 1 | 100.00 | 1258 | 48.54 | 1.22 | 17.20 | 7.92 | 10.50 | 11.13 | 2.32 | 0.09 | 0.13 | 87.81 | -1.00 | 0.00 | 0.00 | 0.00 |
| 2 | 99.00 | 1248 | 48.62 | 1.23 | 17.37 | 7.89 | 10.12 | 11.24 | 2.34 | 0.09 | 0.13 | 87.45 | -1.00 | 1.00 | 0.00 | 0.00 |
| 5 | 96.99 | 1232 | 48.76 | 1.26 | 17.61 | 7.87 | 9.53 | 11.41 | 2.38 | 0.09 | 0.13 | 86.82 | 81.31 | 2.65 | 0.36 | 0.00 |
| 7 | 94.98 | 1231 | 48.83 | 1.28 | 17.49 | 7.95 | 9.43 | 11.41 | 2.40 | 0.10 | 0.14 | 86.56 | 81.02 | 3.27 | 1.75 | 0.00 |
| 12 | 89.96 | 1226 | 49.01 | 1.36 | 17.16 | 8.17 | 9.17 | 11.41 | 2.45 | 0.10 | 0.15 | 85.87 | 80.26 | 4.79 | 5.25 | 0.00 |
| 17 | 84.93 | 1220 | 49.21 | 1.44 | 16.81 | 8.40 | 8.88 | 11.42 | 2.50 | 0.11 | 0.15 | 85.10 | 79.40 | 6.32 | 8.74 | 0.00 |
| 22 | 79.91 | 1214 | 49.43 | 1.53 | 16.42 | 8.64 | 8.57 | 11.43 | 2.56 | 0.11 | 0.16 | 84.22 | 78.44 | 7.86 | 12.23 | 0.00 |
| 27 | 74.90 | 1207 | 49.66 | 1.63 | 15.98 | 8.90 | 8.22 | 11.46 | 2.61 | 0.12 | 0.17 | 83.21 | 77.35 | 9.40 | 15.70 | 0.00 |
| 32 | 69.87 | 1199 | 49.93 | 1.75 | 15.50 | 9.16 | 7.84 | 11.50 | 2.67 | 0.13 | 0.19 | 82.03 | 76.09 | 10.94 | 19.18 | 0.00 |
| 37 | 64.85 | 1190 | 50.22 | 1.88 | 14.95 | 9.43 | 7.42 | 11.57 | 2.73 | 0.14 | 0.20 | 80.65 | 74.63 | 12.50 | 22.65 | 0.00 |
| 42 | 59.83 | 1179 | 50.54 | 2.04 | 14.34 | 9.70 | 6.94 | 11.67 | 2.79 | 0.15 | 0.22 | 79.00 | 72.93 | 14.06 | 26.10 | 0.00 |
| 46 | 56.82 | 1172 | 50.73 | 2.15 | 13.97 | 9.88 | 6.64 | 11.71 | 2.82 | 0.16 | 0.23 | 77.86 | 71.81 | 14.93 | 28.10 | 0.15 |
| 48 | 54.82 | 1170 | 50.77 | 2.22 | 13.83 | 10.04 | 6.50 | 11.58 | 2.86 | 0.16 | 0.24 | 77.12 | 71.24 | 15.19 | 29.14 | 0.85 |
| 53 | 49.81 | 1163 | 50.88 | 2.41 | 13.47 | 10.49 | 6.10 | 11.21 | 2.96 | 0.18 | 0.26 | 75.02 | 69.64 | 15.84 | 31.73 | 2.62 |
| 58 | 44.80 | 1154 | 51.00 | 2.65 | 13.07 | 10.95 | 5.65 | 10.79 | 3.08 | 0.20 | 0.29 | 72.42 | 67.74 | 16.52 | 34.29 | 4.40 |
| 63 | 39.79 | 1144 | 51.14 | 2.95 | 12.60 | 11.42 | 5.12 | 10.30 | 3.20 | 0.23 | 0.33 | 69.15 | 65.42 | 17.20 | 36.83 | 6.18 |
| 65 | 38.75 | 1142 | 51.17 | 3.02 | 12.50 | 11.51 | 5.00 | 10.18 | 3.23 | 0.23 | 0.34 | 68.37 | 64.88 | 17.35 | 37.35 | 6.55 |

Notes: The relative proportions (in wt. %) of the major element oxides and crystallizing phases are shown at ~5 wt. % increments of crystallization, except when a new mineral comes on the liquidus. Olv = olivine; Plg = plagioclase; Cpx – clinopyroxene; Spl = spinel; Fo = forsterite content of crystallizing olivine; An = anorthite content of crystallizing plagioclase. The oxides and parameters not used in the liquid line of descent modeling have been omitted.

Table E-9. D34-2P at low pressure using fractionation model of Langmuir (1992).

| Step | Melt% | T(C) | $SiO_2$ | $TiO_2$ | $Al_2O_3$ | FeO | MgO | CaO | $Na_2O$ | $K_2O$ | $P_2O_5$ | Cr2O3 | Fo | An | Olv% | Plg% | Cpx% | Spl% |
|---|---|---|---|---|---|---|---|---|---|---|---|---|---|---|---|---|---|---|
| 1 | 100.00 | 1297 | 49.59 | 1.02 | 16.19 | 7.64 | 9.07 | 12.89 | 2.17 | 0.06 | 0.05 | 0.131 | -1 | -1 | 0.00 | 0.00 | 0.00 | 0.00 |
| 2 | 99.76 | 1213 | 49.72 | 1.02 | 16.17 | 7.82 | 9.06 | 12.92 | 2.17 | 0.06 | 0.05 | 0.040 | 86.25 | -1 | 0.00 | 0.00 | 0.00 | 0.24 |
| 3 | 99.17 | 1207 | 49.78 | 1.02 | 16.26 | 7.80 | 8.84 | 13.00 | 2.19 | 0.06 | 0.05 | 0.037 | 86.00 | 80.42 | 0.58 | 0.00 | 0.00 | 0.25 |
| 4 | 99.00 | 1207 | 49.79 | 1.02 | 16.25 | 7.80 | 8.83 | 13.00 | 2.19 | 0.06 | 0.05 | 0.037 | 85.97 | 80.39 | 0.63 | 0.13 | 0.00 | 0.25 |
| 8 | 94.98 | 1202 | 49.97 | 1.07 | 15.96 | 7.96 | 8.61 | 13.07 | 2.21 | 0.06 | 0.05 | 0.039 | 85.40 | 79.75 | 1.85 | 2.92 | 0.00 | 0.25 |
| 13 | 89.96 | 1196 | 50.21 | 1.13 | 15.55 | 8.15 | 8.32 | 13.18 | 2.25 | 0.07 | 0.06 | 0.038 | 84.61 | 78.85 | 3.37 | 6.41 | 0.00 | 0.26 |
| 16 | 87.95 | 1194 | 50.28 | 1.15 | 15.42 | 8.24 | 8.21 | 13.18 | 2.26 | 0.07 | 0.06 | 0.038 | 84.28 | 78.51 | 3.86 | 7.70 | 0.23 | 0.26 |
| 19 | 84.93 | 1192 | 50.32 | 1.19 | 15.31 | 8.41 | 8.10 | 13.08 | 2.30 | 0.07 | 0.06 | 0.040 | 83.80 | 78.11 | 4.23 | 9.29 | 1.29 | 0.26 |
| 24 | 79.91 | 1189 | 50.40 | 1.25 | 15.11 | 8.71 | 7.89 | 12.91 | 2.35 | 0.08 | 0.06 | 0.039 | 82.92 | 77.40 | 4.85 | 11.93 | 3.04 | 0.27 |
| 29 | 74.90 | 1186 | 50.49 | 1.33 | 14.89 | 9.03 | 7.66 | 12.71 | 2.41 | 0.08 | 0.07 | 0.042 | 81.93 | 76.62 | 5.47 | 14.57 | 4.79 | 0.27 |
| 34 | 69.87 | 1182 | 50.58 | 1.41 | 14.65 | 9.38 | 7.42 | 12.49 | 2.48 | 0.09 | 0.07 | 0.041 | 80.80 | 75.73 | 6.09 | 17.21 | 6.55 | 0.27 |
| 39 | 64.85 | 1178 | 50.69 | 1.51 | 14.39 | 9.76 | 7.14 | 12.25 | 2.55 | 0.09 | 0.08 | 0.041 | 79.49 | 74.73 | 6.73 | 19.83 | 8.31 | 0.28 |
| 44 | 59.83 | 1173 | 50.80 | 1.63 | 14.10 | 10.17 | 6.83 | 11.98 | 2.63 | 0.10 | 0.08 | 0.044 | 77.97 | 73.59 | 7.38 | 22.44 | 10.07 | 0.28 |
| 49 | 54.82 | 1167 | 50.93 | 1.76 | 13.77 | 10.61 | 6.48 | 11.66 | 2.71 | 0.11 | 0.09 | 0.044 | 76.16 | 72.29 | 8.03 | 25.02 | 11.84 | 0.29 |
| 54 | 49.81 | 1161 | 51.08 | 1.92 | 13.41 | 11.09 | 6.09 | 11.31 | 2.81 | 0.12 | 0.10 | 0.044 | 74.00 | 70.75 | 8.70 | 27.59 | 13.61 | 0.29 |
| 59 | 44.80 | 1152 | 51.25 | 2.11 | 13.00 | 11.59 | 5.63 | 10.89 | 2.91 | 0.13 | 0.11 | 0.045 | 71.34 | 68.92 | 9.38 | 30.14 | 15.38 | 0.30 |
| 65 | 38.81 | 1140 | 51.50 | 2.40 | 12.42 | 12.20 | 5.00 | 10.29 | 3.05 | 0.15 | 0.13 | 0.043 | 67.27 | 66.22 | 10.22 | 33.15 | 17.52 | 0.31 |

Notes: The relative proportions (in wt. %) of the major element oxides and crystallizing phases are shown at ~5 wt. % increments of crystallization, except when a new mineral comes on the liquidus. Olv = olivine; Plg = plagioclase; Cpx – clinopyroxene; Spl = spinel; Fo = forsterite content of crystallizing olivine; An = anorthite content of crystallizing plagioclase. The oxides and parameters not used in the liquid line of descent modeling have been omitted.

Table E-10. 2384-9P at low pressure using fractionation models of Langmuir (1992).

| Step | Melt% | T(C) | $SiO_2$ | $TiO_2$ | $Al_2O_3$ | FeO | MgO | CaO | $Na_2O$ | $K_2O$ | $P_2O_5$ | $Cr_2O_3$ | Fo | An | Olv% | Plg% | Cpx% | Spl% |
|---|---|---|---|---|---|---|---|---|---|---|---|---|---|---|---|---|---|---|
| 1 | 100.00 | 1380 | 49.12 | 1.01 | 17.10 | 7.04 | 9.75 | 11.88 | 2.46 | 0.01 | 0.07 | 0.241 | -1.00 | -1.00 | 0.00 | 0.00 | 0.00 | 0.00 |
| 2 | 99.46 | 1233 | 49.40 | 1.01 | 17.05 | 7.35 | 9.72 | 11.95 | 2.47 | 0.01 | 0.07 | 0.033 | 87.79 | -1.00 | 0.00 | 0.00 | 0.00 | 0.54 |
| 4 | 98.65 | 1224 | 49.49 | 1.02 | 17.19 | 7.32 | 9.41 | 12.05 | 2.49 | 0.01 | 0.07 | 0.028 | 87.49 | 80.14 | 0.79 | 0.00 | 0.00 | 0.56 |
| 5 | 97.99 | 1223 | 49.51 | 1.03 | 17.14 | 7.34 | 9.38 | 12.06 | 2.50 | 0.01 | 0.07 | 0.028 | 87.41 | 80.04 | 0.99 | 0.46 | 0.00 | 0.56 |
| 8 | 94.98 | 1220 | 49.63 | 1.06 | 16.95 | 7.46 | 9.23 | 12.08 | 2.52 | 0.01 | 0.07 | 0.029 | 87.04 | 79.57 | 1.90 | 2.57 | 0.00 | 0.56 |
| 13 | 89.96 | 1215 | 49.84 | 1.12 | 16.60 | 7.66 | 8.95 | 12.12 | 2.57 | 0.02 | 0.08 | 0.031 | 86.36 | 78.72 | 3.41 | 6.07 | 0.00 | 0.56 |
| 18 | 84.93 | 1209 | 50.07 | 1.19 | 16.22 | 7.87 | 8.65 | 12.18 | 2.63 | 0.02 | 0.08 | 0.033 | 85.58 | 77.76 | 4.93 | 9.58 | 0.00 | 0.56 |
| 23 | 79.91 | 1202 | 50.32 | 1.26 | 15.79 | 8.09 | 8.33 | 12.25 | 2.68 | 0.02 | 0.09 | 0.035 | 84.71 | 76.67 | 6.45 | 13.08 | 0.00 | 0.56 |
| 28 | 74.90 | 1194 | 50.59 | 1.35 | 15.33 | 8.32 | 7.97 | 12.35 | 2.73 | 0.02 | 0.09 | 0.037 | 83.69 | 75.44 | 7.97 | 16.57 | 0.00 | 0.56 |
| 33 | 69.89 | 1185 | 50.89 | 1.44 | 14.81 | 8.56 | 7.57 | 12.47 | 2.78 | 0.02 | 0.10 | 0.040 | 82.50 | 74.03 | 9.51 | 20.05 | 0.00 | 0.56 |
| 34 | 69.87 | 1185 | 50.89 | 1.44 | 14.81 | 8.56 | 7.57 | 12.47 | 2.78 | 0.02 | 0.10 | 0.040 | -1.00 | 74.03 | 9.51 | 20.06 | 0.01 | 0.56 |
| 39 | 64.85 | 1180 | 50.99 | 1.54 | 14.57 | 8.91 | 7.30 | 12.23 | 2.87 | 0.02 | 0.11 | 0.039 | 81.30 | 72.95 | 10.13 | 22.68 | 1.78 | 0.57 |
| 44 | 59.83 | 1176 | 51.10 | 1.66 | 14.30 | 9.30 | 7.00 | 11.95 | 2.96 | 0.02 | 0.12 | 0.039 | 79.90 | 71.73 | 10.75 | 25.30 | 3.55 | 0.57 |
| 49 | 54.82 | 1170 | 51.22 | 1.79 | 14.00 | 9.71 | 6.65 | 11.64 | 3.07 | 0.03 | 0.13 | 0.039 | 78.24 | 70.32 | 11.39 | 27.89 | 5.32 | 0.58 |
| 54 | 49.81 | 1163 | 51.35 | 1.95 | 13.67 | 10.16 | 6.27 | 11.28 | 3.19 | 0.03 | 0.14 | 0.039 | 76.24 | 68.66 | 12.02 | 30.48 | 7.11 | 0.58 |
| 59 | 44.80 | 1155 | 51.50 | 2.15 | 13.30 | 10.65 | 5.82 | 10.86 | 3.32 | 0.03 | 0.16 | 0.040 | 73.79 | 66.68 | 12.68 | 33.04 | 8.90 | 0.59 |
| 64 | 39.79 | 1145 | 51.67 | 2.39 | 12.88 | 11.15 | 5.31 | 10.36 | 3.46 | 0.04 | 0.18 | 0.041 | 70.70 | 64.28 | 13.34 | 35.58 | 10.70 | 0.59 |
| 67 | 37.17 | 1138 | 51.77 | 2.54 | 12.63 | 11.41 | 5.00 | 10.07 | 3.55 | 0.04 | 0.19 | 0.039 | 68.74 | 62.80 | 13.69 | 36.89 | 11.65 | 0.60 |

Notes: The relative proportions (in wt. %) of the major element oxides and crystallizing phases are shown at ~5 wt. % increments of crystallization, except when a new mineral comes on the liquidus. Olv = olivine; Plg = plagioclase; Cpx – clinopyroxene; Spl = spinel; Fo = forsterite content of crystallizing olivine; An = anorthite content of crystallizing plagioclase. The oxides and parameters not used in the liquid line of descent modeling have been omitted.

Table E-11. 2384-9P at 2 kbar using fractionation models of Langmuir (1992).

| Step | Melt% | T(C) | $SiO_2$ | $TiO_2$ | $Al_2O_3$ | FeO | MgO | CaO | $Na_2O$ | $K_2O$ | $P_2O_5$ | $Cr_2O_3$ | Fo | An | Olv% | Plg% | Cpx% | Spl% |
|---|---|---|---|---|---|---|---|---|---|---|---|---|---|---|---|---|---|---|
| 1 | 100.00 | 1380 | 49.12 | 1.01 | 17.10 | 7.04 | 9.75 | 11.88 | 2.46 | 0.01 | 0.07 | 0.241 | -1.00 | -1.00 | 0.00 | 0.00 | 0.00 | 0.00 |
| 2 | 99.49 | 1242 | 49.39 | 1.01 | 17.06 | 7.33 | 9.72 | 11.95 | 2.47 | 0.01 | 0.07 | 0.040 | 87.79 | -1.00 | 0.00 | 0.00 | 0.00 | 0.51 |
| 3 | 99.00 | 1236 | 49.44 | 1.02 | 17.14 | 7.31 | 9.54 | 12.01 | 2.48 | 0.01 | 0.07 | 0.038 | 87.61 | -1.00 | 0.49 | 0.00 | 0.00 | 0.52 |
| 5 | 97.99 | 1230 | 49.51 | 1.03 | 17.20 | 7.31 | 9.31 | 12.08 | 2.50 | 0.01 | 0.07 | 0.033 | 87.34 | 79.03 | 1.16 | 0.31 | 0.00 | 0.54 |
| 8 | 94.98 | 1227 | 49.62 | 1.06 | 17.01 | 7.43 | 9.16 | 12.10 | 2.52 | 0.01 | 0.07 | 0.034 | 86.97 | 78.56 | 2.04 | 2.44 | 0.00 | 0.54 |
| 13 | 89.96 | 1222 | 49.82 | 1.12 | 16.66 | 7.63 | 8.89 | 12.15 | 2.57 | 0.02 | 0.08 | 0.036 | 86.30 | 77.71 | 3.53 | 5.97 | 0.00 | 0.54 |
| 18 | 84.93 | 1216 | 50.04 | 1.19 | 16.27 | 7.84 | 8.61 | 12.22 | 2.61 | 0.02 | 0.08 | 0.038 | 85.53 | 76.75 | 5.03 | 9.50 | 0.00 | 0.54 |
| 23 | 79.91 | 1209 | 50.27 | 1.26 | 15.85 | 8.07 | 8.29 | 12.30 | 2.66 | 0.02 | 0.09 | 0.041 | 84.66 | 75.68 | 6.52 | 13.03 | 0.00 | 0.54 |
| 28 | 75.90 | 1204 | 50.44 | 1.33 | 15.52 | 8.26 | 8.04 | 12.34 | 2.70 | 0.02 | 0.09 | 0.043 | 83.89 | 74.78 | 7.60 | 15.72 | 0.24 | 0.54 |
| 29 | 74.90 | 1203 | 50.45 | 1.34 | 15.48 | 8.33 | 7.99 | 12.30 | 2.71 | 0.02 | 0.09 | 0.043 | 83.70 | 74.61 | 7.71 | 16.26 | 0.59 | 0.54 |
| 34 | 69.87 | 1200 | 50.52 | 1.43 | 15.25 | 8.66 | 7.76 | 12.09 | 2.79 | 0.02 | 0.10 | 0.043 | 82.69 | 73.68 | 8.30 | 18.94 | 2.34 | 0.55 |
| 39 | 64.85 | 1196 | 50.60 | 1.52 | 15.01 | 9.03 | 7.50 | 11.86 | 2.87 | 0.02 | 0.11 | 0.043 | 81.52 | 72.65 | 8.90 | 21.60 | 4.10 | 0.55 |
| 44 | 59.83 | 1191 | 50.68 | 1.64 | 14.74 | 9.43 | 7.20 | 11.61 | 2.96 | 0.02 | 0.12 | 0.043 | 80.16 | 71.47 | 9.51 | 24.25 | 5.86 | 0.56 |
| 49 | 54.82 | 1186 | 50.76 | 1.77 | 14.44 | 9.87 | 6.87 | 11.31 | 3.06 | 0.03 | 0.13 | 0.043 | 78.55 | 70.11 | 10.12 | 26.87 | 7.62 | 0.56 |
| 54 | 49.81 | 1180 | 50.85 | 1.92 | 14.11 | 10.35 | 6.50 | 10.98 | 3.17 | 0.03 | 0.14 | 0.044 | 76.62 | 68.53 | 10.74 | 29.49 | 9.39 | 0.57 |
| 59 | 44.80 | 1173 | 50.94 | 2.11 | 13.73 | 10.87 | 6.07 | 10.59 | 3.29 | 0.03 | 0.16 | 0.045 | 74.26 | 66.66 | 11.37 | 32.09 | 11.18 | 0.57 |
| 64 | 39.79 | 1163 | 51.05 | 2.34 | 13.31 | 11.43 | 5.57 | 10.13 | 3.43 | 0.04 | 0.18 | 0.042 | 71.30 | 64.40 | 12.00 | 34.65 | 12.97 | 0.58 |
| 69 | 34.89 | 1152 | 51.15 | 2.62 | 12.83 | 11.99 | 5.00 | 9.59 | 3.58 | 0.04 | 0.20 | 0.044 | 67.60 | 61.68 | 12.64 | 37.13 | 14.75 | 0.59 |

Notes: The relative proportions (in wt. %) of the major element oxides and crystallizing phases are shown at ~5 wt. % increments of crystallization, except when a new mineral comes on the liquidus. Olv = olivine; Plg = plagioclase; Cpx – clinopyroxene; Spl = spinel; Fo = forsterite content of crystallizing olivine; An = anorthite content of crystallizing plagioclase. The oxides and parameters not used in the liquid line of descent modeling have been omitted.

Table E-12. D20-15P at low pressure.

| Step | Melt% | T(C) | $SiO_2$ | $TiO_2$ | $Al_2O_3$ | FeO | MgO | CaO | $Na_2O$ | $K_2O$ | $P_2O_5$ | $Cr_2O_3$ | $H_2O$ | Fo | An | Olv% | Plg% | Cpx% | Spl% |
|---|---|---|---|---|---|---|---|---|---|---|---|---|---|---|---|---|---|---|---|
| 1 | 100.00 | 1353 | 48.98 | 0.94 | 17.41 | 6.97 | 9.84 | 12.03 | 2.44 | 0 | 0.07 | 0.175 | 0 | -1.00 | -1.00 | 0.00 | 0.00 | 0.00 | 0.00 |
| 2 | 99.61 | 1240 | 49.19 | 0.94 | 17.37 | 7.20 | 9.82 | 12.08 | 2.45 | 0 | 0.07 | 0.035 | 0 | 88.99 | -1.00 | 0.00 | 0.00 | 0.00 | 0.39 |
| 3 | 99.00 | 1234 | 49.24 | 0.94 | 17.47 | 7.19 | 9.58 | 12.15 | 2.46 | 0 | 0.07 | 0.032 | 0 | 88.75 | -1.00 | 0.61 | 0.00 | 0.00 | 0.40 |
| 5 | 97.99 | 1230 | 49.30 | 0.95 | 17.46 | 7.21 | 9.45 | 12.19 | 2.48 | 0 | 0.07 | 0.03 | 0 | 88.57 | 81.30 | 1.06 | 0.54 | 0.00 | 0.41 |
| 10 | 92.98 | 1226 | 49.48 | 1.00 | 17.10 | 7.42 | 9.26 | 12.20 | 2.53 | 0 | 0.08 | 0.03 | 0 | 88.01 | 79.83 | 2.42 | 4.20 | 0.00 | 0.41 |
| 15 | 87.95 | 1221 | 49.68 | 1.06 | 16.70 | 7.64 | 9.05 | 12.24 | 2.57 | 0 | 0.08 | 0.031 | 0 | 87.39 | 78.24 | 3.77 | 7.87 | 0.00 | 0.41 |
| 20 | 82.93 | 1215 | 49.88 | 1.12 | 16.28 | 7.88 | 8.81 | 12.29 | 2.62 | 0 | 0.08 | 0.032 | 0 | 86.69 | 76.56 | 5.15 | 11.52 | 0.00 | 0.41 |
| 25 | 77.91 | 1208 | 50.10 | 1.20 | 15.81 | 8.13 | 8.55 | 12.37 | 2.66 | 0 | 0.09 | 0.033 | 0 | 85.89 | 74.76 | 6.52 | 15.16 | 0.00 | 0.41 |
| 30 | 72.89 | 1200 | 50.32 | 1.28 | 15.31 | 8.39 | 8.25 | 12.48 | 2.70 | 0 | 0.10 | 0.034 | 0 | 84.97 | 72.82 | 7.92 | 18.78 | 0.00 | 0.41 |
| 35 | 67.86 | 1190 | 50.56 | 1.37 | 14.76 | 8.67 | 7.91 | 12.63 | 2.74 | 0 | 0.10 | 0.036 | 0 | 83.89 | 70.72 | 9.34 | 22.39 | 0.00 | 0.41 |
| 40 | 63.62 | 1180 | 50.78 | 1.47 | 14.26 | 8.91 | 7.58 | 12.80 | 2.76 | 0 | 0.11 | 0.037 | 0 | 82.81 | 68.83 | 10.56 | 25.41 | 0.00 | 0.41 |
| 41 | 62.84 | 1180 | 50.78 | 1.48 | 14.22 | 8.98 | 7.55 | 12.76 | 2.77 | 0 | 0.11 | 0.035 | 0 | 82.63 | 68.59 | 10.60 | 25.78 | 0.37 | 0.41 |
| 45 | 58.83 | 1176 | 50.80 | 1.57 | 14.05 | 9.32 | 7.37 | 12.52 | 2.84 | 0 | 0.12 | 0.027 | 0 | 81.65 | 67.34 | 10.81 | 27.67 | 2.28 | 0.41 |
| 50 | 53.81 | 1171 | 50.81 | 1.69 | 13.81 | 9.79 | 7.12 | 12.19 | 2.93 | 0 | 0.13 | 0.021 | 0 | 80.24 | 65.64 | 11.06 | 30.03 | 4.69 | 0.41 |
| 55 | 48.81 | 1165 | 50.79 | 1.83 | 13.56 | 10.30 | 6.82 | 11.81 | 3.03 | 0 | 0.14 | 0.017 | 0 | 78.55 | 63.77 | 11.30 | 32.37 | 7.12 | 0.41 |
| 60 | 43.80 | 1158 | 50.76 | 2.00 | 13.28 | 10.88 | 6.48 | 11.39 | 3.15 | 0 | 0.16 | 0.014 | 0 | 76.52 | 61.69 | 11.54 | 34.69 | 9.57 | 0.41 |
| 65 | 38.78 | 1149 | 50.69 | 2.21 | 12.99 | 11.51 | 6.07 | 10.90 | 3.28 | 0 | 0.18 | 0.013 | 0 | 74.02 | 59.34 | 11.76 | 36.98 | 12.07 | 0.41 |
| 70 | 33.77 | 1137 | 50.57 | 2.47 | 12.69 | 12.18 | 5.57 | 10.32 | 3.44 | 0 | 0.21 | 0.013 | 0 | 70.84 | 56.67 | 11.98 | 39.22 | 14.62 | 0.41 |
| 75 | 29.23 | 1123 | 50.40 | 2.76 | 12.42 | 12.78 | 5.00 | 9.70 | 3.62 | 0 | 0.24 | 0.014 | 0 | 67.14 | 53.92 | 12.16 | 41.21 | 16.99 | 0.41 |

Notes: The relative proportions (in wt. %) of the major element oxides and crystallizing phases are shown at ~5 wt. % increments of crystallization, except when a new mineral comes on the liquidus. Olv = olivine; Plg = plagioclase; Cpx – clinopyroxene; Spl = spinel; Fo = forsterite content of crystallizing olivine; An = anorthite content of crystallizing plagioclase. The oxides and parameters not used in the liquid line of descent modeling have been omitted.

Table E-13. 2375-7P at low pressure.

| Step | Melt% | T(C) | $SiO_2$ | $TiO_2$ | $Al_2O_3$ | FeO | MnO | MgO | CaO | $Na_2O$ | $K_2O$ | $P_2O_5$ | $H_2O$ | Fo | An | Olv% | Plg% | Cpx% |
|---|---|---|---|---|---|---|---|---|---|---|---|---|---|---|---|---|---|---|
| 1 | 100.0 | 1204 | 50.22 | 1.38 | 15.32 | 8.63 | 0.17 | 8.29 | 12.02 | 2.72 | 0.09 | 0.11 | 0 | 84.66 | -1.00 | 0.00 | 0.00 | 0.00 |
| 2 | 99.8 | 1202 | 50.24 | 1.39 | 15.35 | 8.62 | 0.17 | 8.21 | 12.05 | 2.73 | 0.09 | 0.11 | 0 | 84.54 | 72.73 | 0.21 | 0.00 | 0.00 |
| 3 | 99.0 | 1201 | 50.27 | 1.40 | 15.30 | 8.65 | 0.17 | 8.17 | 12.06 | 2.73 | 0.09 | 0.11 | 0 | 84.42 | 72.50 | 0.44 | 0.57 | 0.00 |
| 5 | 97.0 | 1198 | 50.34 | 1.43 | 15.14 | 8.73 | 0.17 | 8.08 | 12.09 | 2.75 | 0.09 | 0.11 | 0 | 84.12 | 71.90 | 1.00 | 2.02 | 0.00 |
| 10 | 92.0 | 1191 | 50.51 | 1.50 | 14.73 | 8.94 | 0.18 | 7.82 | 12.19 | 2.77 | 0.09 | 0.12 | 0 | 83.27 | 70.35 | 2.42 | 5.61 | 0.00 |
| 15 | 86.9 | 1182 | 50.69 | 1.59 | 14.29 | 9.16 | 0.18 | 7.54 | 12.32 | 2.79 | 0.10 | 0.12 | 0 | 82.31 | 68.69 | 3.87 | 9.18 | 0.00 |
| 20 | 82.9 | 1175 | 50.83 | 1.67 | 13.95 | 9.33 | 0.19 | 7.30 | 12.41 | 2.81 | 0.10 | 0.13 | 0 | 81.45 | 67.36 | 4.94 | 11.91 | 0.22 |
| 25 | 77.9 | 1171 | 50.84 | 1.76 | 13.78 | 9.66 | 0.19 | 7.12 | 12.17 | 2.87 | 0.11 | 0.14 | 0 | 80.46 | 66.17 | 5.19 | 14.28 | 2.62 |
| 30 | 72.9 | 1167 | 50.83 | 1.86 | 13.60 | 10.00 | 0.20 | 6.92 | 11.91 | 2.94 | 0.12 | 0.15 | 0 | 79.34 | 64.89 | 5.43 | 16.63 | 5.05 |
| 35 | 67.9 | 1162 | 50.82 | 1.97 | 13.41 | 10.38 | 0.21 | 6.69 | 11.63 | 3.01 | 0.13 | 0.16 | 0 | 78.06 | 63.52 | 5.67 | 18.97 | 7.50 |
| 40 | 62.8 | 1157 | 50.80 | 2.10 | 13.21 | 10.78 | 0.21 | 6.45 | 11.32 | 3.09 | 0.14 | 0.17 | 0 | 76.60 | 62.04 | 5.90 | 21.29 | 9.96 |
| 45 | 57.8 | 1151 | 50.75 | 2.25 | 13.00 | 11.20 | 0.22 | 6.16 | 10.97 | 3.18 | 0.15 | 0.18 | 0 | 74.91 | 60.44 | 6.13 | 23.59 | 12.46 |
| 50 | 52.8 | 1143 | 50.69 | 2.43 | 12.78 | 11.64 | 0.23 | 5.84 | 10.59 | 3.27 | 0.16 | 0.20 | 0 | 72.92 | 58.70 | 6.35 | 25.86 | 14.98 |
| 55 | 47.8 | 1135 | 50.61 | 2.63 | 12.56 | 12.09 | 0.24 | 5.46 | 10.16 | 3.38 | 0.18 | 0.22 | 0 | 70.57 | 56.78 | 6.56 | 28.10 | 17.54 |
| 60 | 42.8 | 1124 | 50.49 | 2.87 | 12.34 | 12.53 | 0.25 | 5.02 | 9.67 | 3.51 | 0.20 | 0.25 | 0 | 67.73 | 54.68 | 6.77 | 30.29 | 20.15 |

Notes: The relative proportions (in wt. %) of the major element oxides and crystallizing phases are shown at ~5 wt. % increments of crystallization, except when a new mineral comes on the liquidus. Olv = olivine; Plg = plagioclase; Cpx – clinopyroxene; Spl = spinel; Fo = forsterite content of crystallizing olivine; An = anorthite content of crystallizing plagioclase. The oxides and parameters not used in the liquid line of descent modeling have been omitted.

# APPENDIX F
# REGRESSION ANALYSIS FOR $FE_{8.0}$ AND $NA_{8.0}$

$Na_2O$ and FeO values can be "corrected" for low-pressure fractionation by extrapolating the $Na_2O$ and FeO values along a line of constant slope to 8 wt% MgO. The line is meant to approximate the slope of the liquid lines of decent (LLD), which approximates the change in melt composition produced during crystallization and will fit samples related by fractionation. Samples for individual regions usually form rather smooth trends on plots of oxide abundances as a function of MgO. The best-fit line is meant to approximate the slope of the olivine+plagioclase±clinopyroxene LLD. The problem with using just one line is that there are strong kinks in the slope of the data and the LLD when a new mineral joins the fractionating assemblage. In the Siqueiros data, there is a kink when plagioclase joins the olivine and when clinopyroxene joins the assemblage. In order to fit the trend of the data, two lines of different slope were used to match the kinks in the data (Figures D-1 and D-2). This allowed the samples with higher MgO values to be projected along the shallow olivine slope and the samples with lower MgO along the steeper olivine-plagioclase slope. For this data set, two lines fit reasonably well, but a better fit was obtained by using a second order polynomial (Figures D-3 and D-4). The polynomial was better at fitting the kinks because the Siqueiros data appears to be best explained by more than one LLD and the kinks do not appear to be at the same MgO for each LLD making it difficult to choose two lines to fit the data. The curve of the polynomial was better at fitting all of the data. The $R^2$ was

0.95 for FeO vs. MgO and 0.77 for $Na_2O$ vs. MgO. The equation of the polynomial was then used to extrapolate the data back to 8wt% MgO. The calculated values at 8 wt% MgO of $Na_2O$ and FeO are called $Na_{8.0}$ and $Fe_{8.0}$, respectively.

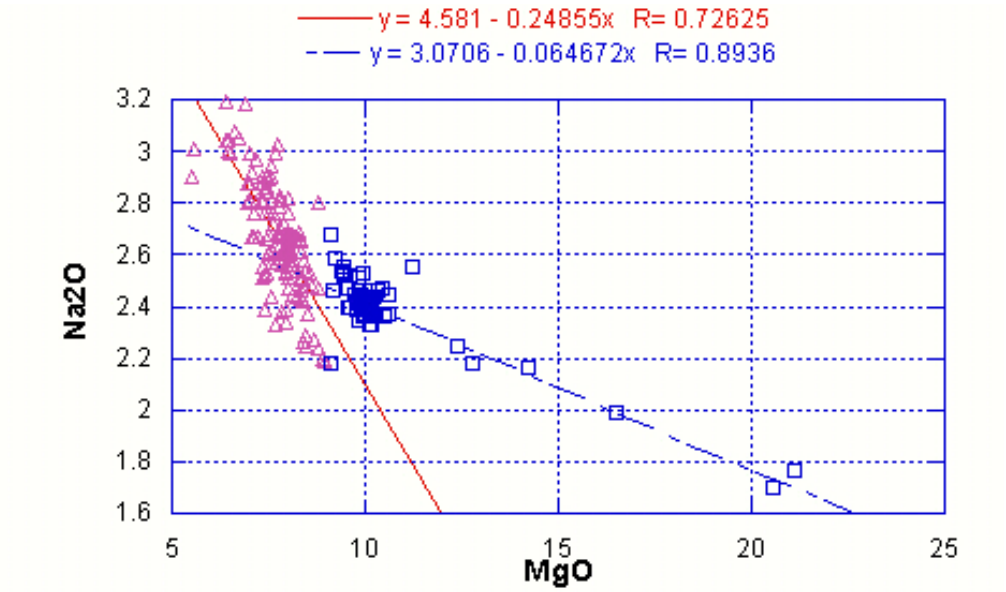


Figure F-1. Linear regression of $Na_2O$. Two best fit-lines used to match the shallow olivine slope and the steeper olivine - plagioclase ± clinopyroxene slope. The kink in the slope set at 9.0 wt% MgO based on the calculated LLDs in chapter 6. A best-fit 2nd order polynomial was used instead to extrapolate data back to 8 wt% MgO.

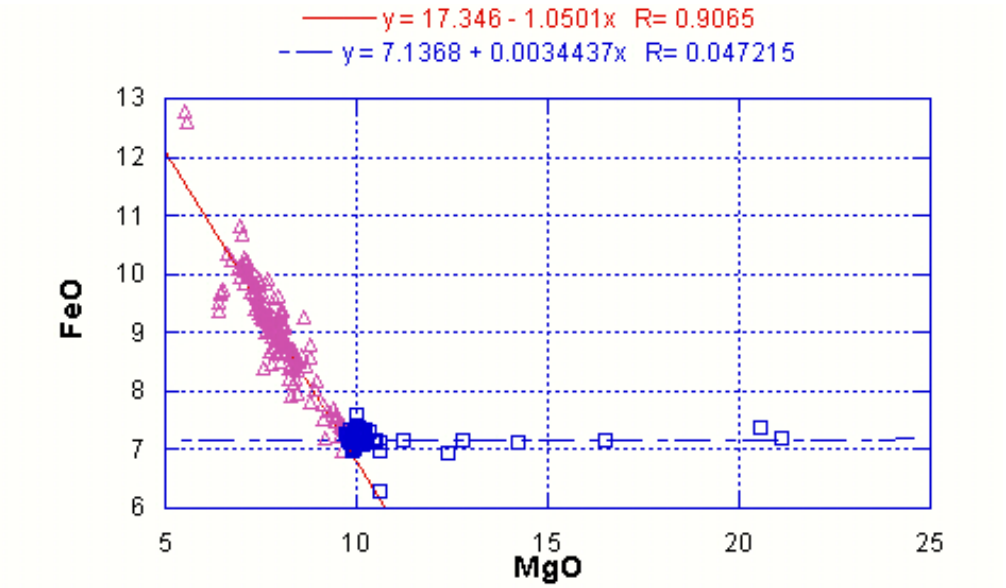


Figure F-2. Linear regression of FeO. Two best fit-lines used to match the shallow olivine slope and the steeper olivine - plagioclase ± clinopyroxene slope. The kink in the slope set at 9.98 wt% MgO based on the calculated LLDs in Chapter 6. A best-fit 2nd order polynomial was used instead to extrapolate data back to 8 wt% MgO.

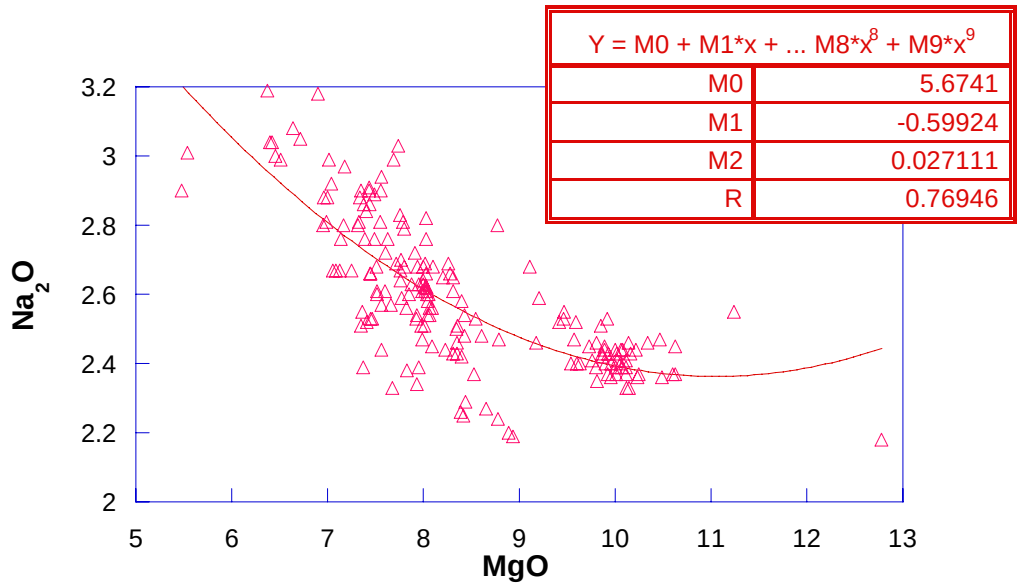


Figure F-3. Polynomial regression of $Na_2O$. The best-fit 2nd order polynomial that was used to extrapolate $Na_2O$ data back to 8 wt% MgO is shown. $Na_{8.0} = Na_2O + -0.59924 \times (8 - MgO) + 0.027111 \times (64 - MgO^2)$.

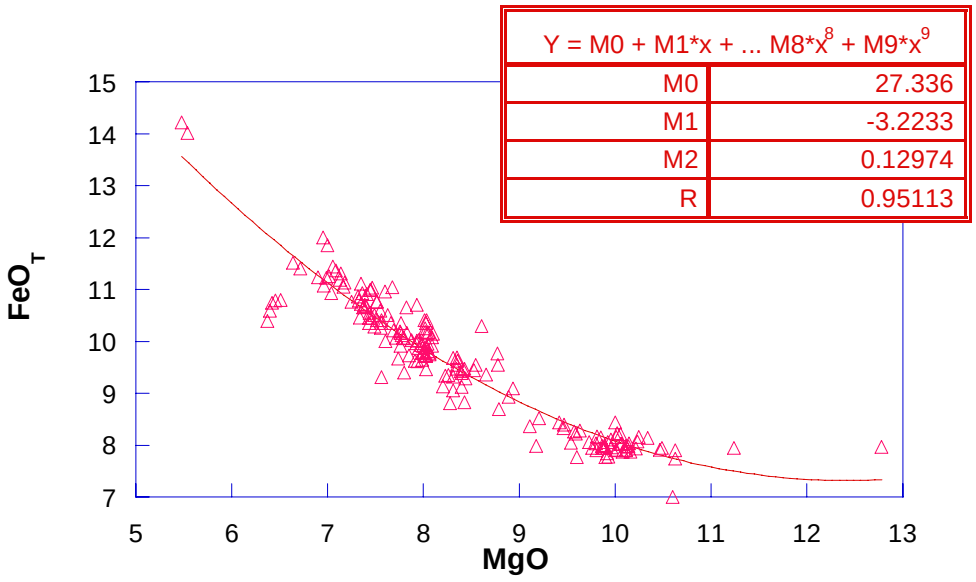


Figure F-4. Polynomial regression of FeO. The best-fit 2nd order polynomial that was used to extrapolate FeO data back to 8 wt% MgO is shown. $Fe_{8.0} = FeO + -3.2233 \times (8 - MgO) + 0.12974 \times (64 - MgO^2)$

LIST OF REFERENCES

Allan, J., R. O. Sack, R. Batiza, Cr-rich spinels as petrogenetic indicators: MORB-type lavas from the Lamont seamount chain, Eastern Pacific, American Mineralogist, 73 (1988) 741-753.

Ariskin, A. A., Nikolaev G. S., An empirical model for the calculation of spinel-melt equilibria in mafic igneous systems at atmospheric pressure: 1. Chromian spinels, Contrib. Mineral. Petrol., 123 (1996) 282-292.

Ballard, R. D., J. Francheteau, T. Juteau, C. Rangan, W. R. Normark, East Pacific Rise at 21 degrees N; the volcanic, tectonic, and hydrothermal processes of the central axis, Earth and Plant. Sci. Lett., 55 (1981) 1-10.

Barnes, S. J. and P. L. Roeder, The range of spinel compositions in terrestrial mafic and ultramafic rocks, J. Petrol., 42(12) (2001) 2,279-2,302.

Batiza, R., B. R. Rosendahl, R.L. Fisher, Evolution of oceanic crust: Petrology and chemistry of basalts from the East Pacific Rise and the Siqueiros Transform Fault, J. Geophys. Res., 82 (1977) 265-276.

Batiza R. and Y. Niu, Petrology and magma chamber processes at the East Pacific Rise-9°30'N, J. Geophys. Res., 97 (1992) 6,779-6,797.

Bazin S., A. J. Harding, G. M. Kent, J. A. Orcutt, C. H. Tong, J. W. Pye, S.C., Singh, P.J. Barton, M.C. Sinha, R.S. White, R.W. Hobbs, J. J. A. Van Avendonk, Three-dimensional shallow crustal emplacement at the 9°03' N overlapping spreading center on the East Pacific Rise: Correlations between magnetization and tomographic images, J. Geophys. Res., 106 (2001) 16,101-16,117.

Beattie P., Olivine-melt and orthopyroxene-melt equilibria, Contrib. Mineral. Petrol., 115 (1993) 103-111.

Bender J. F., C. H. Langmuir, G. N. Hanson, Petrogenesis of basalt glasses from the Tamayo Region, East Pacific Rise, J. Petrol., 25 (1984) 213-254.

Bideau, D. and R. Hekinian, A dynamic model for generating small-scale heterogeneities in ocean floor basalts, J. Geophys. Res., 100 (1995) 10,141-10,162.

Bindeman, I. N., A. M. Davis, M. J. Drake, Ion microprobe study of plagioclase-basalt partition experiments at natural concentration levels of trace elements, Geochim. Cosmochim. Acta, 62 (1998) 1175-1193.

Boudier, F., Nicolas, A., and Ildefonse, B., Magma chambers in the Oman Ophiolite: fed from the top and the bottom, Earth Planet. Sci. Lett., 144 (1996) 239-250.

Bougault, H. and R. Hekinian, Rift valley in the Atlantic Ocean near 36 degrees 50'N; petrology and geochemistry of basalt rocks, Earth Planet. Sci. Lett., 24(2) (1974) 249-261.

Brodholt, J. P. and R. Batiza, Global systematics of unaveraged mid-ocean ridge basalt compositions: comment on "Global correlations of ocean ridge basalt chemistry with axial depth and crustal thickness, J. Geophys. Res., 94 (1989) 4,231-4,239.

Bryan, W. B., G. Thompson, P. J. Michael, Compositional variation in a steady-state zoned magma chamber; Mid-Atlantic Ridge at 36 degrees 50'N, Tectonophysics, 55 (1979) 63-85.

Castillo, P. R., E. Klein, J. Bender, C. Langmuir, S. Shirey, R. Batiza, W. White, Petrology and Sr, Nd, and Pb isotope geochemistry of mid-ocean ridge basalt glasses form 11°45'N to 15°00'N segment of the East Pacific Rise, Geochemistry Geophysics Geosystems$^3$, 1 (2000) paper 1999GC000024.

Castillo, P. R., J. H. Natland, Y. Niu, P. F. Lonsdale, Sr, Nd, and Pb isotopic variation along the Pacific-Antarctic rise-crest, 53-57°S: implications for the composition and dynamics of the South Pacific upper mantle, Earth Planet. Sci. Lett., 154 (1988) 109-125.

Christie, D. M. and J. M. Sinton, Evolution of abyssal lavas along propagating segments of the Galapagos spreading center, Earth Planet. Sci. Lett., 56 (1981) 321-335.

Crane, K., The intersection of the Siqueiros transform fault and the East Pacific Rise, Mar. Geol., 21 (1976) 25-46.

Danyushevsky L. V., The effect of small amounts of $H_2O$ on crystallisation of mid-ocean ridge and backarc basin magmas, J. Volcan. Geoth. Res., 110 (2001) 265-280.

Danyushevsky, L. V., M. R. Perfit, S. M. Eggins, T. J. Falloon, Crustal origin for coupled 'ultra-depleted' and 'plagioclase' signatures in MORB olivine-hosted melt inclusions: evidence from the Siqueiros transform fault, East Pacific Rise, Contrib. Mineral. Petrol., 144 (2003) 619-637.

Danyushevsky, L. V., A. V. Sobolev, L. V. Dmitriev, Estimation of the pressure of crystallisation and $H_2O$ content of MORB and BABB glasses: calibration of an empirical technique, Mineralogy and Petrology, 57 (1996) 185-204.

Detrick, R. S. and G. M. Purdy, The crustal structure of the Kane fracture zone from seismic refraction studies, J. Geophys. Res., 85 (1980) 3759-3777.

Detrick R. S., J. D. Mudie, B. P. Luvendvk, K. C. Macdonald, A near-bottom geophysical survey of a transform fault: Mid-Atlantic Ridge, 37 degrees N, Nature, 246 (1973) 59-61.

Detrick, R. S., P. Buhl, E. E. Vera, J. C. Mutter, J. A. Orcutt, J. A. Madsen, T. M. Brocher, Multi-channel seismic imaging of a crustal magma chamber along the East Pacific Rise, Nature (London), 326(6108) (1987) 35-41.

Dick, H. J. B. and T. Bullen, Chromian spinel as a petrogenetic indicator in abyssal and alpine-type peridotites and spatially associated lavas, Contrib. Mineral. Petrol., 86 (1984) 54-76.

Duke, J. M., Distribution of the period four transition elements among olivine, calcic clinopyroxene and mafic silicate liquid; experimental results, J. of Petrol., 17(4) (1976) 499-521.

Dunn, R. A., D. R. Toomey, S. C. Solomon, Three-dimensional seismic structure and physical properties of the crust and shallow mantle beneath the East Pacific Rise at 9 degrees 30' N, J. Geophys. Res., 105 (2000) 23,537-23,555.

Elthon, Don, The petrology and geochemistry of rocks recovered within the proximal to oceanic fracture zones, From Fox P.J. (ed) Academic Press, 1988, The Tectonics of Oceanic Fracture Zones.

Embley, R. W. and D. S. Wilson, Morphology of the Blanco transform fault zone, NE Pacific; implications for its tectonic evolution, Mar. Geophys. Res., 14 (1992) 25-45.

Falloon, T. J., D. H. Green, H. St. C. O'Neill, W. O. Hibberson, Experimental tests of low degree peridotite melt compositions; implications for the nature of anhydrous near-solidus peridotite melts at 1 GPa, Earth Planet. Sci. Lett., 152 (1997) 149-162.

Fornari, D. J., D. G. Gallo, M. H. Edward, J. A. Madsen, M. R. Perfit, A. N. Shor, Structure and topography of the Siqueiros transform fault system: Evidence for the development of intra-transform spreading centers, Mar. Geophys. Res., 11 (1989) 263-299.

Fornari, D. J., M. R. Perfit, A. Malahoff, R. Embley, Geochemical studies of abyssal lavas recovered by DSRV ALVIN from Eastern Galapagos Rift, Inca Transform, and Ecuador Rift 1. Major element variations in natural glasses and spacial distribution of lavas, J. Geophys. Res., 88 (1983) 10,519-10,529.

Fornari, D. J., M. R. Perfit, J. Casey, K. Kastens, M. Edwards, Final Cruise Report: Siqueiros – Alvin Diving Cruise Atlantis-II 125-25 (1991) (unpublished).

Fornari, D. J., M. R. Perfit, J. F. Allan, R. Batiza, R. Haymon, A. Barone, W.B.F. Ryan, T. Smith, T. Simkin, and M.A. Luckman, Geochemical and structural studies of the Lamont Seamounts: Seamounts as indicators of mantle processes, Earth Planet. Sci. Lett., 89 (1988) 63-83.

Fox, P. J., The effect of transform faults on the character of the oceanic crust. Abstr. Progrm. Geol. Soc. Am., 7 (1978) 403.

Fox, P. J., D. G. Gallo, H. S. Sloan, Ridge-transform intersections; a general model for the bathymetry of fracture zones, EOS Trans. AGU, 62 (1981) 1049-1050.

Goldstein, S. ., M. R. Perfit, R. Batiza, D. J. Fornari, M. T. Murrell, Off-axis volcanism at the East Pacific Rise detected by uranium-series dating of basalts, Nature (London), 367(6459) (1994) 157-159.

Grove, T. L., Origin of magmas, From H. Sigurdsson, B. F. Houghton, S. R. McNutt, R. H. Rymer, J. Stix (eds), San Diego, CA, Academic Press, 2000, Encyclopedia of volcanoes.

Hanson, G. N., Geochemical evolution of the suboceanic mantle, J. Geol. Soc. Lond., 134 (1977) 235-253.

Hart, S. R. and T. Dunn, Experimental cpx/melt partitioning of 24 trace elements, Contrib. Mineral. Petrol., 113 (1993) 1-8.

Hauri, E. H., T. P. Wagner, T. L. Grove, Experimental and natural partitioning of Th, U, Pb and other trace elements between garnet, clinopyroxene and basaltic melts, Chemical Geology, 117 (1994) 149-166.

Haymon, R. M., D. J. Fornari, K. L. von Damm, M. D. Lilley, M. R. Perfit, J. M. Edmond, W. C. Shanks III, R. A. Lutz, J. M. Grebmeier, S. Carbotte, D. Wright, E. McLaughlin, M. Smith, N. Beedle, E. Olson, Volcanic eruption of the mid-ocean ridge along the East Pacific Rise crest at 9 degrees 45-52'N; direct submersible observations of seafloor phenomena associated with an eruption event in April, 1991, Earth Planet. Sci. Lett., 119 (1993) 85-101.

Haymon, R. M., S. Carbotte, D. Wright, N. Beedle, F. Johnson, D. J. Fornari, K. L. von Damm, J. Grebmeier, M. Lilley, E. McLaughlin, E. Olson, J. Edmond, M. R. Perfit, M. Smith, W. C. Shanks III, R. Lutz, J. Seewald, D. Reudelhuber, Active eruption observed on East Pacific Rise, Earth in Space, 4(4) (1991) pp.5.

Hekinian, R., D. Bideau, R. Hebert, Y. Niu, Magmatism in the Garrett transform fault (East Pacific Rise near 13°27'S), J. Geophys. Res., 100 (1995) 10,163-10,185.

Hekinian, R., G. Thompson, D. Bideau, Axial and off-axial heterogeneity of basaltic rocks from the East Pacific Rise at 12°35'N-12°51'N and 11°26'N-11°30'N, J. Geophys. Res., 94 (1989) 17,437-17,463.

Hekinian, R. and G. Thompson, Comparative geochemistry of volcanics from rift valleys, transform faults and aseismic ridges, Contrib. Mineral. Petrol., 57 (1976) 145-162.

Henderson, P., Inorganic Geochemistry, 353p. Pergamon Press, Oxford, 1986.

Herzberg C. and M. J. O'Hara, Plume-associated ultramafic magmas of phanerozoic age, J. Petrol., 43 (2002) 1857-1883.

Hussenoeder, S. A., J. A. Collins, G. M. Kent, R. S. Detrick, Seismic analysis of the axial magma chamber reflector along the southern East Pacific Rise from conventional reflection profiling, J. Geophys. Res., 101 (1996) 22,087-22,105.

Johnson, K. T. M. and R. J. Kinzler, Partitioning of REE, Ti, Zr, Hf, and Nb between clinopyroxene and basaltic liquid: an ion microprobe study, EOS Trans. AGU, 70 (1989) 1,388.

Kastens, K. A., W. B. F. Ryan, P. J. Fox, Structural and volcanic expressions of a fast slipping ridge-transform-ridge plate boundary; Sea MARC I and photographic surveys at the Clipperton transform fault, J. Geophys. Res., 91 (1986) 3469-3488.

Kelemen, P. B., G. Hirth, N. Shimizu, M. Spiegelman, and J.J.B. Dick, A review of melt migration processes in the adiabatically upwelling mantle beneath oceanic spreading ridges, Philos. Trans. R. Soc. London, Ser. A. 355, (1997) 283-318.

Kerr, A. C. and N. T. Arndt, A note on the IUGS reclassification of the high-Mg and picritic volcanic rocks, J. Petrol., 42 (2001) 2169-2171.

Kohut, E. J. and R. L. Nielsen, Low-pressure phase equilibria of anhydrous anorthite-bearing mafic magmas, Geochemistry Geophysics Geosystems$^3$, 4 (2003) paper 2002GC000451.

Lange, R. A. and I. S. E. Carmichael, Densities of $Na_2O$-$K_2O$-CaO-MgO-FeO-$Fe_2O_3$-$Al_2O_3$-$TiO_2$-$SiO_2$ liquids; new measurements and derived partial molar properties, Geochim. Cosmochim. Acta, 51 (1987) 2931-2946.

Langmuir, C. H., E. M. Klein, T. Plank, Petrological systematics of mid-ocean ridge basalts: Constraints on melt generation beneath ocean ridges, AGU Geophysical Monograph, 71 (1992) 183-281.

Langmuir, C. H. and J. F. Bender, The geochemistry of oceanic basalts in the vicinity of transform faults: observations and implications, Earth Planet. Sci. Lett., 69 (1984) 107-127.

Langmuir, C. H. and J. F. Bender, Petrologic and tectonic segmentation of the East Pacific Rise, 5°30'-14°30'N, Nature, 322 (1986) 422-429.

Le Bas, M. J., IUGS reclassification of the high-Mg and picritic volcanic rocks, J. Petrol., 41 (2000) 1467-1470.

Le Roex, A. P. and H. J. B. Dick, Petrography and geochemistry of basaltic rocks from the Conrad fracture zone on the America-Antarctica Ridge, Earth Planet. Sci. Lett., 54 (1981) 117-138.

Lundstrom C. C., D. E. Sampson, M. R. Perfit, J. Gill, Q. Williams, Insights into mid-ocean ridge basalt petrogenesis: U-series disequilibria from the Siqueiros Transform, Lamont Seamounts, and East Pacific Rise, J. Geophys. Res., 104 (1999) 13,035-13,048.

Macdonald, K. C., Linkages between faulting, volcanism, hydrothermal activity and segmentation on fast spreading centers, Geophysical Monograph, 106 (1998) 27-58.

Macdonald, K. C., D. S. Scheirer, S. M. Carbotte, Mid-Ocean Ridges: Discontinuities, Segments and Giant Cracks, Science, 253 (1991) 986-994.

Macdonald, K. C. and P. J. Fox, The axial summit graben and cross-sectional shape of the East Pacific Rise as indicators of axial magma chambers and recent volcanic eruptions, Earth Planet. Sci. Lett., 88 (1988) 119-131.

Macdonald, K. C., P. J. Fox, L. J. Perram, M. F. Eisen, R. M. Haymon, S. P. Miller, S. M. Carbotte, M. H. Cormier, A. N. Shor, A new view of the mid-ocean ridge form the behaviour of ridge-axis discontinuities, Nature, 335 (1988) 217-225.

McKay, G., L. Le, J. Wagstaff, G. Crozaz, Experimental partitioning of rare earth elements and strontium; constraints on petrogenesis and redox conditions during crystallization of Antarctic angrite Lewis Cliff 86010, Geochim. Cosmochim. Acta, 58(13) (1994) 2911-2919.

MacLeod, C. J.and G. Yaouancq, A fossil melt lens in the Oman ophiolite: Implications for magma chamber processes at fast spreading ridges, Earth Planet. Sci. Lett., 176 (2000) 357-373.

Meeker, G.P. and J.E. Quick, OPUS: Old probe-updated software, in: Microbeam Analysis, D.G. Howitt (ed.) (1991) pp. 353-354.

Melson, W. G. and G. Thompson, Petrology of a transform fault and adjacent ridge segments, Phil. Trans. Toy. Sco. London, Ser. A, 268 (1971) 423-441.

Natland, J. H., Partial melting of a lithologically heterogeneous mantle: inferences from crystallization histories of magnesian abyssal tholeiites from the Siqueiros Fracture Zone, From Saunders, A.D. & Norry, M.J. (eds) 1989, Magmatism in the Ocean Basins, Geological Society Special Publication No. 42 41-70.

Natland, J. H. and H. J. B. Dick, Melt migration through high-level gabbroic cumulates of the East Pacific Rise at Hess Deep; the origin of magma lenses and the deep crustal structure of fast-spreading ridges, Proceedings of the Ocean Drilling Program, Scientific Results, 147 (1996) 21-58.

Natland, J. H. and H. J. B. Dick, Origin of melt lenses at the East Pacific Rise: Inferences from textures and compositions of gabbros and dikes at Hess Deep – a pictorial essay, in prep.

Natland, J. H. and W. G. Melson, Compositions of basaltic glasses form the East Pacific rise and Siqueiros fracture zone near 9°N, Initial Rep. Deep Sea Drill Proj., 54 (1980) 705-723.

Orcutt, J. A., B. L. N. Kennett, and L. M. Dorman, Structure of the East Pacific Rise from an ocean bottom seismometer survey, Geophys. J. Roy. Astron. Soc., 45 (1976) 305-320.

Pan, Y. and R. Batiza, Magmatic processes under mid-ocean ridges: A detailed mineralogic study of lavas from East Pacific Rise 9°30'N, 10°30'N, and 11°20'N, Geochemistry Geophysics Geosystems$^3$, 4 (2003) paper 2002GC000309.

Pan, Y. and R. Batiza, Mid-ocean ridge magma chamber processes: Constraints from olivine zonation in lavas from the East Pacific Rise at 9°30'N and 10°30'N, J. Geophys. Res., 107 (2002) 1-13.

Perfit, M. R., D. J. Fornari, A. Malahoff, and R. W. Embley, Geochemical studies of abyssal lavas recovered by DSRV ALVIN from eastern Galapagos Rift, Inca Transform, and Equador Rift 3. Trace element abundances and petrogenesis, J. Geophys. Res., 88 (1983) 10,551-10,572.

Perfit, M. R. and D. J. Fornari, Geochemical studies of abyssal lavas recovered by DSRV Alvin form eastern Galapogos Rift, Inca Transform, and Ecuador Rift; 2, Phase chemistry and crystallization history, J. Geophys. Res., 88 (1983) 10530-10550.

Perfit, M. R., D. J. Fornari, M. C. Smith, C. Langmuir, J. Bender, R. M. Haymon, Fine-scale petrological variations along the East Pacific Rise crest, 9°17'N to 9°54'N: Results from Alvin diving and rock coring during the AdVenture Program [abs.], EOS Trans. AGU, 72 (1991) 491.

Perfit, M. R., D. J. Fornari, M. C. Smith, J. F. Bender, C. H. Langmuir, R. M. Haymon, Small-scale spatial and temporal variations in mid-ocean ridge crest magmatic processes, Geology, 22 (1994) 375-379.

Perfit, M. R., D. J. Fornari, W. I. Ridley, P. D., Kirk, J. Casey, K. A. Kastens, J. R. Reynold, M. Edward, D. Desonie, R. Shuster, S. Paradis, Recent volcanism in the Siqueiros transform fault: picritic basalts and implications for MORB magma genesis, Earth Planet. Sci. Lett., 141 (1996) 91-108.

Perfit, M. R. and W. W. Chadwick, Jr., Magmatism at mid-ocean ridges: Constraints from volcanological and geochemical investigations, Geophysical Monograph, 106 (1998) 59-115.

Pockalny, R. A., P. J. Fox, D. J. Fornari, K. C. Macdonald, M. R. Perfit, Tectonic reconstruction of the Clipperton and Siqueiros Facture Zones: Evidence and consequences of plate motion change for the last 3 Myr, J. Geophys. Res., 102 (1997) 3167-3181.

Ragland, P. C., Basic analytical petrology, Oxford Univ. Press, New York, NY, 1989.

Reynolds, J. R. and C. H. Langmuir, Identification and implications of off-axis lava flows around the East Pacific Rise, Geochemistry Geophysics Geosystems$^3$, 1 (2000) paper 1999GC000033.

Reynolds, J.R., C. H. Langmuir, J. F. Bender, K. A. Kastens, W. B. F. Ryan, Spatial and temporal variability in the geochemistry of basalts from the East Pacific Rise, Nature, 359 (1992).

Reynolds, R.C., Jr., Matrix corrections in trace element analysis by X-ray fluorescence; estimation of the mass absorption coefficient by Compton scattering, American Mineralogist, 48 (1963) 1133-1143.

Ridley, W. I., M. R. Perfit, D. J. Fornari, J. R. Cann, D. K. Smith, Lava-seawater vapor interaction at the mid-ocean ridge crest: an important volcanic process to explain lava transport and flow morphology on the deep sea floor, EOS Trans. AGU, 84 (46) (2002) Fall Meet. Suppl., Abstract.

Ridley, W. I., M. R. Perfit, M. C. Smith and D. J. Fornari, Petrology of a Cumulate Xenolith From The East Pacific Rise at 9$^o$ 50'N: A Snapshot of Axial Magma Chamber Processes, in prep.

Ringwood, A. E., Petrogenesis of Apollo 11 basalts and implications for lunar origin, J. of Geophys. Res., 75(32) (1970) 6453-6479.

Rollinson, J. R. Using geochemical data; evaluation, presentation interpretation, New York, John Wiley & Sons, 1993.

Rosendahl, B. R., R. W. Raitt, L. M. Dorman. L. D. Bibee, D. M. Hussong, and G. H. Sutton, Evolution of oceanic crust: 1. A geophysical model of the East Pacific Rise crest derived from seismic refraction data, J. Geophys. Res., 81 (1976) 5305.

Schouten, H., M. A. Tivey, D. J. Fornari, and J. R. Cochran, Central anomaly magnetization high: Constraints on the volcanic construction and architecture of seismic layer 2A at a fast-spreading mid-ocean ridge, the EPR at 9°30-50'N, Earth Planet. Sci. Lett., 169 (1999) 37-50.

Sigurdsson, H. and J. G. Schilling, Spinels in Mid-Atlantic Ridge basalts: chemistry and occurrence, Earth Planet. Sci. Lett., 29 (1976) 7-20.

Sims, K. W. W., D. J. DePaolo, M. T. Murrell, W. S. Baldridge, S. Goldstein, D. Clague, M. Jull, Porosity of the melting zone and variations in the solid mantle upwelling rate beneath Hawaii; ingerences from 238U-230Th-226Ra and 235U-231Pa disequilibria, Geochim. Cosmochim. Acta, 63 (1999) 4,119-4,138.

Sims, K. W. W., S. J. Goldstein, J. Blichert-Toft, M. R. Perfit, P. Kelemen, D. J. Fornari, P. Michael, M. T. Murrell, S. R. Hart, D. J. DePaolo, G. Layne, L. Ball, M. Jull, J. Bender, Chemical and isotopic constraints on the generation and transport of magma beneath the East Pacific Rise, Geochim. Cosmochim. Acta, 66(19) (2002) 3,481-3,504.

Sinton, J. M., D. S. Wilson, D. M. Christie, R. N. Hey, and J. R. Delaney, Petrologic consequences of rift propagation on oceanic spreading ridges, Earth Planet. Sci. Lett., 62 (1983) 193-207.

Sinton, J. M., and R. S. Detrick, Mid-ocean ridge magma chambers, J. Geophys. Res., 97 (1992) 197-216.

Skulski, T., W. G. Minarik, E. B. Watson, High-pressure experimental trace-element partitioning between clinopyroxene and basaltic melts, Chemical Geology, 117 (1994) 127-147.

Smith, M., Petrologic and geochemical investigations of basalts from the southern Juan de Fuca ridge, Master's thesis (1993) Universtiy of Florida.

Smith, M. C., M. R. Perfit, D. J. Fornari, W. I., Ridley, M. H. Edward, G. J. Kurras, K. L. Von Damm, Magmatic processes and segmentation at a fast spreading mid-ocean ridge: Detailed investigation of an axial discontinuity on the East Pacific Rise crest at 9°37' N, Geochemistry Geophysics Geosystems$^3$, 2 (2001) paper 2000GC000134.

Smith, M. C., M. R. Perfit, and I. R. Jonasson, Petrology and geochemistry of basalts from the southern Juan de Fuca Ridge: Controls on the spatial and temporal evolution of mid-ocean ridge basalt, J. Geophys. Res., 99 (1994) 4787-4812.

Solomon, S. C. and D. R. Toomey, The structures of mid-ocean ridges, Earth Planet. Sci. Lett., 20 (1992) 329-364.

Spiegelman, M. and P. B. Kelemen, Extreme chemical variability as a consequence of channelized melt transport, Geochemistry Geophysics Geosystems$^3$, 4 (2003) paper 2002GC000336.

Spiegelman, M. and P. B. Kelemen, Highway to Hell: Geochemical consequences of channelized melt transport, Geochim. Cosmochim. Acta, 66(15A) (2002) suppl. 1, A731.

Stroup, J. G. and P. J. Fox, Geologic investigations in the Cayman Trough: Evidence for thin crust along the mid-Cayman rise, J. Geol., 89 (1981) 395-420.

Sun, C.-o, R. J. Williams, S-s. Sun, Distribution coefficients of Eu and Sr for plagioclase-liquid and clinopyroxene-liquid equilibria in oceanic ridge basalt; an experimental study, Geochim. Cosmochim. Acta, 38(9) (1974) 1415-1433.

Sun S.-s., W. F. McDonough, Chemical and isotopic systematics of oceanic basalts: implications for mantle composition and process, From Saunders, A.D. and M.J. Norry, Magmatism in the Ocean basins, Geological Society Special Publication, 42 (1989) 313-345.

Takahashi, E., Partitioning of $Ni^{2+}$, $Co^{2+}$, $Fe^{2+}$, $Mn^{2+}$ and $Mg^{2+}$ between olivine and silicate melts, compositional dependence of partition coefficient, Geochim. Cosmochim. Acta, 42(12) (1978) 1829-1844.

Tepley, F. J. III, C. C. Lundstrom, K. W. W. Sims, R. Hekinian, U-series disequilibria in MORB form the Garrett Transform and implications for mantle melting, Earth Planet. Sci. Lett., 223 (2004) 79-97.

Thompson, G., W. B. Byran, R. Ballard, K. Hamuro, W. G. Melson, Axial processes along a segment of the East Pacific Rise, 10°-12° N, Nature, 318 (1985) 429-433.

Tierney, S. E., Distribution and composition of lavas from the southern cleft segment of the Juan de Fuca Ridge; Tectonomagmatic evolution of a ridge-transform intersection, Master's thesis (2003) University of Florida.

Tilley, C. E., Some aspects of magma evolution, Q. J. Geol. Soc. London, 106 (1950) 37-61.

Ulmer, P., The dependence of the $Fe^{2+}$-Mg cation-partitioning between olivine and basaltic liquid on pressure, temperature and compositions; an experimental study to 30 kbars, Contrib. Mineral. Petrol., 101 (1989) 261-273.

Villemant, B., H. Jaffrezic, J. L. Joron, M. Treuil, Distribution coefficients of major and trace elements; fractional crystallization in the alkali basalt series of Chaine des Puys (Massif Central, France), Geochim. Cosmochim. Acta, 45 (1981) 1,997-2,016.

Wendlandt, R. F. and W. I. Ridley, Melting phase relations of a glassy high-MgO basalt from the Siqueiros transform domain, East Pacific Rise (EPR), EOS Trans. AGU, 75 (1994) 720.

Wendt, J. I., M. Regelous, Y. Niu, R. Hekinian, K. D. Collerson, Geochemistry of lavas from the Garrett Transform Fault: insights into mantle heterogeneity beneath the eastern Pacific, Earth Planet. Sci. Lett., 173 (1999) 271-284.

White, S. M., R. M. Haymon, D. J. Fornari, M. R. Perfit, K. C. Macdonald, Correlation between volcanic and tectonic segmentation of fast-spreading ridges: Evidence from volcanic structures and lava flow morphology on the East Pacific Rise at 9°-10°N, J. Geophys. Res., 107 (2002) 7-1-7-20.

# BIIOGRAPHICAL SKETCH

Michelle R. Hays earned her Bachelor of Science degree in environmental studies-earth science from the University of Nebraska at Omaha in 2001. She began graduate studies in geology at the University of Florida in the fall of 2001.